AD-A173 295   THEORETICAL AND EXPERIMENTAL STUDIES IN REACTIVE   1/5
              SCATTERING(U) CALIFORNIA INST OF TECH PASADENA DIV OF
   CHEMISTRY AND CHEMICA..   A KUPPERMANN 11 AUG 86
UNCLASSIFIED AFOSR-TR-86-0878 AFOSR-82-0341   F/G 7/4   NL

				1.0		4.5	2.8	2.5
						5.0		
						5.6	3.2	2.2
						6.3		
							3.6	
				1.1			4.0	2.0
								1.8
	1.25		1.4					1.6
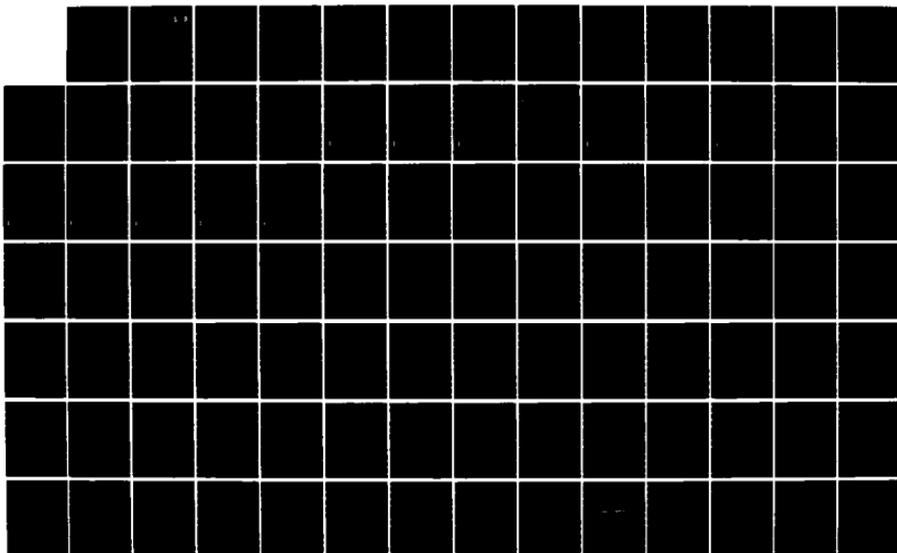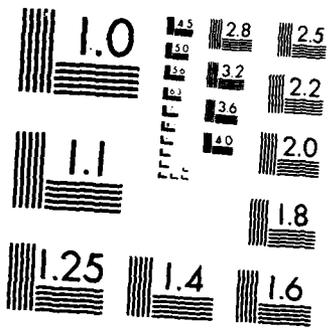
MICROCOPY RESOLUTION TEST CHART
NATIONAL BUREAU OF STANDARDS 1963-A

AFOSR-TR. 86-0870 AUG 1 1 1986

AIR FORCE OFFICE OF SCIENTIFIC RESEARCH
FINAL TECHNICAL REPORT

DTIC
SELECTE**D**
OCT 1 7 1986
D

AD-A173 295

Institution: Division of Chemistry and Chemical Engineering
California Institute of Technology
Pasadena, CA 91125

Title of Project: Theoretical and Experimental Studies in
Reactive Scattering

Project grant number: AFOSR-82-0341

Period: 1 October 82 through 30 September 85

Principal Investigator: *Aron Kuppermann*
Aron Kuppermann

Approved for public release;
distribution unlimited.

DTIC FILE COPY

86 10 8 100

REPORT DOCUMENTATION PAGE

1a. REPORT SECURITY CLASSIFICATION	1b. RESTRICTIVE MARKINGS
Unclassified	

2a. SECURITY CLASSIFICATION AUTHORITY	3. DISTRIBUTION/AVAILABILITY OF REPORT
	Approved for public release;
2b. DECLASSIFICATION/DOWNGRADING SCHEDULE	Distribution unlimited

4. PERFORMING ORGANIZATION REPORT NUMBER(S)	5. MONITORING ORGANIZATION REPORT NUMBER(S)
	AFOSR·TR· 86-0870

6a. NAME OF PERFORMING ORGANIZATION	6b. OFFICE SYMBOL (If applicable)	7a. NAME OF MONITORING ORGANIZATION
California Institute of Technology	NC	AFOSR

6c. ADDRESS (City, State and ZIP Code)	7b. ADDRESS (City, State and ZIP Code)
Division of Chemistry and Chem. Engineering Pasadena, CA 91125	Bldg. 410 Bolling AFB, DC 20332

8a. NAME OF FUNDING/SPONSORING ORGANIZATION	8b. OFFICE SYMBOL (If applicable)	9. PROCUREMENT INSTRUMENT IDENTIFICATION NUMBER
AFOSR	NC	AFOSR-82-0341

8c. ADDRESS (City, State and ZIP Code)	10. SOURCE OF FUNDING NOS.			
	PROGRAM ELEMENT NO.	PROJECT NO.	TASK NO.	WORK UNIT NO.
Bldg. 410 Bolling AFB, DC 20332	61102F	2303	B1	

11. TITLE (Include Security Classification) Theoretical and Experimental Studies in Reactive Scattering

12. PERSONAL AUTHOR(S)
Aron Kupperman

13a. TYPE OF REPORT	13b. TIME COVERED	14. DATE OF REPORT (Yr., Mo., Day)	15. PAGE COUNT
Final	FROM 821001 TO 850930	860811	500

16. SUPPLEMENTARY NOTATION

17. COSATI CODES			18. SUBJECT TERMS (Continue on reverse if necessary and identify by block number)
FIELD	GROUP	SUB. GR.	

19. ABSTRACT (Continue on reverse if necessary and identify by block number)

20. DISTRIBUTION/AVAILABILITY OF ABSTRACT	21. ABSTRACT SECURITY CLASSIFICATION
UNCLASSIFIED/UNLIMITED ☐ SAME AS RPT. ☐ DTIC USERS ☐	

22a. NAME OF RESPONSIBLE INDIVIDUAL	22b. TELEPHONE NUMBER (Include Area Code)	22c. OFFICE SYMBOL
Dr. Wodarczyk		NC

DD FORM 1473, 83 APR EDITION OF 1 JAN 73 IS OBSOLETE.

TABLE OF CONTENTS

QUALITY INSPECTED 1

Accesion For		
NTIS CRA&I		N
DTIC TAB		☐
Unannounced		☐
Justification		
By		
Distribution /		
Availability Codes		
Dist	Avail and / or Special	
A-1		

1. PROJECT ABSTRACT

In this project, we performed accurate calculations of chemical reaction cross sections for collinear and three-dimensional systems of importance for the fundamental aspects of chemical dynamics and for advanced technologies of interest to the United States Air Force. We used some of these calculations to test different transition state theories. We also performed experiments involving beams of He atoms, H atoms and metastable H_3 molecules aimed at the determination of potential energy surfaces involving these systems.

2. COLLINEAR REACTION DYNAMICS

Collinear models of chemical reactions contain the essential element of such processes: the making of a new chemical bond and the breaking of an old one. We have performed several accurate quantum mechanical calculations on such model reactions and used some of the results to test approximate theories on the same systems.

a. Hydrogen atom transfer reactions between hydrocarbon radicals. The free radical abstraction of hydrogen atoms from hydrocarbon molecules is an important elementary step in the pyrolysis of hydrocarbons. Their previous investigation by quantum reactive scattering techniques had not been possible because they involve the transfer of a light species, the H atom, between two much heavier species, the radical and the molecule. The hyperspherical coordinate method we have previously developed for investigating reactive scattering processes is ideally suited for these studies. We modelled the $CH_3 + CH_4 \rightarrow CH_4 + CH_3$ exchange process as a collinear reaction and made extensive calculations of the corresponding reaction probabilities. We discovered that tunnelling was an extremely important process in this system. For example, at an energy of 0.3 Kcal/mole below the top of the barrier, the reaction probability from ground vibrational state reagent to ground vibrational state product has the very large value of 0.8. We also compared these results to the ones obtained using the adiabatic model of Babamov and Marcus. We found that approximation to be quite accurate for the ground-to-ground reactive process, and qualitatively correct for the adiabatic

reactions from the first two excited states. These results are described in detail in the preprint number 11 attached at the end of this report.

b. Hydrogen atom transfer between iodine atoms. We investigated the I + HI→IH + I reaction in the very low translational energy range of 2.8 meV to 4.0 meV (much lower than previously) and discovered a narrow transmission resonance in this range. We used the reaction probabilities obtained at these and at higher energies to calculate rate constants, and found that this resonance does not significantly affect those rate constants. In collaboration with Truhlar and Garrett, these rate constants were then used to test the variational transition state theory with large curvature corrections, and we found the latter to work quite well. These results are described in reprint number 1 attached at the end of this report.

c. Energy partitioning of dissociation products in collision induced dissociation. Using our hyperspherical coordinate approach, we performed accurate quantum mechanical calculations of the partitioning of the collision energy among the fragments of a collision induced dissociation process. These results were compared with those of a classical calculation on the same system. Quantum effects of the order of a factor of 2 were found, as well as quantum oscillations akin to those observed in 3D differential reaction cross sections as a function of scattering angle. The results are described in reprint number 3. The classical results are described in reprint number 6.

3. THREE-DIMENSIONAL REACTION DYNAMICS

a. Hyperspherical coordinates. Extensive work was done on implementing our hyperspherical coordinate approach for three-dimensional reactions. In addition to developing the formalism in complete mathematical detail, we tried several numerical approaches for calculating surface functions. The most accurate one is based on a two-dimensional finite element approach, and is described in reprint number 12. In addition, several variational approaches have been investigated and are still under development. This work is continuing, and when it is completed, a detailed paper describing the results will be published.

b. A state-to-state transition state theory. In collaboration with R. D. Levine, we developed a simple state-to-state transition state theory based on a simple assumption concerning partitioning of the reactive products among different accessible states. This assumption was tested against our accurate 3D quantum calculations on the $H + H_2$ reaction, and was found to be well satisfied. The results obtained are described in detail in reprint number 5.

4. ANISOTROPIC POTENTIALS FOR He + CO_2, OCS, AND CS_2

We performed extensive calculations on the sensitivity of interference oscillations of differential total cross sections to the anisotropy in the atom-molecule potential. We then performed extensive experiments on the He + CO_2, OCS, and CS_2 systems and determined the corresponding anisotropic potential energy functions. The results obtained are described in detail in preprints numbers 9 and 10.

5. PRODUCTION OF A HIGH INTENSITY- HIGH ENERGY BEAM OF H ATOMS AND OF METASTABLE H_3 MOLECULES

We constructed an arc-heated beam of H atoms designed to perform reaction dynamic experiments with this species. The intensity of this beam turned out to be very high, of the order of 10^{22} atoms/sterad/sec and its energy extended as high as 13eV. We also built a Stern-Gerlach inhomogeneous magnetic field velocity selector designed to select a monoenergetic slice of the H atom distribution function, in order to make reaction dynamic studies as a function of translational energy.

In the process of characterizing this beam, we found the presence of a significant intensity of metastable H_3 molecules, having a lifetime in excess of 40 μsec. We proceeded to perform scattering, surface ionization and photoionization experiments with this species, and assigned it to the 2p $^2A'_2$ Rydberg state. The results of these experiments are described in detail in reprint number 2 and preprints numbers 8 and 13.

Also, in the process of characterizing the H + H_3 beam, we detected emission spectra from it which we assigned to a WH species. This is the first spectroscopic observation of such a species and the results obtained are described in preprint number 7.

6. REPRINTS AND PREPRINTS

Enclosed are reprints or preprints of 13 papers published or prepared during the course of this project as follows:

1. Test of Variational Transition State Theory Against Accurate Quantal Results for a Reaction with a Very Large Reaction-Path Curvature and a Low Barrier, D. G. Truhlar, B. C. Garrett, P. G. Hipes and A. Kuppermann, J. Chem. Phys. **81**, 3542 (1984).

2. An Intense Beam of Metastable H_3 Molecules, J. F. Garvey and A. Kuppermann, Chem. Phys. Lett. **107**, 491 (1984).

3. Quantum Mechanical Partitioning of Kinetic Energy in Collision-Induced Dissociation, J. A. Kaye and A. Kuppermann, Chem. Phys. Lett. **115**, 158 (1985).

4. Quantum Mechanical Study of the Reaction Be + FH $(v = 0, 1) \rightarrow$ BeF (v') + H, J. F. Garvey, J. A. Kaye and A. Kuppermann, Chem. Phys. Lett. **118**, 384 (1985).

5. Towards a State-to-State Transition State Theory, A. Kuppermann and R. D. Levine, J. Chem. Phys. **83**, 1671 (1985).

6. Collinear Quasiclassical Trajectory Study of Collision-Induced Dissociation on a Model Potential Energy Surface, J. A. Kaye and A. Kuppermann, J. Chem. Phys. **84**, 1463 (1986).

7. Observation and Analysis of Emission Spectra of Tungsten Hydride, J. F. Garvey and A. Kuppermann. Preprint.

8. Design and Operation of a Stable Intense High Temperature Arc-Discharge Source of Hydrogen Atoms and Metastable Trihydrogen Molecules, J. F. Garvey and A. Kuppermann. Preprint.

9. Sensitivity Analysis of the Differential Scattering Cross-Section to the He + CO_2 Interaction Potential, J. W. Winniczek and A. Kuppermann. Preprint.

10. Anisotropic Intermolecular Potentials for He + CO_2, He + CS_2 and He + OCS from Crossed Beam Scattering Experiments, J. W. Winniczek and A. Kuppermann. Preprint.

11. A Test of the Babamov-Marcus Vibrationally Adiabatic Theory of Hydrogen Atom Transfer Reactions, P. G. Hipes and Aron Kuppermann. Preprint.

12. Three-dimensional Quantum Mechanical Reactive Scattering Using Symmetrized Hyperspherical Coordinates, A. Kuppermann and P. G. Hipes, J. Chem. Phys. 84, 5962 (1986).

13. Total Scattering, Surface Ionization and Photoionization of a Beam of H_3 Metastable Molecules, J. F. Garvey and A. Kuppermann. Preprint.

7. INVITED SEMINARS, CONFERENCES AND LECTURES

During the three year period covered by this report, the principal investigator gave a total of 30 invited seminars, conferences and lectures on topics related to this grant at the following places:

ICPEAC, Oak Ridge, Tennessee, July 1983

Gordon Conference on Few Body Collisions, July 1983

Weizmann Institute, Israel, January 1984

Hebrew University, Israel, February 1984 (2 lectures)

Israel Institute of Technology, March 1984

Shandong University, PRC, April-May 1984 (12 lectures)

Oxford University, June 1984

Cambridge University, July 1984

Kolthoff Lecturer, University of Minnesota, October 1984 (3 lectures)

AFOSR Contractors Meeting, November 1984

University of California at Irvine, February 1985

Sanibel Symposium, Florida, March 1985

NATO Workshop on Chemical Reaction Dynamics, Orsay, France, June 1985 (2 lectures)

AFRPL, September 1985

APPENDICES

Test of variational transition state theory against accurate quantal results for a reaction with very large reaction-path curvature and a low barrier

Donald G. Truhlar
Department of Chemistry, University of Minnesota, Minneapolis, Minnesota 55455

Bruce C. Garrett
Chemical Dynamics Corporation, 1550 West Henderson Road, Columbus, Ohio 43220

Paul G. Hipes and Aron Kuppermann
Arthur Amos Noyes Laboratory of Chemical Physics, California Institute of Technology, Pasadena, California 91125

We present three sets of calculations for the thermal rate constants of the collinear reaction $I + HI \rightarrow IH + I$: accurate quantum mechanics, conventional transition state theory (TST), and variational transition state theory (VTST). This reaction differs from previous test cases in that it has very large reaction-path curvature but hardly any tunneling. TST overestimates the accurate results by factors of 2×10^{10}, 2×10^4, 57, and 19 at 40, 100, 300, and 1000 K, respectively. At these same four temperatures the ratios of the VTST results to the accurate quantal ones are 0.3, 0.8, 1.1, and 1.4, respectively. We conclude that the variational transition states are meaningful, even though they are computed from a reaction-path Hamiltonian with large curvature, which is the most questionable case.

I. INTRODUCTION

Variational transition state theory (VTST), with an approximate treatment of the effects of quantization,[1-4] has now been applied to chemical reactions with a variety of mass combinations and potential energy surfaces. A general conclusion is that the largest deviations of the predicted rate constants from those of conventional transition state theory are associated with symmetric or nearly symmetric systems with a light atom being transferred between two much heavier partners; this was originally concluded on the basis of semiempirical potential energy surfaces,[1-10] and a similar trend has been observed using surfaces based on *ab initio* calculations.[11,12] The predictions of VTST for this kind of system have been checked against experiments for the H/D kinetic isotope effect in $^{37}Cl + H ^{35}Cl \rightarrow H ^{37}Cl + ^{35}Cl$[12] and against accurate quantal reaction probabilities for collinear $Cl + HCl \rightarrow ClH + Cl$.[10] For the latter study accurate quantal scattering calculations and VTST calculations were carried out using the same London–Eyring–Polanyi–Sato (LEPS)-type[13] potential energy surface in order that the comparison of rate constants provides a test of VTST's ability to predict rate constants for a given (realistic) potential energy surface.[10] The test showed that the predictions of VTST, when an appropriate transmission coefficient[12] to account for tunneling is included, are in good agreement with the quantal rate constants. In this article we report a similar comparison of VTST predictions to accurate quantal results, this time for the collinear reaction $I + HI \rightarrow IH + I$. At a given temperature tunneling effects are less important in the present system than in the $Cl + HCl$ system. Thus the present calculation provides a more direct test of the variational choice of the transition state for the over-barrier contribution to the rate constant.

II. CALCULATIONS

A. System

The system is specified by the masses ($m_I = 231\,325m_e$, $m_H = 1837m_e$) and the potential energy surface. The surface is based on the popular extended LEPS formulation[14] with Morse parameters and Sato parameters given in a previous publication,[15] where it is called surface *a*. This surface has a symmetric saddle point at $R_{HI} = 3.366a_0$ with a classical barrier height of 1.353 kcal/mol.

B. Quantal rate constants

Accurate fixed-energy reaction probabilities were calculated by solving the coupled-channel equations in hyperspherical coordinates. The reaction probability as a function of energy has already been reported.[15] To calculate converged thermal rate constants over a wide temperature range, additional fixed-energy reaction probabilities were calculated and the results were thermally averaged.

In the course of these calculations an interesting low-energy resonance was discovered. This resonance has only a very small effect on the thermal rate constants, and it will be discussed in more detail in a subsequent publication.[16]

The accurate quantal rate constants are given in Table I.

C. Generalized transition state theory

The methods used for the generalized transition state theory calculations with classical reaction-coordinate motion are the same as we applied to the $Cl + HCl$ reaction.[12] In particular all vibrational partition functions are based on the Morse I approximation,[1] and the rate constant is calculated by improved canonical variational theory (ICVT).[2]

TABLE I. Accurate quantal rate constants.

$T(K)$	k (cm molecule^{-1} s^{-1})
40	7.03(2)[a]
60	1.23(3)
100	2.12(3)
200	3.89(3)
300	5.26(3)
400	6.31(3)
600	7.69(3)
800	8.55(3)
1000	9.17(3)

[a] Number in parentheses is a power of 10.

Quantal effects on the reaction-coordinate motion are included by the large-curvature, ground-state (LCG)[12] approximation for the transmission coefficient. For comparison we also present results obtained by some alternative procedures. One alternative procedure is to use the WKB approximation instead of the Morse I approximation for the ground-state stretching vibration of the reactant and generalized transition states.[17] This tests the effect of using the true vibrational potential in the generalized-transition-state dividing surface without modifying its shape. In addition we report calculations in which we neglected the transmission coefficient (i.e., set it equal to unity), and in which we calculated it in the small-curvature-tunneling semiclassical adiabatic ground-state (SCTSAG)[18] approximation, by two alternative versions (LCG2[10] and LCG3[19]) of the large-curvature ground-state method, and by the least-action ground-state (LAG)[20] approximation. The transmission coefficients account for quantum mechanical tunneling and nonclassical reflection effects as discussed elsewhere.[12,18–20] Additional calculations were performed using canonical variational theory (CVT[1,2]) and CVT combined with the classical adiabatic ground-state (CAG[2]) transmission coefficient.

The approximate rate constants are compared to the accurate ones in Tables II and III. Both tables include results obtained treating the bound stretching vibrations by the Morse I approximation and also by treating the ground-state stretching vibration by the WKB approximation. Table II shows results obtained by conventional transition state theory with unit transmission coefficient (denoted ‡), by conventional transition state theory with Wigner's lowest-order quantal transmission coefficient[1,8,21] (denoted ‡/W), by CVT and ICVT, and by ICVT combined with four of the

methods to calculate the transmission coefficient. Table III shows additional results obtained with ICVT combined with two of the methods to calculate the transmission coefficient.

III. DISCUSSION

First we compare the ICVT calculations with the various kinds of transmission coefficients. Tables II and III show that all methods for calculating the transmission coefficient of variational transition state theory predict a negligible quantal effect on the reaction coordinate motion, independent of the method used to treat the ground-state stretching vibration. Furthermore, over the whole temperature range considered in the present study, the CVT, CVT/CAG (not shown in tables), and ICVT rate constants agree to better than 1%. Thus, in the interpretive analysis later in this section, we will limit our discussion of the variational transition state theory results to the simplest of these theories, namely CVT with unit transmission coefficient.

Table II shows that improving on the Morse I approximation for the stretching vibration of the generalized transition state does make a quantitative improvement in the accuracy of ICVT at low temperatures where the results are most sensitive to small changes in effective energy barriers. However, in the temperature range of most general interest, 200–1000 K, the improved treatment of the stretching vibration makes a difference of 15% or less and slightly deteriorates the accuracy of ICVT, presumably indicating a small cancellation of errors contributing in part to the accuracy of the CVT calculations with the Morse I approximation. The present comparison of Morse I and WKB approximations is of special interest because large reaction-path curvature can distort the shape of the bound vibrational potentials of generalized transition states and cause the Morse I approximation to be inappropriate. The most important conclusion from the comparison of the Morse I and WKB results in Tables II and III is that even for this extreme mass combination, which contributes very large reaction-path curvature, the differences between the ICVT rate constants calculated with the Morse I and WKB approximations are small compared to typical "chemical accuracy" (say 30%) except at very low temperatures, below 100 K, where all Boltzmann factors become very sensitive to small energy differences. This indicates that the Morse I approximation is not too inaccurate at the variational transition states. For the rest of

TABLE II. Ratios of approximate rate constants to accurate quantal ones.[a]

$T(K)$	‡	‡/W	CVT	ICVT	ICVT/LCG	ICVT/LCG2	ICVT/LCG3	ICVT/LAG
40	1.80×10^{10}	2.86×10^{11}	0.31	0.31(0.63)	0.31	0.32	0.32	0.32
60	7.89×10^{6}	6.01×10^{7}	0.52	0.52(0.83)	0.51	0.52	0.52	0.52
100	1.75×10^{4}	5.92×10^{4}	0.77	0.77(1.02)	0.77	0.77	0.77	0.77
200	2.14×10^{2}	3.42×10^{2}	0.99	0.99(1.14)	0.99	0.99	0.99	0.99
300	5.70×10^{1}	7.21×10^{1}	1.07	1.07(1.16)	1.06	1.07	1.07	1.07
400	3.23×10^{1}	3.71×10^{1}	1.12	1.12(1.19)	1.12	1.12	1.12	1.12
600	2.13×10^{1}	2.27×10^{1}	1.23	1.22(1.27)	1.22	1.22	1.22	1.23
800	1.94×10^{1}	2.01×10^{1}	1.34	1.33(1.38)	1.33	1.33	1.33	1.33
1000	1.93×10^{1}	1.98×10^{1}	1.44	1.42(1.47)	1.42	1.42	1.43	1.42

[a] Morse I approximation for stretches except for numbers in parentheses, which are based on the WKB approximation for ground-state stretches.

TABLE III Ratio of approximate rate constants to accurate quantal ones.

Method $T(K)$	ICVT/SCTSAG		ICVT/LAG	
	300	600	300	600
Morse 1	1.07	1.22	1.07	1.22
WKB	1.16	1.27	1.16	1.27

the discussion we shall limit our attention to the results obtained by the simpler and more widely applied of the two approximations, namely the Morse I approximation.

Comparison of columns 2 and 4 or 5 of Table II shows that there is a very large effect of variationally optimizing the location of the generalized transition state. Conventional transition state theory overestimates the rate constants by very large factors and inclusion of the Wigner transmission coefficient makes the theory even less accurate. Clearly the Wigner transmission coefficient of conventional transition state theory does not provide a meaningful estimate of quantai effects on reaction coordinate motion when conventional transition state theory itself is so inaccurate. This is so because the Wigner transmission coefficient is based on the properties of the saddle point, and, when conventional transition state theory is so inaccurate, saddle point properties do not determine the true dynamical bottleneck. In the conventional theory the transition state is located at the saddle point, whereas in CVT and ICVT it is located to maximize the generalized and the improved generalized free energies of activation, respectively.[2,22] Either of these quantities should be maximized at a location that enhances the validity of the dynamical bottleneck assumption of transition state theory; classically this would correspond to minimizing the number of trajectories that recross the generalized-transition-state theory phase-space dividing surface separating reactants from products.[23–26]

More detailed insight into the origin of the large variational effect for the present reaction is obtained by tabulating some properties of the canonical variational transition states as functions of temperature. This is done in Table IV where these properties are compared to the same quantities evaluated at the saddle point and for reactants. The quantities in Table IV are as follows: s, the value of the reaction coordinate in coordinates[1,25] scaled to a reduced mass of $m_1 m_{HI}/m_{IHI}$; R_{HI} and R_{IH}, the nearest-neighbor distances;

B_F, the curvature[2] of the minimum-energy path in mass-scaled coordinates; V_{MEP}, the potential energy on the minimum-energy path; $\hbar\omega_{str}$, the harmonic frequency (in energy units) of the stretching vibration; and ΔV_a^G, the vibrationally adiabatic ground-state potential curve relative to reactants. The last quantity is defined by

$$\Delta V_a^G(s) = V_a^G(s) - V_a^G(s = -\infty),$$

where

$$V_a^G(s) = V_{MEP}(s) + \epsilon_{str}(n = 0,s)$$

and $\epsilon_{str}(n,s)$ is the quantized energy of the stretching vibration with quantum number n at s obtained by the Morse I approximation. Table IV shows that the variational transition state and its properties are not very sensitive to temperature for this system. This slight dependence on temperature results from the dominance of the ground vibrational state of the stretching vibration. At the saddle point, the reaction-path curvature is very large and this expands the distance between the potential energy contours along the mass-scaled vibrational coordinate, decreasing $\hbar\omega_{str}$ so much that ΔV_a^G is negative. At the variational transition states, V_{MEP} is much lower but $\hbar\omega_{str}$ and $\epsilon_{str}(n = 0,s)$ are much greater, close to their value at reactants, resulting in a small but positive ΔV_a^G. The reaction-path curvature and the deviation of one of the nearest-neighbor distances from its value in the reactants are both very small at the variational transition states; this accounts for the stretching frequency there being close to its reactant value.

The negative value of the ΔV_a^G at the saddle point is responsible for the serious breakdown of conventional transition state theory for this reaction. Because $\Delta V_a^G(s = 0)$ is negative, the conventional transition state theory rate constant actually decreases at low temperature, from 1.26×10^{13} cm molecule^{-1} s^{-1} at 40 K to 1.64×10^5 cm^3 molecule^{-1} s^{-1} at 600 K. At higher temperatures it increases, reaching 2.16×10^5 cm molecule^{-1} s^{-1} at 1000 K. In contrast the CVT rate constant increases monotonically from 2.20×10^2 cm molecule^{-1} s^{-1} at 40 K to 9.43×10^3 cm molecule^{-1} s^{-1} at 600 K to 1.68×10^4 cm molecule^{-1} s^{-1} at 1000 K.

IV. SUMMARY

In previous work we have often found large differences between conventional and variational transition state theory

TABLE IV. Properties of generalized transition states and reactants.

T (K)	s (a_0)	R_{HI} (a_0)	R_{IH} (a_0)	B_F (a_0^{-1})	V_{MEP} (kcal/mol)	$\hbar\omega_{str}$ (cm^{-1})	ΔV_a^G (kcal/mol)
				Conventional transition state			
...	0.000	3.366	3.366	1.06×10^1	1.35	149	-1.764
				Canonical variational transition states			
40	-0.760	4.428	3.047	5.7×10^{-3}	0.513	2135	0.204
200	-0.760	4.428	3.047	5.7×10^{-3}	0.513	2135	0.204
600	-0.772	4.441	3.047	5.7×10^{-3}	0.505	2141	0.204
1000	-0.849	4.521	3.043	5.3×10^{-3}	0.456	2174	0.202
Reactants							
...	$-\infty$	∞	3.024	0.0	0.000	2355	0.000

with quantized generalized transition states and classical re-action-coordinate motion. (We call these differences variational effects.) In the cases where the differences were largest (many orders of magnitude) we also found large quantal effects on reaction-coordinate motion. In the present article we studied a system with large differences between conventional and variational transition state theory but not large quantal effects on reaction-coordinate motion. This study confirms the reality of the large variational effects. Furthermore even when the variational effect is over nine orders of magnitude, variational transition state theory with simple, practical procedures for calculating the quantized energy levels of generalized transition states, gives quantitative estimates of the true quantal rate constants. For 100–1000 K our variational transition state theory rate constants are accurate within a factor of 1.5 or better, although conventional transition state theory is inaccurate by over four orders of magnitude at 100 K and by a factor of 19 at 1000 K.

[1] B. C. Garrett and D. G. Truhlar, J. Phys. Chem. 83, 1079 (1979); 84, 682(E) (1980); 87, 4553(E) (1983).
[2] B. C. Garrett, D. G. Truhlar, R. S. Grev, and A. W. Magnuson, J. Phys. Chem. 84, 1730 (1980); 87, 4554(E) (1983).
[3] D. G. Truhlar and B. C. Garrett, Acc. Chem. Res. 13, 440 (1980).
[4] D. G. Truhlar, A. D. Isaacson, R. T. Skodje, and B. C. Garrett, J. Phys. Chem. 86, 2252 (1982); 87, 4554(E) (1983).
[5] B. C. Garrett and D. G. Truhlar, J. Am. Chem. Soc. 101, 4534 (1979).
[6] B. C. Garrett and D. G. Truhlar, J. Am. Chem. Soc. 101, 5207 (1979).
[7] B. C. Garrett and D. G. Truhlar, J. Am. Chem. Soc. 102, 2559 (1980).
[8] B. C. Garrett, D. G. Truhlar, and A. W. Magnuson, J. Chem. Phys. 74, 1029 (1981).
[9] B. C. Garrett, D. G. Truhlar, and R. S. Grev, in Potential Energy Surfaces and Dynamics Calculations, edited by D. G. Truhlar (Plenum, New York, 1981), p. 587.
[10] D. K. Bondi, J. N. L. Connor, B. C. Garrett, and D. G. Truhlar, J. Chem. Phys. 78, 5981 (1983).
[11] B. C. Garrett, D. G. Truhlar, R. S. Grev, and R. B. Walker, J. Chem. Phys. 73, 235 (1980).
[12] B. C. Garrett, D. G. Truhlar, A. F. Wagner, and T. H. Dunning, Jr., J. Chem. Phys. 78, 4400 (1983).
[13] I. W. M. Smith, Kinetics and Dynamics of Elementary Gas Reactions (Butterworths, London, 1980), p. 43.
[14] P. J. Kuntz, E. M. Nemeth, J. C. Polanyi, S. D. Rosner, and C. E. Young, J. Chem. Phys. 44, 1168 (1966).
[15] J. A. Kaye and A. Kuppermann, Chem. Phys. Lett. 77, 573 (1981).
[16] P. G. Hipes and A. Kupperman (to be published).
[17] B. C. Garrett and D. G. Truhlar, J. Chem. Phys. 81, 309 (1984).
[18] R. T. Skodje, D. G. Truhlar, and B. C. Garrett, J. Chem. Phys. 77, 5955 (1982).
[19] D. G. Truhlar, A. D. Isaacson, and B. C. Garrett, in The Theory of Chemical Reaction Dynamics, edited by M. Baer (Chemical Rubber, Boca Raton, FL, 1984).
[20] B. C. Garrett and D. G. Truhlar, J. Chem. Phys. 79, 4931 (1983).
[21] H. S. Johnston, Gas Phase Reaction Rate Theory (Ronald, New York, 1966), p. 134.
[22] A. Tweedale and K. J. Laidler, J. Chem. Phys. 53, 2045 (1970).
[23] J. C. Keck, Adv. Chem. Phys. 13, 85 (1967).
[24] W. H. Miller, J. Chem. Phys. 61, 1823 (1974).
[25] B. C. Garrett and D. G. Truhlar, J. Phys. Chem. 83, 1052, 3058(E) (1979); 87, 4533(E) (1983).
[26] B. C. Garrett and D. G. Truhlar, J. Phys. Chem. 84, 805 (1980).

AN INTENSE BEAM OF METASTABLE H_3 MOLECULES [*][‡]

James F. GARVEY [+] and Aron KUPPERMANN

*Arthur Amos Noyes Laboratory of Chemical Physics [*], California Institute of Technology,
Pasadena, California 91125, USA*

A method is described for generating a hyperthermal beam of metastable H_3 molecules, intense enough for scattering and absorption spectroscopy experiments. From the flight time of these species between source and detector it is estimated that their lifetime exceeds 40 μs and that they are in the $2p\ ^2A''$ state.

1. Introduction

The existence of H_3 neutral molecules has been reported in the past, both in beams and electric discharges. In one kind of experiment, a high-energy beam of H_3^+ ions is neutralized by charge-exchange with a target gas. This results in a neutral beam from which H_3^+ ions (or their isotopes) are subsequently regenerated by collisions with a second target gas and detected, implying that a neutral specie lived some time between neutralization and reionization [1–3]. In a second type of experiment, the neutral species predissociates into H and H_2 whose translational energy spectrum is then measured [4–6]. Herzberg and co-workers have obtained direct spectroscopic evidence for the existence of a family of Rydberg excited states of H_3 by analyzing the light emitted from a glow discharge in H_2 [7–9]. In addition, Figger et al. [10] have identified the same excited Rydberg states by analyzing the light emitted from H_3 isotopes formed from a corresponding ion beam after neutralization by alkali atoms. Finally, Gellene and Porter [11] have

recently shown that the neutralization of a fast beam of H_3^+ ions by K atoms leads to the formation of metastable H_3 molecules.

In all the experiments described above (excluding Herzberg's which are in the gas phase) a beam of H_3^+ ions (or its isotopes) having energies in the keV to MeV range is neutralized by charge exchange. In the present paper we describe a method for forming a very intense beam of metastable H_3 emanating directly as neutral species from a high-temperature arc-discharge source [12–14], and having translational energies extending from thermal to about 10 eV.

2. Experimental

The beam apparatus is depicted schematically in fig. 1. The arc-discharge source is similar to that described previously.[12–14]. It is placed in a vacuum chamber (VC1), pumped by a 20″ Westinghouse oil diffusion pump, and is connected by a flexible bellows to a test stand consisting of a bell jar (VC2) pumped by a system comprising a 6″ mercury diffusion pump (nominal speed 125 ℓ/s), freon-cooled chevron baffle and liquid nitrogen trap. Differential pumping between these two chambers is provided by a small skimmer (S) with an orifice diameter of about 1 mm with knife-sharp edge. Chamber VC2 contains a beam flag (F), a beam chopper which allows ac detection of the beam (C1), a pair of electric deflector plates which eliminates ions from the beam (D), and an EAI 300 quadru-
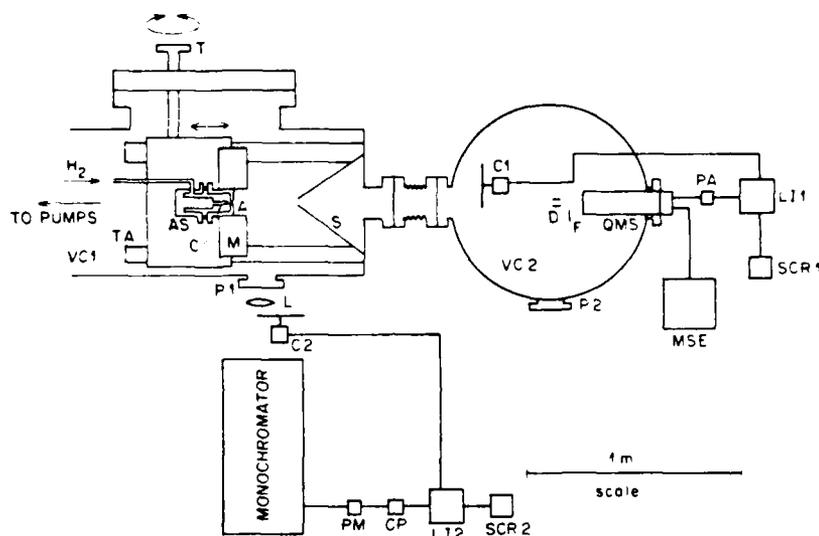
Fig. 1. A schematic view of the top of the machine: VC1, vacuum chamber one; AS, anode assembly; A, anode; C, cathode; M, magnet; S, water-cooled copper skimmer; TA, translation assembly; T, translator; P1, viewport; L, optical lens; C2, 150 Hz chopper; Mono, 0.5 m Jarrell–Ash monochromator; PM, photomultiplier; CP, current preamp; L12, lock-in amplifier; SCR2, strip chart recorder; VC2, vacuum chamber 2; C1, 10 Hz chopper; D, electric field deflectors; F, mechanical flag; QMS, quadrupole mass spectrometer; P2, port; PA, preamp; L11, lock-in amplifier; MSE, mass spectrometer electronics; SCR1, strip chart recorder.

pole mass spectrometer with an electron bombardment ion source (QMS). The arc discharge of the H-atom source can be run continuously with an H_2 stagnation pressure of 50–100 Torr such that the pressure in chamber VC1 is of the order of 10^{-2} Torr and the pressure in chamber VC2 is of the order of 10^{-5} Torr. The source (AS) can be moved with respect to the fixed skimmer from outside of the chamber (T) through the translation stage (TA). It can be operated in two modes. The first is depicted in fig. 1, with the nozzle far away from the skimmer, thereby allowing spectroscopic resolution of the intense red emission of the plasma plume in front of the nozzle. The second moves the nozzle to within 4 cm of the skimmer to maximize the intensity of the beam as measured by the mass spectrometer in chamber VC2.

3. Results and discussion

As shown in fig. 2, during the operation of the discharge we observed a $m/e = 3$ ac ion signal in the mass spectrometer when the beam was run with H_2, and a $m/e = 6$ ion signal when the beam was run with D_2. Fig. 3b shows that by varying the stagnation pressure in our arc-heated source we are able to vary the ratio of the $m/e = 3$ to $m/e = 1$ signal from 0 to about 1. We have determined that these signals are not due to ions which may be present in the beam. The beam passes through an electric field, produced between a pair of deflector plates (D), which has sufficient strength (1 kV/cm) to deflect any charged particles out of the initial beam direction and impeding their entry into the mass spectrometer ionizer. Furthermore, as can be seen in fig. 2, the signal virtually vanishes when the electron beam is turned off.

The possibility that an important source of the $m/e = 3$ signal is H_3^+ formed in the ionizer by some ion–molecule reaction is precluded by observing that under our experimental conditions, the expected signal from that source is less than 10^{-3} of the observed $m/e = 3$ signal. In addition, contribution of the ion source processes $e + H \rightarrow H^* + e^-$; $H^* + H_2 \rightarrow H_3^+ + e^-$, to that signal, a possibility which was considered because of the high H atom intensity component of the neutral beam, was also estimated to be negligible under those
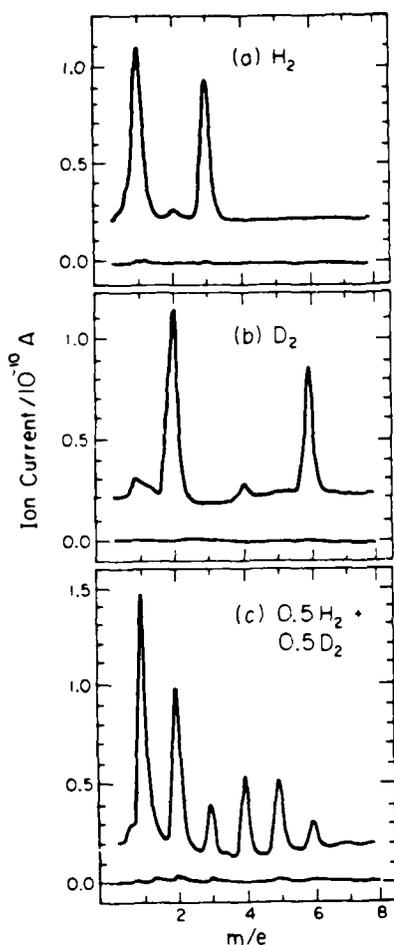
Fig. 2. ac ion current as a function of m/e. In each panel the lower curve is the ac background obtained with the electron beam turned off, and the upper curve is the ac ion current signal shifted upwards by 0.2×10^{-10} A for convenience of display. Electron impact current: 100 μA. Electron accelerating voltage. 60 V. Ion source pressure: 2.1×10^{-5} Torr measured by an uncalibrated ion gauge. (a) H_2 in the molecular beam source; (b) D_3 in that source; (c) an equivalent mixture of H_2 and D_2 in that source. For all the panels, the stagnation pressure in the molecular beam source was 60 Torr. (Nozzle conditions changed slightly.)

Fig. 3. (a) Emission intensity of the H_3 7120 band as viewed through port PI as a function of pressure. (b) Average d ion current as a function of pressure for each of the three masses. Mass spectrometer electron impact current is 100 μA and electron accelerating voltage is 60 V. Error bars represent 90% confidence limit.

conditions. The only possibility remaining is that the observed signal is due to neutral H_3 molecules in the beam. A crude energy analysis of this metastable specie utilizing ion-retarding elements in the optics of the mass spectrometer indicates that a major fraction

of the H_3 has laboratory translational energies in the range of 0–10 eV. From these measurements we can estimate flight times and obtain a lower bound for the lifetime of the observed H_3 species on the order of 40 –100 μs. A calibration of the detector indicates an H_3 intensity on the order of $10^{20} - 10^{21}$ molecules sterad s.

Direct spectroscopic observation of H_3 and its isotopes has come from Herzberg and co-workers [7 –9] who have investigated the light emitted from the cathode regions of a hollow cathode discharge containing H_2 or D_2. The emission bands observed at 5600, 6025 and 7100 Å were assigned to transition between Rydberg states of H_3. All states which were observed were spin doublets with A_1', A_2'', E', or E'' symmetries, the Rydberg electron being in a 2s, 2p, 3s, 3p or 3d type state. The observed 5600 and 7100 Å bands appear broad, apparently due to the fact that they end in the $2s\ ^2A_1'$ state. On the basis of electronic consider-

493

ations this lowest excited state of H_3 is forbidden to predissociate to the $2p^2E'$ repulsive ground state. However, coupling with a vibration of symmetry e' transforms a'_1 to E', making the vibronic predissociation allowed, resulting in the observed line breadth. The 6025 Å band, in contrast, is sharper by two orders of magnitude. The end state of this band is $2p^2A''_2$, the second lowest excited state of H_3. For this state there can be no induced vibrational predissociation since there are no vibrations which can transform an A''_2 state to an E' state.

It also appears that on the basis of accurate ab initio calculations by King and Morokuma [15], which predicts well the observed band positions, the $2p^2A''_2 \rightarrow 2s^2A'_2$ transition has a lifetime on the order of $50\,\mu s$. Thus, this state should indeed be long-lived and appears to be the most likely candidate for the metastable H_3 observed in our beam. We may rule out any higher metastable Rydberg states based on a hydrogenic model for the H_3 state [15,16]. States with principal quantum number $n \geqslant 20$ would be field-ionized by the deflector plates and swept out, while states with $n \leqslant 20$ would have a mean lifetime $< 1\,\mu s$ and never be observed.

As additional confirmation of the presence of H_3 in our beam we observed emission spectra of the plasma plume which appears directly in front of the nozzle of the beam source. These spectra were obtained through a quartz port using a 0.5 m Jarrell–Ash monochromator pointed at the plasma plume from a direction perpendicular to it. As seen in fig. 4, the broad features of our 7100 Å band compares well with Herzberg's spectra. In addition, we observe a sharp reproducible structure which has not yet been assigned.

Fig. 3a shows that the intensity of the 7100 Å band decreases with increasing stagnation pressure, as does the intensity of the detected $m/e = 3$ ion signal (fig. 3b). This indicates a lower electronic temperature at higher pressures and a correlation between the formulation of high Rydberg states of H_3 (as detected by the light emission) with the appearance of the lower metastable $^2A''_2$ state (as detected by the mass spectrometer). We also report the observation of a new broad, featureless band at 7480 Å. On the basis of King and Morokuma's calculation [15] we tentatively assigned this as due to the $2s^2A'_1 \rightarrow 2p^2E'$ transition. This assignment is consistent with the unusually large width (50 Å) of the band due to the repulsive character of
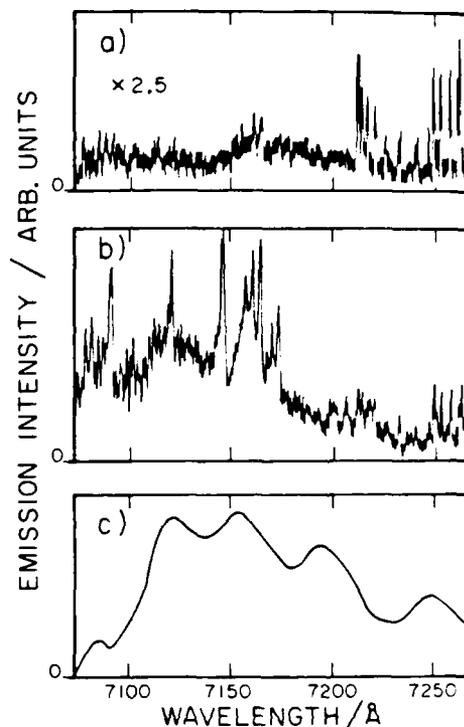

Fig. 4. Emission spectrum viewed through port P1; (a) stagnation pressure = 100 Torr, (b) stagnation pressure = 60 Torr, (c) photometer tracing of 7100 Å band of H_3 observed by Herzberg with sharp H_2 structure removed [8].

the $^2E'$ ground state. If the assignment is correct, then the width of this band is related to the shape of the $^2E'$ potential energy surface in the Franck–Condon region. The intensity of this band increases with increasing stagnation pressure, as opposed to the 7100 Å band, which is also consistent with a lower electronic temperature at higher stagnation pressures.

As expected, this beam is also an intense source of hyperthermal H atoms (see fig. 3b), having a measured intensity in the range of 10^{22} atoms/sterad s and an estimated (as measured by the ion-retardation method mentioned above) energy spread also of about 0–10 eV. It is thus a potentially useful source for scattering experiments of either H or H_3. A similar source for D atom reactive scattering has recently been used by Götting et al. [18].

494

References

[1] P.M. Devienne and J.C. Roustan. Compt. Rend. Acad. Sci. 263B (1966) 1389, 267B (1968) 1279; 268B (1969) 1303.

[2] T. Nagasaki, H. Doi, K. Wada, K. Higashi and F. Fukazawa, Phys. Letters 38A (1972) 381.

[3] N.B. Castro de Faria, M.H. Gaillard, J.C. Poizat and J. Remillieux, Ann. Isr. Phys. Soc. 4 (1981) 134.

[4] M. Vogler and B. Meierjohann, J. Chem. Phys. 69 (1978) 2450.

[5] M. Vogler, Phys. Rev. A19 (1979) 1.

[6] C. Cisneros, I. Alverex, R. Garcia, C.F. Barnett, J.A. Ray and A. Russek, Phys. Rev. A19 (1979) 631.

[7] G. Herzberg, J. Chem. Phys. 70 (1979) 4806; K. Dabrowski and G. Herzberg, Can. J. Phys. 58 (1980) 1238.

[8] G. Herzberg and J.K.G. Watson, Can. J. Phys. 58 (1980) 1250.

[9] G. Herzberg, H. Lew, J.J. Sloan and J K G Watson, Can J. Phys. 59 (1981) 428; G. Herzberg, J.T. Hougen and J.K.G. Watson, Can J Phys 60 (1982) 1261.

[10] H. Figger, M.N. Dixit, R. Maier, W. Schrepp and H Walther, Phys. Rev. Letters 52 (1984) 906.

[11] G.I. Gellene and R.F. Porter, J. Chem. Phys 79 (1983) 5975.

[12] H.L. Knuth, Appl. Mech. Rev. 17 (1964) 751.

[13] W.S. Young, W.E. Rodgers and E.L. Knuth, Rev. Sci Instrum. 40 (1969) 1346.

[14] K.R. Way. S.-C. Yan and W.C. Stwalley, Rev. Sci Instrum 9 (1976) 1049.

[15] H.R. King and K. Morokuma, J. Chem. Phys. 71 (1979) 3213.

[16] R.F. Stebbings, C.J. Latimer, W.P. West, F.B. Dunning and T.B. Cook, Phys. Rev. A12 (1975) 1453.

[17] F.B. Dunning and R.F. Stebbings, Comments At. Mol. Phys. 10 (1980) 9.

[18] R. Gotting, H.B. Mayne and J.P. Toennies, J. Chem. Phys. 80 (1984) 2230.

QUANTUM MECHANICAL PARTITIONING OF KINETIC ENERGY IN COLLISION INDUCED DISSOCIATION [*]

Jack A. KAYE [1,2] and Aron KUPPERMANN

*Arthur Amos Noyes Laboratory of Chemical Physics [3], California Institute of Technology,
Pasadena, CA 91125, USA*

Kinetic energy distributions of atomic products of the collision-induced dissociation $A + BC \rightarrow A + B + C$ on a model triatomic reactive collinear system have been obtained for the first time by an accurate quantum mechanical method and compared with the results of quasi-classical trajectory calculations.

1. Introduction

While there have been many experimental [1] and theoretical [2] studies of the partitioning of energy among the various possible degrees of freedom (electronic, vibrational, rotational, and translational) in simple abstraction or exchange chemical reactions, there is little information on the partitioning of energy in the products of collision-induced dissociation (CID) processes [3]. For electronically adiabatic atom—diatomic molecule processes, which may be represented as

$$A + BC \rightarrow A + B + C. \tag{1}$$

the only degrees of freedom in the product are translational. This information can in principle be obtained from accurate calculations of the collision dynamics for such processes. Its determination from quasi-classical trajectory (QCT) calculations is straightforward, involving integration and analysis of dissociative trajectories, while that from quantum mechanical (QM)

calculations is more complicated. The latter may be obtained from scattering calculations performed using hyperspherical coordinates and local surface functions [4–10].

In this work we present results for the partitioning probabilities, which describe the distribution of the available energy among the three atoms in dissociative collisions for a model reactive collinear atom—diatom molecule collision. To our knowledge, these are the first such results, as previous calculations on these systems [5,8,11] considered only total dissociation probabilities. We review the QM and QCT methods by which these quantities are obtained, compare the results, and discuss their differences. We also summarize the implications of these results for calculations on more realistic systems.

2. Theory and numerical methods

2.1. Quantum mechanical method

The calculation of total dissociation probabilities using hyperspherical coordinates and local surface functions has been outlined by us [5] and by Manz and Römelt [8] previously. The basic formalism for the calculations of the partitioning probabilities has also been given by us previously [5–7]. An alternate formulation (involving a multiple collision expansion)

has also been presented [12], but has not been applied to potentially reactive systems.

We use the notation of ref. [5], in which ABC is the triatomic system and λn_λ represents a bound state of the diatomic reagent. For $\lambda = \alpha$ or γ that reagent is BC or AB, respectively, and n_λ is the corresponding vibrational quantum number. The distances r_λ and R_λ are respectively the Delves mass-scaled [13] diatom internuclear distance and atom to diatom center of mass distance, and $k_{\lambda n_\lambda}$ the mass-scaled relative motion atom–diatom wavenumber. The symbol $\lambda' n'_\lambda$ denotes the product bound states, ρ is the hyperradius $(R_\lambda^2 + r_\lambda^2)^{1/2}$ and α_λ the hyperspherical angle $\tan^{-1}(r_\lambda/R_\lambda)$.

The scattering wavefunction $\psi^{\lambda n_\lambda}$ for a collision involving a bound state λn_λ of the diatomic reagent has an asymptotic behavior which can be written as

$$\lim_{\rho \to \infty} \psi^{\lambda n_\lambda} = \psi_{inc}^{\lambda n_\lambda} + \psi_{bound}^{\lambda n_\lambda} + \psi_d^{\lambda n_\lambda}, \tag{2}$$

where the three terms in the right-hand side represent the incident, final non-dissociated and final dissociated states of the system and are given by [5]

$$\psi_{inc}^{\lambda n_\lambda} = \exp(-ik_{\lambda n_\lambda} R_\lambda)\varphi_{\lambda n_\lambda}(r_\lambda) \tag{3a}$$

$$\psi_{bound}^{\lambda n_\lambda} = \sum_{\lambda' n'_\lambda} (v_{\lambda n_\lambda}/v_{\lambda' n'_\lambda})^{1/2} S_{\lambda' n'_\lambda}^{\lambda n_\lambda}$$

$$\times \exp(ik_{\lambda' n'_\lambda} R_{\lambda'})\varphi_{\lambda' n'_\lambda}(r_{\lambda'}), \tag{3b}$$

$$\psi_d^{\lambda n_\lambda} = \rho^{-1/2} \sum_{n=1}^{N_d} (v_{\lambda n_\lambda}/v_n)^{1/2} S_n^{\lambda n_\lambda}$$

$$\times \exp(ik_n \rho)\varphi_n(\alpha_\lambda; \rho). \tag{3c}$$

In eq. (3c), the subscript n denotes discretized continuum channels, k_n the corresponding ρ-dependent wave numbers, $S_n^{\lambda n_\lambda}$ the bound-to-continuum elements of the scattering matrix and $\varphi_n(\alpha_\lambda; \rho)$ the ρ-dependent nth continuum basis functions. The several v in eqs. (3) are the velocities associated with the corresponding k and $\varphi_{\lambda' n'_\lambda}(r_{\lambda'})$ is the bound state function for the $\lambda' n'_\lambda$ diatom. As $\rho \to \infty$, the eigenvalues of all continuum states tend to zero and all k_n tend to the common value $k = \hbar^{-1}(2\mu E)^{1/2}$, where E is the total energy of the system with respect to three infinitely separated atoms at rest. In principle the sum in eq. (3c) has an infinite number of terms, but in practice it is truncated at a finite N_d, large enough for the probabil-

ities to have converged to a desired accuracy. Eq. (3c) differs from eq. (3) of ref. [5] at finite ρ, but approaches it as $\rho \to \infty$. In the numerical calculations presented here, eq. (3c) has been used.

Let $dP_d^{\lambda n_\lambda}(\alpha_\lambda)$ be the probability for dissociation from the state λn_λ of the diatomic reagent into the angular range α_λ to $\alpha_\lambda + d\alpha_\lambda$ of the system. It is given asymptotically, as $\rho \to \infty$, by

$$dP_d^{\lambda n_\lambda}(\alpha_\lambda) = (j_d^{\lambda n_\lambda}/J_{inc}^{\lambda n_\lambda})\rho \, d\alpha_\lambda, \tag{4}$$

where $j_d^{\lambda n_\lambda}$ is the two-mathematical-dimensional current density associated with eq. (3c) and $J_{inc}^{\lambda n_\lambda}$ is the initial total current flux associated with eq. (3a). Use of these equations furnishes

$$dP_d^{\lambda n_\lambda}(\alpha_\lambda) = \sum_{n,n'=1}^{N_d} \varphi_n(\alpha_\lambda; \rho)\varphi_{n'}(\alpha_\lambda; \rho)[k^{\lambda n_\lambda}/(k_n k_{n'})^{1/2}]$$

$$\times [A_{nn'}(\rho)(\mathrm{Re}\, S_n^{\lambda n_\lambda}\, \mathrm{Re}\, S_n^{\lambda n_\lambda} + \mathrm{Im}\, S_n^{\lambda n_\lambda}\, \mathrm{Im}\, S_n^{\lambda n_\lambda})$$

$$+ B_{nn'}(\rho)(\mathrm{Re}\, S_n^{\lambda n_\lambda}\, \mathrm{Im}\, S_n^{\lambda n_\lambda} - \mathrm{Re}\, S_n^{\lambda}\,^\wedge \mathrm{Im}\, S_n^{\lambda n_\lambda})]\, d\alpha_\lambda. \tag{5}$$

where

$$A_{nn'} = -(1/2\rho)\sin[(k_n - k_{n'})\rho]$$

$$+ k_n \cos[(k_n - k_{n'})\rho], \qquad \lim_{\rho \to \infty} A_{nn'} = k. \tag{6a}$$

$$B_{nn'} = -(1/2\rho)\cos[(k_n - k_{n'})\rho]$$

$$+ k_n \sin[(k_n - k_{n'})\rho], \qquad \lim_{\rho \to \infty} B_{nn'} = 0. \tag{6b}$$

It is convenient to set $\lambda = \alpha$ and to transform from the variable α_α to the fraction $f_A = E_A/E$ of the total system energy which is deposited in the final relative motion of A (which was the incident atom) with respect to the center of mass of the dissociated BC molecule. The corresponding differential probability $dP_{f_A}^{\alpha n_\alpha}$ is given by

$$dP_{f_A}^{\alpha n_\alpha} = |d\alpha_\alpha/df_A| [dP_d^{\alpha n_\alpha}(\alpha_\alpha)/d\alpha_\alpha]\, df_A. \tag{7}$$

where α_α and f_A are interrelated by

$$f_A = [(m_\beta + m_\gamma)/(m_\alpha + m_\beta + m_\gamma)]\cos^2\alpha_\alpha. \tag{8}$$

m_α, m_β, and m_γ being the masses of atoms A, B and C, respectively. The integral of $dP_{f_A}^{\alpha n_\alpha}$ over all possible values * of f_A gives the total dissociation probability

---

* In eq. (8) of ref. [5], we mistakenly gave a value of 0 for the lower limit of integration. This is true only in the limit $\alpha_{max} \to \pi/2$, otherwise E_A^{min} and f_A^{min} are greater than zero.

$P_d^{\alpha n_\alpha}$ from state αn_α of the reagents.

The essence of the hyperspherical coordinate approach is to expand the system's wavefunction in terms of the eigenfunctions in $\varphi_n(\alpha_\lambda; \rho)$ of cuts of the potential at constant ρ. Since the collinear motion of the triatomic system is isomorphic with that of a single particle of mass $\mu = [m_A m_B m_C/(m_A + m_B + m_C)]^{1/2}$ moving in the two-dimensional space described by the coordinates ρ, α and subject to the potential $V(\rho, \alpha)$, this expansion is analogous to the partial wave expansion for the motion of a particle moving on a plane and scattered by a non-central potential. The differential partitioning probabilities $dP_d^{\lambda n_\lambda}/d\alpha_\lambda$ are analogous to differential cross sections for the isomorphic particle.

2.2. Quasi-classical method

The details of the calculation of $dP_{f_A}^{\alpha n_\alpha}/df_A$ by the QCT method have been described elsewhere [6,14]; we briefly outline them here. The equation for $(dP_{f_A}^{\alpha n_\alpha}/df_A)_c$, where the subscript c indicates classical mechanics, is

$$dP_{f_A}^{\alpha n_\alpha}/df_A = \frac{1}{2\pi} \sum_i \frac{1}{|(df_A/d\varphi_{\alpha n_\alpha})_i|} , \quad (9)$$

where $\varphi_{\alpha n_\alpha}$ is the initial phase of the vibration of the diatomic molecule (in radians) and the summation is over all of the regions of the initial range of phases which lead to dissociation, and in which f_A varies continuously with $\varphi_{\alpha n_\alpha}$.

2.3. Potential energy surface

The potential energy surface used is of the rotating-Morse—cubic spline type [15], and has been briefly described elsewhere [5,6]. For the mass combination considered ($m_A = m_B = m_C = 1$ in H-atom mass units), asymptotically there are two bound states in each diatom arrangement channel, with energies of 0.0815 and 0.1885 eV with respect to the bottom of the diatomic molecule well. The Morse parameters [16] of the isolated diatomic molecule are $D_e = 0.22$ eV, $\beta = 1.6$ bohr^{-1}, $R_{eq} = 1.40083$ bohr. Equipotential contour lines of this potential energy surface are displayed in fig. 1 of ref. [5]. The number of bound states was chosen purposefully to be low, in order to permit most of the numerical effort to be devoted to the CID part of the problem.

2.4. Numerical methods

In the hyperspherical coordinate calculations, ten even and ten odd basis functions were used, as was done in ref. [5]. The S matrix was approximately unitary, with deviations being on the order of a few percent. Convergence with respect to the number of channels was of the same magnitude. Integration was carried out to 190 bohr and asymptotic analyses were carried out at 110, 130, 150, 170 and 190 bohr. This is substantially further than the maximum value of $\rho = 64$ bohr used previously [5]. At finite ρ the dissociation probabilities $P_d^{\lambda n_\lambda}$ and the partitioning probabilities oscillate slowly with ρ. The results we present are means and standard deviations of the values of the five different projection distances.

The quasi-classical trajectory calculations were carried out using standard methods [17]. Details of the trajectory calculation have been given elsewhere [6,14].

3. Results

We have calculated the total dissociation probabilities P_v^D as a function of energy at a number of energies up to 0.25 eV above dissociation for the reagent molecule initially in vibrational state v. Values of these probabilities, both quantum and quasi-classical, are given for four energies in table 1. All the quantum mechanical results are averages (indicated by angular brackets) over the five asymptotic analyses described above. We focus attention on the lowest and highest of the energies of table 1: 0.04 and 0.25 eV, respectively.

Detailed data on the structure of the reactivity banding of the QCT calculations are given in table 2, in which we examine the number, width, and properties of the separate regions of the initial phase giving rise to dissociative trajectories. From table 2 it is clear

Table 1
Probabilities of dissociation and related quantities

E' (eV)	$\langle P_0^D \rangle_{QM}$	$\langle P_1^D \rangle_{QM}$	$P_0^D{}_{QCT}$	$P_1^D{}_{QCT}$
0.04	0.0041	0.2033	0	0.107
0.08	0.0021	0.1432	0	0.215
0.16	0.0524	0.1360	0.137	0.150
0.25	0.2018	0.4534	0.268	0.390

Table 2
Detailed structure of dissociative quasi-classical trajectory bands

E (eV)	P^D_{0QCT}	n^{D}_0 a)	$\Delta\varphi_{0j}$ b)	n^{min}_{0j} c)	P^D_{1QCT}	n^{0}_1 a)	$\Delta\varphi_{1j}$ b)	n^{min}_{1j} c)
0.04	0.0	–	–	–	0.107	1	0.67	0
0.08	0.0	–	–	–	0.215	2	0.09	0
							1.26	1
0.16	0.137	2	0.77	0	0.150	3	0.20	1
			0.09	0			0.70	0
							0.04	0
0.25	0.277	2	0.15	0	0.39	2	0.05	0
			1.53	0			2.40	0

a) n^{D}_i is the number of separate regions of initial phase giving rise to dissociative trajectories in collisions of A + BC(v).
b) $\Delta\varphi_{ij}$ is the approximate width in radians of the jth separate region of initial phase giving rise to dissociative trajectories in collisions of A + BC(v) ($\Delta\varphi_{vj} = \varphi^{max}_{vj} - \varphi^{min}_{vj}$, where φ^{max}_{vj} and φ^{min}_{vj} are the phase at the high- and low-phase ends of the jth dissociative region).
c) n^{min}_{vj} is the number of minima in the plot of f_A versus φ in the jth dissociation region for collisions of A + BC(v).

that there may be more than one region of initial phase leading to dissociation, and that these regions may have minima in their plots of f_A versus initial phase. As may be seen from eq. (9), minima in these plots give rise to divergences in $dP^{v/0}_{fA}/df_A$.
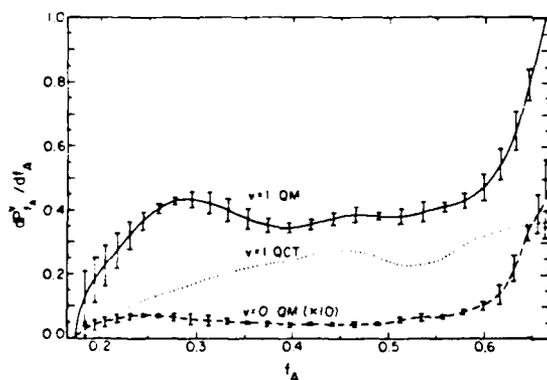

Fig. 1. Plot of the dimensionless partitioning probabilities dP^1_{fA}/df_A as a function of the fraction f_A of the available kinetic energy going into atom A at an energy $E = 0.04$ eV with respect to three infinitely separated atoms at rest. Quantum mechanical (QM) curves are shown for both the $v = 1$ (solid line) and $v = 0$ (dashed line) initial states. The values of dP^0_{fA}/df_A have been multiplied by ten before plotting. All values plotted are the means of the values obtained from the five asymptotic analyses, the error bars indicate one standard deviation about the mean. The plot has been cut off just above $f_A = 0.65$ for reasons described in the text. The quasi-classical (QCT) curve for $(dP^1_{fA}/df_A)_c$ is shown as a dotted line.

Plots of the quantum mechanical partitioning probabilities dP^1_{fA}/df_A as a function of f_A for $E = 0.04$ eV and 0.25 eV are presented in figs. 1 and 2, respectively. Error bars are used to indicate the standard deviations of the calculated partitioning probabilities from their mean. We deleted the portion of the curve nearest to $f_A = 2/3$ as here the calculations are unreliable. This is due to the form of the $d\alpha_\alpha/df_A$ factor in eq. (7):

$$d\alpha_\alpha/df_A = -\tfrac{1}{2}\left[f_A(f^{max}_A - f_A)\right]^{-1/2}. \qquad (10)$$
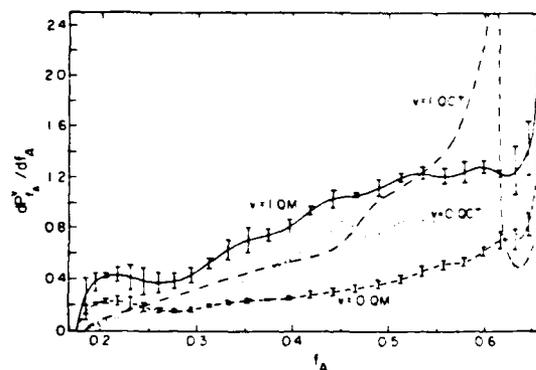

Fig. 2. Plot of the dimensionless partitioning probabilities dP^1_{fA}/df_A as a function of the available kinetic energy going into atom A at an energy $E = 0.25$ eV with respect to three infinitely separated atoms at rest. Quantum mechanical (QM) dP^0_{fA}/df_A dashed line, dP^1_{fA}/df_A solid line. Quasi-classical (QCT) (dP^0_{fA}/df_A), dotted line, (dP^1_{fA}/df_A), dashed-dotted line.

When $f_A = f_A^{max}$ (for this mass combination, when $f_A = 2/3$), this factor diverges and the resulting $dP_{f_A}^i/df_A$ may be large, as may their deviations.

In figs. 1 and 2 we also include plots of the classical partitioning probability $(dP_{f_A}^i/df_A)_c$ for three sets of initial conditions: $E = 0.04$ eV and $v = 0$ and $E = 0.25$ eV and $v = 0$ and $v = 1$. In section 4 we discuss the forms of the quantum mechanical and quasi-classical partitioning probability curves.

4. Discussion and conclusions

The plots of the quantum mechanical partitioning probabilities $dP_{f_A}^1/df_A$ in figs. 1 and 2 all show the same basic structure, with $dP_{f_A}^1/df_A$ increasing fairly smoothly as f_A increases, indicating that the incident atom, in this equi-mass system, tends to retain a large fraction of the available kinetic energy, especially at the higher total energy. There does appear to be some structure in these curves as seen by the existence of shoulders and small maxima. The amplitude of some of the observed oscillations exceeds the magnitude of the error bars and this structure might be real. It is premature to assign too much significance to them, however, as it has been seen in preliminary calculations that termination of integration at a small value of ρ leads to spurious oscillations in the dP_{f_A}/df_A curves, the magnitude of which decreases as ρ increases. If more extensive calculations on this and other systems confirm the presence of such oscillations, the isomorphism with the motion of a particle on a plane, described at the end of section 2.1, would permit a simple interpretation. Indeed, they would be due to the interference between different "partial waves" $\varphi_n(\alpha_\lambda; \rho)$ of eq. (3c) and could be semi-classically interpretable as due to the phase relationships among different classical trajectories leading to the same "scattering angle" α_λ. This perspective would furnish a powerful approach for the analysis of partitioning probabilities.

In general the $dP_{f_A}^0/df_A$ and $dP_{f_A}^1/df_A$ curves have the same overall behavior. The curve for $(dP_{f_A}^1/df_A)_c$ differs appreciably from that for $(dP_{f_A}^0/df_A)_c$ at the same total energy, however. The large spike in $(dP_{f_A}^1/df_A)_c$ in fig. 2 arises because the plot of f_A versus initial phase has a broad inflection region in which $df_A/d\varphi_1 \approx 0$. Thus, by eq. (7), $(dP_{f_A}^1/df_A)_c$ must be-

come large. This is a somewhat unusual occurrence; normally one finds minima in the plot of f_A versus φ_1, giving rise to discontinuities in the plot of (dP_{f_A}/df_A) versus f_A. These discontinuities are purely a consequence of the way in which the classical trajectories behave, in particular the existence of well defined reactivity bands [18]. How the reactivity band structure influences the form of the partitioning probability curves is discussed in detail elsewhere [14].

Because there is not necessarily any close relationship between the reactivity band structure for collisions involving different reactant vibrational states [14], the classical partitioning probabilities for different reactant states at the same total energies can have substantially different forms (i.e. have discontinuities for some reactant states and not for others). The QM partitioning probabilities appear to be fairly similar for the different reactant states, however. Thus, it seems that classical mechanics, while giving a reasonable description for the likelihood of dissociation, gives an incorrect one for the details for the dissociation process. It is quite likely that in higher dimensionality, in which reactivity band structure blurs or disappears altogether [19], more reasonable agreement between the QM and QCT partitioning probabilities may be obtained.

Since dissociation and partitioning probabilities appear to converge reasonably rapidly with basis set size [6] more strongly bound systems should not require an excessive number of continuum states and should thus be amenable to study by the hyperspherical coordinates method. This method may be especially appropriate for studying collision-induced dissociation of van der Waals molecules [20]. Finally, we note that the ability to calculate accurate partitioning probabilities implies the ability to calculate probabilities for three-body recombination reactions, also.

In summary, we have obtained probabilities for the partitioning of kinetic energy among the dissociation products for collinear atom–diatomic molecule collisions by a quantum mechanical method on a model system using hyperspherical coordinates. These coordinates permit an association of these partitioning probabilities with the differential cross section for the scattering of an isomorphic particle confined to move on a plane, and give insight into the scattering process. We have compared these results to those obtained by classical mechanics, and shown that they can behave

quite differently, although there are strong underlying similarities.

References

[1] M.R. Levy, Progr. React. Kinetics 10 (1979) 1;
    R.B. Bernstein, in: Chemical dynamics via molecular beam and laser techniques (Oxford University Press, London, 1982) pp. 55–76.
[2] J.N.L. Connor, Computer Phys. Commun. 17 (1979) 117;
    R.B. Walker and J.C. Light, Ann. Rev. Phys. Chem. 31 (1980) 401.
[3] D.J. Diestler, in: Atom–molecule collision theory, ed. R.B. Bernstein (Plenum Press, New York, 1979) pp. 655–667;
    P.J. Kuntz, in: Atom–molecule collision theory, ed. R.B. Bernstein (Plenum Press, New York, 1979) pp. 669–693.
    D.J. Diestler, in: Numerical integration of differential equations and large linear systems, ed. J. Hinze (Springer, Berlin, 1982) pp. 40–52.
[4] A. Kuppermann, J.A. Kaye and J.P. Dwyer, Chem. Phys. Letters 74 (1980) 257;
    J.A. Kaye and A. Kuppermann, Chem. Phys. Letters 77 (1981) 573; 92 (1982) 574;

[5] J.A. Kaye and A. Kuppermann, Chem. Phys. Letters 78 (1981) 546.
[6] J.A. Kaye, Theoretical Studies of Chemical Reaction Dynamics, Ph.D. Thesis, California Institute of Technology, Pasadena (1982).
[7] J.P. Dwyer, Quantum Mechanical Studies of Molecular Scattering, Ph.D. Thesis, California Institute of Technology, Pasadena (1977).
[8] G. Hauke, J. Manz and J. Römelt, J. Chem. Phys. 73 (1980) 5040;
    J. Römelt, Chem. Phys. Letters 74 (1980) 263; 87 (1982) 259;
    J. Manz and J. Römelt, Chem. Phys. Letters 76 (1980) 337; 77 (1981) 172; 81 (1981) 179.
[9] D.K. Bondi and J.N.L. Connor, Chem. Phys. Letters 92 (1982) 570;
    D.K. Bondi, J.N.L. Connor, B.C. Garrett and D.G. Truhlar, J. Chem. Phys. 78 (1983) 5981.
[10] C.L. Shoemaker, N. AbuSalbi and D.J. Kouri, J. Phys. Chem. 87 (1983) 5389.
[11] K.C. Kulander, J. Chem. Phys. 69 (1978) 5064; Nucl. Phys. A353 (1981) 341c.
[12] L.H. Beard and D.A. Micha, J. Chem. Phys. 73 (1980) 1193.
[13] L.M. Delves, Nucl. Phys. 9 (1959) 391; 20 (1960) 275.
[14] J.A. Kaye and A. Kuppermann, to be published.
[15] J.M. Bowman and A. Kuppermann, Chem. Phys. Letters 34 (1975) 523.
[16] H. Eyring, J. Walter and G. Kimball, Quantum chemistry (Wiley, New York, 1964) pp. 272, 273.
[17] R.N. Porter and L.M. Raff, in: Dynamics of molecular collisions, Part B, ed. W.H. Miller (Plenum Press, New York, 1976) pp. 1–52;
    D.G. Truhlar and J.T. Muckerman, in: Atom–molecule collision theory, ed. R.B. Bernstein (Plenum Press, New York 1979) pp. 505–565.
[18] B.K. Andrews and W.J. Chesnavich, Chem. Phys. Letters 104 (1984) 24.
[19] K.G. Tan, K.G. Laidler and J.C. Wright, J. Chem. Phys. 67 (1977) 5883;
    J.S. Wright, J. Chem. Phys. 69 (1978) 720.
[20] L.M. Raff and D.L. Thompson, J. Chem. Phys. 77 (1982) 6065.

QUANTUM-MECHANICAL STUDY OF THE REACTION
Be + FH($v = 0$, 1) → BeF(v') + H [*]

James F. GARVEY [1], Jack A. KAYE [2] and Aron KUPPERMANN

Arthur Amos Noyes Laboratories of Chemical Physics [3], California Institute of Technology, Pasadena, CA 91125, USA

Exact quantum-mechanical calculations for a collinear model of the reaction Be + FH($v = 0$, 1) have been performed Effects of reagent translational and vibrational excitation on reaction probabilities and product state distributions are examined These quantum results show product state distributions which differ from those of quasi-classical trajectory calculations.

1. Introduction

Over the past decade, there has been substantial interest in the reaction of alkaline earth atoms with hydrogen halides [1–10]

$$M + HX \rightarrow MX + H, \tag{1}$$

where $M = Ca, Sr, Ba$ and $X = F, Cl, Br, I$. Of particular interest has been the way in which reaction rates and product-state distributions vary with changes in the vibrational [2–4] translational [5], and rotational [6–8] state of the HX reagent. Additional studies have focused on the effect of electronic excitation of the metal atom [9,10].

A particularly important conclusion of such studies on the Ba, Sr and Ca + HF reactions is that little of the available product energy in these systems is channeled into product vibration [2]. Additional experiments have shown that increasing the reagents' relative translational energy leads to increased internal excitation of the reaction product [5], and that excitation

of the $v = 1$ state of the reagent in the Ba + HF reaction leads to a reaction rate increase of a factor of three [4].

Accurate theoretical treatment of these reactions is difficult because the large number of electrons present makes calculation of potential energy surfaces prohibitively expensive. For this reason, substantial effort has been made to study the simplest M + HX reaction, that of Be + HF. Considering only the collinear configuration,

$$Be + FH \rightarrow BeF + H, \tag{2}$$
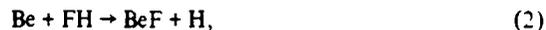
Schor et al. [11] performed ab initio quantum-mechanical calculations of the corresponding potential energy surface, and used that surface (along with an extended LEPS [12] surface designed to mimic the saddle point region of the ab initio surface) in collinear quasi-classical trajectory calculations [10,13]. Diatomics-in-molecules (DIM) surfaces have also been calculated for this reaction [14] (as well as for the reaction Ca + HCl → CaCl + H [15]). Most recently, a three-dimensional potential-energy surface for this system has been calculated [16] and has been fit to a simple form in a three-dimensional quasi-classical trajectory calculation [17].

In this work, quantum-mechanical calculations are carried out on the collinear Be + FH reaction (2) using the extended LEPS surface of Schor et al. [11] for HF ($v = 0,1$). This surface has the same barrier and position as the ab initio one, but a more gently curved reac-

[1] Work performed in partial fulfillment of the requirement for the Ph.D. in Chemistry at the California Institute of Technology.

[2] Present address: Goddard Space Flight Center, Code 616, Greenbelt, MD 20771, USA.

[3] Contribution No. 7084.
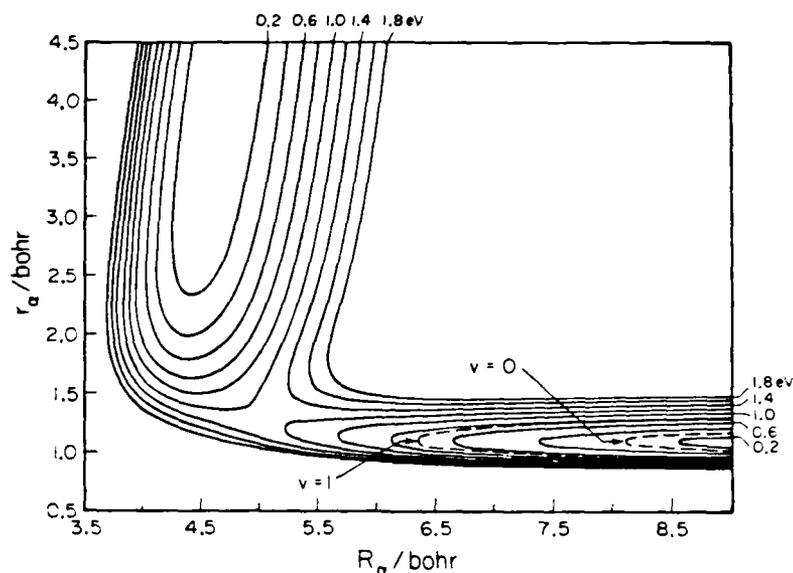
Fig. 1. Contour plots of the extended LEPS potential energy surface for the collinear Be + FH reaction in Delves' scaled coordinated system. The solid curves are equipotential contours spaced each by 0.2 eV. The zero of energy is the bottom of the HF well. Contours corresponding to the isolated HF($v = 0, 1$) energy are also shown.

tion path. As a result, the quasi-classical dynamics on these two surfaces differ [11], and analogous differences in their quantum dynamics are expected. In this study, we compare the quantum and quasi-classical dynamics [11,13] on the LEPS surface only. We consider specifically the effect of HF vibrational excitation and of the reagents' relative translational excitation on the total reaction probability and the product vibrational state distributions.

2. Calculation

Reaction probabilities were calculated using the coupled-channel method of Kuppermann, which has been discussed in detail previously [18]. Between 20 and 27 basis functions were used in these calculations with the larger number being used only at the high-energy end of the calculations (1.4 eV above the HF ground state). Flux conservation was always 3% or better, and at lower energies substantially better than that. A contour plot of the equipotentials in the BeFH configuration of the surface used in the Delves mass-weighted coordinate system [18] is shown in fig. 1.

With respect to the bottom of the HF well, this surface is exoergic by 0.022 eV and has a barrier height of 1.21 eV. The positioning of the energy levels of HF and BeF is given in table 1.

Table 1
Energy levels of HF and BeF in eV [a]

v	HF	BeF
0	0.28	0.075
1	0.77	0.23
2	1.24	0.38
3	1.69	0.53
4		0.68
5		0.82
6		0.97
7		1.11
8		1.28
9		1.39
10		1.52
11		1.66

[a] The common zero energy is the bottom of the HF well with the Be atom removed to infinity.

3. Results and discussion

The collinear quasi-classical trajectory calculations of Schor et al. [11] display reaction probabilities which rise extremely sharply (over a range of about 0.01 eV) from threshold to unity, and which do not decrease with increasing energy in the range of energies studied. The dynamical threshold translational energies for the Be + FH(v) → BeF(all) + H reaction is 1.06 eV for $v = 0$ and 0.80 eV for $v = 1$. The exact quantum curves also rise from 0 to 1. They have a sigmoid shape, achieving the value of 0.01 at translational energies of 0.98 eV and 0.75 eV for $v = 0$ and $v = 1$ respectively, and a value of 0.99 at 1.18 eV and 0.90 eV respectively. Over the translational energy range of 1.23 to 1.5 eV the $v = 0$ probability drops from 1.00 to 0.97 whereas the quasi-classical one remains equal to 1.00. In summary, the quantum results for HF($v = 0$) differ from the quasi-classical ones in that the reaction probability rises more gradually to unity with increasing energy and then decreases slightly at higher energies. For HF($v = 1$), the quantum-mechanical probabilities rise more rapidly to unity than they do for HF($v = 0$). The phenomenological thresholds (defined as the translational energy at which the reaction probability equals 0.01) calculated in the quantum-mechanical calculations were slightly lower than those in the trajectory calculations.

The difference between the quantum phenomenological thresholds for the $v = 0$ and $v = 1$ reactions is 0.23 eV. Since the spacing of these two HF vibrational levels is approximately 0.49 eV, one sees that HF vibrational excitation is only partially (47%) effective in promoting reaction. Such relative inefficiency is not too surprising given that the configuration of the saddle point is more similar to that of the reagents than that of the products. Vibrational enhancement of reaction in this system is only slightly more than in the reaction

$$D + FH \rightarrow DF + H \qquad (3)$$

in which excitation of HF to $v = 1$ was calculated to lead to a 0.22 eV reduction in the threshold to reaction [19].

The disposal of energy in the products also shows similarities between the quasi-classical and quantum-mechanical calculations. In fig. 2, the fraction of available energy going into product vibration (f_{vib}) as

a function of reagent translational energy is shown for these calculations. Both indicate that this fraction is approximately 0.35 for ground-state reagents. For HF($v = 1$), both treatments furnish values of f_{vib} near 0.45 in the 0.9 to 1.00 eV translational energy, although the quantum-mechanical result starts falling rapidly with decreasing energy at slightly higher energies.

Pronounced differences were observed between the BeF product vibrational state distributions in the two calculations, however. Histogram plots of these distributions at selected energies for ground (fig. 3) and vibrationally excited (fig. 4) reagents show these differences clearly. For $v = 0$, the quasi-classical distributions have sharp lower and upper cut-offs, whereas the quantum ones have a more Gaussian-like shape. For $v = 1$, both the quasi-classical and quantum results are quite broad; the quasi-classical ones are slightly bimodal whereas the quantum ones are very clearly bimodal.

Bimodal distributions of product vibrational states have been seen in other collinear quantum-mechanical systems [20], primarily for light–heavy–heavy (LHH) systems such as

$$H + Cl_2 \rightarrow HCl + Cl. \qquad (4)$$
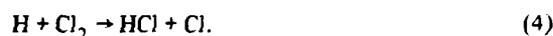
Quasi-classical trajectory calculations have been seen to display less structure in their product state distributions [21], as has also been observed here. Bimodal product vibrational state distributions have not been
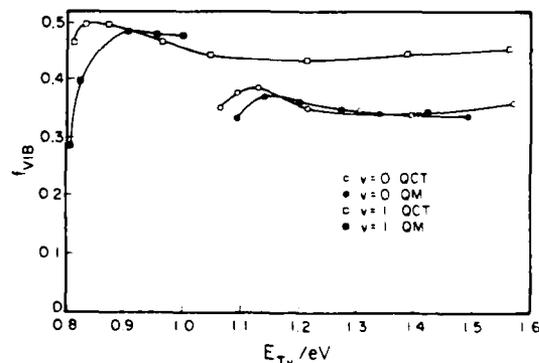

Fig. 2. Fraction f_{vib} of available energy going into vibration of the BeF product as a function of reagent translational energy for HF($v = 0, 1$). Open symbols represent the quasi-classical trajectory calculations of Schor et al. [13], while solid symbols represent the quantum-mechanical results.
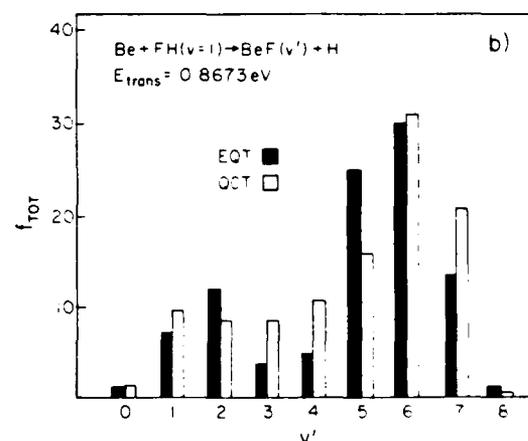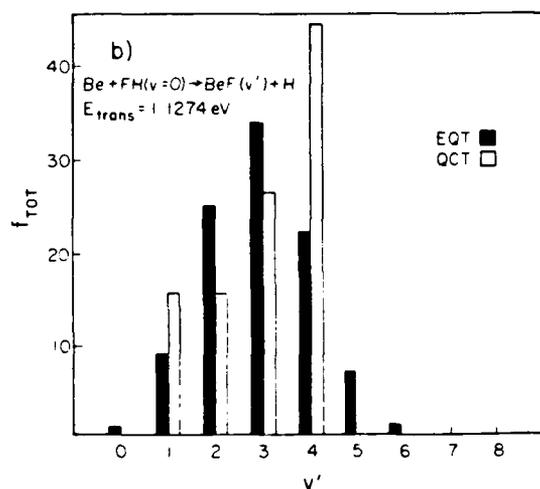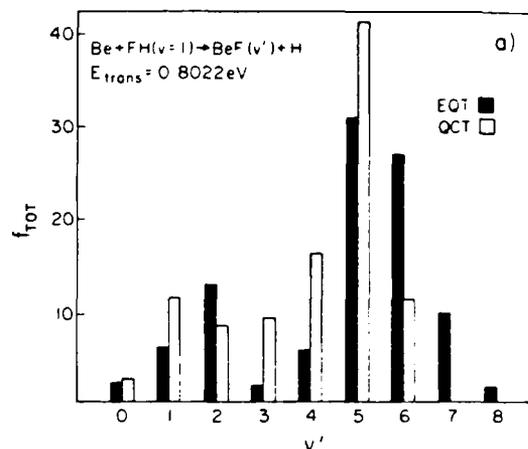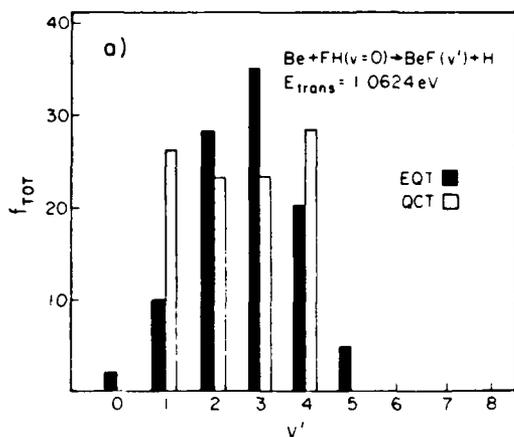
Fig. 3. Product vibrational state distribution of BeF formed in the reaction Be + FH($v = 0$) → BeF(v') + H for energies shown. Open bars are quasi-classical trajectory values taken from the results of Schor et al. [11], while solid bars are from the quantum-mechanical calculations.

Fig. 4. Product vibrational state distribution of BeF formed in the reaction BeF + FH($v = 1$) → BeF(v') + H for energies shown. Symbols are as in fig. 3.

observed experimentally in these systems, although unusual distributions differing substantially from standard unimodal ones have been observed [22]. Recent work in converting one-dimensional probabilities to three-dimensional ones suggests that with properly energy- and state-selected reagents, bimodal product vibrational state distributions might well be observable in the three-dimensional world [23].

As has been discussed previously [24], the bimodal product-state distribution in the quantum-mechanical calculations is due to a Franck—Condon reflection pattern, where the state-to-state reaction probabilities have a close correspondence to the probability density distribution of the vibrationally excited reagent. Classically, one may interpret the bimodal product state distribution for $v = 1$ reagents to be due to two different types of trajectories. One type samples the repulsive wall at small values of R_α and gives rise to high vibrational state products whereas the other passes

387

from the reagent to the product region leaving the saddle point to its left and producing lower vibrational energy products (see fig. 1). The latter type of trajectory does not occur for $v = 0$ because for ground-state reagents only the region of configuration space close to the minimum energy path is explored.

4. Conclusions

The major results of this study are as follows:

(1) Vibrational energy is only moderately (just under 50%) effective in promoting reaction.

(2) Quantum-mechanical and quasi-classical trajectory calculations give approximately equal values of the fraction of available energy going into product vibration (0.35 for $v = 0$, 0.45 for $v = 1$), but the details of the product-state distributions differ markedly.

(3) A bimodal BeF vibrational state distribution has been obtained in the reaction of vibrationally excited ($v = 1$) reagents. Similar distributions have been seen for L + HH reactions (the reverse of the H + HL reaction being considered here).

Acknowledgement

References

[1] H.W. Cruse, P.J. Dagdigian and R.N. Zare, Faraday Discussions Chem. Soc. 55 (1973) 277.

[2] J.G. Pruett and R.N. Zare, J. Chem. Phys. 64 (1976) 1774.

[3] Z. Karny and R.N. Zare, J. Chem. Phys. 68 (1978) 3360.

[4] A. Torres-Filho and S.G. Pruett, J. Chem. Phys. 72 (1980) 6736; 77 (1982) 740.

[5] A. Gupta, D.S. Perry and R.N. Zare, J. Chem. Phys. 72 (1980) 6237;
A. Siegel and A. Schultz, J. Chem. Phys. 72 (1980) 6227.

[6] Z. Karny, R.C. Estler and R.N. Zare, J. Chem. Phys. 69 (1978) 5199.

[7] C.K. Man and R.C. Estler, J. Chem. Phys. 75 (1981) 2779.

[8] R.A. Altkorn, F.E. Bartoszek, J. DeHaven, G. Hancock, D.S. Perry and R.N. Zare, Chem. Phys. Letters 98 (1983) 212.

[9] U. Brinkmann and H. Telle, J. Phys. B10 (1977) 133.

[10] F. Engelke and K.H. Meiwes-Broer, Chem. Phys. Letters 108 (1984) 137.

[11] H. Schor, S. Chapman, S. Green and R.N. Zare, J. Chem. Phys. 69 (1978) 3790.

[12 P.J. Kuntz, E.M. Nemeth, J.C. Polanyi, S.D. Rosner and C.E. Young, J. Chem. Phys. 44 (1966) 1168.

[13] H. Schor, S. Chapman, S. Green and R.N. Zare, J. Phys. Chem. 83 (1979) 920.

[14] P.J. Kuntz and A.C. Roach, J. Chem. Phys. 74 (1981) 3420;
A.C. Roach and P.J. Kuntz, J. Chem. Phys. 74 (1981) 3435;
J.L. Schreiber and P.J. Kuntz, J. Chem. Phys. 76 (1982) 1872.

[15] A.D. Isaacson and J.T. Muckerman, J. Chem. Phys. 73 (1980) 1729.

[16] S. Chapman, M. Dupuis and S. Green. J. Chem. Phys. 78 (1983) 93.

[17] S. Chapman. J. Chem. Phys. 81 (1984) 262.

[18] A. Kuppermann, in: Theory of scattering; papers in honor of Henry Eyring. Theoretical chemistry: advances and perspectives, Vol. 6A (Academic Press, New York, 1981), and references therein.

[19] J.A. Kaye, Ph.D. Thesis, California Institute of Technology, Pasadena (1982).

[20] J.N.L. Connor, W. Jakubetz and J. Manz, J. Chem. Phys. 63 (1976) 674;
J.K.C. Wong and P. Brumer, Chem. Phys. Letters 68 (1979) 517;
J.N.L. Connor, W. Jakubetz, A. Lagana, J. Manz and J.C. Whitehead, J. Chem. Phys. 65 (1982) 29.

[21] J.N.L. Connor, J.C. Whitehead, W. Jakubetz and A. Lagana, Nuovo Cimento 63B (1981) 459.

[22] A.M.G. Ding, L.J. Kirsch, D.S. Perris, J.C. Polanyi and J.L. Schreiber, Faraday Discussions Chem. Soc. 55 (1973) 252;
B. Hildebrandt, H. Vanni and H. Heydtmann, J. Chem. Phys. 84 (1984) 125.

[23] W. Jakubetz, J. Chem. Phys. 88 (1984) 271.

[24] D.R. Herschbach, Faraday Discussions Chem. Soc. 55 (1973) 233;
M.S. Child, Mol. Phys. 35 (1978) 759;
M.S. Child and K.B. Whaley, Faraday Discussions Chem. Soc. 67 (1979) 479.

Towards a state-to-state transition state theory

A. Kuppermann

Arthur Amos Noyes Laboratory of Chemical Physics.[a] *California Institute of Technology, Pasadena, California 91125-0001*

R. D. Levine

The Fritz Haber Molecular Dynamics Research Center, The Hebrew University, Jerusalem 91904, Israel

We assume that, having arrived at the transition state, the branching into the different product states is independent of the initial quantum states of the reactants. This assumption plus the familiar transition state approximation (that the reaction rate is the rate of the passage across the barrier) yields an expression for the state-to-state cross section in terms of the state-to-all one, as well as microcanonical rate constants. Models, adiabatic correlations, purely statistical considerations, or collinear computations can provide the required input for the theory. Exact quantal computations on the 3D H + H_2 reaction are found to satisfy the assumed factorization quite well. Furthemore, reaction probabilities derived from a line-of-centers model, with a barrier height dependent on the approach angle, account for the probabilities derived from the exact quantal computation.

I. INTRODUCTION

There are a number of motivations for the development to be discussed in this paper. One, mentioned in the title, is to formulate a state-to-state theory which, upon summing over product states and averaging over an equilibrium distribution of reactant states, will yield the conventional transition state theory TST.[1]

Another is to provide a framework where exact collinear reaction probabilities can be used to compute three-dimensional state-to-state cross sections.[2] Alternatively, one can employ reaction probabilities derived from models for such calculations. One such model[3] based on a line-of-centers approach is used here to compare against the results of exact quantal computations[4] for the 3D H + H_2 reaction. Then, one can regard the present development as a natural extension of the phase space theory[5] to reactions with a tight transition state.[6,7] These and other topics closely related to our development have received extensive discussion in the literature. Hence, the list of references in this paper can in no way be complete and we apologize beforehand for our omissions.

The discussion in this paper considers systems at a constant total energy. Results at a given temperature can be obtained by appropriate Boltzmann averages and will be presented elsewhere with additional applications.

In Sec. II we derive a set of exact relations involving state-to-state, state-to-all, and all-to-all cross sections or rate constants in a form appropriate for subsequent TST developments. In Sec. III we introduce a state-to-state reaction cross section factorization, and use it to develop a state-to-state TST. That factorization is tested in Sec. IV against exact 3D H + H_2 quantal calculations. In Sec. V we show that in an adiabatic formalism the condition for validity of the corresponding all-to-all microcanonical rate constant is equivalent to that for the thermal TST one derived previously.[8] A

simple line-of-centers model is used in Sec. VI to calculate state-to-state and state-to-all cross sections for that reaction and shown to be in agreement with accurate quantum mechanical calculations. Section VII summarizes the conclusions reached.

II. STATE-TO-STATE, STATE-TO-ALL, AND ALL-TO-ALL RELATIONS

Let us consider the partitioning of a polyatomic system into a pair of molecules designated by the arrangement channel index λ and let n_λ represent the set of quantum numbers needed to specify the internal states of those molecules when they are infinitely apart. Let $Q^{\lambda n_\lambda}_{\lambda' n'_\lambda}(E)$ be the integral cross section for the $\lambda n_\lambda \rightarrow \lambda' n'_\lambda$ process at total energy E, which is a bimolecular reaction for $\lambda' \neq \lambda$. The corresponding state-to-state rate constant is given by

$$K^{\lambda n_\lambda}_{\lambda' n'_\lambda}(E) = v_{\lambda n_\lambda}(E) Q^{\lambda n_\lambda}_{\lambda' n'_\lambda}(E)$$
$$= [k^2_{\lambda n_\lambda}(E)/\pi\hbar\rho_{\lambda n_\lambda}(E)] Q^{\lambda n_\lambda}_{\lambda' n'_\lambda}(E). \quad (2.1)$$

where $\rho_{\lambda n_\lambda}$ is the density of states per unit volume of the relative translational motion of the λ molecules, and $k_{\lambda n_\lambda}$ and $v_{\lambda n_\lambda}$ the corresponding wave number and velocity. These three quantities are interrelated by

$$\rho_{\lambda n_\lambda}(E) = (1/h^3)4\pi\mu_\lambda^2 v_{\lambda n_\lambda} = (1/h^2)2\mu_\lambda k_{\lambda n_\lambda}, \quad (2.2)$$

where μ_λ is the reduced mass of the pair of λ molecules. Summing Eq. (2.1) over n'_λ gives

$$K^{\lambda n_\lambda}_{\lambda'}(E) = [k^2_{\lambda n_\lambda}(E)/\pi\hbar\rho_{\lambda n_\lambda}(E)] Q^{\lambda n_\lambda}_{\lambda'}(E), \quad (2.3)$$

where the $Q^{\lambda n_\lambda}_{\lambda'}$ and $K^{\lambda n_\lambda}_{\lambda'}$ are, respectively, the state-to-all cross section and rate constant. Multiplying Eq. (2.3) by $\rho_{\lambda n_\lambda}$ and summing over n_λ gives[9]

$$K^{\lambda}_{\lambda'}(E) = [\pi\hbar\rho_\lambda(E)]^{-1} \sum_{n_\lambda} k^2_{\lambda n_\lambda}(E) Q^{\lambda n_\lambda}_{\lambda'}(E), \quad (2.4)$$

where ρ_λ and $K^\lambda_{\lambda'}$ are, respectively, the total density of states

per unit volume and the all-to-all microcanonical rate constant defined by[9]

$$\rho_\lambda(E) = \sum_{n_\lambda} \rho_{\lambda n_\lambda}(E) \tag{2.5}$$

and

$$K_\lambda^\lambda(E) = [\rho_\lambda(E)]^{-1} \sum_{n_\lambda} \rho_{\lambda n_\lambda}(E) K_\lambda^{\lambda n_\lambda}(E). \tag{2.6}$$

Equations (2.1), (2.3), and (2.4) express the state-to-state, state-to-all, and all-to-all rate constants at a fixed total energy in terms of appropriate cross sections and serve as a bridge between dynamics and rate theory.[10,11]

According to the principle of microscopic reversibility[9]

$$k_{\lambda n_\lambda}^2(E) Q_{\lambda' n_\lambda'}^{\lambda n_\lambda}(E) = k_{\lambda' n_\lambda'}^2(E) Q_{\lambda n_\lambda}^{\lambda' n_\lambda'}(E). \tag{2.7}$$

Summing over n_λ' furnishes

$$k_{\lambda n_\lambda}^2 Q_\lambda^{\lambda n_\lambda} = \pi h \rho_\lambda(E) K_{\lambda n_\lambda}^\lambda(E), \tag{2.8}$$

where $K_{\lambda n_\lambda}^\lambda$ is the total rate constant into state n_λ of λ reaction products from a microcanonical ensemble of λ' reagents at energy E and is given by

$$K_{\lambda n_\lambda}^\lambda(E) = \rho_\lambda^{-1}(E) \sum_{n_\lambda'} \rho_{\lambda' n_\lambda'}(E) K_{\lambda n_\lambda}^{\lambda' n_\lambda'}(E). \tag{2.9}$$

In the spirit of TST, we write the factor $h\rho_\lambda \cdot K_{\lambda n_\lambda}^\lambda$ on the right-hand side of Eq. (2.8) as the product of a number N_λ^λ and a probability $P_{\lambda n_\lambda}^\lambda$ and rewrite that equation as

$$k_{\lambda n_\lambda}^2 Q_\lambda^{\lambda n_\lambda} = \pi N_\lambda^\lambda(E) P_{\lambda n_\lambda}^\lambda(E), \tag{2.10}$$

where the $P_{\lambda n_\lambda}^\lambda$ are normalized over n_λ:

$$\sum_{n_\lambda} P_{\lambda n_\lambda}^\lambda(E) = 1. \tag{2.11}$$

Equation (2.10) is not an approximation, but together with Eq. (2.11) it constitutes a unique definition of the quantities N_λ^λ and $P_{\lambda n_\lambda}^\lambda$. Indeed, we obtain immediately from these equations the equivalent defining expressions

$$N_\lambda^\lambda(E) = \pi^{-1} \sum_{n_\lambda} k_{\lambda n_\lambda}^2(E) Q_\lambda^{\lambda n_\lambda}(E) \tag{2.12}$$

and

$$P_{\lambda n_\lambda}^\lambda(E) = \frac{k_{\lambda n_\lambda}^2(E) Q_\lambda^{\lambda n_\lambda}(E)}{\sum_{n_\lambda} k_{\lambda n_\lambda}^2(E) Q_\lambda^{\lambda n_\lambda}(E)}. \tag{2.13}$$

It is easy to prove from microscopic reversibility that N_λ^λ and N_λ^λ are equal, which is an important property for a TST formulation, as developed in Sec. III, since these numbers will be eventually associated with the number of states of the transition state accessible at energy E and should not depend on whether we approach it from the λ' or the λ' directions.

Replacing Eq. (2.10) on the right-hand side of Eq. (2.4) and using Eq (2.11) gives for the microcanonical rate constant[10,12]

$$K_\lambda^\lambda(E) = \frac{N_\lambda^\lambda(E)}{h\rho_\lambda(E)}. \tag{2.14}$$

This expression, although exact, has the same form as the

corresponding TST equation, in which N, rather than being defined by Eq. (2.12), is the number of transition state states mentioned in the previous paragraph.

Let us now define a set of state-to-state reaction probabilities[13]

$$\bar{P}_{\lambda' n_\lambda'}^{\lambda n_\lambda}(E) = Q_{\lambda' n_\lambda'}^{\lambda n_\lambda}(E) / Q_{\lambda' n_\lambda'}^{\lambda n_\lambda}(E). \tag{2.15}$$

which are obviously normalized over n_λ'. Using Eq. (2.10) we get

$$Q_{\lambda' n_\lambda'}^{\lambda n_\lambda}(E) = [\pi/k_{\lambda n_\lambda}^2(E)] N_\lambda^\lambda(E) P_{\lambda n_\lambda}^\lambda(E) \bar{P}_{\lambda' n_\lambda'}^{\lambda n_\lambda}. \tag{2.16}$$

Once more, this expression is exact but has a form appropriate for TST. In the same spirit we define the transmission factors

$$T_{\lambda n_\lambda}^\lambda(E) = P_{\lambda n_\lambda}^\lambda(E) N_\lambda^\lambda(E) \tag{2.17}$$

and

$$\bar{T}_{\lambda' n_\lambda'}^{\lambda n_\lambda}(E) = \bar{P}_{\lambda' n_\lambda'}^{\lambda n_\lambda}(E) N_\lambda^\lambda(E) \tag{2.18}$$

in terms of which Eq. (2.16) can be rewritten in the equivalent exact form

$$Q_{\lambda' n_\lambda'}^{\lambda n_\lambda}(E) = [\pi/k_{\lambda n_\lambda}^2(E)] T_{\lambda n_\lambda}^\lambda(E) \bar{T}_{\lambda' n_\lambda'}^{\lambda n_\lambda}(E) / N_\lambda^\lambda(E). \tag{2.19}$$

Equations (2.16) or (2.19) are useful for the development of state-to-state reaction cross section theories by replacing in them the N, P, $\bar{P}$, T, or $\bar{T}$ by appropriate approximations.

III. STATE-TO-STATE REACTION CROSS SECTION FACTORIZATION AND TRANSITION STATE THEORY

So far we have only used formal developments, without any approximations. We will now make the first one, by assuming that the following relation holds:

$$\bar{P}_{\lambda' n_\lambda'}^{\lambda n_\lambda}(E) = P_{\lambda' n_\lambda'}^\lambda. \tag{3.1}$$

This expression is equivalent to

$$\frac{Q_{\lambda' n_\lambda'}^{\lambda n_\lambda}(E)}{Q_\lambda^{\lambda n_\lambda}(E)} = \frac{k_{\lambda n_\lambda}^2(E) Q_\lambda^{\lambda n_\lambda}(E)}{\sum_{n_\lambda} k_{\lambda n_\lambda}^2(E) Q_\lambda^{\lambda n_\lambda}(E)}. \tag{3.2}$$

Replacement of Eq. (3.1) into Eq. (2.15) gives

$$Q_{\lambda' n_\lambda'}^{\lambda n_\lambda}(E) = Q_\lambda^{\lambda n_\lambda}(E) P_{\lambda' n_\lambda'}^\lambda(E). \tag{3.3}$$

This factorization implies that the n_λ, n_λ' dependence of $Q_{\lambda' n_\lambda'}^{\lambda n_\lambda}$ can be expressed as the product of a factor that depends on n_λ only and one on n_λ' only.[14] This is in the spirit of TST, in the sense that the partitioning of the reaction flux among the products should not depend on how the system reached its transition state.

Using the definition of $Q_\lambda^{\lambda n_\lambda}$ and the microscopic reversibility expression (2.7) we rewrite Eq. (3.2) as

$$\frac{Q_{\lambda' n_\lambda'}^{\lambda n_\lambda}(E)}{Q_\lambda^{\lambda n_\lambda}(E)} = \frac{\sum_{n_\lambda} k_{\lambda n_\lambda}^2(E) Q_{\lambda' n_\lambda'}^{\lambda n_\lambda}(E)}{\sum_{n_\lambda} k_{\lambda n_\lambda}^2 Q_\lambda^{\lambda n_\lambda}(E)}. \tag{3.4}$$

Generally speaking, it is not expected that this expression should be valid, since it formally contains an n_λ dependence on its left-hand side but not on its right-hand side. However, if the factorization property (3.3) is satisfied, the n_λ dependencies in the numerator and denominator of the left-hand

TABLE I Rotational branching probabilities $\overline{P}_{j'}^{j}$ for $H + H_2 \rightarrow H_2 + H$ at $E = 0.6$ eV.

j'			
j	0	1	2 ·
0	0.262	0.473	0.265
1	0.255	0.482	0.263
2	0.257	0.472	0.272

side of Eq. (3.4) cancel, eliminating this inconsistency.

With the help of Eq. (3.1), we can cast Eqs. (2.16) and (2.19) in the approximate form

$$Q_{\lambda' n_{\lambda'}}^{\lambda n_\lambda}(E) = \left[\pi/k_{\lambda n_\lambda}^2(E) \right] N_\lambda^\lambda(E) P_{\lambda n_\lambda}^\lambda(E) P_{\lambda' n_{\lambda'}}^\lambda(E) \tag{3.5}$$

$$= \left[\pi/k_{\lambda n_\lambda}^2(E) \right] T_{\lambda n_\lambda}^\lambda(E) T_{\lambda' n_{\lambda'}}^\lambda(E)/N_\lambda^\lambda(E).$$

The description of a test of this equation is given in Sec. IV.

We now introduce TST in Eq. (3.5) by replacing $N_\lambda^\lambda(E)$ by $N_{\lambda'}^\lambda(E)$, the total number of transition state states[15] or activation barrier tops whose energies do not exceed E. The most obvious way of defining such barrier is based on adiabatic correlations between the transition state and the states of the reagents.[8] We also replace $P_{\lambda n_\lambda}^\lambda$ by an approximate probability $P_{\lambda n_\lambda}^{\lambda, \text{app}}$, which is still normalized over n_λ as in Eq. (2.11) but is otherwise arbitrary, no longer needing to satisfy Eq. (2.13). We then get the following state-to-state TST cross section expression:

$$Q_{\lambda' n_{\lambda'}}^{\lambda n_\lambda}(E) = \left[\pi/k_{\lambda n_\lambda}^2(E) \right] N_{\lambda'}^\lambda(E) P_{\lambda n_\lambda}^{\lambda \text{app}}(E) P_{\lambda' n_{\lambda'}}^{\lambda \text{app}}(E)$$

$$= \left[\pi/k_{\lambda n_\lambda}^2(E) \right] T_{\lambda n_\lambda}^{\lambda \text{app}}(E) T_{\lambda' n_{\lambda'}}^{\lambda \text{app}}(E)/N_{\lambda'}^\lambda(E), \tag{3.6}$$

where the T^{app} are related to the corresponding P^{app} by an expression analogous to Eq. (2.17) in which N_λ^λ is replaced by $N_{\lambda'}^\lambda$. Replacement of this expression into Eq. (2.10) and

comparison of the result with Eq. (2.8) gives

$$\rho_{\lambda n_\lambda}(E) K_\lambda^{\lambda n_\lambda}(E) = \frac{1}{h} N_{\lambda'}^\lambda(E) P_{\lambda n_\lambda}^{\lambda \text{app}}(E). \tag{3.7}$$

Summing this expression over n_λ and using Eq (2.6) and the normalization condition of the $P_{\lambda n_\lambda}^{\lambda \text{app}}$ results finally in

$$K_\lambda^\lambda(E) = \frac{N_{\lambda'}^\lambda(E)}{h\rho_\lambda(E)}. \tag{3.8}$$

This is the correct TST version of Eq. (2.14) and shows that regardless of the choice of the normalized model $P_{\lambda n_\lambda}^{\lambda \text{app}}$ used for the calculation of the state-to-state cross section $Q^{\lambda n}$, we will always get the correct TST microcanonical all-to-all rate constant $K_\lambda^\lambda(E)$.

IV. A TEST OF FACTORIZATION

Using the state-to-state reaction cross sections for the H + H$_2$ system obtained from an exact quantal calculation,[4] we have tested the factorization assumption of Sec III The energy used was 0.6 eV, for which only the ground vibrational state of the reagent and product is open.

The first test was on the summed and averaged cross sections. Replacing in Eq. (2.15) n_λ by j, m_j and summing over m_j' and averaging over m_j we get, for the summed and averaged cross sections,

$$Q_{j'}^j = Q^j \overline{P}_{j'}^j. \tag{4.1}$$

Using the values of $Q_{j'm_j'}^{jm_j}$ of Table VI of Ref. 4 (and reproduced in Table II of this paper) we calculated the Q^j and $Q^{j'}$, and from those we obtained the values of $\overline{P}_{j'}^j$ given in Table I. From the relatively small variation of these quantities with j we conclude that the factorization of $Q_{j'}^j$, into a j dependent (but j' independent) factor and a j' dependent (but j independent) factor is a very good one for this case. This is in agreement with the Franck–Condon model proposed and tested previously.[16]

TABLE II Integral reactive cross sections $Q_{j'm_j'}^{jm_j}$ for the H + H$_2 \rightarrow$ H$_2$ + H reaction at $E = 0.6$ eV.[a]

jm_j \ $j'm_j'$	00	11	10	1 − 1	22	21	20	2 − 1	2 − 2
00	0.432e-01	0.322e-02	0.717e-01	0.322e-02	0.227e-03	0.474e-02	0.338e-01	0.474e-02	0.227e-03
	0.432e-01	0.337e-02	0.726e-01	0.337e-02	0.226e-03	0.462e-02	0.327e-01	0.462e-02	0.226e-03
11	0.337e-02	0.549e-03	0.596e-02	0.835e-03	0.488e-04	0.709e-03	0.261e-02	0.127e-02	0.774e-04
	0.354e-02	0.276e-03	0.595e-02	0.276e-03	0.185e-04	0.379e-03	0.268e-02	0.379e-03	0.185e-04
10	0.751e-01	0.596e-02	0.128	0.596e-02	0.380e-03	0.812e-02	0.578e-01	0.812e-02	0.380e-03
	0.761e-01	0.595e-02	0.128	0.595e-02	0.398e-03	0.815e-02	0.577e-01	0.815e-02	0.398e-03
1 − 1	0.337e-02	0.835e-03	0.596e-02	0.549e-03	0.774e-04	0.127e-02	0.261e-02	0.709e-03	0.488e-04
	0.354e-02	0.276e-03	0.595e-02	0.276e-03	0.185e-04	0.379e-03	0.268e-02	0.379e-03	0.185e-04
22	0.262e-03	0.538e-04	0.419e-03	0.855e-04	0.111e-04	0.811e-04	0.209e-03	0.134e-03	0.146e-04
	0.262e-03	0.205e-04	0.441e-03	0.205e-04	0.137e-05	0.281e-04	0.199e-03	0.281e-04	0.137e-05
21	0.549e-02	0.783e-03	0.890e-02	0.140e-02	0.811e-04	0.113e-02	0.407e-02	0.228e-02	0.134e-03
	0.537e-02	0.419e-03	0.902e-02	0.419e-03	0.281e-04	0.575e-03	0.407e-02	0.575e-03	0.281e-04
20	0.391e-01	0.288e-02	0.638e-01	0.288e-02	0.209e-03	0.407e-02	0.286e-01	0.407e-02	0.209e-03
	0.380e-01	0.297e-02	0.639e-01	0.297e-02	0.199e-03	0.407e-02	0.288e-01	0.407e-02	0.199e-03
2 − 1	0.549e-02	0.140e-02	0.897e-02	0.783e-03	0.134e-03	0.228e-02	0.407e-02	0.113e-02	0.811e-04
	0.537e-02	0.419e-03	0.902e-02	0.419e-03	0.281e-04	0.575e-03	0.407e-02	0.575e-03	0.281e-04
2 − 2	0.262e-03	0.855e-04	0.419e-03	0.538e-04	0.146e-04	0.134e-03	0.209e-03	0.811e-04	0.111e-04
	0.262e-03	0.205e-04	0.441e-03	0.205e-04	0.137e-05	0.281e-04	0.199e-03	0.281e-04	0.137e-05

[a] The top number in each entry is the exact quantal value from Ref. 4, and the bottom one the result of a least-mean-square fit of Eq. (3.5)

In order to test the detailed state-to-state factorization assumption, we least-mean-square fitted the mentioned $Q_{j'm'j}^{m}$ values by Eq. (3.5), using N and the six quantities $P_{j\,m_j}$ ($j = 0,1,2$) as parameters. The results are given in Table II, where the top number in each entry represents the accurate quantal calculation of Ref. 4 and the lower one the fitted values. The resulting optimal probability parameters are given in the second column of Table III. From these parameters, we can calculate the P_j by summing over the m_j. The results are

$$P_0 = 0.262,$$

$$P_1 = 0.481,$$

$$P_2 = 0.257.$$

These values are in good agreement with the $\overline{P}_j$ values of Table I, which is an indication of the overall validity of Eq. (3.1) when used for the summed and averaged quantities.

A comparison between the quantal and fitted cross sections of Table II indicates an overall qualitative agreement between them, showing that the factorization expression (3.5) is reasonable even on a single quantum state (rather than averaged) level.

The optimal value of N is 5.89. We used Eq. (30) of Ref. 17 to compute the transition state $N_{\ddagger}$ for this system at 0.6 eV. The result was 172. Therefore, although the factorization assumption works quite well, microcanonical TST for this system at this energy is too large by a factor of about 30. This is consistent with deviations between thermal TST and quantal results found previously.[4,8]

V. AN ADIABATIC STATE-TO-STATE TRANSITION STATE THEORY

As a result of the remarks of Sec. III, we conclude that a necessary and sufficient condition for the validity of microcanonical all-to-all TST is that N_{λ}^{λ} , (E), defined after Eq. (2.12), be equal to $N_{\lambda_{\ddagger}}^{\lambda}$, (E), defined after Eq. (3.5). On the other hand, it was previously proven[8] that a necessary and sufficient condition for the validity of thermal adiabatic TST is that certain reaction probabilities (not those defined in this paper so far) be step functions of the energy. The mathematical language used on that proof invoked an adiabatic correlation between each state of the reagents and a corresponding state of the transition state. This implies, physically, that the evolution of the system follows separate adiabatic path-

TABLE III. Probability parameters P_{jm}.

j,m_j	P_{jm}	
	a	b
0,0	0.262	0.172
1,0	0.440	0.417
1, ± 1	0.0204	0.02
2,0	0.198	0.308
2, ± 1	0.0280	0.03
2, ± 2	0.0014	0.0012

[a] From fit to quantal results.—See Sec. IV.
[b] From model described in Sec. VI.

ways. Since the microcanonical TST involves less averaging than the thermal one, it is important to show that (in the framework of an adiabatic formalism) the condition for validity of the former is not less restrictive than that of the latter. We will now show that these two necessary and sufficient conditions are acutally equivalent. As a result, we shall be able, from Eq. (2.13), to provide explicit expressions for the transition probabilities (or the transmission coefficients) which appear in Eq. (3.6). These are the central practical results of the section. Of course, both the proof and the explicit results are dependent on the aforementioned adiabatic correlation.

The state-to-state cross section can be expressed as

$$Q_{\lambda'n_{\lambda}'}^{\lambda n_{\lambda}} (E) = \frac{\pi}{k_{\lambda n_{\lambda}}^2(E)} \sum_{J=0}^{\infty} (2J + 1) \left| [1 - S'(E)]_{\lambda'n_{\lambda}'}^{\lambda n_{\lambda}} \right|^2,$$

(5.1)

where J is the system's total angular momentum quantum number, I is the identity matrix and S' a scattering matrix whose open part is symmetric and unitary. As a result, the J partial wave $\lambda n_{\lambda} \to \lambda' n_{\lambda}'$ transition probability defined by

$$p_{\lambda'n_{\lambda}'}^{J\lambda n_{\lambda}} (E) = \left| [S'(E)]_{\lambda'n_{\lambda}'}^{\lambda n_{\lambda}} \right|^2$$

(5.2)

is normalized with respect to $\lambda' n_{\lambda}'$:

$$\sum_{\lambda'n_{\lambda}'} p_{\lambda'n_{\lambda}'}^{J\lambda n_{\lambda}} (E) = 1.$$

(5.3)

Summing Eq. (5.1) over n_{λ}' for $\lambda' \neq \lambda$ (i.e., for reactive processes) we get

$$Q_{\lambda'}^{\lambda n_{\lambda}}(E) = \frac{\pi}{k_{\lambda n_{\lambda}}^2(E)} \sum_{JM} p_{\lambda'}^{J\lambda n_{\lambda}}(E),$$

(5.4)

where

$$p_{\lambda'}^{J\lambda n_{\lambda}}(E) = \sum_{n_{\lambda}'} p_{\lambda'}^{J\lambda n_{\lambda}}(E)$$

(5.5)

is the state-to-all J partial wave reaction probability and M is the quantum number of the projection of the total angular momentum of the system on a laboratory-fixed axis. This probability is degenerate, with respect to M, lies (as any probability should) in the range

$$0 \leqslant p_{\lambda'}^{J\lambda n_{\lambda}}(E) \leqslant 1$$

(5.6)

and is normalized with respect to λ' but not with respect to n_{λ}. Replacing Eq. (5.4) into Eq. (2.12) we get the exact expression

$$N_{\lambda}^{\lambda} (E) = \sum_{u_{\lambda}} p_{\lambda}^{\lambda u_{\lambda}}(E),$$

(5.7)

where u_{λ} represents the set of quantum numbers J, M, n_{λ}.

As described previously,[8] we now define a set of curvilinear coordinates consisting of a reaction coordinate q and a set of transverse coordinates $\mathbf{p}$, such that as q changes from $-\infty$, to 0, $+\infty$ the system evolves from the separated reagent molecules in the λ arrangement channel, to the saddle point of the potential energy surface between arrangement channels λ and λ' to the separated product molecules in the λ' arrangement channel. Let H (p,q) be the Hamiltonian of the system for a fixed q, which describes the transverse $\mathbf{p}$

motion. For each q let us consider the simultaneous eigenfunctions of H (p;q), the square of the systems's total angular momentum and its component along the laboratory-fixed axis mentioned above. Let the corresponding energy eigenvalues be denoted by $E_\lambda^{\lambda u_\lambda}(q)$. The $E_\lambda^{\lambda u_\lambda}$ vs q curves usually represent barriers which at the saddle point have values $E_\lambda^{\lambda u_\lambda}(0)$, and in general have maxima $E_\lambda^{\lambda u_\lambda,max}$ which occur at values $q_\lambda^{\lambda u_\lambda,max}$ of q which depend on J and n_λ (in addition to λ and λ'). The $E_\lambda^{\lambda u_\lambda}(-\infty)$ are the energy eigenvalues of the separated reagents, and are independent of λ'.

It was previously proven[x] that if we use the $E_\lambda^{\lambda u_\lambda,max}$ to calculate the transition state partition functions, a necessary and sufficient condition for the validity of all-to-all thermal adiabatic TST is that

$$p_\lambda^{\lambda u_\lambda}(E) = H(E - E_\lambda^{\lambda u_\lambda,max}) = 0 \text{ for } E < E_\lambda^{\lambda u_\lambda,max}$$
(5.8)
$$= 1 \text{ for } E > E_\lambda^{\lambda u_\lambda,max},$$

where H denotes the Heavyside step function. Note however that it is possible in principle to use alternative (i.e., nonadiabatic) correlation schemes to define the transition state energy levels and corresponding partition functions.[1x] The relation of adiabatic TST to generalized TST has been discussed recently.[1v] We now wish to calculate what $N_\lambda^\lambda(E)$ Eq. (5.8) implies. Replacement of this equation into Eq. (5.7) shows that $N_\lambda^\lambda(E)$ is in this case equal to the total number of $E_\lambda^{\lambda u_\lambda}(q)$ barriers (i.e., u_λ sets) for which $E_\lambda^{\lambda u_\lambda,max} < E$. This is by definition the number $N_{\lambda:}^\lambda(E)$ of transition state states whose energy is below E. If we changed the definition of $E_\lambda^{\lambda u_\lambda,max}$ and used the new $E_\lambda^{\lambda u_\lambda,max}$ to compute the partition functions of the transition state in this modified TST, the modified $N_{\lambda:}^\lambda(E)$ would still be the number of u_λ sets for which the new $E_\lambda^{\lambda u_\lambda,max} < E$.[20] We thus conclude that Eq. (5.8) is a sufficient condition for the validity of

$$N_\lambda^\lambda(E) = N_{\lambda:}^\lambda(E),$$
(5.9)

and therefore for the validity of microcanonical transition state theory.

Let us now show that Eq. (5.8) is a necessary condition for the validity of Eq. (5.9) and therefore that Eqs. (5.8) and (5.9) are equivalent. Indeed, replacing Eq. (5.9) into Eq. (5.7) and changing the summation index to $\bar{u}_\lambda$ we get

$$\sum_{\bar{u}_\lambda} p_\lambda^{\lambda u_\lambda}(E) = N_{\lambda:}^\lambda(E).$$
(5.10)

We now order the u_λ according to a criterion of increasing $E_\lambda^{\lambda u_\lambda,max}$ and designate by $u_\lambda - 1$ the set of quantum numbers which immediately precedes u_λ according to this criterion. Then, over the entire E range, defined by

$$E_\lambda^{\lambda u_\lambda - 1,max} < E < E_\lambda^{\lambda u_\lambda,max},$$
(5.11)

the left-hand side of Eq. (5.10) contains $N_\lambda^\lambda(E)$ terms. Since, according to Eq. (5.6), none of them can exceed unity, the only way in which Eq. (5.10) can be satisfied is if all those terms are unity over this energy range. By allowing E to assume all possible values, we conclude that we must have, in general,

$$p_\lambda^{\lambda u_\lambda}(E) = 1 \text{ for } E > E_\lambda^{\lambda u_\lambda,max}.$$
(5.12)

It is furthermore implicit in any adiabatic TST theory, microcanonical or thermal, that the corresponding $p_\lambda^{\lambda'r}(E)$ must vanish for $E < E_\lambda^{\lambda u_\lambda,max}$. As a result of this and of Eq. (5.12), Eq. (5.8) is valid, and the conditions for validity of adiabatic microcanonical and thermal TST are inded equivalent, as stated.

We turn now to deriving explicit expressions for the transition probabilities in terms of the barrier heights (or energy levels) of the transition state. With the notation introduced after Eq. (5.7) we get, replacing Eq. (5.8) into Eq. (5.4), the adiabatic state-to-all TST cross section

$$Q_\lambda^{\lambda n,ATST}(E) = \frac{\pi}{k_{\lambda n_\lambda}^2(E)} \sum_{JM} H(E - E_\lambda^{\lambda u_\lambda,max}).$$
(5.13)

Using this result in Eqs. (2.13) and (3.5) we get the corresponding ATST probabilities and state-to-state cross sections. To implement a calculation of these quantities it suffices to obtain the heights $E_\lambda^{\lambda u_\lambda,max}$ of the barriers which adiabatically connect the λu_λ state of the reagents with the λ' products. A calculation of the cross section given by Eq. (5.13) for the H + H_2 exchange reaction has been reported previously.[x]

VI. MODEL REACTION PROBABILITIES

A model for the reaction cross section as a function of the orientation angle has been described in Ref. 3 and successfully tested for the H + D_2 reaction. Using θ for the angle between the diatom axis and the vector from the center of mass of the diatom to the atom the result is

$$\sigma_R(\theta) = \pi d^2[1 - E_0(\theta)/E_{tr}],$$
(6.1)

where $E_0(\theta)$ is the barrier height for a fixed orientation and E_{tr} is the relative translation energy.

To convert Eq. (6.1) to quantal cross sections we average σ_R over a probability distribution of θ for a given j, m_j state, according to[21]

$$Q_R^{jm_j} = \int \sigma_R(\theta)|Y_{jm_j}(\theta,\varphi)|^2 \sin\theta \, d\theta \, d\varphi.$$
(6.2)

We performed this integration numerically, using the $E_0(\theta)$ form Fig. 1 of Ref. 3. The resulting Q^{jm_j} cross sections were used in Eq. (2.10) to compute the model P_{jm_j}. The corresponding values are given in the third column of Table III. The agreement with the ones obtained by the accurate quantal cross sections described in Sec. IV and given in the second column of Table III is quite reasonable [but the numerical values based on Eq. (6.2) are sensitive to the precise value of the translational energy, particularly for $j = 2$]. Using these P_{jm_j} together with Eqs. (2.12) and (3.5) we can calculate the state-to-state cross sections from a remarkably simple model.

The addition theorem of spherical harmonics insures that the degeneracy-averaged reaction cross section

$$Q_R^j = \frac{1}{2j+1} \sum_{m_j} Q_R^{jm_j}$$
(6.3)

is given by the classical[1] angle-averaged value

$$Q_R^{\prime} = \frac{1}{4\pi} \int \sigma_R(\theta)\sin\theta\,d\theta\,d\varphi. \qquad (6.4)$$

VII. CONCLUSIONS

From a rather simple factorization assumption, given by Eq. (3.3), and tested for the H + H_2 system at 0.6 eV, we were able to obtain a simple expression which permits the calculation of state-to-state cross sections in terms of state-to-all cross sections. This assumption also permitted the development of a microcanonical TST theory for state-to-state and state-to-all processes.

ACKNOWLEDGMENTS

[1]For a recent review see D. G. Truhlar, W. L. Hase, and J. T. Hynes, J. Chem. 87, 2664 (1983)

[2]For the computation of state-to-all cross sections see J. M. Bowman, G. Z. Ju, and K. T. Lee, J. Chem. Phys. 86, 2232 (1982)., and references cited therein

[3]R. D. Levine and R. B. Bernstein, Chem. Phys. Lett. 105, 467 (1984)

[4]G. C. Schatz and A. Kuppermann, J. Chem. Phys. 65, 4668 (1976)

[5]J. D. Light, Discuss. Faraday Soc. 44, 14 (1967)

[6]The present results are not however the quantal version of the Strong Coupling Theory of A. F. Wagner and E. K. Parks, J. Chem. Phys. 65, 4343

(1976) The essential difference is that the present state-to-state results are guaranteed to reproduce the transition state theory rate (Ref. 7)

[7]One can also consider extensions of the present results such that the averaged rate is that of the "unified" statistical theory [W. H. Miller, J. Chem. Phys. 65, 2216 (1976)] which is intermediate between a "loose" and a "tight" transition state.

[8]A. Kuppermann, J. Chem. Phys. 83, 171 (1979)

[9]R. D. Levine, Quantum Mechanics of Molecular Rate Processes (Clarendon, Oxford, 1969), p 116

[10]C. A. Coulson and R. D. Levine, J. Chem. Phys. 47, 1235 (1967)

[11]Reference 9, Section 2.6.3, Eq. (6.48)

[12]R. A. Marcus, J. Chem. Phys. 45, 2138 (1966)

[13]These should not be confused with other kinds of reaction probabilities, such as the square of the absolute values of the elements of the reactive part of the scattering matrix introduced in Eq. (5.2)

[14]Factorization properties of this type have been invoked in a variety of contexts. Closest perhaps to our approach is its use to express the reaction rate out of specific states of the reagents in terms of reaction rates into selected states of the reagents from selected states of the products for the reversed reaction [K. G. Anlauf, D. H. Maylotte, J. C. Polanyi, and R. B. Bernstein, J. Chem. Phys. 51, 5716 1969, and R. A. Marcus ibid 53, 604 (1970).] Note however that the relation between the detailed forward and reverse rate constants can be obtained without invoking the factorization assumption [H. Kaplan, R. D. Levine, and J. Manz, J. Chem. Phys. 13, 447 1976 or R. D. Levine, in The New World of Quantum Chemistry, edited by B. Pullman and R. Parr (Reidel, Dordect, 1976.]

[15]Reference 9, Section 3.4.0, Eq. 4.15 in particular, or Ref. 12 Eq. 9 in particular. See also K. Morokuma, B. C. Eu, and M. Karplus, J. Chem. Phys. 51, 5193 1969 and S. H. Lin, K. H. Lau, and H. Eyring ibid 55, 5657 (1971)

[16]G. C. Schatz and J. Ross, J. Chem. Phys. 62, 3162 1977

[17]S. H. Harms and R. E. Wyatt, J. Chem. Phys. 62, 3162 1975

[18]An example of such an alternative scheme is to use the principle of conservation of translational momentum [R. D. Levine and R. B. Bernstein, Molecular Reaction Dynamics (Clarendon, Oxford, 1974, Chap. 1)]

[19]D. G. Truhlar, A. D. Isaacson, and B. C. Garrett, in The Theory of Chemical Reaction Dynamics, edited by M. Baer (Chemical Rubber, Boca Raton, FL, 1984, Appendix I

[20]Even if two u, sets have the same $E_\alpha^{\prime\,max}$ they contribute separately to $N_\alpha(E)$. Therefore, these $E_\alpha^{\prime\,max}$ have at least a $2J + 1$ degeneracy corresponding to the M quantum number

[21]J. M. Bowman and K-T Lee, J. Chem. Phys. 72, 5071 (1980)

Collinear quasiclassical trajectory study of collision-induced dissociation on a model potential energy surface[a]

Jack A. Kaye[b] and Aron Kuppermann

Arthur Amos Noyes Laboratory of Chemical Physics,[c] California Institute of Technology, Pasadena, California 91125

Quasiclassical trajectory calculations have been carried out at energies above the threshold for collision-induced dissociation for a model symmetric collinear atom–diatomic molecule system. Exact quantum mechanical calculations have shown that quasiclassical trajectories give a qualitatively correct picture of the dynamics in this system, in so far as reaction and total dissociation probabilities are concerned. Trajectories leading to dissociation are found to lie almost entirely in well-defined reactivity bands, with the exception of a few occurring in a small chattering region in which the outcome of the trajectory is extremely sensitive to its initial conditions. The energy distribution functions of the dissociated atoms are obtained and shown to vary substantially with initial conditions (reagent vibrational and translation energy). The form of these distributions is, to a major extent, determined by the position and width of the reactivity bands. The different dissociation reactivity bands are shown to be associated with different types of trajectories. Part of the vibrational enhancement of dissociation arises from the fact that the simplest possible trajectory leading to dissociation (one which crosses the symmetric stretch line only once prior to the onset of dissociation) is not obtained with ground state reagents.

I. INTRODUCTION

The collision-induced dissociation (CID) of diatomic molecules

$$A + BC \rightarrow A + B + C \qquad (1)$$

is a process of great fundamental interest in chemistry, particularly at the high temperatures associated with shock waves, both in the laboratory[1] and in interstellar space.[2] The *ab initio* calculation of CID rates has proven to be extremely difficult, as one must have accurate methods for calculating the potential energy surface for the collision, solving for the dynamics, and then integrating the coupled rate equations to obtain expressions for the rate of disappearance of the diatomic molecule.

The development of accurate methods for solving for the dynamics has been especially difficult. Kinematic and quasiclassical trajectory (QCT) calculations have been extensively used to study CID.[3] The number of studies incorporating quantum mechanical effects, either by a semiclassical or a purely quantum mechanical approach, is much smaller.[4-11] Most of these studies have been restricted to collinear collisions in which reactive processes of the type

$$A + BC \rightarrow AB + C \qquad (2)$$

are not permitted. Noncollinear collisions in nonreactive systems have been studied by a semiclassical method by Rusinek.[5(a)] There have been published, however, three purely quantum calculations in which reaction and dissociation were allowed to compete, all of them for collinear collisions:

the wave packet approach pioneered by Kulander,[6,10(b)] the hyperspherical coordinate coupled-channel method developed independently in our laboratories,[7] and by Hauke, Manz, and Römelt,[8] and the multiple collision approach of Beard and Micha[9] (which has been applied to a nonreactive system).

The availability of accurate quantum mechanical (QM) results for CID has increased interest in QCT studies. In particular, Kaye and Kuppermann[7(b)] have shown that for the collinear model system they studied, the QCT results for the reaction probabilities and the total CID probabilities were qualitatively similar to the QM ones. Since the model system involves light masses (each of the atoms A, B, C have a mass equal to that of a hydrogen atom) and weakly bound (by 0.22 eV) molecules, quantum effects might be expected to be important. This suggests that QCT calculations might be useful predictors of the gross features of CID in reactive systems. Good agreement between CID probabilities from semiclassical[5(b)] and quantum mechanical[4(c)] calculations for a model collinear nonreactive system has also been reported. One must approach this with some caution, however, as in a different nonreactive system, Gray et al.[10a] have obtained major differences in the dissociation probability between their QCT results and the QM results of Knapp and Diestler[11] for the same system.

In order to help gain a better understanding of the dynamics of this model system, we describe in this paper a reactivity band analysis of the QCT results. Reactivity bands are those regions of the two-dimensional space spanned by the system's energy and the initial diatomic reagent vibrational phase in which the outcome of the collision (chemical reaction, dissociation, or nonreaction) is the same.

Such analyses have been extensively applied to collinear reactive systems below dissociation[12-14] and have also been applied to a collinear nonreactive system above dissociation.[10a] A classical phase space analysis of CID in such a

system has recently been performed.[14(a)] We examine bandedness in the plots of trajectory outcome (reaction, nonreaction, dissociation) as a function of initial vibrational phase of the diatomic molecule and the relative kinetic energy. A discussion of the regions separating nonreactive, dissociative, and reactive bands for the collinear $H + H_2$ system has also been published recently.[14(b)]

We also consider the variation of the vibrational action of the diatomic product of nonreactive and reactive collisions with initial vibrational phase. In dissociative collisions we examine how the partitioning of the energy among the three product atoms varies with initial vibrational phase and reagent translational energy. We also examine individual trajectories in order to understand the origin of the reactivity bands.

II. CALCULATION PROCEDURE

The QCT calculations have been performed using standard methods.[15] The model potential energy surface used has been described previously[7(b)]; we repeat here its basic features. It is of the rotating Morse-cubic spline type[16] and has asymptotic Morse oscillator parameters[17] of $D_e = 0.22$ eV, $R_{eq} = 1.400\,83$ bohr, and $\beta = 1.6$ bohr^{-1}. There is a barrier to exchange of 0.14 eV. Equipotential contours of this surface are plotted, together with selected trajectories, in several of the figures in this paper (see Sec. IV). A schematic diagram showing the features of this potential energy surface along its minimum energy path and the energy levels of the two vibrational states is presented in Fig. 1.

The trajectories were obtained with an integration time step of 5.41×10^{-17} s. Energy was conserved to four digits in these calculations. Integration of trajectories began with the distance from the incident atom to the center of mass of the diatomic molecule at 12 bohr.

To determine dissociation probabilities and rough boundaries for reactivity bands, we initially calculated 100 trajectories per energy at regularly spaced values of the initial vibrational phase Φ. At selected energies, we substantially narrowed the phase grid near the boundaries of the reactivity bands. Below dissociation we calculated 50 trajectories
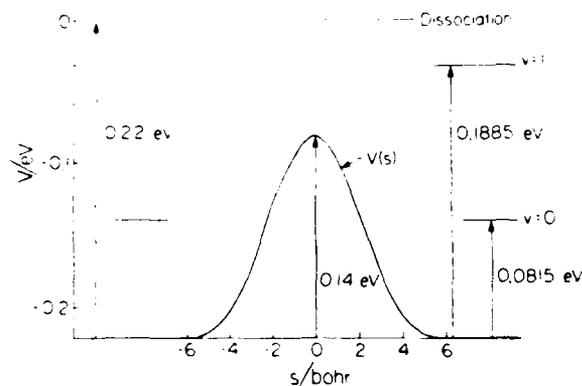

FIG 1 Schematic diagram of the potential energy function characteristics along the minimum energy path s is the distance along the path measured from the saddle point configuration. and $V(s)$ is the corresponding potential energy The horizontal lines indicate the energy levels of the bound states of the isolated diatomic molecules and of the dissociated configuration

per energy at regularly spaced ($\pi/25$ rad) values of the initial vibrational phase and subsequently narrowed the grid near the band boundaries.

We have also determined the partitioning of kinetic energy among the atoms after the collision. The quantity of greatest interest is the fraction f_X^D (X = A, B, C) of the available kinetic energy E' (the energy of the system with respect to the three infinitely separated atoms at rest) in dissociative collisions in each of the atoms at the end of the collision. [This quantity is labeled E in Refs. 7(b) and 7(d).] In dissociative collisions, the collision was defined to be over when both internuclear distances R_{AB} and R_{BC} were greater than 6.0 bohr and were increasing with time. The sums of the kinetic and potential energies of the AB and BC pairs were each required to be greater than D_e. The corresponding fractions f_A^N for atom A in nonreactive collisions and f_C^R for atom C in reactive collisions are defined similarly. In these cases, the available kinetic energy is defined as the difference between the total energy and the potential energy (measured with respect to the bottom of the isolated diatomic molecule well) when the trajectory was terminated. Plots of these quantities vs initial vibrational phase will connect smoothly to the f_A^D and f_C^D curves across the boundary of the reactivity bands. From the fractional energy vs initial vibrational phase data, one may calculate the probability $(dP'_{f_A})_c$ of the fractional kinetic energy f_A of atom A after dissociation being in the range $f_A + df_A$ for a collision in which the diatomic molecule is initially in state v. It is connected to the slope of the curve relating the initial vibrational phase Φ_i (in radians) which gives rise to a dissociative trajectory to the final atom A fractional kinetic energy by

$$(dP'_{f_A})_c = df_A \frac{\pi}{2} \sum_i |d\Phi_i/df_A|_i. \qquad (3)$$

The summation extends over all of the separate regions of initial phase giving rise to dissociation known as dissociative phase segments. The subscript c emphasizes the classical nature of this probability. The $(\frac{1}{2}\pi)$ factor is included so that $(dP'_{f_A})_c$ will be appropriately normalized:

$$\int_{f_A^{min}}^{f_A^{max}} (dP'_{f_A})_c = (P_i^D)_c. \qquad (4)$$

where $(P_i^D)_c$ is the total dissociation probability for a molecule initially in state v. The limits of integration in Eq. (4). f_A^{min} and f_A^{max}, can easily be shown to be given by[18]

$$f_A^{min} = \frac{m_B + m_C}{m_A + m_B + m_C} \frac{m_A m_C}{m_A m_C + m_B(m_A + m_B + m_C)}, \qquad (5a)$$

$$f_A^{max} = \frac{m_B + m_C}{m_A + m_B + m_C}. \qquad (5b)$$

For the system being considered, they lead to $f_A^{min} = 1/6$ and $f_A^{max} = 2/3$. As a result of Eqs. (3) and (4) we have

$$(P_i^D)_c = \frac{1}{2\pi} \sum_i (\Delta\Phi_i)_i. \qquad (6)$$

where $(\Delta\Phi_i)_i$ is the width of the dissociative phase segment i.

The evaluation of the derivative in Eq. (3) is complicated by the possibility of minima or maxima in the f_A vs Φ curves

which permits $\Phi(f_A)$ to be a multiple valued function of f_A. We separate those regions in which $d\Phi/df_A$ is positive and negative and then separately obtain the derivatives by a three-point finite difference procedure. The resulting derivatives are then used as the input for a cubic spline procedure which permits their calculation as a function of f_A. We next sum the absolute values of the derivatives over all branches of each dissociative reactivity band and over all such dissociative reactivity bands, and divide by 2π for normalization purposes. The resulting curve (called a partitioning probability curve) may contain some numerical noise associated with the numerical differentiation procedures; we have visually smoothed these as well as the spline-induced oscillations.

III. RESULTS

We have studied collisions up to energies beyond twice the dissociation energy. In this energy range both reaction and dissociation occur. Plots of the reaction and dissociation probability vs initial relative translational energy E_i are shown for initial reagent states $v = 0$ and $v = 1$ (the only ones possible) in Figs. 2 and 3, respectively. For both initial reagent states, the reaction probability is zero below a threshold energy, increases rapidly with energy to a large value (0.86 for $v = 0$, 0.96 for $v = 1$), and then decreases to zero (for $v = 0$) or a value just above zero ($v = 1$). It then increases monotonically with energy. The dissociation probabilities for the $v = 0$ and $v = 1$ reagents behave quite differently from each other, however. In the $v = 0$ case, no dissociation is observed until F_0 is substantially (0.08 eV) above its energetic threshold; as the energy increases beyond that, the probability increases slowly, reaching a value of 0.27 at the highest energy studied. For the $v = 1$ case, disso-


FIG. 3. Probabilities for reaction P_1^R (solid line) and dissociation P_1^D (dashed line) in collisions of vibrationally excited molecules as a function of the reagent translational energy E_1, and total energy collision energy E. (See Fig. 2 caption for details.)

ciation sets in at 0.02 eV above its energetic threshold, increases rapidly with energy to a maximum of 0.33 and then decreases rapidly to 0.02 before again increasing with energy up to a value 0.39 at the highest energy studied. It should be emphasized that all of these results are qualitatively similar to the exact quantum mechanical results for this system presented in Ref. 7(b).

We next examined bandedness in plots of trajectory outcome vs initial vibrational phase and relative translational energy. Plots of the reactivity bands for this system are shown in Figs. 4 and 5 for reagent states $v = 0$ and 1, respectively, for energies above the threshold for CID. Unlike reactivity band plots normally used in studies of reactive atom-diatomic molecule collisions at energies below dissociation,[12,13] in which there are only two possible outcomes of a trajectory (reaction or nonreaction), there are three possible outcomes here: reaction (R), indicated by shaded regions of the figures; dissociation (D), indicated by the speckled regions, and nonreaction (N), indicated by the clear regions. The dissociative band centered near 2.0 rad and 0.17 eV

FIG. 2 Probabilities for reaction P_0^R (solid line) and dissociation P_0^D (dashed line) in collisions of ground vibrational state molecules as determined by quasiclassical trajectory calculations as a function of the collision energy. The reagent translational energy E_0 is indicated on the lower abscissa, the total energy E (sum of the vibrational energy —measured with respect to the bottom of the isolated diatom potential energy well—and the translational energy) is indicated on the upper abscissa. The arrow points to the energy at which the dissociation channel becomes energetically accessible. The detailed nature of the reaction probability curve close to threshold is only approximately correct due to the limited number of trajectories computed in that energy region.


FIG. 4 Reactivity band plot for reaction and dissociation in collisions of ground state molecule. Reactive (R) bands are indicated by shading, dissociative (D) bands are indicated by speckling. The solid white region is nonreactive (N). Both the translational energy E_0 (left ordinate) and the total energy E (right ordinate) are indicated. E is defined in the caption for Fig 2
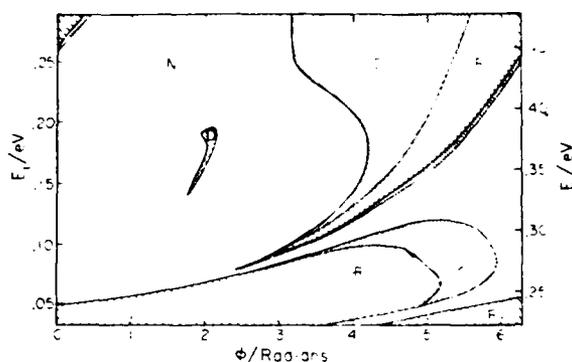
FIG 5. Reactivity band plot for reaction and dissociation in collisions of vibrationally excited molecules. Band type is indicated as in Fig 4. Axis labeling is also as in Fig 4. No effort is made to accurately portray the band structure in the chattering region. (See the text.)

FIG. 7. Final action v_f as a function of the initial phase Φ for a collision involving a ground state diatomic molecule at a reagent translational energy E_0 of 0.388 eV. A solid line is used to connect results of nonreactive trajectories, a dashed line is used to connect results of reactive trajectories. The shaded areas indicate those regions of the initial phase giving rise to dissociative trajectories, in which the action cannot be defined in the usual way. N, D, and R indicate nonreactive, dissociative, and reactive regions, respectively. The trajectories were begun with the distance from atom A to the center mass of BC being 12 bohr.

translational energy for $v = 1$ in Fig. 5 is enlarged in Fig. 6.

Fairly well-defined bands are seen to exist above dissociation. When one decreases the difference between neighboring initial phases substantially (to about 0.002 rad), one may find blurring of the boundaries and formation of a "chattering" region[13,19,20(a),21] in which the outcome of the trajectory varies strongly with small changes in the initial phase. This effect is most severe below 0.10 eV translational energy in the $v = 1$ case, where the high energy reaction and dissociation bands come to a cusp (see Fig. 5). For example, at 0.085 eV initial reagent translational energy, between 2.50 and 2.70 rad initial phase, there are four separate dissociative segments, two reactive segments, and one nonreactive segment obtained when the grid spacing of 0.002 rad is used. The total width of all the dissociative segments in this region is 0.052 rad. The dissociation probability produced by this region is only 0.8%, which is far smaller than the contribution at this energy from the large band centered at 5.5 rad. Chattering is also seen near the boundary between reactive and nonreactive bands at energies below dissociation.

We next consider the variation of the vibrational energy of the diatomic molecule resulting from reactive or nonreactive collisions. Normally, to examine this quantity one pre-

pares plots of the actions of the diatomic molecule at the end of the trajectory as a function of initial phase at a sequence of energies.[10(a),12,20,21] At energies above dissociation, one cannot calculate the action in the usual way, and one is left with gaps in the action vs phase plots. Examples of these plots are shown in Figs. 7 and 8 for the highest energies studied (reagent translational energies of 0.388 eV for $v = 0$ and 0.2815 eV for $v = 1$). Solid lines are used to indicate nonreactive processes and dashed lines are used to indicate reactive ones. The shaded regions mark those regions of initial phase in which the trajectories are dissociative and hence no action can be defined. In both of these figures, the dissociation is seen to occur between regions of high final action in reactive and nonreactive collisions (the maximum allowable final action in this system is 1.981, which is related to the fact that it only supports two bound states). This is quite reasonable behavior, as for dissociation to occur there must be more than the dissociation energy present in each diatomic molecule. Hence, the transition between reactive or nonreactive regions is expected to occur where the final action of the diatomic molecule equals its maximum value.

A somewhat different behavior is shown in Fig 9, in which we plot the final action vs initial phase in a collision

FIG 6 Enlarged view of the small dissociative band (from Fig 4) in collisions of vibrationally excited molecules. All markings and axes are as in Fig. 4
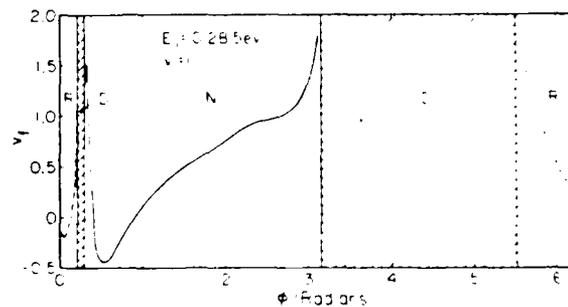

FIG 8 Final action v_f as a function of initial phase Φ for a collision involving vibrationally excited molecules at a reagent translational energy E_0 of 0.2815 eV. All markings are as in Fig 7
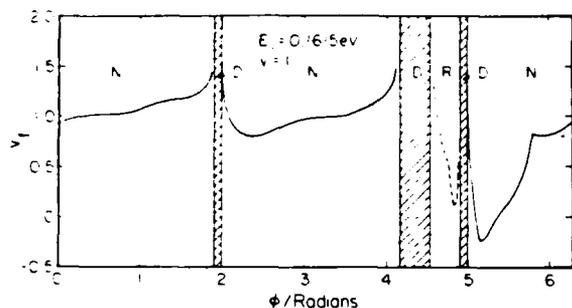
FIG. 9 Final action v_f as a function of initial phase Φ for a collision involving vibrationally excited molecules at a reagent translational energy E_1 of 0 1615 eV. All markings are as in Fig. 7.

FIG. 10. Final action v_f as a function of initial phase Φ for a collision involving ground state molecules at a reagent translational energy E_1 of 0 178 eV. All markings are as in Fig 7. Note the expanded scale of the ordinate

with $v = 1$ reagent and a reagent translational energy of 0.1615 eV. Here there are three dissociative regions. Two are found between the reactive and nonreactive initial phase segments, and one is in the middle of the large nonreactive segment. The latter is part of the small dissociative band located near 2 rad initial phase between 0.15 and 0.20 eV initial reagent translational energy in Fig. 5 (and enlarged in Fig. 6). As the initial phase for reactive trajectories is varied so it closely approaches that in the dissociative region, the final action increases, suggesting that the consideration of dissociation as a limiting case of vibrational excitation is an appropriate concept.

There is a substantial difference between the product state distribution in collisions with $v = 1$ reagent at initial relative energies of 0.2815 eV (Fig. 8) and at 0.1615 eV (Fig. 9). At the higher energy, the likelihood of vibrational deexcitation, as measured by the large region of initial phase over which the final action is substantially smaller than one, is significantly greater than at the lower energy. At the lower energy, from $\Phi = 0$ to the second dissociative segment (at 4.15 rad), the final action never becomes smaller than 0.8. Thus, increasing translational energy seems to lead to increasing vibrational nonadiabaticity in nonreactive collisions. The small likelihood of reaction in these high translational energy regions makes it difficult to draw any conclusions concerning that process. A similar trend has been observed in the exact quantum mechanical calculations on this system.[22]

Further evidence of the tendency towards vibrational adiabaticity at low energies can be seen by considering a collision with $v = 0$ molecules at an energy (0.178 eV initial translational energy) at which only nonreactive collisions occur—no dissociation or reaction was found. A plot of the final action as a function of initial phase for this collision is given in Fig. 10. The near adiabaticity may be seen by noting that the total range of final actions in the figure is from $- 0.12$ to 0.19, corresponding to final vibrational energies of 0.0639 and 0.1079 eV, respectively (the zero point energy of the diatomic reagent is 0.0818 eV). Hence, at most 15% of the initial translational energy was converted to vibrational energy in the collision. Another interesting feature of this figure is its relatively complicated structure. In spite of the fact that all collisions are nonreactive and nearly adiabatic,
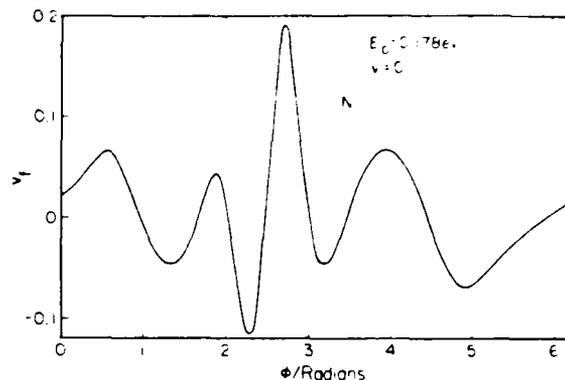
there is still a strong variation in the dependence of the final action on the initial phase.

To indicate what happens when the boundary regions between the reactivity bands become blurred, we present in Fig. 11 a plot of final action vs initial phase for the collision with a $v = 1$ molecule at a relative translational energy of 0.085 eV for initial phases in the range 2.40–3.10 rad. In this region one sees five separate dissociative segments, four of which occur between 2.50 and 2.70 rad. These may be thought of as being distinct from the larger dissociative segment between 2.90 and 3.10 rad. The latter band is part of the large dissociative band seen in the lower right-hand portion of Fig. 5. The action vs initial phase curves are fairly smooth between the dissociative segments. Away from the lower tip of the large dissociation and reaction band in Fig. 5, the boundaries are smoother. Figure 11 seems to represent, then, an upper limit to the complexity of such a diagram.

We next consider the partitioning of kinetic energy among the three atoms in dissociative collisions and also among the final atoms and diatom in reactive and nonreactive collisions. In all cases the collision partners are A and BC. The calculation of the energy partitioning fraction f_X has been described in Sec. II. Plots of these quantities as a function of the initial phase are shown in Figs. 12–17 for
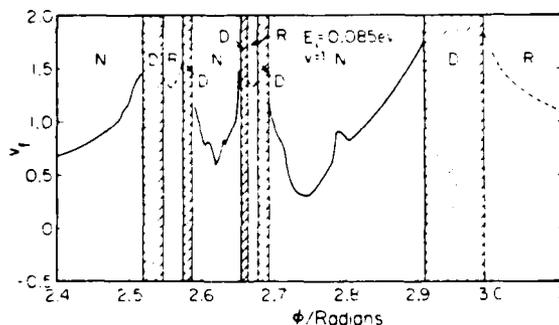

FIG. 11 Final action v_f as a function of the initial phase Φ for a collision involving vibrationally excited molecules at a reagent translational energy E_1 of 0.085 eV. The initial phases are limited to the chattering regions described in the text and the regions of slightly lower and higher initial phase. All markings are as in Fig 7.
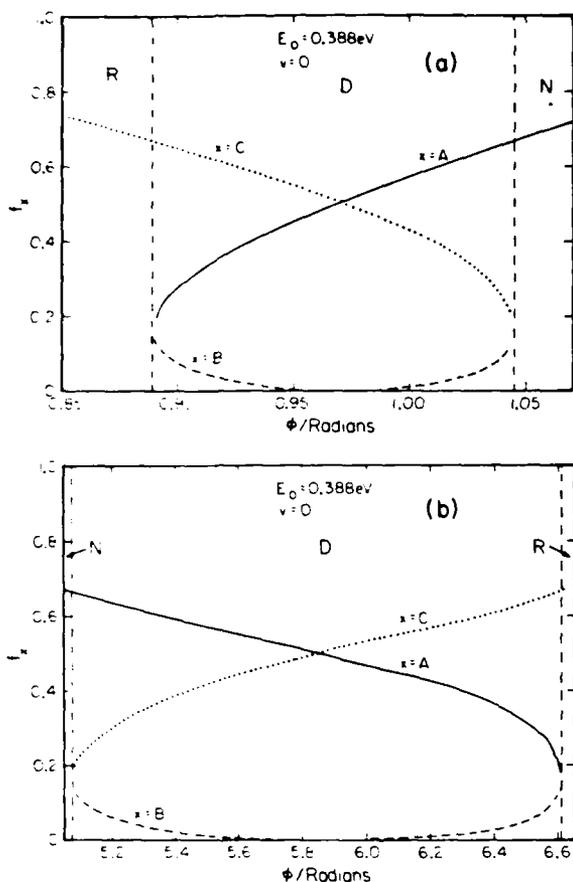
FIG. 12 Final energy fractions f_X (X = A, B, C) (defined in Sec. II) as a function of the initial phase Φ for the dissociative bands seen in collisions of ground state molecules at a reagent translational energy E_0 of 0.388 eV. A solid line is used for atom A, a dashed line for atom B, and a dotted line for atom C. A dashed-dotted line marks the approximate boundary between bands. The curve for atom A is continued into the nonreactive region and the curve for atom C is continued into the reactive region by a procedure described in the text. (a) The small band from 0.90 to 1.03 rad initial phase; (b) the large band from 5.10 to 6.60 rad.


FIG. 14. Final energy fractions f_X as a function of initial phase Φ for dissociative bands in collisions of vibrationally excited molecules at a reagent translational energy E_1 of 0.2815 eV. (a) The small band from 0.25 to 0.31 rad; (b) the large band from 3.20 to 5.50 rad. All markings are as in Fig. 12.

FIG 13 Final energy fractions f_X as a function of initial phase Φ for dissociative bands in collisions of ground state molecules at a reagent translational energy E_0 of 0.233 eV. All markings are as in Fig. 12.

initial phases near which dissociation occurs for a variety of initial conditions. A few important features are observed in these figures, and we review these here.

First, the curves are quite smooth in the dissociation regions. At the border between reactive and dissociative collisions, f_C smoothly matches onto the f_C^R curve, and at the border between nonreactive and dissociative collisions, f_A smoothly matches onto the f_A^N curve. In all cases, the matching occurs at a value of the energy fraction of 2/3; this is the maximum value f_A or f_C can take in the dissociative region for a system of three equal masses. The small values of f_B are also a requirement of the mass combination (for the case of three equal masses, f_B is required to be smaller than 1/6).

Second, two types of partitioning curves are seen. For those dissociative bands confined between one reactive and one nonreactive band, f_A and f_C must both have regions where they are large ($\approx 2/3$) and small ($\approx 1/6$). For those bands confined between two nonreactive bands, the f_A vs phase curve must have a minimum. The presence of such a minimum will have a major effect on the partitioning probabilities to be presented below. In principle, one might obtain

FIG. 16. Final energy fractions f_X as a function of initial phase Φ for dissociative bands in collisions of vibrationally excited molecules at a reagent translational energy E_1 of 0.015 eV. All markings are as in Fig. 12.
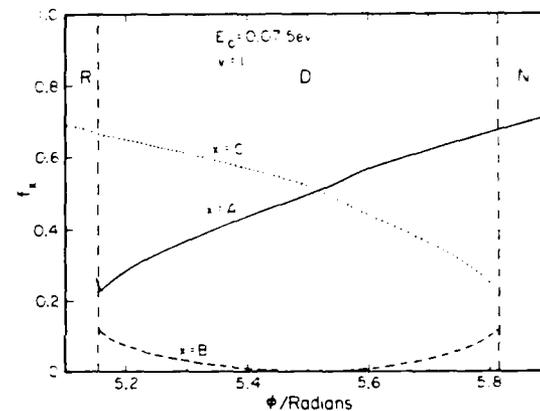

FIG. 17. Final energy fractions f_X as a function of initial phase Φ for dissociative bands in collisions of vibrationally excited molecules at a reagent translational energy of E_1 of 0.0715 eV. All markings are as in Fig. 12.

FIG. 15. Final energy fractions f_X as a function of initial phase Φ for dissociative bands in collisions of vibrationally excited molecules at a reagent translational energy E_1 of 0.1815 eV. (a) band from 2.04 to 2.12 rad; (b) band from 4.25 to 4.80 rad. (c) band from 5.32 to 5.36 rad. All markings are as in Fig. 12.

dissociative bands confined between two reactive ones, but such bands have not yet been observed.

Finally, we present results for the partitioning probability $(dP'_{f_A}/df_A)_c$ defined in Sec. II. These are shown in Figs. 18–23 for the six sets of initial conditions for which energy fractions were shown as a function of initial phase in Figs. 12–17. The partitioning probabilities in the first and last of the former figures are compared with the corresponding quantum mechanical ones elsewhere.[7(d)] As mentioned pre-

FIG. 18. Partitioning probability $(dP'_{f_A}/df_A)_c$ (see Sec. II) as a function of energy fraction f_A of atom A for dissociation in collisions of ground state molecules at a reagent translational energy E_0 of 0.388 eV.
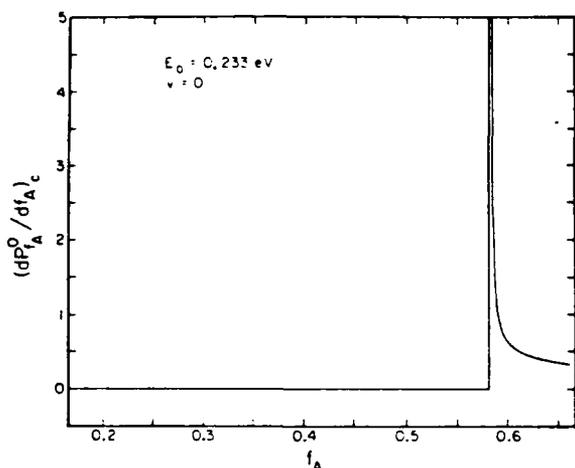
FIG. 19. Partitioning probability $(dP^0_{f_A}/df_A)_c$ as a function of energy fraction f_A for atom A for dissociation in collisions of ground state molecules at a reagent translational energy E_0 of 0.233 eV. The probability is zero for values of the energy fraction f_A below that at which it diverges (≈ 0.58).
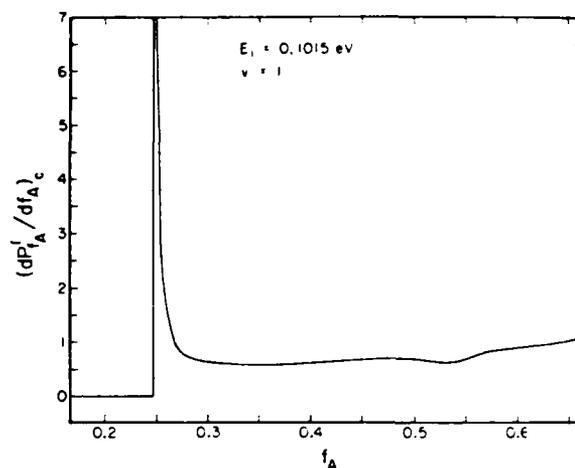
FIG. 22. Partitioning probability $(dP^1_{f_A}/df_A)_c$ as a function of energy fraction f_A for atom A for dissociation in collisions of vibrationally excited molecules at a reagent translational energy of 0.1015 eV. The probability is zero for values of the energy fraction f_A below that at which it diverges (≈ 0.25).
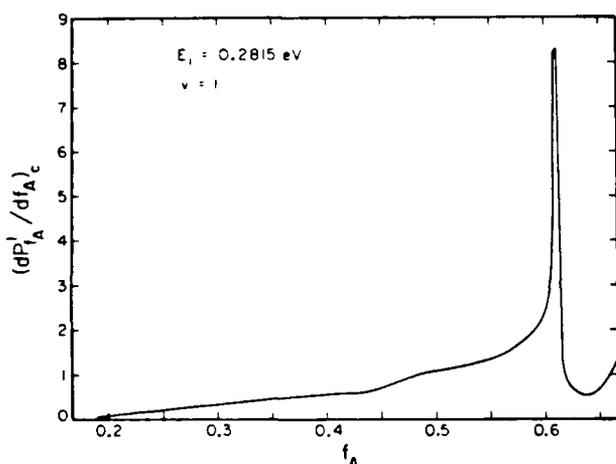
FIG 20 Partitioning probability $(dP^1_{f_A}/df_A)_c$ as a function of energy fraction f_A for atom A for dissociation in collisions of vibrationally excited molecules at a reagent translational energy E_1 of 0.2815 eV.
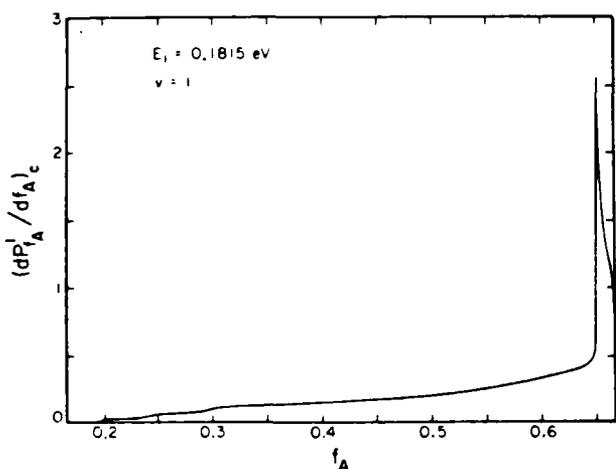
viously (see Sec. II), there are some numerical difficulties involved in generating these curves, due to the necessity of interpolating and differentiating the f^D_X vs phase curves, as well as in obtaining highly accurate f^D_X values in regions where it is nearly independent of phase, thus making a major contribution to $(dP^r_{f_A}/df_A)_c$ as can be seen from Eq. (3). The details of the curves are less certain (and of less interest) than their broad, overall shape, which is expected to be less sensitive to numerical methods. They all appear quite different from each other, and we can rationalize much of their form simply from the reaction and dissociation probabilities, the kinematics of the system, and the existence of well-defined dissociation bands in the reactivity band plots (Figs. 4–6). We will consider this issue in greater detail in Sec. IV.

There are a few features of Figs. 18–23 which will prove to be of most interest. First is the tendency of the partitioning

FIG 21 Partitioning probability $(dP^1_{f_A}/df_A)_c$ as a function of energy fraction f_A for atom A for dissociation in collisions of vibrationally excited molecules at a reagent translational energy E_1 of 0.1815 eV.
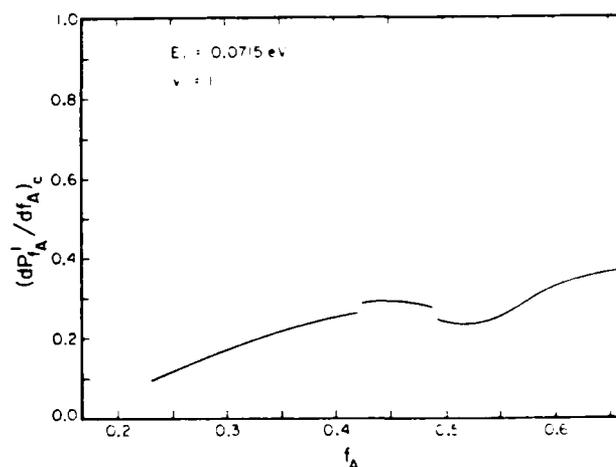
FIG 23 Partitioning probability $(dP^1_{f_A}/df_A)_c$ as a function of energy fraction f_A for atom A for dissociation in collisions of vibrationally excited molecules at a reagent translational energy of 0.0715 eV

probabilities to have their maxima near the maximum allowable energy fraction of 2/3, although this is not uniformly true (see particularly Fig. 22, in which the partitioning probability diverges at an $f_A = 0.25$). Second, in four out of the six cases studied, the partitioning probability either has poles (Figs. 19 and 22) or sharp peaks (Figs. 20 and 21).

IV. DISCUSSION

In this section we consider first the implication of the bandedness of dissociative trajectories as seen in the reactivity band plots (Figs. 4–6). In particular, we will focus on how this bandedness, when coupled with the calculated reaction probabilities and the kinematics of the collision, can be seen to lead to the general structure of the partitioning probability curves, such as those shown in Figs. 18–23. We then consider the origins of the bandedness of the dissociative trajectories and show that a close relationship can be established between the separate bands and different types of trajectories leading to dissociation.

A. Implications of the dissociative reactivity bands

Trajectories which lead to dissociation have been found to occur, as a general rule, in well-defined bands in the reactivity band plots (Figs. 4–6). Exceptions to this trend are found for collisions of a $v = 1$ molecule in which the reagent translational energy is in the range from 0.07 to 0.10 eV. In this region, the trajectory outcome may vary substantially with small changes in the initial phase of the diatomic molecule. This is somewhat reminiscent of the observation of chattering regions in the final action vs initial phase plots seen in reactive atom–diatomic collisions (at energies well below dissociation), particularly the $H + H_2$,[13,20(a)] $F + H_2$,[19,21] and $Cl + HCl$[23] reactions. Unlike in those cases, where the outcome of the trajectory appears to be random, seemingly smooth (but quite short) curves of final action vs initial phase can be obtained by the use of sufficiently small grid spacing (0.002 rad).

In most cases, dissociative trajectories can be thought of as limiting cases of reactive or nonreactive collisions giving rise to vibrational excitation of products. This can be seen in two interrelated ways. For values of the initial phase only slightly different from those of the trajectories which lead to dissociation, the diatomic molecules remaining at the end of the collision will be highly vibrationally excited. If one considers the fractional energy as a function of initial phase, such as that plotted in Figs. 11–17, one sees that the curve of atom A smoothly matches onto that for atom A in nonreactive collisions and that for atom C smoothly matches onto that for atom C in reactive collisions.

The nature of the dissociative segment (defined by the type of nondissociative segments between which it is confined at a given energy) will play a major role in determining the appearance of the partitioning probability curves. If the dissociative segment is confined between one reactive and one nonreactive segment, the partitioning probability curve should cover essentially all the accessible regions of energy fractions (1/6–2/3 in this case). If, on the other hand, the segment is confined between two nonreactive or two reactive

ones, the partitioning probability curves will cover only a subset of the allowable energy fractions and must have at least one place where they diverge. This divergence occurs at values of f_A for which the f_A vs initial phase curves show extrema, as can be seen from Eq. (3). For the simplest case in which the dissociative segment is confined between two nonreactive segments, the divergence will occur at a minimum of f_A, and the dissociation probability below the singularity will vanish while above the singularity, it is continuous. Such curves are observed in Figs. 19 and 22. For the other simple case, a maximum in f_A will occur and the dissociation probability will vanish above the singularity and be continuous below it. Trajectories corresponding to this case have not been observed in the present system. More complicated situations might arise. More generally, one may, in principle, find curves of f_A vs ϕ for dissociative segments confined between two nonreactive ones having $n + 1$ minima and n maxima (leading to $2n + 1$ divergences in partitioning probability curves). Similarly, for dissociative bands confined between two reactive ones, there may be $n + 1$ maxima and n minima. No such curves (multiple minima and maxima) were observed, however.

These figures demonstrate that the value of the energy fraction at which the partitioning probability diverges can be quite close to its maximum or minimum permitted value. Precisely at what values of the energy fraction the partitioning probability diverges will depend on the shape of the dissociation and reaction reactivity bands at the energy being considered. If for instance, one is at an energy fairly near the onset of the reaction band, the minimum in the energy fraction vs phase plot will occur at a value of the energy fraction close to 1/6. This is the case in Fig. 22 (for which the important reaction and dissociation reactivity bands may be seen in Fig. 5). If the energy is such that one is not close to the onset of the reaction band, the minimum will occur at values of the energy fraction close to 2/3.

These discontinuities are very similar in appearance to those associated with rainbow scattering observed in the classical scattering of a particle by a spherically symmetric potential.[24] In that problem, the differential cross section is zero on the high angle side of the rainbow, while it has a smooth dependence on the deflection angle or the low angle side. These rainbows are analogous to the discontinuities here because the partitioning of the energy among the atomic products of CID is related to the asymptotic orientation of the classical trajectory with respect to the coordinate axes when plotted in the usual Delves mass-weighted coordinate system.[7(b)]

Certain types of curves of energy fraction vs phase in dissociative collisions which might in principle occur have not been observed in these studies. For instance, in no cases were curves with more than one minimum or maximum obtained. Hence, the partitioning probability diverges at one and only one energy fraction if it diverges at all. As mentioned earlier, no dissociative bands confined between two reactive bands were observed. Such bands would lead to partitioning probability plots opposite to those in Figs. 19 and 22: at all energy fractions above that at which the singularity occurs the probability would vanish. There seems to be no

reason why such bands should not exist, so we assume that their absence is a function of the particular potential energy surface and mass combination used.

The fact that reactive processes are less probable than nonreactive ones at the energies studied suggests that in dissociative collisions one may be more likely to find kinetic energy distributions in which atom A has the greatest portion of the available energy. This would give rise to the partitioning probability being dominated by high energy fractions. The range of energy fractions allowable is kinematically determined simply by the masses of the colliding particles, are given in Eqs. (5), which explains why only certain numerical regions of the energy fraction are allowed. Changing the masses would, therefore, change the partitioning probabilities of both kinematic and dynamic reasons.

The structure of the reactivity band plot differs very strongly for $v = 0$ and $v = 1$ molecule collisions, and this fact, coupled with the definite manner in which the position and width of the reactivity bands have been shown to determine the partitioning probabilities, suggest that one might obtain substantially different kinetic energy distributions from dissociation from the two reagent states at the same total energy. The same statement applies to translational energy. The simplest way of obtaining such different behaviors would be to locate an energy at which the dissociation from $v = 0$ occurs totally from a band which is confined between two nonreactive bands, while that from $v = 1$ occurs from one or more bands confined between one reactive and one nonreactive band. Thus, not only may the outcome of the collision (reaction, nonreaction, or dissociation) depend on the initial state, but the intimate details of dissociation may also be a function of the initial state.

B. Origin of the dissociative reactivity bands

Formation of reactivity bands in atom–diatomic molecule collisions has been observed in a variety of systems at energies below dissociation[12,13,20(a)]; banding has also been observed in a nonreactive system studied at energies above dissociation.[10(a)] The present paper is, to our knowledge, the first reactivity band study of dissociation in a reactive system. To explain the origin of reactivity bands, we are interested in understanding the nature of the trajectories which comprise each band. In particular, we focus on two questions. First, we want to know whether each separate band corresponds to different types of trajectories. Second, we want to know what happens near the boundaries between bands, especially in the chattering regions, such as that shown in Fig. 11, in which the outcome of the trajectory is extremely sensitive in the initial conditions of the trajectory.

Wright and Tan[12(c)] have shown in their study of the collinear T + HT system on the SSMK surface[25] that the two lowest energy reaction reactivity bands are comprised of different types of trajectories. In the lower energy band, reactive trajectories cross the symmetric stretch line only once, while in the higher energy band, they cross the symmetric stretch line three times. Representative trajectories are shown in Fig. 8 of Ref. 12(c). A similar correspondence can be drawn between the two reaction regions in Fig. 5 for collisions in which the diatom is initially in the $v = 1$ state. For
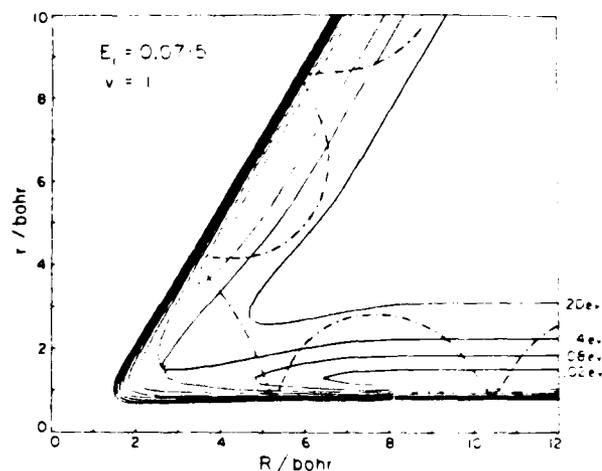
FIG. 24 Plot of typical reactive trajectory in the low energy reaction reactivity band for collisions of a vibrationally excited molecule. The trajectory is for an initial translational energy of 0.0715 eV and initial vibrational phase of 3.4558 rad. The integration of the trajectory was begun with $R = 12.8952$ bohr. The trajectory is superimposed on a plot of the potential energy surface for the system in Delves mass-scaled coordinates. Contours are drawn every 0.06 eV starting from 0.02 up to 0.50 eV with respect to the bottom of the well of the isolated diatomic molecule. The ✕ marks the saddle point for the reaction. Note that there is only one crossing of the symmetric stretch line.

the $v = 0$ case we show in Fig. 4 only the high energy reaction region; there is another one at lower energies responsible for the large values of P_0^R seen in Fig. 2. Trajectories comprising the lower reaction band in the $v = 1$ case cross the symmetric stretch line once (Fig. 24) while those in the higher band cross it three times (Fig. 25). Reactive trajectories must cross the symmetric stretch line an odd number of times; thus, these are the simplest kind of reactive trajectories possible. The same behavior is seen in collisions of ground state molecules; we do not show them here.
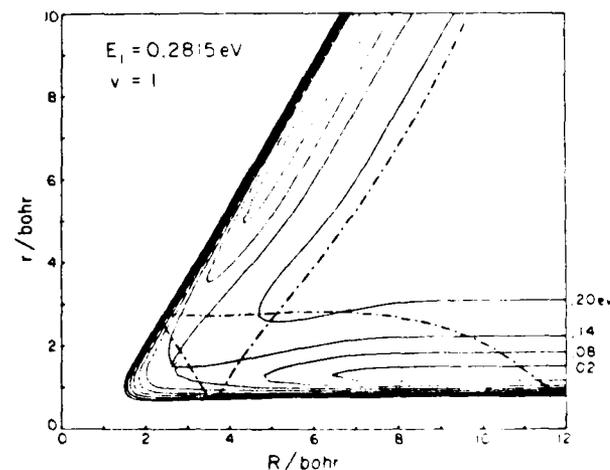

FIG. 25 Plot of a typical reactive trajectory in the high energy reaction reactivity band for collisions of vibrationally excited molecules. Trajectory is for initial translational energy of 0.2815 eV and initial vibrational phase of 0.2817 rad. All markings are as in Fig. 24

We next consider the nature of trajectories leading to dissociation. We focus our attention first on the single dissociation band (Fig. 4) for collisions of ground state molecules and two large bands (Fig. 5) for collisions of $v = 1$ molecules. We consider the small band for $v = 1$ isolated in the large nonreactive band and the overall chattering region later. Typical dissociative trajectories are shown in Figs. 26–28 for the dissociative band in $v = 0$ collisions, the first dissociative band in $v = 1$ collision, and the second such band in $v = 1$ collisions, respectively. In Figs. 26 and 28, the trajectory crosses the symmetric stretch line three times; in Fig. 27 the symmetric stretch line is crossed only once. The three crossings for Figs. 26 and 28 are associated with two internal collisions in the strong interaction region, the first between A and B and the second between B and C. For Fig. 27 the single crossing of the symmetric stretch line is also associated with two internal collisions, but in inverse order, the first between B and C and the second between A and B. This suggests that the separate dissociation bands are each comprised of trajectories crossing the symmetric stretch line a different number of times, just as was seen for reactive transitions. Andrews and Chesnavich[14(b)] have also noted that dissociative trajectories may originate on either side of the symmetric stretch line in symmetric (A–B–A) systems. Compared to the reactive case, things are not quite so simple in the dissociation case, however, as the trajectory need not cross the symmetric stretch line an odd number of times. In fact, trajectories which cross it twice have been observed in both of the $v = 1$ reactivity bands. The last crossing of the symmetric stretch line may occur (as does that in the trajectory shown in Fig. 27) at large values of the internuclear coordinates. Whether or not such a crossing takes place will depend on the partitioning of the energy among the three atoms. The final crossing may be thought to occur while the atoms are in the process of dissociating, even if the crossing occurs at fairly small values of the internuclear coordinates. Thus, the first dissociation reactivity band in the reactivity plot (in Fig. 5) may be thought of as being comprised of trajectories which cross the symmetric stretch line once pri-
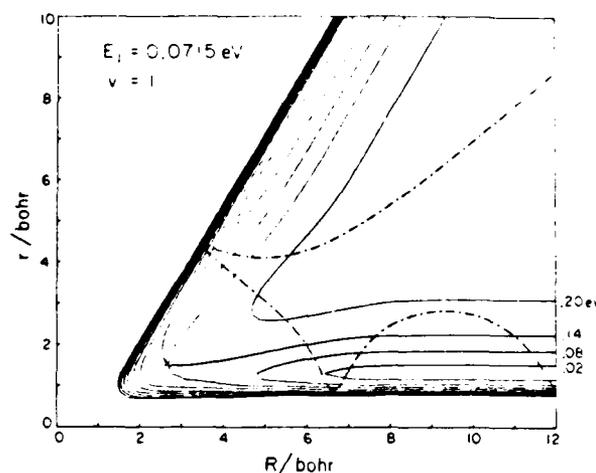
FIG. 27. Plot of a typical dissociative trajectory in the low energy dissociation reactivity band for collisions of vibrationally excited molecules. Trajectory is for initial translational energy of 0.0715 eV and initial vibrational phase of 5.3407 rad. All markings are as in Fig. 24.

or to the process of actually dissociating (during which they may again cross that line). In the second dissociation band for $v = 1$ and the only such band for $v = 0$, two crossings take place prior to the onset of dissociation, after which a third crossing may occur.

These observations allow one to make a simple physical picture to account for the observed vibrational enhancement of CID in this system. The simplest trajectory which may lead to dissociation does not occur when the molecule is in its ground state. It occurs when the molecule is in its excited state. Since more complicated trajectories appear to contribute only at higher energies, low energy dissociation is prevented in the ground state case. The qualitative agreement between the quasiclassical trajectory calculations and the exact quantum ones reported previously[7] indicate that this simple classical picture may be a reasonable one to use in
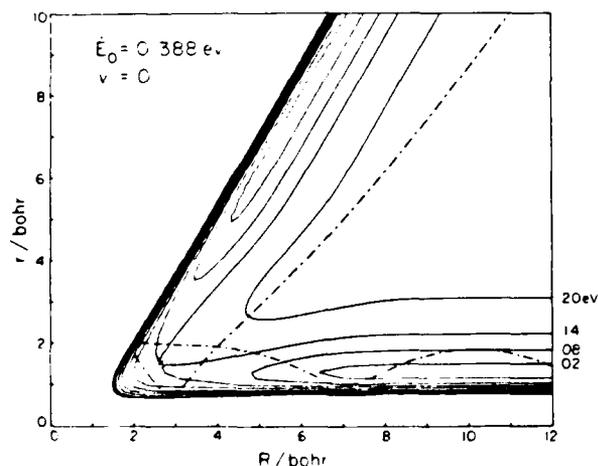
FIG 26 Plot of a typical dissociative trajectory in collisions of ground state molecules Trajectory is for initial translational energy of 0.388 eV and initial vibrational phase of 0.3142 rad All markings are as in Fig. 24.
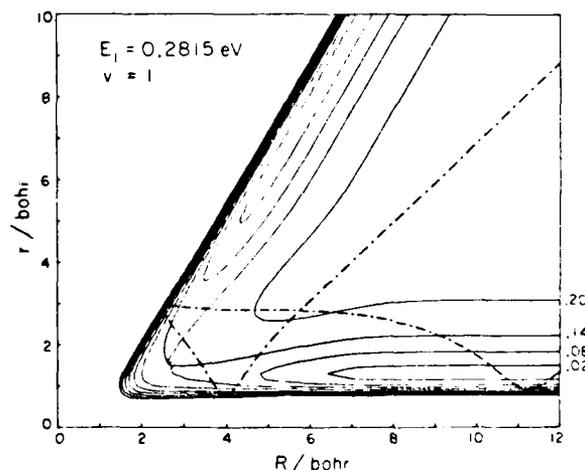

FIG 28. Plot of a typical dissociative trajectory in the large, high energy dissociation reactivity band for collisions of vibrationally excited molecules. Trajectory is for initial translational energy of 0.2815 eV and initial vibrational phase of 5.3407 rad All markings are as in Fig 24.
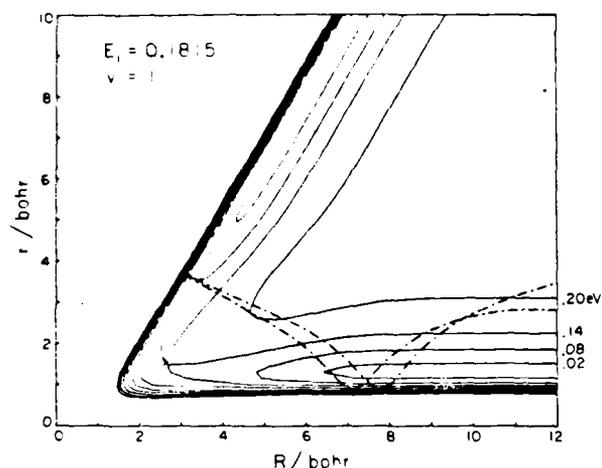
FIG. 29. Plot of a typical dissociative trajectory in the small dissociation reactivity band imbedded in the large nonreaction band for the collision of a vibrationally excited molecule. Trajectory is for initial translational energy 0.1815 eV and initial vibrational phase of 2.12 rad. All markings are as in Fig. 24.

FIG. 31. Plot of a dissociative trajectory in the chattering region shown in Fig. 11. Initial conditions are the same as for the trajectory in Fig. 29, except that the initial vibrational phase is 2.66 rad. All markings are as in Fig. 24.

attempting to understand the calculated vibrational enhancement of CID in this system.

We next wish to consider the small dissociation band seen in Fig. 5 (and enlarged in Fig. 6) near 2 rad and 0.18 eV reagent translational energy. A typical trajectory for this band is shown in Fig. 29. This trajectory is quite different from the dissociative ones seen in Figs. 26 and 28. This should not be surprising, however, and this small dissociative band is imbedded in a large nonreactive band and the other dissociative bands tend to be confined between reactive and nonreactive bands. Examination of nonreactive trajectories near the boundaries between the nonreactive and dissociative reactivity bands indicates that differences between the trajectories within them are quite small and become important only at large values of the internuclear coordinates.

This is a case then, in which the final outcome of the trajectory is not seen until well after the collision might be thought to be finished (R_{AB} large and increasing, R_{BC} fairly small).

We finally consider the chattering regions indicated in Fig. 11. In the regions of initial phase from 2.5 to 2.7 rad, the outcome of the trajectory varies greatly with small changes in the initial phase. Such regions have been observed in studies of reactions below dissociation, particularly the $H + H_2$[13,20(a)] and $F + H_2$[19,21] reactions. In these regions, the trajectories become very complicated, frequently bouncing back and forth many times in the strong interaction regions of the potential energy surface. Atom B is said to "chatter" between atoms A and C, hence the name chattering regions.

In this case, the trajectories in the chattering regions are not overly complicated. Three such trajectories are shown in Figs. 30–32 corresponding to initial conditions shown in Fig. 11. The initial phase differs by 0.01 rad (0.57°) between each

FIG. 30. Plot of a nonreactive trajectory for the collision of a vibrationally excited molecule in the chattering region shown in Fig. 11. Trajectory is for an initial translational energy of 0.085 eV, and an initial phase of 2.65 rad. All markings are as in Fig. 24.
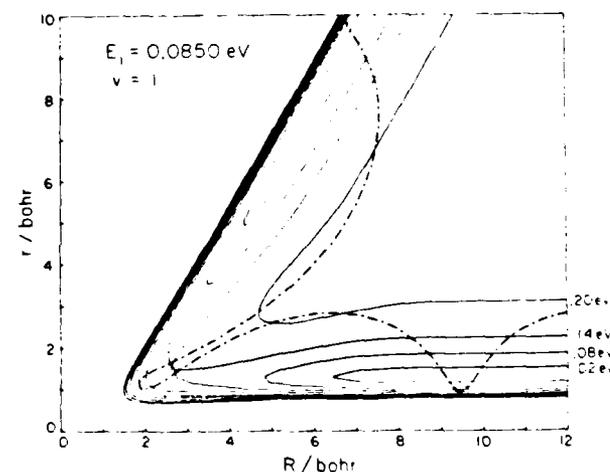
FIG. 32. Plot of a reactive trajectory in the chattering region shown in Fig. 11. Initial conditions are the same as for the trajectory in Fig. 30, except that the initial vibrational phase is 2.67 rad. All markings are as in Fig. 24.

trajectory. The dominant feature of the trajectories is clear: trajectories in this region involve motion more or less along the symmetric stretch line. The extreme sensitivity of the trajectory outcome to the initial phase can be rationalized as follows. In moving the symmetric stretch line, the trajectory can naively be viewed as having "forgotten" from where it was begun, and therefore it is reasonable that a small perturbation to the trajectory could seriously alter its course.

At energies below dissociation motion exactly along the symmetric stretch line would constitute that of a trapped trajectory—one which could oscillate back and forth forever, never leaving the interaction regions of the potential energy surface.[26] In the language of Pollak and Pechukas, such motion constitutes a trapped trajectory of the first kind.[27] These trajectories are frequently found at the boundary between reactive and nonreactive bands in atom–diatomic molecule systems at energies below dissociation.[12,13,21,22] At energies above dissociation, trapped trajectories of the first kind (in which the trajectory oscillates back and forth forever between the two different equipotential lines for the given total energy) do not exist. A trajectory can change its character continuously from reactive to nonreactive or vice versa by going through an intermediate stage of dissociative trajectories. Thus, the requirement shown by Pechukas and Pollak that trapped trajectories must occur at the boundary between reactive and nonreactive bands at energies below dissociation is not applicable at energies above dissociation.[25] Andrews and Chesnavich[14(b)] have, in fact, shown the necessity of having dissociative trajectories occurring with initial conditions between those of nonreactive and reactive trajectories. Nothing in these statements, however, precludes the possiblity of formation of trapped trajectories of the second or third kinds.[27] No such trapped trajectories (or nearly trapped ones) were observed, although we have not carried out a systematic search for them.

CONCLUSIONS

We have performed a reactivity band analysis of CID in a model collinear reactive atom–diatomic molecule system on which nonreactive, reactive, and dissociative processes are possible. Quasiclassical trajectories are believed to provide a reasonable view of the dynamics in this system because of the qualitative similarity in the reaction and dissociation probabilities calculated by trajectories and by exact quantum mechanical calculations.[7]

CID is shown to occur almost entirely in well-defined bands in initial phase–initial translational energy space, the exception being a small contribution from dissociative trajectories in a chattering region in which the outcome of the trajectory is extremely sensitive to the initial vibrational phase of the reagent molecule. Dissociation may be thought of as a limiting case of vibrational excitation, as nondissociative (reactive or nonreactive) trajectories with initial conditions only slightly different from those leading to dissociation result in a diatomic molecule product which is highly vibrationally excited. In most cases, dissociative reactivity bands found are confined between one reactive and one nonreactive band; in the rest, they may be found between two

nonreactive bands. In no instances were dissociative bands confined between two reactive bands.

The partitioning of kinetic energy among the three atomic products of dissociative collisions was calculated and shown to be a smooth function of the initial phase throughout the dissociation band. Kinematic considerations require that most of the available kinetic energy go onto the end atoms (A or C). The fraction of the available kinetic energy in the end atoms, as a general rule, matches smoothly onto that of the free atom in nondissociative collisions (atom A in nonreactive collisions, atom C in reactive ones).

From the curves of final energy fraction vs initial phase we have been able to calculate the partitioning probability, that is, the likelihood of the dissociation process to distribute the available energy in a given way. Plots of the partitioning probabilities vs final energy fraction for six different sets of initial conditions (reagent vibrational state and translational energy) display a wide range of behavior. The general form of these partitioning probability curves can be inferred solely by examination of the reactivity band plots.

The different dissociative reactivity bands found for the reaction of vibrationally excited ($v = 1$) molecules have been shown to be comprised of different kinds of trajectories. The band which dominated at low energies (and ends at reagent translational energies about 50% above the dissociation energy) is seen to arise from trajectories which cross the symmetric stretch line only once prior to the onset of actual dissociation, while the higher energy band arises from trajectories which cross the symmetric stretch line an additional time. The single dissociation band observed in collisions of ground state molecules is seen to be made up of trajectories which cross the symmetric stretch line twice prior to dissociation. Hence, the vibrational enhancement of CID can be thought of as being due to the inability of ground state molecules to dissociate by the simplest possible trajectory; dissociation from such ground states is only possible by a more complex procedure, which only becomes important at higher energies.

The chattering region is seen to arise from trajectories which at some point follow the symmetric stretch line very closely. Since the available energy is greater than the dissociation energy, motion along the symmetric stretch line does not constitute a trapped trajectory. The existence of a dissociation channel allows for a smooth transition from reactive to nonreactive trajectories via an intermediate region of dissociative trajectories. As a result, trapped trajectories need not occur at the boundary between reactive and nonreactive trajectories.

Our analysis has been restricted to a single model of a potential energy surface for a collinear collision. In a reactive system, changes in the masses of the atoms have been shown to produce major changes in the structure of the reactivity bands.[12(b)] Exact quantum mechanical calculations on isotopically substituted versions of the model system studied here (mass combinations 10–1–10 and 1–35–1) indicate that the effect of mass on dissociation is strong.[24] Large changes in the reactivity band structure can be expected. Thus one must use caution in attempting to make generalizations on the basis of the reactivity bands for one system.

Removal of the collinearity restriction might be expected to lead to substantial changes in the reactivity bands. In studies of the two- and three-dimensional T + HT reaction, Wright[12(e)] has shown a disappearance of the bandedness observed in the collinear reaction, which is due to the diminished importance of multiple collisions (which involve multiple crossing of the symmetric stretch line) in noncollinear collisions. Thus, in three-dimensional systems, the richness of the banded structure obtained here might be expected to be substantially reduced.

ACKNOWLEDGMENTS

[1]R. L. Belford and R. A. Strehlow, Annu. Rev. Phys. Chem. 20, 247 (1969)

[2]A. Dalgarno and W. G. Roberge, Astrophys. J. 233, L25 (1979); D. Hollenbach and C. F. McKee, Astrophys. J. Supp. Ser. 41, 555 (1979); W. Roberge and A. Dalgarno, Astrophys. J. 255, 176 (1982).

[3]P. J. Kuntz, in Atom-Molecule Collision Theory, edited by R. B. Bernstein (Plenum, New York, 1979), pp. 669-692, and references therein.

[4](a) D. J. Diestler, in Atom-Molecule Collision Theory, edited by R. B. Bernstein (Plenum, New York, 1979), pp. 655-667, and references therein, (b) G. D. Barg and A. Askar, Chem. Phys. Lett 76, 609 (1980); (c) C. Leforestier, G. Bergeron, and P. C. Hiberty, ibid. 84, 385 (1981); P. M. Hunt and S. Sridharan, J. Chem. Phys. 77, 4022 (1982).

[5](a) I. Rusinek, J. Chem. Phys. 72, 4518 (1980), (b) I. Rusinek and R. E. Roberts, ibid. 68, 1147 (1978).

[6](a) K. C. Kulander, J. Chem. Phys. 69, 5064 (1978), Nucl. Phys. A 353, 341c (1981), (b) C. Leforestier, Chem. Phys. 87, 241 (1984).

[7](a) A. Kuppermann, J. A. Kaye, and J. P. Dwyer, Chem. Phys. Lett. 74, 257 (1980); (b) J. A. Kaye and A. Kuppermann, ibid. 78, 546 (1981); (c) J. P. Dwyer, Ph.D. thesis, California Institute of Technology, 1977, (d) J. A. Kaye and A. Kuppermann, Chem. Phys. Lett. 115, 158 (1985)

[8](a) A. Hauke, J. Manz, and J. Römelt, J. Chem. Phys. 73, 5040 (1980), (b) J. Manz and J. Römelt, Chem. Phys. Lett. 77, 172 (1980).

[9]L. H. Beard and D. A. Micha, J. Chem. Phys. 73, 1193 (1980).

[10](a) J. C. Gray, G. A. Fraser, and D. G. Truhlar, Chem. Phys. Lett. 68, 359 (1979); (b) J. C. Gray, G. A. Fraser, D. G. Truhlar, and K. C. Kulander, J. Chem. Phys. 73, 5726 (1980); (c) J. C. Gray and D. G. Truhlar, ibid. 76, 5350 (1982).

[11]E. W. Knapp and D. J. Diestler, J. Chem. Phys. 67, 4969 (1977).

[12](a) J. S. Wright, K. G. Tan, K. J. Laidler, and J. E. Hulse, Chem. Phys. Lett. 30, 200 (1975); (b) J. S. Wright, K. G. Tan, and K. J. Laidler, J. Chem. Phys. 64, 970 (1976); (c) J. S. Wright and K. G. Tan, ibid 66, 104 (1977); (d) K. G. Tan, K. J. Laidler, and J. S. Wright, ibid 67, 5883 (1977); (e) J. S. Wright, ibid. 69, 720 (1978); (f) K. J. Laidler, K. G. Tan, and J. S. Wright, Chem. Phys. Lett. 46, 56 (1977).

[13]R. E. Howard, A. C. Yates, and W. A. Lester, Jr., J. Chem. Phys. 66, 1960 (1977).

[14](a) P. M. Hunt and M. S. Child, J. Phys. Chem. 86, 1116 (1982); (b) B. K. Andrews and W. J. Chesnavich, Chem. Phys. Lett. 104, 24 (1984)

[15]R. N. Porter and L. M. Raff, in Dynamics of Molecular Collisions, Part B, edited by W. H. Miller (Plenum, New York, 1976), pp. 1-52; D. G. Truhlar and J. T. Muckerman, in Atom-Molecule Collision Theory, edited by R. B. Bernstein (Plenum, New York, 1979), pp. 505-565

[16]J. M. Bowman and A. Kuppermann, Chem. Phys. Lett. 34, 523 (1975).

[17]H. Eyring, J. Walter, and G. Kimball, Quantum Chemistry (Wiley, New York, 1944), pp. 272-273.

[18]In Ref. 7(b), Eq. (8) implies erroneously that $f_A^{min} = 0$.

[19]J. S. Hutchinson and R. E. Wyatt, J. Chem. Phys. 70, 3509 (1979).

[20](a) J. W. Duff and D. G. Truhlar, Chem. Phys. Lett. 4, 1 (1974); (b) J. R. Stine and R. A. Marcus, ibid. 29, 575 (1974); (c) N. Sathyamurthy, ibid. 59, 95 (1978); (d) M. S. Child and K. B. Whaley, Faraday Discuss. Chem. Soc. London 67, 57 (1979).

[21]F. Schnabel and S. Chapman, Chem. Phys. Lett. 57, 189 (1978).

[22]J. A. Kaye and A. Kuppermann (unpublished)

[23]J. A. Kaye, Ph.D. thesis, California Institute of Technology, 1982

[24](a) H. Pauly and J. P. Toennies, Adv. At. Mol. Phys. 1, 258 (1965), (b) E. A. Mason, J. Chem. Phys. 62, 667 (1957).

[25]I. Shavitt, R. M. Stevens, F. L. Minn, and M. Karplus, J. Chem. Phys. 48, 2700 (1968)

[26]P. Pechukas and E. Pollak, J. Chem. Phys. 67, 5976 (1977)

[27]E. Pollak and P. Pechukas, J. Chem. Phys. 69, 1218 (1978).

Observation and Analysis of Emission Spectra of Tungsten Hydride[*]

James F. Garvey[†] and Aron Kuppermann

Arthur Amos Noyes Laboratory of Chemical Physics[§]

California Institute of Technology, Pasadena, Ca., 91125

Abstract: We report in this paper the first observation of electronic emission spectra due to the tungsten monohydride radical. This emission originates from the plasma generated by a DC discharge through hydrogen flowing between a tungsten anode rod and a tungsten cathode nozzle of a hydrogen atom beam source. By analyzing this spectrum rotational constants and bond distances have been derived for this radical and its deuterated analog. This data should be useful in assessing the accuracy of calculation methodology developed for relativistic systems.

1. Introduction

One of the oldest techniques for the observation of emission spectroscopy from molecules and radicals is through excitation by an electric discharge. The first time this technique was employed to observe emission from a non-monatomic radical was by Oldenberg[1] in 1934, when he observed OH in a discharge sustained through moist hydrogen. Since then electric discharges have been of great utility in the observation of the emission spectroscopy of excited species. In an attempt to characterize our hydrogen discharge beam source[2] we spectroscopically dispersed the visible emission of the plasma plume which appears in front of our nozzle during normal operation of the arc discharge. In addition to the expected H atom Balmer lines and H_3 Rydberg state emission bands, we observed in the 6800 Å region of the spectrum very sharp transitions converging to two band heads shaded to the red. We report here the observation and analysis of these bands.

2. Experimental

The beam apparatus is depicted schematically in figure 1. The arc-discharge source has been described previously[2] and is similar to other sources of this type[3-5]. It is placed in a vacuum chamber (VC1), pumped by a 20″ Westinghouse oil diffusion pump, and is connected by a flexible bellows to a test stand consisting of a bell jar (VC2) pumped by a 6″ mercury diffusion pump (nominal speed 125 l/s), attached to a freon-cooled chevron baffle and liquid nitrogen trap. Differential pumping between these two chambers is provided by a small conical copper skimmer (S) with an orifice diameter of about 1 mm with knife-sharp edge. Chamber VC2 contains a beam flag (F), a beam chopper (C1) operated at 10 Hz which allows ac detection of the beam, a pair of electric deflection plates (D) which eliminates ions from the beam, and an EAI 300 quadrupole mass spectrometer (QMS) with an electron bombardment ion source.

The discharge through H_2 in this H-atom source can be run continuously with a hydrogen stagnation pressure of 50-100 torr, such that the pressure in VC1 is of the order of 10^{-2} torr and the pressure in VC2 is of the order of 10^{-5} torr. The source (AS) can be moved with respect to the fixed skimmer with the help of a translation control knob (T) placed outside of the chamber and attached to a translation assembly (TA). This allows the nozzle to be moved to within 4 cm of the skimmer to maximize the intensity of the beam as measured by the mass spectrometer in VC2.

It is also possible to run in the mode depicted in figure 1 with the nozzle ~ 20 cm away from the skimmer, thereby allowing spectroscopic resolution of the intense red emission of the plasma plume in front of the nozzle. That light was focused onto the slits of a 0.5 meter Ebert scanning Jarrel-Ash monochromator by lens L, after being chopped at ~ 100 Hz by C2. The entrance and exit slits were set at an opening of 75 μ, which corresponds to a resolution of about 0.5 Å (or about 1 cm^{-1}) in the 6800 Å region. The wavelength scale of that spectrometer was calibrated with light from an Fe-Ne cathode discharge tube to an accuracy of 0.5 Å. The light, after dispersion by the monochromator, is detected by a photomultiplier tube coupled to a Princeton Applied Research model 181 current sensitive preamplifier. The signal is then processed by a Princeton Applied Research model HR-8 lock-in amplifier tuned to the frequency of the chopper, C2. This provides excellent discrimination against any background or stray light originating after the chopper. The output of the lock-in is fed to a strip chart recorder and the monochromator is made to scan the desired spectral region smoothly. The signal intensity was sufficiently large to preclude any difficulty in achieving good signal-to-noise ratio. In all cases the stagnation pressure was 60 torr. Figures 2 and 3 show, respectively, the emission spectrum obtained with H_2 or D_2 in the discharge. The observed spectral lines are given in Tables I and II and are accurate to one wavenumber.

In a previous paper[2] we have reported emission due to excited Rydberg states

of H_3 present in arc-heated beam. However, it was clear from the first observation of the lines in the 6800 Å bands that they could not be due to H_3 emission since this structure was so sharp. In addition the rotational spacing of the peaks was too small for it to be attributed to that molecule. Likewise, all other spectral features which we have observed and assigned to H_3 show prominent intensity changes when the stagnation pressure is altered[2]. In contrast, these 6800 Å bands show no significant change in intensity over the pressure range of 55 to 90 torr.

Attempts to identify this spectrum with previously observed spectra, including those of H_2 and CuH, proved unsucessful, leading to the conclusion that a new emission, possibly of a new species, was invloved. Throughout the operation of the arc discharge, considerable erosion from the tungsten anode nozzle and copper holder has been observed. It was natural then to assume that the emission might be due to a metal-containing species resulting from that erosion. Changing the discharge gas to deuterium creates a wavelength shift in the two bands consistent with what one would expect for a hydrogen-containing species.

The emission spectrum of the lowest electronically excited singlet state of CuH $(A\ ^1\Sigma^+)$ has been previously observed[6-9a] to occur in the region of 4280 Å, but we did not find the corresponding emission lines. The emission spectrum of the associated triplet state has so far not been observed, but for it to be the source of the lines in Table I and II the singlet-triplet splitting in this species should be about $8600\ cm^{-1}$. Although no *ab initio* calculations of this splitting have been performed, it seems that its value should be significantly less than $8600\ cm^{-1}$. These remarks suggest that the observed 6800 Å bands are not due to CuH.

In attempting to detect the presence of metal-containing species in our beam, we scanned the mass spectrometric detector in VC2 through $m/e = 250$. No peaks were found in the m/e range of 64 to 66 (corespnding to CuH), but were found in the m/e range 181 to 187 (corresponding to WH). The resolution of our instrument in that mass range was $\sim$ 3 mass units. This is insufficient to observe individual peaks, but the overall envelope was consistent with that of a species containing a W atom (albeit inadequate for distinguishing between W and WH). We therefore investigated the possibility that our 6800 Å emission bands might be due to a species containing one W and one or more H (or D) atoms.

In an attempt to determine the number of hydrogens which this candidate species contained we preformed experiments with a mixture containing 50% H_2 and 50% D_2 molecules in the discharge gas. If the species was a monohydride there would only be two emission spectra observed, one for the mono-hydride and one for the mono-deuteride. If it was a dihydride there would be three sets of spectra observed for MH_2, MD_2 and MHD. We observed only two sets of spectra, the one which we had observed in running with pure H_2 and another one we could also observe when running with pure D_2, concluding therefore that we were observing the electronic spectrum of a monohydride. This working hypothesis was confirmed by the analysis of the spectra described below.

3. Analysis

The analysis of diatomic electronic emission spectra has been carefully described in Herzberg's classic books[9b,10]. The rotational energy levels of a diatomic species are given by[11]

$$F(J) = \frac{E_r}{hc} = BJ(J+1) - DJ^2(J+1)^2 + \dots . \tag{1}$$

where

$$B = \frac{h}{8\pi^2 c \mu r^2} \tag{2}$$

is the rotational constant, μ is the reduced mass, r is the bond distance, and J is the rotational angular momentum quantum number. D is a centrifugal correction term which may be approximated by

$$D = \frac{4B^3}{\omega^2} \tag{3}$$

where ω is the vibrational frequency in cm^{-1}.

The rotational structure of a given vibronic transition depends on the type of electronic states involved. For a $\Sigma \leftarrow \Sigma$ transition the rotational selection rule is $\Delta J = \pm 1$. Transitions corresponding to $\Delta J = J^{lower} - J^{upper} = +1, -1$ are designated as P and R branches respectively. Together they form a simple series of lines represented by the expression

$$\nu = \nu_o + (B'_\nu + B''_\nu)m + (B'_\nu - B''_\nu)m^2 \tag{4}$$

where ν is the transition frequency (in cm^{-1}, usually), B'_ν and B''_ν are the rotational constants for the upper and lower states, ν_0 is called the band origin or the zero line and m is equal to -J and $J + 1$ for the P and R branches respectively, J being the final rotational state angular momentum quantum number. This formula can be represented graphically using the frequency of the transition as the abscissa and the quantity m as the ordinate. For $B'_\nu \neq B''_\nu$ this representation yields a parabola with a horizontal axis and is called the Fortrat parabola[9c]. The vertex of the parabola is associated with a band head. If the upper and lower electronic states have different electronic orbital angular momenta (such as in a $\Sigma \leftarrow \Pi$ transition), then an additional rotational branch called a Q branch (for which m equals J), corresponding to $\Delta J = 0$, exists. The lines of this third branch lie more closely together than for the P or R branches, forming a different parabola[9c].

In the case of our observed emission bands for both the hydride and the deuteride, two prominent band heads appear. This indicates that the electronic angular momentum of the initial state differs from that of the final one. Our assignments for

the P, Q and R branches for both spectra appear at the top of Figures 2 and 3. We can now construct Fortrat parabolas, to examine the accuracy of our fits. Figures 4 and 5 display the Fortrat parabolae for the hydride and deuteride, respectively.

Since tungsten hydride has four d and one s valence electrons, one can expect that the electronic states involved will have sextet multiplicity and that transitions between the lowest different electronic angular momentum states will be of the type $^6\Sigma^+ \leftarrow ^6\Pi$. With high multiplicities many more P, Q, and R branches may exist having different band heads[9d]. This is due to the different angular momenta in the molecule: electronic spin, electronic orbital and molecular rotation angular momentum all contributing to the total angular momentum of the molecule. These additional branches complicate the interpretation of the spectra. Very few $\Sigma \leftarrow \Pi$ systems have been studied with multiplicities greater than 3. The first to be analyzed in detail were due to Nevin: the first negative bands of oxygen (the $^4\Pi_u \leftarrow ^4\Sigma_g^-$ transition of O_2^+)[12-14] and the MnH bands at 5677 and 6237 Å representing a $^7\Sigma \leftarrow ^7\Pi$ transition[15]. If Hund's case (a) (where it is assumed that the spin-orbit coupling is large, while the coupling of the molecular rotation with the electronic motion is weak) strictly applied to the Π states, there would be 48 and 147 branches, respectively[9e]. If instead Hund's case (b) (where the coupling of the spin with the internuclear axis is weak and as a consequence the spin is coupled to the axis of rotation of the molecule) applied there would be only 12 and 21 branches[9e]. In the case of the O_2^+ bands Nevin identified 40 branches while for MnH he identified 49. Also in the spectra of FeCl, a $^6\Sigma \leftarrow ^6\Pi$ and a $^4\Sigma \leftarrow ^4\Pi$ transition has been identified by Miescher[16] and Muller[17].

Due to the observation of only two strong band heads (as shown in Figures 2 and 3) and due to our resolution, (~ 0.5 Å or ~ 1 cm^{-1}) we were not able to deal fully with the electronic multiplicity of the spectra. It should be noted that unassigned transitions that extended down to 6580 Å for the hydride and 6620 Å for the deuteride, appeared to be associated with the vibronic band in question. Whether these peaks are due to excited vibrational bands of this transition or are associated with additional rotational branches due to the expected high multiplicity is unknown. The structure in this series of peaks could be fit to several sets of parabolae, but due to their low intensities and absence of any clear band head, a reliable assignment was not possible. However, the existence of additional rotational branches can not at present be excluded.

We then attempted to treat the clear set of P, Q, and R branches of Figures 2 and 3 as if the electronic transition had singlet multiplicity, in order to derive a rotational constant and bond distance for the upper and lower states. This would be a strictly correct procedure if Hund's case (b) applied. Historically, rotational constants are derived by the use of combination differences[9f]. Though useful for a preliminary analysis the method implicitly assumes that no perturbations due to other electronic states are present[18,19]. A program developed by Zare and coworkers[19-21] that employs all measured line positions and iteratively compares their values with those calculated from numerically diagonalized model Hamiltonians with adjustable molecular constants represents a better approach, and we employed that program.

For our fit we used 5 molecular constants in the Hamiltonian: ν_0, the orgin of the band under study and the B and D constants (see equations (2) and (3)) for both the upper and lower states. As a result, the Fortrat parabolae are quartic rather than quadratic. The lines listed in Tables I and II were fit using this program. The numbers in parentheses represent the difference between the observed line position and the calculated one (using the program described above). The curves in Figures 4 and 5 are the Fortrat parabolae generated by the calculated lines. For both the hydride and deuteride cases the overall fit is satisfactory in view of the approximations and data accuracies involved.

From the rotational constants listed in Tables III and IV we are able to calculate bond distances by using equation (2). Likewise, we are also able to crudely estimate the fundamental vibrational frequency of the metal hydride by using the centrifugal distortion constant and equation (3). These values are also listed in Tables III and IV.

The errors given in those two tables were obtained as follows. The Fortrat 'parabolae' obtained by the procedure described above were distorted by the maximum amounts permitted by the differences between the observed and calculated line positions. From these extreme parabolae, extreme values of the 5 constants for each state were obtained and their excursion away from the iteration procedure were taken to be the errors.

It should be noted that with our current resolution the bond distances listed for the hydride are good to $\sim 1\%$ and those for the deuteride to $\sim 3\%$. This is due to the fact that the deuteride spectrum is considerably more congested then the hydride one, due to the closer spacing of the corresponding rotational lines. The relative errors in the values of the D constants are rather large because they are associated with small rotational stretch effects. In turn, these result in large relative errors in the fundemental vibration frequencies ν of the states involved, which as a result are only qualitatively given by these experiments.

Table I

Experimental Transition Energies of WH (in cm^{-1}) and their Assignments^a

J	R	Q	P
0	14,844.2 (−3.2)^b		
1	14,853.9 (−1.8)	14,833.8 (−3.0)	
2	14,861.0 (−1.7)	14,831.1 (−3.5)	14,820.0 (+4.2)
3	14,866.5 (−1.8)	14,828.6 (−2.6)	14,805.4 (+2.3)
4	14,870.9 (−1.7)	14,825.5 (−1.1)	14,788,7 (−0.7)
5	14,876.5 (+1.2)	14,822.7 (+1.9)	14,771.9 (−2.9)
6	14,883.5 (+7.3)	14,816.7 (+3.2)	14,758.7 (−4.7)
7	14,880.6 (+5.3)	14,809.7 (+4.6)	14,743.1 (+0.5)
8	14,873.4 (+0.9)	14,799.6 (+4.3)	14,727.3 (+2.3)
9	14,866.5 (−1.1)	14,781.6 (−2.2)	14,711.3 (+4.7)
10	14,857.8 (−2.6)	14,768.0 (−2.8)	
11	14,849.5 (−1.3)	14,749.5 (−6.4)	
12	14,840.9 (+2.4)	14,733.3 (−6.1)	
13		14,716.7 (−4.1)	
14		14,700.0 (−0.2)	
15		14,683.0 (+5.7)	

a) These energies are accurate to about ± 1 cm^{-1}

b) The numbers in parenthesis are the differences between the observed and fitted values. See text.

Table II

Experimental Transition Energies of WD (in cm^{-1}) and their Assignments[a]

J	R	Q	P
0	14,830.6 (−5.0)[b]		
1	14,838.4 (−1.6)		
2	14,843.7 (−0.2)		
3	14,849.1 (+1.5)		14,815.0 (+0.8)
4	14,853.3 (+2.5)	14,821.5 (−4.9)	14,808.5 (+1.2)
5	14,857.7 (+4.1)		14,803.8 (+4.2)
6		14,816.4 (−4.0)	14,791.1 (+0.3)
7	14,860.9 (+3.2)	14,812.6 (−3.6)	14,783.7 (+2.9)
8	14,862.9 (+4.2)	14,808.9 (−1.8)	14,770.1 (+0.7)
9		14,803.4 (−0.8)	
10	14,857.2 (−1.0)		
11	14,855.3 (−1.0)		
12	14,850.9 (−2.1)		
13	14,846.1 (−1.9)		
14	14,841.4 (+0.2)		
15	14,834.2 (+2.0)		

a) These energies are accurate to about 1 cm^{-1}

b) The numbers in parenthesis are the differences between the observed and fitted values. See text.

Table III

Spectroscopic Constants of WH

$\nu_{\text{o}} = 14{,}842 \pm 1 \text{ cm}^{-1}$

	Upper State ($^6\Pi$)	Lower State ($^6\Sigma$)
B/cm^{-1}	$4.72 \pm .11$	$5.29 \pm .13$
D/cm^{-1}	$2.7 \pm 0.5 \times 10^{-3}$	$2.3 \pm 0.4 \times 10^{-3}$
$r_e/\text{Å}$	$1.89 \pm .02$	$1.78 \pm .02$
ν/cm^{-1}	394 ± 60	512 ± 62

Table IV

Spectroscopic Constants of WD

$\nu_{\text{o}} = 14{,}833 \pm 5 \text{ cm}^{-1}$

	Upper State ($^6\Pi$)	Lower State ($^6\Sigma$)
B/cm^{-1}	$2.33 \pm .11$	$2.53 \pm .13$
D/cm^{-1}	$2.1 \pm 1.6 \times 10^{-3}$	$3.1 \pm 2.2 \times 10^{-3}$
$r_e/\text{Å}$	$1.91 \pm .05$	$1.83 \pm .05$
ν/cm^{-1}	156 ± 184	145 ± 144

4. Discussion

We can now check the consistency of our identification of the metal atom in the monohydride and monodeteride as tungsten by comparing the corresponding constants and analyzing the magnitude of the isotope effect.

A large isotope effect in the rotational constants is expected because of the large difference in the reduced mass of the two molecules. Let the suprescripts H and D refer to quantities associated with WH and WD respectively.

The rotational constants of these two isotopic molecules are related by

$$B^D = \rho^2 B^H \tag{5}$$

where

$$\rho = (\frac{\mu^H}{\mu^D})^{\frac{1}{2}} \tag{6}$$

and the μ are reduced masses. Other molecular constants have simple dependences on ρ. In the case of the centrifugal distortion constant, calculations made by Dunham[22] have show that

$$D^D = \rho^4 D^H \tag{7}$$

is a very good approximation. The investigation of the isotope effect in electronic band spectra has had an historically important role in the early discovery of new isotopes of very small abundance[23,24].

As a check of the correctness of our assignment of the spectra as due to tungsten hydride we can see how well the rotational constants obey equation 5. From the definition of ρ given by equation (6) the value of ρ^2 should be 0.50. From the rotational constants in Tables III and IV and equation (5) we get values for ρ of 0.48 $\pm$ 0.04 and 0.49 $\pm$ 0.03 for the ground and excited states respectively, indicating a consistency of the observed isotope effect on the rotational constants with theory. Equation (7) is also satisfied by the data but within such large error bars so as to not be very informative.

An additional isotope effect which is expected[25] involves the position of the 0-0 band (the band origin). In the present case the band origin for WD lies (9 ± 6) cm^{-1} to the red of the one for WH. A consistency check of this shift can be obtained by observing that the energy difference between the mimima of the upper and the lower potential energy curves can be independently calculated from the data for the WH and WD molecules. The respective values are $(14.90\pm0.08) \times 10^3$cm^{-1} and $(14.83 \pm 0.23) \times 10^3$cm^{-1}, which are equal to one another within experimental accuracy, as expected. The large errors in these quantities are due to the inaccuracy in the zero point energies, to which the electronic spectra measured are not very sensitive. Nevertheless, within this large error bars, the isotope effect on the position of the band origin is consistent with our data.

In summary, our assignment of the observed spectra to a monohydride and monodeuteride of a heavy element is consistent with all of the observed isotope effects.

In addition, we must examine the physical reasonability of the spectroscopic constants obtained. Unfortunately, there have been no spectra reported for tungsten or for molybdenum hydride and only sparse data for chrominum hydride. Kleman and co-workers[26] and O'Connor[27,28] have published CrH spectra. O'Connor analyzed the band at 11611 cm^{-1} which he atttributes to a A $^6\Sigma^{(+)} \leftarrow X$ $^6\Sigma^{(+)}$ transition. He was able to assign the twelve P and R branches and derive rotational constants such that he derived a bond distance of 1.655 Å for the ground state and 1.787 Å for the upper state, with vibrational frequencies of 1581.2 cm^{-1} and 1479.4 cm^{-1}, respectively. For the alkali hydrides[29] and the hydrogen halides[30] it has been observed that as one goes down the periodic table the bonds become weaker, the bond length longer and the vibrational frequencies smaller. The same trend is observed between CrH and WH, on the basis of our assignment. Furthermore, the internuclear distance in H_2 is 0.746Å [31a] and the distnace between nearest neighbors in tungsten at 25°C is 2.741Å [31b]. As a simple approximation, we estimate the WH distance in its ground electronic state as the arithmetic mean of those two values, namely 1.74 Å. This value is in good agreement with our spectroscopic result of (1.78 ± 0.02)Å.

Relativistic effects are of importance in this system because of the high atomic weight of the W atom. In recent years approximate methods have been developed and applied to calculations of the electronic energy of such systems[32-34]. The present results should be useful in testing the validity of those methods.

5. Other Possible Systems

The electronic spectra of many metal hydrides have not yet been obtained. As of 1984 there were no hydride spectra[35,36] of the large majority of the lanthanides and actinides as well as of Y, Zr, Nb, Mo, Ru, Rh, Os and Ir. Of the known spectra about half have not been rotationally analyzed, a third have not been vibrationally analyzed and about 15% are of uncertain identification[35]. By adding metal carbonyls to the hydrogen gas which sustains the discharge it might be possible to generate electronically excited states of metal hydrides whose emission spectra have not yet been observed. Another way of generating new metal hydrides might be through the use of different metals as nozzles. We have attempted to do this useing a molybdenum nozzle but were unable to sustain a discharge due to rapid deformation under the high temperature conditions of the plasma.

In the case of metal nitrides, there are very few systems which have been studied (as of 1984)[35,36]. The Kunth type of discharge source we have employed has also been very successful in the generation of nitrogen atoms through the use of N_2 as the discharge gas[37,38]. Metal nitride emission spectra from these sources have not been reported so far, but our results suggest that attempts in this direction be made.

Another possibile for use of these sources is the generation of metal clusters. In the present work we tried to minimize the amount of erosion from the tungsten electrodes, but conversely one can try to increase this erosion. In attempting to stabilize his hydrogen discharge W. C. Stwalley[39] positioned, exterior to the nozzle, a sacrificial tungsten electrode. His observation was that this electrode was corroded by the discharge. This technique could perhaps be employed for generating tungsten clusters.

In general, the high electronic temperature provided by this arc discharge source presents interesting possibilities for the generation and detection of novel molecular species.

6. Conclusions

We have assigned some observed emission spectra from a plasma obtained from an arc discharge through hydrogen or deuterium, with tungsten electrodes, as due to WH and WD respectively. All the observed isotope effects and the magnitudes of the spectroscopic constants obtained are consistent with this assignment. Additional heavy metal hydride as well as other systems might be studied by this technique. Many of these systems are of interest for testing relativistic molecular quantum mechanical calculation methods

7. References

1. O. Oldenberg, *J. Chem. Phys.*, **2**, 713 (1934).

2. J. Garvey and A. Kuppermann, *Chem. Phys. Lett.*, **107**, 491 (1984).

3. E. L. Knuth, *Appl. Mech. Rev.*, **17**, 751 (1964).

4. W. S. Young, W. E. Rodgers and E. L. Knuth, *Rev. Sci. Instrum.*, **40**, 1346 (1969).

5. K. R. Way, S. -C. Yang, and W. C. Stwalley, *Rev. Sci. Instrum.*, **9**, 1049 (1979).

6. A. Heimer and T. Heimer, *Z. Physik*, **84**, 222 (1933).

7. T. Heimer, Dissertation (Stockholm, 1937).

8. H. Schuler, H. Gollnow and H. Haber, *Z. Physik*, **111**, 508 (1939).

9. G. Herzberg, *Molecular Spectra and Molecular Structure, I. Spectra of Diatomic Molecules*, D. Van Nostrand Company, Inc., N. Y., a) p. 526 b) p. 66, c) p. 172, d) p. 260, e) p. 266, f) p. 168, (1950).

10. G. Herzberg,*The Spectra and Structures of Simple Free Radicals, An Introduction to Molecular Spectroscopy*, Cornell University Press, Ithaca, p. 18. (1970).

11. L. Pauling and E. B. Wilson, Jr., *Introduction to Quantum Mechanics*, McGraw-Hill, N. Y. (1935).

12. T. E. Nevin, *Nature (London)*, **140**, 1101 (1937).

13. T. E. Nevin, *Phil. Trans. Roy. Soc., London*, **237**, 471 (1938).

14. T. E. Nevin, *Proc. Roy. Soc., London*, **174**, 371 (1940).

15. T. E. Nevin, *Proc. Roy. Irish Acad. A*, **48**, 1 (1942).

16. E. Miescher, *Helv. Phys. Acta*, **11**, 463 (1938).

17. W. Muller, *Helv. Phys. Acta*, **16** 3 (1943).

18. N. Aslund, *Arkiv for Fysik*, **30**, 377 (1965).

19. R. N. Zare, A. L. Schmeltekopf, W. J. Harrop, and D. L. Albritton, *J. Mol. Spectrosc.*, **46**, 37 (1973).

20. D. L. Albritton, W. J. Harrop, A. L. Schmeltekopf, R. N. Zare, and E. L. Crow, *J. Mol. Spectrosc.*, **46**, 67 (1973).

21. D. L. Albritton, A. L. Schmeltekopf, J. Tellinghuisen, and R. N. Zare, *J. Mol. Spectrosc.*, **53**, 311 (1974).

22. J. L. Dunham, *Physic Rev.* **34**, 438 (1929), **41**, 721 (1932).

23. G. H. Dieke and H. D. Babcock, *Proc. Nat. Acad. Amer.*, **13**, 670 (1927).

24. W. H. J. Childs and R. Mecke, *Z. Physik*, **86**, 344 (1931).

25. F. A. Jenkins and A. McKellar, *Physic Rev.*, *42*, 464 (1932).

26. B. Kleman and B. Liljeqvist, *Arkif For Fysik*, **9**, 345 (1955).

27. S. O'Connor, *Proc. R. Ir. Acad.*, **50A**, 123 (1967).

28. S. O'Connor, *J. Phys. B.*, **2**, 541 (1969).

29. F. A. Cotton and G. Wilkinson, *Advanced Inorganic Chemistry*, Interscience Publishers, New York, p. 182 (1972).

30. R. S. Berry, S. A. Rice, and J. Ross, *Physical Chemistry*, John Wiley and Sons, New York, p. 312 (1980).

31. *Internation Table for X-ray Crystallography*, Kynoch Press, Birmingham, England, (1962), a) v. 3, p. 258, eds. H. Ondik and D. Smith, b) v. 3, p. 278, eds. W. Hume-Rothery and K. Lonsdale.

32. D. D. Koelling, D. E. Ellis and R. J. Bartlett, *J. Chem. Phys.*, **65**, 3331 (1976).

33. P. A. Christiansen, K. Balasubramanian and K. S. Pitzer, *J. Chem. Phys.*, **76**, 5087 (1982).

34. K. Balasubramanian, *Chem. Phys. Lett.*, **114**, 201 (1985).

35. R. Grinfeld, *Proceedings of the Tenth Colloquium Spectroscopicum Internationale*, eds. E. R. Lippincott and M. Margoshes, Spartan Books, Washington, D. C. (1962).

36. K. P. Huber and G. Herzberg, *Molecular Spectra and Molecular Structure, IV. Constants of Diatomic Molecules*, Van Nostrand Reinhold Co. (1979).

37. R. L. Love, J. M. Herrmann, R. W. Bickes, Jr., and R. B. Bernstein, *J. Am. Chem. Soc.*, **99**, 8316 (1977).

38. K. Tabayashi, S. Ohshima, and K. Shobatake, *J. Chem. Phys.*, **80**, 5335 (1984).

39. W. C. Stwalley, private communication.

8. Figure Captions

Figure 1. A schematic view of the top of the machine: VC1 and VC2, vacuum chambers; AS, anode assembly; A, anode; C, cathode; M, magnet; S, water-cooled copper assembly; TA, Translation assembly; T, translator; P1 and P2, viewports; L, optical lens; C1 and C2, choppers; PM, photomultiplier; CP, current preamp; LI1 and LI2, lock-in amplifiers; SCR1 and SCR2, stripchart recorders; D, electric field deflectors; F, mechanical flag; QMS, quadrupole mass spectrometer; PA, preamplifier; MSE, mass spectrometer electronics.

Figure 2. Emission spectrum around 6800 Å with H_2 in the arc source. Assigned rotational transitions for WH appear above spectrum. The letters P, Q, and R refer to the corresponding spectral branches.

Figure 3. Emission spectrum around 6800 Å with D_2 in the arc source. Assigned rotational transitions for WD appear above spectrum. The letters P, Q, and R refer to the corresponding spectral branches.

Figure 4. Fortrat parabolae for WH. Open symbols represent observed spectral lines while smooth curve represents the fit to those lines.

Figure 5. Fortrat parabolae for WD. Open symbols represent observed spectral lines while smooth curve represents the fit to those assigned lines.
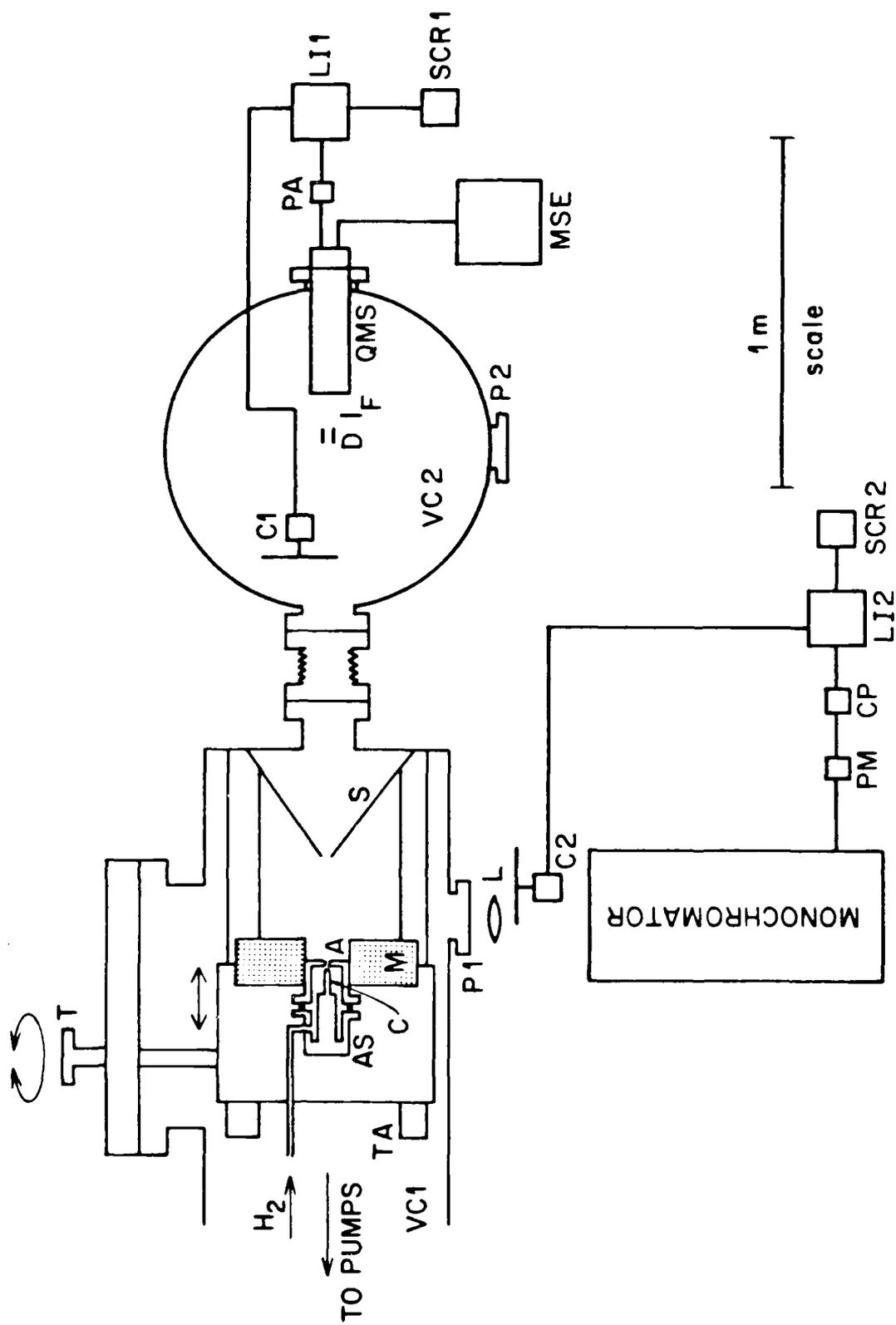
Figure 1
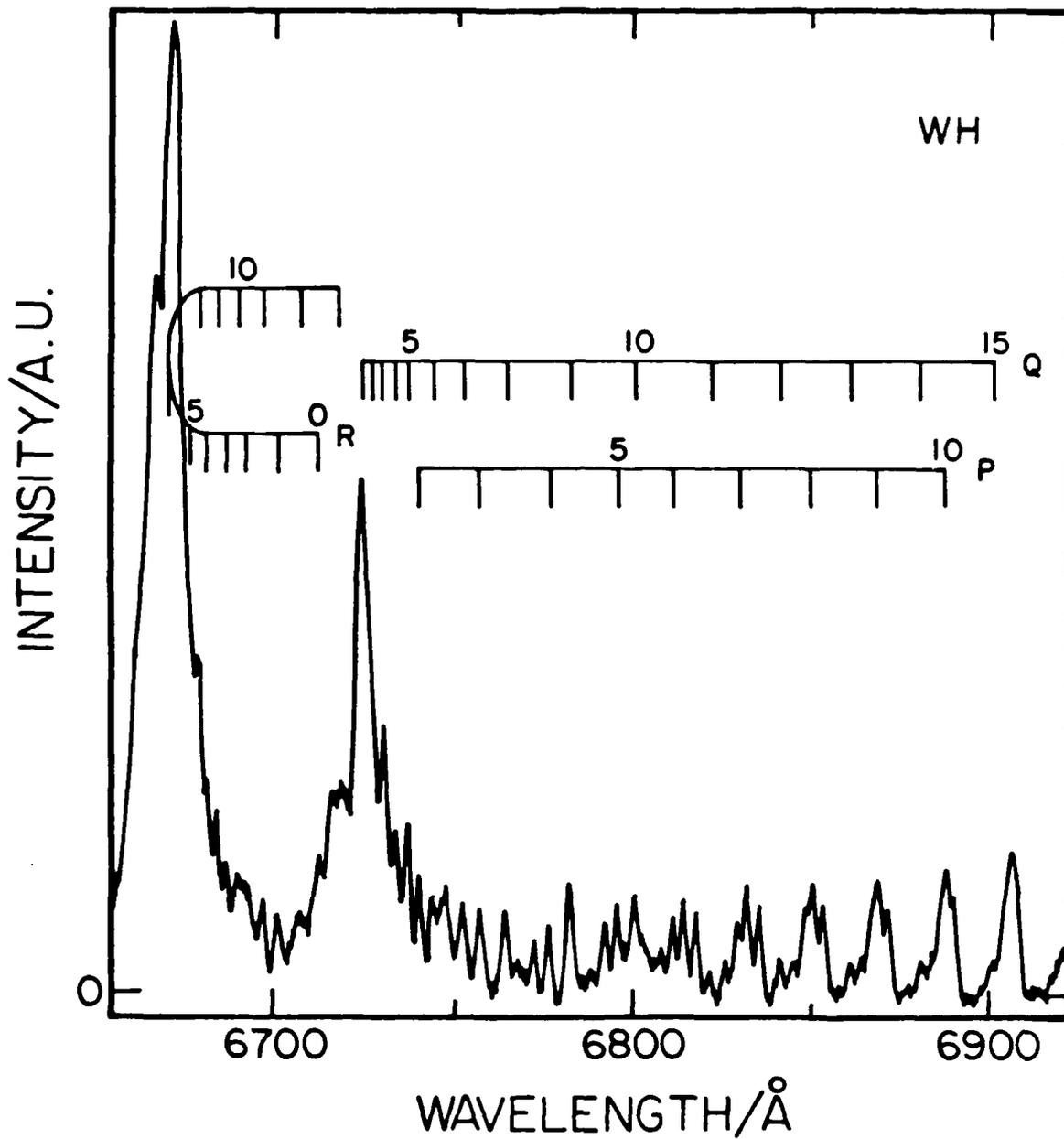
Figure 2
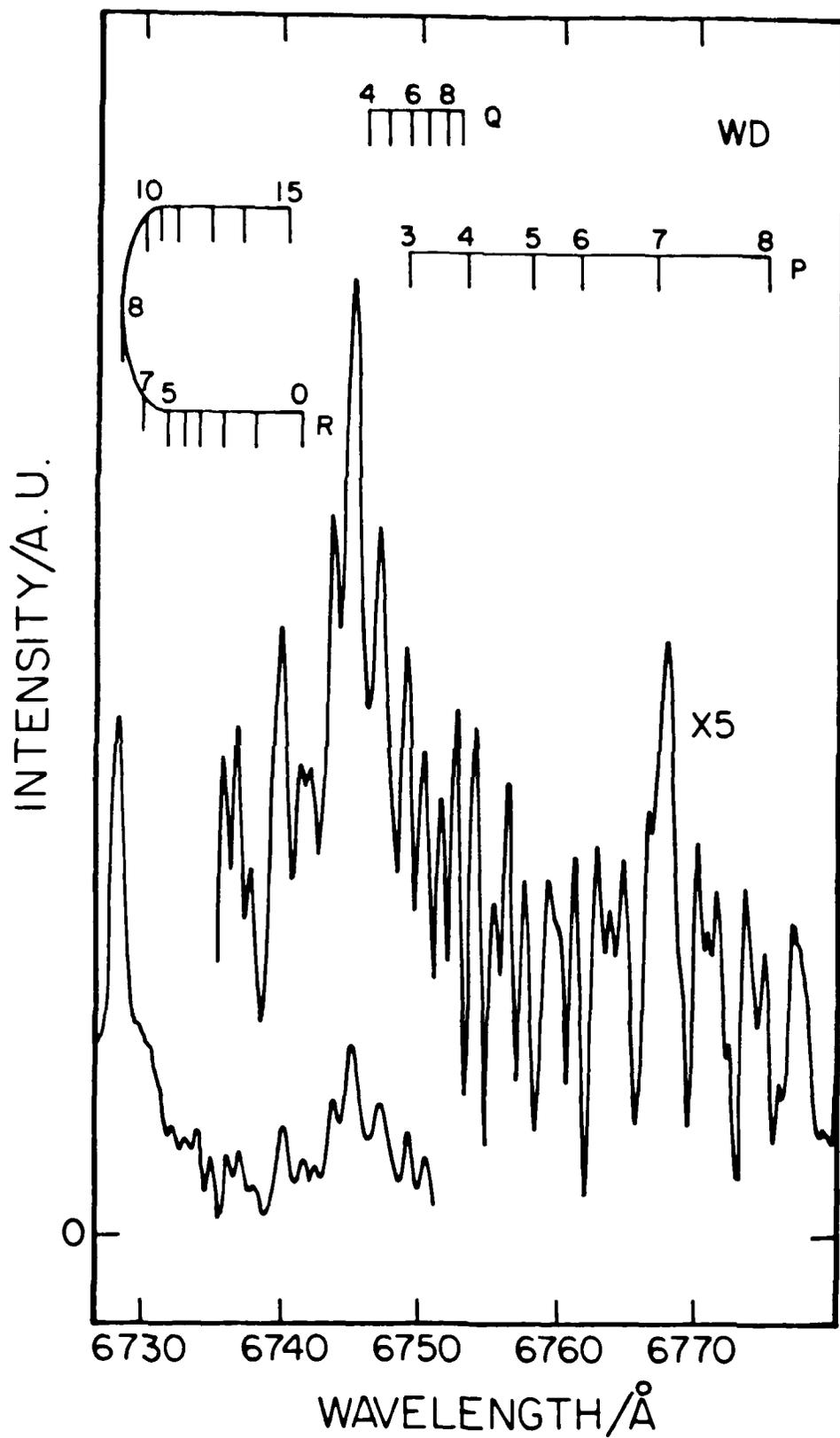
Figure 3
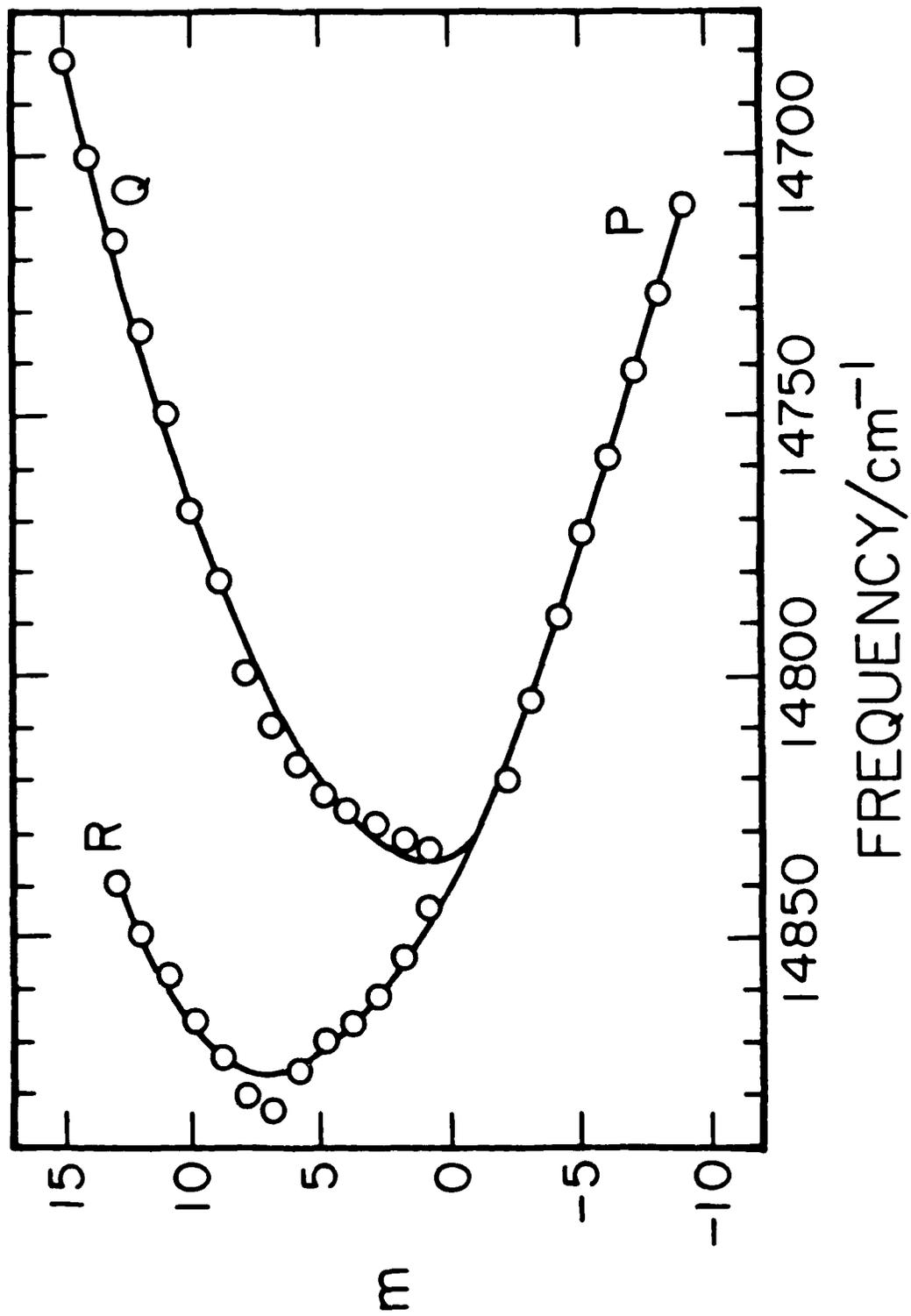
Figure 4
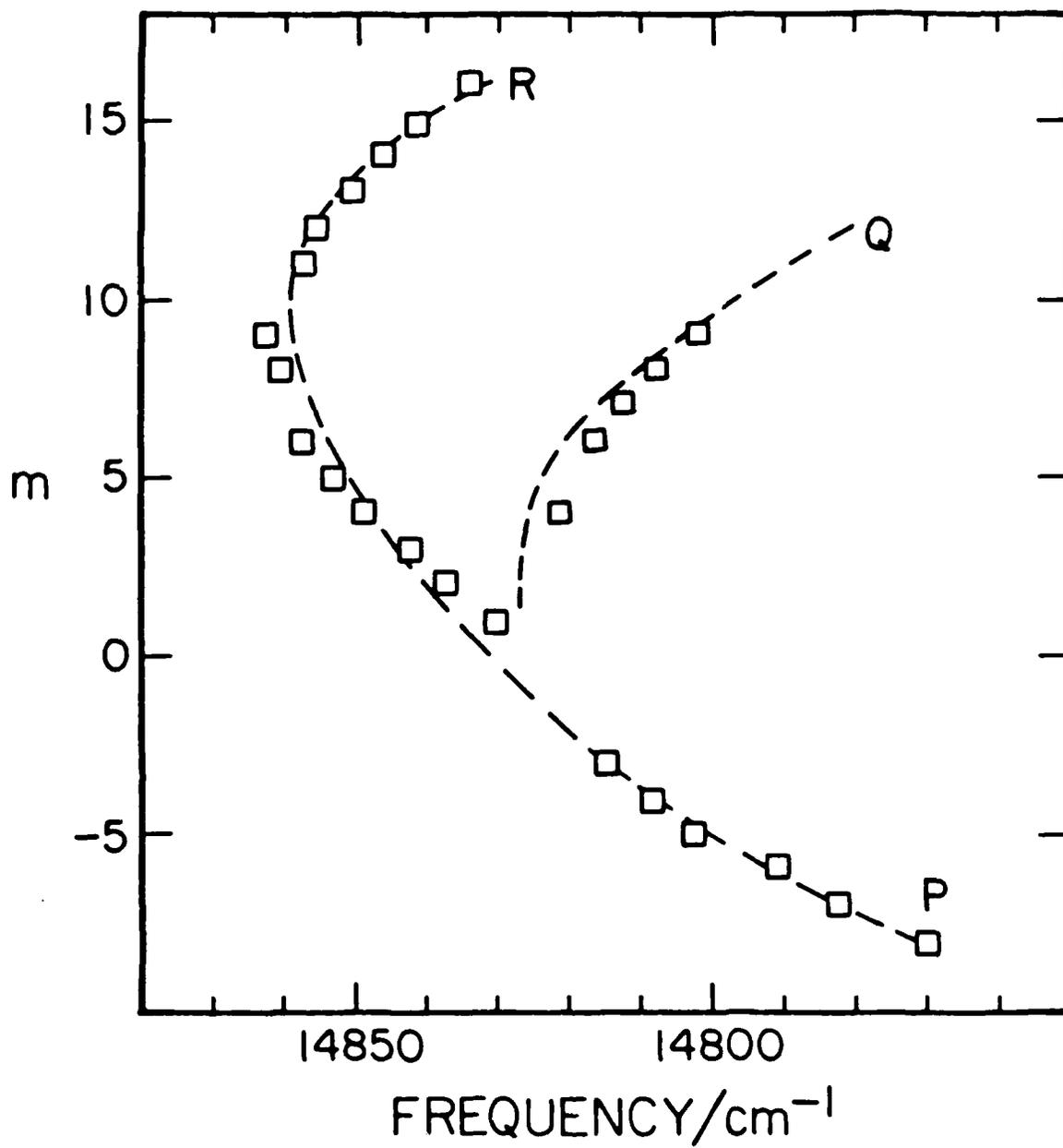
Figure 5

Design and Operation of a Stable Intense High Temperature Arc – Discharge Source of Hydrogen Atoms and Metastable Trihydrogen Molecules[*]

James F. Garvey[†] and Aron Kuppermann

Arthur Amos Noyes Laboratory of Chemical Physics[§]

California Institute of Technology, Pasadena, Ca., 91125

Abstract: We report a design for a stable intense beam source of hyperthermal hydrogen atoms. The basis for the design is an arc heater used first by Kunth for the generation of high translational energy He-Ar beams. In the case of hydrogen atom generation this source is very unstable due to the corresponding higher temperatures which are generated by the plasma discharge. We have substantially eliminated these difficulties by the insertion of discharge-localizing insulators, and the use of a tungsten nozzle mounted in the center of a 1 kilogauss electromagnet. This source generates exceptionally high hydrogen atom beam intensities of $\sim 10^{22}$ atoms sec^{-1} sterad^{-1} with translational energy distribution functions which extend to 18 eV and whose peak occurs at energies as high as 13 eV. In addition metastable H_3 molecules having an intensity between 10^{20} and 10^{21} molecules sec^{-1} sterad^{-1} are formed.

[†] Work performed in partial fulfillment of the requirement for the Ph.D in Chemistry at the California Institute of Technology. Present address: Dept. of Chemistry, UCLA, Los Angeles, Ca. 90024.

[§]Contribution No. 7234

1. Introduction

The use of molecular beams to elucidate the dynamics of molecular collisions has been widely demonstrated. However, due to the high barrier heights of most reactions only a relatively small number of systems have been studied[1,2] by this technique. It would therefore be attractive to be able to produce neutral atomic beams with translational energies in the 1-20 eV energy range, a regime which would permit the dissociation of all chemical bonds. Many different sources for the generation of such hyperthermal beams have been devised[3-7] but all suffer from various drawbacks, such as low intensities, instabilities, metastable state atomic species and poor duty factors.

The most promising approach for the generation of fast atoms lies in the plasma jet technique[8,9] where the nozzle is one of the electrodes between which an arc is struck. The resulting effective stagnation temperature can be ten thousand degrees or higher. Despite the obvious advantages of these arc-discharges their operation is not straightforward. A major difficulty is that corrosion of the anode and cathode surfaces creates dimensional instabilities in the electrodes making the discharge itself unstable. With this problem in mind Kunth and co-workers[10-12] developed an arc heater for argon which; (a) had lower electrode erosion rates, (b) a more stable arc, (c) higher thermal efficiency, and (d) greater ease of construction and maintenance.

In the generation of hyperthermal hydrogen atoms, early work was unsuccessful in sustaining a continous H_2 plasma beam source with a DC discharge[13]. It was not until Stwalley and coworkers[14,15] adapted the Kunth source to operate with H_2 that hydrogen atoms with hyperthermal energies were generated. However, this source still suffered from instabilities due to the high temperature of the plasma.

We report in this paper an improved design for this discharge source which is capable of producing routinely much greater beam intensities than have been previously been observed, having in addition enhanced stability and reliability.

2. Source Design

Following the design of Knuth and coworkers[9-11] an arc-heated source was constructed. The concept of the source is a simple one in that gas is introduced into the area between a fixed anode and a movable cathode tip. Placing the source in a vacuum chamber causes the gas to flow through the nozzle into the chamber due to the large pressure differential. An arc is initiated with a high voltage pulse applied between the anode and cathode. The plasma flame created extends, due to the expansion of gas through the nozzle, beyond the anode itself, thus carrying away much of the heat generated. As described later, this arc produces very high temperatures which demands efficient cooling of the components of the source to avoid their destruction.

In the original use of this design we achieved little success in creating and sustaining a reliable hydrogen plasma. These difficulties were surmounted by a total redesign which in turn generated new insights as to what parameters were importan. in creating a stable discharge. What follows is a description of the evolution of the system.

The cathode portion of the source is shown in figure 1. It consists of a water-cooled hollow tube [A] with a cylindrical cathode rod [B] attached to the front of the tube by two set screws [C] placed perpendicularly to each other. This rod is made of 2% thoriated tungsten and is capable of withstanding temperatures in excess of 3000 K. Many different shapes for the tip of the rod have been tried, with the best one having the end rounded. While running the source this rod tends to erode in such a way that tungsten sputters off it and will sometimes clog the nozzle. After an extended run its tip is shaped to a sharp point by this process. The hollow tube [A] is fitted inside a support structure [D] in such a way that it can be moved 3/4" back or forth with respect to this structure. A bellows [E] is welded between the tube and the support structure to provide a vacuum tight assembly. Once set the position of the tube may held in place with the help of three teflon screws connecting the outside casing [F] with the support structure [D]. The hole for one of these screws is shown

in figure 1 [G].

Two gas inlets are drilled at sharp angles through the cathode support structure [D] (i.e., nearly tangentially to its inner surface) on opposite sides of the chamber located between the cathode and the anode. This has the effect of causing the gas to swirl around inside the source creating a more stable flow through the nozzle and thereby stabilizing the arc. It has been observed that when one of these inlets is clogged the arc will not operate, probably due to gradients in the gas density making the discharge medium less uniform and therefore unstable. The entire cathode section (except the cathode itself) is now made of stainless steel and the gas inlets are welded to is such as not to become loose at the high temperatures generated.

The anode assembly, as shown by an expanded view in figure 2, consists of a large cylindrical brass piece [D1 & D2] which has six water cooling channels bored into it. The front of the device (at the right side of the figure 2) holds the nozzle anode assembly through which the gas passes and to which the arc is struck. It appears that a large part of the problem we had in the past with creating a stable discharge was due to the difficulty of keeping the arc confined to the small region between the tip of the cathode and the nozzle. What apparently occurred is that once the arc was struck between the cathode tip and the anode nozzle, it would migrate to the back of the anode housing creating an internal arc which would severly damage the source. To circumvent this problem it was decided that the anode section of the source should be shielded from the cathode everywhere except near the tip of the cathode rod. This was accomplished by inserting a macor cylinder [E] between the anode and cathode regions. With this insulator in place the arc remains limited to the small region between the cathode tip and the anode. After prolonged use the only damage to the macor cylinder is a slight charring at its exit hole. A problem that this geometry does not eliminate is that the arc will sometimes strike along the inside area of the nozzle (figure 2 [C]) causing severe erosion of its surface.

Since much heat is generated at or near the exit aperture of the nozzle, this part has been designed for easy replacement. In principle a material which is highly conductive electrically and thermally would make an excellent nozzle. We initially

followed the example of Stwalley and co-workers[15] by using a replaceable copper nozzle which simply screwed into the front of the brass anode. Using this design we quickly encountered the same problem they had, namely that during a typical run the nozzle opening would enlarge from an initial 2 mm diameter to as much as 6 mm after about 1/2 hour operation. We tried, as they did, to use molybdenum as the material for the nozzle but it melted too easily. After many attempts with these materials we eventually came to the conclusion that the nozzle would have to be made out of a material having a substantially higher melting point, such as tungsten. However, due to the grave difficulties in machining that metal a simpler nozzle design was essential. Also because of the poorer thermal conductivity of tungsten, efficient cooling was critical in order to avoid having the nozzle aperture enlarge as much as with the other materials used. The optimal design involved cutting a 1/8" thick disk of 2% thoriated tungsten from a .375" welder's rod. A 1.2 mm hole is then drilled into this disk with a carbide drill. This disk is shown as part [B] in figure 2. It is held in place by two copper pieces (parts [A] and [C]) which are threaded into the brass anode housing [D]. These copper pieces provide excellent thermal contact between the tungsten nozzle and that water−cooled housing. This design has been much more successful in that we are able to run repeatedly (5 to 8 times, several hours each time) using the same nozzle, before nozzle replacement is necessary.

When assembled, the anode and cathode are joined by six teflon screws. One of the corresponding screw holes is indicated by H in figure 1. The assembled source is shown in figure 3. The anode and cathode are electrically insulated from one another by a teflon spacer and a Viton O-ring which also provides a vacuum seal between these two components. Great care must be taken in acertaining that a seal has been established since otherwise less gas will pass through the nozzle and the plasma will become hot enough to damage the anode. Likewise, when tightening the six teflon screws it is necessary that the cathode rod remain centered with respect to the anode body. If the rod should be off axis, damage will occur to the copper pieces which retain the tungsten nozzle, because the arc will strike localized regions of those pieces preferentially and the nozzle hole itself will enlarge in an asymmetric fashion, i.e., it

will open up in the region to which the rod is pointing, causing the plume to be off axis, with a concomitant decrease in the detected beam intensity.

Once the system is assembled, the space between the cathode tip and the anode nozzle forms a small chamber into which the gas is introduced via the inlet lines. To ensure that the cathode is insulated from the rest of the chamber (thus preventing any shorts) all water lines to it are made of 1/4" polyethylene tubing. The metal gas inlet line is insulated from the anode by a piece of glass tubing.

When the system is assembled the cathode tip to anode nozzle distance can be adjusted by compressing the cathode bellows (figure 1, [E]) with the help of 3 teflon screws. One of the corresponding screwholes is indicated by G in figure 1. Trial and error have shown the optimum gap between the tip of the cathode and the surface of the anode disk to be 0.5mm; if it is smaller than that value the nozzle hole will immediately short out to the cathode rod and if it is much larger the arc will be extinguished during the changeover from argon to hydrogen. This distance appears to be fundamental to the stable operation of the system. For example, Toennies and co-workers[16] have recently developed a source similar to the one described here and had great difficulty maintaining a stable discharge until they also began to run using the parameters just described.

Power for our arc source is provided by a Westinghouse type WS variable current arc welder supply. This unit can generate a maximum current of 180 A and an open circuit voltage of 90 VDC. A Westinghouse 0−150 VDC meter is used to monitor the output voltage, while a 0−250 ADC ammeter is used to monitor the current. The arc itself is started by using a 200 A lamp starter (Hanovia model 29912) which generates a high voltage pulse.

Figure 4 shows a schematic top view of the entire machine, with the arc source [AS] installed. The source is placed in a vacuum chamber [VC1] pumped by a 20" Westinghouse oil diffusion pump. That chamber is connected by a flexible bellows to a test stand consisting of a bell jar [VC2] pumped by a system comprising a 6" mercury diffusion pump, a freon-cooled chevron baffle and a liquid nitrogen trap. Differential pumping between these two chambers is provided by a skimmer [S] with

an orifice diameter of about 1 mm having a knife-sharp edge. Chamber VC2 contains a beam flag [F], a beam chopper [C1] which modulates and allows ac detection of the beam, a pair of electric deflector plates which eliminate ions from the beam [D], and an EAI 300 quadrupole mass spectrometer with an electron bombardment ion source [QMS].

The arc source is mounted so as to have its nozzle is in the center of a 6" diameter by 1.4" thick electromagnet [M]. This device has no ferromagnetic core and is formed by wrapping approximately 450 turns of 14 gauge armored polythermaleze insulated antenna wire (Belden, 8009−500) around an aluminum support structure. The magnet is typically operated at 20 volts and 20 amperes which provides a 1 kG axial field. Because of the heat generated by this electromagnet it is water cooled by 2 layers of 3/16" copper tubing which are imbedded in the wire windings and by a brass cooling channel which acts as the inner sleeve of the magnet. The assembled arc source is surrounded by this cooling channel during operation of the discharge. We have found that the 1 kG field is of critical importance in stabilizing the plasma. This stabilization occurs by providing a force perpendicular to the direction of motion of the ions. For ions moving along the magnet's axis the magnitude of this force is zero. For ions moving off axis, this force tends to make them spiral around the axial direction thereby confining them to the center of the free jet expansion. In Stwalley's and co-workers[15] and Kunth's and co-workers[9−12] original design the nozzle was placed at the exit edge of the magnet. In this configuration Stwalley[17] observed that his discharge characteristics were independent of magnetic field and that he could operate his arc source with that field entirely turned off. In our apparatus, in which the nozzle is located in the center of the magnet, the magnetic field greatly influences the plasma, such that by decreasing that field from 1000 gauss to about 700 or 600 gauss one can visually observe that the lumimous plasma displays a larger divergence. This effect is reversible in that by increasing the applied magnetic field the beam becomes narrower and better defined. In contrast to Stwalley's[17] observation, we have found it impossible to operate the discharge without a magnetic field of at least 500 gauss.

As shown in figure 4, the magnet [M] is mounted on a movable rail track so that once the arc is operating the arc source and the magnet may be jointly moved closer to the downstream skimmer [S] via a mechanical vacuum feedthrough [T] mounted on a 10" flange which permits the whole translation assembly [TA] to be moved back and forth.

3. Operation of Source

Any attempt to start the discharge in pure H_2 results in the destruction of the source and anything within its vicinity due to the unstable nature of this hot arc. It was found by Stwalley and coworkers[15] that a safe, reliable way to generate a hydrogen atom beam with this technique is to first start the plasma with argon and then gradually switch over to molecular hydrogen. This technique is so delicate that they filmed the changeover in order to document the operation[18]. A second—by—second table of the values of flow rates, voltage, and source pressure with some pertinent description is available[19]. Our current technique is very similar to theirs.

After evacuating VC1 and VC2 (figure 4), a flow of argon is established. The flow is regulated by a valve attached to a Dwyer gas flowmeter until a constant flow, equivalent of 7 standard cubic feet per hour, is achieved. The stagnation pressure was measured by a 0 to 1 atmosphere Wallace & Tiernan gauge on that line and was about 340 torr. At this time the pressure in VC1 is about 50 microns, and that in VC2 about 4×10^{-4} torr.

The argon arc is now initiated by turning on the Hanovia lamp starter which provides the voltage pulse between the anode and the cathode. The welder power supply indicates a voltage of 15 V and a current of 100 A. For 5 to 10 seconds after the start of the discharge, streams of sparks will sometimes be emitted from the nozzle. Eventually the discharge will stabilize and a steady intense light blue plume will be observed.

Once the discharge appears stable, hydrogen gas is *slowly* mixed into the argon flow. The gas is introduced into the system via a Granville—Phillips variable leak valve (series 203). No visible change appears in the plasma until approximately 24 torr partial pressure of hydrogen has been introduced. At this time there is a dramatic change in the appearance of the plume: it becomes much reduced in size and turns less intense and its color becomes a beautiful crimson red. The hydrogen flow is continuously increased until the hydrogen pressure reaches 150 torr. The intensity of the plasma emission (as detected by the naked eye) continues to decrease as the hydrogen flow increases. This procedure takes approximately ten minutes.

Once this hydrogen pressure has been reached the argon flow is slowly turned off, which results in a decrease of the arc current and an increase in its voltage. It is however vital that during this changeover the current be kept at a constant value of 100 A or the discharge will be extinguished. This is achieved by manually increasing the power supplied. During the decrease in the argon flow the emission becomes progressively more intense and the cooling water flowing through the anode and the cathode progressively hotter. It is at this point that the greatest chance of losing the discharge occurs, if the proper procedure is not carefully followed. The argon should be slowly turned off over a period of 10 minutes. If the current is kept at a constant value of 100 A, the voltage will rise from the initial 15 V to 45 V at the end of this operation.

Once the argon flow has been totally turned off and the electric current and hydrogen gas flow have stabilized, a brilliant diffuse crimsom red plume is observed at about 150 torr stagnation pressure. According to Stwalley and co-workers[15], who call the discharge at this time the 'standard' discharge, reducing the H_2 pressure but keeping the input power constant will produce a more intense beam of hydrogen atoms. Indeed, by slowly lowering the H_2 pressure to 70 torr the discharge is observed to go into this 'pencil' mode having the appearence of a sharp very intense beam of white light surrounded by a diffuse dull red plume. After the beam is placed in this mode further lowering of the stagnation pressure to 55 torr produces a much higher flux of hydrogen atoms as measured by the mass spectrometer (figure 4). Under these conditions the pressure in VC2 (figure 4) is about 2×10^{-5} torr while in VC1 it can be anywhere from 0.1 to 1 torr, depending on how much use the nozzle has previously had, and on how much its diameter may have changed during the current run. After about 25 minutes the voltage to the source will appear to drop to a value of ab jut 30 volts, and stay at that value for the rest of the run. Under these conditions the beam becomes quite stable and may be operated for a long time, 5 hours being the longest we have kept it on before deciding to turn it off.

The nozzle is at first operated far away ($\sim$ 17 cm) from the skimmer. Once the pencil mode is stabilized the source may be brought closer to the skimmer using

the translation assembly ([TA] in figure 4). After being placed within 8 cm of the latter there is a dramatic increase in the observed hydrogen atom beam intensity. This intensity steadily increases as the source is brought closer to the skimmer. 2 cm is the closest the source has ever been brought to the skimmer without the latter deforming due to heating. Normally it is operated 3 to 4 cm. away. However if the beam is returned to the 'standard' mode it is possible to bring the source even closer without fear of damaging the skimmer. This is undoubtly due to the plasma temperature being much lower when there is more gas flowing through the discharge, at constant power input.

The procedure which has been outlined above provides a reliable routine which results in a stable high temperature (pencil) arc source. The CW arc discharge in the H-atom source can be run continuously for many hours with a H_2 stagnation pressure of 50-100 torr such that the pressure in chamber VC1 is of the order of 10^{-1} torr and in VC2 of the order of 10^{-5} torr. The source can be used for 5 to 8 times (as stated previously) before it becomes necessary to replace its tungsten nozzle.

4. Results

With this source we are able to generate a beam of H atoms with 95% of the H_2 present in the beam dissociated as estimated by the relative height of the m/e = 1 and m/e = 2 peaks measured by using the mass spectrometer in VC2 (figure 4). With the help of absolute mass spectral peak intensity measurements we are able to estimate the H atom beam flux per unit solid angle as 1.3×10^{22} atoms s^{-1} sterad^{-1}.[20] Stwalley and coworkers[15] determined a lower bound of 4×10^{17} and an upper bound of 1×10^{20} atoms s^{-1} sterad^{-1} for their beam source. The reason for our significantly greater intensity, which is consistent with all our operating conditions, appears unclear at present. However, the nature of these discharges can apparently change appreciably from what would otherwise be considered simple modifications in the arc source. We feel one reason for our larger intensities lies in the higher degree of collimation of the beam which we are able to achieve due to the focusing of the plasma by the applied magnetic field.

We have also observed that under appropriate conditions this source can produce a beam of metastable H_3 molecules having an intensity of the order of 10^{20} to 10^{21} molecules s^{-1} sterad^{-1}.[20] This intensity is sufficiently high to permit interesting spectroscopic and dynamics experiments to be performed with this molecule.

We have also been able to make a crude energy analysis of the H atom beam by application of a repulsive potential to the first lens of the quadrupole mass spectrometer such that only ions having translational energies greater than needed to overcome that repulsive potential are able to pass through the mass analysis system and be detected. By scanning this repulsive potential and measuring the corresponding decrease in intensity, one can measure an approximate intergral of the energy distribution function. Numerical differentiation of this curve furnishes a crude estimate of the energy distribution function.

Performing this measurement while operating the H atom source in the 'pencil' mode at a stagnation pressure of 55 torr we measure an H atom energy distribution function with a maximum intensity at 13 eV and a FWHM of 5 eV. By contrast,

Stwalley's and co-workers' [15] distribution (measured by deflection of the H atom beam by an inhomogenours magnetic field) has a maximum at 5 eV and a FWHM of 5 eV. This difference in hydrogen atom translational energy indicates that our discharge is considerably hotter than theirs. This higher temperature may also in part account for our higher intensities.

If the stagnation pressure is increased to 70 torr (for which the beam is still in the pencil mode) the intensity maximum in the translational energy distribution is observed to shift down to 8 eV and the FWHM is reduced to 3 eV. Increasing the stagnation pressure (in the pencil mode) not only decreases the translational energy of the hydrogen atoms but also decreases the intensity of the beam as well. It appears from these results that increasing the stagnation pressure, at constant arc power, decreases the effective temperature of the plasma. As a result, the stagnation pressure may be used as a crude means of shifiting the overall translational energy of the beam. The intensity maxima in the energy distribution function of H_3 at 70 torr stagnation pressure also occurs at 8 eV but the FWHM is now 7 eV.

It should be noted that the high intensity and broad energy distribution function of the H atoms produced coupled with an appropriate velocity selector[21], could provide a beam of monoenergtic hydrogen atoms whose translational energies would be continously tunable from 0.1 to 5 eV. Such a source should be of great utility for a whole family of reactive scattering experiments.

6. References

1. R. B. Bernstein, *Chemical Dynamics via Molecular Beam and Laser Techniques*, New York : Oxford University Press (1982).

2. M. A. D. Fluendy and K. P. Lawley, *Chemical Applications of Molecular Beam Scattering*, Chapter 8, London : Chapman and Hall (1973).

3. D. R. Herschbach, *Disc. Far. Soc.*, **33**. 149 (1962).

4. N. G. Utterback, *Phys. Rev.*, **129**, 219 (1963).

5. G. T. Skinner, *Physics of Fluids*, **4**, 1172 (1961).

6. J. P. Toennies, W. Weley, and G. Wolf, *J. Chem. Phys*, **61**, 2461 (1974).

7. M. A. D. Fluendy, R. M. Martis, E. E. J. Muschlitz, and D. R. Herschbach, *J. Chem. Phys.*, **46**, 2172 (1967).

8. R. W. Kessler and B. Koglin, *Rev. Sci. Instr.*, **37**, 682 (1966).

9. E. L. Kunth, *Applied Mechanics Rev.*, **17**, 751, (1964).

10. E. L. Kunth, UCLA Department of Engineering Report #66−19, (April 1966).

11. W. S. Young, W. E. Rodgers, and E. L. Kunth, *Rev. Sci. Instrum.*, **40**, 1346, (1969).

12. W. S. Young, UCLA Department of Engineering Report #69-39 (July 1969).

13. G. Clausnitzer, *Nucl. Instrum. Methods*, **23**, 309, (1963).

14. K. R. Way, S.−C. Yang, and W. C. Stwalley, *Abstracts of the IXth International Conference on the Physics of Electronic and Atomic Collisions*, Univ. Washington P., Seattle, 957, (1975)

15. K. R. Way, S.−C. Yang, and W. C. Stwalley, *Rev. Sci. Instrum.*, **47**, 1049, (1976).

16. R. Gotting, H. R. Mayne, and J. P. Toennies, *J. Chem. Phys.*, **80**, 2230, (1984).

17. W. C. Stwalley, private communiation.

18. K. R. Way, S.−C. Yang, and W. C. Stwalley, *Operation of a Superthermal*

15

Arc—Heated Hydrogen Atom Source. This film may be rented from Media Library Audio Visual Center, University of Iowa, Iowa City, 1A 52242, Catalog No. U–30354.

19. K. R. Way, S.–C. Yang, and W. C. Stwalley, United States Energy Research and Development Administration Report COO–2326–11 (11 Feburary 1976). Alternatively, see AIP document No. PAPS RSINA 47–1049–17 for 16 pages of arc documentation material.

20. J. F. Garvey and A. Kuppermann, *Chem. Phys. Lett.*, **107**, 491 (1984).

21. R. R. Herm and D. R. Herschbach, UCRL-10562, UC-34 Physics (October, 1962).

7. Figures and Captions

Figure 1. Scale drawing of cathode assembly: A, hollow tube; B, thoriated tungsten cathode rod; C, set screw hole; D, support structure; E, bellows; F, outside casing; G and H, teflon screw holes. Originally the assembly (other than the cathode) was made out of brass but is now made out of stainless steel.

Figure 2. Expanded view of anode assembly: A, threaded copper front holder; B, thoriated tungsten nozzle anode; C, threaded copper back holder; D (1 and 2) brass anode housing; E, macor cylinder.

Figure 3. Cross sectional view of assembled anode and cathode structures.

Figure 4. A schematic top view of the apparatus: VC1 and VC2, vacuum chambers; AS, anode assembly; A, anode; C, cathode; M, electromagnet; S, water–cooled copper skimmer; TA, translation assembly; T, translator; P1 and P2, viewports; L, optical lens; C1 and C2, choppers; PM, photomultiplier; CP, current preamplifier; LI1 and LI2, lock–in amplifiers; SCR1 and SCR2, stripchart recorders; D, electric deflector plates; F, mechanical flag; QMS, quadrupole mass spectrometer; PA, preamplifier; MSE, mass spectrometer electronics.

GAS INLET

O-RING GROOVE

H

C
D
G

F

E

2 cm

A

WATER IN

WATER OUT

B

FIGURE 1.

FIGURE 2.

O RING

TEFLON
GASKET

2 cm
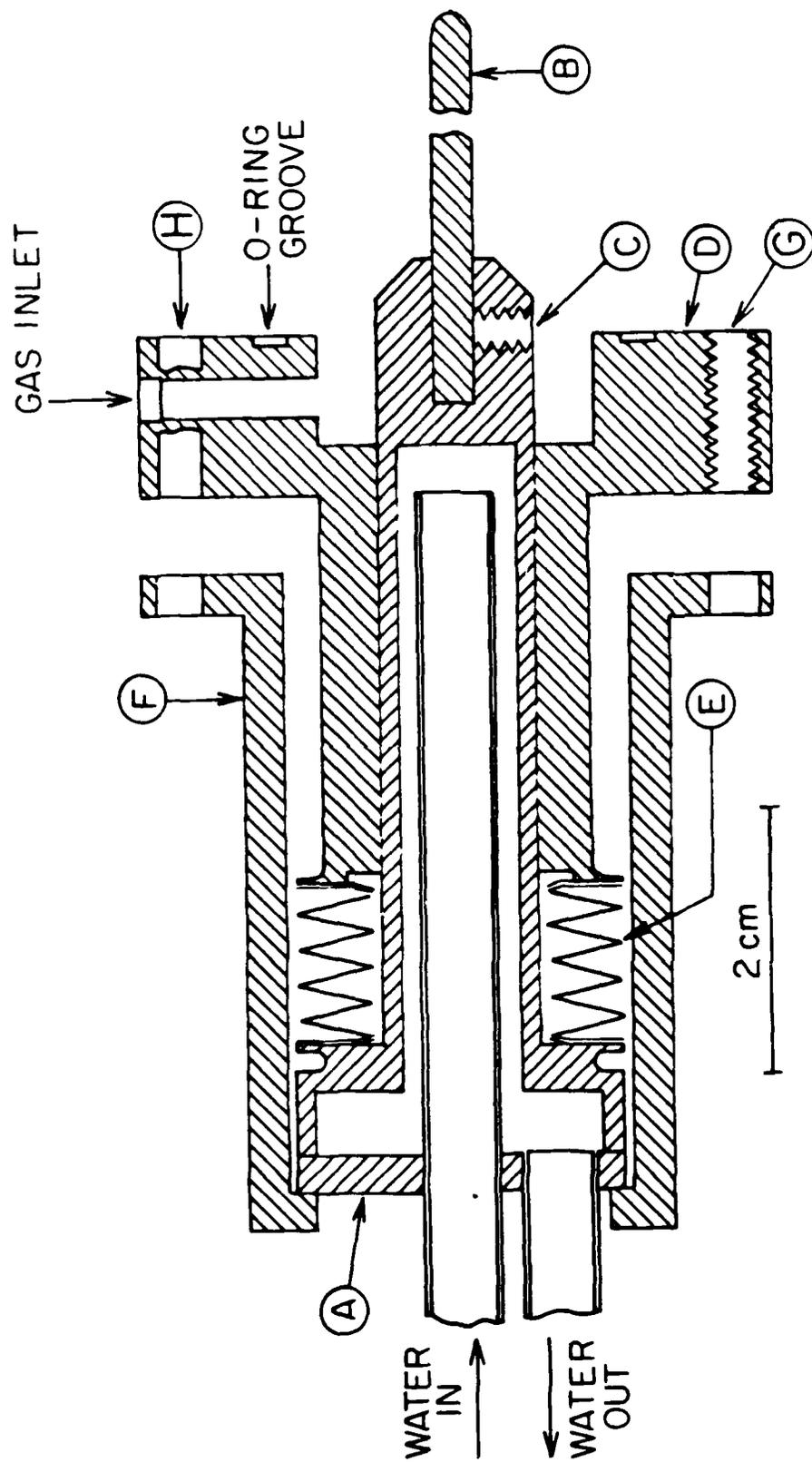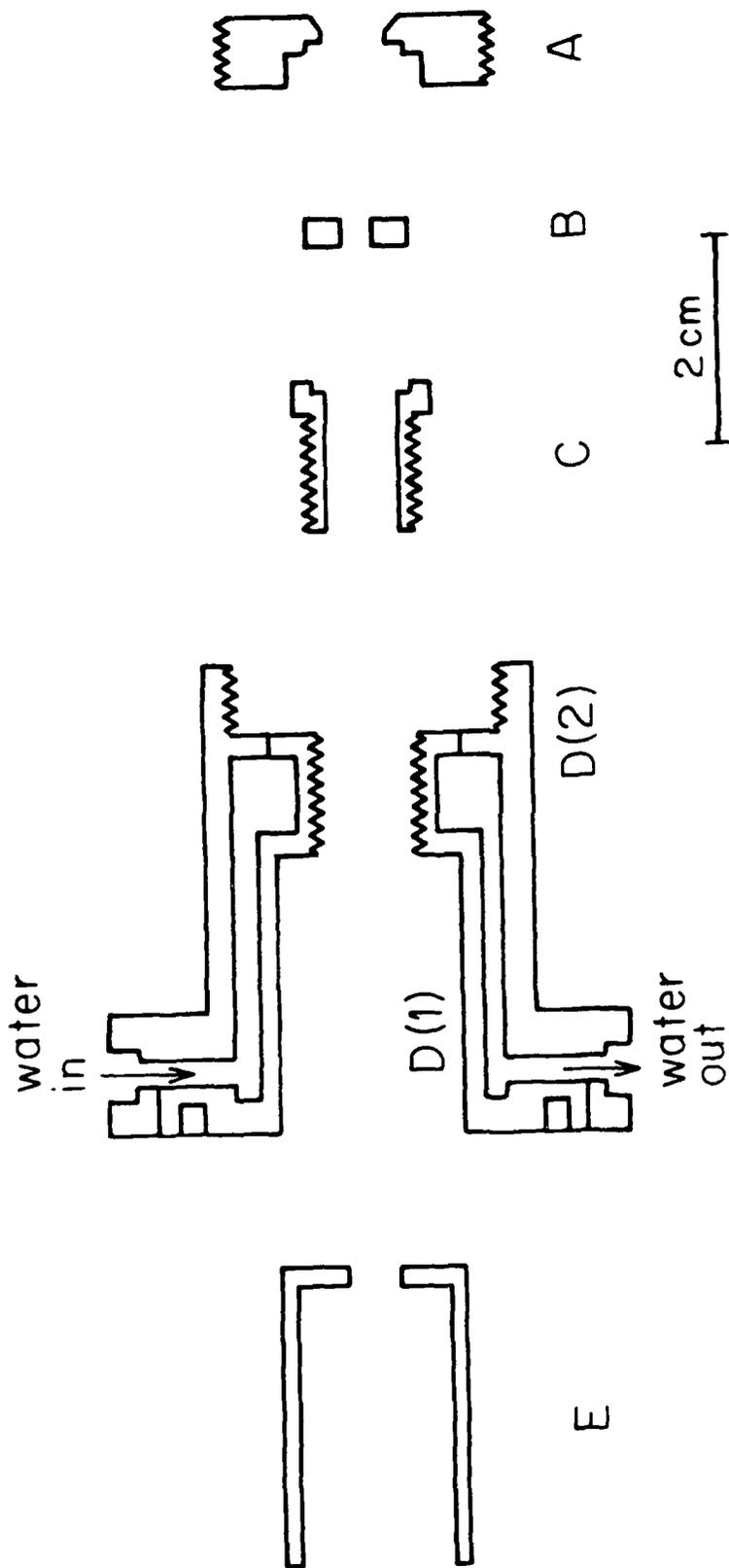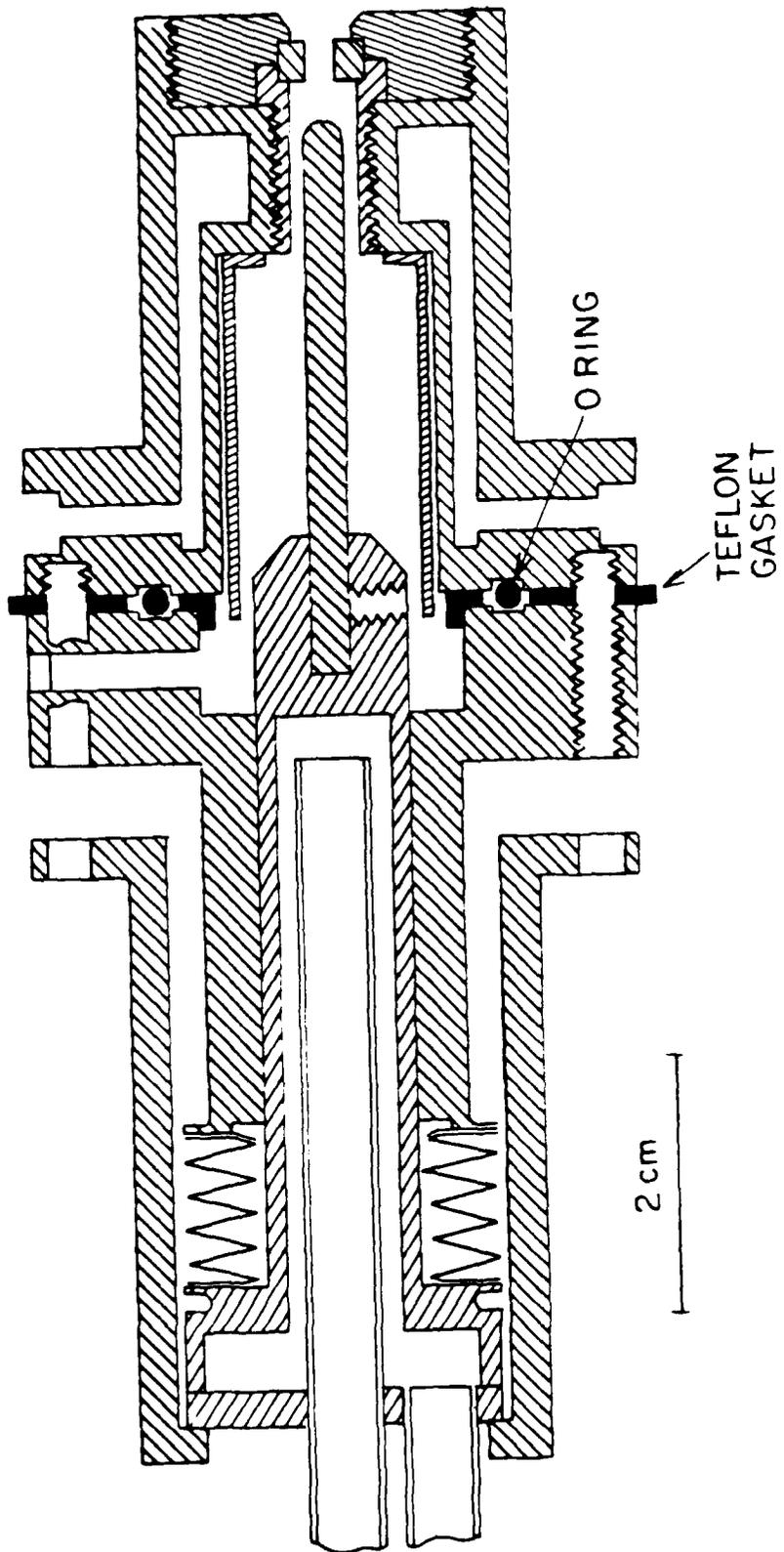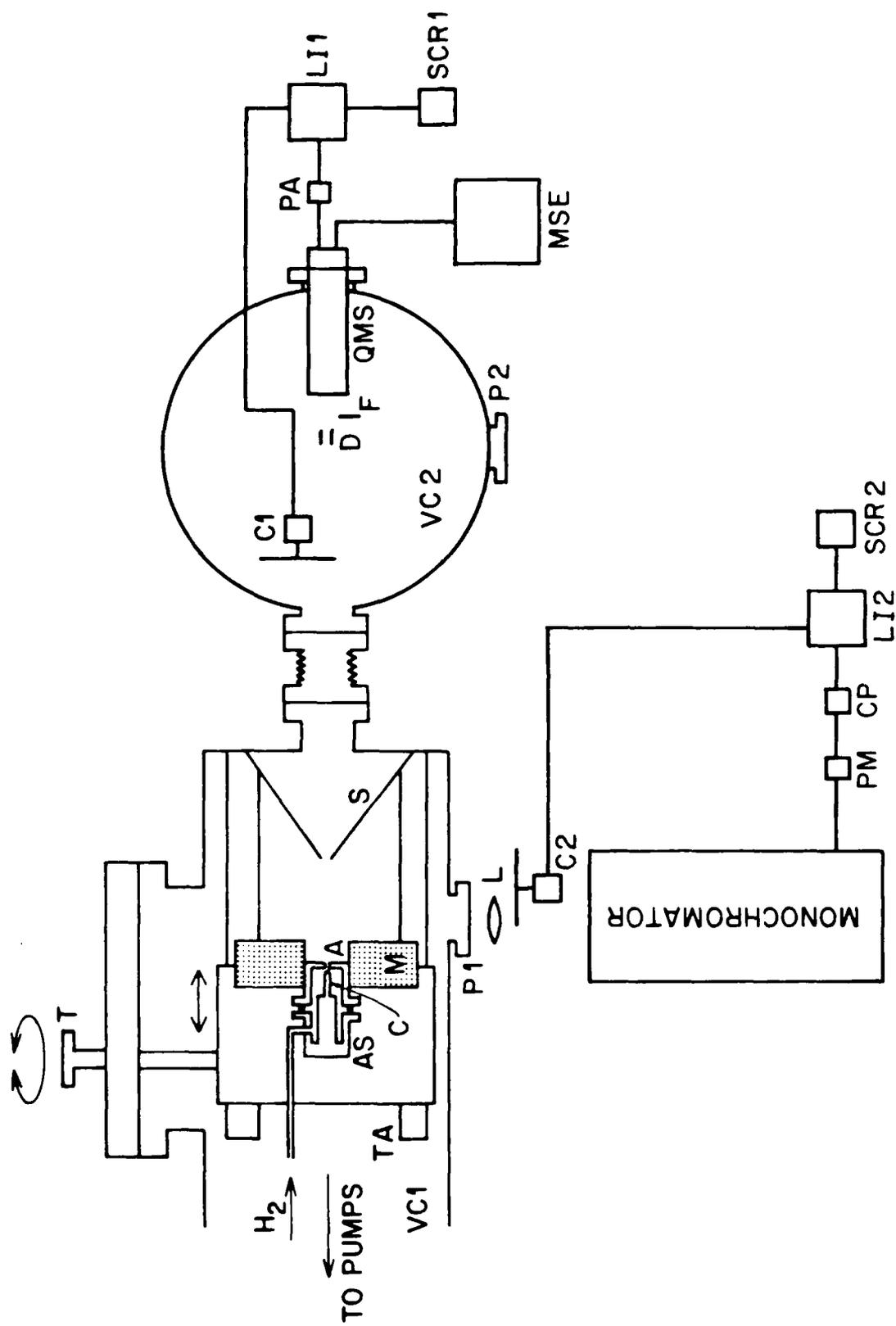
FIGURE 3.

FIGURE 4.

Sensitivity Analysis of the
Differential Scattering Cross-Section to the
He + CO$_2$ Interaction Potential [a]

Jarosław W. Winniczek [b] and Aron Kuppermann

Arthur Amos Noyes Laboratory of Chemical Physics [c]
California Institute of Technology, Pasadena, California 91125

(received   )

A detailed sensitivity analysis of the total and rotational state-to-state differential cross-section (DCS) is performed on an empirical potential energy surface for He + CO$_2$. The infinite order sudden approximation is used to calculate the cross-sections. The sensitivity analysis consits of: 1) a large scale modification of the parameters that determine the anisotropic potential, and 2) an infinitesimal variation of these parameters to obtain a relative sensitivity function for the DCS. From these we demonstrate the effect each potential parameter has on the cross-sections. Despite the fact that this highly quantum system displays no classical effects such as rainbow scattering, we have

shown that the quantal DCS oscillations contain significant information regarding the depth and width of the potential well and its anisotropy. Much of this information can be extracted from total-DCS scattering data. However the rotationally inelastic DCS contain a substantial amount of additional information regarding the shape of the potential energy surface.

1. INTRODUCTION

Interaction potentials between an atom and a molecule have been and continue to be subjects of significant theoretical as well as experimental analysis.[1-30] The experimentalists have sought ways to extract information on the shape of the potential from observed phenomena such as differential scattering cross-sections, integral cross-sections, transport phenomena, and relaxation spectroscopy.[9] The theorists have devised means for calculating and predicting the observed phenomena and associating them with various regions of the potential energy surface.[4-7,13,14,18-22] The anisotropy of these potentials results in the interconversion of translational and rotational energy during an encounter of the molecule with the atom. The most efficient theoretical tool for studing the outcome of such collisions is the infinite order sudden approximation (IOSA),[24] which we will use in the course of this paper, under conditions appropriate for its vadidity. The measurement of differential scattering cross sections in a crossed molecular beam apparatus is a very sensitive tool for the dermination of atom-molecule potentials. The region of the potential to which such data are most sensitive is the vicinity of the attractive well. Since this well results from the balance between the competing long-range atractive and the short range repulsive forces, its *ab-initio* evaluation is more difficult than for the adjacent regions. As a result, the experimental approach is the best one for the detrmination of the potential well characteristics.
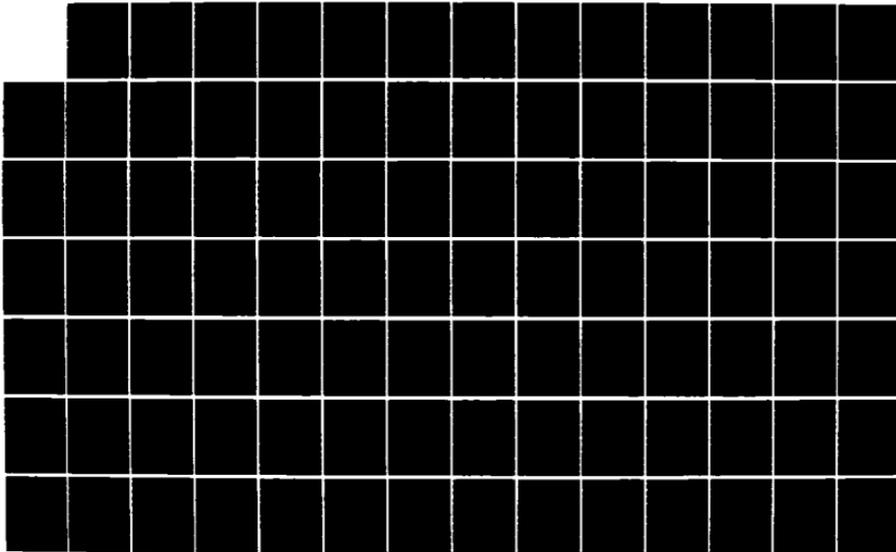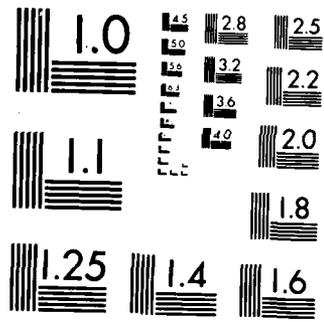
MICROCOPY RESOLUTION TEST CHART

NATIONAL BUREAU OF STANDARDS 1963 A

The extraction of potentials from scattering data begins by proposing a physically reasonable model for the potential. The model is characterized by several parameters that define the specific shape of the potential, such as well depth, well minimum position, well width, repulsive wall steepness, and various features of the anisotropy. Initial values of these parameters are chosen judiciously, and are then used to simulate the observed scattering data. A least squares alogorithm is employed to adjust these parameters such that the best possible agreement is achieved between the observed and calculated cross-sections. As a result, the interpretation and analysis of scattering experiments is very dependent on theoretical considerations. In particular one wishes to know: a) how do various features of the potential effect the observed cross-section? b) how sensitive are the data to a given parameter and therefore how significant is this parameter?

These questions have been addressed by many investigators in a variety of ways. Cross[24] used semiclassical theory to show that anisotropic potentials have differential cross-sections with dampened rainbow and quantal oscillations. Using the IOSA, Pack [25] has shown that the rainbow oscillation dampening is due to anisotropies in the potential well depth, while the quantal oscillation dampening is primarily caused by anisotropies in the position of the well depth minimum. In several instances computed IOSA integral rotational state-to-state cross-sections were found to be very sensitive to the

anisotropic topography.[14,19-21] Rotationally inelastic rainbow structure has been related to details of the anisotropic potential energy surface.[5-7,] Numerous experimentalists have successfully fitted potentials to their data only if those potentials contained anisotropy.[3,9,10,15-17]

A potential that has received considerable attention is one for He + CO_2. The repulsive wall as well as its anisotropy have been calculated by several methods[21,22]. The anisotropic long-range dispersion coefficients were evaluated by Pack.[35,36] Parker et al.[10,9] measured the differential cross-section from which they obtained an anisotropic potential for the well region. Recently we remeasured the differential cross-sections for that system, and proposed a new potential which we believe to be more accurate.[3]

In this paper we wish to probe and answer the questions regarding the significance and sensitivity of the parameters which specify the He + CO_2 potential. Some of the above mentioned papers employed classical scattering theory in arriving at many of their conclusions. Classical mechanics is not applicable to this highly quantal system which shows no evidence of rainbow scattering. Some have used rather rigid and inflexible potentials, such as the Lennard-Jones, which was shown to be unsatisfactory for modeling real potentials.[18]

This study has been undertaken to establish a clearer connection between the observed differential cross-sections and the potential energy surface for He + CO_2. Although we have chosen a specific system for

this analysis, we feel that the majority of the conclusions will apply to similar systems, *i.e.*, highly quantum systems with collision energies and rotational energy spacings analogous to those for He + CO_2. Our approach is two fold; a) We conduct a large scale sensitivity analysis by selectively modifing the parameters of our empirical potential to elucidate the effects they have on the scattering. b) We then conduct an infinitesimal sensitivity analysis by taking the partial derivatives of the cross-sections with respect to a given potential parameter; the sensitivities of all the parameters will be compared to each other and the relative significance of each parameter will be accessed.

The infinitesimal sensitivity analysis has been stimulated by the work of Rabitz and coworkers rf 11-14, allthough our approach is much less general and less elegant, it nonetheless is completely adequate in satisfing the goals of this paper.

Eno and Rabitz[11-14] have developed the formal theory of sensitivity analysis for collision process. The basic premise of the theory is to determine how variations in one quantity are affected by variations in an other quantity. The first application is obtaining the variations of cross-sections with variations in a feature of the interaction potential. The theory is highly generalizable to other applications, such as variation of one state-to-state cross-section with a different state-to-state cross-section, variations of one potential parameter with an other. All of these can be obtained from a single solution of the scattering problem, with

relatively little additional computational effort.

Eno and Rabitz[13] have evaluated the parameter sensitivities for an assumed He + CO_2 anisotropic potential. This potential is an inflexible Lennard-Jones type, and hence does not fully resemble the empirical potential[3]. In addition they reported sensitivities for differential cross-sections with an initial ground rotational state ($j = 0$). If He + CO_2 sensitivity results are to be a useful guide for the experimentalist, one should present calculations that most closely model the conditions of the experiment. Under most experimental conditions it is not practical or possible to produce CO_2 molecules in their ground state.[3,10] Even if CO_2 molecules were prepared in their ground states the small energy loss by the helium in exciting the CO_2 to a higher rotational state could not be observed with current time-of-flight molecular beam apparati. The rotational constant for CO_2 is so much smaller than the collision energy, a transition from the ground rotational state would change the scattered He energy (and hence flight time to the detector) by such a small amount that the transition would be obscured by the spreads in energy of the He and CO_2 beams.

Schinke et al.[6] have pointed out that the rotational rainbow (not to be confused with the classical rainbow) is a structure highly sensitive to the potential anisotropy. Eno and Rabitz[13] have confirmed this with their sensitivity analysis. However both of these studies have been performed on the initial ground state of the target molecule. For higher

ground states and larger changes in rotational quantum number the rotational rainbows become much less pronounced and move to higher scattering angles.[6,13] In fact Schinke et al.[6] recommend that experiments be conducted at the initial ground state of the target molecule and at higher scattering angles. As we stated before, for the case of CO_2 it is not practical to have it in its ground state. Also, large scattering angles are difficult to attain experimentally, since the signal is usually very low at high angles. For practical purposes it is best to concentrate on small scattering angles. We will then concentrate on conditions that best model experimental conditions, and as we will show the majority of significant information regarding the potential will be contained in the range of scattering angles easily observable.

In section 2 we briefly summarize the IOS approximation and present the needed expressions for the total and state-to-state differential cross-sections. In section 3 we review our model potential. In sections 4 and 5 we present the calculation methods. We demonstrate the inappropriateness of classical rainbow scattering analysis for our model system in section 6. Before considering anisotropic scattering we analyze a spherical analog of our model potential in section 7. The fully anisotropic potential sensitivities for the total differential cross-section are presented in section 8. In section 9 we discuss the rotational state-to-state differential cross-sections by way of the large scale sensitivity analysis, and employ the infinitesimal sensitivity analysis in section 10.

In section 11 we briefly discuss the results of a set of analyses at two collision energies above and below the 65 meV used in sections 4 thru 10. Finally we summarize our findings in section 12.

2. CROSS-SECTIONS

We have used the infinite order sudden approximation (IOSA) to calculate the total (elastic and inelastic) and rotational state-to-state differential scattering cross-sections (DCS). Since this formalism has been reviewed and outlined by many authors we will only present the salient points of the IOSA.

In the systems to be considered, the target molecules are essentially all in their ground vibrational states and the collision energies are well below the threshhold for producing vibrational excitations.[33] Therefore, it is reasonable to treat the target molecule as a rigid rotor of length R (the distance between the end atoms) having a moment of inertia I. Let $\underset{\sim}{r}$ be the position vector of the incident atom with respect to the center-of-mass of the molecule and γ be the angle between $\underset{\sim}{r}$ and the oriented molecular axis $\underset{\sim}{R}$. The nuclear motion Hamiltonian for this system is therefore

$$\hat{H} = -\frac{\hbar^2}{2\mu r}\frac{\partial^2}{\partial r^2}r + \frac{\hat{L}^2}{2\mu r^2} + \frac{\hat{j}^2}{2I} + V(r,\gamma) \tag{1}$$

where μ is the atom-molecule reduced mass, and $\hat{L}$ and $\hat{J}$ are the orbital angular momentum and molecular angular momentum operators, respectively.

The Schrödinger equation can be solved for the above Hamiltonian by expanding the wave function in eigenfunctions of the total angular momentum operator $\hat{\mathbf{J}} \equiv \hat{J} + \hat{L}$ and its projection $\hat{\mathbf{J}}_z$ about a space

fixed axis z. This results in a set of coupled radial differential equations; the coupling being due to the matrix elements of $V(r, \gamma)$ obtained using these eigenfunctions. Under the conditions of our calculation it is valid to decouple these equations, by imposing the centrifugal sudden (CS)[29,30] and energy sudden (ES)[27,28] approximations, collectively known as the infinite order sudden approximation (IOSA).[24] The CS approximation is introduced by replacing the orbital angular momentum operator with its eigenvalue form[29,30]

$$\hat{L}^2 \simeq \hbar^2 \bar{l}(\bar{l}+1) \qquad (2)$$

while to implement the ES approximation the molecular angular momentum operator is replaced with its eigenvalue form[27,28]

$$\hat{j}^2 \simeq \hbar^2 \bar{j}(\bar{j}+1) \qquad (3)$$

where $\bar{l}$ and $\bar{j}$ are appropriately chosen effective quantum numbers.

The resulting set of decoupled differential equations are

$$\left[\frac{d^2}{dr^2} + k_j^2 - \frac{\bar{l}(\bar{l}+1)}{r^2} - \frac{2\mu}{\hbar^2}V(r, \gamma)\right]\phi_{\bar{l}}(r; \gamma) = 0 \qquad (4)$$

where the wave vector is

$$k_j^2 = \frac{2\mu}{\hbar^2}\left[E - \frac{\hbar^2 \bar{j}(\bar{j}+1)}{2I}\right] \qquad (5)$$

E being the total energy of the system and ϕ_l is an effective scattering wave function for a angle of incidence γ. These equations can be solved

for a given $\bar{l}$ and γ in a manner analogous to a spherical problem, by requiring that the wave function must vanish at the origin, and at large r behave as

$$\phi_{\bar{l}} \xrightarrow[r \to \infty]{} k_j^{-1/2} \left\{ e^{-i(k_j r - \bar{l}\pi/2)} - e^{i[k_j r - \bar{l}\pi/2 + 2i\eta_{\bar{l}}(\gamma)]} \right\} \qquad (6)$$

where $\eta_{\bar{l}}(\gamma)$ is the phase shift for a given fixed atom-molecule orientation, which is obtained in a manner identical to that for a spherical scattering problem[31,32], and the resulting scattering amplitude is given by

$$f^{k_j}(\gamma \mid \theta) = \frac{i}{2k_j} \sum_l (2l+1) \left\{ 1 - e^{2i\eta_l(\gamma)} \right\} P_l(\cos\theta) \qquad (7)$$

It can be shown that the rotational state-to-state differential cross-section is given in this approximation by[24]

$$\sigma(j' \leftarrow j \mid \theta) = \frac{k_j^2}{(2j+1)k_{j'}^2} \sum_{m_j} | < j' m_j | f^{k_j}(\gamma \mid \theta) | j m_j >_{\mathrm{BF}} |^2 \qquad (8)$$

where the matrix elements of $f(\gamma \mid \theta)$ are evaluated in the spherical harmonics of the body-fixed coordinates - BF.[23] It should be noted that this result is independent of the choice of $\bar{l}$.

Equation (8) can be simplified for calculational purposes by expanding $f^{k_j}(\gamma \mid \theta)$ in Legendre polynomials

$$f^{k_j}(\gamma \mid \theta) = \sum_i F_i^{k_j}(\theta) P_l(\cos\gamma) \qquad (9)$$

where

$$F_i^{k_j}(\theta) = (i + 1/2) \int_0^\pi P_i(\cos\gamma) f^{k_j}(\gamma \mid \theta) \quad \sin\gamma \; d\gamma \qquad (10)$$

This then leads to the expression for the differential cross-section

$$\sigma(j' \leftarrow j \mid \theta) = \left(\frac{k_j}{k_j}\right)^2 \sum_{j''} \frac{1}{2j''+1} C^2(j, j'', j'; 0, 0, 0) \mid F_{j''}^{k_j}(\theta) \mid^2 \quad (11)$$

The total differential cross-section is the sum of all state-to-state cross-sections $\sigma(j' \leftarrow j \mid \theta)$ from an initial state j over all energetically allowed final states j'. The cross-section in equation (11) can be summed and simplified if the effective IOSA rotational quantum number $\bar{j}$ is set equal to j (the initial rotational state). By way of the completeness of the spherical harmonics and the addition theorem for the spherical harmonics it can be shown that the total differential cross-section is

$$\sigma(\theta) = 1/2 \int_0^\pi |f^{k_j}(\gamma \mid \theta)|^2 \sin\gamma \; d\gamma \qquad (12)$$

This expression, for a given initial relative translational energy, is independent of the initial rotational state j, and hence represents the total differential cross-section for any initial state.

It has been demonstrated that the IOSA is valid in cases where the relative collision energy is much larger than the spacing between rotational levels and larger than the attractive part of the potential. Since we will consider collision energies of 35 to 95 meV we are well

within the range validity for the He + CO_2 interaction where the typical CO_2 rotational spacings are less than 6 meV, and where the He + CO_2 well depth is less than 7 meV.

3. POTENTIALS

In order to obtain realistic results and fulfill the objectives of this paper we will use a realistic potential for our cross-section and sensitivity calculations. Our potential is based on one extracted from experimental crossed-beam data. We represent the anisotropy by giving an angular γ dependence to the parameters of an otherwise spherical potential,

$$V(r,\gamma) = V\left[r, \epsilon(\gamma), r_m(\gamma), \beta(\gamma)\right] \tag{13}$$

where ϵ is the well depth, r_m is the well minimum position, and β is a shape parameter which depends on the parameterization of V. Some parameterizations may have more than one shape parameter, all of which may have angular dependence. In this paper we will expand the well minimum position and the well depth to second order in Legendre polynomials

$$r_m(\gamma) = r_m^{(0)} + r_m^{(2)} P_2(\cos\gamma) \tag{14a}$$

$$= r_m^{(0)}[1 + qP_2(\cos\gamma)] \tag{14b}$$

and

$$\epsilon(\gamma) = \epsilon^{(0)} + \epsilon^{(2)} P_2(\cos\gamma) \tag{15a}$$

$$= \epsilon^{(0)}[1 + aP_2(\cos\gamma)] \tag{15b}$$

where we have defined the anisotropies of the well minimum position and depth as $q \equiv r_m^{(2)}/r_m^{(0)}$ and $a \equiv \epsilon^{(2)}/\epsilon^{(0)}$ respectively. Due to the symmetry of the CO_2 molecule the first order Legendre term is zero.

The shape of $V(r, r_m, \epsilon, \beta)$ is charterized by the highly flexible Morse-Morse-spline-van der Waals (MMSV) potential which may be written as

$$V(r) = \frac{\epsilon}{\omega}\left\{ e^{2(\beta' - r\beta\omega/r_m)} - 2e^{(\beta' - r\beta\omega/r_m)} \right\} \qquad (16a)$$

$$\text{for} \quad r < r_o$$

$$V(r) = \epsilon\left[e^{2\beta(1 - r/r_m)} - 2e^{\beta(1 - r/r_m)} \right] \qquad (16b)$$

$$\text{for} \quad r \leq r_i$$

$$V(r) = \left[S_1(r_{sv} - r)^2 + S_3 \right](r_{sv} - r)$$
$$+ \left[S_2(r - r_i)^2 + S_4 \right](r - r_i) \qquad (16c)$$

$$\text{for} \quad r_i < r < r_{sv}$$

$$V(r) = -\frac{C_6}{r^6} - \frac{C_8}{r^8} \qquad (16d)$$

$$\text{for} \quad r \geq r_{sv}$$

$$\text{with} \quad \omega = \frac{\beta' - \ln 2}{\beta - \ln 2}$$

where $r_o = r_m(1 - \ln 2/\beta)$ is the zero of both Morse funtions, and $r_i = r_m(1 + \ln 2/\beta)$ is the inflection point of the second Morse function. The spline coefficients S_1, S_2, S_3 and S_4 are determined by continuity conditions imposed on the potential and its derivative at r_i and r_{sv}. The Spline-van der Waals junction is maintained at $r_{sv}/r_m = 1.6,$[3,9,10,18] and

the constant ω is used to impose a smooth transition between the two Morse functions.

This parameter-expansion MMSV potential is a good choice for this study since the various features of the potential are neatly segregated into specific parameters; the well minimum position ($r_m^{(0)}$), the well depth ($\epsilon^{(0)}$), their anisotropies (q and a), the well width (β),and the repulsive wall steepness (β'). Table I lists the values of these parameters as used in this study, obtained from an empirically derived potential,[3] the long range dispersion terms for this potential were computed by Pack[36]). In the course of this study we will change some of these values one by one to see what effect the change has on the cross-sections and the sensitivities.

4. SENSITIVITY CALCULATIONS

Extensive work has been done by Eno and Rabitz[11-14] on formal sensitivity analysis in quantum collison theory. However, since the aims of this study are less probing and less demanding, we can adopt a simpler and less general approach to analyzing the sensitivity of observable data, *i.e.*, cross-sections, to the interaction potential; one that will serve as a useful guide to interpreting experimental scattering data. We wish to know how sensitive the differential scattering cross-section is to a parameter specifing the corresponding potential? In other words, for a given potential and collision energy, by what fraction will the cross-section change for a small change in the parameter. If this change is small enough we can expand the cross-section σ in the potential parameter p_k as

$$\sigma = \sigma^0 + \left(\frac{\partial \sigma}{\partial p_k}\right)_{p_k} (p_k - p_k^0) \tag{17}$$

where σ can refer to a state-to-state or a total differential cross-section, and the super-scripted σ^0 and p_k^0 refer to a reference choice of parameters. In order to facilitate comparison between sensitivities for various parameters and for different scattering angles as well as different initial and final conditions, we define a reduced and unitless relative sensitivity

$$S(\sigma; p_k) \equiv \frac{p_k}{\sigma} \left(\frac{\partial \sigma}{\partial p_k} \right) \tag{18}$$

This quantity gives the fractional change in the cross-section for a fractional change in the parameter. This may be written as

$$\frac{\Delta \sigma}{\sigma} = S(\sigma; p_k) \left(\frac{\Delta p_k}{p_k} \right) \tag{19}$$

For a given potential and collision energy we calculated the phase shifts $\eta_l(\gamma)$ in equation (7), via Numerov integration[38] for low values of l and via the JWKB method[37,31] for higher values (the switch over taking place between $l = 15$ and 25). In general it is sufficient to use 48 approach angles γ in order to obtain good values for state-to-state cross-sections (total differential cross-sections are convergent with only 12 approach angles). Using equations (7) and (10) we determined the expansion scatttering amplitudes $F_j^{k,j}(\theta)$. These are then used to obtain all state-to-state differential cross-sections from equation (11).

The sensitivities are determined by the finite difference method, which from equation (19) is expressed as

$$S(\sigma; p_k) = \left(\frac{p_k}{\Delta p_k} \right) \frac{\sigma(p_k + \Delta p_k) - \sigma(p_k)}{\sigma(p_k)}$$

The Δp_k is $10^{-4} p_k$ and the cross-section is calculated at p_k and $p_k(1 + 10^{-4})$ for a collision energy of 65 meV. Collision energies of 35 and 95 meV are also considered in section 11. The masses of the He and CO_2 are 4.0026 and 44.0098 amu, respectively.[33] They are used along

with the C-O bond distance[33] to determine the moment of inertia I (eq. 5).

The computational time for these sensitivities is rather small, 30 minutes on our VAX 11/780 computer for a given energy and a given potential with 10 parameter p_k varied.

5. THE METHOD

In order to investigate the effect the potential parameters have on the differential cross-section we have calculated the cross-sections and their sensitivities for several physically reasonable values of a given parameter. We start with the above mentioned parameter-expansion MMSV potential, the parameters for which are given in Table I. We then change one parameter and determine its effect on the cross-sections and sensitivities. Since there are ten parameters that specify this potential and since we wish to consider several initial values of each of these parameters above and below their actual values, we can easily generate well over several hundered figures representing the dependence of the differential cross-sections on these parameters. This is definately undesirable, nor is it very informative. Hence we will show only some of the figures and summarize the key features of the others in tabular form.

We have constructed various potentials based on the one in Table I, for which we give the designation M. In order to be able to refer to these modified potentials we will classify them by the symbols outlined in Tables II and III. The first table (II) lists the spherical potential constructed from the empirical anisotropic MMSV potential (M). This potential is generated by setting q, a, $C_6^{(2)}$, and $C_8^{(2)}$ equal to zero in Eqs. 14 and 15. The other table (III) lists variations in the anisotropic potential.

Various sensitivity features which are not plotted will be compared to those that are plotted, in Tables V thru IX. The two characteristics of the sensitivity functions which we will compare are: their overall magnitude, abbreviated as "mag.", and their oscillations with scattering angle, abbreviated as "osc.". A trend in either of these properties as a function of an increase of a parameter, energy or inelasticity is indicated with several adjectives. By "same" magnitude we mean that the magnitudes of the two sensitivities are within a factor of 1.2 of each other for all angles. Magnitudes that are "similar" (abbrev. "siml.") are within a factor of 1.2 at most angles with some larger variations up to factor of 1.5 for some ranges of angles. Changes in magnitude are marked as "increasing" ("incr.") or "decreasing" ("decr."). A "slight" ("sl.") increase or decrease is less than a factor of 2, and is usually over the entire range, unless marked otherwise; while "significant" ("sig.") change is a change by a factor of 10 or more.

Changes in oscillation control are more difficult to quantify. By "same" we mean that the sensitivity oscillations cross zero at the same angles for the two sensitivities being compared. "Similar" indicates the same number of zero crossings but with some at different angles. A "significant" increase or decrease in oscillation control means there was at least a factor of 2 change in the number of zero crossings; while a "slight" change is one for less than a factor of 1.2 or just a change in the positions of the crossings.

6. CLASSICAL BEHAVIOR

It is well known[3,9,10,15-18] that helium-molecule scattering data exhibit very pronounced quantum effects, as is evident by the broad oscillations in the differential cross-section. Let us nonetheless summarize the characteristcs of classical scattering using different central field potentials. To this effect we calculate the classical deflection function given by[2]

$$\Theta(b) = \pi - 2b \int_{r_c}^{\infty} dr \; \frac{1}{r^2 \sqrt{1 - V(r)/E - b^2/r^2}} \qquad (20)$$

where r_c is the classical turning point of the potential, and b is the classical impact parameter which can be expressed in terms of the partial wave angular momentum quantum number l

$$b = \frac{l + 1/2}{k} \qquad (21)$$

The classical differential cross-section is given as[2]

$$\sigma(\theta) = \sum_i \frac{b_i}{\sin\theta \; | \frac{d\Theta}{db_i} |} \qquad (22)$$

the sum is over all b_i for which $\Theta(b_i)$ exists such that $\theta = | \Theta(\bmod \pi) |$.

It is clear that as $\frac{d\Theta}{db}$ approaches zero the cross-section approaches infinity. The scattering angle at which this occurs is known as the rainbow angle. In Figure 1 we plot the deflection function versus the reduced impact parameter (actually $bk - \frac{1}{2} = l$). The minimum of $\Theta(l)$

is indicative of the rainbow angle, while the inflection of $\Theta(l)$ will yield the pre-rainbow minimum of the cross-section.

Table IV summarizes the positions of the rainbow maxima and the corresponding oscillation minima for different spherical potentials. The rainbow angle is most strongly affected by the well depth and well width, and only slightly by the well minimum position. The well mimimum position does however, have a strong effect on the impact parameter (or l) at which the rainbow angle occurs. With behavior in mind let us analyze to quantum DCS for the SM potential given in Figure 2. The lowest scattering angle oscillation occurs at 4.5 degrees and it is very dampened. The next oscillation is much more pronounced having a well defined minimum at 7.7 degrees and a maximum at 9.8 degrees. Only this second oscillation is close enough to the rainbow to be considered as a vestige of that classical feature. If that is indeed the case it should not be strongly affected by changes in well minimum position (r_m), while its angular position should be shifted most by the well depth or well width. In order to verify whether this is or is not the case, we present in Figure 3 comparative plots for several different MMSV potentials. From Figure 3a we observe that increasing r_m shifts all of the oscillations closer together and modifies their relative intensities, while variations in ϵ or β have only a marginal influence on their positions (Figures 3a and 3b). Hence, we can conclude that there is no evidence of any rainbow structure in this highly quantum system. Despite the fact that this fingerprint of

well depth is not observable, we will show that the quantal oscillations
do contain significant well depth and width information.

7. DCS SENSITIVITIES FOR SPHERICAL POTENTIALS

Before we deal with the effects of potential anisotropy on the differential scattering cross-section (DCS), we will discuss the influence of the parameters of a spherical MMSV potential on the DCS. As mentioned in the previous section, the position of the DCS oscillations is most strongly influenced by the well position (r_m) with some small shifts due to changes in the well depth (ϵ) and width (β).

We draw attention to the intensity of the oscillations for various values of r_m, ϵ, and β in Figure 3. An increase in ϵ (Fig. 3a) tends to intensify most of the oscillations, even the low angle one becomes clearly visible at high ϵ. The only exception to this rule is the second oscillation (at $\sim 7.5°$) which decreases slightly in intensity with increasing ϵ. If the well is made narrower, i.e. β is increased (Fig. 3c) the high angle oscillations (above $15°$) increase in intensity, while the intensity of the low angle oscillations decreases. The intensity of the oscillation at ~ 12 degrees does not change appreciably with β. The intensity behavior is less regular for variations in r_m (Fig.3a). The overall pattern is for the oscillation amplitude to decrease somewhat with increasing r_m - while the overall DCS increases as does the frequency of the oscillations. However, the lowest angle oscillation is first dampened as r_m increases, but as r_m becomes even larger it reappears.

It is clearly evident that despite no indication of rainbow scattering, the spherical potential DCS contains information pertaining to the well

depth and width, and it is known that r_m has a greater influence over the cross-section than any of the other parameters. Since r_m effectively determines the size of the scattering target it will in turn determine the overall magnitude of the cross-section. The positions of the DCS oscillations will also be most influenced by the size of the scattering target. This may be visualized by analogy to the diffraction of light through a slit, where the slit width is analogous to the target size. As the slit width is decreased the diffraction pattern spacings increase and broaden out. The same is true for scattering; as r_m decreases the oscillations broaden out and decrease in frequency as a function of angle. However, it is unrealistic to expect *a priori* that the well depth and width have a small or negligible influence on the shape of the DCS. After all, they both deterime the shape and value of the potential at a given r. The value of the potential can in turn be related (in classical terms) to the degree of deflection the probe particle will be subject to for a given impact parameter.

In Figure 4 we plot the sensitivities for the six parameters of the MMSV-(SM) potential. The above mentioned observations and expectations are clearly evident in the plots. The r_m sensitivity is the greatest by an overall factor of 10 above that for ϵ or β. The overall sensitivities for ϵ and β are very similar, while the β' sensitivity is slightly smaller than that for β. The C_6 and C_8 sensitivities are lower by a factor of 100 and 1000, respectively, than that for r_m at angles below

25 degrees. Above 25 degrees, the C_6 sensitivity becomes similar to that for C_8, both being about 1000 times lower than for r_m. The most pronounced feature of all of these sensitivities is their oscillation between positive and negative values, such that an increase in a parameter will shift $\sigma(\theta)$ up at one angle and down at another. In other words, all the potential parameters have an influence on the DCS oscillations and magnitude.

Comparing the sensitivities $S(\theta; \epsilon)$ and $S(\theta; \beta)$ we observe that for θ less than 15 degrees they have in general opposite signs; while for θ between 15 and 35 degrees they usually have the same sign. Beyond 35 degrees their behavior is not well correlated. Even the small dampened DCS oscillation at 4.5 degrees shows strong sensitivity to both ϵ and β. However if this oscillation is dampened further by setting ϵ low and β high (potential SBEHL in Table II) the sensitivity in this region decreases and loses its oscillatory structure. In general many of the gross features of the sensitivities are preserved if a parameter is altered by a physically reasonable amount, as in Table II.

The β' sensitivity shows very similar structure to the β one in the range of 10 to 20 degrees. Beyond 20 degrees the overall magnitude of $S(\theta; \beta')$ remains relatively constant as the regularity of the oscillations decreases significantly; whereas at angles below 10 degrees overall magnitude of the sensitivity drops rapidly with angle. From classical scattering theory we would not expect a parameter that controls the

close (low r) features of the potential to have any effect on small angle scattering. Since for $r \geq r_o$ (potential zero crossing) β' has no effect on the potential, we would not expect to see any β' sensitivity for those impact parameters which do not sample the potential in the region $r < r_o$. For the MMSV-SM potential these impact parameters correspond classically to scattering angles of less than 15 degrees, below which $S(\theta; \beta')$ starts to decrease, dropping to zero at 0 degrees. Yet because this is a highly quantum system the sensitivity does not drop to zero instantly at 15 degrees.

Similar classical scattering arguments can be used to explain why the C_6 and C_8 sensitivities are largest at small angles. Large impact parameters imply larger distances of closest approach, where the potential is weak and produces a small scattering angle. Hence the far reaches of the potential, as determined by C_6 and C_8, will have significant influence on small angle scattering. For scattering angles less than 7 degrees the C_6 sensitivity is within a factor of two of the r_m, ϵ, and β sensitivities. The C_8 sensitivity is much smaller then the one for C_6 at angles less than 25 degrees, and is not important in defining the shape of the DCS. Above 25 degrees both $S(\theta; C_6)$ and $S(\theta; C_8)$ have approximately the same small magnitude and should play a minor role in the appearance of the differential scattering cross-section.

The sensitivities described above have been calculated for specific values of the potential parameters. What happens to these sensitivities

if one of the key parameters r_m, ϵ, or β is changed by a large although physically reasonable amount (as in Table II)? As we stated before, there is no benefit in plotting all of the sensitivities for every parameter change. Instead we have summarized, in Table V the changes that do occur in the sensitivities as each of these parameters is individually lowered or raised above its normal value (see also Section 5). Two key features of the sensitivities are the effects they imply on the overall magnitude and oscillations of the DCS. We will use the expression "oscillation control" as the effect of the parameter on the amplitude of the oscillations in the differential cross-section. This control manifests itself in the sensitivity versus angle curve as oscillations above and below zero. For example, we say that r_m exhibits strong oscillation control (Fig. 4a), while β' exhibits a poorer oscillation control (Fig. 4d), especially in ther range of 40 to 55 degrees.

Superficially, most of the sensitivities were not significantly affected by large, allthough physically reasonable, changes in a parameter. The most notable exceptions are the C_6 and C_8 sensitivites for changes in r_m and β. The increase of r_m moves both the Morse inflection point r_i and the spline-van der Waals junction to larger r where the van der Waals part of the potential is weaker. Therefore the van der Waals part makes up a smaller portions of the potential, and hence it has less less effect on the magnitude of the potential. Similarly, as β increases the well narrows, the inflection point r_i moves to smaller r, and the r_{sv} remains

the same. This makes the spline region wider and results in a greater influence of the van der Waals region, giving the C_6 and C_8 coefficients a greater control of the DCS.

The other variations in sensitivities are more subtle and are not as readily predictable. However, a clue to understanding some of this behavior is realizing that β and β' are dimensionless parameters that govern the well and repulsive wall shapes, respectively. The actual slope of the potential, in the attractive and repulsive regions, is governed by ϵ and r_m. Hence any change of these parameters is expected to affect the sensitivity of parameters that also control the slope, i.e. β and β'.

8.   TOTAL DCS SENSITIVITIES FOR ANISOTROPIC POTENTIALS

It is well known, as discussed in the introduction, that the anisotropy of r_m (q in eq. 14) has a much greater influence on the appearance of the DCS than does the anisotropy of ϵ (a in eq. 15). Yet it has been demonstrated[3] that a is essential in fitting potentials to experimental data; q as the only anisotropy term cannot adequately account for all the features of the observed DCS. Similar conclusions can be drawn from the total differential cross-sections (*i.e.*, summed over all final states) plotted in Figure 5. Variations of q from 0.1 to 0.5 show how significantly the oscillations can be dampened. For $q = 0.1$ the DCS is very similar to the one for a purely spherical potential (see Figure 2), despite the presence of ϵ anisitropy. However, both these values of q are physically unrealistic. The well minimum position anisotropy should follow the shape and size of the CO_2 molecule. Since the C-O bond distance is 1.16 Å, it then is expected that the difference between $r_m(\gamma = 0)$ and $r_m(\gamma = \pi/2)$ be approximately this distance. This is indeed the case for $q = 0.21$ (the experimentally fitted value) which results in a difference of 1.10 Å, whereas the difference is 0.53 Åfor $q = 0.1$ and 2.63 Åfor $q = 0.5$.

There are no easy clues that can be used to predict the well depth anisotropy (a), and as Figure 5b shows a has a much more subtle effect on the total DCS than q. An increase in a dampens some oscillations, i.e. at 5 and 9 degrees; while others become more

pronounced, especially at 15 degrees. Hence, well depth anisotropy information is contained not in overall oscillation dampening but in relative dampening and relative intensities of the oscillation. Just as in the spherical potential case, the total DCS was determined mainly by r_m, with fine variations in oscillation intensity resulting from the well depth and shape. Consequently, for anisotropic potentials the angular dependent well minimum position $r_m(\gamma)$ determines the main features of the total DCS. The well depth anisotropy and shape parameters gives the oscillatory structure of the cross-section.

In Figure 6 we present the effects of varying the shape parameters β and β'. As was the case for the spherical potential, an increase of β increases the oscillation amplitudes above 10 degrees and reduces those below that angle. Also the magnitude of the DCS above 10 degrees remains about the same, while below it drops with increasing β. We know that classical low angle scattering is due to trajectories that sample regions of the potential for large distances of closest approach r_c. For this distance equal to 3.8 Å(the value of r_i for the SM potential) the resultant scattering angle is about 8 degrees (for the scattering energy of 65 meV considered in this paper). The deflection angle for $r_c = 5.6$ Å(the value of r_{sv}) is 1 degree. As β increases the well narrows and the spline region between r_i and r_{sv} becomes shallower, and a smaller fraction of the trajectories are scattered in to the region between 1 and 8 degrees. Similarly as the well narrows the DCS exhibits sharper quantum

interference oscillations.

The repulsive wall shape parameter β' has little effect on scattering below about 16 degrees, the scattering angle corresponding to a classical closest approach distance radius of 3.1 Å, the value of r_o. Above 16 degrees, however, the increase of β' decreased the total DCS (Fig. 6b). The reason seems to be that as β' increases the wall becomes steeper and less likely to be penetrated, yielding a lower cross-section at the larger scattering angles.

In the framework of the above observations let us now consider the sensitivities for these parameters. The sensitivites to $r_m^{(0)}$, $\epsilon^{(0)}$, q, a, β and β' are presented in Figure 7, and to the van der Waals coefficients $C_6^{(0)}$, $C_8^{(0)}$, $C_6^{(2)}$, and $C_8^{(2)}$ in Figure 8. We can compare these sensitivities to those for the spherical limit of this potential (Fig. 4). The presence of anisotropy has significantly altered these sensitivites. Those for $r_m^{(0)}$, β and $C_6^{(0)}$ have increased in overall magnitude; while those for ϵ, β' and $C_8^{(0)}$ have decreased. The oscillation control has been reduced for ϵ and β', whereas for the other parameters it has remainded relatively the same in so far as the frequency of the sensitivity oscillations is concerned, with only some changes in their relative amplitudes. This is particularly true for $S(\theta; r_m^{(0)})$. The r_m sensitivity for the spherical potential has a progression of oscillations with alternating crests (postitive) and troughs (negative) of equal width and equal magnitude; whereas the $r_m^{(0)}$ sensitivity has large troughs (negative) and small and narrow peaks

(postitive). An increase in $r_m^{(0)}$ tends to lower the DCS oscillation troughs much more than it raises the crests. This is effectively a decrease in oscillation control. The peak to trough height does not increase as much for the anisotropic potential as for the spherical one for an increase in $r_m^{(0)}$, since for the spherical potential the troughs move down as much as the peaks move up, while for the anisotropic potential the troughs move down, but the peaks move up only slightly.

The sensitivity to the spherical average of the well depth $\epsilon^{(0)}$ is reduced slightly by the introduction of anisotropy, as can be seen from a comparison of Figures 7b and 4b. There is also some reduction of oscillation control, especially for low scattering angles ($\theta < 20°$). The DCS oscillation at 4 degrees is still influenced by $\epsilon^{(0)}$ such that an increase will deepen the trough of the oscillation. In general, the inclusion of anisotropy has reduced the precision with which well depth information can be extracted from a measured DCS. However, this is not as unfortunate as it may seem, since the DCS also contains information pertaining to the anisotropy. Also, the presence of anisotropy permits CO_2 rotational energy transfer, which can be observed as inelastic scattering. This inelastic scattering, as we shall see later, contains additional information which can be used to extract the various potential parameters, as well as the well depth, more accurately and more precisely.

The DCS oscillation dampening properties of the well minimum

position anisotropy q are clearly evident in Figure 7c. The sensitivity, $S(\theta; r_m^{(0)})$, is positive in regions of the DCS troughs, and negative in regions of DCS crests. The DCS dampening properties of a are very sinmilar to those of q, as is seen by comparing Figure 7d with Figure 7c. From 0 to 7.5 degrees the two sensitivites are of similar magnitude, while between 8 and 35 degrees the $S(\theta; q)$ magnitude rises up to 10 times that of $S(\theta; a)$. Therefore the scattering below 7.5 degrees should be most important in defining a, particularly since a has a greater oscillation control than q for the DCS oscillation at 4 degrees. Even in the range of 7.5 to 14 degrees $S(\theta; a)$ is one third of $S(\theta; q)$ indicating that a has a significant influence on the DCS. For low angle scattering ($\theta \leq 20°$) a provides much more oscillation control than $\epsilon^{(0)}$ and hence serves an indispensable function in modeling the real potential. In fact, it has been demonstrated[3] that a calculated DCS cannot be sucessfully fitted to experimental DCS scattering data with potential models that do not include well depth anisotropy.

The sensitivity to the well width parameter β has increased with the introduction of anisotropy, as indicated by comparing Figures 7e and 4c. The overall magnitude of this sensitivity has incresed, up to a factor of three, above 12 degrees; and oscillation control has also increased some (below 20 degrees). Indeed, the sensitivity to β is the second most intense one after $S(\theta; r_m^{(0)})$, greater than the $\epsilon^{(0)}$ sensitivity. Its importance should not be underemphasized, particularly for this

anisiotropic potential, although it is not obvious why the sensitivity should increase with increased anisotropy. This sensitivity of the DCS to the β parameter has not been previously realized.

The sensitivity to β' (Figure 7f) shows essentially the same behavior as in Figure 6b; very little sensitivity at low angles with only very minor oscillation control, and a negative sensitivity at higher angles. As mentioned above, scattering below 15 degrees corresponds to classical trajectories that do not approach the repulsive wall, hence this region $(0 < \theta < 15°)$ represents penetration into the classically forbidden region of the repulsive part of the potential. For the scattering angles above $15°$ oscillation control disappears and the sensitivity to β' demonstrates that a steeper wall (higher β') reduces the DCS magnitude.

The sensitivities to the dispersion coefficients are plotted in Figure 8. The only important coefficient, one with the largest magnitude by far, is $C_6^{(0)}$. The sensitivities to the other dispersion parameters is so low that they do not significantly affect the DCS. Since these coefficients are calculated theoretically, their sensitivities provide a guide as to how accurately those calculations must be performed. The sensitivities to the anisotropy terms $C_6^{(2)}$ and $C_8^{(2)}$ can be expected to be small because the van der Waals region extends ranging from r_{sv} to infinity and has some influence on the spline region. As the He atom traverses the van der Waals region the CO_2 molecule rotates thereby changing γ. The DCS then reflects the spherical averge of the dispersion terms. The well and

wall regions will be traversed more quickly by the He atom, and hence the anisotropy of this part of the potential will not be severely averaged over γ.

Table VI summarizes the significant changes that occur in the sensitivities if q, a, or β are changed above or below their nominal values. In general the sensitivities are not substantially affected by these changes; most of the differences are subtle. Some sensitivites increase as a parameter is increased, and upon a further increase of the parameter they drop again in magnitude. Only $S(\theta; a)$ increases significantly in magnitiude as a is raised; it also gains oscillation control as q is increased. In addition, a narrowing of the well i.e., and increase in β makes the well a sharper target which in turn increases the sensitivity of the well minimum position $(r_m^{(0)})$. Other than these there are no regular or predictable trends in the small variations of these sensitivities.

9. STATE-TO-STATE DIFFERENTIAL CROSS-SECTIONS

The anisotropy of the He + CO_2 interaction potential allows for the coupling and transfer of energy between the rotation of the CO_2 molecule and the relative translational energy between it and the helium atom. The total differential cross-sections, discussed in the previous sections of this paper, are the sums of a large set of rotational state-to-state transitions (Equation 12), and therefore they are less sensitive to the details of the the potential then the individual cross-sections would be. In this section we will show these state-to-state cross-sections depend on the characteristics of the potential. We have chosen as an example an initial state $j = 12$, which lies in the range of rotational states that the CO_2 is likely to occupy at all but the lowest temperatures. The discussions and conclusions for $j = 12$ can be easily carried over to other initial states j, from $j = 4$ to $j = 30$.

In Figure 9 we plot the full range of rotational transitions from $j = 12$. For a given change in $\Delta j = j' - j$ (where j' is the final rotational state) the shapes of the DCS curves for the rotational gain ($\Delta j > 0$) are very similar to the one for rotational loss ($\Delta j < 0$), for the same $|\Delta j|$. The major difference is that the rotational $\Delta j > 0$ transitions have DCS's which in magnitude are greater than those for the corresponding $\Delta j < 0$ trasitions. We will therefore focus our attention on the former without compromising detail or completeness of conclusions.

Elastic scattering dominates at low scattering angles. Inelastic

transitions for $\Delta j = 2$ become important for scattering angles θ above 10 degrees. Transitions for $\Delta j > 6$ are not significant for angles below 40 degrees. Beyond 40 degrees the $\Delta j = 8$ DCS has minor significance. Transitions with $\Delta j > 8$ although not shown in Figure 9, contribute very little to the total DCS, and are extremely small at all angles. We also do not show DCS's from initial states other than $j = 12$. These other transitions have virtually identical characteristics to those for $j = 12$. However, $j = 0$ is an exception in that DCS's for small Δj (2 and 4) are greater than those for the other inelastic ones and the elastic ones for angles above 10 or 15 degrees.

In Figure 10 we probe the effects of varying the potential well minimum position anisotropy q. The anisotropy parameter q elongates the potential along the CO_2 molecular axis (if it is positive). As this happens the torque about the center-of-mass of the CO_2 imparted by the He atom to the CO_2 molecule will increase, which increases the amount of translational to rotational energy exchange. We then expect a potential with a larger q to have greater inelastic cross-sections, as is borne out in Figures 10a and 10b. For $q = 0.5$ (high value) inelastic scattering is substantial even at 4 degrees (for Δj between 2 and 8). For $q = 0.1$ (low value) even $\Delta j = 4$ scattering has little effect on the total scattering. At 12 and 18 degrees (Fig. 10a) the DCS for the $\Delta j = 2$ transition is comparable in magnitude to that of the elastic DCS. The elastic DCS curve for $q = 0.1$ has oscillations of greater amplitude than the one for

$q = 0.21$. As q increases the elastic DCS oscillations dampen while those for inelastic transition DCS ($\Delta j > 2$) tend to increase. The elastic DCS decreases with q and so do the DCS's for small Δj transitions. The magnitude of the total DCS is unchanged by the value of q (Figure 5a), and since inelasticity increases with q, the elastic DCS should therefore decrease.

There are problems with potentials having large large values of q, and thereby relatively large differential cross-section for large Δj. The IOS approximation is only valid for cases where rotational transitions occur at small impact parameter and for relatively small changes in the rotational energy. A potential with a large q does not meet these criteria, and hence the results shown in Figure 10b, are not a good approximation to those the exact ones. Nonetheless, we can still use the results to show the trends that occur as q changes. Similar caution is required for low q potentials where the target molecule has a small moment of inertial I (a light diatom such as H_2, or even N_2 is an example). The small I is indicative of large spacings between rotational levels; a condition to which the IOSA is not applicable.

Variations in the well depth anisotropy a do not have as dramatic an effect on the DCS's as does q. Yet, as is evident from examining Figures 11a and 11b, the influence is significant. The differences in state-to-state DCS's are most apparent at low scattering angles, as a increases (in absolute value) from -0.2 to -0.9. We expect, based upon the discussion

of spherical potentials, the well depth information to be concentrated at scattering angles in the range of greatest classical sampling of the well region, i.e. 4 to 20 degrees. An increase in a dampens the oscillations for all inelastic DCS's, particularly for larger Δj's, while the DCS's increase in magnitude especially at low angles.

To account for these observations, we probed further by making several modifications in the well depth and its anisotropy. First, we plot the state-to-state DCS's for two extreme values of the overall well depth $\epsilon^{(0)}$ (2.5 and 7.5 meV) with the anisotropy a unchanged at -0.5. For an increasing $\epsilon^{(0)}$ the trends, as shown in Figures 12a and 12b, are: the inelastic DCS amplitudes increases; the elastic DCS magnitude increases between 4 and 20 degrees; and the DCS oscillation magnitudes also increase somewhat abvove 25 degrees. For a negative a the well is deeper than the spherical average $\epsilon^{(0)}$ at angles greater than the zero point of the second order Legendre polynomial $P_2(\cos\gamma)$ ($\cos\gamma = 1/\sqrt{3}$ or $\gamma \approx 54.7°$). We can make this region shallower than $\epsilon^{(0)}$ and place the very minimum of the potential on the molecular axis ($\gamma = 0$, or π) rather than perpendicular to it ($\gamma = \pi/2$), by setting a to a positive value. Figures 13 show the DCS's for two different values of a positive: a +0.5 and +0.1. For scattering angles below 12 to 22 degrees (depending on the Δj of the transition) the inelastic DCS's increase in overall magnitude and decrease in oscillation amplitude as a is increased. Above these angles the DCS magnitude drops slightly and the oscillations intensify.

To complete the test we set the well depth anisotropy a to $+0.3$ and $\epsilon^{(0)}$ to 2.5 and 5.5 meV, Figures 13c and 13d respectively. Once again the deepening of the well produces an increase of the magnitude of the inelastic DCS for low scattering angles (12 to 22 degrees).

In summary, the increase of the well depth increases the inelastic DCS regardless of the anisotropy. The increase of the magnitude of the well depth anisotropy also increaes the inelastic DCS. An increase in the magnitude of a will deepen the well somewhere. Since the inelastic DCS's apparently sense a depth increase, regardless of the sign of a, they must be influenced by regions of the potential above and below the approach angle γ corresponding to the zero of $P_2(\cos\gamma)$. This is consistent with the arguments presented in the discussion of the well minimum anisotropy q: the most effective translational-rotational energy transfer will occur at approach angles γ for which the torque is greatest, i.e. somewhere away from both parallel and perpendicular approaches.

Figures 14a and 14b show elastic and inelastic DCS's for extreme values of the potential well width parameter β. As we demonstrated in the Sections 7 and 8, an increase in β results in an increase in the low angle scattering and an increase in DCS oscillation amplitudes. The same is observed for the state-to-state DCS's. An increase in β narrows the well so that the values of the potential in the well region decrease for all r other than r_m at a fixed γ. A narrower well will have a repulsive wall which starts at a larger r and has an initially steeper slope (before

β' becomes influential), and therefore the effective target size increases as does the cross-section. As β increases, the inelastic DCS increases at scattering angles which classically correspond to collisions with the repulsive wall of the potential, as can be seen by comparing Figures 14a, 9b and 14b for which β is 5.0, 7.2 12.0 respectively.

When we discussed the effects of the repulsive wall shape parameter on the total DCS, we observed that an increase in β' decreases the scattering intensity at higher angles with virtually no effect on the oscillations. A similar observation is made for state-to-state DCS's for small Δj (≤ 4). For the larger Δj (≥ 6) the reverse is true, i.e. the high angle state-to-state DCS's increase with increasing wall steepness. There is no discernable difference in the state-to-state DCS's for variations in β' at angles below 15 degrees, and only above 35 degrees is the difference reasonably significant. At 60 degrees the largest variation is for the $\Delta j = 8$ DCS, with less than a factor of 2 increarse in the DCS for a change in β' from 5.0 to 12.0.

10. STATE-TO-STATE DCS SENSITIVITIES

In the previous section we observed the response of the state-to-state differential cross-sections to relatively large changes in potential parameters. We now turn to the sensitivities of equation 18, to gauge the response of the state-to-state DCS to very small parameter changes. How do they compare to the total DCS sensitivities? How do they change as the inelasticity increases?

In Figure 15 we plot the sensitivities of the $j = 12$ to $j = 14$ DCS sensitivities to the parameters $r_m^{(0)}$, $\epsilon^{(0)}$, q, a, β and β'. We observe only one significant change over the total DCS sensitivities of Figure 7, otherwise the two sets of sensitivities are very similar. The change is in the q sensitivity $S(\theta;q)$ which shows a very significant loss of oscillation control and an overall increase in magnitude. The sensitivities to the $C_6^{(0)}$ and $C_6^{(2)}$ coefficients do show some increase in magnitude over those for the total DCS. In Table VII we compare these sensitivities to the sensitivities for the total DCS, the elastic $j = 12$ DCS, and a variety of inelastic ($j = 12$ to $j = 4, 6, 8, 10, 14, 16, 18, 20$) DCS.

The difference between the total and state-to-state sensitivities for q is quite remarkable, compare Figures 7c and 15c respectively. The increase in magnitude was expected since the elongation of the potential should be and is the primary feature responsible for translational-rotational energy exchange. The significant loss of oscillation control indicates that the primary dampening mechanism of the total DCS

oscillations is the fact that the phases of the inelastic DCS oscillations differ from each other and from those of the elastic DCS (see Figures 9 and 10). As q increases in magnitude the inelastic DCS's increase and therefore contribute more to the total DCS. Since the oscillation peaks of $j' \leftarrow j$ DCS occur roughly at the same angles as the troughs of the adjacent DCS for which the j' differ by 2, the oscillations of the total DCS will dampen. The state-to-state inelastic DCS oscillations are not dampened at all by q; actually, a large q tends to increase the large Δj oscillations (compare Figures 10a and 10b). The state-to-state elastic DCS oscillations, however, are dampened by an increasing q; and the $S(\theta; q)$ is very similar to the one for the total DCS with only minor decrease in oscillation control (we did not plot the elastic sensitivity since it is so similar to the total).

The q sensitivity in Figure 15d is positive for $\theta < 20$ degrees and negative for $\theta > 25°$. As Δj increases the sensitivity becomes positive for all angles and increases in magnitude up to 20 times for $j' = 4 \leftarrow j = 12$ over the $12 \leftarrow 12$ elastic process (Table VII). This effect was observed in Figure 10, where for small angles the DCS increases with q, while at larger angles ($\theta > 20°$) the DCS decreases for small Δj and increases for larger Δj. Classical trajectories with small values of the distance of closest approach correspond to small impact parameters and have large scattering angles. Large angle scattering is due to collisions that approach the repulsive wall, for which smaller Δj DCS decrease while

larger Δj increase with increasing q. If a trajectory approaches the repulsive wall and scatters at large angles it will be able to transfer a greater amount of energy than at lower angles and therefore the total DCS will be dominated by larger Δj transitions.

The spherical average of the well depth minimum position $r_m^{(0)}$ has a very strong effect on the high inelasticity DCS. For $\Delta j = 8$ the sensitivity $S(\theta; r_m^{(0)})$ increases by a factor of 500 over the one for the total DCS (Table VII). The repulsive wall shape parameter β' sensitivity also shows a significant increase for larger Δj, up to a factor of 100. Since large Δj transitions occur at the wall, the parameters that control the position and shape of that wall ($r_m^{(0)}$ and β' respectively), should have the greatest influence on the corresponding inelstic DCS. A larger $r_m^{(0)}$ means a larger target and hence a greater DCS. A larger β' means a steeper wall and hence a more effective inelastic DCS (as we observed at the end of the previous section).

The sensitivity to the well depth anisotropy parameter a is rather strongly affected by large Δj transitions; the $\Delta j = 8$ sensitivity increases up to 30 times over the one for the total DCS. This confirms the observations and discussions of the previous section, according to which an increase in the magnitude of a increases the inelastic DCS.

The increase of sensitivities for the dispersion terms, particularly the anisotropy terms $C_6^{(2)}$ and $C_8^{(2)}$, with increasing inelasticity (Table VII), is unimportant because the corresponding state-to-state DCS is

extremely small (Figures 9a and 9b), especially at low scattering angles where elastic transitions dominate.

Table VIII summarizes the effects of parameter changes on the $j = 12$ to $j' = 14$ DCS sensitivities. It is similar to the analogous table (VI) for the total DCS sensitivities. Many of the conclusions reached regarding Table VI are equally applicable to Table VIII. We include this table only for completeness sake, and refer the reader to previous discussions, since there is no additional insight that can be presented.

11. DIFFERENT SCATTERING ENERGIES

All of the above analyses were for a single relative kinetic energy of 65 meV. What happens to the DCS's and their sensitivities at energies above and below this value? We have made calculations at 35 meV and 95 meV and summarize their results below with emphasis on the differences between the studies at these energies and those at 65 meV. The IOS approximation is valid over this energy range.

The positions of the DCS oscillations depend not only upon the well minimum location but also on the kinetic energy and hence the wavelength. As the energy increases the wavelength decreases and hence the spacing of the oscillations decreases. The magnitudes of the total DCS and also the inelastic DCS decrease with increasing energy for scattering angles below 30 degrees. At scattering angles above 30 degrees kinetic energy has a negligible

effect on the magnitude of all the DCS's. Inelastic DCS's for small Δj also decrease with increasing energy; while for large Δj they increase. This is expected since the large Δj DCS's depend upon the repulsive wall collisions (see previous section); a larger energy makes the wall region more accessible.

Table XI list the changes in sensitivities for the total and $j = 12$ to $j = 14$ DCS's as the initial kinetic energy increases. Overall, the sensitivities were not very significantly altered. The well depth sensitivity showed a factor of 5 decrease only for scattering angles above

17 degrees (as the kinetic energy is raised from 35 to 95 meV). The sensitivities for β and $C_6^{(0)}$ were the virtually the same for 35 and 95 meV but much greater for 65 meV. The $C_8^{(2)}$ sensitivity showed a marked increase with energy.

Classically, one would expect that at a lower kinetic energy. the probing of the well region would be greater and the probing of the wall lesser. This is the case to a small extent for our system, but not significantly so. The β' sensitivity increases only slightly, indicating a slight increase in the probing of the repulsive wall. The minor decrease in the $\epsilon^{(0)}$ sensitivity indicates very little decrease in the probing of the well; most of the decrease in $S(\theta; \epsilon^{(0)})$ is for angles above the classical range of well sampling. The other well parameter β has the most sensitivity at an intermediate energy (65 meV); at the extreme energies (35 and 65 meV) the $S(\theta; \beta)$'s are identical.

The specific choice of a scattering energy to experimentally probe the He + CO_2 potential, or one for a similar system is not important. The higher energies in this range yield cross-sections with more classical behavior, and will sample more of the repulsive wall. At the lower energies the behavior is more quantal in nature, and hence the scattering will be less a function of how a trajectory samples the well region, than how a wave is distorted by the total potential. It is not appropriate or very useful to invoke trajectory concepts in attempting to predict parameter sensitivities at low energies. Therefore, it is not very beneficial

to measure cross-sections for quantal scattering systems at very low scattering energies, since similar information can be obtained at room temperature energies. The only advantage of lower energy studies is the increase in elastic cross-section at intermediate scattering angles; a factor of 2 increase is observed in the range of 5 to 15 degrees as the energy drops from 95 to 35 meV. The disadvantage is that the inelastic cross-sections decrease for these conditions. The best course of action is to measure the cross-sections at many energies, and use the combined data to extract a potential.

12. CONCLUDING REMARKS

In this paper we have investigated the effect of several anisotropic interaction potential parameters on observable differential cross-sections for the scattering of He by CO_2 at an energy of 65 meV. Relative sensitivity functions for the DCS were introduced to quantify the influence of each parameter. We also performed a large scale sensitivity analysis by calculating the cross-sections at several physically reasonable values of each of the potential parameters. The following conclusions were reached:

1. The DCS (total and inelastic) are most sensitive to the location of the potential well mimimum r_m, particularly the spherical average of $r_m(\gamma)$. It has, by far, the greatest effect on the overall magnitude of the DCS especially at low angles, and on the positions of the quantal oscillations.

2. The quantal oscillations of the total DCS versus scattering angle θ curves are dampened primarily by the presence of anisotropy in the position of the well minimum r_m. The dampening is due to the fact that the inelastic DCS's have oscillations with troughs and crests at different θ. The state-to-state DCS's are not dampened by the anisotropy of r_m, but their relative magnitudes are very dependent on this anisotropy.

3. Although the He + CO_2 system is highly quantal and therefore its DCS shows no classical rainbow behavior, it is still possible to

extract siginficant information regarding the depth and width of the well from DCS measurments. The sensitivities to these parameters exteneed well beyond what would be expected classically. The low angle DCS oscillations increase with the well depth. Increasing the well width increases the amplitude of low angle $(\theta < 12°)$ oscillations and decreases the high angles ones. The increase of well depth also increases the inelasticity of the collision.

4. The elastic and inelastic DCS is highly sensitive to the width of the well. The sensitivity to it is actually somewhat greater than to the well depth. However the range in experimentally determied values for the reduced well width (parameterized by β for the MMSV potential, $\beta = 5.5$ to 8.2) is much smaller than the range of values of well depth (2.5 to 7.0 meV).

5. The anisotropy of the well depth ϵ is clearly discernable in the total DCS, primarily in the shape of the oscillations. It has little effect on the dampening of the oscillations. An increase in its absolute value increases the inelasticity.

6. There is little change in parameter sensitivities for scattering at energies other than 65 meV. At 35 meV the increase in sensitivity in the well depth is less than a factor 1.5 over that for 95 meV, indicating that classical arguments are not very useful in predicting sensitivities.

Although we considered a specific case, the above conclusions are

valid for systems with similar characterstics: collision energy, reduced mass, and rotational energy spacing. The techniques outlined should prove beneficial in interpreting total and inelastic diffential cross-section data, and in assigning significance to the features of the potentials that are obtained from the data.

3.13 REFERENCES

1. *Atom-Molecule Collision Theory: A Guide for the Experimentalist* R. B. Bernstein ed. (Plenum, New York, 1979).

2. R. B. Bernstein, *Chemical Dynamics via Molecular and Laser Techniques*, (Clarendon Press, Oxford 1982)

3. J. W. Winniczek and A. Kuppermann, (to be submitted).

4. R. J. Cross, Jr., *J. Chem. Phys.* **52**, 5703 (1970).

5. (a) H. R. Mayne and M. Keil, *J. Phys. Chem.* **88**, 883 (1984); (b) M. Keil and H. R. Mayne, *Chem. Phys. Lett.* **85**, 456 (1982).

6. (a) R. Schinke, W. Müller, W. Meyer, and P. McGuire, *J. Chem. Phys.* **74**, 3916 (1981); (b) R. Schinke, H. J. Korsch, and D. Poppe, *J. Chem. Phys.* **77**, 6005 (1982).

7. F. Wolf and J. J. Korsch, *J. Chem. Phys.* **81**, 3127 (1984).

8. G. Scoles, *Ann. Rev. Phys. Chem.* **31**, 81 (1980).

9. M. Keil and G. A. Parker, *J. Chem. Phys.* **82**, 1947 (1985).

10. (a) G. A. Parker, M. Keil, and A. Kuppermann, *J. Chem. Phys.* **78**, 1145 (1983); (b) M. Keil, G. A. Parker, and A. Kuppermann, *Chem. Phys. Lett.* **59**, 443 (1978).

11. (a) J. T. Hwang and H. Rabitz, *J. Chem. Phys.* **70**, 4609 (1979); (b) L. Eno and H. Rabitz, *J. Chem. Phys.* **71**, 4824 (1979); (c) L. A. Elsava, L. Eno, and H. Rabitz, *J. Chem. Phys.* **73**, 4998 (1980).

12. L. Eno and H. Rabitz, *J. Chem. Phys.* **75**, 1728 (1981).

13. L. Eno and H. Rabitz, *J. Chem. Phys.* **74**, 3859 (1981).

14. L. Eno and H. Rabitz, *J. Chem. Phys.* **72**, 2314 (1980).

15. R.T Pack, G. A. Pfeffer, and J. P. Toennies, *J. Chem. Phys.* **80**, 4940 (1984).

16. M. Faubel, K. H. Kohl, J. P. Toennies, and F. A. Gianturco, *J. Chem. Phys.* **78**, 5629 (1984).

17. M. Faubel, K.-H. Kohl, and J. P. Toennies, *Faraday Discuss. Chem. Soc.* **73**, 205 (1982).

18. M. Keil and A. Kuppermann, *J. Chem. Phys.* **69**, 3917 (1978).

19. P. M. Agrawal and L. M. Raff, *J. Chem. Phys.* **74**, 3292 (1981)

20. P. M. Agrawal and L. M. Raff, *J. Chem. Phys.* **75**, 2163 (1981).

21. C. L. Stroud and L. M. Raff, *J. Chem. Phys.* **72**, 5479 (1980).

22. G. A. Parker, R. L. Snow, and R. T Pack, *J. Chem. Phys.* **64**, 1668 (1976)

23. R. T Pack, *J. Chem. Phys.* **60**, 633 (1974)

24. G. A. Parker and R. T Pack, *J. Chem. Phys.* **68**, 1585 (1978).

25. R. T Pack, *Chem. Phys. Lett.* **55**, 197 (1978).

26. G. Rotzoll and A. Lübbert, *J. Chem. Ph/s.* **71**, 2275 (1979).

27. V. Khare, *J. Chem. Phys.* **68**, 4631 (1978).

28. D. Secrest, *J. Chem. Phys.* **62**, 710 (1975).

29. P. McGuire and D. J. Kouri, *J. Chem. Phys.* **60**, 2488 (1974).

30. R. T Pack, *J. Chem. Phys.* **60**, 633 (1974).

31. D. S. Saxon, *Elementary Quantum Mechanics* (Holden-Day, San Francisco, 1968).

32. A. S. Davydov, *Quantum Mechanics* (Pergamon, Oxford 1976), 2nd edition, tr. D. ter Haar.

33. G.Herzeberg, *Molecular Spectra and Molecular Structure III. Electronic Spectra and Electronic Structure of Polyatomic Molecules*, (Van Nostrand Reinhold, New York, 1966).

34. The vibrational energies for the three vibrational modes of $CO2_2$ are given in ref. 22, and are 291.26 meV, 172.11 meV and 82.75 meV; at a temperature of 298 K these states have a ground state relative populations of 100.0%, 99.9% and 96.0%, respectively.

35. R. T Pack, *J. Chem. Phys.* **64**, 1659 (1976).

36. R. T Pack, *J. Chem. Phys.* **61**, 2091 (1974).

37. R. T Pack, *J. Chem. Phys.* **60**, 633 (1974).

38. K. Smith, *The Calculation of Atomic Collision Processes* (Wiley, New York 1971).

TABLE I. MMSV Anisotropic Parameter Expansion Potential[a] Parameters

Parameter	Symbol	Value
well minimum (spherical average)	$r_m^{(0)}$	3.5 Å
well minimum anisotropy	q	0.21
well depth (spherical average)	$\epsilon^{(0)}$	4.3 meV
well depth anisotropy	a	-0.50
well shape[b]	β	7.2
wall shape[b]	β'	7.2
Spline-van der Waals joint	$\rho_{sv} = r_{sv}/r_m$	1.6
van der Waals coefficients	$C_6^{(0)}$	9.98 meV Å⁶
	$C_6^{(2)}$	2.31 meV Å⁶
	$C_8^{(0)}$	46.4 meV Å⁸
	$C_8^{(2)}$	48.4 meV Å⁸

a) see equations 14, 15, and 16; this potential will
   be designated as M
b) in some cases these parameters will be expanded
   in Legendre polynomials (as in eqs. 14 or 15)

TABLE II. Modified Spherical Potentials

Characteristic	Parameter Value	Potential
unmodified potential[a]	-	SM
low r_m	$r_m = 2.5$ Å	SRL
high r_m	$r_m = 4.5$ Å	SRH
low ϵ	$\epsilon = 2.5$ meV	SEL
high ϵ	$\epsilon = 7.5$ meV	SEH
low β	$\beta = 4.0$	SBWL
high β	$\beta = 10.0$	SBWH
low β'	$\beta' = 4.0$	SBRL
high β'	$\beta' = 10.0$	SBRH
low β and β'	$\beta = \beta' = 4.0$	SBL
high β and β'	$\beta = \beta' = 10.0$	SBH
low ϵ and high β	$\epsilon = 2.5$ meV $\beta = 10.0$	SBEHL

a) Spherical limit of the MMSV anisotropic potential in Table I, i.e. $q = 0$ and $a = 0$ (also $C_6^{(2)}$ and $C_8^{(2)}$ are zero)

TABLE III. Modified Anisotropic Potentials

Characteristic	Parameter Value	Potential
unmodified potential[a]	-	M
zero q	$q = 0$	Q0
low q	$q = 0.1$	QL
high q	$q = 0.5$	QH
zero a	$a = 0$	A0
low a	$a = -0.2$	AL
high a	$a = -0.9$	AH
low β	$\beta = 5.0$	BWL
high β	$\beta = 12.0$	BWH
low β'	$\beta' = 5.0$	BRL
high β'	$\beta' = 12.0$	BRH
anisotropic β[b]	$\beta^{(2)}/\beta^{(0)} = 0.62$ $a = 0.0$	BA
low positive a	$a = 0.1$	PAL
high positive a	$a = 0.5$	PAH
low ϵ	$\epsilon = 2.5$ meV	EL
high ϵ	$\epsilon = 7.5$ meV	EH
positive a low ϵ	$a = 0.3$ $\epsilon = 2.5$ meV	PAEL
positive a high ϵ	$a = 0.3$ $\epsilon = 7.5$ meV	PAEH

a) the anisotropic MMSV potential of Table I
b) β ansiotropy is introduced by way of a Legendre expansion
  (eq. 14 or 15).

TABLE IV. Classical Rainbow Scattering Angles

Potential[a]	θ_r/deg	$l(\theta_r)$[b]	$\theta_{r\ min}/deg$[c]
SM	8.9	40	7.5
SRL	6.8	28	4.3
	8.8	43	8.5
SRH	9.2	52	7.7
SEL	5.0	40	3.8
SEH	16.0	41	13.3
SBWL	7.0	43	2.9
SBWL	10.8	40	9.1
M			
$\gamma = 0$	4.5	48	4.0
$\gamma = \pi/4$	7.8	42	6.0
$\gamma = \pi/2$	11.0	36	9.1
A0			
$\gamma = 0$	9.1	48	7.1
$\gamma = \pi/4$	9.0	42	7.6
$\gamma = \pi/2$	8.7	37	7.6
Q0			
$\gamma = 0$	4.1	39	3.4
$\gamma = \pi/4$	7.7	40	6.7
$\gamma = \pi/2$	11.4	40	10.0

a) See tables II and III for potential symbols
b) The reduced impact parameter for the rainbow angle (eq. 21)
c) Location of the rainbow minimum

TABLE V. Sensitivity Variations as a Function of Parameter Increase for Spherical Potentials

Sensitivity[a] and characteristic	Parameter Increasing		
	r_m	ϵ	β
$S(\theta; r_m)$			
mag.	siml.	incr. $(10\times\ 15°<\theta<20°)$	incr. $(\theta>20°)$ decr. $(\theta<20°)$
osc.	same	incr.	decr. $(\theta>30°)$
$S(\theta; \epsilon)$			
mag.	incr. (low r_m)	incr.	incr. $(\theta>25°)$
osc.	same	decr. $(10°<\theta<15°)$	incr.
$S(\theta; \beta)$			
mag.	sl. incr.	sl. decr.	same
osc.	same	decr. $(\theta>30°)$	incr. $(\theta>25°)$
$S(\theta; \beta')$			
mag.	incr. (low r_m)	same	same
osc.	sig. incr.	sig. incr.[b]	incr. $(\theta>15°)$
$S(\theta; C_6)$			
mag.	decr. $(\times 10)$	same	incr. $(\times 50\ \theta>25°)$
osc.	simil.	var.[c]	same
$S(\theta; C_8)$			
mag.	decr. $(\times 10)$	same	same
osc.	simil.	var.[c]	same

a) See sec. 5 of text for a full description of this table and symbols
b) Especially small at low ϵ
c) Variable number of oscillations for different ranges of θ

TABLE VI. Sensitivity Variations as a Function of Parameter Increase for Anisotropic Potential Total DCS

Sensitivity[a]	Parameter Increasing		
characteristic	q	a	β
$S(\theta; r_m^{(0)})$			
mag.	simil.[b]	simil.[b]	sig. incr.[c]
osc.	simil.[b]	sl. decr.	same
			sig. incr.$(\theta > 20°)$[c]
$S(\theta; \epsilon^{(0)})$			
mag.	same	incr.	same
osc.	decr.	incr.	same
$S(\theta; q)$			
mag.	simil.[d]	simil.[d]	same
osc.	simil.[b]	same	simil.
$S(\theta; a)$			
mag.	same	sig. incr.	same
osc.	simil.	same	simil.
	incr. $(5\times \; \theta < 8°)$		
$S(\theta; \beta)$			
mag.	simil.[b]	simil.[b]	simil.[b]
osc.	simil.[b]	simil.[b]	simil.[b]
$S(\theta; \beta')$			
mag.	same	same	same
osc.	same	same	incr.

a) See sec. 5 of text for a full description of this table and symbols

b) Highest at intermediate value of the parameter and similar at extereme
   values

c) The increase is for value of β changing from 4.0 to 7.2 only

d) Increase only for higher value of parameter

TABLE VII. Comparison of Inelastic Sensitivities

Sensitivity[a] and characterisitc	increase in Δj for $j = 12$	Comparison with total DCS $S(\theta; p_k)$	
		elastic $j = 12$	inelastic $j = 12 \to 14$
$S(\theta; r_m^{(0)})$			
mag.	incr. ($\times$ 500)	same	incr. ($\theta < 6°$)
osc.	same	same	same
$S(\theta; \epsilon^{(0)})$			
mag.	sl. incr.	same	simil.
osc.	decr.	sl. incr.	sl. incr.
$S(\theta; q)$			
mag.	incr. ($\times 20$)	simil.	incr.
osc.	sig. decr. $S(\theta; q) > 0$	decr.	v. sig. decr.
$S(\theta; a)$			
mag.	incr.($\times 30$)	simil.	incr.
osc.	decr.	simil.	sl. decr.
$S(\theta; \beta)$			
mag.	incr.	same	incr. ($\times 10\ \theta < 10°$)
osc.	same	same	same
$S(\theta; \beta')$			
mag.	incr. ($\times 100\ \Delta j = 8$)	same	sl. incr.
osc.	incr.	same	simil.

(continued)

TABLE VII. *(continuation)*

Sensitivity[a] and characterisitc	increase in Δj for $j = 12$	Comparison with total DCS $S(\theta; p_k)$	
		elastic $j = 12$	inelastic $j = 12 \rightarrow 14$
$S(\theta; C_6^{(0)})$			
mag.	incr.	simil.	incr.
osc.	same	same	simil.
$S(\theta; C_8^{(0)})$			
mag.	sl. incr.	decr. (×10)	sl. decr.
osc.	decr.	decr.	decr.
$S(\theta; C_6^{(2)})$			
mag.	incr. (×100 $\Delta j=8$)	simil.	incr. (×10 $\theta<5°$)
osc.	same	decr.	decr.
$S(\theta; C_8^{(2)})$			
mag.	incr. (×10 $\Delta j=8$)	same	simil.
osc.	decr.	decr.	simil.

a) See sec. 5 of text for a full description of this table and symbols

TABLE VIII. Sensitivity Variations as a Function of Parameter Increase for Anisotropic Potential $j = 12 \rightarrow j = 14$ DCS

Sensitivity[a] and characteristic	Parameter Increasing		
	q	a	β
$S(\theta; r_m^{(0)})$			
mag.	same	simil.[b]	incr.
osc.	sl. decr.	simil.	sl. incr.
$S(\theta; \epsilon^{(0)})$			
mag.	sl. decr.	incr.	same
osc.	sl. decr.	same	same
$S(\theta; q)$			
mag.	sl. incr.	same	same
osc.	sl. incr.	sl. incr.	sl. incr.
$S(\theta; a)$			
mag.	decr.	sig. incr.($\times 100$)	sl. decr.
osc.	sl. decr.	sl. incr.	same
$S(\theta; \beta)$			
mag.	simil.[b]	sl. decr.	incr. ($\theta < 6°$)
osc.	siml.[b]	sl. decr.	same
$S(\theta; \beta')$			
mag.	simil.	same	same
osc.	simil.	sl. decr.	sig. incr.

a) See sec. 5 of text for a full description of this table and symbols
b) Highest at an intermediate value of the parameter
and similar at extreme values

**TABLE IX. Variations in Sensitivities
with Increasing Energy**

Sensitivity[a] and characteristic	total DCS	$j = 12 \to j = 14$ DCS
$S(\theta; r_m^{(0)})$		
mag.	same	sl. decr. (@ 95 meV)
osc.	sl. incr.	same
$S(\theta; \epsilon^{(0)})$		
mag.	decr. ($\times 5$ $\theta > 17°$)	same
osc.	sl. incr.	same
$S(\theta; q)$		
mag.	incr. ($\times 2$ $\theta > 25°$)	same
osc.	same	simil.
$S(\theta; a)$		
mag.	same	same
osc.	same	same
$S(\theta; \beta)$		
mag.	simil.[b]	simil.[b]
osc.	simil.[b]	sl. incr.
$S(\theta; \beta')$		
mag.	incr.	sl. incr.
osc.	same	same

TABLE IX. *(continuation)*

Sensitivity and characteristic	total DCS	$j = 12 \to j = 14$ DCS
$S(\theta; C_6^{(0)})$		
mag.	simil.[c]	simil.[c]
osc.	simil.[c]	simil.[c]
$S(\theta; C_8^{(0)})$		
mag.	same	same
osc.	same	same
$S(\theta; C_6^{(2)})$		
mag.	same	sl. decr.
osc.	same	simil.
$S(\theta; C_8^{(2)})$		
mag.	incr.	sig. incr.
	($\times 10$ 95 *meV*)	($\times 100$ 95 *meV*)
osc.	same	sl. incr.

a) See sec. 5 of text for a full description of this table and symbols
b) Similar at 35 and 95 meV but 10 times greater at 65 meV,
    also the oscillations are increased at 65 meV
c) Similar at 35 and 95 meV but 100 times greater at 65 meV,
    also the oscillations are significantly increased at 65 meV

Figure 1. Deflection function for the spherical MMSV potential (SM
Table II) at a collision energy of 65 meV.
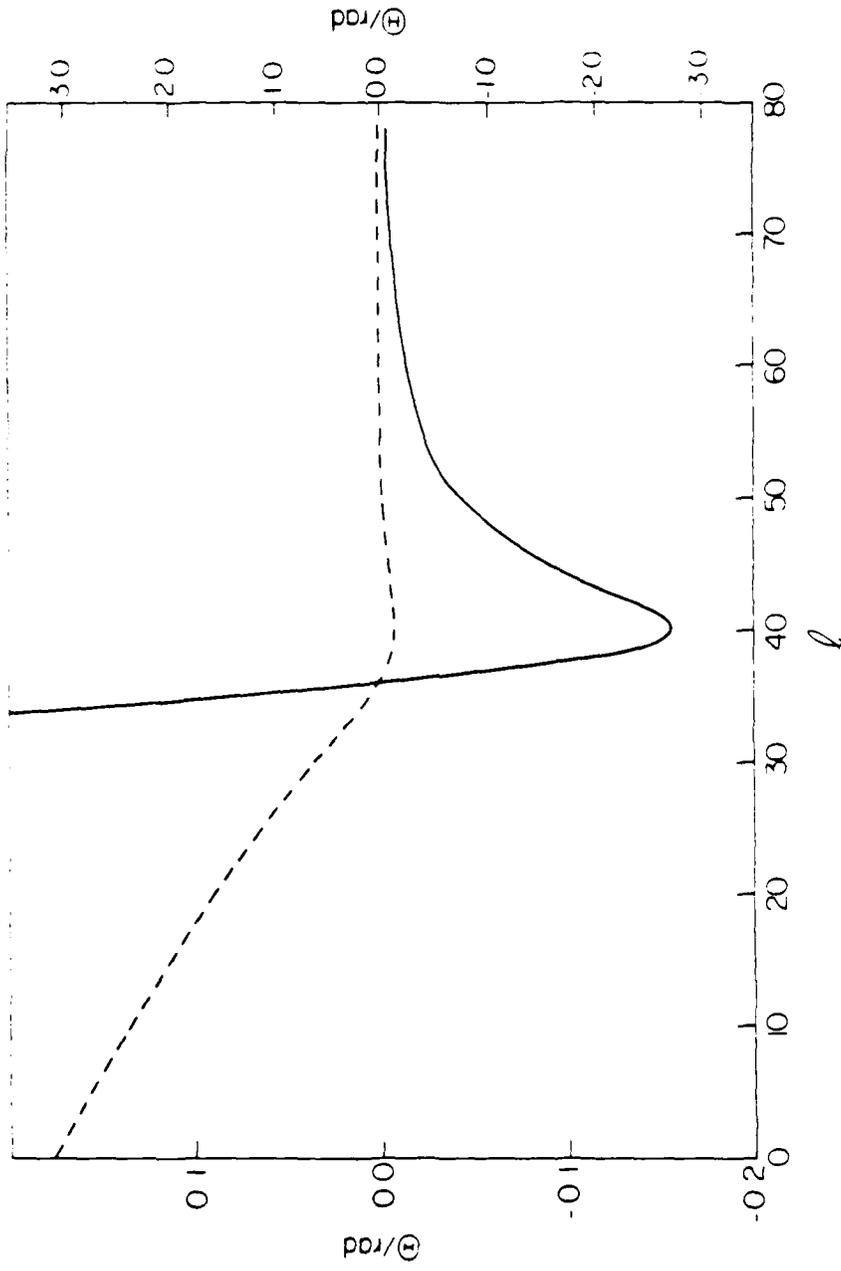
Figure 1.

Figure 2. Differential cross section (in the center-of-mass reference
frame) for the spherical MMSV potential (SM Table II) at
a collision energy of 65 meV.
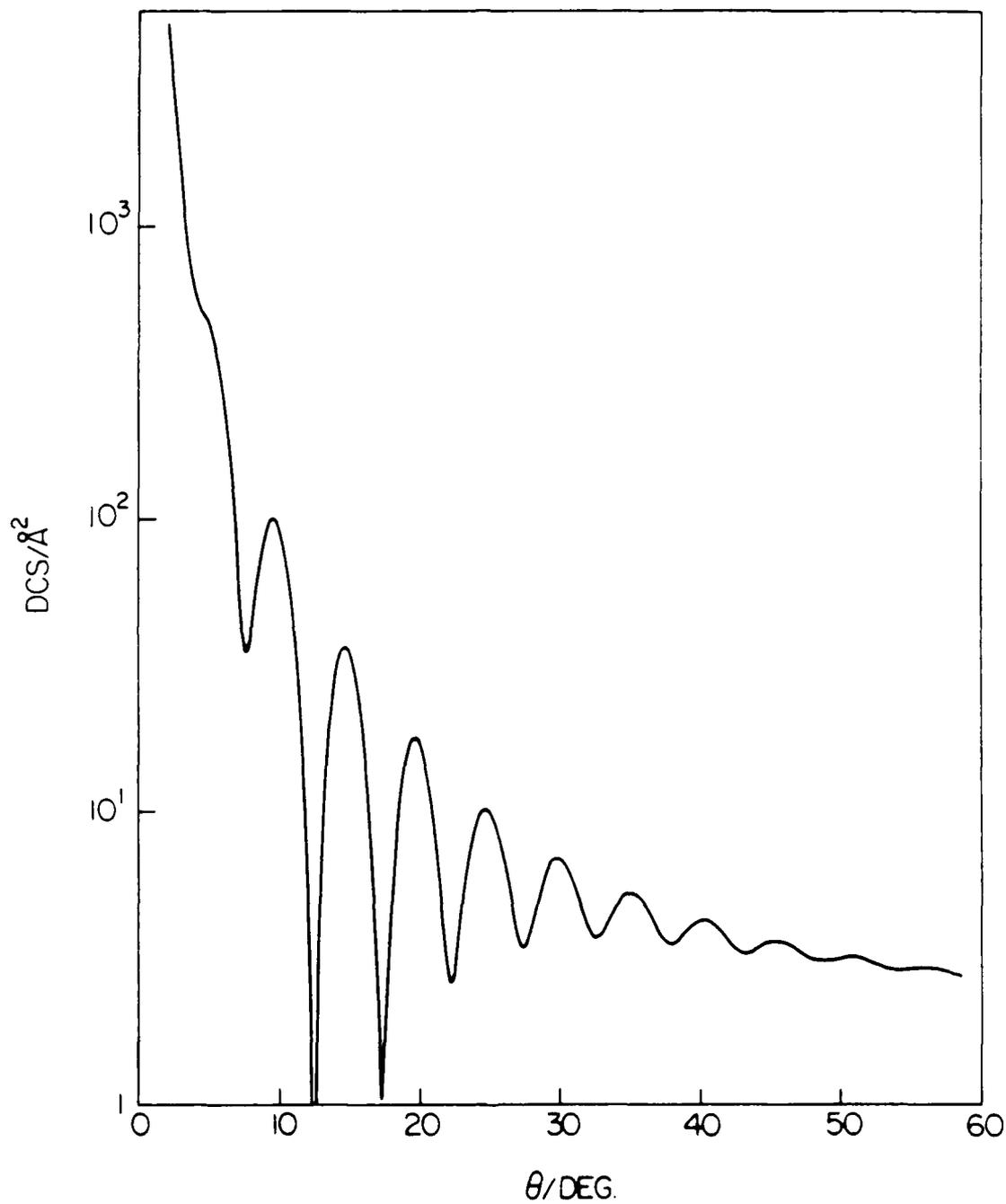
Figure 2.

Figure 3. Comparison of differential cross sections for variations of parameters r_m, ϵ, and β of the spherical MMSV potential. The center curve (in each of the three sets of curves) is for the SM potential (Table II). For clarity, the upper curves are shifted upwards by a factor of 10 while the lower curves are shifted downwards by the same factor. For panels a, b, and c the upper curves correspond to the SRH, SEH, and SBH potentials (Table II), respectively, and the lower curves correspond to the SRL, SEL, and SBL potentials, respectively.
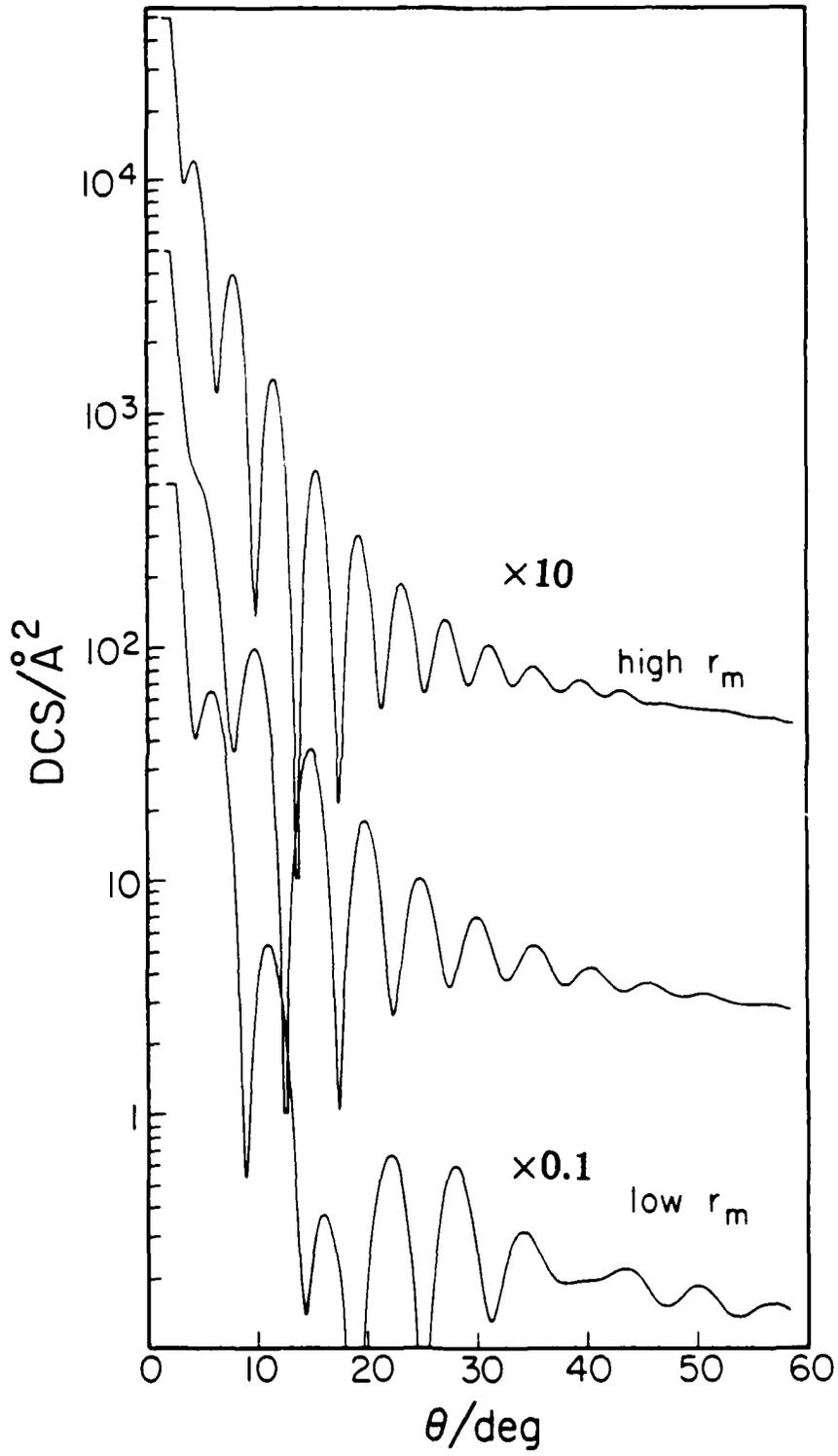
Figure 3a.
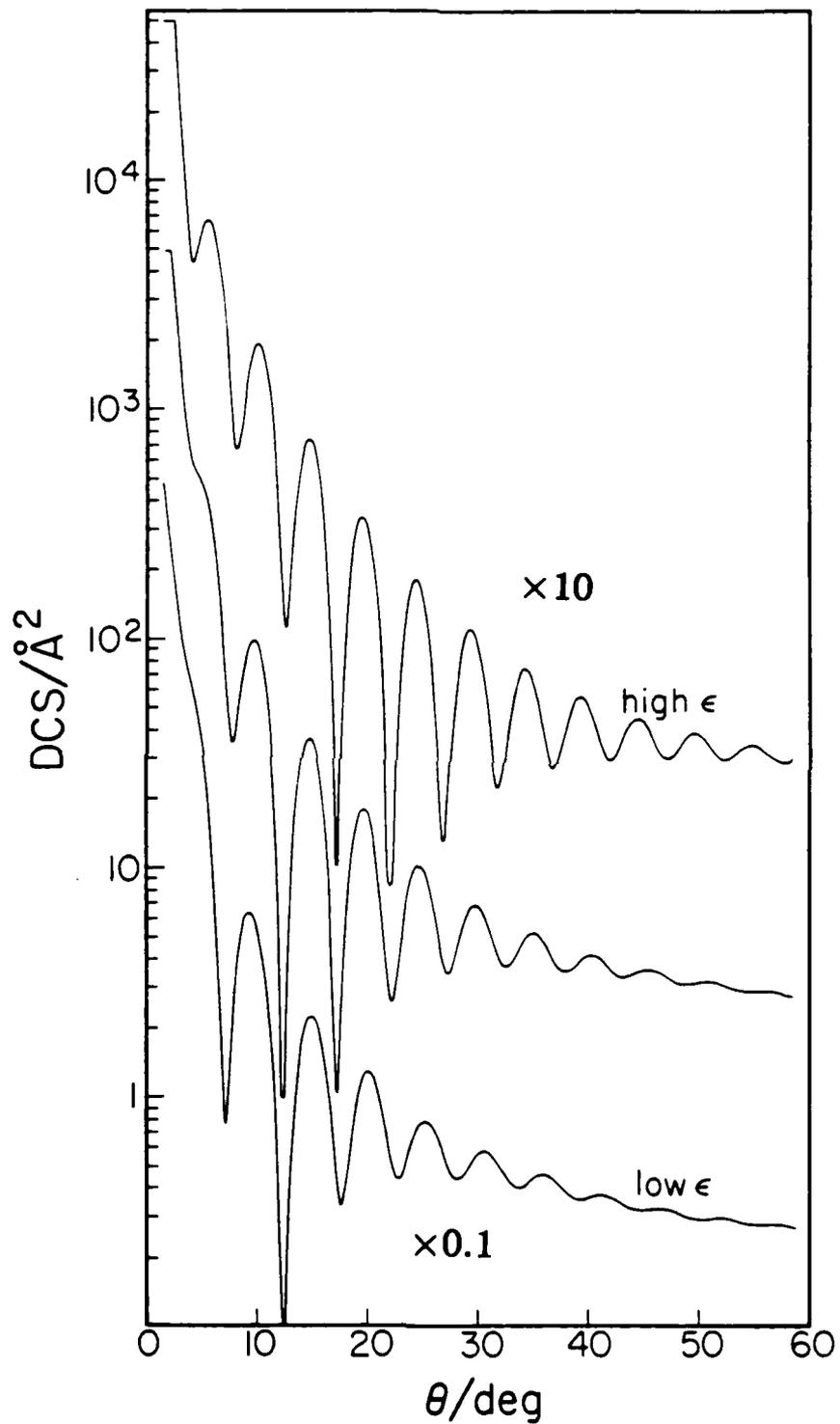
Figure 3b.
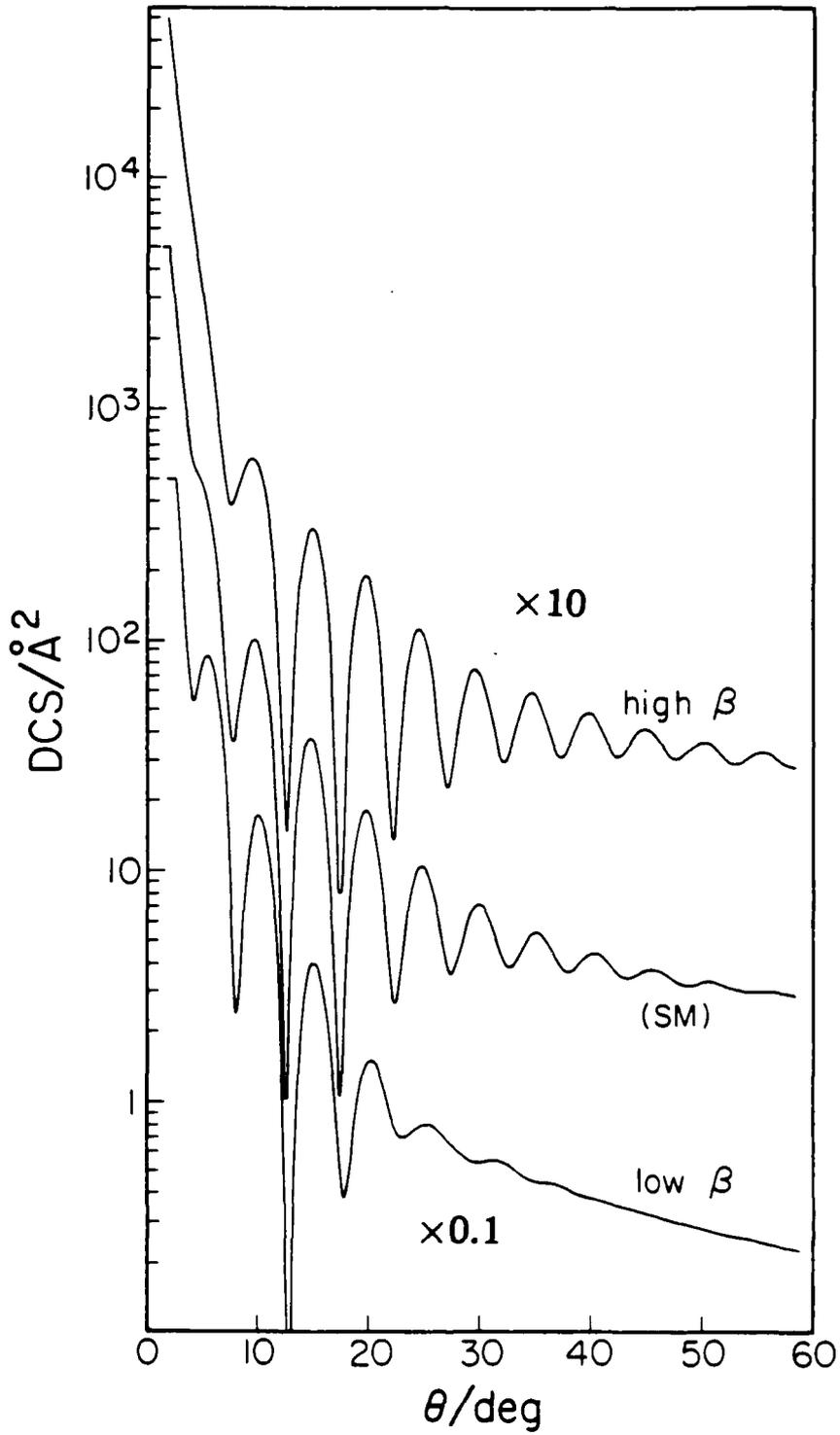
Figure 3c.

Figure 4. Sensitivity functions for the SM (Table II) potential for the parameters r_m, ϵ, β, β', C_6, and C_8. The solid curves are for positive values of the sensitivities, while the dashed curves are for negative values of the sensitivities.
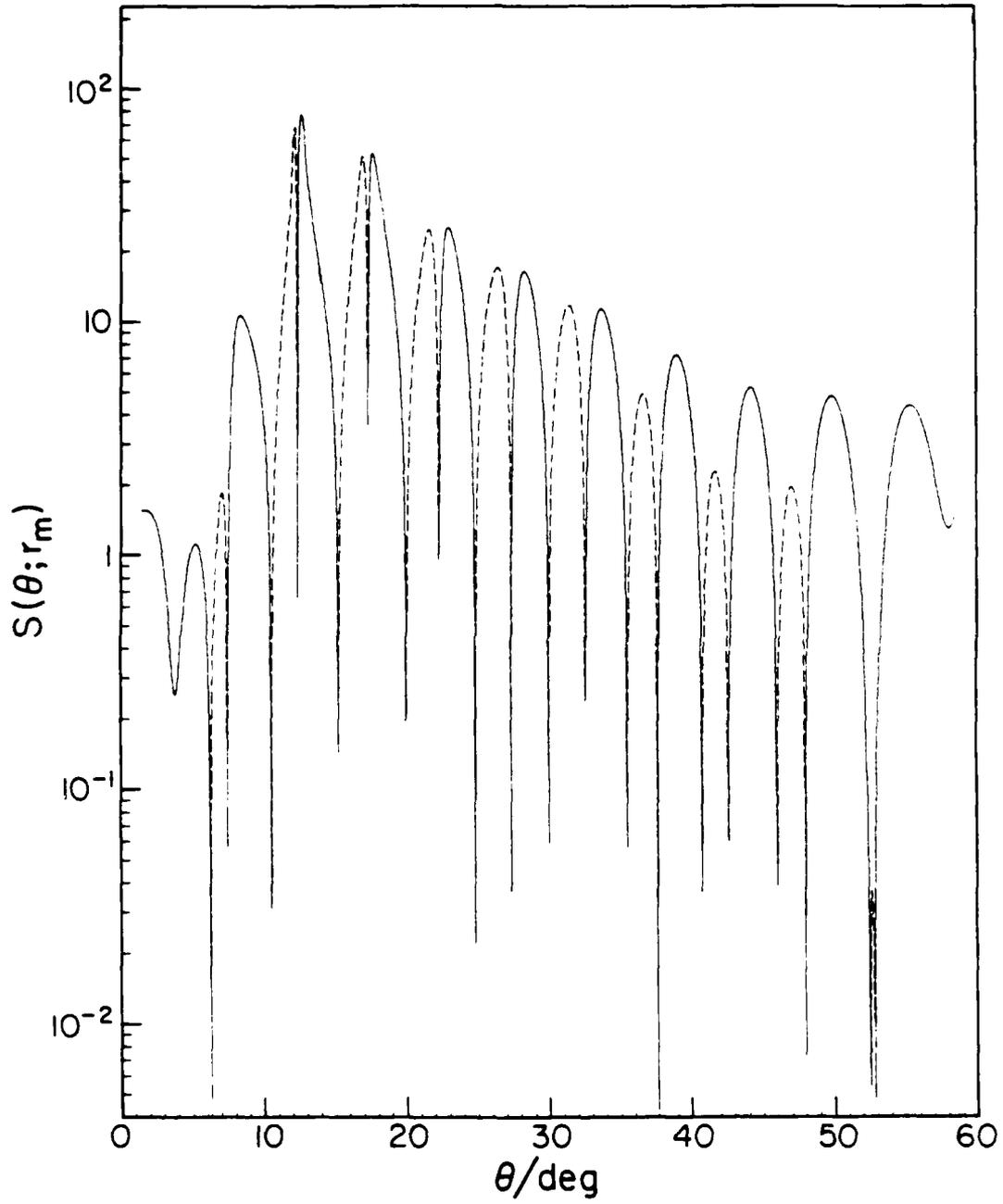
Figure 4a.
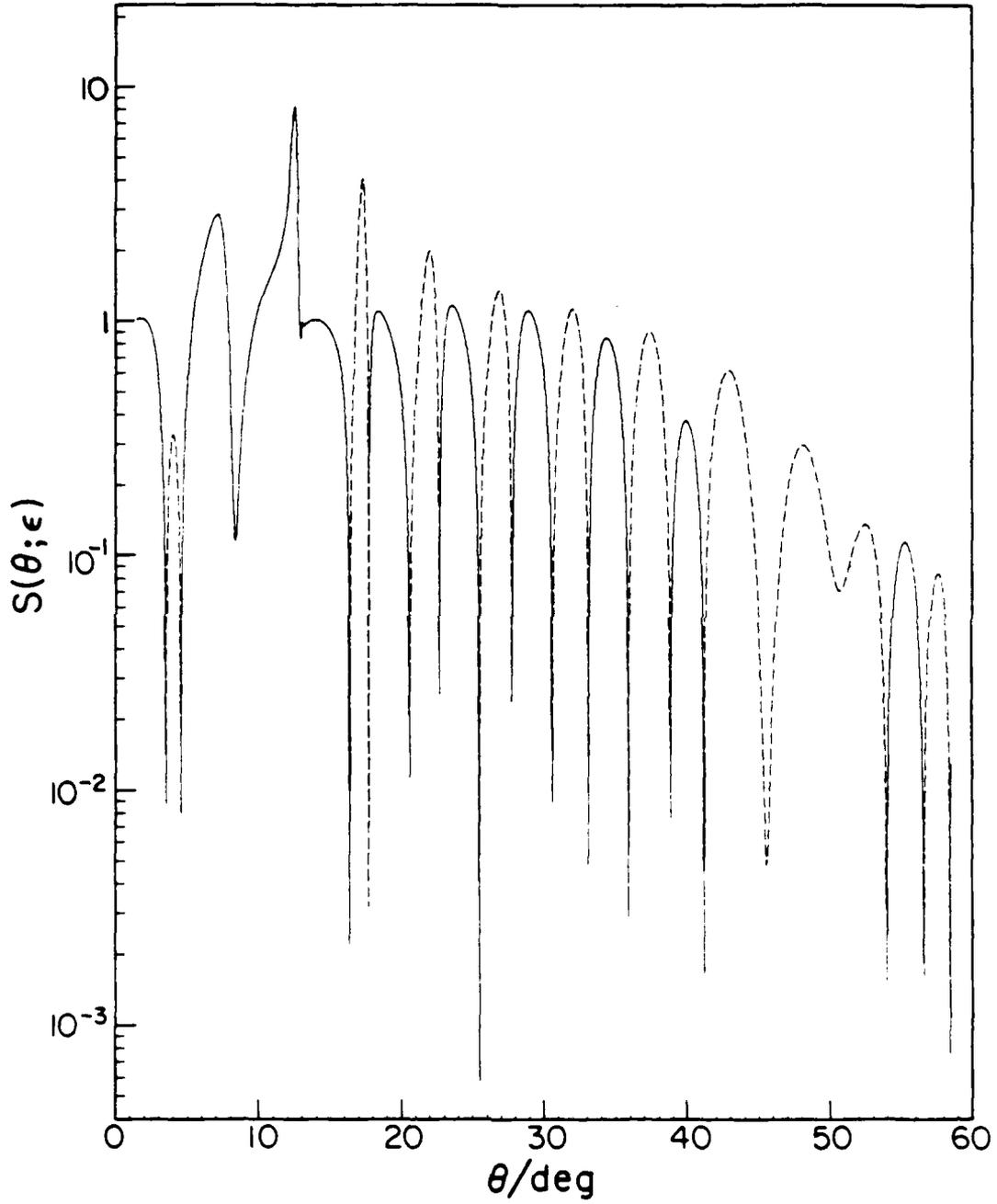
Figure 4b.
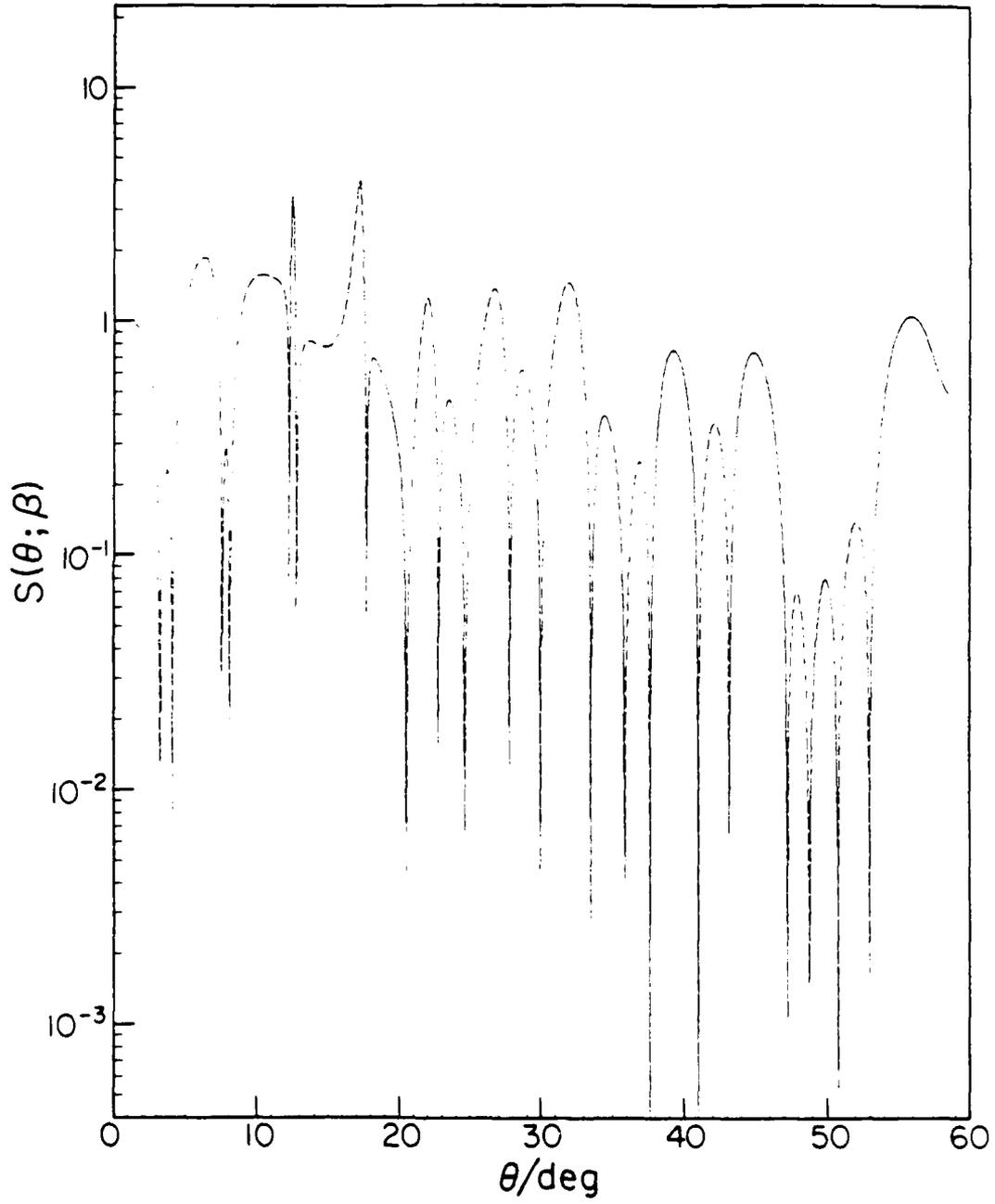
Figure 4c.
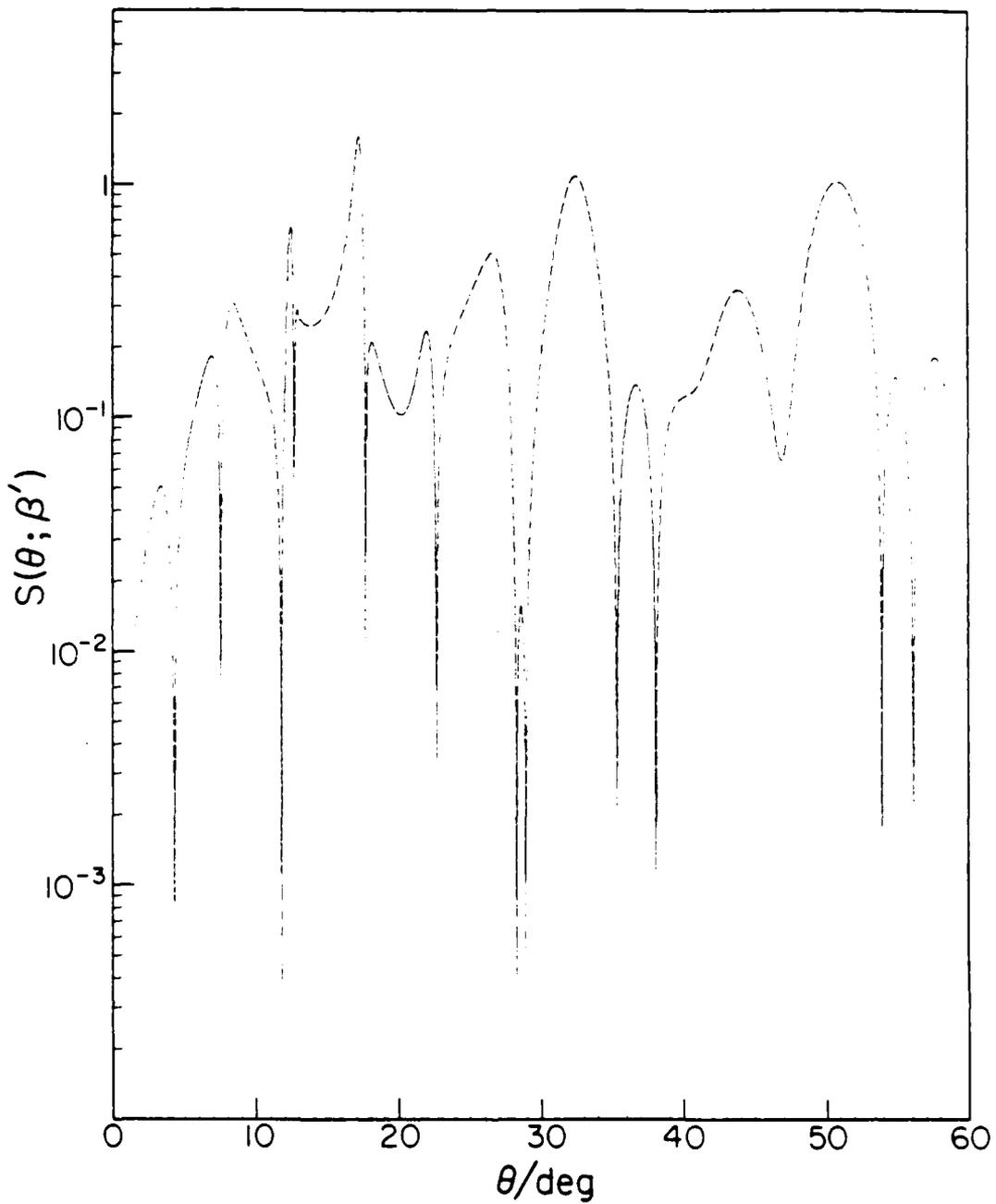
Figure 4d.
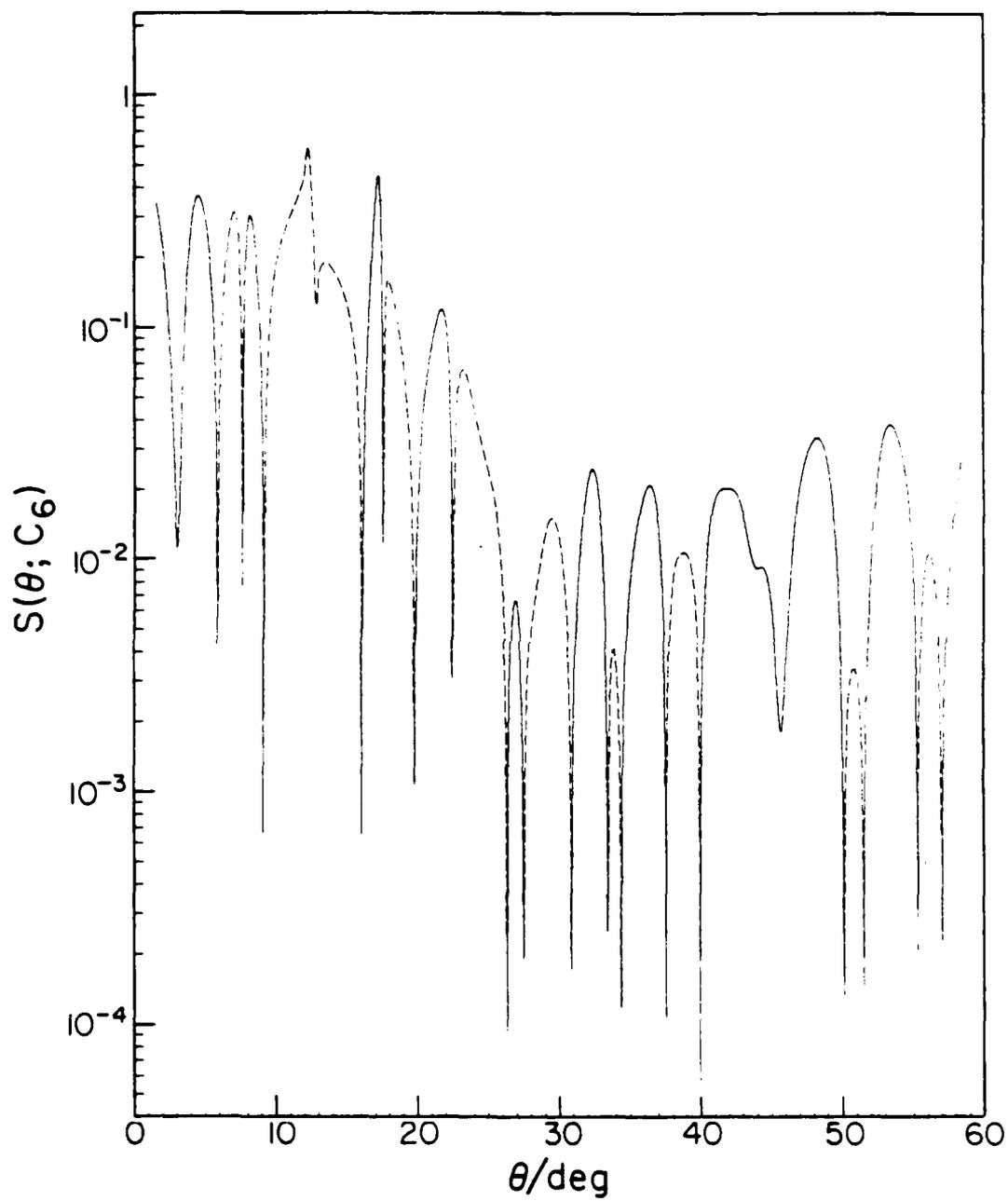
Figure 4e.
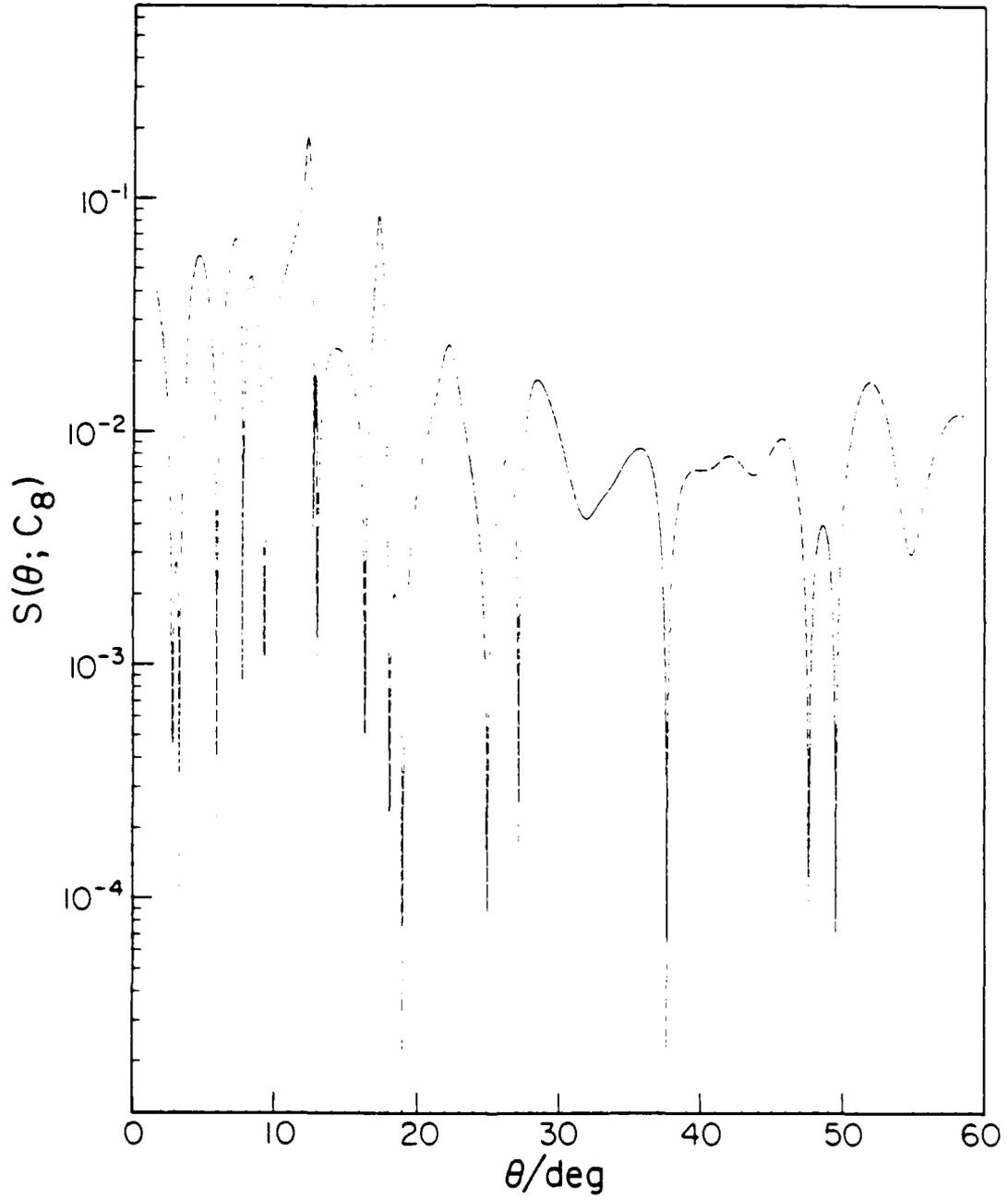
Figure 4f.

Figure 5. Comparison of differential cross sections for variations of the anisotropy parameters q, and a for the MMSV potential given in Table I and its variations given in Table III. The center curve (in the two set of curves) is for the M potential (Table III). For clarity, the upper curves are shifted upwards by a factor of two; while the lower curves are shifted downwards by the same factor. For panels a, and b the upper curves correspond to the QH and AH potentials, respectively, and the lower curves correspond to the QL and AL potentials, respectively.
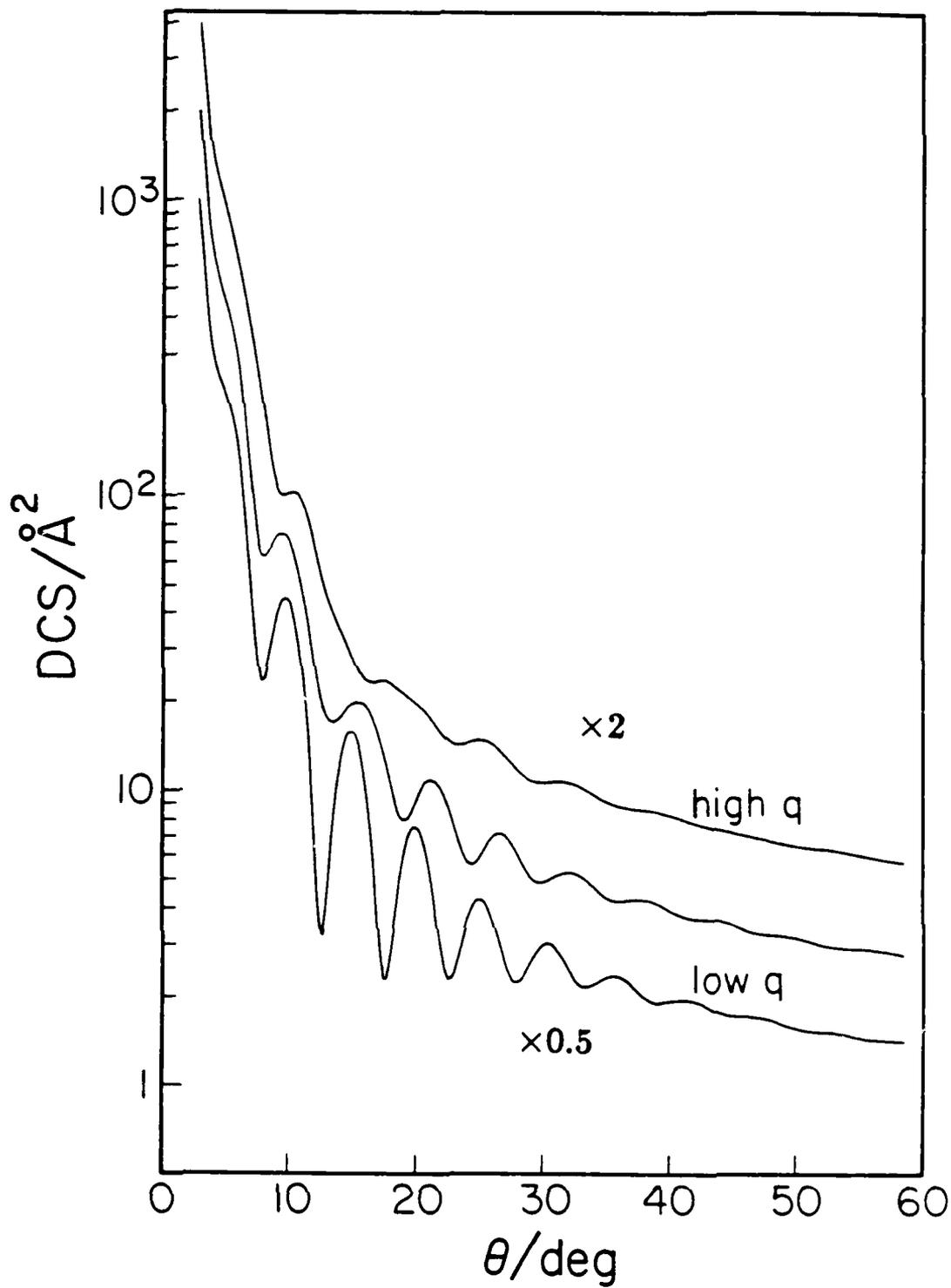
Figure 5a.
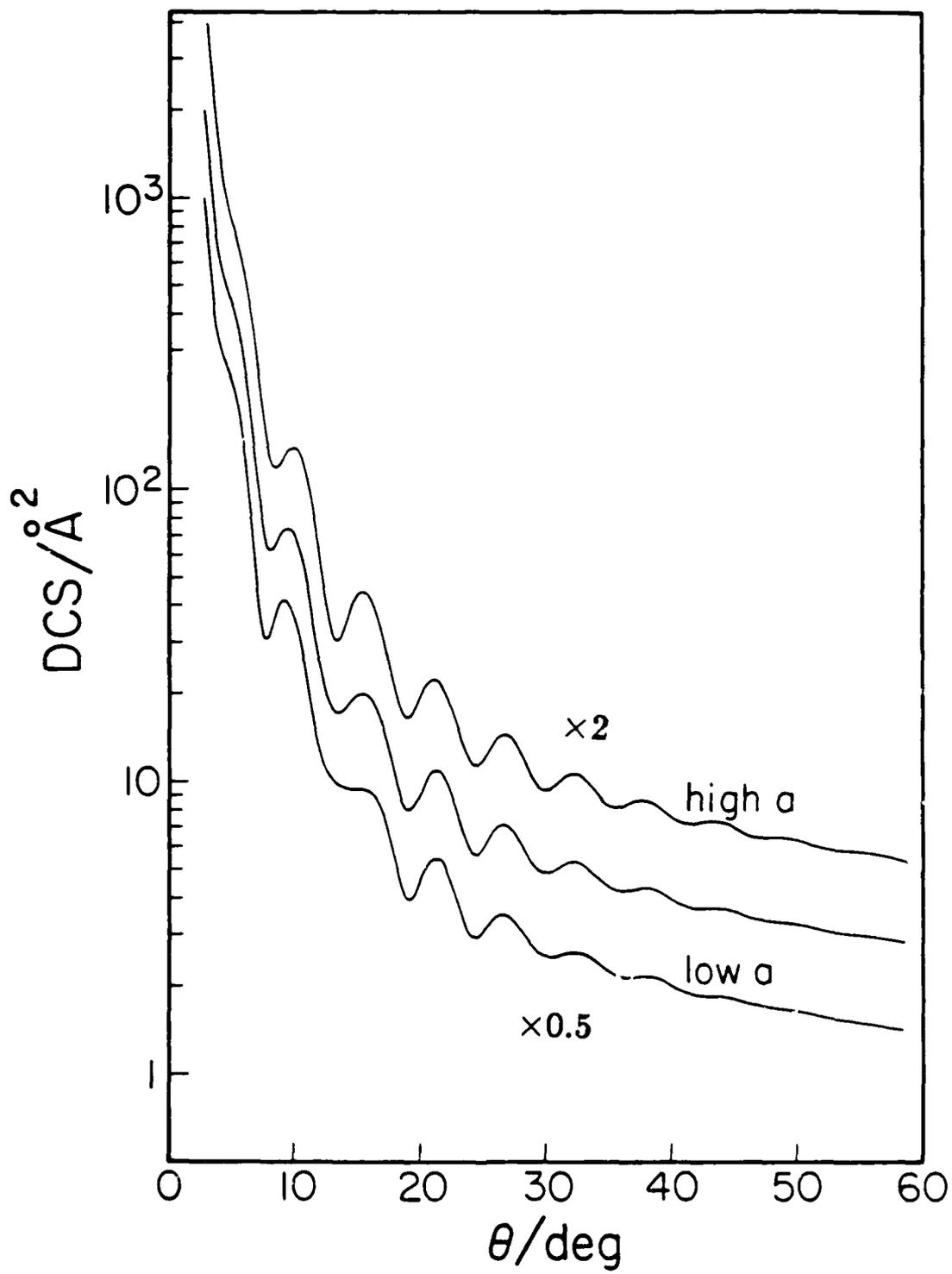
Figure 5b.

Figure 6. Comparison of differential cross sections for variations of
the well shape parameter β and the repulsive wall shape
parameter β' for the MMSV potential given in Table I and
its variations given in Table III. The center curve (in the
two set of curves) is for the M potential (Table III). For
clarity, the upper curves are shifted upwards by a factor
of two, while the lower curves are shifted downward by
the same factor. For panels a and b the upper curves
correspond to the BWH and BRH potentials, respectively,
and the lower curves correspond to the BWL and BRL
potentials, respectively.
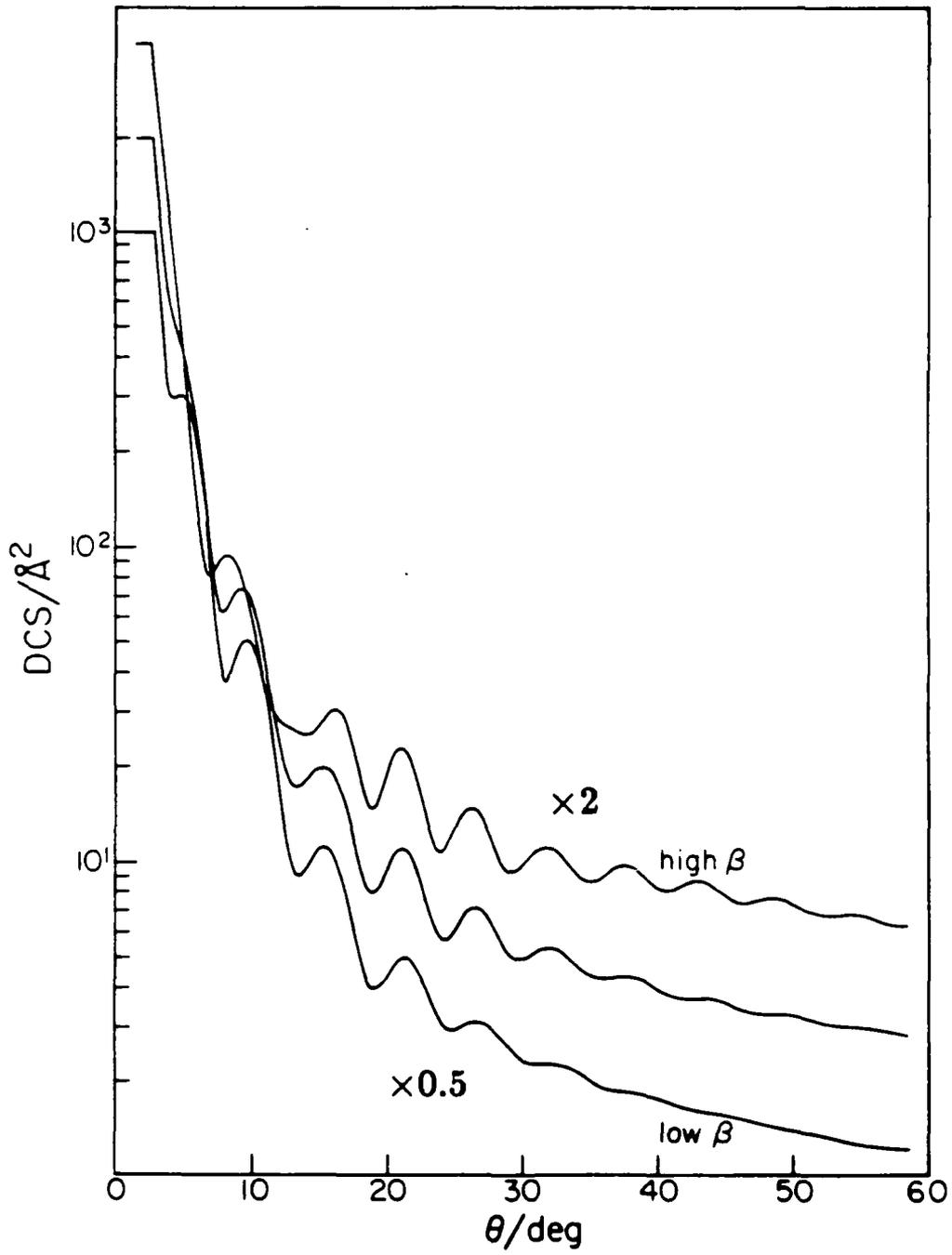
Figure 6a.
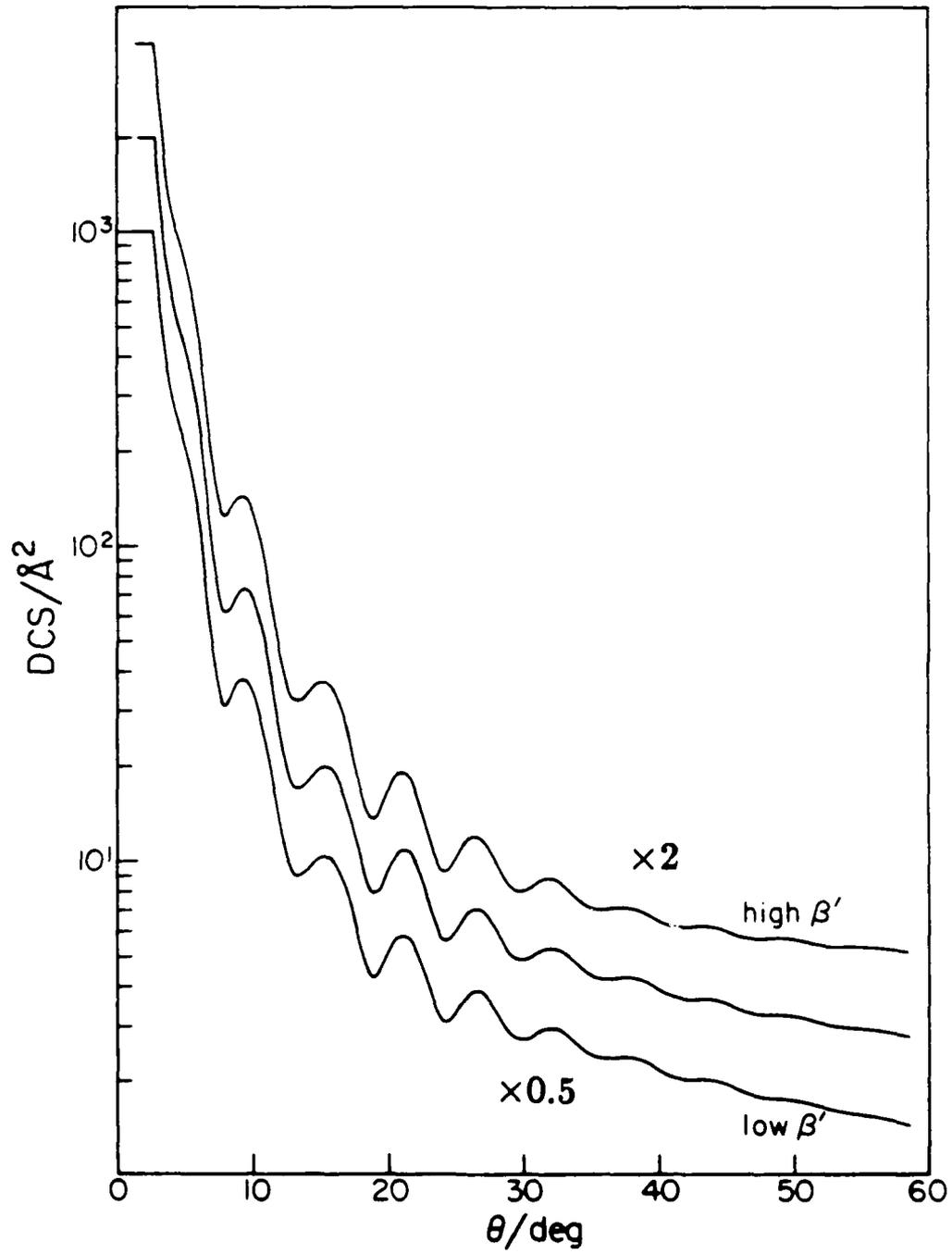
Figure 6b.

Figure 7. Total DCS sensitivity functions for the M (Table I)
anisotropic potential for the parameters $r_m^{(0)}$, $\epsilon^{(0)}$, q, a,
β and β'. The solid curves are for positive values of the
sensitivities, while the dashed curves are for negative values
of the sensitivites.
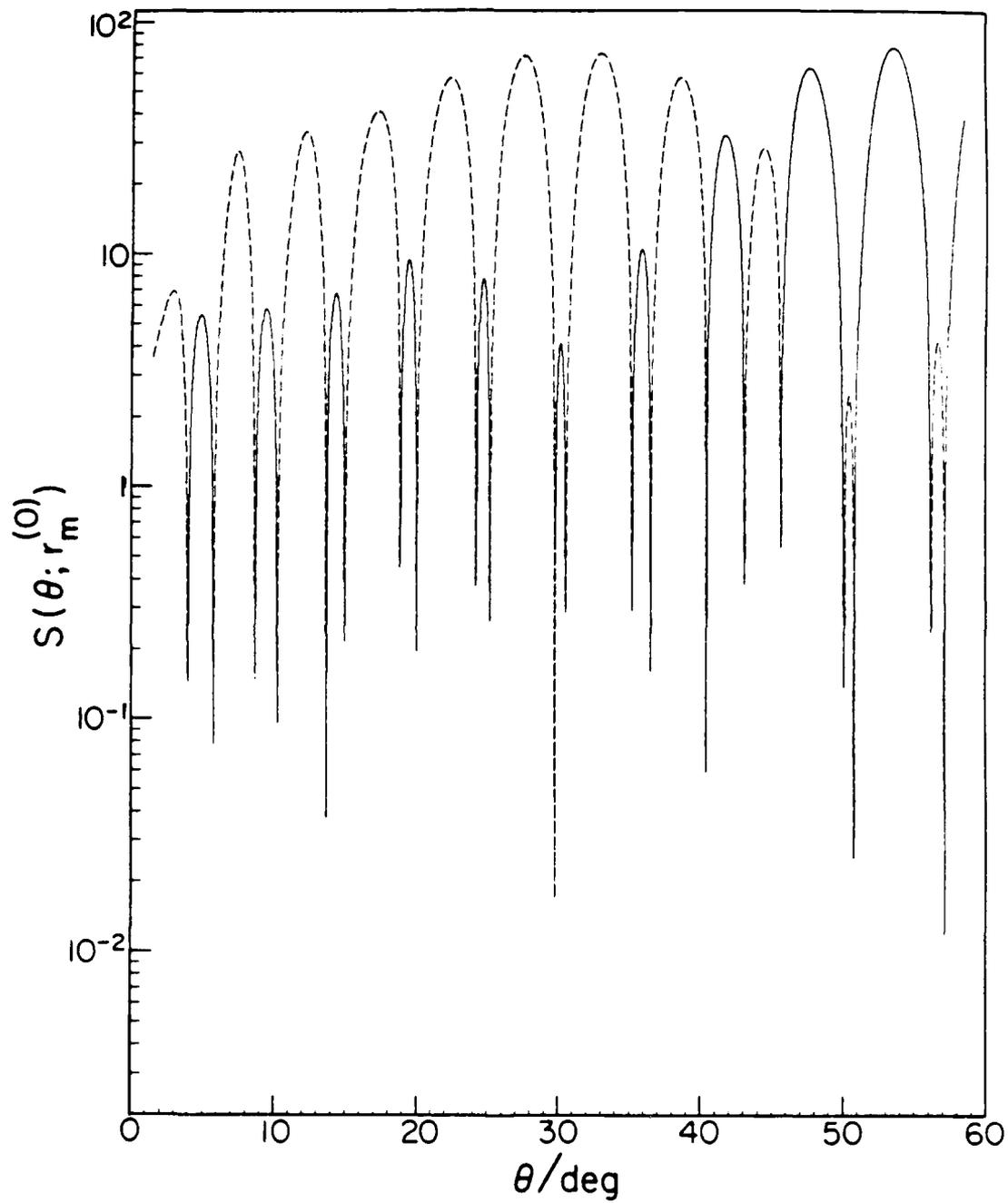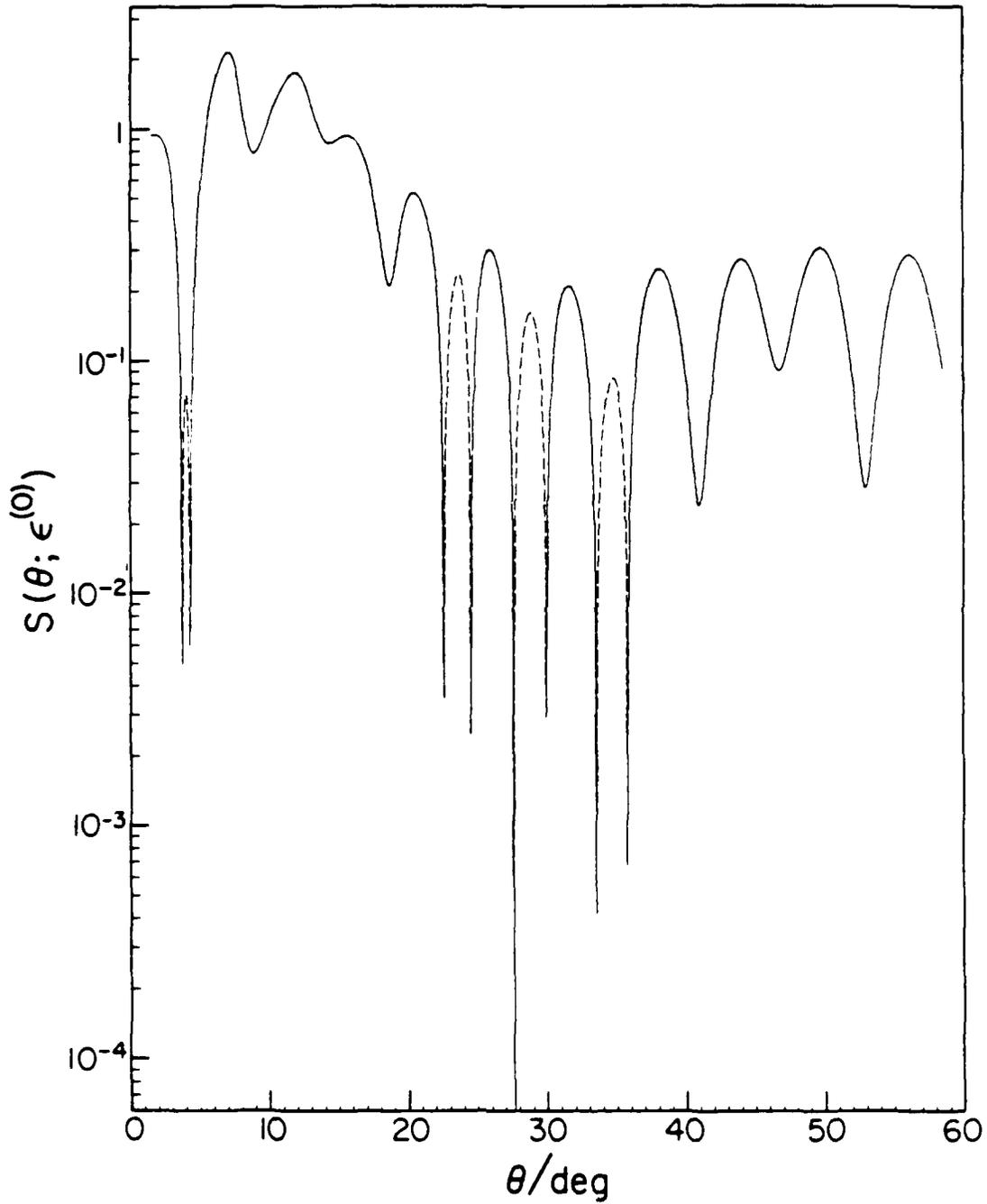
Figure 7a.

Figure 7b.
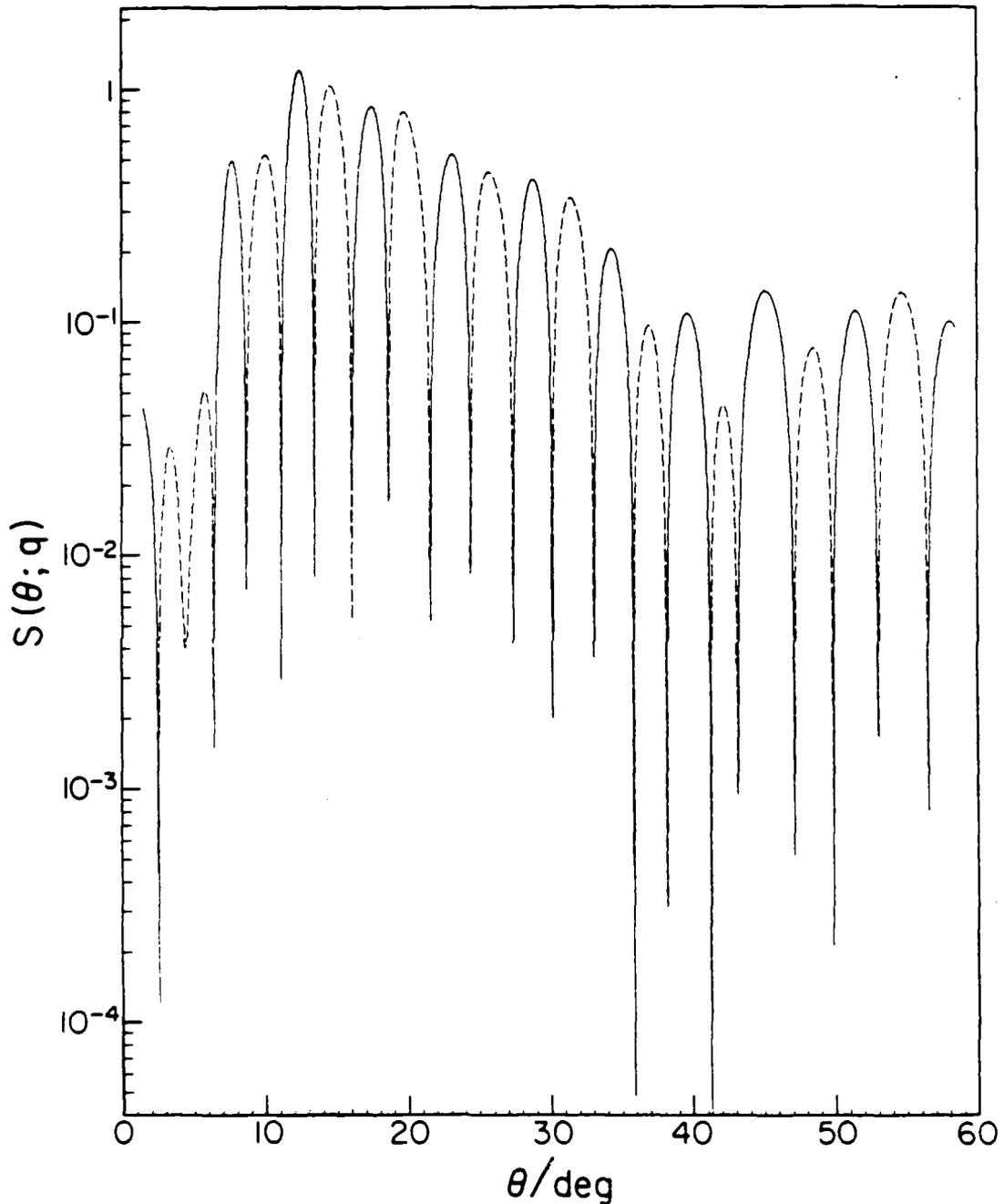
Figure 7c.
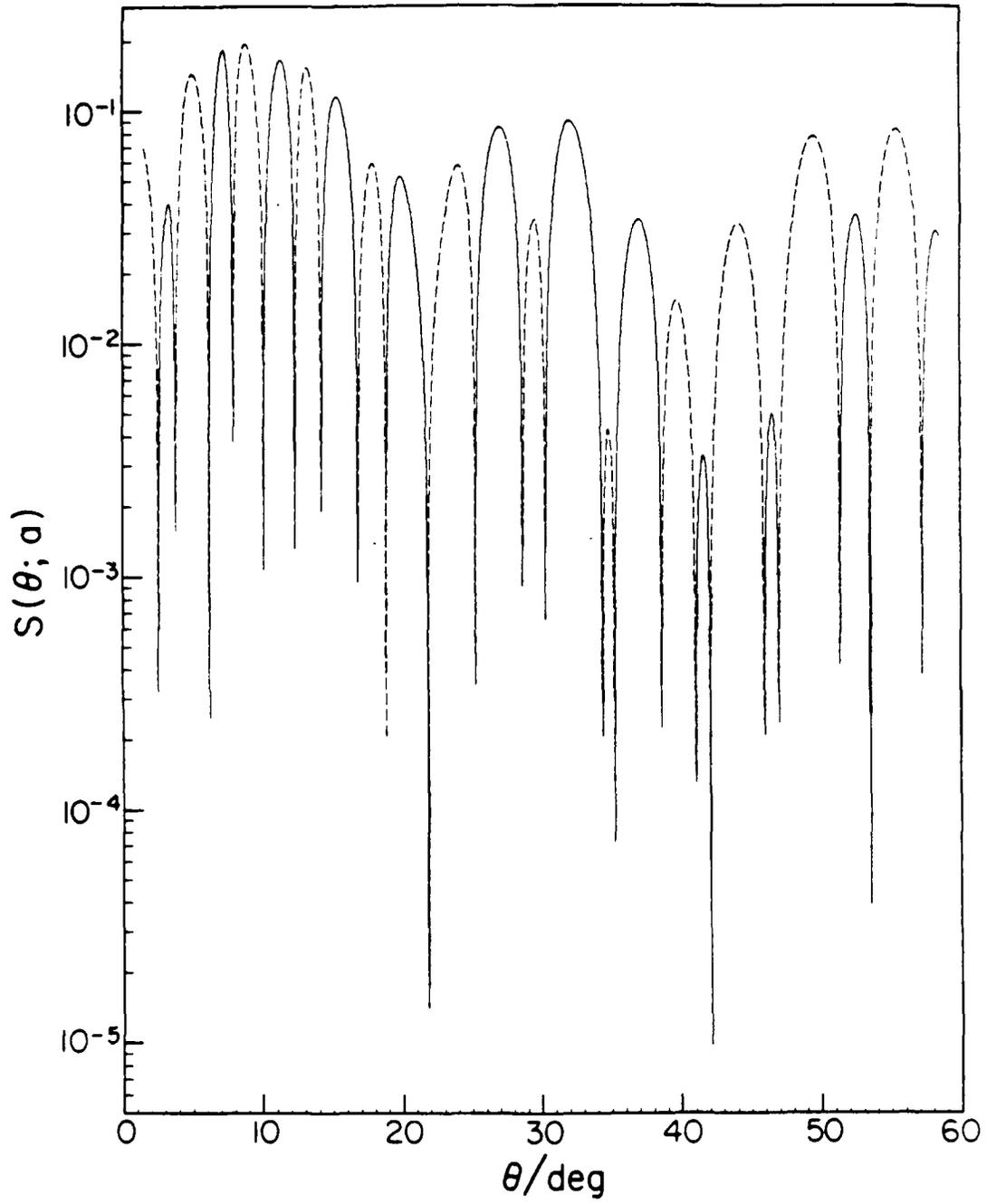
Figure 7d.
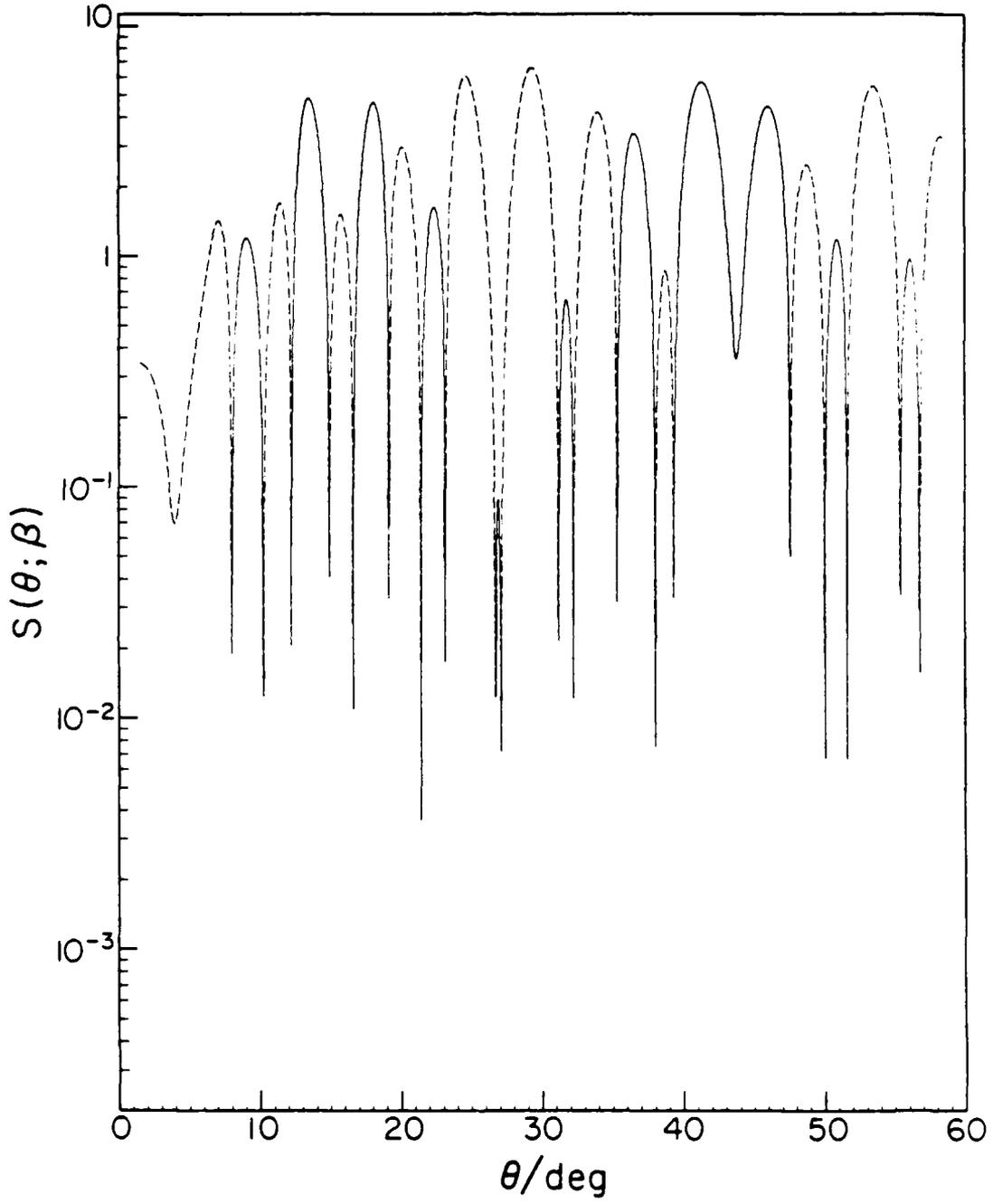
Figure 7e.
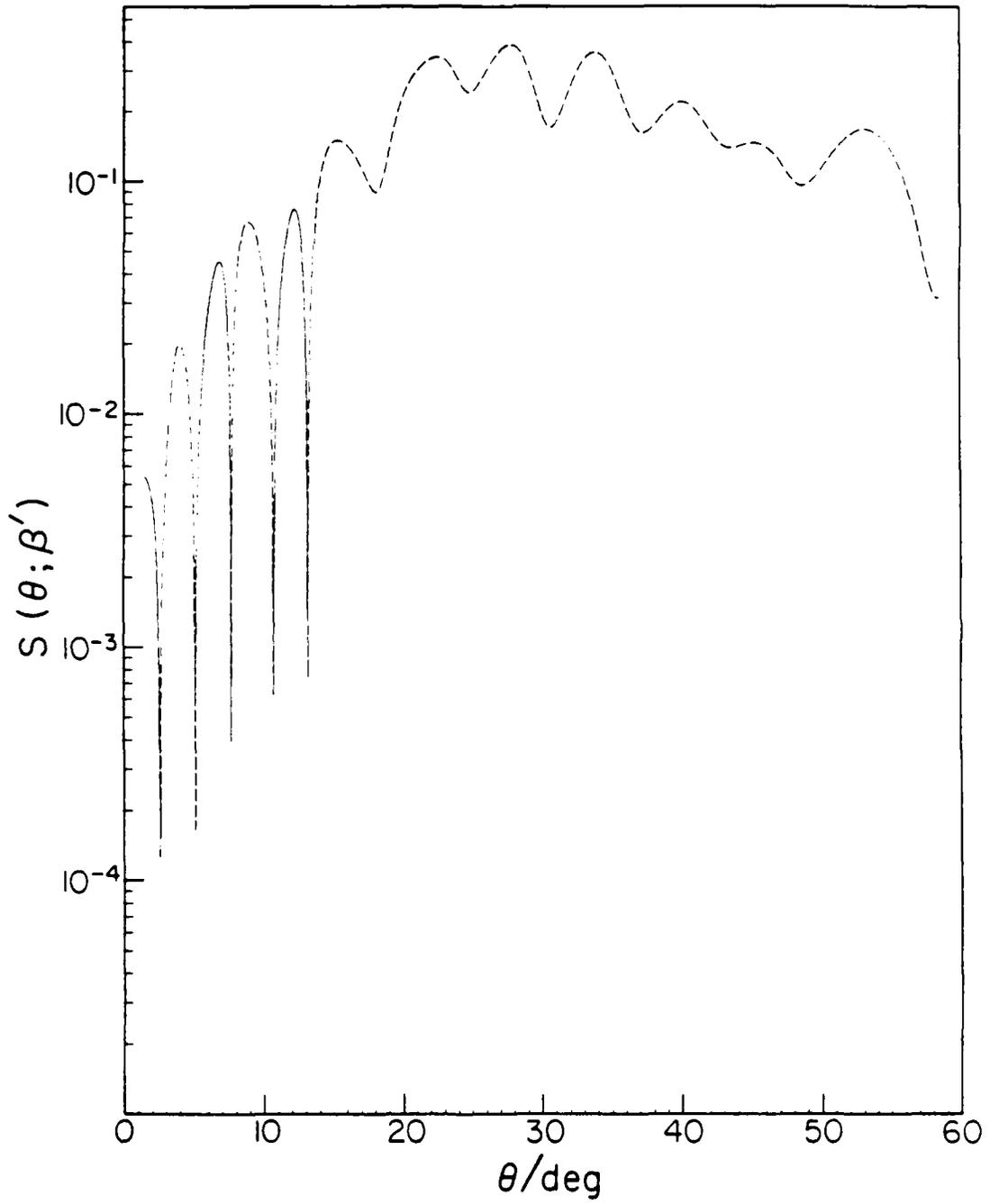
Figure 7f.

Figure 8. Total DCS sensitivity functions for the M (Table I) aniso-
tropic potential for the long range dispersion coefficients
$C_6^{0)}$, $C_6^{2)}$, $C_8^{0)}$ and $C_8^{2)}$. The solid curves are for positive
values of the sensitivities, while the dashed curves are for
negative values of the sensitivities.
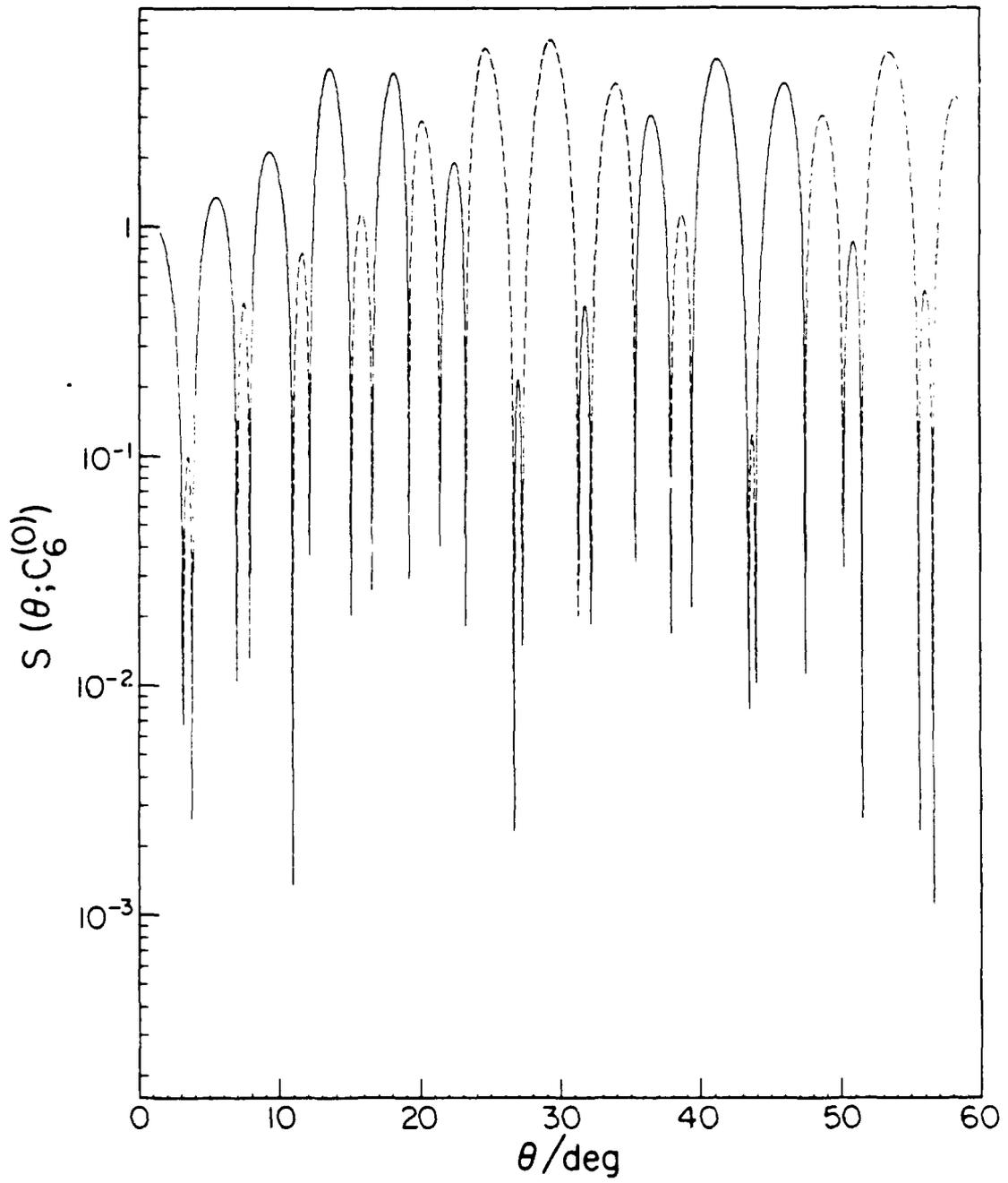
Figure 8a.
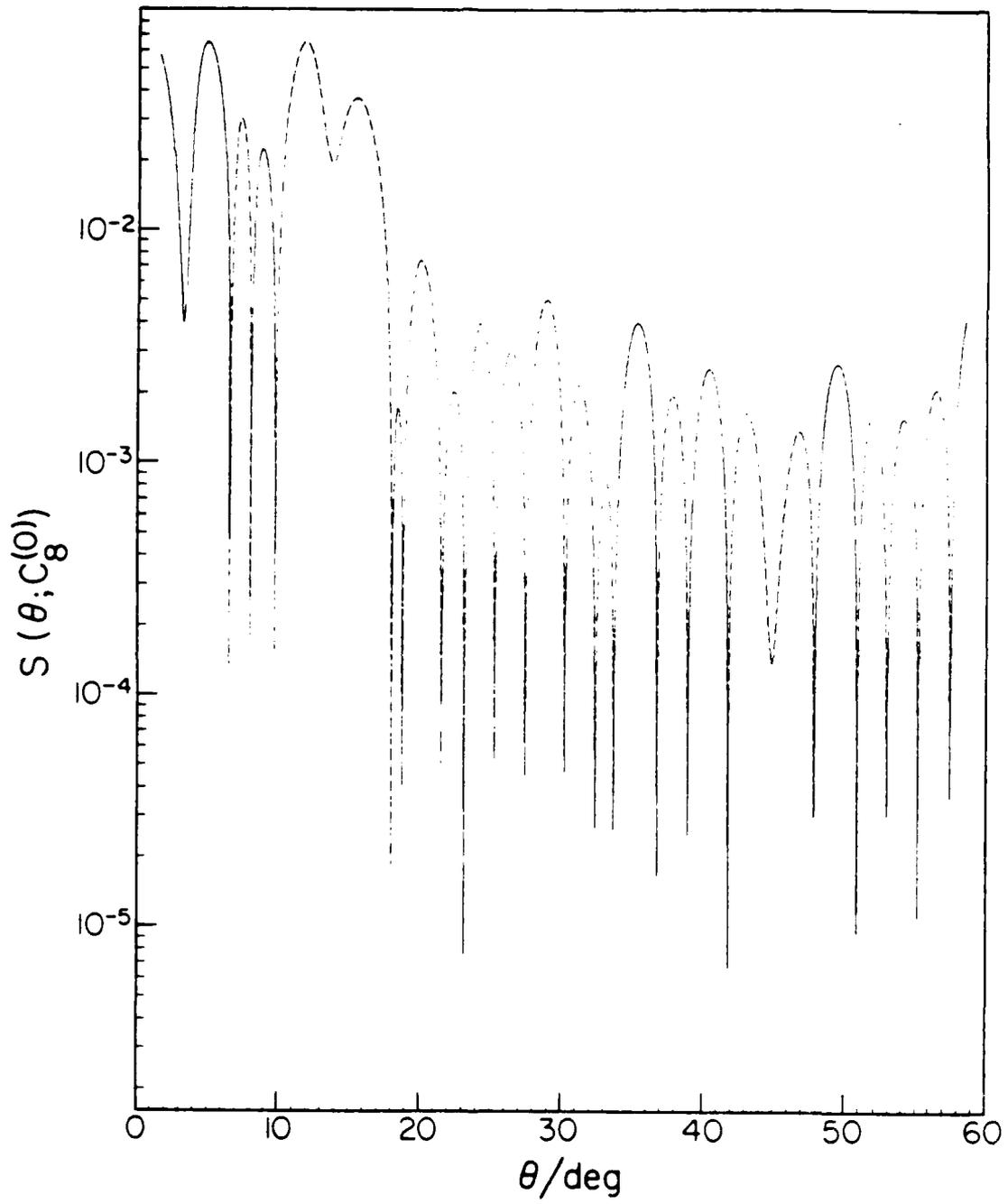
Figure 8b.
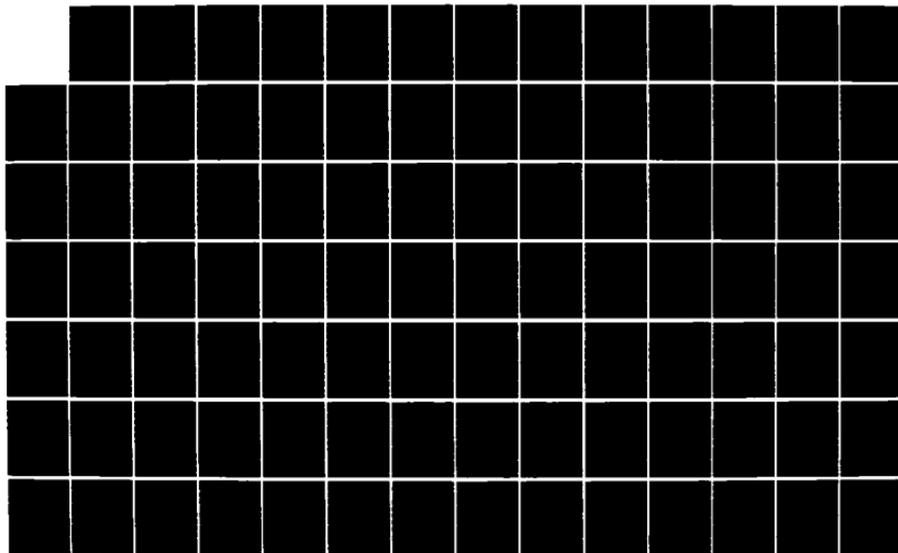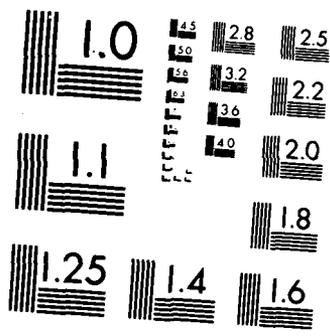
MICROCOPY RESOLUTION TEST CHART
NATIONAL BUREAU OF STANDARDS 1963-A
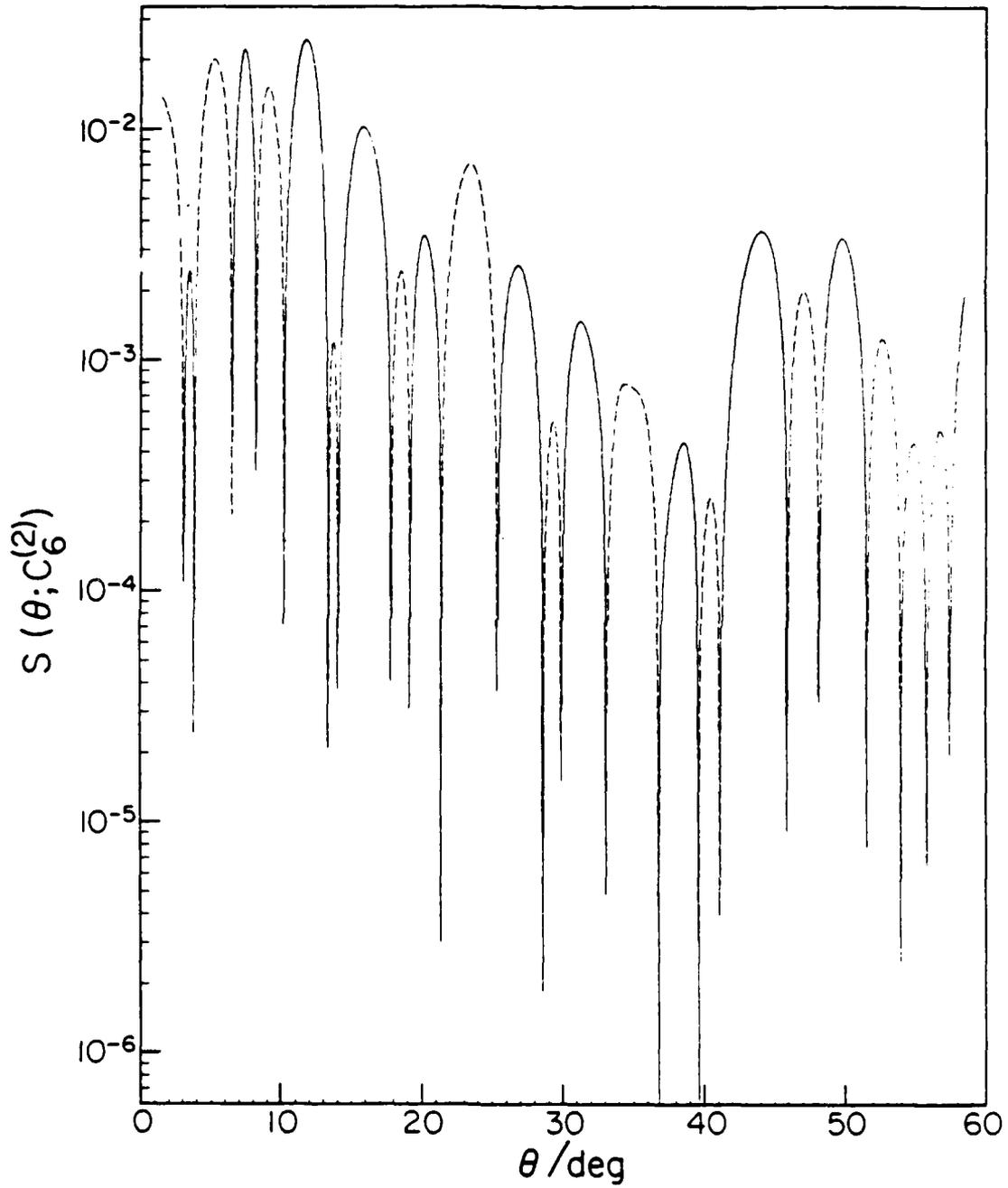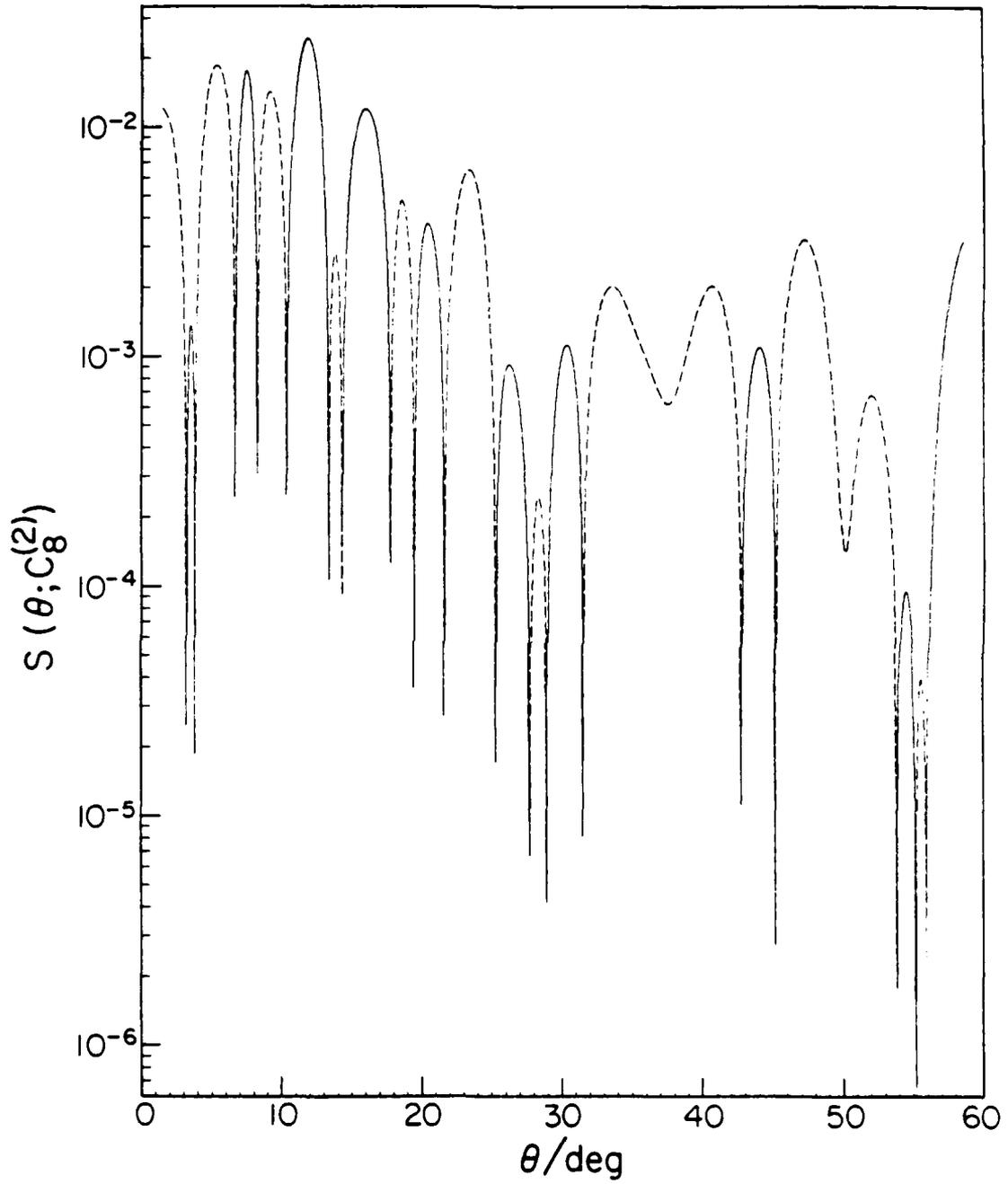
Figure 8c.

Figure 8d.

Figure 9. Rotational state-to-state differential cross sections for the anisotropic potential M (Table I) from initial state $j = 12$. Figure a shows the rotational energy loss cross sections final $j' = 12$, 10, 8, 6, and 4. While b shows the energy gain cross sections, final $j' = 12$, 14, 16, 18, and 20. The upper curve in both figures is for the elastic cross-section; the curves below it are progressively more inelastic. An increase in inelasticity corresponds to decrease in cross section, particularly at low scattering angles. The curves for alternating $j' \leftarrow j$ cross sections are plotted with dashes for distinguishability.
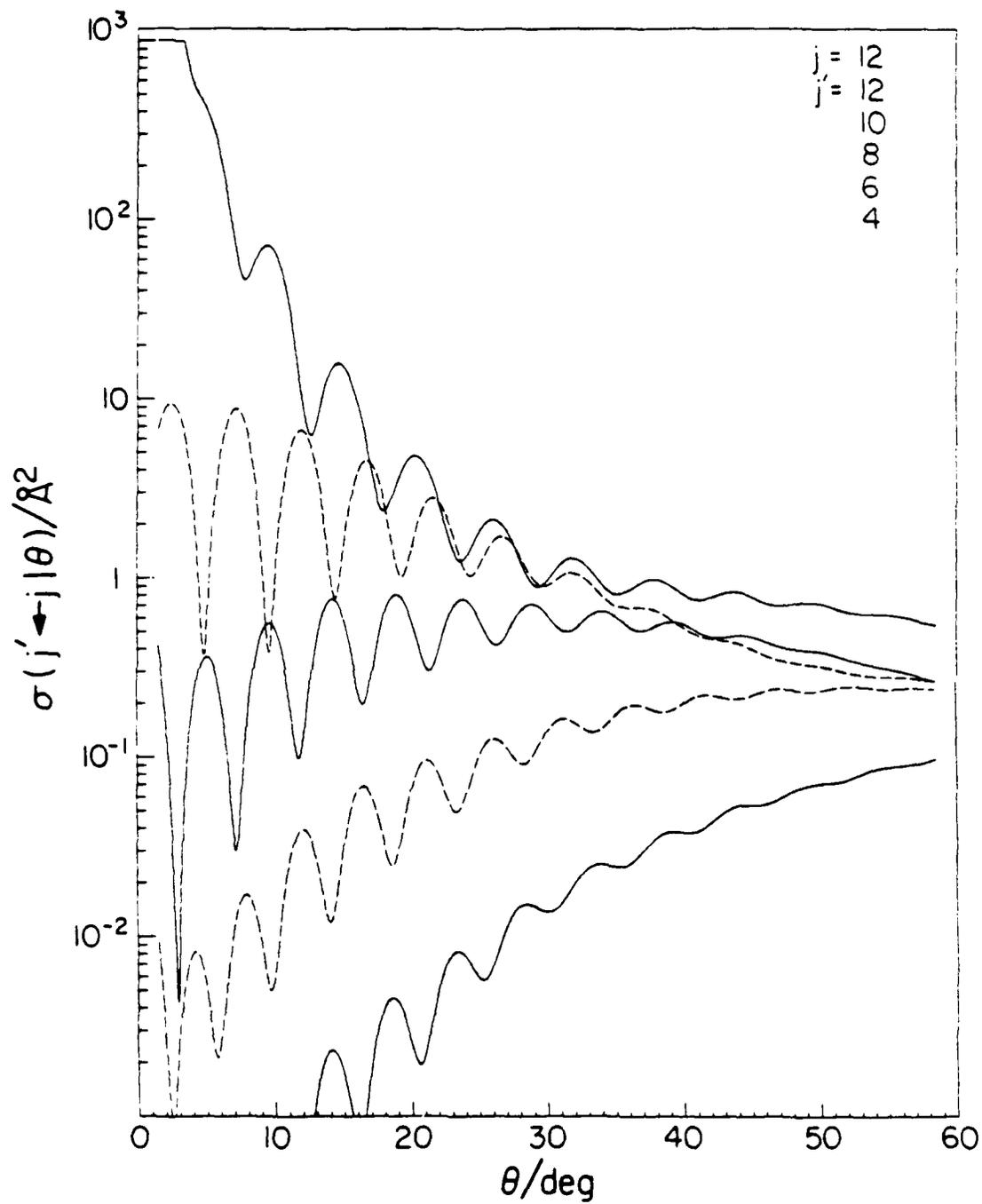
Figure 9a.
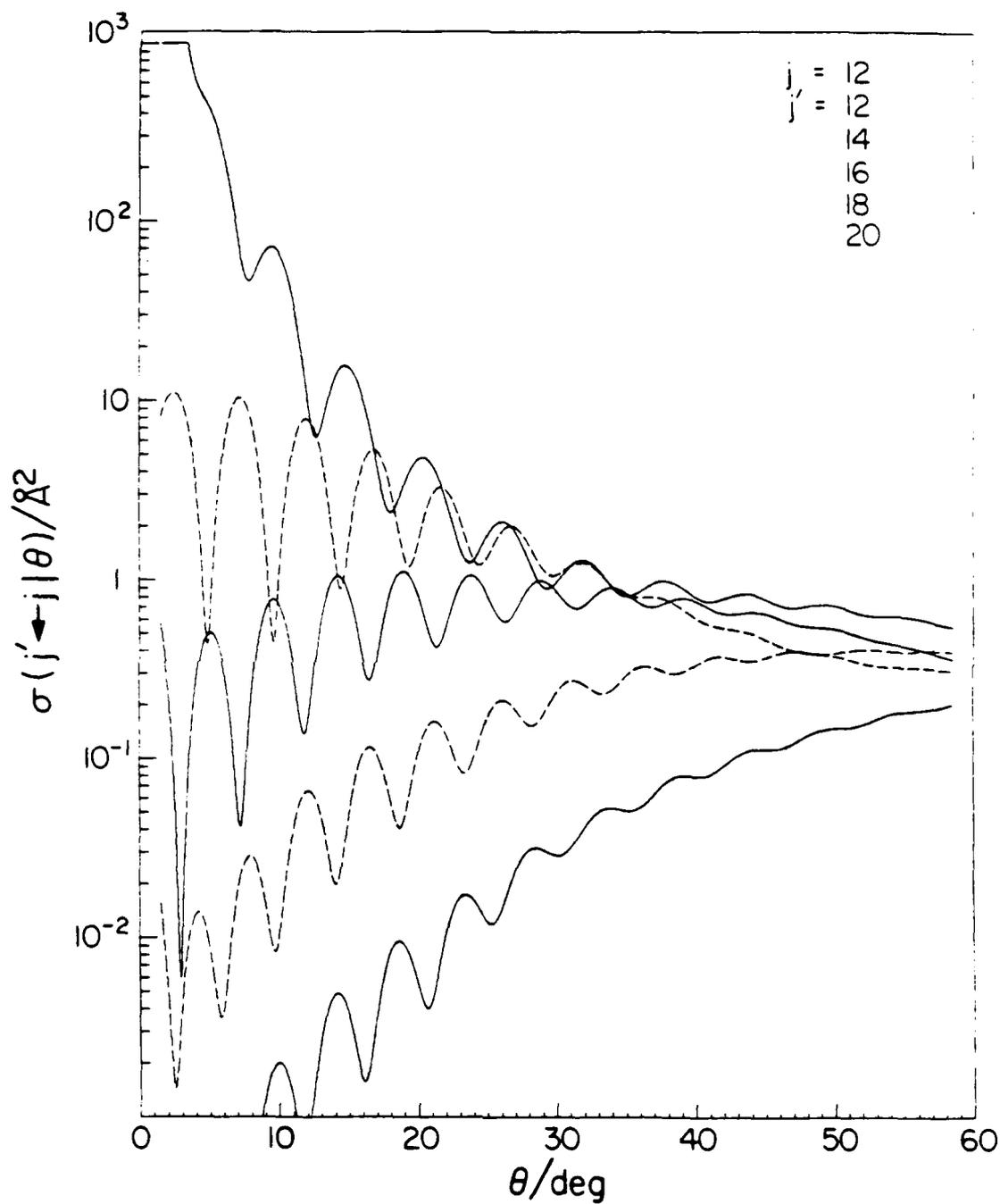
Figure 9b.

Figure 10. Rotational state-to-state differential cross sections for high

and low values of the parameter q (the well minimum

position anisotropy). The values are given in Table III;

Fig. 10a (low q) is for the QL potential, while 10b (high q)

is for the QH. The same transitions are shown as in Figure

9b (rotational energy gain cross sections).
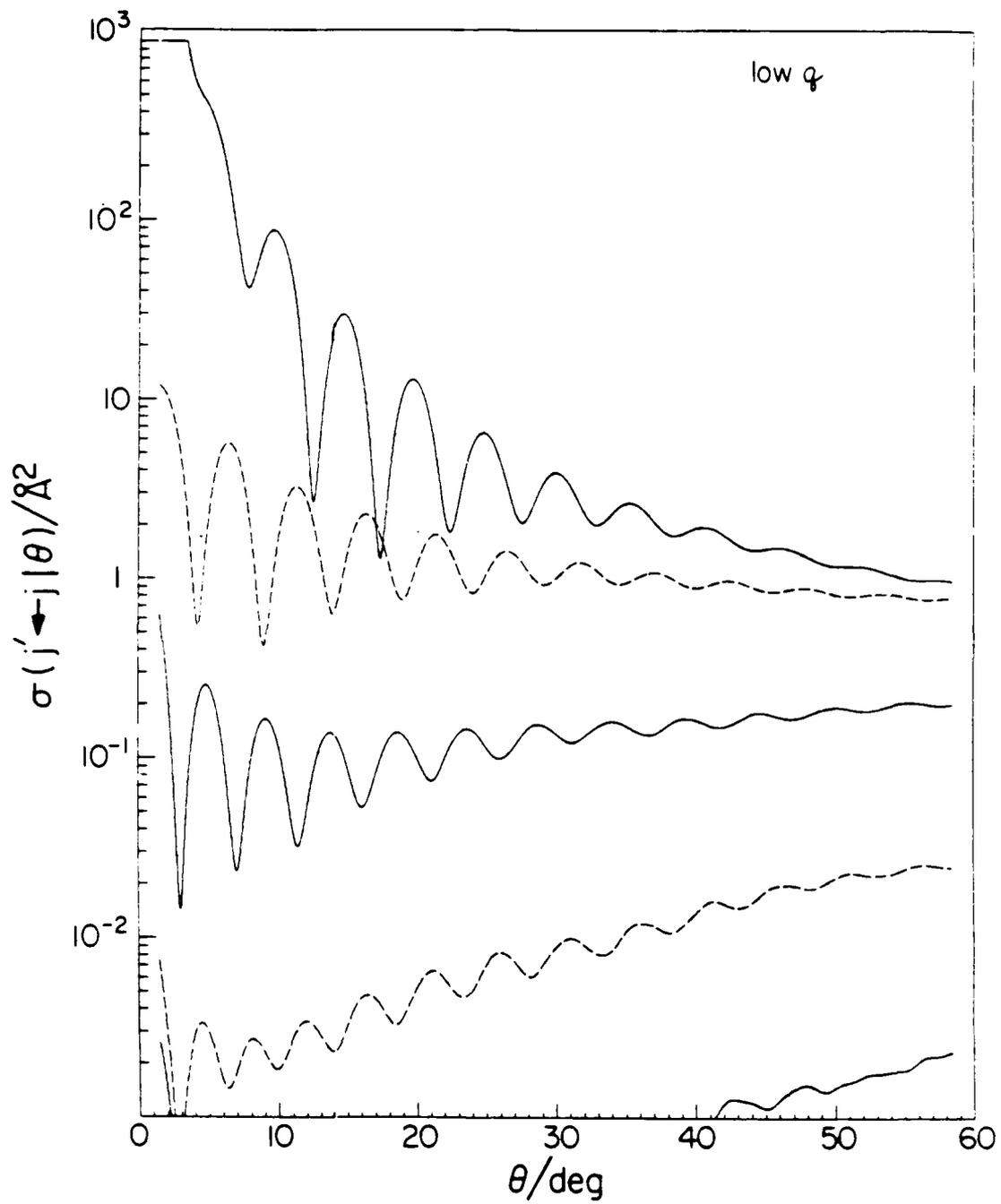
Figure 10a.
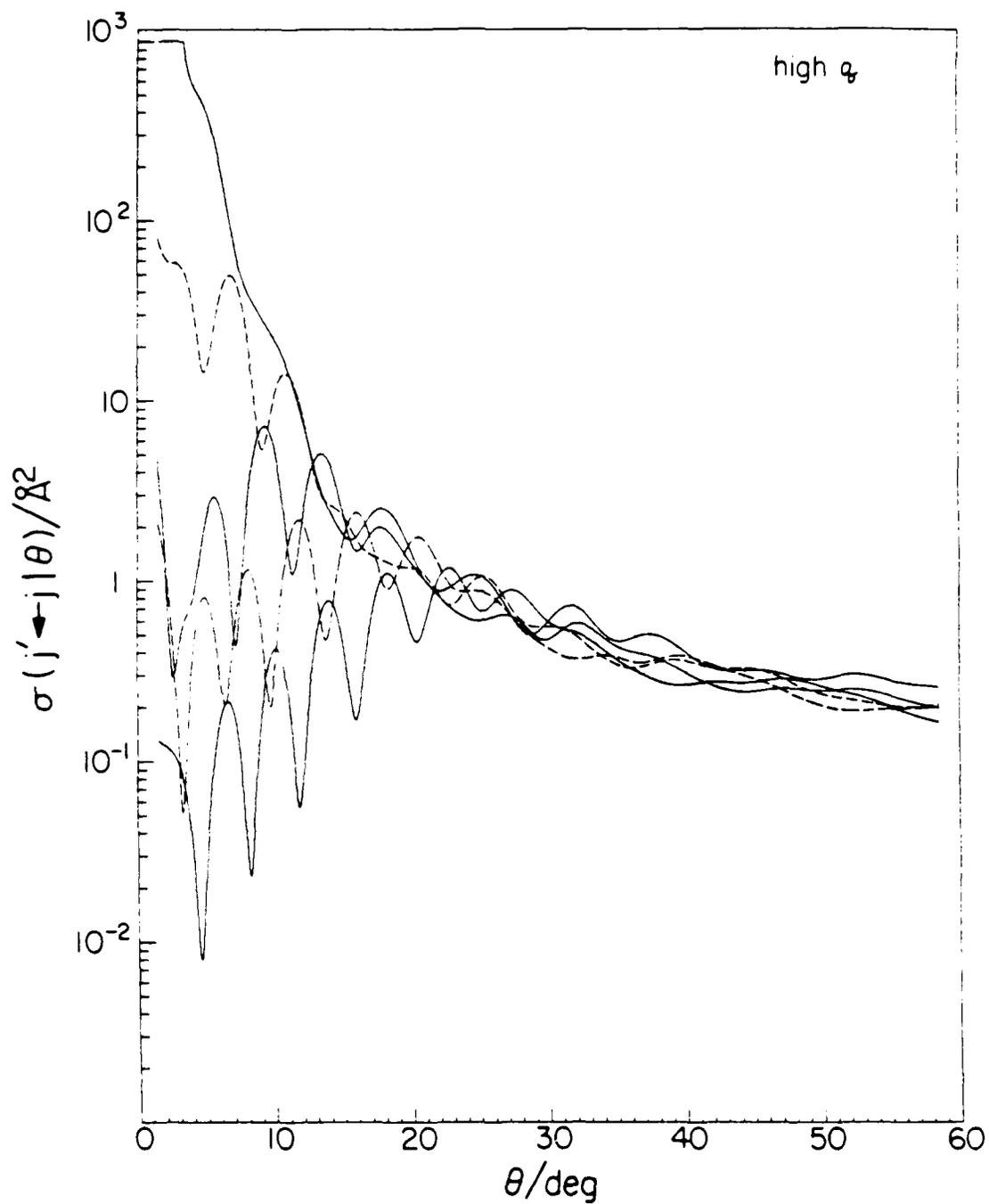
Figure 10b.

Figure 11. Rotational state-to-state differential cross sections for high and low values of the parameter a (the well depth anisotropy). The values are given in Table III; Fig. 11a (low a) is for the AL potential, while 11b (high a) is for the AH. The same transitions are shown as in Figure 9b (rotational energy gain cross sections).
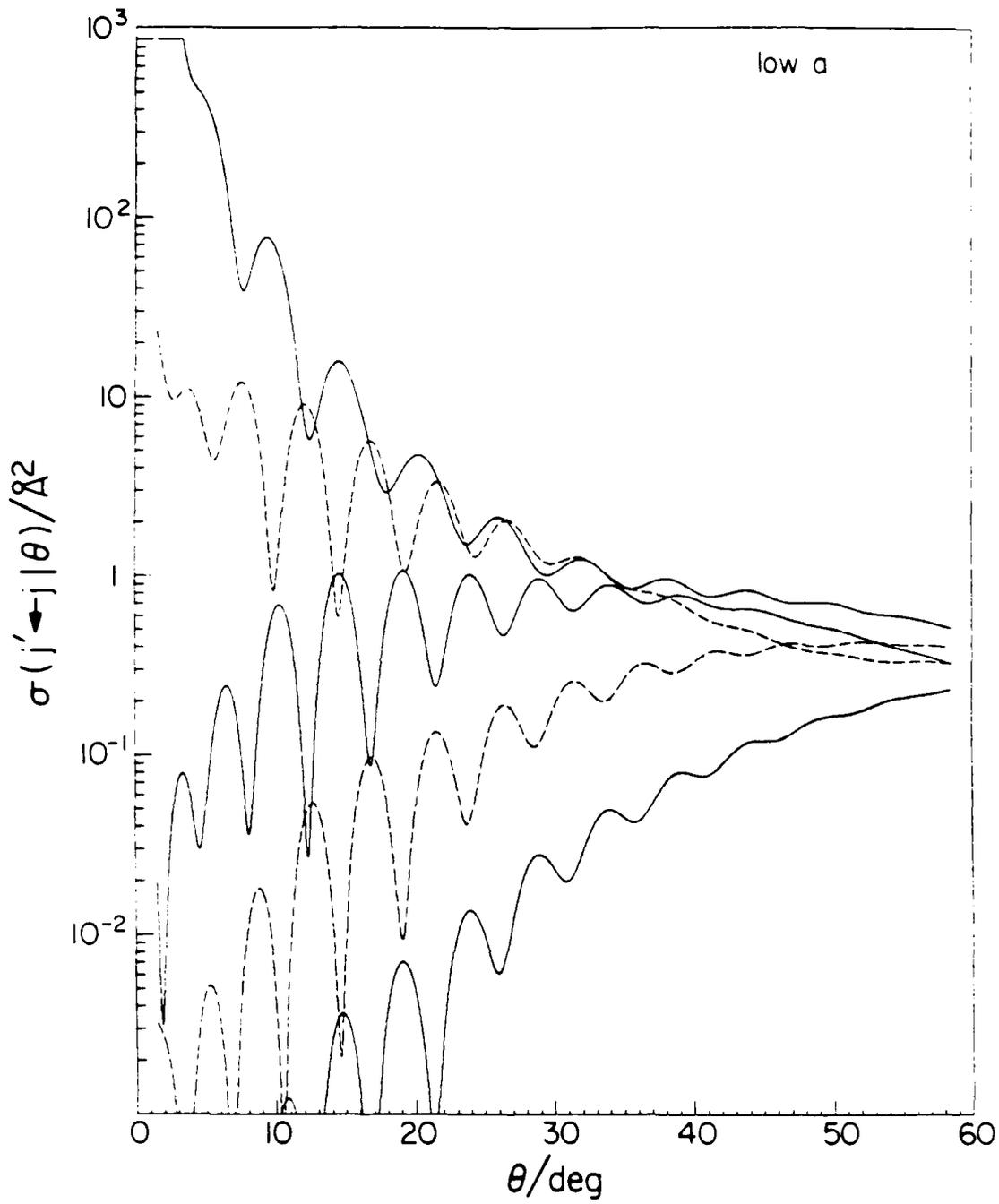
Figure 11a.
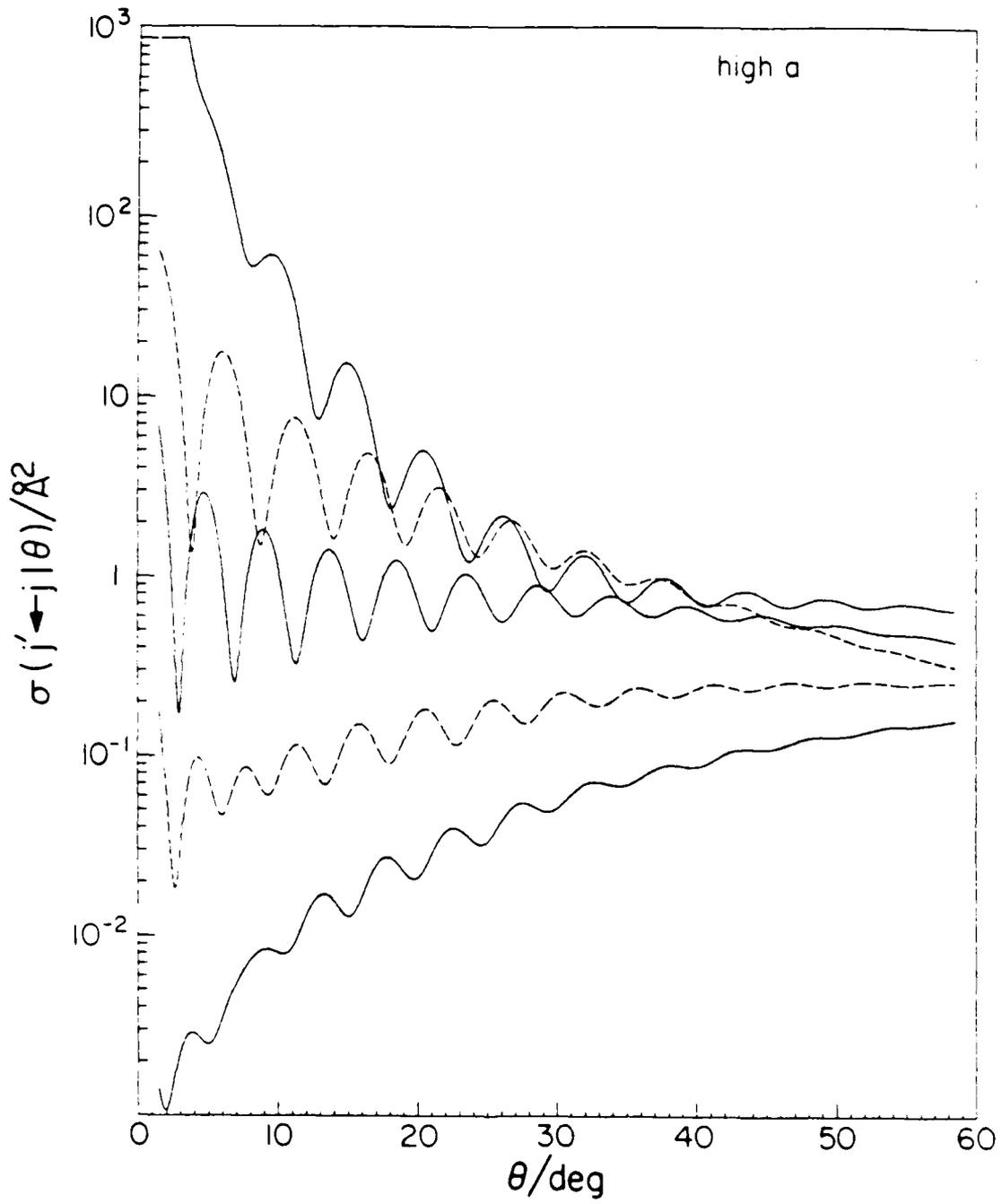
Figure 11b.

Figure 12. Rotational state-to-state differential cross sections for high and low values of the parameter $\epsilon^{(0)}$ (the spherical average of the well depth). The values are given in Table III; Fig. 12a (low $\epsilon^{(0)}$) is for the EL potential, while 12b (high $\epsilon^{(0)}$) is for the EH. The same transitions are shown as in Figure 9b (rotational energy gain cross sections).
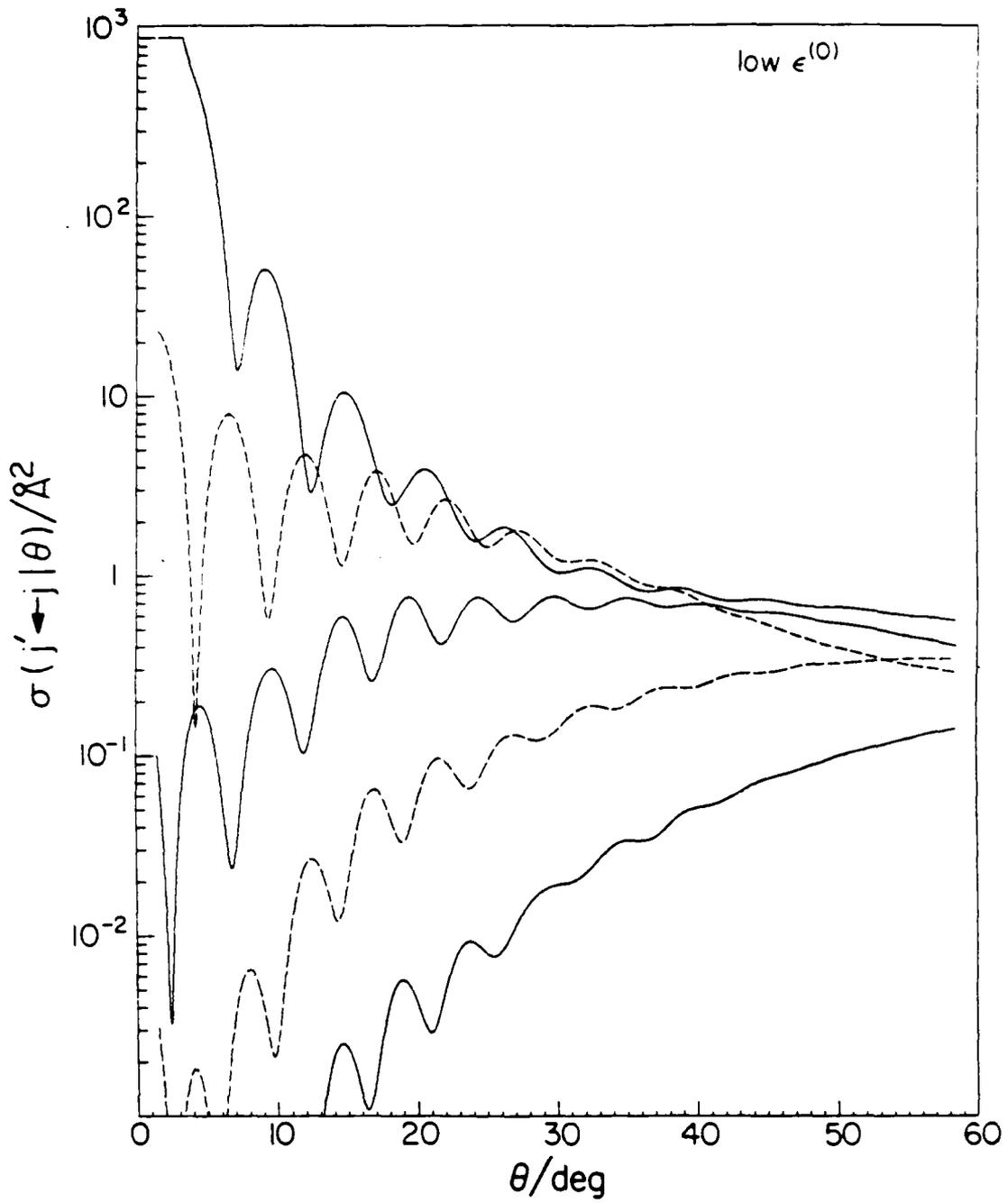
Figure 12a.
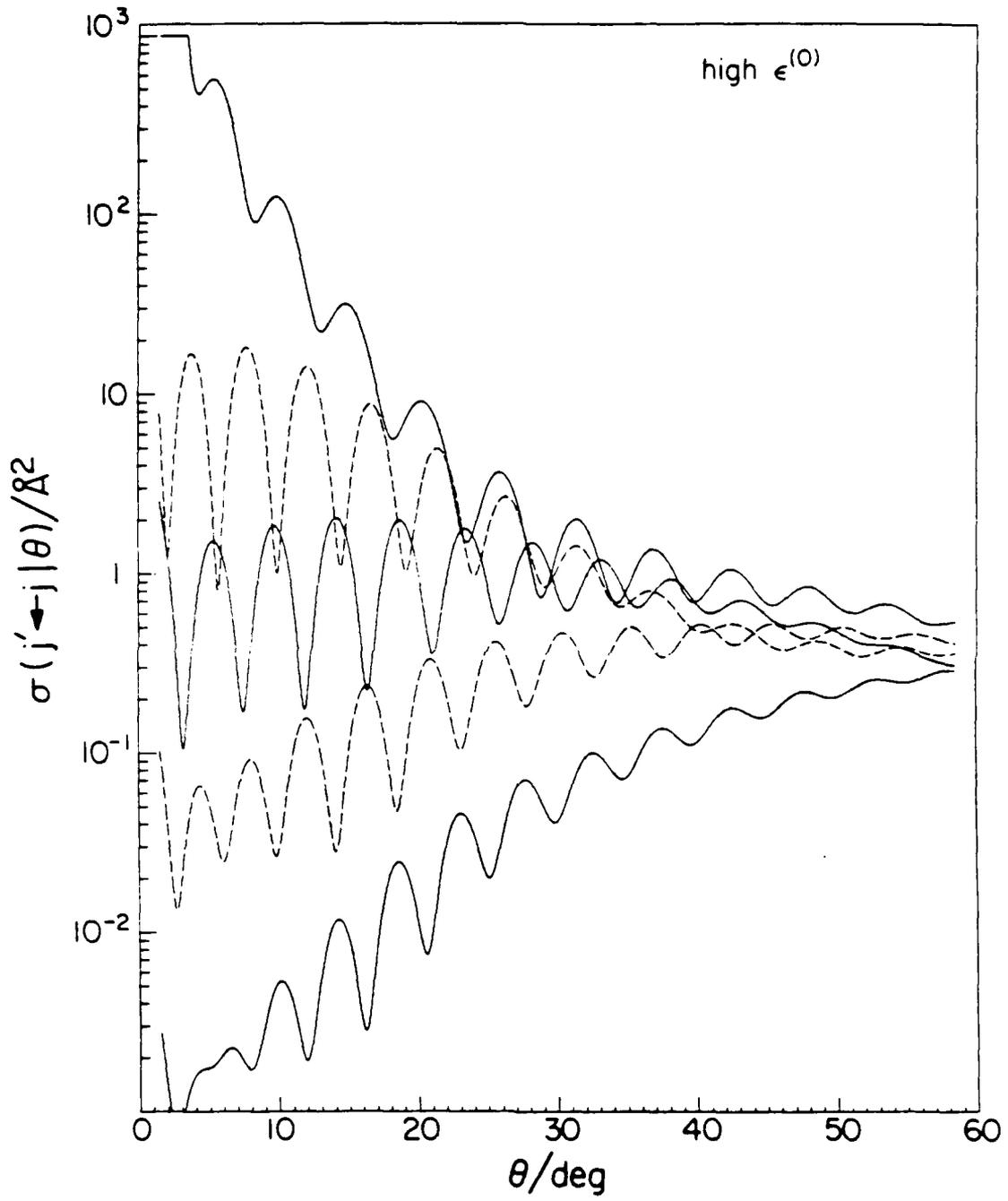
Figure 12b.

Figure 13. Rotational state-to-state differential cross sections for potentials with a "reversed" well depth anisotropy, i.e. a is a positive value. Figures 13a and 13b are for the PAL (low positive a) and PAH (high positive a) potential of Table III, respectively. Figures 13c and 13d are for potentials with an intermediate positive value of a (+0.3) with low (PAEL) and high (PAEH) values of the spherical average of the well depth $\epsilon^{(0)}$, respectively. The same transitions are shown as in Figure 9b (rotational energy gain cross sections).
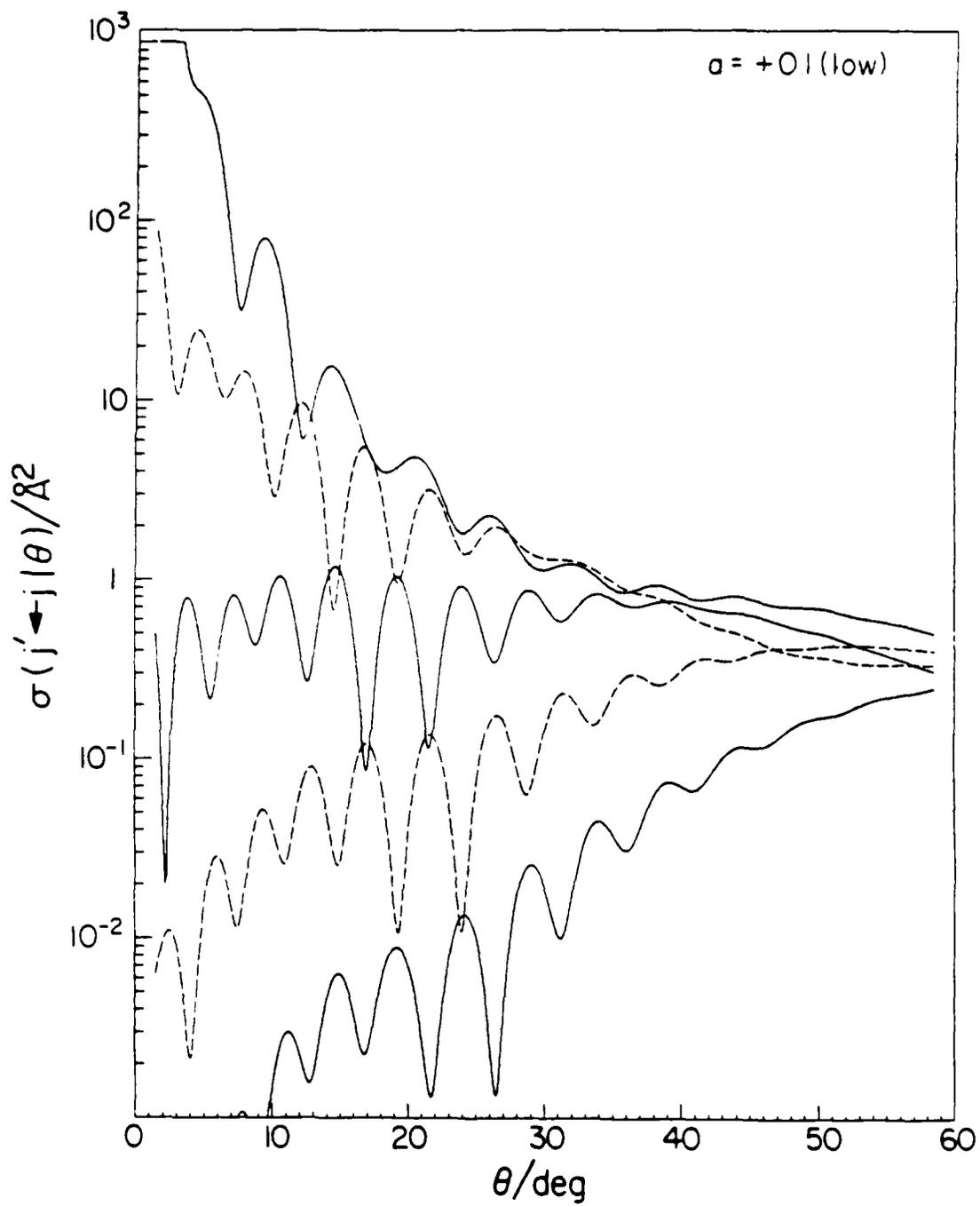
Figure 13a.
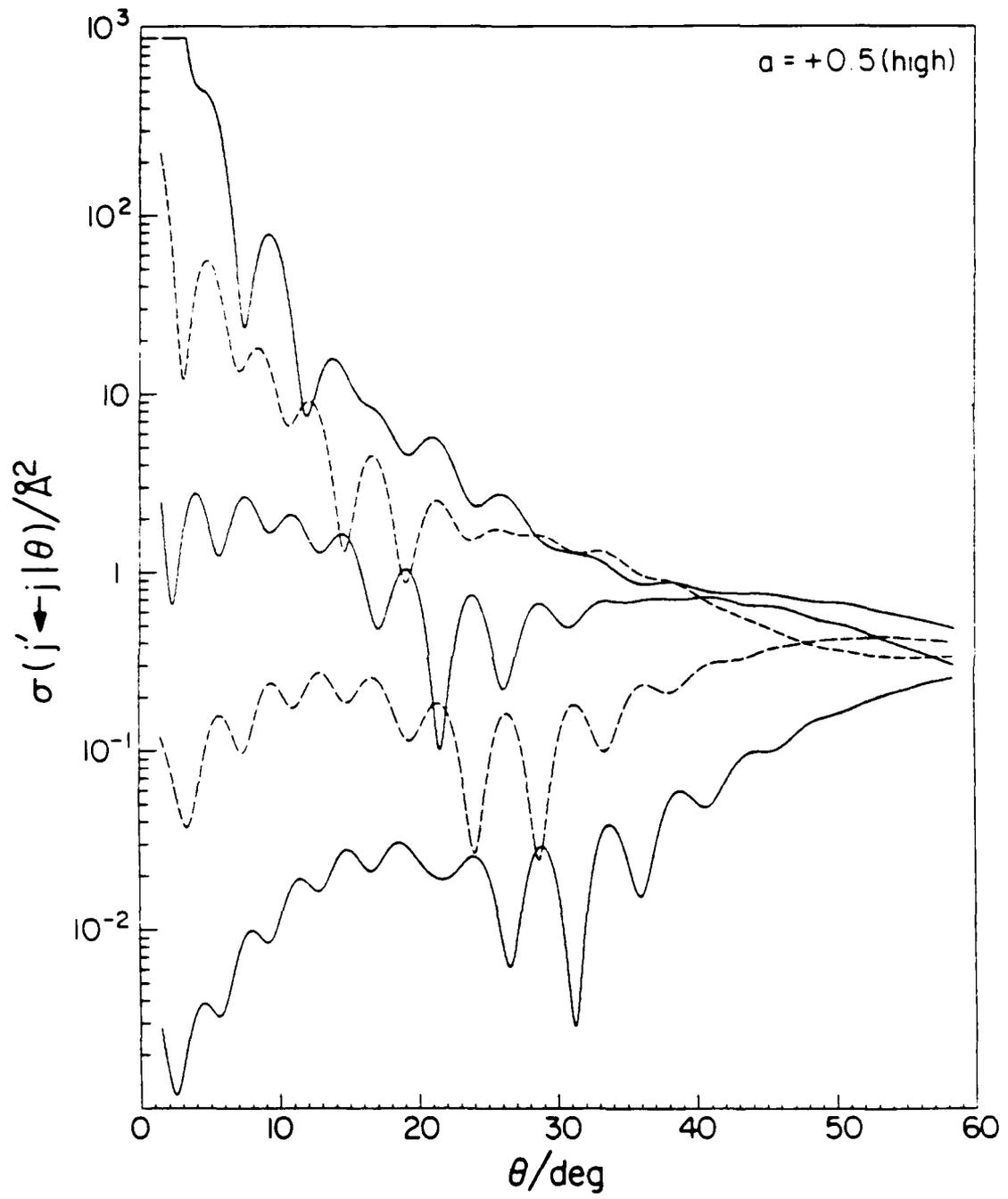
Figure 13b.
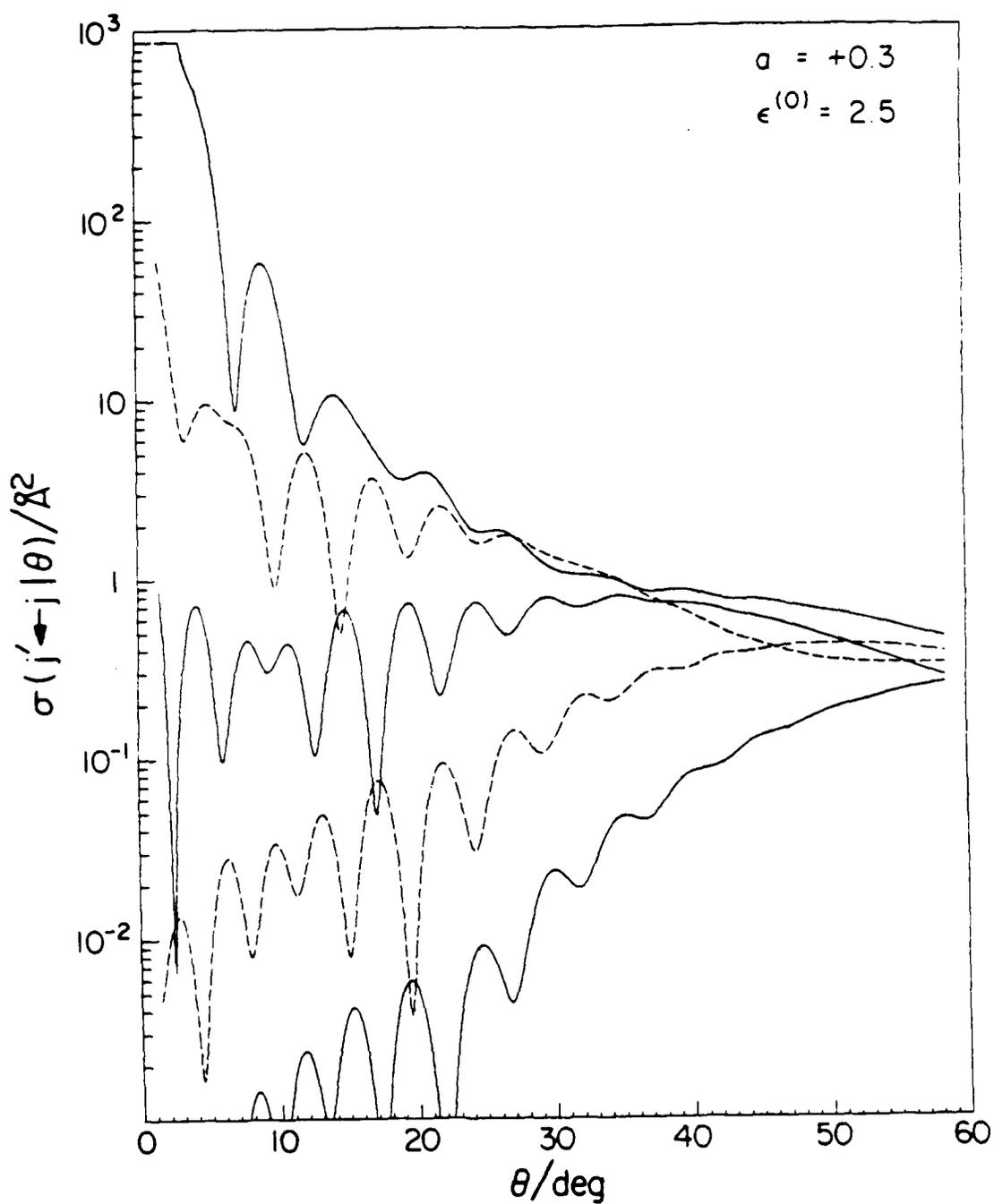
Figure 13c.
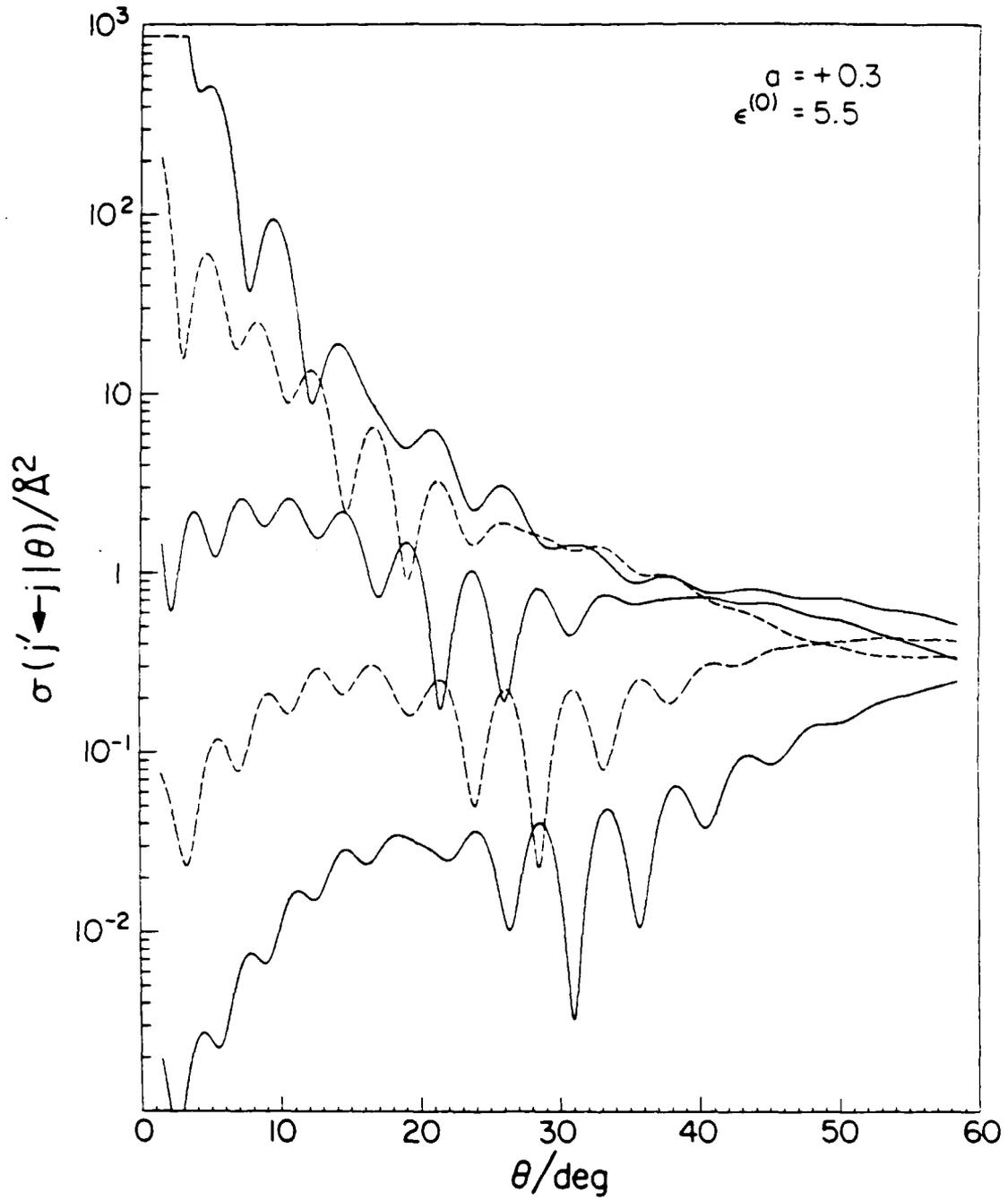
Figure 13d.

Figure 14. Rotational state-to-state differential cross sections for high
and low values of the well width parameter β. The values
are given in Table III; Fig. 14a (low β) is for the BWL
potential, Fig. 14b (high β) is for the BWH. The same
transitions are shown as in Figure 9b (rotational energy
gain cross sections).
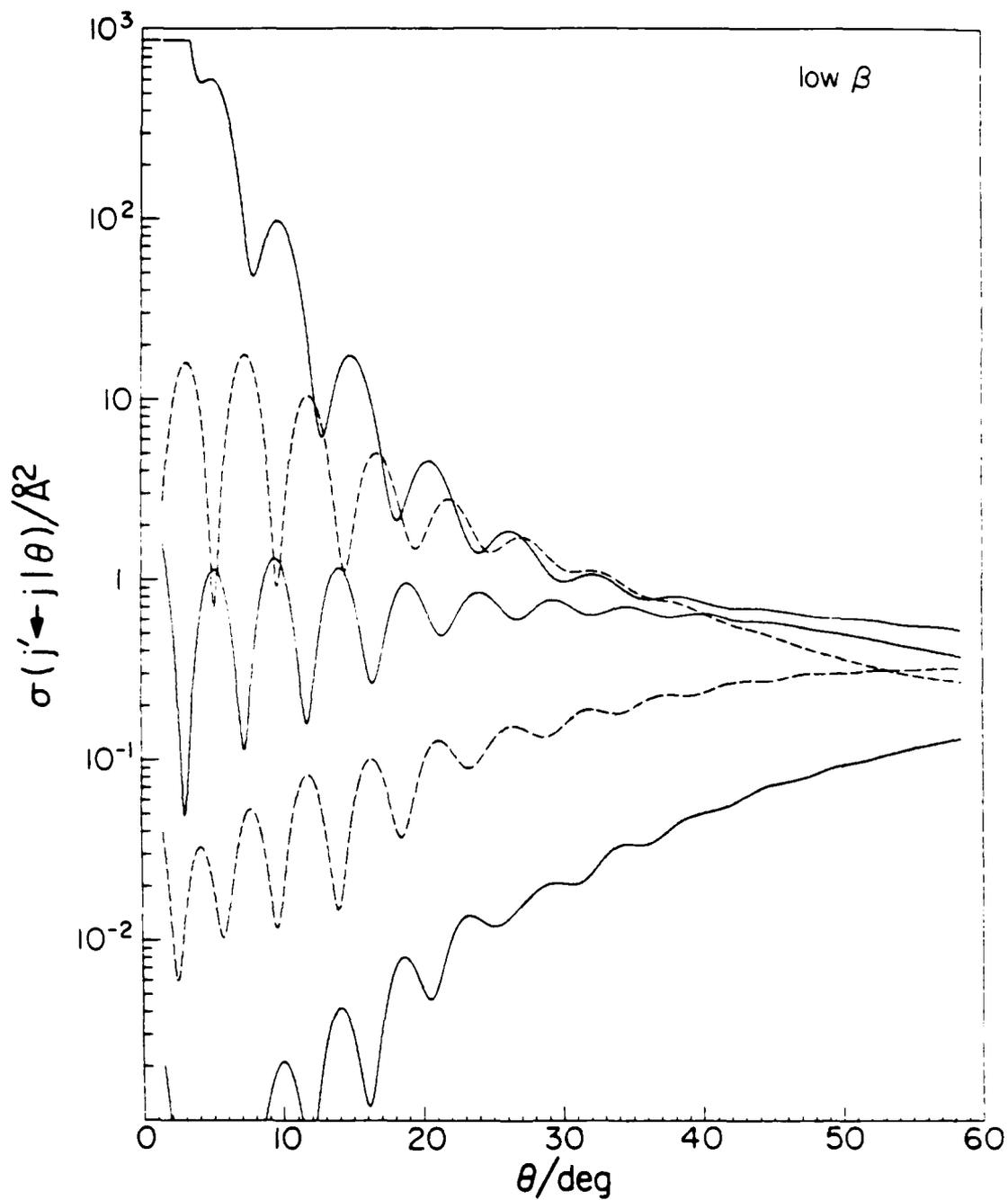
Figure 14a.
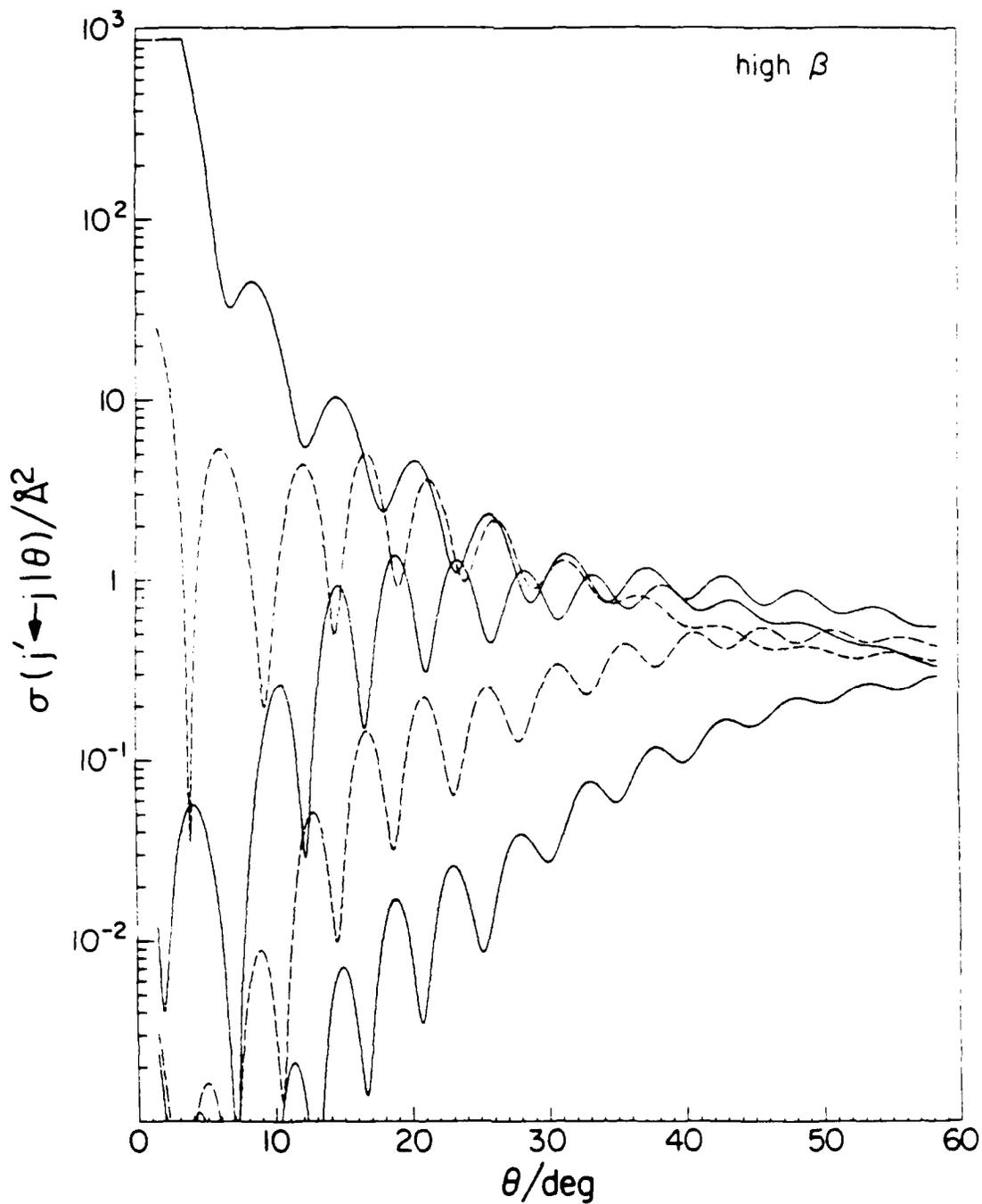
Figure 14b.

Figure 15. Rotational state-to-state $j = 12$ to $j = 14$ DCS sensitivity

functions for the M (Table I) anisotropic potential for the

parameters $r_m^{(0)}$, $\epsilon^{(0)}$, q, a, β and β'. The solid curves

are for positive values of the sensitivities, while the dashed

curves are for negative values of the sensitivities.
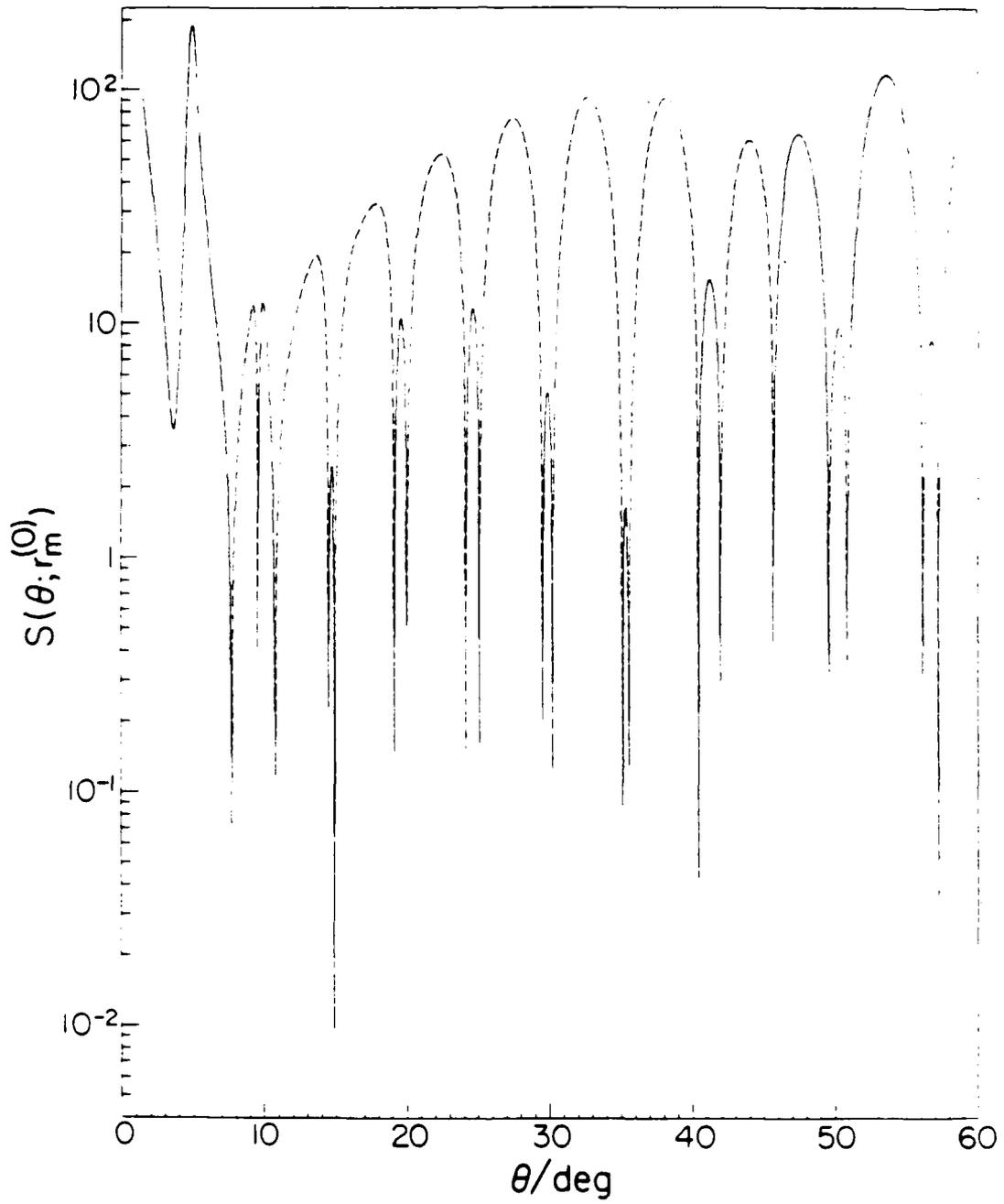
Figure 15a.
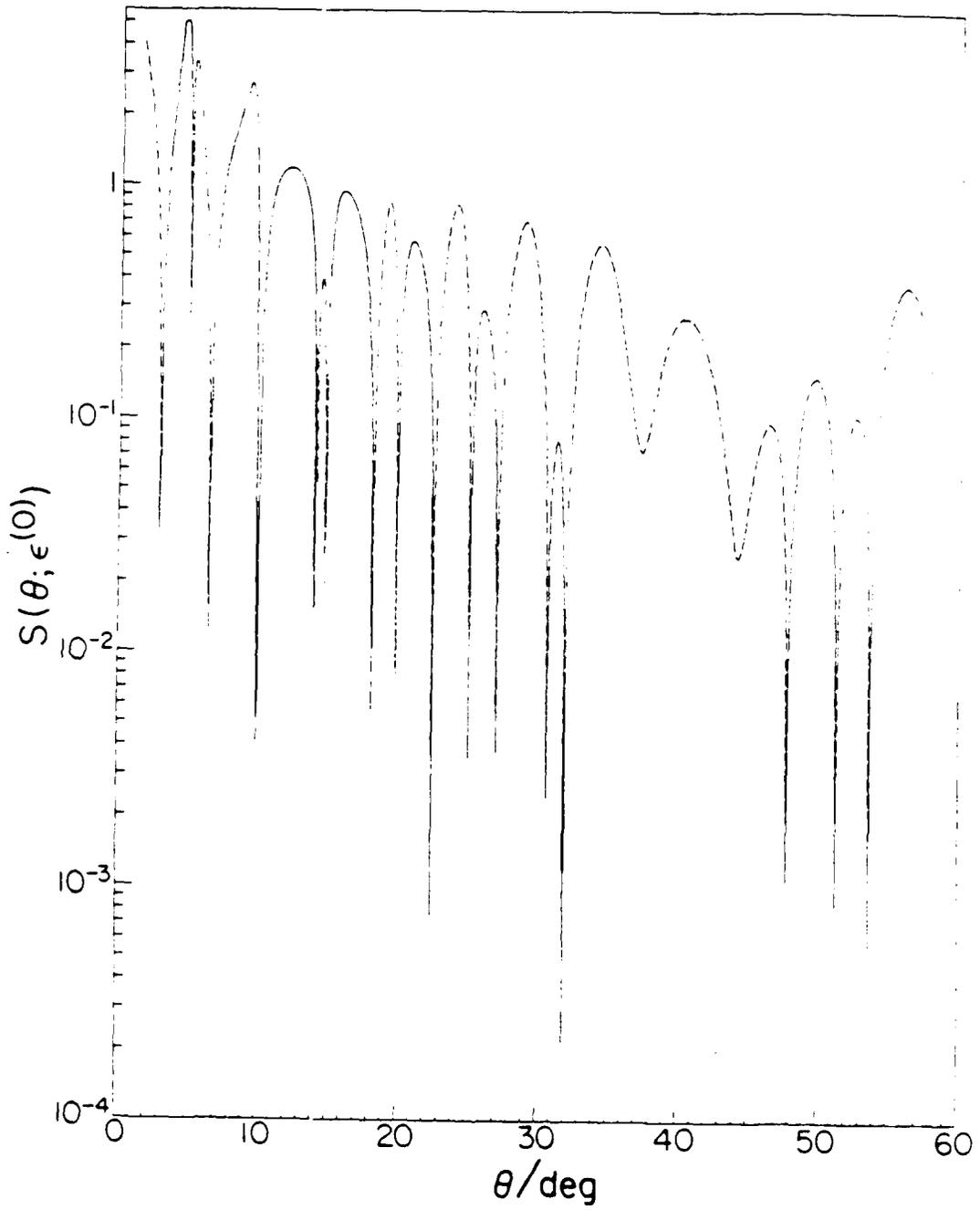
Figure 15b.
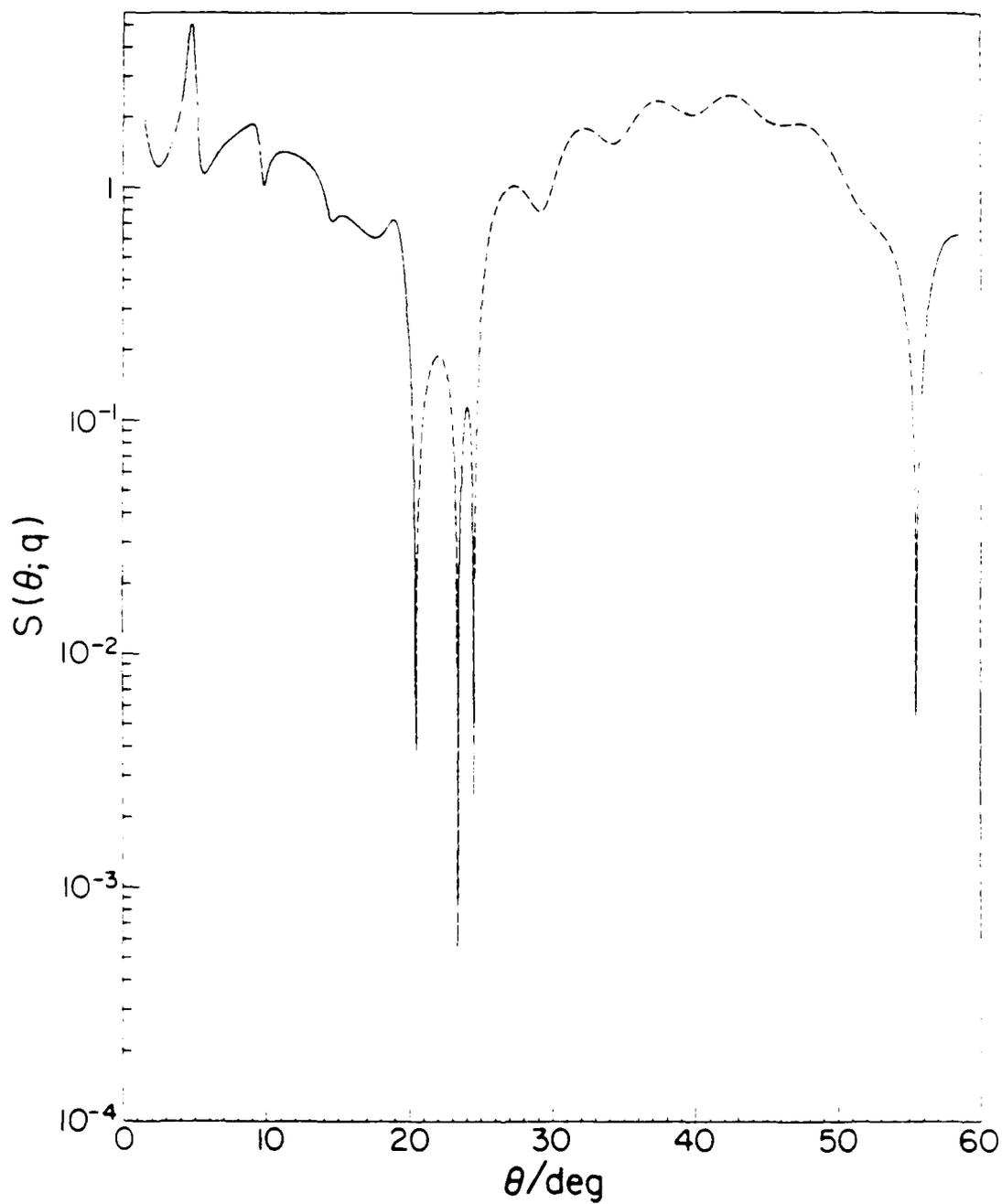
Figure 15c.
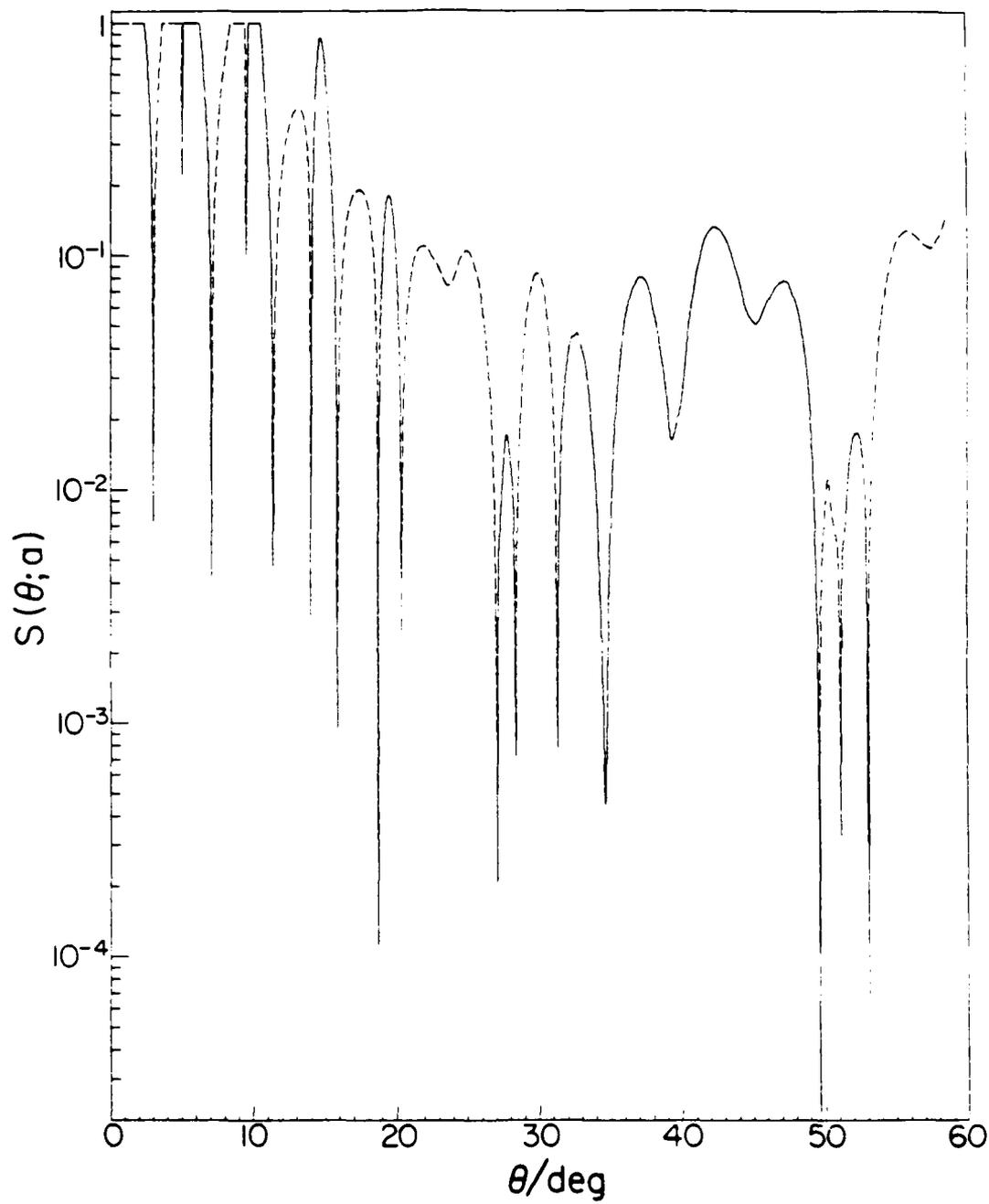
Figure 15d.
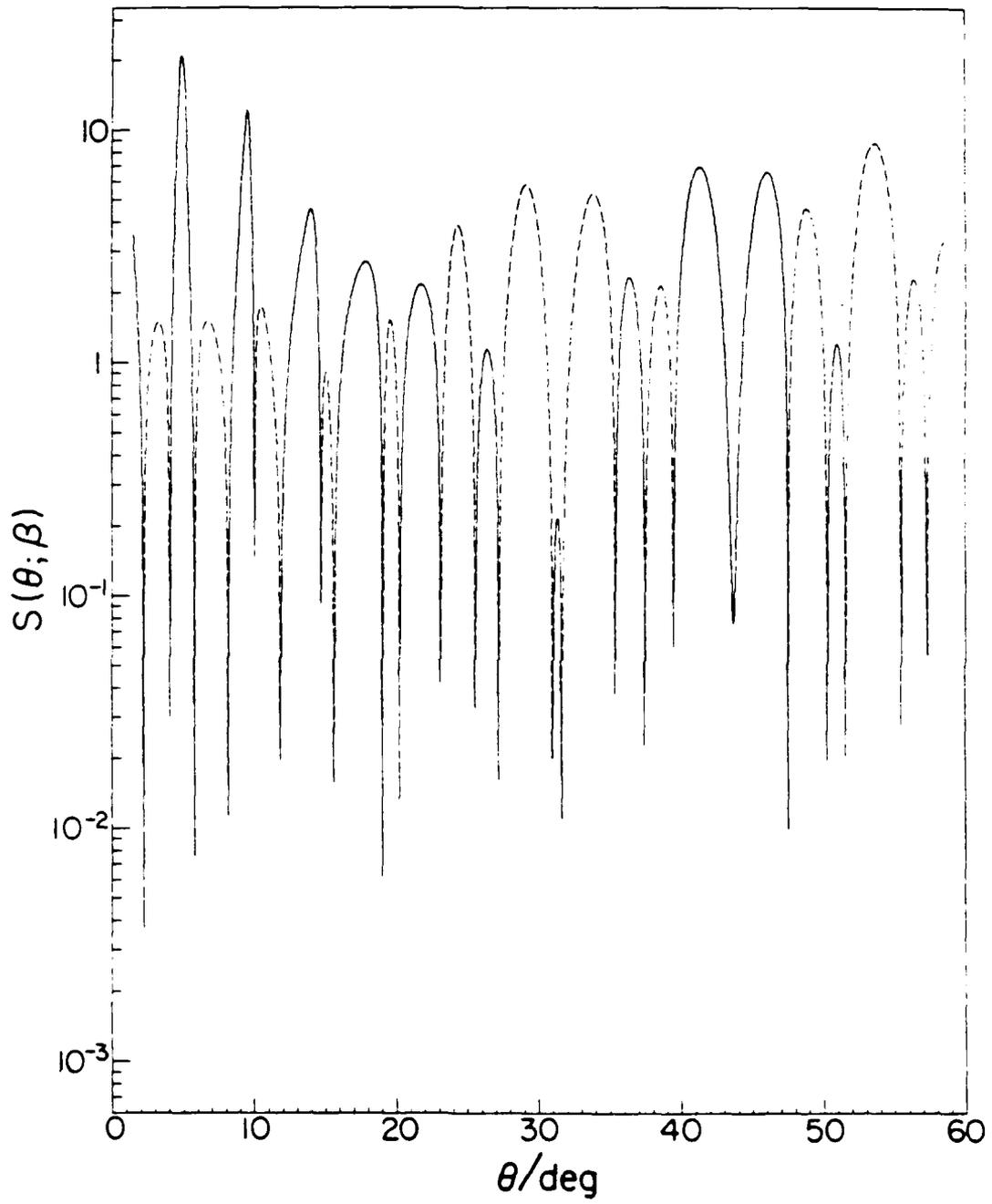
Figure 15e.
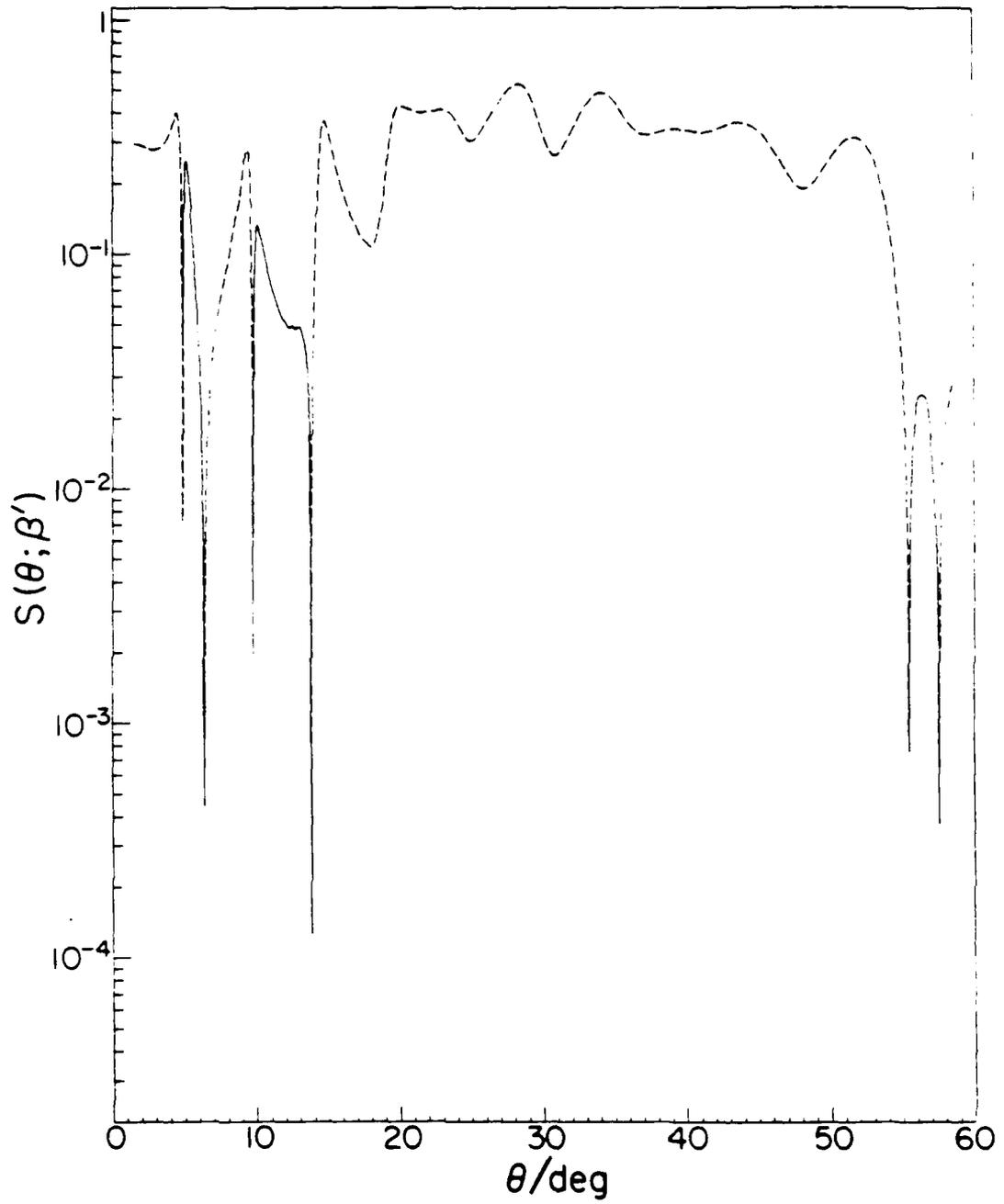
Figure 15f.

Anisotropic Intermolecular Potentials for He + CO_2, He + CS_2, and He + OCS from Crossed Beam Scattering Experiments [a]

Jaroslaw W. Winniczek [b] and Aron Kuppermann

Arthur Amos Noyes Laboratory of Chemical Physics [c]
California Institute of Technology, Pasadena, California 91125

(received   )

Crossed molecular beams total (elastic and inelastic) differential scattering cross sections have been measured for He + CO_2, CS_2, OCS at a relative collision energy of about 65 meV. Anisotropic interaction potentials were extracted from these data, by way of an infinite order sudden approximation analysis. Several different anisotropic potential models were used in this analysis. The necessity for considering the anisotropy in the position of the well minimum as well as of its depth is demonstrated. A potential is proposed for He + OCS that reflects the symmetry of OCS, with a minimum number of modeling parameters.

---

1. INTRODUCTION

Interaction potentials between an atom and a molecule have been and continue to be subjects of a large body of theoretical and experimental work.[1,2] The successful application of the infinite order sudden approximation (IOSA) to many systems has made possible the prediction of a wide range of phenomena.[1-3,11-13] However, the prediction from first principles of these potentials is still difficult in the range where there is a transition between the long range attractive van der Waals forces and the short range repulsive forces. The accurate determination of the potential requires the analysis of a variety of experimental data; the differential cross section (DCS) is one of the most sensitive observables to the potential.

A potential that has attracted a particularly large interest is one for He + CO_2.[3-6,11-15] Which of its characteristics account for various features of the DCS? How uniquely can they be obtained from the data? Is there evidence for potential anisotropy in the data and how can it be studied?

These questions have been addressed previously. Pack[14] showed that anisotropy of r_m dampens the DCS quantal oscillations, while ϵ anisotropy has a much smaller effect on on the DCS. Eno and Rabitz[7] computed sensitivity coefficients for Pack's[14] Lennard-Jones potential to show that the DCS is most sensitive to r_m, with decreasing sensitivity

for ϵ, r_m anisotropy, and ϵ anisotropy. Raff and coworkers[11,12] compared the effects of variations of potential energy surface topography on the observed integral inelastic cross sections and total differential cross sections for He + CO_2; they found that the total (elastic plus inelastic) DCS is by far more sensitive to potential anisotropy than the state resolved integral cross sections. Faubel et al.[9,10] measured the He + O_2 and He + N_2 DCS's, where the total DCS oscillations are very slightly dampened and potential anisotropy can only be extracted by measuring the rotationally inelastic DCS. The DCS for He + CO_2 was first observed by Keil et al.[5] and further analyzed by Parker et al.[4] to extract a potential which provied a good fit to their data. Recently, Keil and Parker[3] fitted the He + CO_2 DCS along with a large set of data which included integral cross sections, transport properties, and linewidths. However, as we will point out, they did not correctly account for certain instrumental parameters in analyzing the DCS data. Because of this problem they could not obtain the correct He + CO_2 potential.

In this paper we present and analyze total (elastic and inelastic) differential scattering cross section data for He + CO_2, CS_2 and OCS. In section 2 we summarize the infinite order sudden approximation (IOSA) and show that it is valid for the analysis of the data collected. In section 3 we list various anisotropic potential forms used to fit our data. In section 4 we describe our crossed-molecular beam apparatus and its operating conditions. In section 5 we describe the data analysis

procedure used to extract an interaction potential from the data. In section 6 we present our data and various potential models that fit the data. We demonstrate the need for anisotropy in well minimum position as well as in the well depth in order to account for all the features of the scattering data. An anisotropic potential for He + OCS is proposed that includes the lack of an inversion center with a minimum number of variable parameters. In section 7 we calculate various bulk properties for He + CO_2 from our best fit potential and compare them to reported experimental measurements. The paper concludes with a summary of our results and conclusions in section 8.

2. THEORY

The theoretical basis for extraction of non-spherically symmetric potentials from differential scattering cross-section data for atom-linear molecule collisions is the infinite order sudden approximation (IOSA) for rotationally inelastic transitions. Parker and Pack have presented an excellent derivation of the IOSA;[13] hence we will only demonstrate its highlights and how it applies specifically to obtaining non-spherical intermolecular potentials. At the collision energies under consideration here, vibrational excitations are not accessible, while vibrational deexcitations are not possible since the molecules of interest herein are in their vibrational ground states.[23] Therefore, it is reasonable to treat the target molecule as a rigid rotor of length R (the distance between the end atoms) and with a moment of inertia I. Let r be the position vector of the incident atom with respect to the center-of-mass of the molecule and γ be the angle between r and the oriented molecular axis R. The nuclear motion Hamiltonian for this system is therefore

$$\hat{H} = -\frac{\hbar^2}{2\mu r}\frac{\partial^2}{\partial r^2}r + \frac{\hat{L}^2}{2\mu r^2} + \frac{\hat{j}^2}{2I} + V(r,\gamma) \tag{1}$$

where μ is the atom-molecule reduced mass, and $\hat{L}$ and $\hat{J}$ are the orbital angular momentum and molecular angular momentum operators, respectively.

Solution of the corresponding nuclear motion Schrödinger equation can be achieved by expanding the scattering wave function in eigenfunctions of the total angular momentum $\hat{\mathbf{J}} \equiv \hat{J} + \hat{L}$. This yields a set of radial differential equations in the coefficients of this expansion coupled by the matrix elements of $V(r, \gamma)$ in the expansion basis set. These equations can be decoupled by imposing the centrifugal sudden approximation[18,19] and the energy sudden approximation.[16,17] This involves replacement of the orbital and molecular angular momentum operators in (1) by the constants

$$\hat{L}^2 \simeq \hbar^2 \bar{l}(\bar{l} + 1) \tag{2}$$

and

$$\hat{J}^2 \simeq \hbar^2 \bar{j}(\bar{j} + 1) \tag{3}$$

where $\bar{l}$ and $\bar{j}$ are effective angular momentum quantum numbers which are chosen differently to accommodate various versions of the theory. Collectively, these two approximations are known as the IOSA,[13] which yields the decoupled ordinary differential equations

$$\left[\frac{d^2}{dr^2} + k_j^{-2} - \frac{\bar{l}(\bar{l} + 1)}{r^2} - \frac{2\mu}{\hbar^2} V(r, \gamma) \right] \phi_{\bar{l}}(r; \gamma) = 0 \tag{4}$$

in terms of which the differntial cross sections of interest can be calculated as indicated below. Equation (4), in which γ plays the role of a parameter (since it does not appear in differential operators), can

be solved in a manner analogous to a spherical potential problem,[21] by requiring that the wave function vanish at the origin and that at large r it behave as

$$\phi_l \xrightarrow[r\to\infty]{} k_{\bar{j}}^{-1/2}\left\{e^{-i(k_{\bar{j}}r - l\pi/2)} - e^{i[k_{\bar{j}}r - l\pi/2 + 2i\eta_l(\gamma)]}\right\} \qquad (5)$$

where $\eta_l(\gamma)$ is the phase shift for a given fixed atom-molecule orientation and the wave vector $k_{\bar{j}}$ is given by[13]

$$k_{\bar{j}}^2 = \frac{2\mu}{\hbar^2}\left[E - \frac{\hbar^2 \bar{j}(\bar{j}+1)}{2I}\right] \qquad (6)$$

for a given total energy E.

The scattering amplitude for a given angle of incidence γ is obtained in a manner identical to that for a spherical scattering problem[21]

$$f^{k_{\bar{j}}}(\gamma \mid \theta) = \frac{i}{2k_{\bar{j}}}\sum_l (2l+1)\left\{1 - e^{2i\eta_l(\gamma)}\right\}P_l(\cos\theta) \qquad (7)$$

It can be shown that the rotational state-to-state differential cross-section is given in this approximation by[13]

$$\sigma(j' \leftarrow j \mid \theta) = \frac{k_{\bar{j}}^2}{(2j+1)k_{\bar{j}}^2}\sum_{m_j}|<j'm_j|f^{k_{\bar{j}}}(\gamma \mid \theta)|jm_j>_{\text{BF}}|^2 \qquad (8)$$

Note that this result is independent of the choice of l. (The matrix elements of $f(\gamma \mid \theta)$ are evaluated in the spherical harmonics of the body-fixed coordinates - BF).

The implication of the IOSA is that the approach angle γ does not change appreciably during the collision.[13,15,17] This can be related to two operationally more tangible conditions which ensure the validity of the IOSA: a) the relative collision translational energy is large compared to the spacing between rotational energy levels - i.e., the collision is not strongly influenced by the rotation b) rotational transitions occur at small impact parameters, i.e., at low values of orbital angular momentum. The first condition is easily met by the systems considered in this paper where the relative collisional energy of 65 meV is much greater than the largest spacing of 6 meV between consecutive open rotational states. The second condition is met by systems which have a small well depth relative to the collisional energy, implying that the incident atom is mainly influenced by the repulsive wall of the interaction potential which occurs at short distances r. The well depths for the collisions studied herein and other helium-molecule systems are less than 8 meV.[3-5,8-10,28-36]

The total differential cross-section, from a state j to all accessible states j', can be obtained by summing equation (8) over all j'. If $\bar{j}$ is chosen to be equal to j then this sum yields

$$\sigma(\theta) = 1/2 \int_0^\pi |f(\gamma \mid \theta)|^2 \sin \gamma \, d\gamma \qquad (9)$$

This expression is independent of the initial rotational state j, and hence represents the total differential cross-section for all initial states.

3. POTENTIAL MODELS

In order to insure a reasonable uniqueness and reliability of the potential derived from experimental data, we have employed several parametrized models for the He-molecule potential. These include highly flexible central field potentials as well as anisotropic potentials. The spherical models were chosen to demonstrate their inappropriateness as models of the interaction of He with the molecules considered in this work. The anisotropic potential models were chosen for their simplicity, flexibility and physical reasonability. Simplicity is an important criterion, since an excess of parameters in a least-squares fitting procedure can lead to an over-determined system with high correlations between parameters, yielding a final potential that is not unique.

3.1. Anisotropy Parameterization

We consider three forms for expressing the anisotropy of a potential.

1) Legendre expansion representation

A reasonably obvious form for expressing the angular dependence of an atom-rigid linear molecule potential is a Legendre polynomial expansion

$$V(r, \gamma) = \sum_{n=0}^{\infty} V_n(r) P_n(\cos \gamma) \qquad (10)$$

The $V_n(r)$'s are spherical-type potentials with several parameters each. If the expansion proceeds beyond $n = 2$ the number of parameters becomes too large to insure the uniqueness and independence of each parameter.

2) Multi-center representation

An alternate means for constructing an atom-molecule anisotropic potential is to express it as a sum of pairwise isotropic atom-atom potentials:[4]

$$V(r, \gamma) = \sum_{i=1}^{n} V_i(r_i) \qquad (11)$$

where

$$r_i = [r^2 + z_i^2 - 2rz_i \cos \gamma]^{1/2} \qquad (12)$$

and z_i is the distance from the center-of-mass of the molecule to the center of atom i; it may be positive or negative.

3) Angular-dependent parameter representation

A third way of specifying anisotropy, is by giving a γ dependence to the parameters of an otherwise spherical potential,[14]

$$V(r, \gamma) = V\left[r, \epsilon(\gamma), r_m(\gamma), \beta(\gamma)\right] \tag{13}$$

where ϵ is the well depth, r_m is the well minimum position, and β is a shape parameter which depends on the parameterization of V. Some parameterizations may have more than one shape parameter, all of which may have angular dependence. The angular dependence of any parameter A (such as ϵ, r_m, β) may be expressed in terms of Legendre polynomials[14]

$$A(\gamma) = \sum_{n=0}^{\infty} A^{(n)} P_n(\cos \gamma) \tag{14}$$

In general, for symmetric molecules, the expansion is carried only to two non-vanishing terms $n = 0$ and $n = 2$, because an excess of parameters may not yield a unique potential via the least squares procedure as the data are not sensitive enough for their determination. Another parameterization for $A(\gamma)$ (also for symmetric molecules), especially useful for r_m, is an elliptical form[5]

$$r_m(\gamma) = r_{m\perp} \left[\frac{1 + q \sin^2 \gamma}{1 + q}\right]^{1/2} \tag{15}$$

where

$$q \equiv \left[\frac{r_{m\perp}^2}{r_{m\parallel}^2} - 1\right] \tag{16}$$

while $r_{m\perp}$ is r_m for the $\gamma = \frac{\pi}{2}$ configuration and $r_{m\parallel}$ is r_m for $\gamma = 0$ or π.

Since each parameter has been given an angular dependence, the angular dependence of the potential can be complicated such that its expansion contains Legendre polynomials to large orders. We then expect that the angular-dependent parameter representation would be the most flexible potential form.[4,5]

3.2. Shape Parameterization

The shape of the anisotropic potential in any of the three representations given above can be expressed in terms of well known spherical-like potentials. The potentials we consider are:

1) Lennard-Jones (LJ)[24a]

$$V(r) = \epsilon\left[\left(\frac{r_m}{r}\right)^{12} - 2\left(\frac{r_m}{r}\right)^{6}\right] \tag{17}$$

This potential is quite simple, but not very flexible. The width of the well is fixed and is approximately fitted by a $\beta = 6.3$ Morse potential of equal depth and well position.

2) Morse [41]

$$V(r) = \epsilon\left[e^{2\beta(1-r/r_m)} - 2e^{\beta(1-r/r_m)}\right] \tag{18}$$

The shape parameter β gives the Morse much greater flexibility in

specifying the well width than the LJ. It determines not only the well width but also the long range van der Waals' part of the potential to which scattering experiments do not have much sensitivity. The van der Waals dispersion terms are quite amenable to theoretical calculation, and inculsion of them in a potential is appropriate for improving the Morse potential.

3) Lennard-Jones-Dispersion (LJ8)

The Lennard-Jones potential may be modified to include the C_6 dispersion term. This gives some flexibility to the well width but it is subject to the control of the dispersion term [4]

$$V(r) = \frac{2\epsilon r_m^{12} - C_6 r_m{}^6/2}{r^8} - \frac{C_6}{r^6} - \frac{3\epsilon r_m{}^8 - 3C_6 r_m{}^2/2}{r^8} \qquad (19)$$

4) Morse-Spline-van der Waals (MSV)

A better parameterization is one in which the dispersion and well width are more independent. At short distances we use the Morse potential, while at long distances we use the van der Waals dispersion potential. The two are joined with a cubic spline.[28,36,37]

$$V(r) = \epsilon \left[e^{2\beta(1-r/r_m)} - 2e^{\beta(1-r/r_m)} \right] \qquad (20a)$$

$$\text{for} \quad r \leq r_{MS}$$

$$V(r) = \left[S_1 (r_{SV} - r)^2 + S_3 \right] (r_{SV} - r)$$

$$+ \quad [S_2(r - r_{MS})^2 + S_4](r - r_{MS}) \qquad (20b)$$

$$\text{for} \quad r_{MS} < r < r_{SV}$$

$$V(r) = -\frac{C_6}{r^6} - \frac{C_8}{r^8} \qquad (20c)$$

$$\text{for} \quad r \geq r_{SV}$$

where $r_{MS} = r_m(1 + \ln 2/\beta)$ is the inflection point of the Morse function. The spline coefficients S_1, S_2, S_3 and S_4 are determined by continuity conditions imposed on the potential and its derivative at r_{MS} and r_{SV}. The Spline-van der Waals junction is maintained at $r_{SV}/r_m = 1.6$.[27-30]

5) Morse-Morse-Spline-van der Waals (MMSV)

The MSV potential still has some inflexibility since the well width parameter β also affects the repulsive wall. This interdependence can be removed by using a different Morse function for the repulsive region to yield [27,36,37]

$$V(r) = \frac{\epsilon}{\omega} \left\{ e^{2(\beta' - r\beta\omega/r_m)} - 2e^{(\beta' - r\beta\omega/r_m)} \right\} \qquad (21a)$$

$$\text{for} \quad r/r_m < 1 - \ln 2/\beta$$

$$V(r) = V_{\text{MSV}}(r) \qquad (21b)$$

$$\text{for} \quad r/r_m \geq 1 - \ln 2/\beta$$

$$\text{where} \quad \omega = \frac{\beta' - \ln 2}{\beta - \ln 2}$$

The constant ω is used to impose a smooth transition between the two Morse functions.

6) Simons-Parr-Finlan-Dunham (SPFD)

Another very flexible potential is the SPFD (Simons-Parr-Finlan-Dunham) potential which includes a van der Waals term. It is esentially a polynomial in r^{-1} and is given by [38-40]

$$V(r) = \epsilon \left\{ b_0 \lambda^2 \left(1 + \sum_{i=1}^{N} b_i \lambda^i \right) - 1 \right\} \qquad (22a)$$

$$\text{for} \quad r \leq r_f$$

$$V(r) = -\frac{C_6}{r^6} - \frac{C_8}{r^8} \qquad (22b)$$

$$\text{for} \quad r > r_f$$

$$\text{where} \quad \lambda = 1 - \frac{r_m}{r}$$

The two highest order shape parameters b_{N-1} and b_N are fixed by smoothness conditions in joining to the van der Waals point at r_f, which is made equal to $1.6 r_m$. In general N is 2 or 3, giving one or two shape parameters, b_0 and b_1. The SPFD potential is not well behaved for $r < 0.6 r_m$, and oscillates in that region. This problem can be eliminated by replacing it by an exponential of the form[24] $V(r) = A e^{-br}$ for $r < r_W$, where A and b are fixed by smoothness at r_W. The choice for r_W is usually $0.7 r_m$, and has little effect on the final results since experimental data are not sensitive to this highly repulsive region.

7) Hartree-Fock Dispersion (HFD) [32,33]

$$V(r) = \epsilon e^{\beta(1-r/r_m)} - \frac{C_6}{r^6} - \frac{C_8}{r^8} e^{-(\alpha r_m/r - 1)^2} \qquad (23a)$$

$$\text{for} \quad r < \alpha r_m$$

$$V(r) = \epsilon e^{\beta(1-r/r_m)} - \frac{C_6}{r^6} - \frac{C_8}{r^8} \qquad (23b)$$

$$\text{for} \quad r \geq \alpha r_m .$$

Only one of ϵ, β, or α can be specified for a given potential: the other two are fixed by the requirement that at r_m the potential be equal to $-\epsilon$ and its derivative vanish. For the purposes of this study we will either vary α or ϵ, in addition to r_m.

The potentials with the correct long range behavior are the MSV, MMSV, SPFD, and HFD. We would then expect that they should give the most accurate representation of the potential. The long range dispersion terms constrain the potential in regions where the sensitivity of the experiment is low, while giving it the necessary flexibility in regions of greater sensitivity. The van der Waals dispersion term coefficients C_6 and C_8 for He + CO_2 have been accurately calculated by Pack.[26] Both coefficients have significant anisotropy which can represented by a second order Legendre expansion

$$C_n(\gamma) = C_n^{(0)} + C_n^{(2)} P_2(\cos \gamma)$$

where $n = 6$ or 8

The differential cross-section is most sensitive to the spherical average of the C_6 coefficient $C_6^{(0)}$.[6] The sensitivitites for the anisotropy of C_6 ($C_6^{(2)}$) and for the C_8 coefficient with its anisotropy ($C_8^{(0)}$ and $C_8^{(2)}$) are at least a factor of 50 smaller than for than for $C_6^{(0)}$.[6] In the fitting procedure described in section 5 the dispersion coefficients are assumed to be known, i.e., are not treated as fitting parameters. Therefore for the purposes of this paper, $C_6^{(0)}$ must be known with the greatest accuracy, while the other coefficients are less significant and need not be known as accurately. This is fortunate since at present calculations for the dispersion terms for He + CS_2 and He + OCS have not been published, and hence they must be approximately derived from those for He + CO_2 and the polarizibilities $\alpha(X)$ [24ab,25,26], where $X = CO_2$, CS_2, and OCS. For $C_6^{(0)}$ a quite reliable relation is

$$C_6^{(0)}(X) = C_6^{(0)}(CO_2)\frac{\alpha(X)}{\alpha(CO_2)}$$

The expressions for the other coefficients are more complicated and are less accurate.

The disperison term for the multi-center potentials is splined into each of the three centers i using

$$V_i(r_i)_{VDW} = \frac{-1}{3}\left(\frac{C_6(\gamma)}{r^6} + \frac{C_8(\gamma)}{r^8}\right)$$

where r_i is the distance from the center i to a point in space with the coordinates (r, γ), and is given by equation (12). As a result, in

the dispersion region the $V_i(r_i)$ contain γ-dependent parameters. This means that physically the potential is no longer a sum of three spherically symmetric potentials having different centers, over the full range of r. This procedure is adopted because of numerical convenience, since the resulting fits are not strongly affected by it.

For the multi-center potential we use the spectroscopic bond distances[22] to locate the origins of each of the central potentials from the center-of-mass of the molecule; the z_i in equation (12) is not treated as an adjustable parameter in the least-squares parameter fitting procedure. This provides a reasonable constraint on the potential, such that the least-squares algorithm produces a physically acceptable potential.

4. EXPERIMENTAL

The crossed molecular beam apparatus used in these experiments is depicted in Figure 1. The basic constituents are a doubly differentially pumped supersonic primary (probe) beam source, an effusive secondary (target) beam source, and a doubly differentially pumped mass spectrometer. The beams cross at right angles, while the mass spectrometer detects the scattered signal at angles in the plane or out of the plane of the beams. This section will attempt to present a reasonably thorough description of the apparatus, with emphasis on improvements made since previous descriptions.[28,42-45] The primary and secondary beam sources along with the movable detector are mounted on a 130 cm diameter base (Fig. 1). The base is covered by a stainless steel bell jar, which may be raised to permit access to internal components. The 1250 liter vacuum chamber is pumped by four liquid nitrogen (l -N_2) trapped 6 inch oil diffusion pumps and 2 l -N_2 and refrigeration-trapped mercury pumps with a total pumping speed of 1850 l/sec. Pressures as low as 2×10^{-8} torr can be achieved with no load on the system.

The primary beam (PB) is produced via a supersonic expansion through a 70 micron diameter nozzle (Nz) consisting of platinum or molybdenum electron microscope aperture. The central portion of the resultant beam is collected by a 0.64 mm diameter conical brass skimmer

(Sk) at a distance of 11 mm from the nozzle. The edge of the skimmer aperture is sharp and has an inner surface half-angle of 28 degrees and outer surface angle of 34 degrees. The skimmer-nozzle distance is remotely variable, and was optimized at 11 mm for strongest scattered signal and smallest background. The gas that does not pass through the skimmer is pumped by a 6 inch oil diffusion pump (DP1) with a 250 l/sec pumping speed for helium (400 l/sec for air). The pressure in this chamber is 2×10^{-3} torr[48] with a 1300 torr stagnation pressure of He behind the nozzle. This pressure is limited by the pumping speed of DP1, and not by dimer formation. After passing the skimmer the beam enters a second differentially pumped chamber. This is pumped by a 100 l/sec (for helium) mercury diffusion pump. Under the above conditions the pressure in this chamber is 4×10^{-5} torr.[48] The chamber contains a chopper (Ch) to modulate the beam at 160 Hz for lock-in signal detection. Also enclosed in the chamber is a slotted-disk velocity selector (VS)[47] used for measuring the beam velocity distribution; it is moved out of the beam path during scattering experiments. The beam emerges into the scattering chamber through a collimating aperture (1.52 mm diamter) 79 mm from the scattering center.

The velocity distribution data obtained with the VS consist of signal from the mass-spectrometer as a function of the selector rotational frequency to which the velocity is directly proportional. These (after correction for the fact that a mass spectrometer is a number density

detector rather than a flux detector) are fitted via least-squares to the function [46]

$$f(v) = cv^3 e^{-\frac{m}{2kT_s}(v-v_s)^2} \tag{24}$$

where m is the mass of the beam molecule. In this expression there are two variable parameters T_s and v_s. The constant c is determined be requiring $f(v)$ to be normalized over v. The gas stream temperature T_s and stream velocity v_s are related to the effective nozzle stagnation temperature T_0, a Mach number M, and the heat capacity ratio $\gamma = C_p/C_v$ [46]

$$T_s = \frac{T_0}{1 + \frac{\gamma-1}{2}M^2} \tag{25}$$

and

$$v_s^2 = \frac{kT_s \gamma M^2}{m} \tag{26}$$

The secondary beam (SB) enters the scattering center directly from a capillary array (CA), located 6 mm before it. The array consists of 2 micron diameter glass tubules 610 microns long fused into a single disk, with a 50% open area to gas flow.[49] The array is held in place by an o-ring which vacuum seals and exposes a 1.6 mm diameter region of the disk. This assembly is mounted on a block which may be tilted up via a remotely activated pneumatic bellows so as to uncross the beams. In the

crossed position the bellow presses the source assembly firmly against a fixed flat surface to ensure precise alignment.

The secondary beam conditions are chosen to maximize the intensity, mimimize the angular spread and eliminate secondary collisions of the primary beam with secondary beam molecules. The first criterion requires the greatest stagnation pressure behind the capillary array, while the other two require a lower stagnation pressure. Also, a lower stagnation pressure reduces the formation of van der Waals dimers. An optimum pressure occurs in the range of 3 to 5 torr. This results in a scattering chamber pressure of approximately 3×10^{-7} torr, for condensible (on l-N_2 cooled surfaces) gases such as CO_2, CS2, and OCS. These pass through the capillary array with little expansion cooling as their low Mach number ($M \approx 1$) indicates . This was determined by measuring the velocity distribution of the secondary beam, with the capillary array placed in the position of the primary beam nozzle.

The optimal operating condition of the beam sources are summarized in Table I. The angular distributions were measured using the mass spectrometer, and characterized approximately by the shape of a cosine squared distribution.

Primary beam atoms that are scattered by the secondary beam, pass through a detector entrance aperture of 1.52 mm diameter, 8.0 cm from the scattering region. This aperture is equipped with a gate valve (GV) which separates the scattering (main) chamber from a buffer

chamber. A second aperture, also 1.52 mm in diameter, 4.5 cm away from the first one, isolates this buffer chamber from the main part of the mass spectrometer (MS) vacuum chamber. The center of the mass spectrometer ionization region is located 2.4 cm from that second aperture. The penumbral cone determined by these apertures is 4 degrees and spans a 5.8 mm diameter at the scattering region. The umbral cone angle is 0.67 degrees with a 1.6 mm diameter span at the scattering center. This ensures that the entire scattering region is in full view of the mass spectrometer. The angular resolution, as determined from the angles subtended by the umbral and penumbral projections at the ionization region, is in the range 0.67 to 1.41 degrees. However, the overall apparatus angular resolution $(\Delta\theta_{lab})$ is a composite of this and the size of the scattering volume. The value of this parameter is crucial; a correct potential cannot be obtained from the data without it. For the beam conditions under consideration, the overall angular apparatus resolution was determined to be 1.5 degrees by a careful analysis of He + Ar scattering data. The potential parameters for an MMSV and a SPFD potential were fitted along with $\Delta\theta_{lab}$ to the He + Ar scattering data obtained on our apparatus. The potential parameter values agreed with those obtained at other laboratories.[33-36] The same value of $\Delta\theta_{lab}$ was obtained by making it the only variable parameter and fitting it to our data with the SPFD potential parameters fixed at values obtained at those laboratories. This is a new value of the resolution parameter and

superseds the value of about 1.9 deg. which we previously reported.[28-30] The main reason for this change is that the previous value of $\Delta\theta_{lab}$ was obtained by fitting the data to a very rigid Lennard-Jones potential.[24] We will discuss the implications of this change in $\Delta\theta_{lab}$ on the He + CO_2 potential in section 6.

The detector buffer chamber is pumped by a 5 l/sec ion pump and the mass spectrometer chamber is pumped by a 25 l/sec ion pump. During experiments a liquid helium cryopump (CP) carries most of the pumping load of the main MS chamber. The pump is surrounded by a l-N_2-cooled jacket. The ionizer (I) directly below the cryo-pump is cooled with l-N_2 to reduce radiation heating of the pump. This shielding allows the pump to operate for over four hours with an initial fill of one liter of liquid He. The cryo-pump has an estimated pumping speed of 300 to 400 l/sec at pressures 7.0 to 15×10^{-10} torr. A bake-out is necessary in order to maintain these pressures.

The mass-spectrometer ionizer is a high-efficiency electron-impact device, [50] operated at 15 mA to 25 mA emission current. The ions produced in it are focused into a quadupole mass filter and after mass selection are detected by a Channeltron[51] electron multiplier. The Channeltron may be operated in a pulse counting (digital) mode or current measuring (analog) mode. In the pulse counting mode the Channeltron pulses are passed through a pulse amplifier-discriminator[52] and proceed to a gated phase sensitive pulse counter.[53] The counter

is controlled and read by a PDP11/03 computer.[54] The gating signal originates at a photodiode light sensor on the primary beam chopper (Ch); it is amplified, shaped, phase shifted and then serves as the gate for the counter. The computer reads the counter at twice the 160 Hz chopper frequency, i.e., when the chopper passes the primary beam and when it blocks the beam. The computer then subtracts the "blocked" signal from the "unblocked" to obtain a phase sensitive digital lock-in reading. Due to the finite length of the read cycle, followed by a counter clear pulse, the counter has a reduced duty time of 95%. This, however, is not a problem since we further gate our signal to an 85% duty time so as not to count pulses while the primary beam intensity rises and falls as the chopper teeth edges cross the beam path. The duration of the gate is maintained by a quartz oscillator to ensure precision and reproducibility of each gate pulse.

In the analog detection mode the Channeltron current is measured by a home-built electrometer with a sensitivity of about 50 picoamperes.[56] The electrometer output goes into a PAR HR-8 phase sensitive lock-in amplifier,[55] which also makes use of the chopper photodiode. The lock-in output is read by an analog-to-digital converter of the PDP-11/03.

As stated above, the mass-spectrometer has two angular degrees of freedom. It may by positioned from 12 degrees below the plane of the beams to 40 degrees above that plane. Motion in the plane of the beams ranges from -20 to 110 degrees, where the positive angular direction is

from the primary beam to along the secondary beam, with the primary beam axis serving as the orgin. The positioning reproducibility in both directions is better than ±0.05 degrees.

Accurate and precise alignment is a necessary prerequisite for good scattering intensity measurements. The principal axis of alignment consists of: the primary beam nozzle, the skimmer, the exit aperture, a 0.05 mm alignment pin placed at the scattering center, the two detection apertures and cross-hairs at the back of the mass spectrometer housing. All of these are made to lie along a line to the specified tolerances of 0.05 mm with the aid of a precision surveyor's telescope. After this alignment is completed the secondary beam source is aligned with the scattering center pin, where the latter is rotated to 90 degrees from the primary beam axis.

The in- and out-of-plane angles are measured wth the help of two sychro position sensors.[57] The accuracy of these sensors is determined by measuring the distance along a rotation arc at a large radius. The agreement of the sensor readings with these measurements is within 0.05 degrees. The accuracy with which the detector tracks the scattering center is measured as the distance from the scattering center pin to the front aperture. The maximum variation is 0.1 mm over the full range of both angular degrees of freedom; this corresponds to a maximum deviation of 0.1 degrees in the tracking of the scattering center, which occurs at large (c.a. 40 deg.) out-of-plane angles.

Data are collected in the range of 2 to 20 degrees (out of the plane of the beams) at intervals of 0.25 degree for up to 10 degrees, every 0.5 degree up to 15 degrees and every degree thereafter. We use the digital pulse counting mode for these experiments in preference over the analog mode since it is inherently simpler and requires shorter measurement times at larger angles for equivalent data quality. The modulated signal is accumulated at a given angle with the beams crossed, thereafter the secondary beam source is tilted up to uncross the beams and the modulated component of the background signal is measured and then subtracted from the crossed signal. A reference signal at 4.5 degrees is repetitively measured after every three to five successive angles to provide a normalization and to compensate for any drift in sensitivity. The entire angular scattering intensity distribution is measured six times, giving a total accumulation time of 5 minutes per angle at low angles to 2 hours at the largest angles. These six measurements are averaged; the standard deviation at each angle defines the error bars for use in the weighted least squares procedure.

5. DATA ANALYSIS

The process of extracting a potential from differential cross-section data begins by proposing a good model of the potential with a reasonable initial guess of the appropriate parameters. This model is the basis of a computer simulation of the data. A least-squares fitting procedure is employed to iteratively adjust the potential parameters until the best possible match is made between experimental and modeled data.

The simulation of data can be divided into two parts a) calculation of the cross-section in the center-of-mass frame by means outlined in the theory section for a range of relative collision energies and scattering angles; b) transformation of these results to a laboratory reference frame and averaging over the velocity and angular distributions of the beams as well as the effective resolution of the detector.

Rotationally inelastic collisions occur for systems with anisotropic potentials. In general, this inelasticity should be considered in transforming the total differential cross sections to the laboratory frame. However, since the changes in rotational quantum number are small[6] and the collision energy is much greater than the rotational spacings[6] for the systems under consideration, it is possible to transform the total differential cross sections as if they were purely elastic without any loss of accuracy.[15]

The DCS calculation is done as follows:

(1) The phase shifts are calculated at a set of relative collision velocities w_n and approach angles γ (see equation 5). The w_n are picked to represent the full range of collision velocities as determined from the operating conditions of the beams. The approach angles are chosen to correspond to Gauss-Legendre integration points. The phase shifts are calculated to a specified precision by the JWKB method[58,20b] or for the low partial waves in some cases, by Numerov integration[59] of the Schrödinger equation (eq. 4).

It was found that a 12-point Gauss-Legendre quadrature over γ is virtually identical to a 48-point quadrature for the conditions of our calculation. The inversion symmetry of CO_2 and CS_2 further reduces the number of points by a half, requiring the phase shift calculation at only six values of γ.

(2) The scattering amplitudes are calculated using equation (7) for a set of center-of-mass scattering angles θ_m. The partial wave summation is truncated when several successive phase shifts become less than a specified value (usually 0.001 radian). This requires phase shifts to be calculated up to a maximum l which lies in the range 150 to 350 depending on the target molecule considered.

(3) The square of the scattering amplitude is integrated over the approach angle γ, using equation (9). This yields center-of-mass differential cross-sections $\sigma(w_n, \theta_m)$ at relative collision velocities

w_n and scattering angles θ_m.

The transformation and averaging procedure is done as follows:

(1) A set of Gaussian integration points is obtained for the distribution of beam velocities based on the characteristics summarized in Table I. The range of integration is specified by cut-off probabilities of the velocity distributions; the integration points are designated v_{pi} and v_{sj} for the primary and secondary beams, respectively.

(2) A set of Gaussian integration points are obtained for the spread of beam interaction angles, designated at ς_k. The ς_k are determined from a convolution of the individual beam spreads as given in Table I.

(3) Cross sections $\sigma(w_{ijk}, \theta_m)$ are interpolated from $\sigma(w_n, \theta_m)$ where the w_{ijk} are the relative collision velocities corresponding to $\{v_{pi}, v_{sj}, \varsigma_k\}$.

(4) The center-of-mass cross-sections $\sigma(w_{ijk}, \theta_m)$ are transformed to the laboratory reference frame by multiplying by the Jacobian factor[62] $J_{lab}^{ijk}(\theta_m)$ (appropriate for a number density detector)[28] to yield $I(\theta_{lab}^{ijk})_{ijk}$, a laboratory scattering intensity, where θ_{lab}^{ijk} depends on θ_m. By interpolation the $I(\theta_{lab}^{ijk})_{ijk}$ are converted to $I(\theta_{lab}^c)_{ijk}$, where the θ_{lab}^c are a set of θ_{lab} angles used subsequently in a quadrature.

(5) A Gaussian quadrature (summation of $I(\theta_{lab}^c)_{ijk}$) over $v_p, v_t,$ and ς (i, j, k) yields $I(\theta_{lab}^c)$.

(6) At each angle θ_{lab}^c, the $I(\theta_{lab}^c)$ are averaged over the effective angular width of the detector. We say "effective" since this resolution represents not only the angular width of the detector but also contributions from the finite scattering volume. For these experiments the effective angular resolution angle is 1.5 degrees FWHM with an assumed cosine squared distribution in θ_{lab}. The scattering intensities averaged over the effective angular range of the detector are interpolated to give $I(\theta_{lab}^c)$ at the experimental angles θ_{lab}^c.

The least-squares procedure for the potential parameter determination is done by minimizing the quantity[60]

$$\chi^2 = \sum_{i=1}^{n} w_i [F_i - \alpha I_i(p_1, ..., p_k)]^2 \qquad (27)$$

with respect to the parameters $p_1, ..., p_k$ for laboratory angles $\theta_{lab\ i}$ ($i = 1, ..., n$). The F_i are the measured scattering intensities; the I_i are the calculated intensities based on the potential parameters which are being optimized; and the w_i are weighting factors which are given in terms of the experimental error bars (or standard deviations) ΔF_i

$$w_i = (\Delta F_i)^{-2} \qquad (28)$$

Since the experimentally measured intensities F_i are arbitrarily normalized, the calculated intensities I_i must be scaled to them. The scaling factor α is obtained in closed form by minimizing χ^2 with respect to α.

Following Keil and Kuppermann[27] we use a "goodness-of-fit" statistical index

$$G \equiv (\Delta\alpha/\alpha)_{0.95} = \frac{1}{\alpha}t(n-k)_{1-0.05}\left[\frac{\chi^2}{(n-k)\sum_{i=1}^{n}w_i I_i^2}\right] \qquad (29)$$

where $t(n-k)_{1-y}$ is Student's t-distribution for a confidence level y of the scaling factor α, with n data and k adjusted parameters.

The parameters are optimized according to a nonlinear weighted least-squares regression algorithm introduced by Marquardt.[61] The process is iterative, requiring five to fifteen cycles before convergence is attained, depending upon an initial guess for the parameters.

6. RESULTS AND DISCUSSION

The scattering intensities of He colliding with CO_2, CS_2, and OCS are plotted in Figures 2, 3, and 4 respectively, as a function of the laboratory scattering angle. The data have been multiplied by the sine of the laboratory scattering angle θ so as to emphasize quantal oscillations and display their relative contribution to the integral cross section.[1] While prominent oscillations have been observed for scattering of He with various diatomics [9,10,29] and highly symmetric polyatoms such as CH_4 and SF_6,[8,30] our current data by comparison show a substantial dampening of these oscillations, as has been previously observed for He + CO_2 and other highly anisotropic systems.[3,4] The rainbow scattering angle structure is completely obscured as is the case for systems with spherical potentials. [6,33]

The questions that form immediately are: what features of the potential account for the oscillation dampening? How unique are these features? And, how well can these be extracted from the data?

As we mentioned in the introduction, these questions have been addressed previously. However, we claim that the He + CO_2 potential presented by Keil et al.[5], Parker et al.[4], and Keil and Parker[3] is inaccurate for the fact that all three of these papers used the value of angular resolution of the detector of Keil et al.[28] which we showed to be incorrectly determined (see Section 4.). Although many of the qualitative

conclusions reached by Keil and Parker[3,4,5] will remain the same, the actual potential that we present will naturally be different. The angular resolution of the detector determines how the detection system dampens the observed oscillations. Therefore to correctly account for the actual quantal oscillation dampening it is necessary to distinguish it from the intrumental dampening. Since Keil and Parker used an angular resolution that was too large, they underestimated the extent of the quantal dampening. Keil et $al.$[28] made a similar mistake for He + Ar where they obtained a well that was too shallow and also too wide; Aziz et $al.$[35] have pointed out the possible source of this error and reported the correct He + Ar potential. There are many factors that contribute to the dampening of the oscillation; the r_m anisotropy is the most pronounced. The shape of the well, i.e. the well depth and particularly well width contribute significantly to the shape of the oscillations.[6] In fact the width parameter is very important one; it can dampen the oscillation more significantly than the well depth.[6] Low angle He + CO_2 DCS oscillations ($\theta < 12°$) are dampened by a decrease in well width, while higher angle oscillations ($\theta > 12°$) are dampened by an increase.[6] An increase in well depth dampens oscillations only in the range $5° < \theta \leq 12°$; outside this range the oscillations increase with increasing well depth.[6] The angular range for the He + CO_2 and He + Ar experiments is 2 to 20 degrees. For most of this range the an increase of well width can be compensated for by an decrease in the depth; very roughly we can say that the well

capacity (depth times width) remains fixed. Only the first and last oscillations (or dampened remenants) in this range do not follow this "fixed well capacity rule." From this one may deduce as to why the Keil *et al.* He + Ar well is too shallow and too wide. In fact the widths of the Keil and Parker[3,4,5] He + CO_2 potentials are consitently greater than those reported for other He scattering system[8-10,33-35] (except those reported by Keil *et al.*[28-30]). On this basis we feel that the questions mentioned in the previous paragraph must be consided again, with careful accounting of all DCS oscillation dampening factors.

We first may address the uniqueness question by suggesting that a spherical potential may be constructed with appropriate values for its parameters, that can model our data without resorting to anisotropic potentials. Referring again to Figures 3 through 4, we note that the calculated scattering intensity curves for the best spherical fit have significantly more oscillatory structure than our data, for all three systems. The parameters for these spherical fits are given in Table II. We have used the very flexible SPFD and MMSV[27] forms (equations 21 and 22). The goodness-of-fit statistic G (eq. 29) and the relative χ^2 (eq. 27) reflect a rather poor fit for CS_2 and OCS and at best a marginal fit for CO_2. Even though previous experience dictates that for these experiments G in the range of 1.8 to 2.0% gives acceptable fits (G less than 1.3% gives very good fits),[4,27-30] we should not *a priori* give full credence to the results. The well depth ϵ, is very large, much

deeper than reported for helium collisions with various diatomics, such as CO,[29] which were satisfactorily modeled with spherical potentials. It is also much deeper than the spherical average of the well depth for our anisotropic fits to He + CO_2, which as shown below, is in the range of 3.8 to 4.3 meV, depending on the potential model used. It is also much deeper than the well depth of the spherical average of these anisotropic potentials, which is about 2.8 meV. Presumably if these experiments and data reduction methods are not capable of detecting potential anisotropy, they should then sample the spherical average of the actual potential and not the spherical limit potential (the potential constructed from the spherical averages of the angle-dependent parameters of the actual potential). The same can be said for the well width and repulsive steepness parameters, which yield a very narrow well with a steep repulsive part, which is inconsistent with previous empirical isotropic[33,34] and anisotropic potentials[3,8-10] as well as our anisotropic fits. Clearly therefore the spherically symmetric potential model does not satisfactorily represent the interaction of He with CO_2, CS_2 and OCS; and hence we must include anisotropy into the potential models. This is consistent with the conclusions reached previously for similar systems.[4,5]

In section 3 we have proposed several means of including anisotropy and several means of characterizing the radial shape of the anisotropic potential. Since the various combinations would produce well over a

hundred different potential models, it would not be practical, or very informative to present an exhaustive survey. We will concentrate only on several reasonable choices for He + CO_2. The best of these will be used to analyze He + CS_2 and He + OCS.

6.1. Potentials for He + CO_2

In Tables III and IV we present the best fit results for a variety of multi-center and parameter expansion potentials for He + CO_2. Conspicuously absent are the results for Legendre expansion potential fits of equation (10). We repeatedly tried different types of fits to the $V_n(r)$ with terms up to second order, but with minimal success.[4,8] The major problem associated with these potentials is multiple minima along a radius of constant γ, in the repulsive region, and in some cases an attractive region at small r for γ close to the molecular axis. Both of these characteristics tended to develop in the process of least squares adjustment of potential parameters, and are physically unacceptable. Also, the parameters tend to be highly correlated, yielding a potential of questionable uniqueness. In addition, if we examine equation (10) we see no reason for the $V_n(r)$ to have a general shape of the spherical potentials in section 3.2 . The shape of $V(r, \gamma)$ at a fixed γ should have a form given by those potentials, but there is no a priori basis for selecting $V_n(r)$ to have one of those forms. However, is is reasonable that the $n = 0$ term should be shaped that way since it is the spherical average

of the potential.[1,9,10] We have expanded all our resultant potentials (of Tables III and IV) to $n = 6$ order, and found that only the $n = 0$ terms had a repulsive region at small r, a well at 3 to 4 Ångstroms and weak monotonically decreasing attractive region at large r, as required physically. In many cases the $n = 2$ terms could also be described by this behavior, and in certain cases the $V_2(r)$ were the negatives of a typical van der Waals potential. But no $n = 4$ (or greater) term could be described as a van der Waals type, and most of the potentials in Tables III and IV have significant $V_6(r)$ terms. We therefore conclude that the Legendre expansion potentials are unsuitable as good models for He + CO_2 and similar systems using equations (17) thru (23) for the form of the r-dependent coefficients, and we forgo them in further consideration and discussion.

The multicenter potentials in Table III all give very good fits to the data, as is evident by the low values of G or χ^2. Varying six parameters in place of five produces somewhat better fits if we compare MSV-m1 to MSV-m2 and SPFD-m2 to SPFD-m3. However, an even better improvement in fit is acheived if the six parameters are chosen differently as in MMSV-m and SPFD-m1. The MMSV-m emphasizes and improves the shape of the repulsive region by separating it from the parameters that define the shape of the well. The function of the b_1 shape parameter in the SPFD is not as region specific, and we have a better fit in the SPFD-m1 where the b_0's for each of the centers are different and the

b_1's are fixed. The Morse-m yielded the best fit with six parameters; but since it does not include the long range van der Waals forces and differs significantly from the other multi-center potentials it has to be taken cautiously. The validity of the multi-center and parameter expansion potentials will be discussed later.

The angular-dependent parameter potentials of Table IV give a range of fits to the data; most are very good. Especially noteworthy are the four parameter LJ8-e and the three parameter HFD-e. In the case of the HFD we were unable to vary additional parameters, such as the anisotropy of α or the values of $\epsilon^{(0)}$ and $\epsilon^{(2)}$, since this variation yielded a potential with unacceptable behavior at certain angles. The LJ-e gives a good fit despite its lack of long range dispersion terms, but the results are deceptive; the anisotropy of the well depth is unrealistically extreme, producing well depth ranging from 0.04 $(\gamma = 0)$ to 5.24 meV $(\gamma = \pi/2)$. The other potentials have values of $r_m(\gamma)$ close to one another, and while the agreement in well depths is not as good, it is still quite reasonable.

The angular-dependent parameter potentials give a particularly straightforward visualization of the anisotropy, especially the elliptical parameterization of $r_m(\gamma)$ - much better than the multi-center potentials, which nonetheless fully account for the anisotropy (as we shall see later). Yet one may wonder how real these anisotropies are? Even though, they do give much better fits to the data than the spherical potentials. This improvement in fit might, for example, be due to a greater number of

parameters in the region of sensitivity of these experiments. The results of Table V will clear up some of these questions, as shown below.

The best fit potential of Table IV is SPFD-e. Let us determine the degradation in this fit as the potential anisotropy is decreased. First we lessen the anisotropy of ϵ by decreasing $\epsilon^{(2)}/\epsilon^{(0)}$ to -0.47 and keeping it fixed at this value while optimizing the remaining parameters. The well minimum ($r_m(\gamma)$) does not change appreciably, but the average well depth increases, and the well narrows (b_0 is larger), with a slight reduction in quality of fit. We now remove all depth anisotropy (setting $\epsilon^{(2)} = 0$) and optimize b_1 instead. As can be seen by the results of test B, the well deepens and narrows even further with a significant decrease in the quality of fit. Perhaps the choice of b_1 as the new variational parameter was not a good one, since the optimized value is close to original fixed value of -6.1. Let us instead introduce anisotropy in the shape parameter b_0 (test C). The fit is better than for test B but not as good as for test A in which there was some ϵ anisotropy. The interesting fact is that the anisotropy of b_0 is such that the well is wider at the angles for which the previous fits (with ϵ anisotropy) gave a deeper well, ($\gamma = \pi/2$), and narrower at the angles for which previously the well was shallower ($\gamma = 0$). In very general terms, the fitting procedure is trying to keep the well capacity (depth times width) somewhat constant. However, if the well depth has the anisotropy given in Table IV, the inclusion of b_0 anisotropy in SPFD-e produces no marked improvement in

parameters in the region of sensitivity of these experiments. The results of Table V will clear up some of these questions, as shown below.

The best fit potential of Table IV is SPFD-e. Let us determine the degradation in this fit as the potential anisotropy is decreased. First we lessen the anisotropy of ϵ by decreasing $\epsilon^{(2)}/\epsilon^{(0)}$ to -0.47 and keeping it fixed at this value while optimizing the remaining parameters. The well minimum ($r_m(\gamma)$) does not change appreciably, but the average well depth increases, and the well narrows (b_0 is larger), with a slight reduction in quality of fit. We now remove all depth anisotropy (setting $\epsilon^{(2)} = 0$) and optimize b_1 instead. As can be seen by the results of test B, the well deepens and narrows even further with a significant decrease in the quality of fit. Perhaps the choice of b_1 as the new variational parameter was not a good one, since the optimized value is close to original fixed value of -6.1. Let us instead introduce anisotropy in the shape parameter b_0 (test C). The fit is better than for test B but not as good as for test A in which there was some ϵ anisotropy. The interesting fact is that the anisotropy of b_0 is such that the well is wider at the angles for which the previous fits (with ϵ anisotropy) gave a deeper well, ($\gamma = \pi/2$), and narrower at the angles for which previously the well was shallower ($\gamma = 0$). In very general terms, the fitting procedure is trying to keep the well capacity (depth times width) somewhat constant. However, if the well depth has the anisotropy given in Table IV, the inclusion of b_0 anisotropy in SPFD-e produces no marked improvement in

the potential nor does it change the other parameters, and the resulting final $b_0{}^{(2)}/b_0{}^{(0)}$ is small (less than 0.02).

Table IV shows a greater agreement between the position of the well minima and of their anisotropies for the several potential models than the well depths and their anisotropies. This suggests and other ample evidence confirms[6,7] that our data are more sensitive to the well position than to its depth. We can then assume that the omission of r_m anisotropy and inclusion of ϵ anisotropy will produce a poorer fit to the data. This is indeed the case to a small extent (in Table V, thest D gives G = 1.69% wheras thest B gives G = 1.61%). This test D is however still much better than the spherical case. The striking feature of the results obtained by eliminating the r_m anisotropy (compare test D and A in Table V) is the increase in the well depth, and in its anisotropy as well as a narrowing of its width. The inclusion of shape anisotropy (test E) has a minor effect on the results or on the quality of fit (as compared to test D). The ϵ anisotropy provides the proper regulation of the well capacity, and it is of the correct sign though somewhat greater than the ones in Table IV, in the range of -0.47 to -0.70, which provide a better fit than test E.

In Fig. 5 we have plotted the laboratory scattering intensity for these anisotropy tests. All of the curves are very similar at angles below 5 degrees. The potentials with no r_m anisotropy (tests D and E) show the most deviation in the region at 4.5 degrees. The region

from 5 to 9 degrees demonstrates the need for both r_m and ϵ anisotropy; the oscillations are not as dampened if only r_m or ϵ anisotropies are present, nor does the inclusion of β anisotropy with that for r_m properly dampen this oscillation. The range from 7 to 20 degrees demonstrates the importance of r_m anisotropy, which alone is responsible for significant dampening of quantum oscillations. Yet this region is influenced by ϵ or β anisotropies. The curves with no ϵ anisotropy do fall within the upper ranges of the data error bars, so the effectiveness of this region in establishing ϵ or β anisotropy is rather marginal. The role of r_m anisotropy is absolutely essential in establishing the He + CO_2 potential. Although $r_m(\gamma)$ is the most important parameter, and should be determined first before adjusting the other parameters, it is nonetheless evident that well depth anisotropy does play a crucial role in defining the potential and the resulting laboratory scattering intensity, and it is not just an arbitrary parameter chosen to improve the quality of fit.

We fitted our data to several potential models and obtained well positions and their anisotropies. Even if well depth anisotropy is ignored the final best fit $r_{m\perp}$ and q are very close to the results in Table IV. The two parameters which specify $r_m(\gamma)$ are crucial in determining the well depth and shape parameters, as is evident from Table V. Our experience in constructing the results of Table IV indicates that these $r_m(\gamma)$ parameters should be determined first before any other

anisotropy is introduced. Otherwise, starting the fitting procedure at arbitrary initial values of all potential parameters and varying r_m and ϵ anisotropies produces very unsatisfactory results. We therefore conclude that the parameters which specify $r_m(\gamma)$ are the ones which are most precisely determined, and from the discussion in the previous paragraph, are crucial in establishing the values of the other parameters. However, $r_m(\gamma)$ cannot be the only angle-dependent parameter. The well depth must also have such a dependence.

In Table VI we present several features of each of the best potentials from Tables III and IV which have been reduced to and MMSV form. Features of interest are the minimum location r_m, well depth ϵ, the well width as characterized by β, and the repulsive steepness as characterized by β'. β is derived by finding the zero crossing of the potential and its inflection point; we present both. β' is found by fitting it to eq. 21a with all other parameters given. These five features are evaluated at $\gamma = \pi/2, \pi/4$, and 0; expanded to zeroth and second Legendre orders; and determined for the spherical average of the potential.

With some reservation we included the analysis of the potential at $\gamma = 0$. Our experimental data are not very sensitive to regions near the molecular axis, and misleading conclusions can be drawn if too much weight is placed upon the shape of the potential in these regions. A configuration space analysis shows that the solid angle element (which contributes to eq. (9)) will be greatest at $\gamma = \pi/2$, while at $\gamma = 0$ it

will be zero. On these grounds the helium atom is more likely to hit the molecule perpendicular to its axis than along that axis. This means that about 70% of the sensitivity lies in the range $\gamma = \pi/4$ to $\gamma = \pi/2$ ($\cos(\pi/4) \approx 0.7$). The differential scattering cross-section will mainly be influenced by this portion of the potential (unless it favors the collinear orientation so strongly as to force most collisions to occur in an aligned configuration; a situation which does not occur in the systems being considered). The extracted potential will be most similar to the real potential in this range, while in the range near the axis it will reflect the intrinsic biases of the given model as that model tries to best match the regions of highest sensitivity. Care should be taken so as not to infer too much from the structure of the model potential near $\gamma = 0$.

All of the potential models in Table VI agree very well on the position and anisotropy of the well minimum. Despite the warnings of the previous paragraph the agreement is very good even at $\gamma = 0$. The standard deviation for $r_m(\gamma)$ is approximately 1% for each of the the three values of γ given. It can be said with reasonable confidence that $r_m(\gamma)$ is model-independent and that we have established its angular dependence. The minima location follows the overall shape of the CO_2 molecule; the difference between $r_m(0)$ and $r_m(\pi/2)$ is about 1.1 Å which correlates with the CO bond distance of 1.16 Å. This correspondence is not an internal bias of any of the potentials used; all of these are capable of a wide range of behavior including elongation perpendicular to the

CO_2 axis.

As expected, there is less agreement among the potentials in Table VI regarding the well depth and its anisotropy. The expectation is motivated by the above discussions regarding the need for well depth anisotropy. Although it is clear that $\epsilon(\gamma)$ has γ dependence, it is not completely clear how this relates to the width of the well; every potential in Table VI manipulates ϵ and β differently. The first drive in the fitting process is to establish $r_m(\gamma)$, to which the cross-section is most sensitive; it is not as sensitive to the other parameters which are therefore much more subject to the biases of a given model.

We have observed that the parameters of the fitted multi-center potentials exhibit a greater correlations between various parameters than for the angular dependent parameter potentials.. This is due to the fact that for the former potentials a changes in one of the parameters affects the potential globally in more pronounced way than for the latter potential. As an example, let us compare the MSV-m1, MSV-m2, and MMSV-m potentials to each other. For these potentials the well width and wall shape parameters are specified in different ways. The MSV-m1 is a six-fitted-parameter potential; the r_m, ϵ and β for each center are adjusted in the fitting procedure. The MSV-m2 is a five-fitted-parameter potential; the β's for the three centers are set equal to one another in the fitting procedure. The MMSV-m is a six-fitted-parameter potential, where the β's for the three centers are made equal to each other as

well as the the β'''s and are therefore treated as two fitting parameters. The MSV-m1 and MSV-m2 potentials are very similar to each other in quality of fit and value (Table VI). They differ the most at and near $\gamma = \pi/2$, where the MSV-m1 is deeper, narrower, and steeper (on the wall). In general, the well is narrower when β is higher, and the wall becomes steeper when β' increases. The MMSV-m potential provides a somewhat better fit than the two MSV-m ones. It is not as similar to either of them as they are to each other: the well is shallower and wider; the minimum position is greater; and the wall is steeper for all γ. The repulsive wall shape parameter β' has a strong influence on the fitting of the other parameters for these potentials. This influence is also observed if we compare the angular-dependent parameter potentials MSV-e and MMSV-e although it is not as pronounced.

A potential that gave a very good fit, but one which we can reject is the Morse-m. It has an extreme anisotropy in well depth (the latter ranging from 1.9 to 8.13 meV), and a very narrow and steep well. By contrast the Morse-e potential gave a very poor fit with a shallow and wide well. This extreme behavior of both potential is caused primarily by inadequate flexibility in the form of the Morse potential for which the well parameters determine the behavior in the van der Waals dispersion region.

The other potentials are much more difficult to reject; all are quite physically reasonable. We may suspect to some extent those that have

a rather steep repulsive wall, such as the MMSV-e or even the MMSV-m. However, a selection of potentials for He interacting with various molecules[1-5,8-10,27-30] shows that many MMSV type potentials do have larger β' than β (eq. 21), also sensitivity analysis shows[6] that the DCS is much less sensitive to β' than to β making β' a less relaible parameter. Otherwise there is no reason to favor any of the potentials in Table VI other than by the quality of fit. The two best "fits" are the SPFD-m1 and SPFD-e. We have chosen to depict these graphically in Figures 6 through 9. In both cases the contours (Figures 6 and 8) are smooth. The fixed angle plots (Figures 7 and 9) further confirm a regular and smooth potential. The contours for the two potentials do have similar overall features, but the details are different. This is expected, since there simply is not enough information in the data (Figure 2) to unequivocally establish the shape of the potential. These contours should be viewed as representing the basic features of the real potential but not the specific details.

6.2. Potentials for He + CS_2

The best potential fits for He + CS_2 data are presented in Tables VII and VIII. We have chosen the potential forms that gave the best fits for He + CO_2. The quality of fit to experimental data is not as good as for He + CO_2, but nonetheless reasonably good. Substantial improvement in quality of fit occurs if the repulsive wall is made steeper

as in the MMSV-e (Table VII) or MMSV-m (Table VIII). The poorer fit of the other potentials is manifest at scattering angles above 14 degrees (see Fig. 3 - note: $I(\theta) \sin\theta$ is not plotted for MSV-m). At angles below 14 degrees agreement between the various models is very good.

The characteristics of the He + CS_2 potentials are presented in Table IX. All of the potentials have similar well positions, depths and widths. The Morse-m deviates the most from the average of the others - but since it does not have the correct long-range behavior we reject it more readily than the others (as in the case of He + CO_2). The MMSV-m has the shallowest well and greatest r_m anisotropy. Since it provides the best fit to the data we claim it as most representative of the real potential. The contours and sectional views are shown in Figures 10 and 11.

The reliability level of the He + CS_2 potentials is lower than for He + CO_2. This is based on the larger fluctuation between the various forms and the poorer fits to the data. We can attribute some of these differences to the van der Waals dispersion coefficients. The CS_2 ones were obtained from the accurately calculated CO_2 coefficients by the use of a polarizibility correction (see end of Sec. 3) and are therefore less accurate than those for CO_2.

6.3. Potentials for He + OCS

The best potential fits for He + OCS data are presented in Tables X

and XI, with Table XII displaying the features transformed to a common MMSV form. Once again we have used those potential forms that gave the best and most physically reasonable results for the He + CO_2 system. As is evident from the tables, all the potentials afforded very good fits. However, since the dispersion constants are not as well known for He + OCS we should hold less trust in these results than in the He + CO_2 ones.

In Table X we present the best fits for two different three-center MSV potentials. In these cases we decided to use three different centers and fit only five parameters; $r_m(O)$, $\epsilon(O)$, $r_m(S)$, $\epsilon(S)$ and one β assumed to be the same for all three centers. We chose the $r_m(C)$ and $\epsilon(C)$ parameters for the carbon center as the average of the corresponding He + CO_2 and He + CS_2 multi-center potential values. For those systems we found that the central atom potential had less effect on the cross-section than the outer atom potential. In addition varying the C-centered potential produced smaller changes in the potential or the quality of fit, as most of these changes were compensated for by the two outer potentials. The difference between the MSV-m1 and MSV-m2 potentials is in the way the van der Waals dispersion terms are included. For the MSV-m2 they are included in the same way as outlined at the end of section 3. For the MSV-m1 the potential centered at the carbon was splined to a zero valued dispersion term, while the O centered potential was splined one half of the He + CO_2 term, and the S centered potential

was splined to one half of the He $+ CS_2$ term. These dispersion terms were evaluated using the r_i (eq. 11 amd 12) and not r as was done for the other multi-center potentials (end of section 3).

The MSV-m1 fitted the data better than the MSV-m2, and hence we display it in Figures 12 and 13 which show the potential as contours and angular sectional views, respectively. From Table XII we see that the two potetials are not so different considering the fact that we cannot expect too much detail regarding the potential from our data. The position of the repulsive wall is in agreement with those for He $+ CO_2$ and He $+ CS_2$, being greater at the S end, as can be seen by comparing the values of r (for $\gamma = 0, \pi$) at which the potentials crosses zero (see Figs. 12, 8 and 10). The well is deeper at the S end as would be expected from bond polarizabilities of -C=S and -C=0,[24ab,25] (the former being greater) and from the He $+ CO_2$ and CS_2 potential parameter results. However, the well near the O in OCS is much shallower than in CO_2, and hence physically unrealistic. This emphasizes our previous warning on trusting the characteristics of a potential in a region of low sensitivity near the molecular axis. We must be even more cautious with a lower symmetry potential extracted from our limited data. Yet, we can consider the MSV-m1 or MSV-m2 potentials to be very reasonable models which display many of the overall features of the real potential.

The angle-dependent potentials were defined for systems with a center of symmetry. As a result, when applied to the asymmetric OCS

system, they are expected to represent the average of the two halves of the correct potential about the plane perpendicular to the OCS-axis and passing through the center-of-mass of the molecule. We did not attempt to employ angle-dependent potentials without an inversion center since these would have too many degrees of freedom; expansion of $r_m(\gamma)$ and $\epsilon(\gamma)$ to second or third order with β would give seven to nine parameters, an excessive number for the information content of the DCS data. The centro-symmetric potential fits to the OCS data are given in Table XI. The Morse-e potential gives a good fit, but is physically very unreasonable; both the r_m and ϵ anisotropies are extreme and reversed. The MMSV-e is such a good fit that no useful or additional informaion can be obtained by including more parameters in fitting the data. Also, the amplitudes in the DCS oscillations (see Figure 4) are significantly dampened, and it would be unrealistic to expect them to reflect the subtle details of the actual potential.

In Table XII we show an average of the MSV-m1 and MSV-m2 potentials about the center-of-mass of the OCS, to facilitate comparison between the centrosymmetric MMSV-e potential. The MSV-m1-average shows a good similarity to the MMSV-e, while the MSV-m2-average is rather different from the MMSV-e. On the basis of the MSV-m1-average we can consider the MMSV-e to be a reasonable approximation to a center-of-mass average of the actual potential.

—

7. INTEGRAL CROSS SECTIONS AND BULK PROPER-
TIES

The validity of our He + CO_2 potential can be tested by its ability to predict a variety of observed phenomena, which include integral cross section $Q(v_{He})$ (as a function of He velocity), binary diffusion coefficient $D_{He,CO_2}(T)$, viscosity curvature $\eta_{He,CO_2}(T)$, and second virial coefficient $B_{He,CO_2}(T)$. The expressions for these quantities have been derived and presented in several publications[13,2], and hence we will forgo listing them here. The figures in which we compare experimental data to our calculations are sufficent in substantiating the validity of our potential. All of the bulk property calculations are for the SPFD-e potential.

Butz *et al.*[63] have measured the total integral cross sections $Q(v_{He})$ as a function of the velocity of a He beam interacting with a cell of CO_2 gas. To model these data the total integral cross sections are calculated at a range of collision energies they are then averaged over the distribution of velocities of the bulk CO_2 gas and the He beam. In Figure 14 we show calculations of $Q(v_{He})$ on our SPFD-e potential (Table IV) and compare then to the data of Butz *el al.*.[63] Our potential predicts averaged integral cross sections that for all velocities are about 3% lower than the experimental; however there is very good agreement in the relative intensities. Butz *el al.* have given a 15 % upper error limit on their measurements which includes estimates of the extent of systematic

errors to which experiments of this type are highly susceptible.[64,65] Our calculations are well within these error bars.

In Figure 15 we compare experimental[66] binary diffusion coefficients $D_{He,CO_2}(T)$ for He in CO_2 to those calculated from our potential . The agreement is excellent for the entire measured temperature range of 180 to 600 K.

In Figure 16 we compare calculated mixture viscosity coefficients to experimental viscosities $\eta_{x_{CO_2}}(T)$ at two mole fractions x_{CO_2} of CO_2 to ones obtained experimentally by Kestin and Ro[67]. We also compare the interaction viscosity (transport of momentum along a velocity gradient) coefficients $\eta_{He,CO_2}(T)$ to those extracted from Kestin and Ro's data by Keil and Parker[3]. The interaction viscosity coefficients η_{He,CO_2} can be extracted from the experimental mixture viscosities; they cannot be measured directly. (The mixture viscosities are a function of the mole fraction of the two constituents, the interaction viscosity coefficients, and the binary diffusion coefficient.) For all three cases the agreement is once again excellent.

Finally, in Figure 17 we compare the calculated second virial coefficients $B(T)$ to experimentally measured ones.[68] The agreement is very good at temperatures above 200 K and fair below. The experimental data are from three different laboratories; the points with the largest error bars are from the one source[68a], while the ones with the smallest error bars are from a different source[68b]. Its is difficult to determine

how conservatively or liberally these error bars were assigned by the respective authors. Our assessment is that the low error bars may be reported somewhat conservatively, and hence our potential has allowed a very accurate calculation of the second virial coefficient as function of temperature.

Our He + CO_2 potential is capable of predicting a variety of observables. However, we should point out that the bulk properties disscussed above, can be equally well predicted by the Parker-Keil-Kuppermann[4,5] and Keil-Parker[3] potentials. Yet these potential are rather different from ours. In fact, Parker and Pack[13,31] have proposed a He + CO_2 potential that was able to predict the viscosity and diffusion coefficients very well but failed to predict the integral and differential cross-section data. It is therefore, quite evident that the bulk properties are much less sensitive to the potential energy surface topography then is the differential cross-section. This is not surprising since the expressions for the diffusion, viscosity and virial coefficients are integrals over several variables, and thereby contain significant averaging. The total integral cross section curve is rather structureless, and at low velocities of He includes large energy averaging over the CO_2 velocity. The variety of potentials that could easily yield the same bulk properties is much larger than those that could reproduce a similar differential cross section. These properties are only useful in substantiating the validity of the potentials which are extracted from crossed beam DCS data.

8. CONCLUSIONS

We have measured the total differential scattering cross-sections (DCS) for He + CO_2, CS_2, and OCS. From these we obtained realistic interaction potentials that exhibit significant anisotropies in well minimum position as well as in the well depth. Isotropic potentials do not satisfactorily represent the potential that produces the scattering data. Clearly the scattering data is not the result of a spherical average of the real potential. This is particularly evident if they are compared to He + atom and He + diatomic-molecule scattering data.[9,10,29]

With He + CO_2 we have clearly demonstrated that not only is the well minimum position (r_m) anisotropy important in accounting for the observed data, but the depth (ϵ) anisotropy is also detected and accounts for many features in the DCS. Although the r_m anisotropy accounts for most of the dampening of the quantal oscilations; ϵ anisotropy is also responsible for some of the dampening as well as for the shape of the oscillation. Also very important is the width of the well, to which we were unable to ascribe any anistropy. Crucial to the extraction of a potential from the DCS was a knowledge of the long term dispersion coefficients. Potential forms that do not have provisions for them, could not be sucessfully fitted to the DCS; either the potential was physically unreasonable or the fit was poor.

Two models for characterizing the potential anisotropy which have demonstrated a high degree of flexibility as well as simplicity are the

parameters expansion potential to second order in Legendre polynomials; and the multi-center potential. These were coupled with two very flexible spherical-like potential forms, to correctly describe the shape of the potential along a given angle of approach. Both the MMSV (or MSV) and the SPFD forms have good control of well depth as well as including the needed dispersion terms.

Both the parameter expansion and multicenter models have allowed us to extract very similar potentials from the DCS. In all three cases we found that r_m corresponds to the geometry of the molecule (CO_2, CS_2 and OCS). While the potential minimum is located perpendicular to the molecular axis. In the case of He + OCS, we have proposed a non-centro-symmetric potential constructed of three MSV potentials centered on the three OCS nuclei. Only five parameters were adjusted; the C-centered MSV was chosen on the basis of the He + CO_2 and He + CS_2 potentials.

Although our results yield the most accurate and detailed potentials for these systems to date, nonetheless we cannot state that these models are identical with the actual potential in every aspect. First of all, any technique that relies on a collision to probe the potential will be most sensitive to that potential in the regions where the collision is most probable; perpendicular to the axis of the CO_2, CS_2, and OCS molecule. Second, our experiment detects a wide range of rotationally inelastic collisions which are unresolved and thereby dampen many features in

the total DCS. However, these result provide significant limits on the range of many potential parameters and unambiguously establish the presence of certain features.

ACKNOWLEDGEMENTS

2.9 REFERENCES

1. G. Scoles, *Ann. Rev. Phys. Chem.* **31**, 81 (1980).
2. *Atom-Molecule Collision Theory: A Guide for the Experimentalist* R. B. Bernstein ed. (Plenum, New York, 1979).
3. M. Keil and G. A. Parker, *J. Chem. Phys.* **82**, 1947 (1985).
4. G. A. Parker, M. Keil, and A. Kuppermann, *J. Chem. Phys.* **78**, 1145 (1983).
5. M. Keil, G. A. Parker, and A. Kuppermann, *Chem. Phys. Lett.* **59**, 443 (1978).
6. J. W. Winniczek and A. Kuppermann, (to be submitted).
7. L. Eno and H. Rabitz, *J. Chem. Phys.* **74**, 3859 (1981).
8. R.T Pack, G. A. Pfeffer, and J. P. Toennies, *J. Chem. Phys.* **80**, 4940 (1984).
9. M. Faubel, K. H. Kohl, J. P. Toennies, and F. A. Gianturco, *J. Chem. Phys.* **78**, 5629 (1984).
10. M. Faubel, K.-H. Kohl, and J. P. Toennies, *Faraday Discuss. Chem. Soc.* **73**, 205 (1982).
11. P. M. Agrawal and L. M. Raff, *J. Chem. Phys.* **75**, 2163 (1981).
12. C. L. Stroud and L. M. Raff, *J. Chem. Phys.* **72**, 5479 (1980).
13. G. A. Parker and R. T Pack, *J. Chem. Phys.* **68**, 1585 (1978).
14. R. T Pack, *Chem. Phys. Lett.* **55**, 197 (1978).
15. G. Rotzoll and A. Lubbert, *J. Chem. Phys.* **71**, 2275 (1979).
16. V. Khare, *J. Chem. Phys.* **68**, 4631 (1978).
17. D. Secrest, *J. Chem. Phys.* **62**, 710 (1975).
18. P. McGuire and D. J. Kouri, *J. Chem. Phys.* **60**, 2488 (1974).
19. R. T Pack, *J. Chem. Phys.* **60**, 633 (1974).
20. D. S. Saxon, *Elementary Quantum Mechanics* (Holden-Day, San Francisco, 1968).
21. A. S. Davydov, *Quantum Mechanics* (Pergamon, Oxford 1976), 2nd edition, tr. D. ter Haar.
22. G.Herzeberg, *Molecular Spectra and Molecular Structure III. Electronic Spectra and Electronic Structure of Polyatomic Molecules*, (Van Nostrand Reinhold, New York, 1966).
23. The vibrational energies for $CO2_2$, CS_2 and OCS are given in ref. 22, the lowest of which is the CS_2 bending mode: 396.7 cm^{-1} for which 80%

of the CS_2 molecules are in the ground state at a temerature of 298 K. The other two CS_2 vibrational modes have a 96% and a 100% ground state relative populations. For CO_2 the ground state relative populations for the three vibrational modes are 97%, 100% and 100%. For OCS these populations are 92%, 98% and 100%.

24. J. O. Hirshfelder, C. F. Curtiss, and R. B. Bird, *Molecular Theory of Gases and Liquids* (Wiley, New York 1964); (a) page 22 and 32, (b) page 950, (c) page 949.

25. N. J. Bridge and A. S. Buckingham, *Proc. R. Soc. Edinburgh Sect.* **A295**, 334 (1966).

26. R. T Pack, *J. Chem. Phys.* **64**, 1659 (1976).

27. M. Keil and A. Kuppermann, *J. Chem. Phys.* **69**, 3917 (1978).

28. M. Keil, J. T. Slankas, and A. Kuppermann, *J. Chem. Phys.* **70**, 482 (1979).

29. M. Keil, J. T. Slankas, and A. Kuppermann, *J. Chem. Phys.* **70**, 482 (1979).

30. J. T. Slankas, M. Keil, and A. Kuppermann, *J. Chem. Phys.* **70**, 1482 (1979).

31. R. T Pack, *J. Chem. Phys.* **61**, 2091 (1974).

32. J. Hepburn, G. Scoles, and R. Penco, *Chem. Phys. Lett.* **36**, 451 (1975).

33. K. M. Smith, A. M. Rulis, G. Scoles, R. A. Aziz, and V. Nain, *J. Chem. Phys.* **67**, 152 (1977).

34. K. M. Smith, A. M. Rulis, G. Scoles, R. A. Aziz, and G. Duquette *J. Chem. Phys.* **63**, 2250 (1975).

35. R. A. Aziz, P. W. Riley, U. Buck, G. Maneke, J. Schleusener, G. Scoles, and U. Valbusa, *J. Chem. Phys.* **71**, 3637 (1979).

36. C. H. Chen, P. E. Siska, and Y. T. Lee, *J. Chem. Phys.* **59**, 601 (1973).

37. A. L. J. Burgmans, J. M. Farrar, and Y. T. Lee, *J. Chem. Phys.* **64**, 1345 (1976).

38. R. W. Bickes and R. B. Bernstein, *Chem. Phys. Lett.* **26**, 457 (1974).

39. J. L. Dunham, *Phys. Rev.* **41**, 721 (1932).

40. G. Simons, R. G. Parr, and J. M. Finlan, *J. Chem. Phys.* **59**, 3229 (1973).

41. P. M. Morse, *Phys. Rev.* **34**, 57 (1929).

42. A. Kuppermann, R. J. Gordon, and M. J. Coggiola,
    Faraday Discuss. Chem. Soc. **55**, 145 (1973).

43. M. J. Coggiola, Ph. D. thesis, California Institute of Technology 1975.

44. J. T. Slankas, Ph. D. thesis, California Institute of Technology 1979.

45. M. Keil, Ph. D. thesis, California Institute of Technology 1978.

46. J. B. Anderson and J. B. Fenn, *Phys. Fluids* **8**, 780 (1965).

47. H. U. Hostettler and R. B. Bernstein, *Rev. Sci. Instrum.* **31**. 872 (1960).

48. This is the corrected pressure which takes into account the fact that a
    Bayard-Alpert ion gauge has a sensitivity for helium 10 times smaller
    than that for air.

49. Galileo Electro-Optics Corp., Sturbridge, Massachusetts.

50. Extranuclear Laboratories Inc., Pittsburgh, Pennsylvania.

51. Channeltron Model No. 4816, Galileo Electro-Optics Corp., Sturbridge,
    Massachusetts.

52. Model A-101. AMPTEK Inc., Bedford, Massachusetts.

53. The phase sensitive counter is an in-house built counter with a Phase
    Control Unit (phase shifter) model 4114 Evans Electronics, Berkeley,
    California.

54. Digital Equipment Corporation, Maynard, Massachusetts.

55. Princeton Applied Research Corporation, Princeton, New Jersey.

56. The electrometer is in-house built by the Department of Chemistry Elec-
    tronics Suport Group. The chief part of the unit is a high performance
    FET operational amplifier with a 100 Mega Ohm electrometer feedback;
    Model LH0022CH, National Semiconductor Corp., Santa Clara, Califor-
    nia.

57. Angular position encoder manufactured by: Clifton Precision, div. of
    Litton Systems Inc., Chatsworth, California; and Bendix Corporation,
    South Montrose, Pennsylvania; Decoder and display manufactured by
    Data Device Corporation, Bohemia, New York.

58. R. T Pack, *J. Chem. Phys.* **60**, 633 (1974).

59. K. Smith, *The Calculation of Atomic Collision Processes* (Wiley, New
    York 1971).

60. N. R. Draper and H. Smith, *Applied Regression Analysis* (Wiley, New
    York 1966).

61. D. W. Marquardt, *J. Soc. Indust. Appl. Math.* **11**, 431 (1963)

62. T. T. Warncock and R. B. Bernstein, *J. Chem. Phys.* **49**, 1878 (1966).

63. H. P. Butz, R. Feltgen, H. Pauly, and H. Vehmeyer, *Z. Physik* **247**, 70 (1971).

64. E. W. Rothe, Ph. D. Thesis, University of Michigan (1959).

65. C. A. Linse, J. J. H. Van Den Biesen, E. H. Van Veen, C. J. N. Van Den Meijdenberg, and J. J. M. Beenakker, *Physica* **99A**, 145 (1979).

66. (a) S. C. Saxena and E. A. Mason, *Mol. Phys.* **2**, 379 (1959); (b) B.K.Annis, A. E. Humphereys, and E. A. Mason, *Phys. Fluids* **12**, 78 (1969); (c) R. E. Walker, N deHass, and A. A. Westenberg *J. Chem. Phys.* **32**, 1314 (1960) (d) J. C. Giddings and S. L. Seager, *Ind. Eng. Chem. Fundam.* **1**,277 (1962); (e) S. L. Seager, L. R. Geertson, and J. C. Giddings, *J. Chem. Eng. Data* **8**, 168 (1963); (f) J. N. Holsen and M. R. Strunk, *Ind. Eng. Chem. Fundam.* **3**, 143 (1964); (g) B. A. Ivankin and P. E. Suetin, *Soviet Phys. Tech. Phys.* **9**, 866 (1964); (h) A. E. Loiko, G. A. Ivankin, and P. E. Suetin, *ibid.* **19**, 434 (1974); (i) N. D. Kosov and A. F. Bogatyrev, *Teplofiz. Massoperenos* **7**, 497 (1968); (j) A. G. Karpushin adn N. D. Kosov, *Fizika (Alma-Alta)* **1**, 127 (1970); (k) I. Nagata and T.Hasegawa, *J. Chem. Eng. Jpn.* **3**, 143 (1970); (l) K. R. Harris, T. N. Bell, and P. J. Dunlop, *Can. J. Chem.* **50**, 1874 (1972); (m) P. S. Arora, H. L. Robjohns, I. R. Shankland, and P. J. Dunlop, *Chem. Phys. Lett.* **59**, 478 (1978).

67. (a) J. Kestin and S. T. Ro, *Ber. Bunsenges. Phys. Chem.* **78**, 20 (1974); (b) R. DiPippo, J. Kestin, and K. Oguchi, *J. Chem. Phys.* **46**, 4758 (1967)

68. (a) T. L. Cottrell and R. A. Hamilton, *Trans. Faraday Soc.* **52**, 156 (1956); (b) R. C. Harper, Jr. and J. G. Miller, *J. Chem. Phys.* **27**, 36 (1957); (c) J. Brewer, Tech. Ref. AD663448 (1967) Available from the Clearinghouse for Federal Scientific and Technical Information; (d) T. N. Bell and P. J. Dunlop, *Chem. Phys. Lett.* **84**, 99 (1981).

Table I. Molecular Beam Characteristics

Characteristic	Probe Beam	Target Beam		
Gas	He	CO_2	CS_2	OCS
Stagnation Temperature/K	298	298	298	298
Stagnation Pressure/torr	1330	4.4	4.4	4.4
Angular Spread FWHM[a]/degrees	1.0[b]	3.0[b]	3.0[b]	3.0[b]
Most probable velocity/(km/sec)	1.76	0.49[c]	0.37[c]	0.42[c]
Velocity FWHM ($\Delta v/v$)	0.12	0.8	0.8	0.8
Mach number	12.7	1.06	1.06	1.06
Effective Heat capacity ratio γ	1.06	2.20	2.20	2.20

[a] Full width at half maximum.

[b] The effective detector acceptance angle of 1.5 deg is greater than the actual detector acceptance angle (see text) since it includes the effects of the finite size of the scattering volume.

[c] These most probable velocities give a relative collision energy of 65 meV with helium.

Table II. Spherical Potential Best Fits

System/Potential	r_m	ϵ	B or b_0 [a]	B' or b_1 [a]	r_s/r_m [a]	C_w [b]	G/χ [c]	χ^2 [c]
He + CO_2								
MMSV	3.34	6.09	11.39	19.12	1.37	0.82	2.00	72.4
SPFD	3.34	5.96	104.5	-7.33	1.40	0.84	2.09	74.9
SPFD	3.39	6.21	107.6	-7.25	1.41	1.0	2.17	87.7
He + CS_2								
SPFD	3.82	5.52	65.67	-5.70	1.67	0.98	3.59	156.6
He + OCS								
SPFD[d]	3.94	5.79	85.92	-7.19	1.34	1.781	3.08	204.2
SPFD[e]	3.97	6.33	147.8	-9.49	1.32	0.623	2.28	112.5

a B and B' apply to the MMSV potential (eq. 21) while b_0 and b_1 apply to the SPFD potential (eq. 22); r_s is the van der Waals spline point.

b C_w is a multiplier for the C_6 and C_8 van der Waal's coefficients, i.e., C'_6 or $8 = C_w C_6$ or 8.

Table II. Continued

---

[c] See equations 27 to 29.

[d] Use C_6 and C_8 for He + CO_2.

[e] Use C_6 and C_8 for He + CS_2.

Table III. Multicenter Potentials for He + CO_2

Potential Type[a]	Center[b]	$r_m/\text{Å}$	ϵ/meV	Shape(1)[c]	Shape(2)[c]	G/%[d]	χ^2[d]
MSV-m1	C	3.14	3.19	11.00			
	O	3.14	1.54	6.47		1.15	23.9
MSV-m2	C	3.18	2.88	7.90			
	O	3.15	1.24	7.90[e]		1.18	26.1
MMSV-m	C	3.26	3.27	5.37	13.26		
	O	3.45	0.51	5.37[e]	13.26[e]	1.08	21.3
SPFD-m1	C	3.21	4.51	77.15	-6.0[f]		
	O	3.37	0.66	22.84	-6.0[f]	1.05	19.9
SPFD-m2	C	3.12	3.51	66.52	-7.04		
	O	3.22	0.82	66.52[e]	-7.04[e]	1.11	22.5
SPFD-m3	C	3.15	3.33	60.66	-6.0[f]		
	O	3.21	0.98	60.66[e]	-6.0[f]	1.15	24.6
Morse-m	C	3.22	4.83	17.11	-		
	O	3.23	1.74	4.21	-	0.99	18.5

[a]Refer to equation (11). Potentials at each center are of the same spherical type, as discussed in section IIIB. The designation "-m" is for classification and refers to multicenter.

[b]The C-O bond distance is fixed at 1.162 Å. For systems with long range van der Waals dispersion terms each center contributes one third of the dispersion. The dispersion terms are given as:

$$C_6 = 9.98 + 2.31\ P_2\ (\cos \gamma)\ \text{eV}\cdot\text{Å}^6 \qquad \text{and}$$

$$C_8 = 46.4 + 48.4\ P_2\ (\cos \gamma)\ \text{eV}\cdot\text{Å}^8$$

They are splined to the potential at $r/r_m = 1.6$ for all cases.

Table III. continued

---

[c]The shape parameters are defined by equations (18), (20), (21), and
(22) for the Morse, MSV, MMSV, and SPFD parameterizations respectively.
The second shape parameter for MMSV or SPFD is β' or b_1 respectively.

[d]G is the goodness-of-fit statistic of eq. (29); while χ^2 is unitless
as defined by eqs. (27) and (28).

[e]This parameter is the same as the analogous one for the potential
centered at the C. Both were varied as one parameter.

[f]This parameter is fixed and was not varied via least squares.
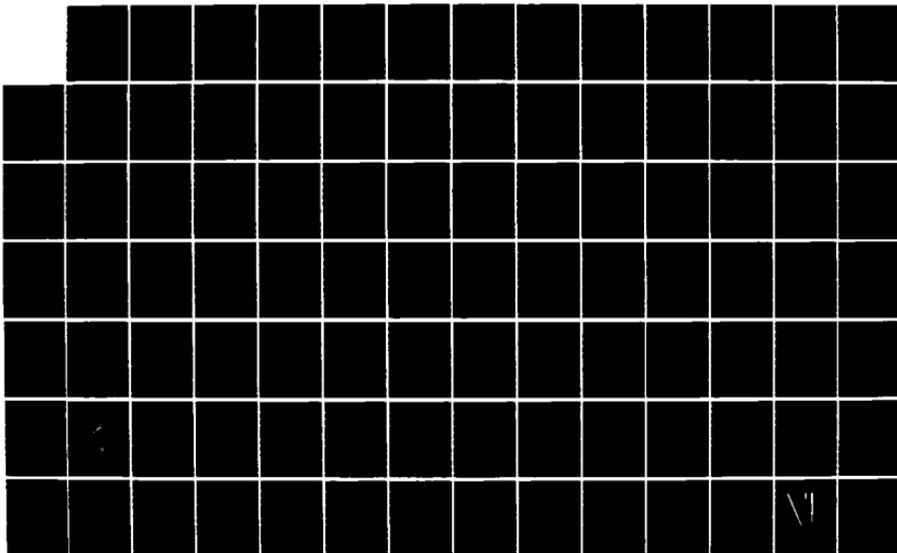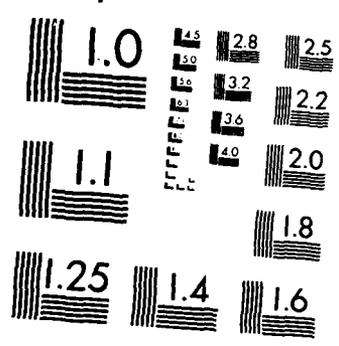
MICROCOPY RESOLUTION TEST CHART
NATIONAL BUREAU OF STANDARDS-1963-A

Table IV. Angular-dependent-parameter potentials for He + CO_2

Potential type[a]	r_{mi}/Å[b]	q^b	$\epsilon^{(0)}$/meV[c]	$\epsilon^{(2)}/\epsilon^{(0)}$[c]	shape(1)[d]	shape[d']	G/g^e	χ^2 [e]
SPFD-e	3.10	-0.477	3.99	-0.697	54.45	-6.14[f]	0.99	18.3
MSV-e	3.11	-0.437	4.29	-0.477	7.05		1.27	31.5
MMSV-e	3.11	-0.437	4.19	-0.568	6.91	16.16	1.16	26.5
HFD-e	3.19	-0.424	(3.61)[g]	(-0.727)[g]	(6.08)[g]	(α=1.07)[g]	1.63	50.1
LJ8-e	3.14	-0.465	3.70	-0.690			1.23	29.8
LJ-e	3.13	-0.490	3.51	-0.988			1.30	33.0
Morse-e	3.22	-0.548	3.23	-0.687	5.00		2.50	117.8
	$r_m^{(0)}$/Å[h]	$r_m^{(2)}/r_m^{(0)}$[h]						
SPFD-p	3.54	0.226	3.88	-0.773	52.57	-6.1[f]	0.99	18.4
MSV-p	3.41	0.206	4.35	-0.439	7.11		1.40	36.6
LJ8-p	3.56	0.224	3.69	-0.679			1.24	30.1

[a]Refer to equation (13). The designations "e" and "p" are for classification and refer to elliptical expansion of $r_m(\gamma)$ and second order Legendre expansion of $r_m(\gamma)$. The dispersion terms used in the

Table IV. continued

KSV, MMSV, SPFD, HFD and LJ8 are

$C_6 = 9.98 + 2.31 P_2 (\cos \gamma) eV \cdot \mathring{A}^6$ and $C_8 = 46.4 + 48.4 P_2 (\cos \gamma) eV \cdot \mathring{A}^8$;

and are splined at $r/r_m = 1.6$

[b] Elliptical expansion of $r_m(\gamma)$ is given by eqs (15-16).

[c] Legendre expansion of $\epsilon(\gamma)$ is given by eq. (14).

[d] This shape parameter is β of eqs. (18, 20 and 21) or b_0 of eq. (22).

[d'] This shape parameter is β' of eq. (21), or b_0 of eq. (22).

[e] G is defined by eq. (29), the "goodness-of-fit" statistic. χ^2 is given by eqs. (27-28) and is unitless.

[f] This parameter is fixed in the least squares fitting procedure.

[g] The well depth and its anisotropy are derived. The shape parameter corresponds to β of eq. (20) and was derived from the zero crossing of the potential. Only three parameters were varied; $r_{m\parallel}$, q, and α [see eq. (23)].

[h] Legendre expansion of $Y_m(\gamma)$ is given by eq. (14).

- 75 -

Table V. SPFD[a] angular-dependent-parameter potentials to test anisotropy for He + CO_2

Test	$r_m/Å$[b]	q[b]	$e^{(0)}/meV$[c]	$e^{(2)}/e^{(0)}$[c]	$b_0(0)$[d]	$b_0^{(2)}/b_0(0)$[d]	b_1	G/χ[e]	χ^{2}[e]
A	3.09	-0.480[f]	4.34	-0.470[f]	60.06	0[f]	-6.1[f]	1.12	25.3
B	3.09	-0.440	4.83	0[f]	67.10	0[f]	-5.90	1.61	48.2
C	3.09	-0.490	3.98	0[f]	58.99	0.616	-6.1[f]	1.41	36.8
D	3.39	0[f]	5.77	-0.802	103.93	0[f]	-7.15	1.69	52.4
E	3.39	0[f]	5.76	-0.802	103.80	0.052	-7.14	1.67	52.0

[a]See equation (22). Note: see a) of table III.

[b]See equations (15) and (16).

[c]See equation (14).

[d]The first shape parameter b_0 was expanded to a second Legendre order eq. (14).

[e]See eq. (29) for G and eqs. (27) and (28) for χ^2 which is unitless (reduced).

[f]This parameter was fixed in the least squares fitting.

Table VI. Summary of Characteristics of Best Fit Potentials for He + CO_2

Potential type[a]	Characteristic[b]	$r_m/Å$	ϵ/meV[c]	β_z^d	$\beta_\perp^d$	β_γ^d
MSV-m1	$\gamma = \pi/2$	3.11	5.93	9.72	11.0	10.5
	$\gamma = \pi/4$	3.67	4.08	7.04	13.0	7.20
	$\gamma = 0$	4.2	2.8	8.0	8.5	8.9
	$L = 0$	3.45	4.62	8.27	9.13	9.43
	$L = 2$	0.74	-2.21[f]	-1.37[g]	-1.26[g]	-2.21[g]
	S	3.75	2.72	7.50	8.53	7.49
MSV-m2	$\gamma = \pi/2$	3.12	4.96	7.64	8.29	7.62
	$\gamma = \pi/4$	3.72	4.14	8.08	8.69	8.01
	$\gamma = 0$	4.2	2.8	9.7	9.8	10.4
	$L = 0$	3.51	4.24	7.90	8.38	8.32
	$L = 2$	0.74	-1.36[f]	1.54[f]	1.54[f]	1.64[f]
	S	3.85	2.69	8.35	9.13	8.97
MMSV-m	$\gamma = \pi/2$	3.26	4.30	5.23	5.34	13.15
	$\gamma = \pi/4$	3.78	2.81	8.38	3.06	13.77
	$\gamma = 0$	4.2	2.4	10.7	8.5	17.8
	$L = 0$	3.59	3.41	7.30	5.55	14.23
	$L = 2$	0.71	-1.45	3.05[f]	1.18[g]	4.82[f]
	S	3.93	2.44	9.63	6.09	15.06

Table VI. continued

Potential type[a]	Characteristic[b]	$r_m/\overset{\circ}{A}$	ε/meV[c]	β_z[d]	β_i[d]	β_r[d]
SPFD-m1	$\gamma = \pi/2$	3.20	5.83	7.92	8.10	7.51
	$\gamma = \pi/4$	3.69	3.11	7.30	8.60	9.30
	$\gamma = 0$	4.3	2.1	7.9	7.3	11.3
	$L = 0$	3.50	4.28	7.88	8.59	8.40
	$L = 2$	0.72	-2.86[f]	0[f]	-0.71[f]	2.00[f]
	S	3.79	2.45	7.71	8.98	10.84
SPFD=m2	$\gamma = \pi/2$	3.10	5.07	8.07	8.71	8.10
	$\gamma = \pi/4$	3.79	3.68	7.67	11.3	7.99
	$\gamma = 0$	4.2	2.6	9.8	13.0	10.0
	$L = 0$	3.53	3.98	7.92	8.78	8.52
	$L = 2$	0.80[f]	-1.51[f]	1.08[f]	0.30[f]	0.93[f]
	S	3.92	2.60	7.82	9.00	12.90
SPFD-m3	$\gamma = \pi/2$	3.12	5.14	7.54	8.28	7.39
	$\gamma = \pi/4$	3.76	3.78	7.54	10.1	7.58
	$\gamma = 0$	4.2	2.7	9.1	6.6	9.7
	$L = 0$	3.52	4.10	7.62	8.06	7.93
	$L = 2$	0.78	-1.59[f]	1.10[f]	0.85	1.34[f]
	S	3.87	2.59	7.45	8.91	12.94
Morse-m	$\gamma = \pi/2$	3.21	8.13	14.6	15.8	16.9
	$\gamma = \pi/4$	3.29	4.12	13.5	21.5	18.3

Table VI. continued

Potential type[a]	Characteristic[b]	r_m/Å	ϵ/meV[c]	β_z[d]	β_i[d]	β_r[d]
	$\gamma = 0$	4.3	1.9	5.4	5.4	4.9
	$L = 0$	3.42	5.78	12.15	13.55	16.59
	$L = 2$	0.71[f]	5.22[f]	-7.71[g]	-8.91[g]	-3.58[g]
	S	3.28	4.38	14.02	17.91	17.95
SPFD-e	$\gamma = \pi/2$	3.10	5.38	7.54	9.33	7.67
	$\gamma = \pi/4$	3.74	3.29	7.54	8.04	7.71
	$\gamma = 0$	4.3	1.2	7.5	8.6	7.7
	$L = 0$	3.52	3.99	7.54	8.53	7.69
	$L = 2$	0.81	-2.78	0	0	0
	S	3.76	2.50	6.85	7.15	7.83
MSV-e	$\gamma = \pi/2$	3.11	5.31	7.08	7.10	7.08
	$\gamma = \pi/4$	3.67	3.77	7.03	7.03	7.03
	$\gamma = 0$	4.2	2.2	7.0	7.0	7.0
	$L = 0$	3.48	4.29	7.05	7.05	7.05
	$L = 2$	0.70	-2.05	0	0	0
	S	3.66	2.91	6.80	7.11	7.22
MMSV-e	$\gamma = \pi/2$	3.11	5.38	6.91	6.91	16.16
	$\gamma = \pi/4$	3.67	3.60	6.91	6.91	16.16
	$\gamma = 0$	4.2	1.8	6.91	6.91	16.16
	$L = 0$	3.48	4.19	6.91	6.91	16.16
	$L = 2$	0.70	-2.38	0	0	0
	S	3.65	2.89	9.40	7.38	15.25

Table VI. continued

Potential type[a]	Characteristic[b]	r_m/Å	ϵ/meV[c]	β_z^d	β_i^d	β_r^d
HFD-e	$\gamma = \pi/2$	3.19	5.22	5.98	4.33	6.29
	$\gamma = \pi/4$	3.73	2.70	6.14	5.36	6.46
	$\gamma = 0$	4.2	1.6	6.2	7.2	6.5
	$L = 0$	3.55	3.61	6.08	6.37	6.40
	$L = 2$	0.69	-2.62	0.15	0.34	0.16
	S	3.65	2.78	6.02	6.07	6.44
LJ8-e	$\gamma = \pi/2$	3.14	4.98	6.42	6.03	7.79
	$\gamma = \pi/4$	3.76	3.06	6.71	6.43	7.97
	$\gamma = 0$	4.3	1.1	6.5	6.3	7.8
	$L = 0$	3.55	3.67	6.59	6.61	7.90
	$L = 2$	0.78	-2.55	0.17^f	0.17^f	0.11^f
	S	3.72	2.63	6.61	6.58	7.92
SPFD-p	$\gamma = \pi/2$	3.14	5.38	7.44	8.60	7.66
	$\gamma = \pi/4$	3.74	3.13	7.44	8.58	7.69
	$\gamma = 0$	4.3	0.9	7.4	8.9	7.6
	$L = 0$	3.54	3.88	7.44	8.41	7.67
	$L = 2$	0.80	-3.00	0^f	0^f	0
	S	3.75	2.48	6.79	7.05	7.83

Table VI. continued

Potential type[a]	Characteristic[b]	$r_m/\text{Å}$	ϵ/meV[c]	β_z[d]	β_i[d]	β_r[d]
LJ8-p	$\gamma = \pi/2$	3.16	4.94	6.44	6.06	7.80
	$\gamma = \pi/4$	3.06	3.76	6.71	6.59	7.97
	$\gamma = 0$	4.4	1.2	6.6	6.3	7.9
	$L = 0$	3.56	3.69	6.60	6.61	7.90
	$L = 2$	0.80	-2.50	0.19[f]	0.19[f]	0.12[f]
	S	3.75	2.56	6.62	6.63	7.92
Average[h]	$\gamma = \pi/2$	3.14	5.2	7.2	7.4	8.8
		(0.05)	(0.4)	(1.1)	(1.4)	(2.8)
	$\gamma = \pi/4$	3.73	3.4	7.3	7.9	8.8
		(0.04)	(0.5)	(0.6)	(2.5)	(2.8)
	$\gamma = 0$	4.2	2.0	8.0	8.1	9.9
		(0.07)	(0.7)	(1.4)	(1.8)	(3.5)
	$L = 0$	3.52	4.0	7.3	7.6	9.1
		(0.04)	(0.7)	(1.0)	(0.7)	(1.6)
	$L = 2$	0.75	-2.3	0.5	0.2	0.7
		(0.04)	(0.7)	(1.0)	(0.7)	(1.5)
	S	3.77	2.6	7.5	7.6	9.9
		(0.09)	(0.2)	(1.1)	(1.2)	(3.1)

[a]Please refer to tables III and IV for details concerning potential types.

[b]The characteristics include: profiles of the potential at approach angles $\gamma = \pi/2$, $\pi/4$, and 0; Legendre expansion of the potential parameters for orders $L = 0$ and $L = 2$, and the shape of the spherical average of the potential (S).

Table VI. continued

[c]The well minimum is found numerically using Newton's method for the
zero of the potential derivative. The "L = 0" and "L = 2" are the
Legendre projections of the parameter (as a function of angle
$\chi(\gamma)$ ($\chi = r_m, \epsilon, \beta$).

$$\chi_L = (L + \tfrac{1}{2}) \int_{-1}^{1} \chi(\gamma)\, P_L(\cos \gamma)\, d \cos \gamma$$

[d]The β's are the MMSV type (eqs. 20 and 21). β_z is found from the
zero point of the potential r_z,

$$\beta_z = \frac{\ln 2}{1 - r_z/r_m}$$

β_i is found from the potential's inflection point r_z ($\frac{d^2 V(r_z)}{dr^2} = 0$)

$$\beta_i = \frac{\ln 2}{r_i/r_m{}^{-1}}$$

The value β in the repulsive region is found by iteratively
fitting β' in equation (21a) with given $\beta = \beta_z, \epsilon$, and r_m to the
potential at $r = 0.8\, r_z$.
[f]Expansion terms of higher Legendre order exist for this parameter,
and are at least 5% of the zeroth term.
[g]Expansion terms of higher Legendre order exist for this parameter,
and are at least 25% of the zeroth order.
[h]The value of the above parameters (except for Morse -m) are
averaged. The standard deviations are in parentheses below each
parameter.

Table VII. Angular-dependent-parameter potentials for He + CS_2

Potential Type[a]	$r_m/\text{Å}$[b]	q[b]	$\epsilon^{(0)}/\text{meV}$[c]	$\epsilon^{(2)}/\epsilon^{(0)}$[c]	shape(1)[d]	shape(2)[d']	G/χ^e	χ^{2e}
MMSV-e	3.58	-0.506	4.28	-0.549	7.53	20.3	1.59	32.8
MSV-e	3.51	-0.543	4.31	-0.579	7.38		1.87	41.0
SPFD-e	3.61	-0.510	4.25	-0.658	62.0	-6.1[f]	1.84	39.4

[a] See note a of Table IV except of the dispersion terms which are $C_6 = 33.28 + 10.64\ P_2\ (\cos\gamma)$,

$C_8 = 137.21 + 160.20\ P_2\ (\cos\gamma)$.

[b-e] see corresponding notes of Table IV.

[f] This parameter is fixed, but if it is varied with the others there is no change in the quality of

fit or in b_1, which changes to -6.11.

Table VIII. Multicenter Potentials for He + CS$_2$

Potential Type[a]	Center[b]	r_m/Å	ε/meV	shape(1)[c]	shape(2)[c]	G/%[d]	χ^2[d]
MSV-m	C	3.68	4.04	8.44		1.80	38.2
	S	3.64	0.98	9.17			
MMSV-m	C	3.76	3.94	6.80	19.56	1.26	18.5
	S	3.90	0.52	6.80[e]	19.56[e]		
SPFD-m1	C	3.67	5.34	67.22	-6.0[f]	1.82	38.8
	S	4.11	0.33	25.08	-6.0[f]		
SPFD-m2	C	3.52	5.04	70.38	-8.91	1.88	41.4
	S	4.07	0.18	70.38[e]	-8.91[e]		
Morse-m	C	3.69	4.80	17.12		1.43	25.9
	S	4.80	1.71	4.02			

[a] See note a of Table III.

Table VIII. Continued.

^{b} The C-S bond distance is fixed at 1.554 Å. The van der Waal's dispersion terms are:

C_6 = 33.28 + 10.64 P_2 (cos γ); C_8 = 137.21 + 160.20 P_2 (cos γ). Each center contributes one-third of the dispersion. These are splined to the potential at r/r_m = 1.6.

$^{c-f}$ See corresponding notes of Table III.

Table IX. Summary of Characteristics of Best Fit Potentials for He + CS_2

Potential type[a]	Characteristic[b]	$r_m/Å$	ϵ/meV[c]	β_z[d]	β_i[d]	β_r[d]
MMSV-e	$\gamma = \pi/2$	3.58	5.46	7.53	7.63	20.34
	$\gamma = \pi/4$	4.41	3.70	7.53	7.56	20.34
	$\gamma = 0$	5.1	1.9	7.5	7.5	20.3
	$L = 0$	4.13	4.28	7.53	7.53	20.34
	$L = 2$	1.03	-2.35	0.0	0.0	0.0
	S	4.53	2.31	11.19	8.95	19.49
MSV-e	$\gamma = \pi/2$	3.51	5.55	7.38	7.38	7.38
	$\gamma = \pi/4$	4.43	3.68	7.38	7.38	7.38
	$\gamma = 0$	5.2	1.8	7.4	7.4	7.4
	$L = 0$	4.11	4.31	7.38	7.38	7.38
	$L = 2$	1.14	-2.49	0.0	0.0	0.0
	S	4.56	2.18	6.79	7.39	7.51
SPFD-e	$\gamma = \pi/2$	3.61	5.64	7.88	8.21	7.61
	$\gamma = \pi/4$	4.45	3.55	7.88	8.54	7.66
	$\gamma = 0$	5.2	1.5	7.9	8.2	7.6
	$L = 0$	4.16	4.25	7.88	8.69	7.64
	$L = 2$	1.05	-2.79	0.0	-0.11	0.03
	S	4.55	2.27	7.02	7.51	7.90

Table IX. Continued.

Potential type[a]	Characteristic[b]	$r_m/\text{Å}$	ε/meV[c]	$\varepsilon_z{}^d$	$\varepsilon_\ell{}^d$	$\varepsilon_r{}^d$
MSV-m	$\gamma=\pi/2$	3.63	5.38	8.29	8.94	8.38
	$\gamma=\pi/4$	4.41	4.07	8.85	11.95	9.45
	$\gamma=0$	5.1	2.6	11.0	12.1	12.7
	$L=0$	4.11	4.47	8.79	9.39	9.44
	$L=2$	1.02[f]	-2.06[f]	1.96[f]	2.07[g]	2.70[g]
	S	4.69	2.20	9.57	11.00	11.0
MMSV-m	$\gamma=\pi/2$	3.73	4.92	6.71	7.17	21.12
	$\gamma=\pi/4$	4.52	3.11	10.55	5.91	25.86
	$\gamma=0$	5.1	2.1	13.7	8.6	32.9
	$L=0$	4.20	3.79	10.17	7.31	22.02
	$L=2$	0.99[f]	-1.94[g]	5.91[g]	0.90[f]	7.58[g]
	S	4.85	2.07	14.41	15.31	24.18
SPFD-ml	$\gamma=\pi/2$	3.67	5.99	7.81	7.77	7.56
	$\gamma=\pi/4$	4.54	2.69	5.84	3.92	9.51
	$\gamma=0$	5.2	1.8	8.1	8.3	10.2
	$L=0$	4.15	4.06	7.39	8.40	8.49
	$L=2$	1.11[f]	-3.17[g]	-0.35[g]	-0.08[f]	1.70[f]
	S	4.67	2.00	7.01	6.60	10.10

Table IX. Continued.

Potential type[a]	Characteristic[b]	r_m/Å	ε/meV[c]	$\beta_z{}^d$	$\beta_i{}^d$	$\beta_r{}^d$
SPFD-m2	$\gamma=\pi/2$	3.54	5.28	8.66	11.83	9.32
	$\gamma=\pi/4$	4.60	3.37	7.22	8.02	6.42
	$\gamma=0$	5.2	1.6	9.6	9.5	11.3
	L=0	4.22	3.66	7.58	9.35	8.84
	L=2	1.13[f]	-1.99	1.68[g]	1.66[g]	-1.25[g]
	S	4.70	2.37	8.62	10.76	7.93
Morse-m	$\gamma=\pi/2$	3.76	5.43	13.20	20.26	18.21
	$\gamma=\pi/4$	5.62	2.26	4.50	4.49	3.86
	$\gamma=0$	6.3	2.0	5.2	5.3	5.2
	L=0	4.96	3.06	6.98	10.13	12.08
	L=2	1.82	-1.97[g]	-5.35[g]	-12.03[g]	-14.59[g]
	S	5.52	2.18	4.43	4.48	3.61
Average-h	$\gamma=\pi/2$	3.61 (0.07)	5.5 (0.3)	7.8 (0.6)	10.0 (5.)	12.0 (6.)
	$\gamma=\pi/4$	4.48 (0.07)	3.5 (0.4)	8.4 (1.6)	7.6 (2.5)	12.0 (8.)
	$\gamma=0$	5.2 (0.05)	1.9 (0.3)	11. (6.)	8.8 (1.6)	15. (9.)
	L=0	4.15 (0.04)	4.1 (0.3)	8.3 (0.9)	8.3 (0.9)	12. (6.)
	L=2	1.07 (0.06)	-2.4 (0.4)	1. (2.)	0.6 (0.9)	1.5 (3.)
	S	4.65 (0.11)	2.2 (0.1)	9.2 (2.8)	9.7 (3.0)	12.6 (6.6)

Table IX. Continued

---

[a] Please refer to Tables VII and VIII for details concerning
the potential types

[b - g] See corresponding notes for Table VI

[h] The averages are for all the above potentials (except for
Morse-m) with the standard deviations given in paren-
thesis.

Table X. Three-center MSV Potentials For He + OCS

Potential[a] Type	Center[b]	$Z/\overset{\circ}{A}$[b]	$r_m/\overset{\circ}{A}$	ϵ/meV	β	G^C	χ^{2C}
MSV-ml[d]	C	0.523	3.80	0.69	6.23	1.07%	26.3
	S	-1.037	3.90	3.75	6.23[f]		
	O	1.683	3.90	0.17	6.23[f]		
MSV-m2[e]	C	0.523	3.79	0.63	5.84	1.16	28.6
	S	-1.037	3.68	2.95	5.84[f]		
	O	1.683	4.14	0.72	5.84[f]		

[a] Refer to equation (11). These are three center potentials with an MSV spherical potential at each center.

[b] The distance z is from the center-of-mass of the OCS molecule, c is fixed in the least-squares parameter fitting procedure.

[c] See eq. (29) for G and eqs. (27-28) for χ^2.

[d] The long range dispersion part of this potential was constructed by giving the MSV potential centered at the O one-half of the He + CO_2 dispersion terms as given in Table III (see eq. (20c)), and by giving the MSV potential centered at the S one-half of the He + CS_2 dispersion terms. While the C-centered MSV is given dispersion terms of value zero.

[e] The long range dispersion part of this potential was constructed in the same manner as for the He + CO_2 and CS_2 multi-centered potentials. The dispersion coeficients are the same as given in Table X (footnote g).

Table XI. Angular-dependent-parameter Potentials for He + OCS

Potential Type[a]	$r_{m_1}/Å$[b]	q[b]	$\epsilon^{(0)}/meV$[c]	$\epsilon^{(2)}/\epsilon^{(0)}$[c]	β	β'	G[d]	χ^2[d]
Morse-e	4.50	0.978	3.04	1.14	5.16		1.19%	31.6
MMSV-e[e]	3.59	-0.474	4.34	-0.228	7.38	5.90	1.17	29.6

[a] Refer to equation (13). The designation "-e" classifies the potential as having an elliptical form for $r_m(\gamma)$.

[b] Elliptical form for $r_m(\gamma)$ is given by eqs. (15-16).

[c] Legendre expansion of $\epsilon(\gamma)$ is given by eq. (14).

[d] G is defined by eq. (29). χ^2 is given by eqs. (27-28).

[e] Approximated dispersion terms for He + OCS are given as (see text for derivation)

$C_6 = 21.63 + 6.37 P_2 (\cos\gamma)$ eV · Å⁶ and $C_8 = 91.81 + 104.30 P_2 (\cos\gamma)$ eV · Å⁸

Table XII. Summary of Characteristics of Best Fit Potentials for He + OCS

Potential Type[a]	Characteristic[b]	$r_m/Å$	ϵ/meV[c]	β_z[d]	β_t[d]	β_r[d]
MMSV-e	$\gamma=\pi/2$	3.59	4.83	7.36	7.36	5.90
	$\gamma=\pi/4$	4.32	4.09	7.36	7.36	5.90
	$\gamma=0$	4.9	3.3	7.36	7.36	5.90
	L=0	4.07	4.33	7.36	7.36	5.90
	L=2	0.92	-0.99	0.0	0.0	0.0
	S	4.43	2.61	6.63	7.38	6.30
MSV-m1	$\gamma=0$	5.2	0.8	7.9	13.5	7.8
	$\gamma=\pi/4$	4.34	1.60	6.34	6.39	6.32
	$\gamma=\pi/2$	3.76	4.60	5.80	5.92	5.71
	$\gamma=3\pi/4$	4.55	4.07	7.06	6.90	7.01
	$\gamma=\pi$	4.9	3.9	7.9	7.6	7.9
	L=0	4.21	3.51	6.40	6.52	6.42
	L=1	-0.10	-1.56	-0.46	-0.36	-0.29
	L=2	0.92	-1.70	1.27	1.04	1.44
	L=3	0.35	-0.30	0.32[f]	0.17[f]	0.39
	S	4.53	2.34	6.90	7.02	7.03
MSV-m2	$\gamma=0$	5.7	1.2	7.5	8.0	8.0
	$\gamma=\pi/4$	4.95	1.59	6.34	6.50	6.15
	$\gamma=\pi/2$	3.62	4.17	5.31	5.69	5.23
	$\gamma=3\pi/2$	4.34	3.75	6.10	6.71	6.00

Table XII. Continued.

Potential Type[a]	Characteristic[b]	$r_m/\text{Å}$	ε/meV[c]	$\beta_2^{\ d}$	$\beta_i^{\ d}$	$\varepsilon_r^{\ d}$
MSV-m2	$\gamma=\pi$	4.7	4.7	6.7	8.3	7.1
(Continued)	$L=0$	4.28	3.14	5.93	6.14	6.08
	$L=1$	0.43	-1.64	0.18	0.23	-0.05
	$L=2$	1.10	-0.91	1.19	1.04	1.65
	$L=3$	0.10^g	0.21^g	-0.03^f	0.22^f	0.53^f
	S	4.79	1.72	6.23	6.24	6.61
MSV-m1[h]	$\gamma=0$	5.4	1.8	7.3	7.5	8.0
	$\gamma=\pi/4$	4.70	2.29	5.94	5.13	6.45
	$\gamma=\pi/2$	3.62	4.17	5.31	6.22	5.23
MSV-m2[h]	$\gamma=0$	5.0	2.2	7.8	9.6	8.0
	$\gamma=\pi/4$	4.51	2.79	6.91	6.83	6.90
	$\gamma=\pi/2$	3.76	4.60	5.80	6.07	5.71

[a] Please refer to tables X and XI for details concerning the potential types.

[b] The characteristics include: Profiles of the potential at approach angles $\gamma=0$, $\pi/4$, $\pi/2$, and for the non-centrosymmetric potential, also at $\gamma=3\pi/4$ and π; Legendre expansion of the potential parameters for orders up to $L=3$ (the $L=1$ and $L=3$ terms are zero for the centro-symmetric potentials); and the shape of the spherical average of the potential (S).

Table XII. Continued.

c) - g) See corresponding notes for Table VI.

h) Average of the corresponding non-centrosymmetric potential
about a plane perpendicular to the molecular axis and passing
through the center-of-mass of the OCS; i.e., $V(r,\gamma)$ =
1/2 $[V(r,\gamma) + V(r,\pi - \gamma)]$.

Figure 1. Vertical cut view of the crossed molecular beam apparatus, drawn approximately to scale. DP = diffusion pumps, PB = primary beam source - beam axis is parallel to drawing, Nz = nozzle (64 mm), Sk = skimmer, VS = velocity selector, Ch = beam modulation chopper, SB = secondary beam source - beam axis is perpendicular to plane of drawing, θ_h = in plane angle of detector as measured from the PB axis, θ_v = out-of-plane angle of detector, MS = mass spectrometer detector, GV = gate valve in front of the mass spectrometer entrance apperture, IP_b = 5 l/sec ion pump for buffer chamber, I = ionizer and ion focus lenses (l-N_2 cooling coils around filament not shown), CEM = Channeltron electron multiplier (Model 4816), CP = liquid He cryopump (350 l/sec), IP = 25 l/sec ion pump, IG = ionization gauge, BV = bake out and vent valve.
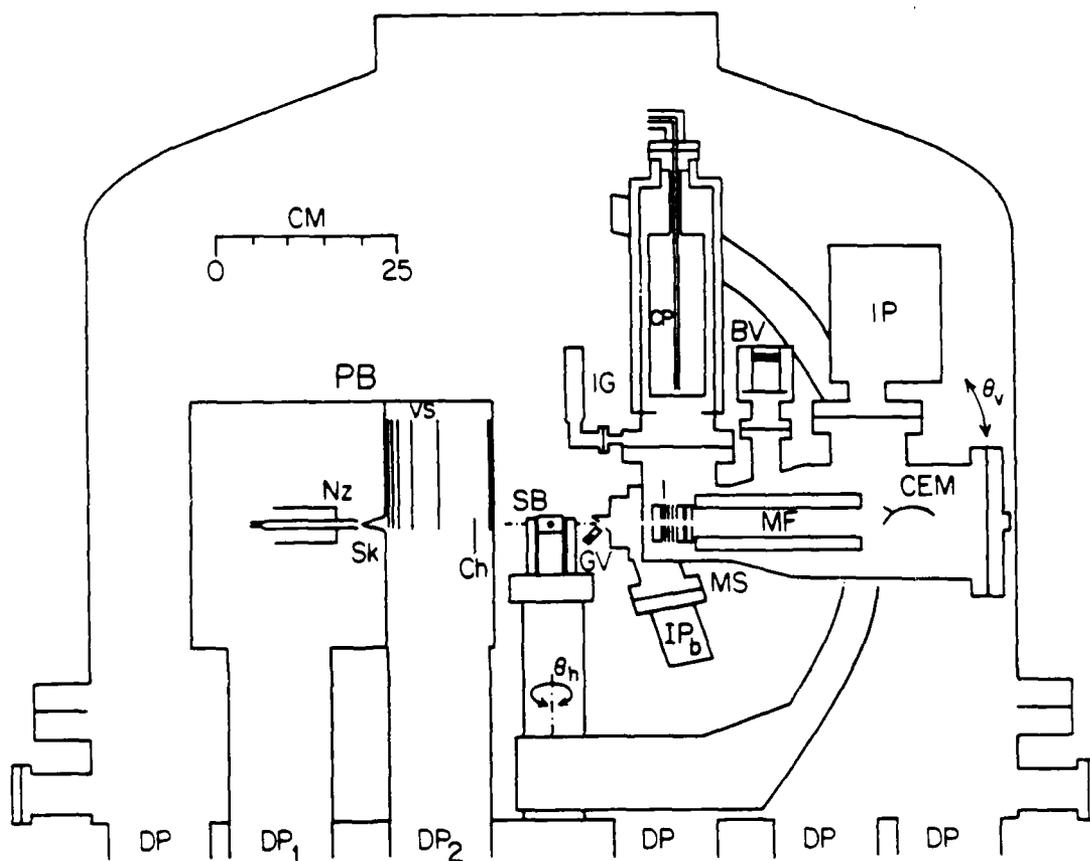
Figure 1.

Figure 2. Laboratory differential cross section for out-of-plane scattering of He by CO_2. Experimental points are plotted with their error bars. The solid curve is the calculated cross-section from the best fit anisotropic potential SPFD-e (see Table IV). The broken curve is for the best fit spherical potential (see Table II).
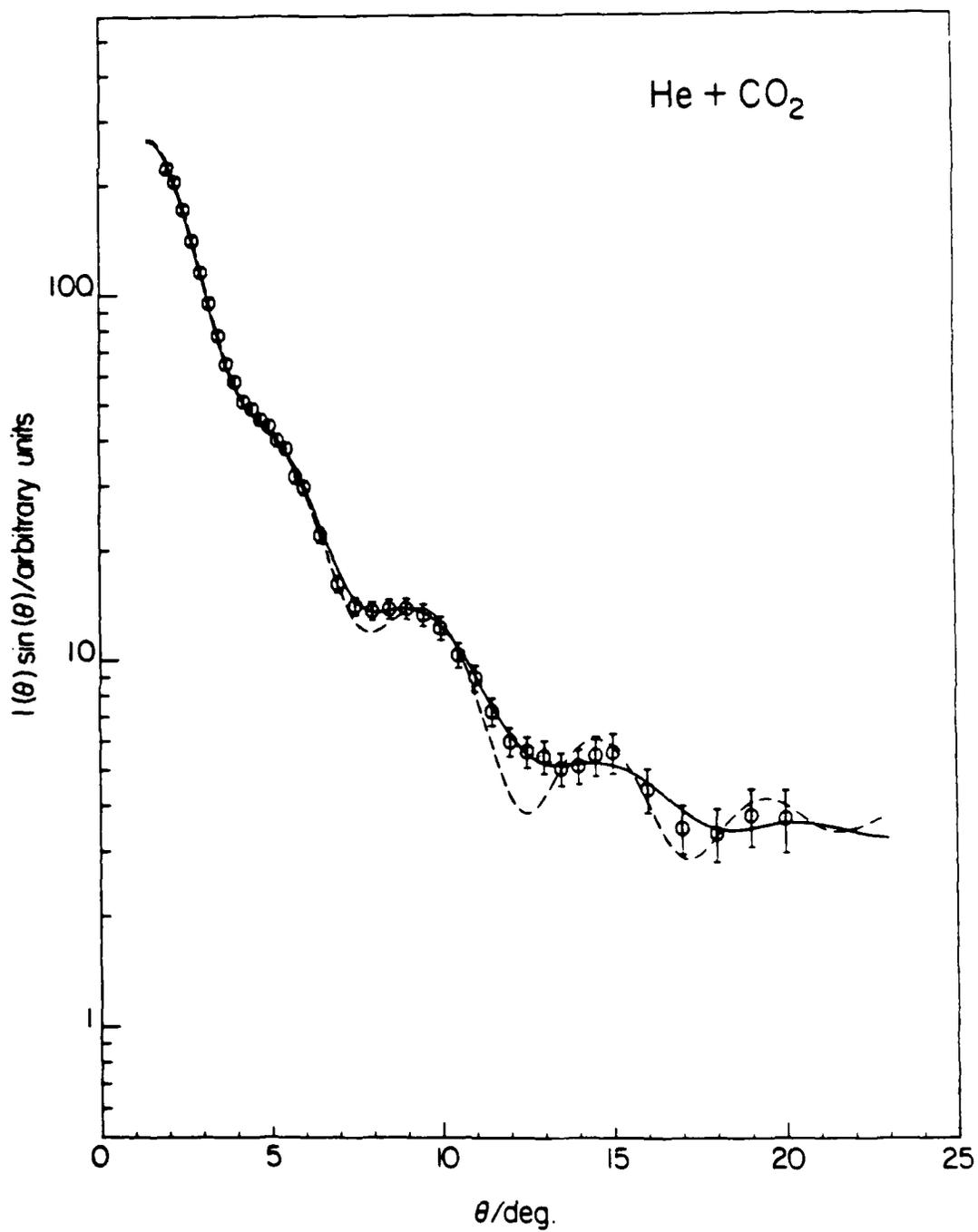
Figure 2.

Figure 3. Laboratory differential cross section for out-of-plane scattering of He by CS_2. Experimental points are plotted with their error bars. The solid curve is the calculated cross section for the best fit anisotropic potential MMSV-m (see Table VIII). The broken curve is for the best fit spherical potential (see Table II).
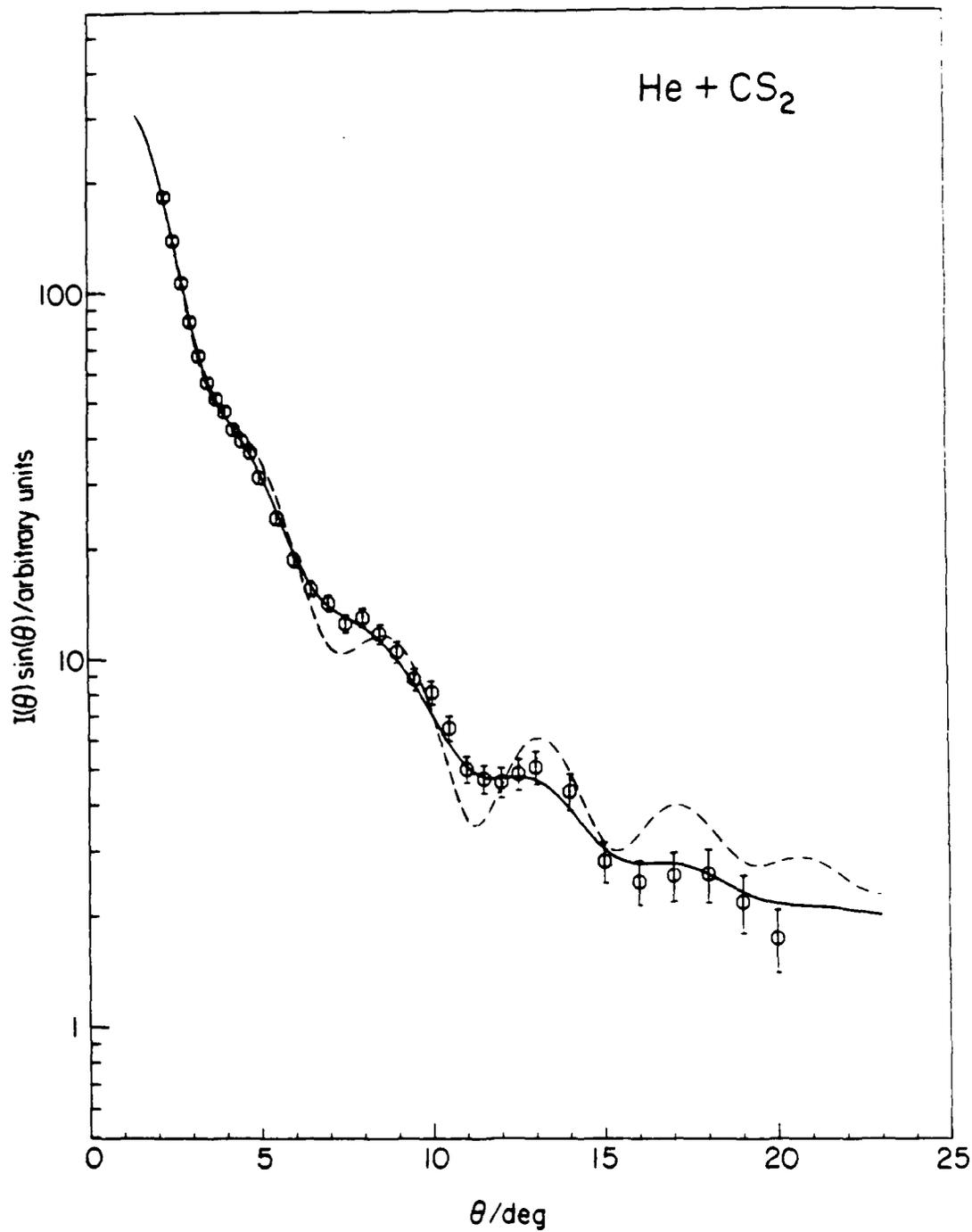
Figure 3.

Figure 4. Laboratory differential cross section for out-of-plane scattering of He by OCS. Experimental points are plotted with their error bars. The solid curve is the best fit anisotropic potential, the three-center MSV (see Table X). The broken curve is for the best fit spherical potential (see Table II).
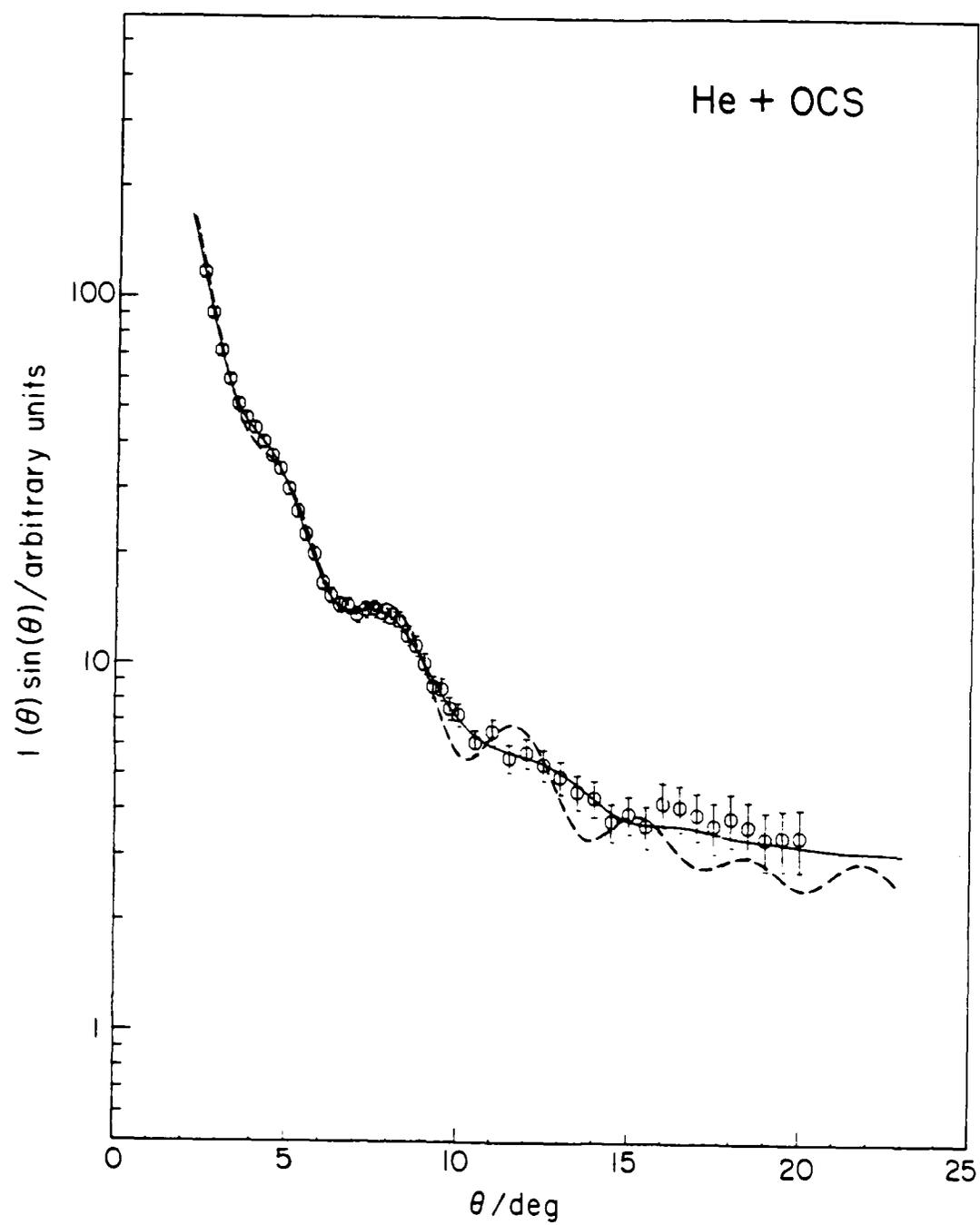
Figure 4.

Figure 5. Calculated laboratory cross sections for test of He + CO_2 anisotropy. The potentials are those listed in Table V. The solid curve is for a potential with r_m and ϵ anisotropy (test A). The long dashed curve is for the potential with no ϵ anisotropy (test B). The short dashed curve is for the potential with r_m and β anisotropy (test C). The short-long dashed curve is for the potential with no r_m anisotropy (tests D and E, for which the plot are indistinguishable).
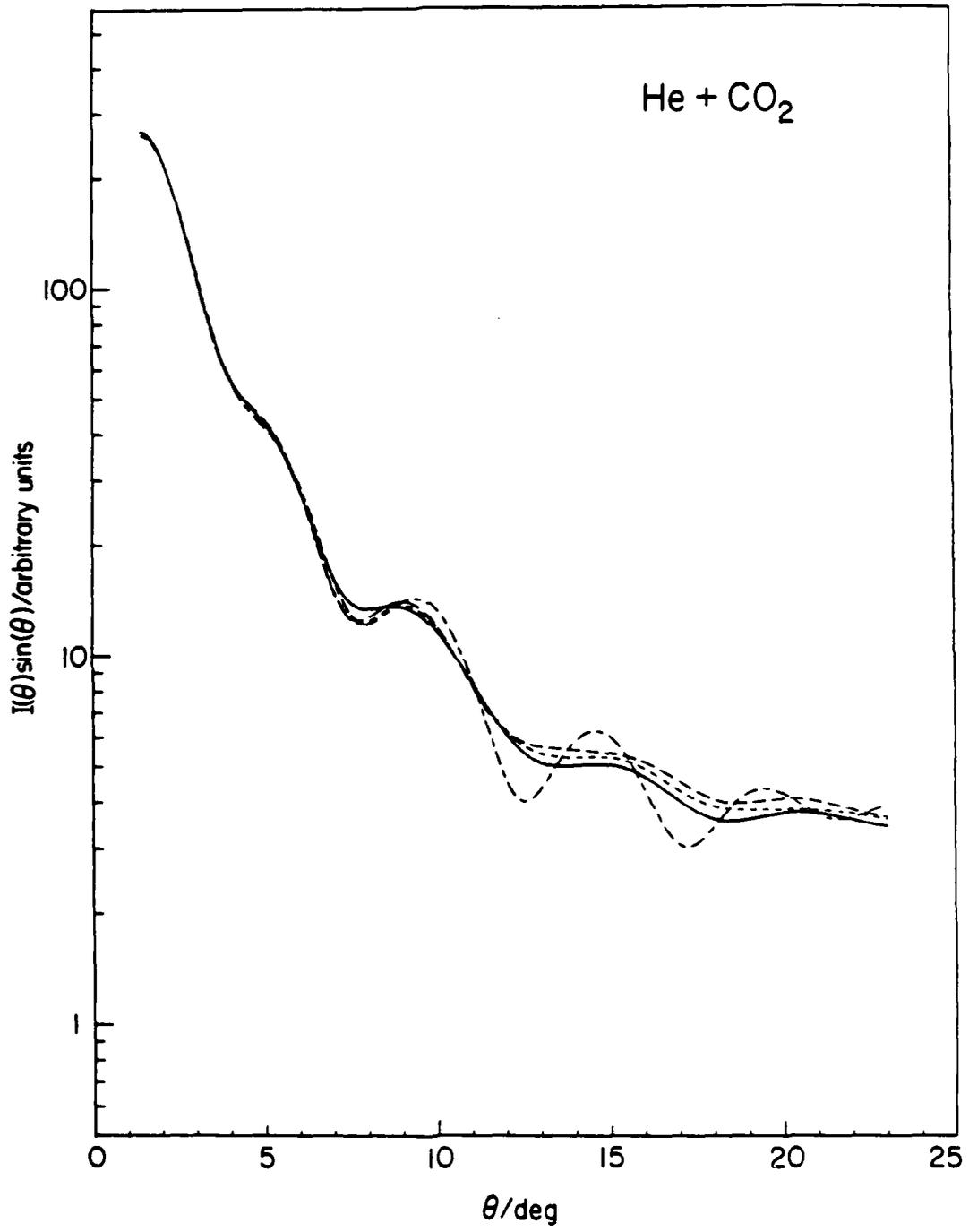
Figure 5.

Figure 6. Equipotential contours for the He + CO_2 SPFD-m1 potential (see Tables III and VI). The indicated contour values are in meV, while the tick marks are in Ångstroms. The attractive region is indicated by solid curves, the repulsive by the small dashes, and the zero of the potential by the large dashes. The minimum of the potential is -5.83 meV at r = 3.20 Åand $\gamma = \pi/2$. The saddle point is at r = 4.3 Å$\gamma = 0$ (and also $\gamma = \pi$) with a value of 2.1 meV. The centers of the C and O atoms are separated by 1.1621 Å.
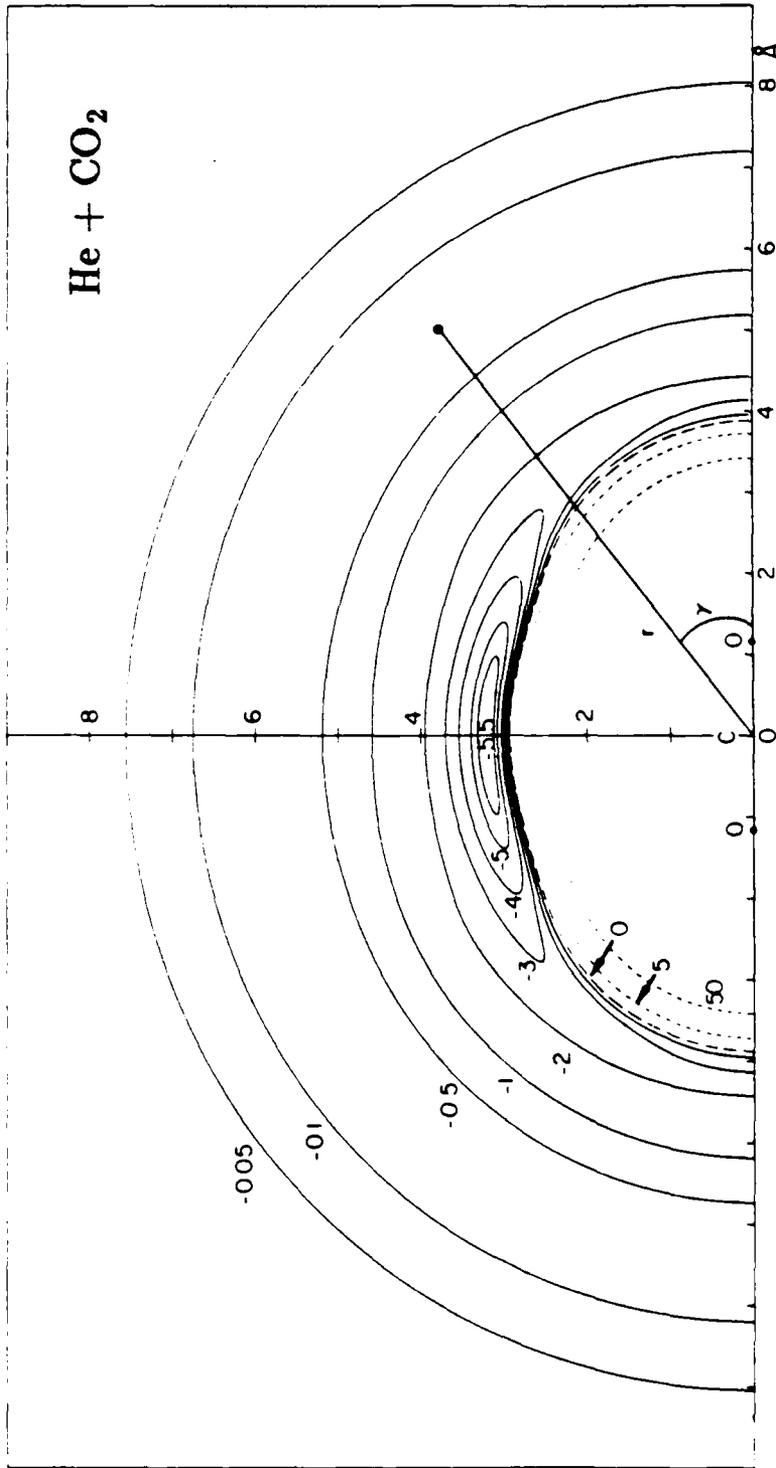
Figure 6.

Figure 7. He + CO_2 SPFD-m1 potential for three fixed approach angles γ, 0, 45, and 90 degrees and the spherical average of the potential (dashed curve). Please refer to Table VI for numerical details.
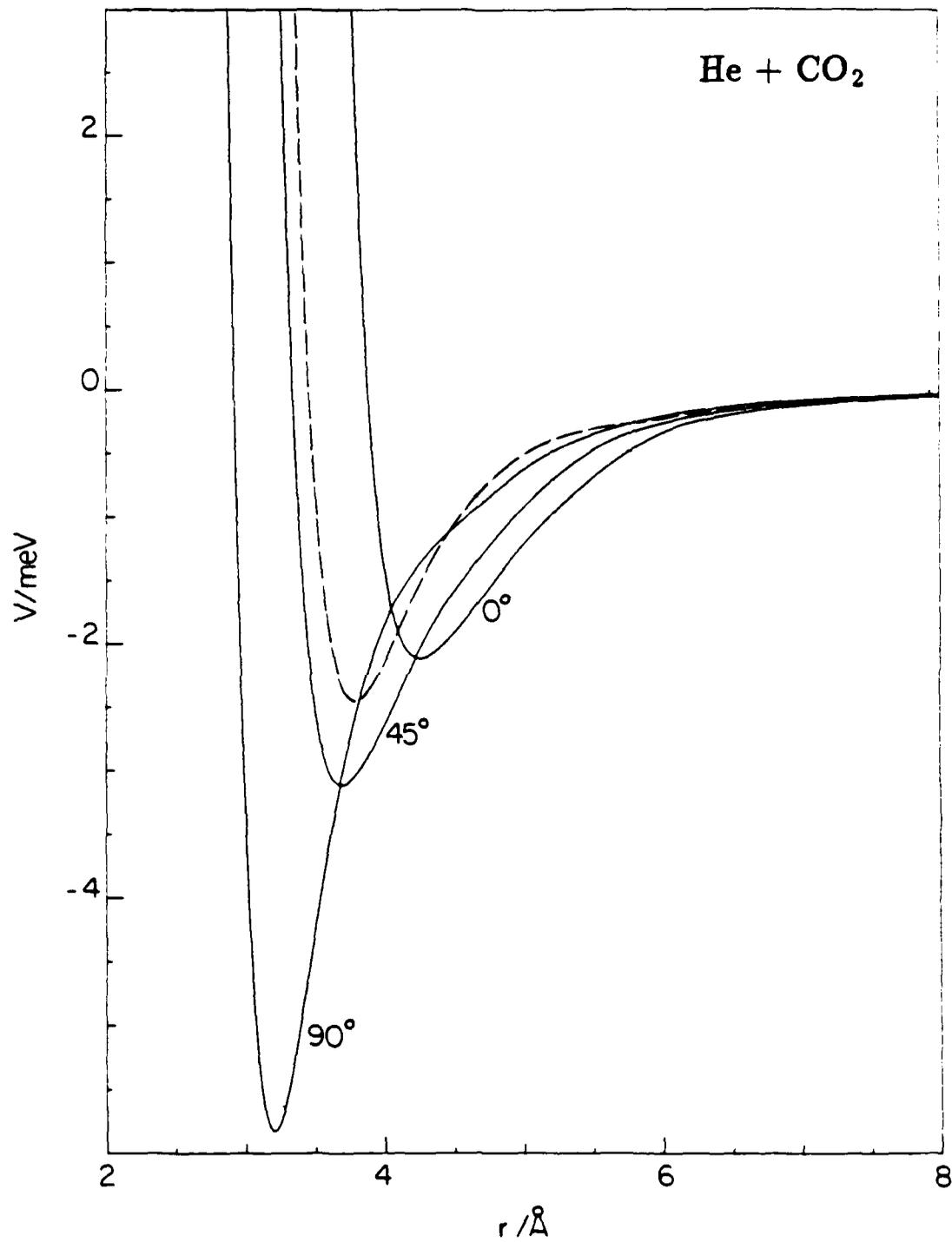
Figure 7.

Figure 8. Equipotential contours for the He + CO_2 SPFD-e potential (see Tables III and VI). The indicated contour values are in meV, while the tick marks are in Ångstroms. The attractive region is indicated by solid curves, the repulsive by the small dashes, and the zero of the potential by the large dashes. The minimum of the potential is -5.38 meV at r = 3.10 Åand $\gamma = \pi/2$. The saddle point is at r = 4.3 Å$\gamma = 0$ (and also $\gamma = \pi$) with a value of 1.2 meV. The centers of the C and O atoms are separated by 1.1621 Å.
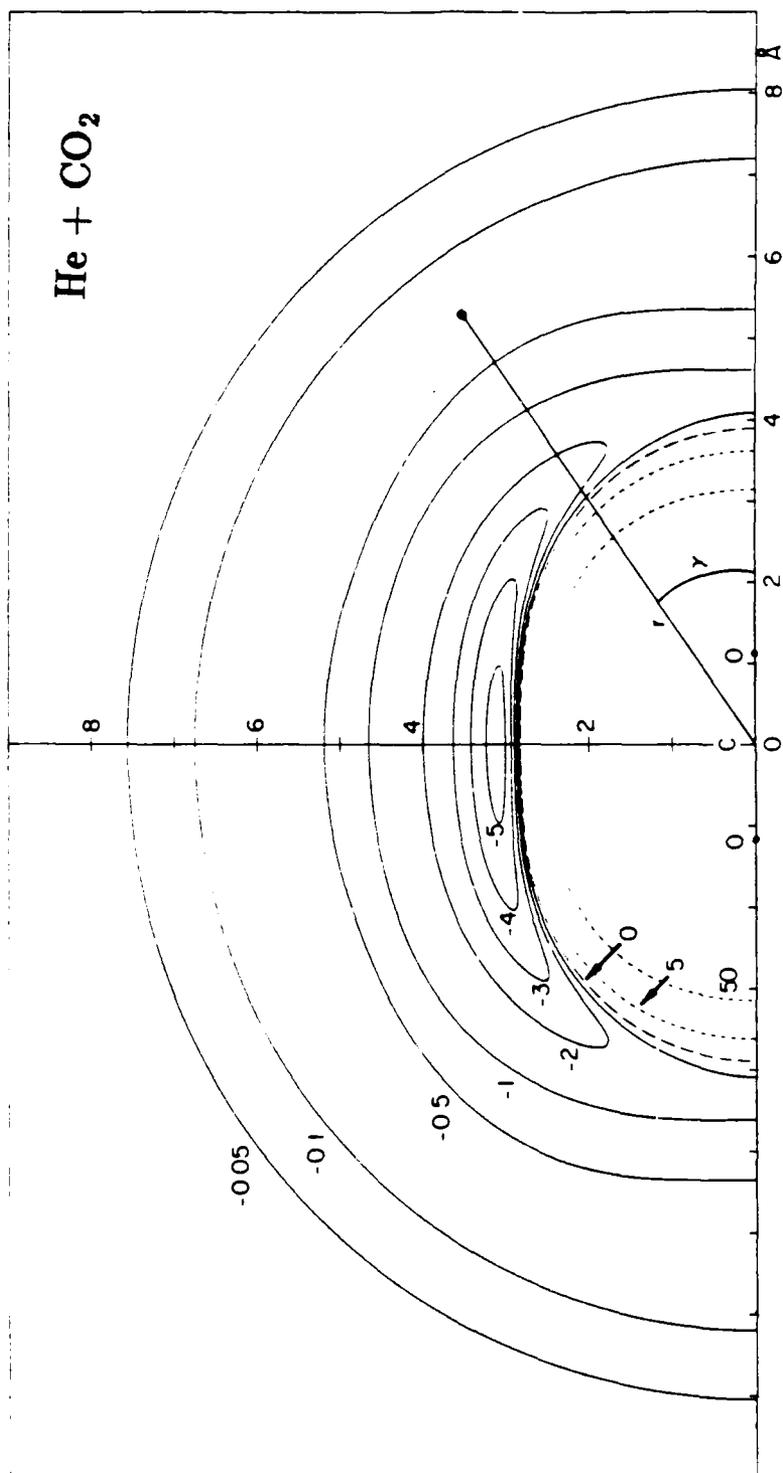
He + CO₂

Figure 8.

Figure 9. He + CO_2 SPFD-e potential for three fixed approach angles γ, 0, 45, and 90 degrees and the spherical average of the potential (dashed curve). Please refer to Table VI for numerical details.
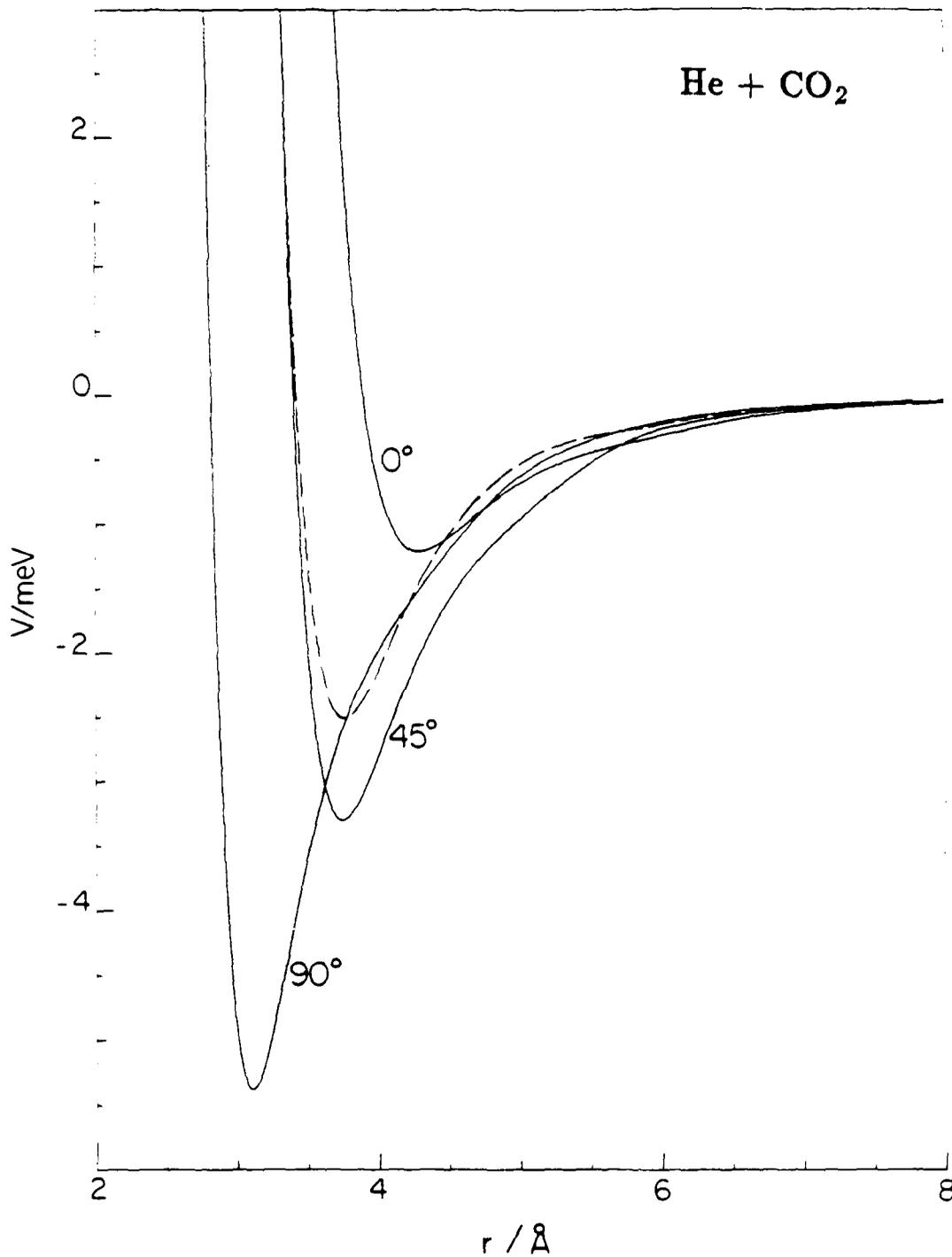
Figure 9.

Figure 10. Equipotential contours for the He + CS_2 MMSV-m potential (see Tables VII and IX). The indicated contour values are in meV, while the tick marks are in Ångstroms. The attractive region is indicated by solid curves, the repulsive by the small dashes, and the zero of the potential by the large dashes. The minimum of the potential is -4.92 meV at $r = 3.73$ Åand $\gamma = \pi/2$. The saddle point is at $r = 5.1$ Å$\gamma = 0$ (and also $\gamma = \pi$) with a value of 2.1 meV. The centers of the C and S atoms are separated by 1.554 Å.
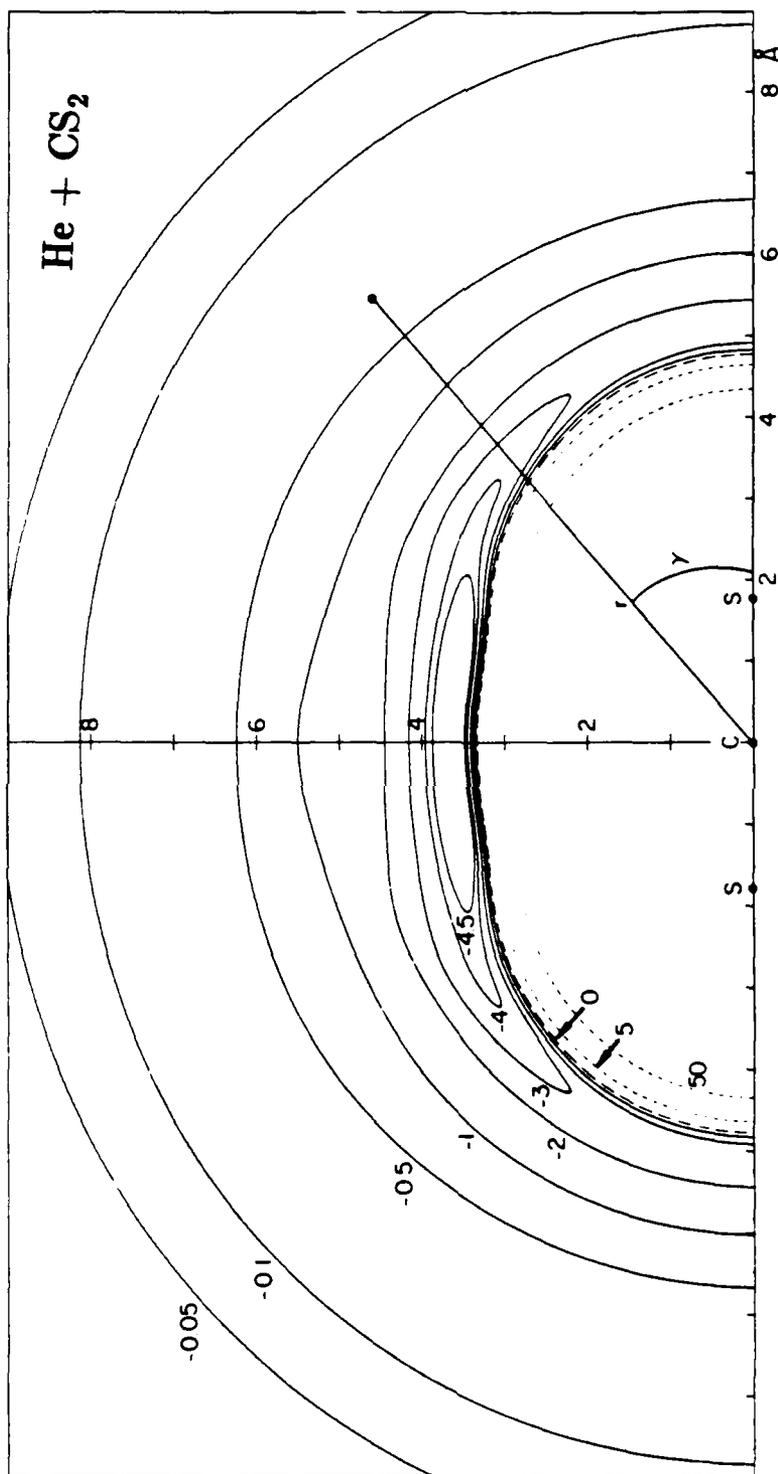
Figure 10.

Figure 11. He + CS_2 MMSV-m potential for three fixed approach angles γ, 0, 45, and 90 degrees and the spherical average of the potential (dashed curve). Please refer to Table IX for numerical details.
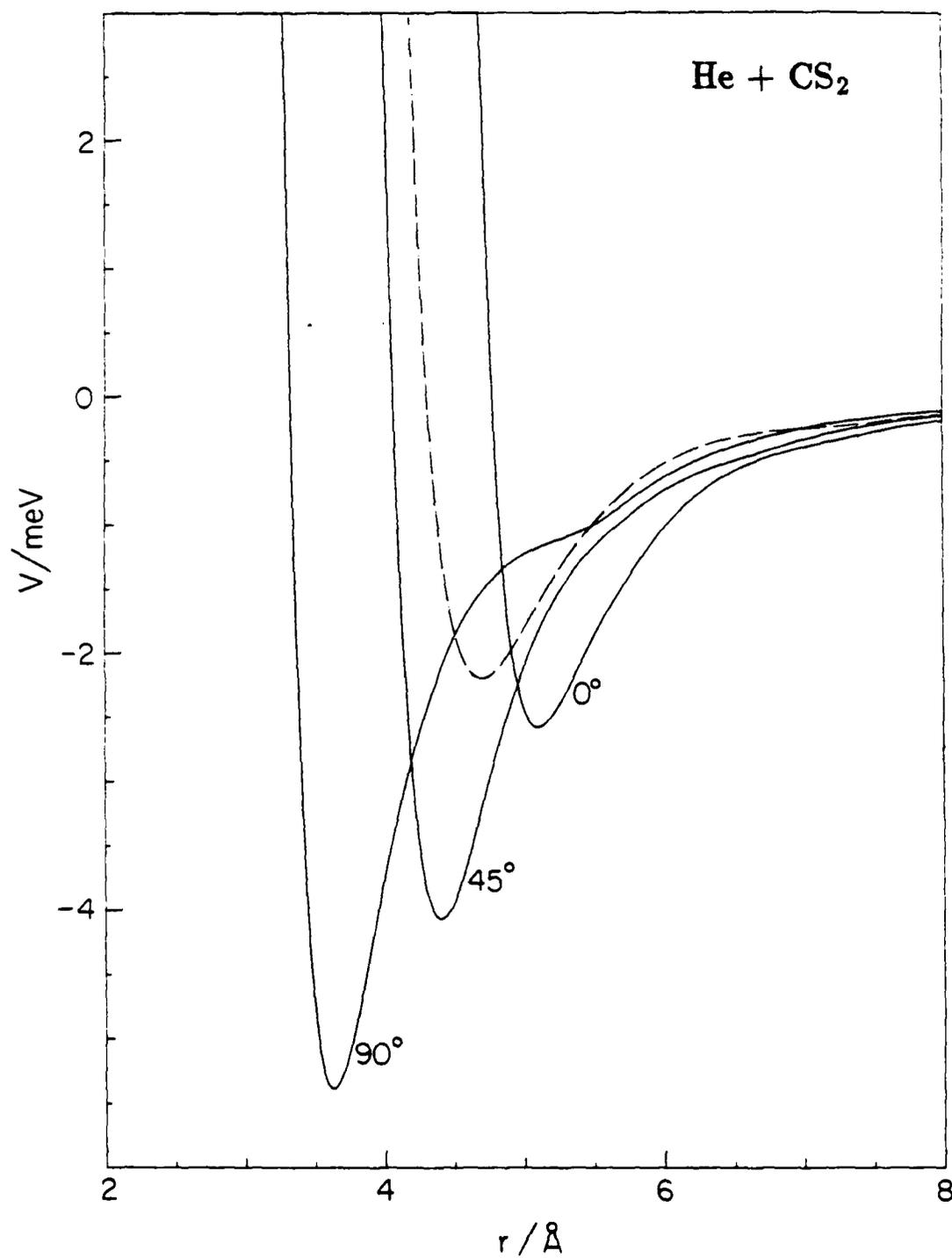
Figure 11.

Figure 12. Equipotential contours for the He + OCS MSV-m1 potential (see Tables X and XII). The indicated contour values are in meV, while the tick marks are in Ångstroms. The attractive region is indicated by solid curves, the repulsive by the small dashes, and the zero of the potential by the large dashes. The minimum of the potential is -4.6 meV at $r = 3.76$ Åand $\gamma = \pi/2$. One saddle point is at $r = 5.2$ Å$\gamma = 0$ with a value of -0.8 meV, the other saddle point is at $r = 4.9$ Å$\gamma = \pi$ with a value of -4.9 meV. The distance between the nuclei of the C and S atoms 1.560 Å, and the distance between the nuclei of the C and O atoms is 1.160 Å.
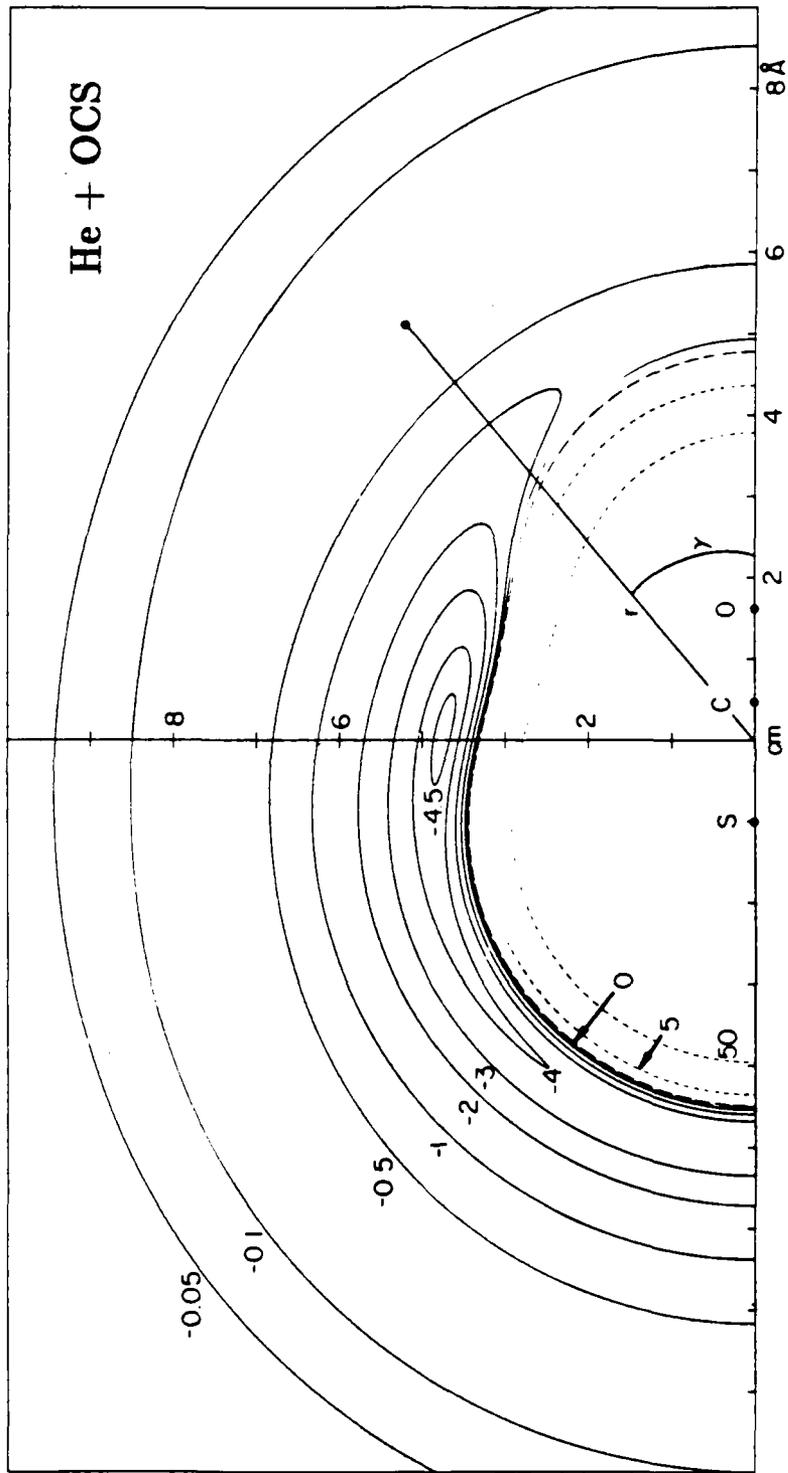
Figure 12.

Figure 13. He + CS_2 MMSV-m potential for three fixed approach angles γ, 0, 45, 90, 135, and 180 degrees and the spherical average of the potential (dashed curve). Please refer to Table XII for numerical details.
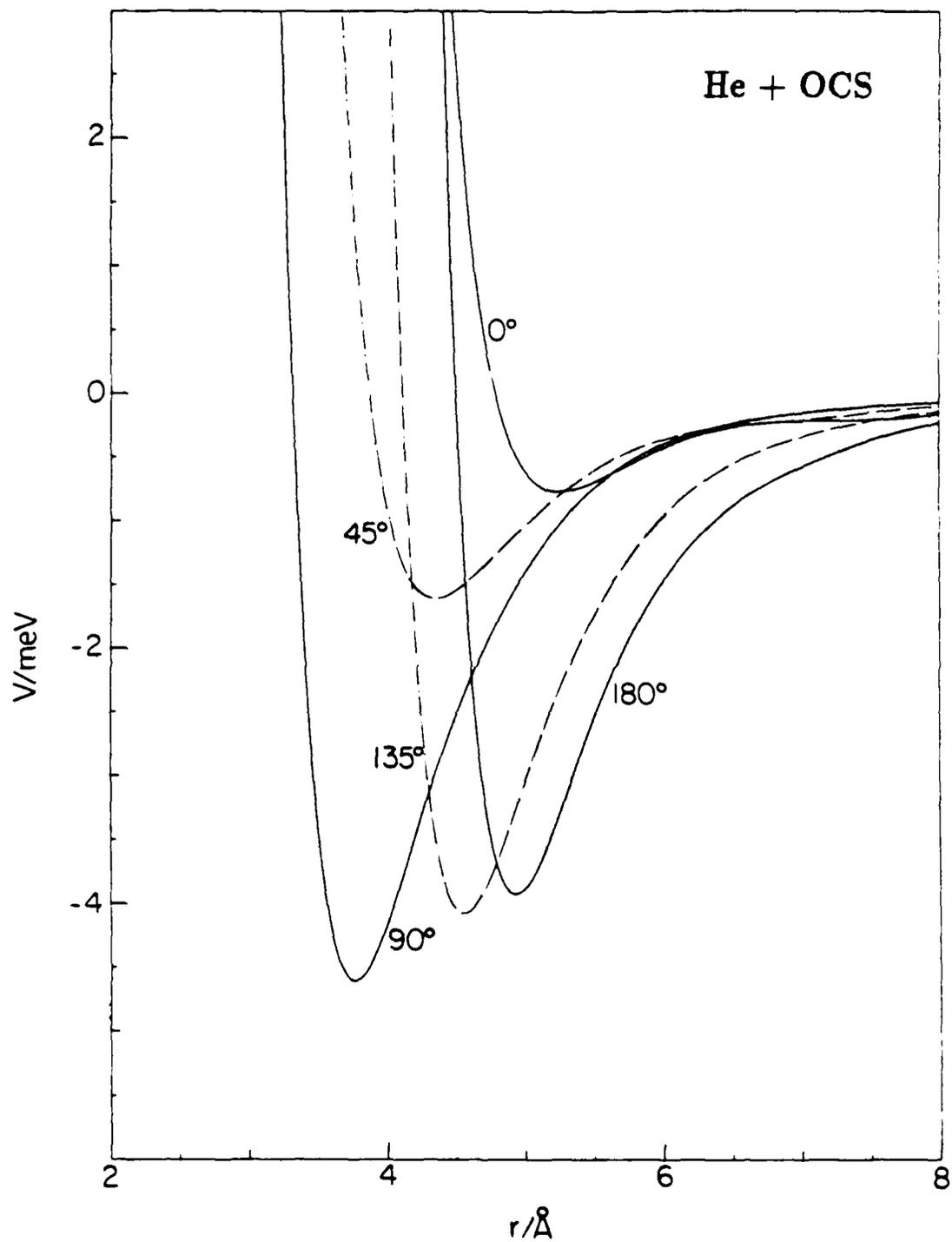
Figure 13.

Figure 14. Total integral cross sections as a function of the He beam velocity v_1. Points are from data of Butz et al. . The curve is a calculation for the He + CO_2 SPFD-e potential (Table IV). The ordinate scale is designed to exaggerate oscillatory behavior.
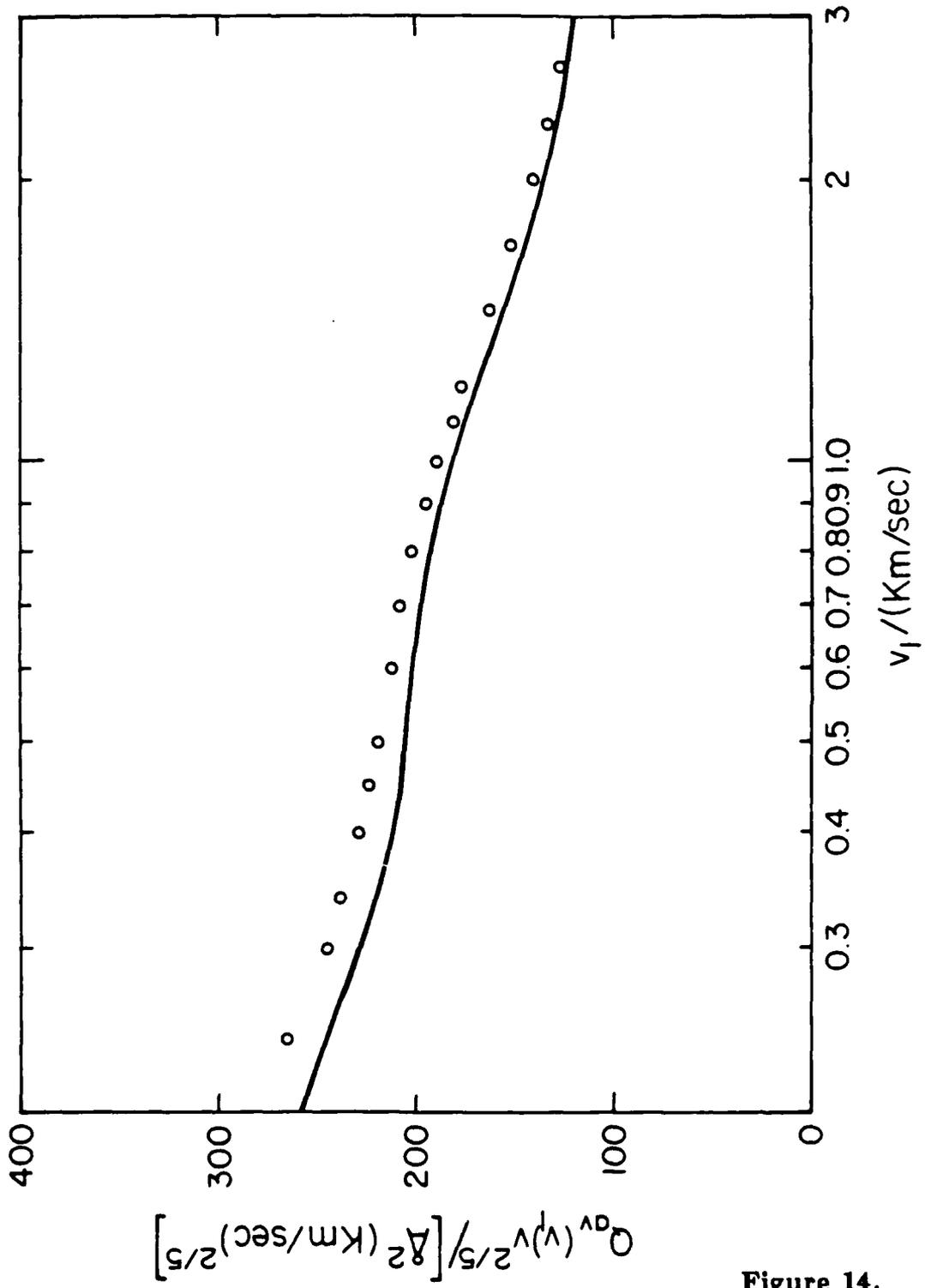
Figure 14.

Figure 15. Interaction diffusion coefficients as a function of temperature. Points are from various references (see text). The curve is a calculation for the He + CO_2 SPFD-e potential (Table IV).
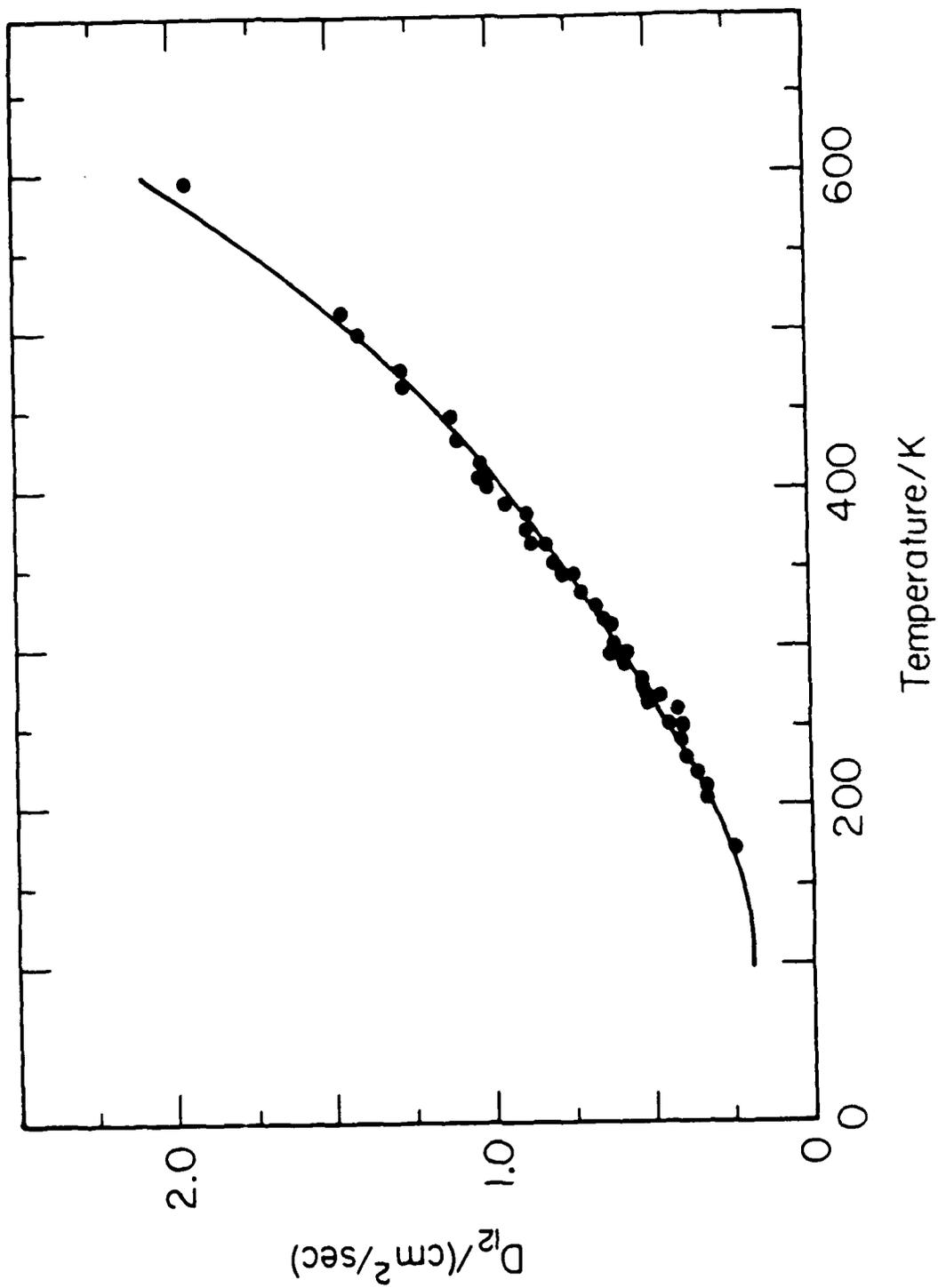
Figure 15.

Figure 16. Mixture viscosity coefficients as a function of temperature for two different mole fractions of CO_2: $x_{CO_2} = 0.0928$ (upper curve) and $x_{CO_2} = 0.6015$ (center curve). The lower curve is for the interaction viscosities η_{12}. See text for references on the points. The curves are calculations for the He + CO_2 SPFD-e potential (Table IV).
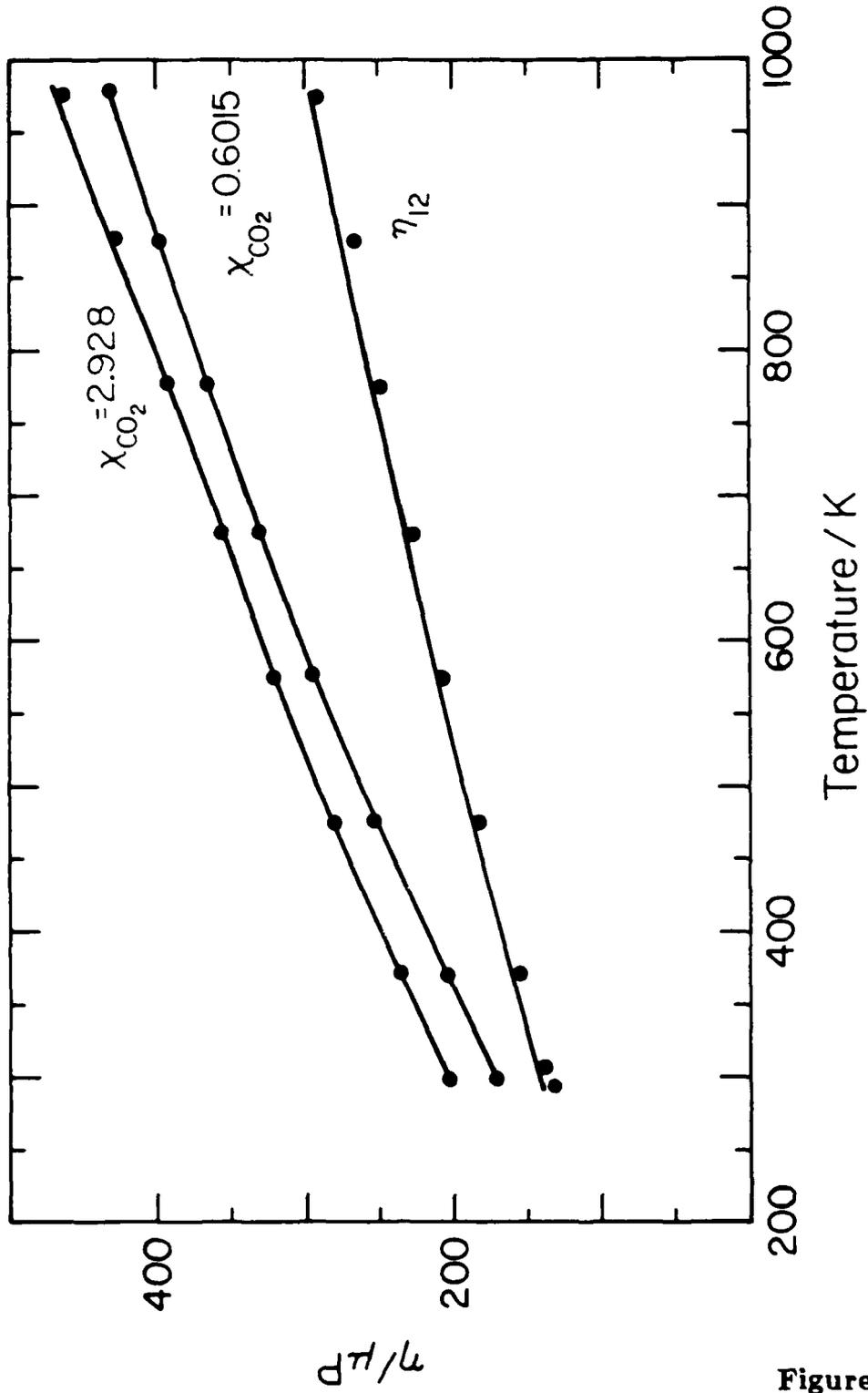
Figure 16.

Figure 17. Interaction second virial coefficients as a function of temperature. The curve is a calculation for the He + CO_2 SPFD-e potential (Table IV). See text for references on the points.
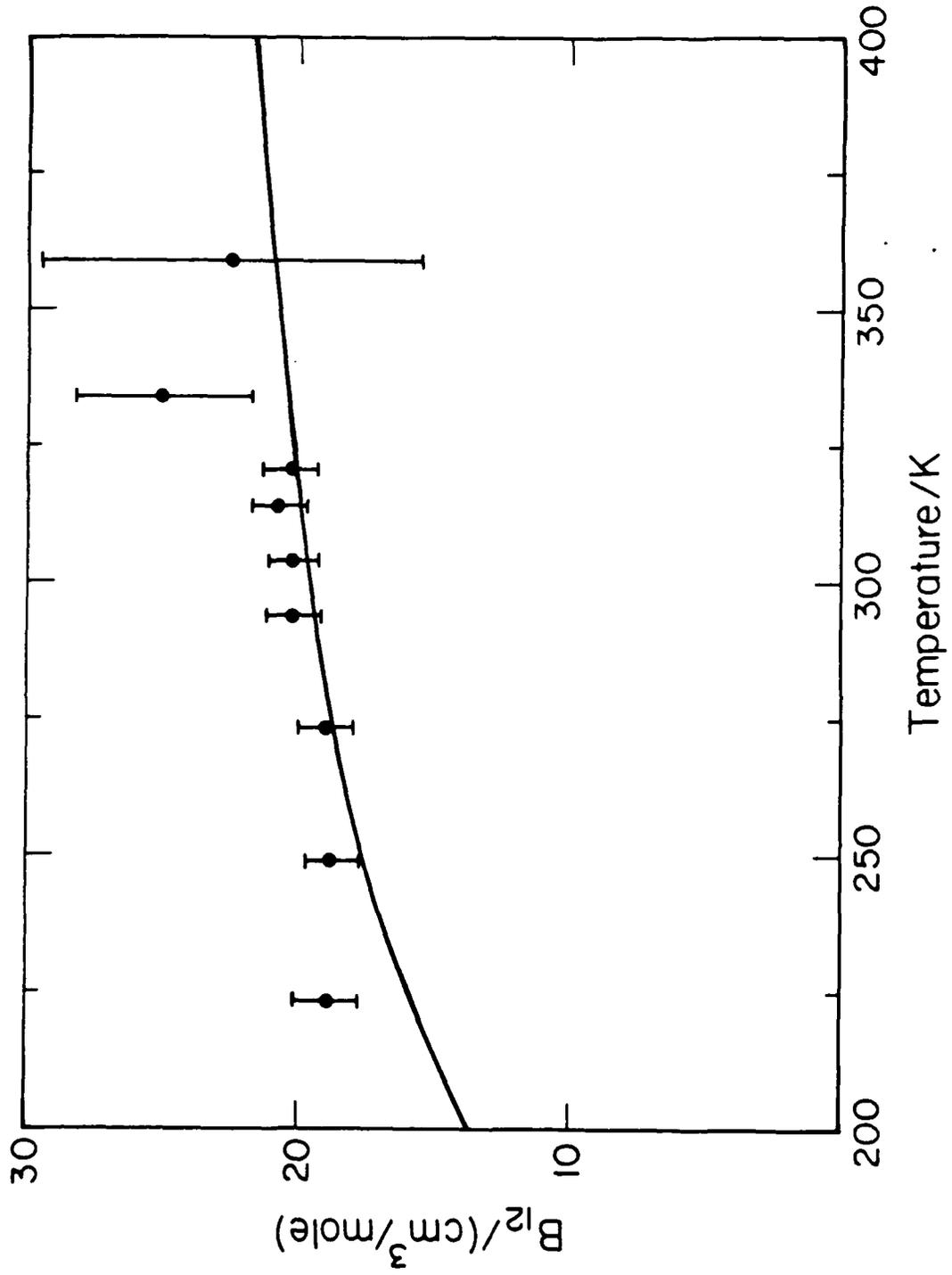
Figure 17.

50. W. S. Young, W. E. Rodgers, and E. L. Kunth, *Rev. Sci. Instrum.*, **40**, 1346 (1969).

51. K. R. Way, S.-C. Yang, and W. C. Stwalley, *Rev. Sci. Instrum.*, **9**, 1049 (1976).

52. J. F. Garvey and A. Kuppermann, *Rev. Sci. Inst. um.*, in press.

53. K. C. Kulander and M. F. Guest, *J. Phys. B: Atom. Moles. Phys.*, **12**, L501 (1979).

54. D. Datz and E. H. Taylor, *J. Chem. Phys.*, **25**, 389 (1956).

55. E. F. Greene, A. Persky, and A. Kuppermann, *J. Chem. Phys.*, **49**, 2347 (1968).

56. Oriel Corporation Catalog, Stamford, Conn., p. D30 (1979).

57. S. Rosin and I. Rabi, *Phys. Rev.* **48**, 373 (1935).

58. R. D. Levine and R. B. Bernstein, *Molecular Reaction Dynamics*, Oxford University Press, New York (1974)., a) p.16 , b) p.86.

59. E. W. Rothe, Ph.D thesis, University of Michigan (1959). Available from University Microfilms, Inc., Ann Arbor, Michigan

60. P. Rosenberg, *Phys. Rev.*, **61**, 528 (1942).

61. L. Loeb, *Kinetic Theory of Gases*, McGraw-Hill, New York (1934).

62. R. B. Bernstein, *Chemical Dynamics via Molecular Beam and Laser Techniques*, Oxford University Press p. 77 (1982).

63. G. Das, A. F. Wagner, and A. C. Wahl, *J. Chem. Phys.*, **68**, 4917 (1978).

64. E. W. Rothe and R. B. Bernstein, *J. Chem. Phys.*, **31**, 1619 (1959).

65. J. Peter Toennies, W. Welz, and G. Wolf, *J. Chem. Phys.*, **71**, 614 (1979).

66. A. A. Radzig and B. M. Smirnov, *Reference Data on Atoms, Molecules, and Ions*, Springer-Verlag p.408, (1985).

67. A. Streitwieser, Jr., and C. H. Heathcock, *Introduction to Organic Chemistry*, Macmillan Publishing Co. (1976) p.96.

68. K. T. Gillen, A. M. Rulis, and R. B. Bernstein, *J. Chem. Phys.*, **54**, 2831, (1971).

69. I. Langmuir and K. H. Kingdon, *Proc. Roy. Soc. (London)*, **A107**, 61 (1925).

70. M. J. Copley and T. E. Phipps, *Phys. Rev.*, **48**, 960 (1935).

71. E. Ya. Zandberg and N. I. Ianov, *Usp. Fig. Nauk.*, **67**, 581 (1959).

72. E. F. Green, J. T. Keeley and M. A. Pickering, *Surf. Sci.*, **120**, 103 (1982).

73. K. T. Gillen, C. Riley, and R. B. Bernstein, *J. Chem. Phys.*, **50**, 4019 (1969).

74. K. P. Wojciechowski, *Surface Sci.*, **55**, 246 (1976).

75. V. N. Kondratiev, *Bond Dissociation Energies, Ionization Potentials and Electron Affinities*, Mauka Publishing House, Moscow, (1974).

76. W. E. Lamb, Jr. and R. C. Retherford, *Phys. Rev.*, **79**, 549 (1950).

77. I. A. Sellin, *Phys. Rev.*, **136**, A1245 (1964).

78. V. L. Tal'roze and E. L. Frankenvich, *Zh. fiz. Khim.*, **34**, 2709 (1960).

79. K. P. Warne, *J. Chem. Phys.*, **46**, 502 (1967).

80. G. Gioumousis, and D. P. Stevenson, *J. Chem. Phys.*, **29**, 294 (1958).

81. K. R. Ryan and J. H. Futrell, *J. Chem. Phys.*, **43**, 3009 (1965).

82. E. Rabinowitsch, *Trans. Faraday Soc.*, **33**, 283 (1937).

83. K. Takayanagi and H. Suzuki, *Cross Section for Atomic Processes, Vol. 1*, Research Information Center Institute of Plasma Physics, Nagoya University, Nagoya, Japan (1975).

84. S. A. Edelstein and T. F. Gallagher, *Advances Atomic Mol. Phys*, **14**, 365

41

(1978).

85. K. Takayanagi, *Comments Atomic Mol. Phys.*, **6**, 177 (1977).

86. R. F. Stebbings, *Science*, **193**, 537 (1976).

87. H. A. Bethe and E. E. Salpeter, *Quantum Mechanics of One-and Two-Electron Atoms*, Springer-Verlag, Berlin (1957).

88. J. R. Hiskes, C. B. Tarter, and D. A. Moody, *Phys. Rev.*, **133**, A424 (1964).

89. E. Fermi, *Nuovo Cim.*, **11**, 157 (1934).

90. C. Lanczos, *Z. Physik*, **68**, 204 (1931).

91. D. S. Boudreaux and P. H. Cutter, *Phys. Rev.*, **149**, 170 (1966).

92. M. G. Inghram and R. Gomer, *Z. Naturforsch.*, **10a**, 863 (1955)

93. E. W. Muller and K. Bahadur, *Phys. Rev.*, **102**, 624 (1956).

94. F. Kirchner, *Naturwiss*, **41**, 136 (1954).

95. R. Gomer, *J. Chem. Phys.*, **21**, 1869 (1953).

96. D. S. Bailey, J. R. Hiskes, A. C. Riviere, *Nucl. Fusion*, **5**, 41 (1965).

97. R. F. Stebbings, C. J. Latimer, W. P. West, F. B. Dunning and T. B. Cook, *Phys. Rev. A.*, **12**, 1453 (1975).

98. P. M. Koch, L. D. Gardner, and J. E. Bayfield, in *Fourth International Conference on Beam Foil Spectroscopy, Gatlinburg, Tenn.* Plenum, New York (in press).

99. D. K. Kleppner, M. G. Littman, and M. L. Zimmerman, in *Atoms and Molecules in Rydberg States*, eds. R. F. Stebbings and F. B. Dunning, Cambridge University Press, Cambridge, England (in press).

100. L. Allen, D. G. C. Jones, and D. G. Schofield, *J. Opt. Soc. Am.*, **59**, 842 (1969).

101. M. Karplus and R. N. Porter, *Atoms & Molecules: An Introduction For Students of Physical Chemistry*, Benjamin/Cummings Publishing Co., p. 139 (1970).

6. Figures and Captions

Figure 1. A schematic view of the top of the machine: VC1, arc source vacuum chamber; AS, anode assembly; A, anode; C, cathode; M, magnet; S water-cooled copper skimmer; TA, translation assembly; T, translator; P1,2 viewports; L, optical lens; C2, 150 Hz chopper; PM, photomultiplier; CP, current preamplifier; LI 1,2, lock-in amplifiers; SCR 1,2, strip chart recorders; VC2, bell jar vacuum chamber; C1, 10 Hz chopper; D, electric field deflectors plates; F, mechanical flag; QMS, quadrupole mass spectrometer; PA, EAI preamplifier (ESA-75); MSE, mass spectrometer electronics.

Figure 2. AC ion current as a function of m/e. In each panel the lower curve is the AC background obtained with the electron beam turned off, and the upper curve is the AC mass spectrometer ion current signal (with the beam chopped at 10 Hz) shifted upwards by 0.2×10^{-10}A for convenience of display. Electron impact current: $100\,\mu$A. Electron accelerating voltage: 60V. Ion source pressure: 2.1×10^{-5} torr measured by an uncalibrated ion gauge. (a) H_2 in the molecular beam source; (b) D_2 in that source; (c) and equimolar mixture of H_2 and D_2 in that source. For all the panels the stagnation pressure in the molecular beam source was 60 torr. (Nozzle conditions changed slightly.)

Figure 3. DC ion current as a function of pressure for m/e = 1, 2, and 3. Mass spectrometer electron impact current is $100\,\mu$A and electron accelerating voltage is 60 V. Error bars represent 90% confidence limit.

Figure 4. Energy level diagram for H_3. The vertical arrows indicate the two electronic transitions we observed previously[48].

Figure 5. Top cross sectional view of photoionization/scattering cell with mounting flanges. Hatched area of drawing indicates the pipe walls.

Figure 6. A schematic view of the top of the machine with scattering cell installed.

Labels are the same as in figure 1 with the following additions: L, quartz lens; ML, 200 watt high pressure mercury lamp; PS, power supply for mercury lamp; QW, quartz window; IG, ion gauge; CAT, time-averaging computer; X-Y, x-y recorder; SM, spherical mirror.

Figure 7. Fractional attenuation of mass spectrometer signal as a function of argon pressure within the stagnant gas cell for $m/e = 1$, 2, and 3. I_o is the intensity of the species with no gas in the cell and I is the corresponding intensity with gas in the cell. The pressure was measured with an uncalibrated Schulz-Phelps gauge. Lines are least squares fits to the points. The path length in the gas cell is 4 inches. The beam stagnation pressure is 57 torr.

Figure 8. Pictorial representation of the $2p_z$ Rydberg orbital is of H_3 molecules in the $2p$ $^2A_2''$ state. The solid points represent the nuclei. The Rydberg orbital perpendicular to the plane of the nuclei and is represented by a 90 % boundary surface of a hydrogenic $2p_z$ orbital[101].

Figure 9. Fractional attenuation of mass spectrometer signal as a function of target gas pressure measured with an uncalibrated Shulz-Phelps gauge for $m/e = 1$. I_o is the intensity of that species with no gas in the cell and I is the corresponding intensity with gas in the cell. Lines are least squares fit to points. The path length of the gas cell is 2 inches. The beam stagnation pressure is 65 torr. Solid symbols: Ar target. Open symbols: propane target.

Figure 10. Fractional attenuation of mass spectrometer signal as a function of target gas pressure measured with an uncalibrated Schulz-Phelps gauge for $m/e = 3$. I_o is the intensity of this species with no gas in the cell and I is the corresponding intensity with gas in the cell. Lines are least squares fit to the points. The path length in the gas cell is 2 inches. The beam stagnation pressure is 65 torr. Solid symbols: Ar target. Open symbols: propane target.

Figure 11. Ionization efficiency (I_{eff}) as a function of tungsten filament temperature

for the production of H^+ and H_3^+ ions, (a) stagnation pressure = 80 torr, (b) stagnation pressure = 75 torr, (c) stagnation pressure = 70 torr.

Figure 12. Natural logarithm of the ionization efficiency (I_{eff}) plotted as a function of the inverse of the tungsten filament temperature, for the production of H^+ and H_3^+ ions, (a) stagnation pressure = 80 torr, (b) stagnation pressure = 75 torr, (c) stagnation pressure = 60 torr. Lines represents least squares fits to the points.

Figure 13. Ionization efficiency (I_{eff}) as a function of platinum filament temperature for the production of H^+ and H_3^+ ions, (a) stagnation pressure = 75 torr, (b) stagnation pressure = 65 torr, (c) stagnation pressure = 60 torr.

Figure 14. Natural logarithm of the ionization efficiency (I_{eff}) plotted as a function of the inverse platinum filament temperature for the production of H^+ and H_3^+ ions, (a) stagnation pressure = 75 torr, (b) stagnation pressure = 65 torr, (c) stagnation pressure = 60 torr. Lines represent a least squares fit to the points.

Figure 15. Mass spectrum of molecular beam. (a) electron impact mass spectrum (b) background-corrected photoionization mass spectrum generated by irradiation of beam with mercury lamp. Smooth line indicates fit to data points. The stagnation pressure was set at 100 torr and 95 torr as indicated.

Figure 16. Mass spectrum of molecular beam. (a) electron impact mass spectrum (b) background-corrected photoionization mass spectrum generated by irradiation of beam with mercury lamp. Smooth line indicates fit to data points. The stagnation pressure was set at 90 torr and 80 torr as indicated.

Figure 1

Figure 2

Figure 3

SPHERICAL MIRROR

TOP DEFLECTION PLATE

INTERCHANGABLE APERTURE

GAS CELL

$10\frac{1}{2}$"

OUTER MOUNTING FLANGE

INNER MOUNTING FLANGE

SET SCREW

TURNING RING →

LOCKING RING →

ION GAUGE →   ← GAS INLET

QUARTZ WINDOW

1"
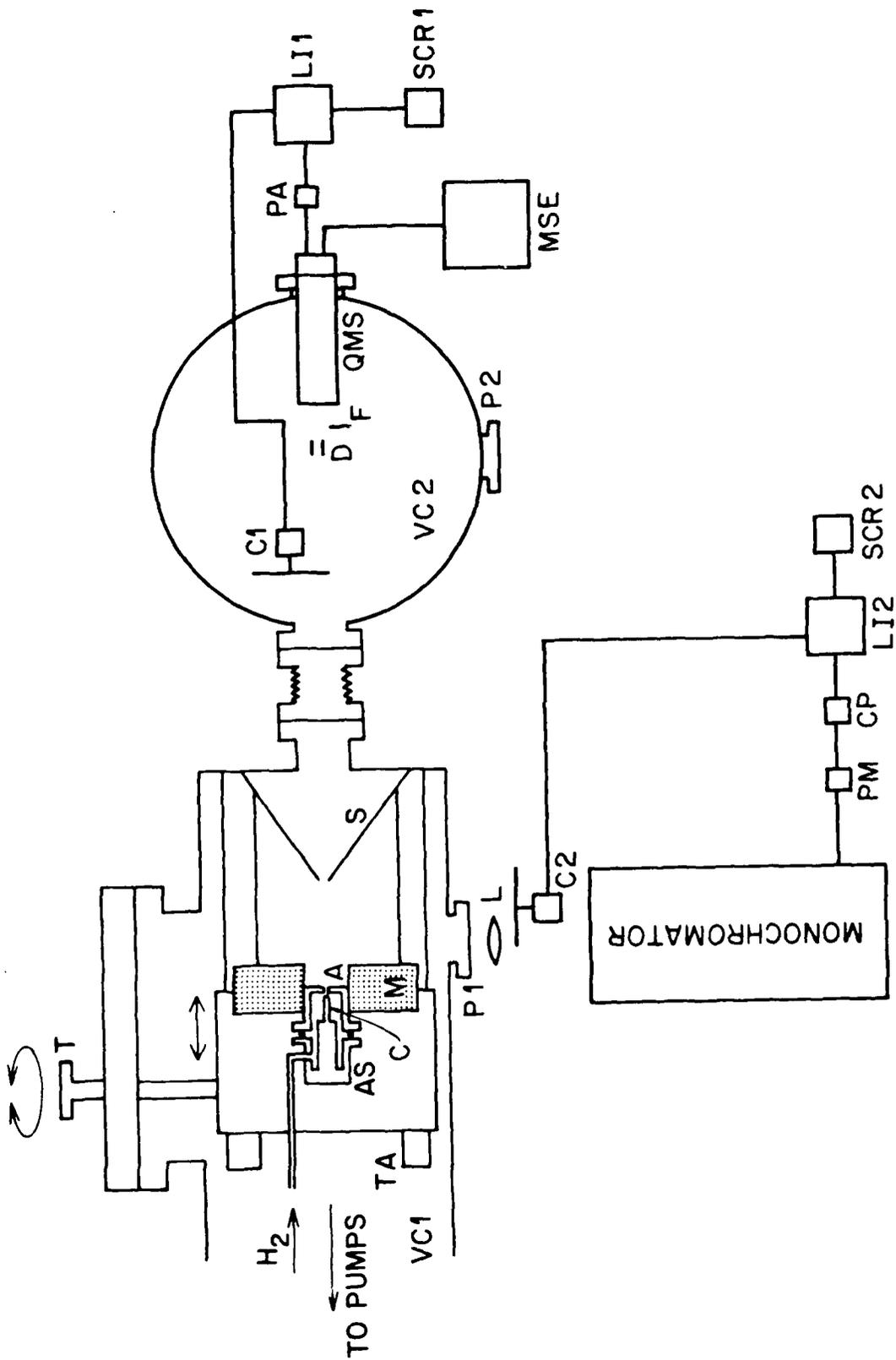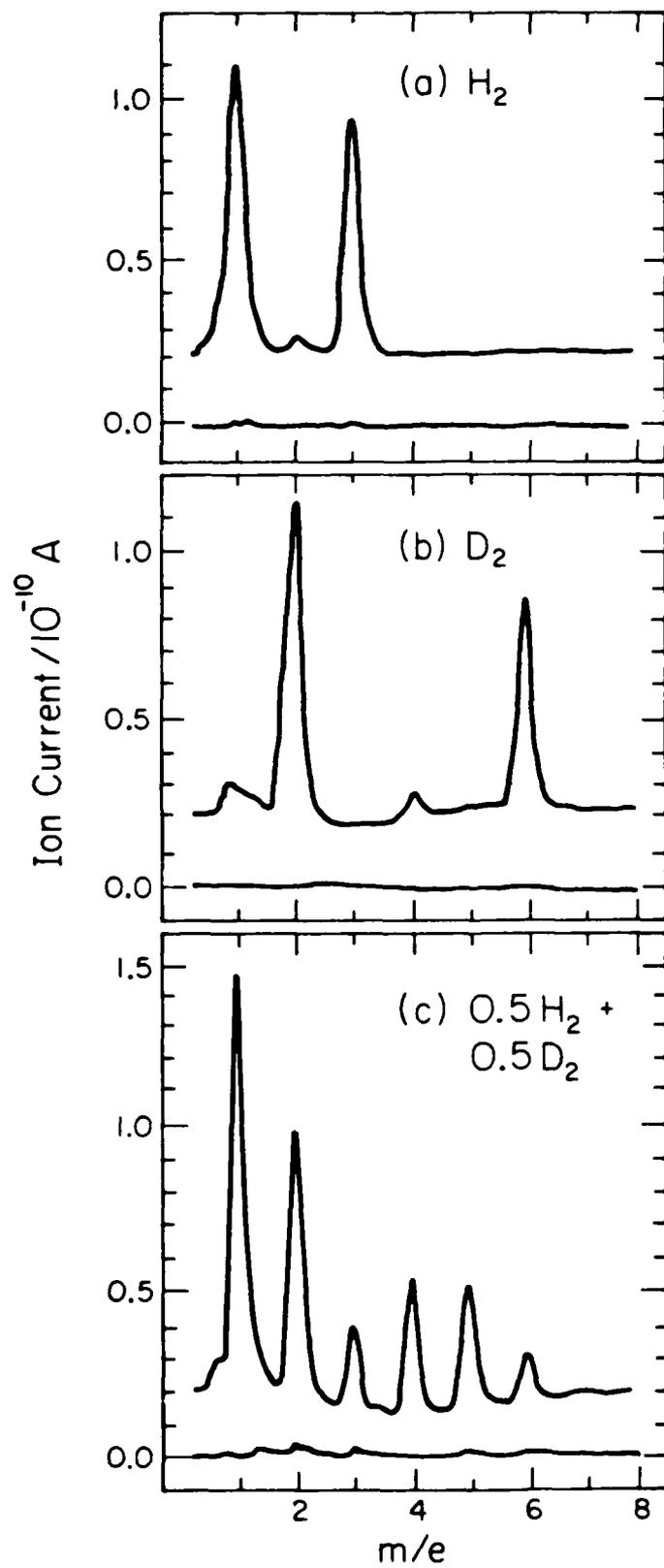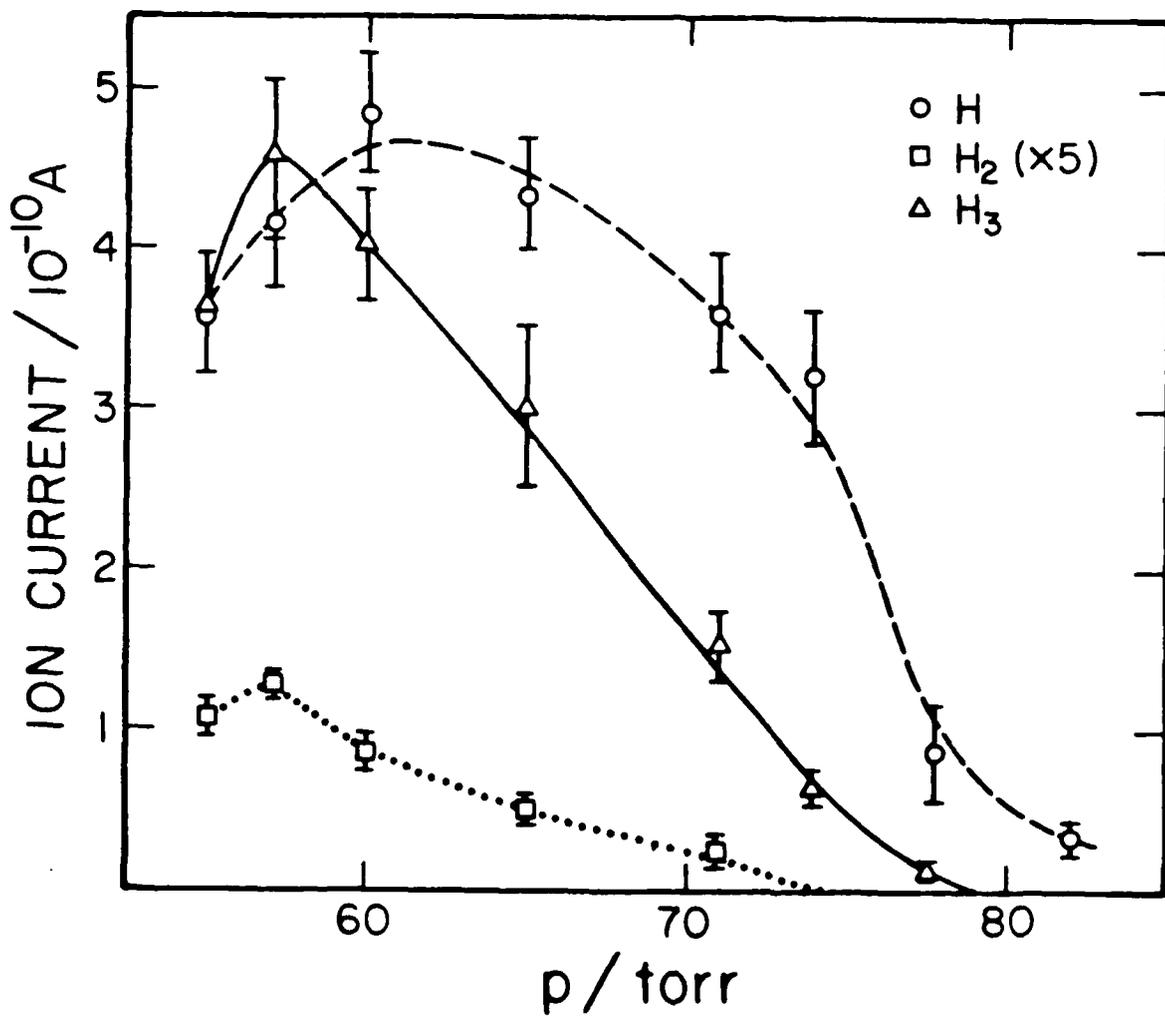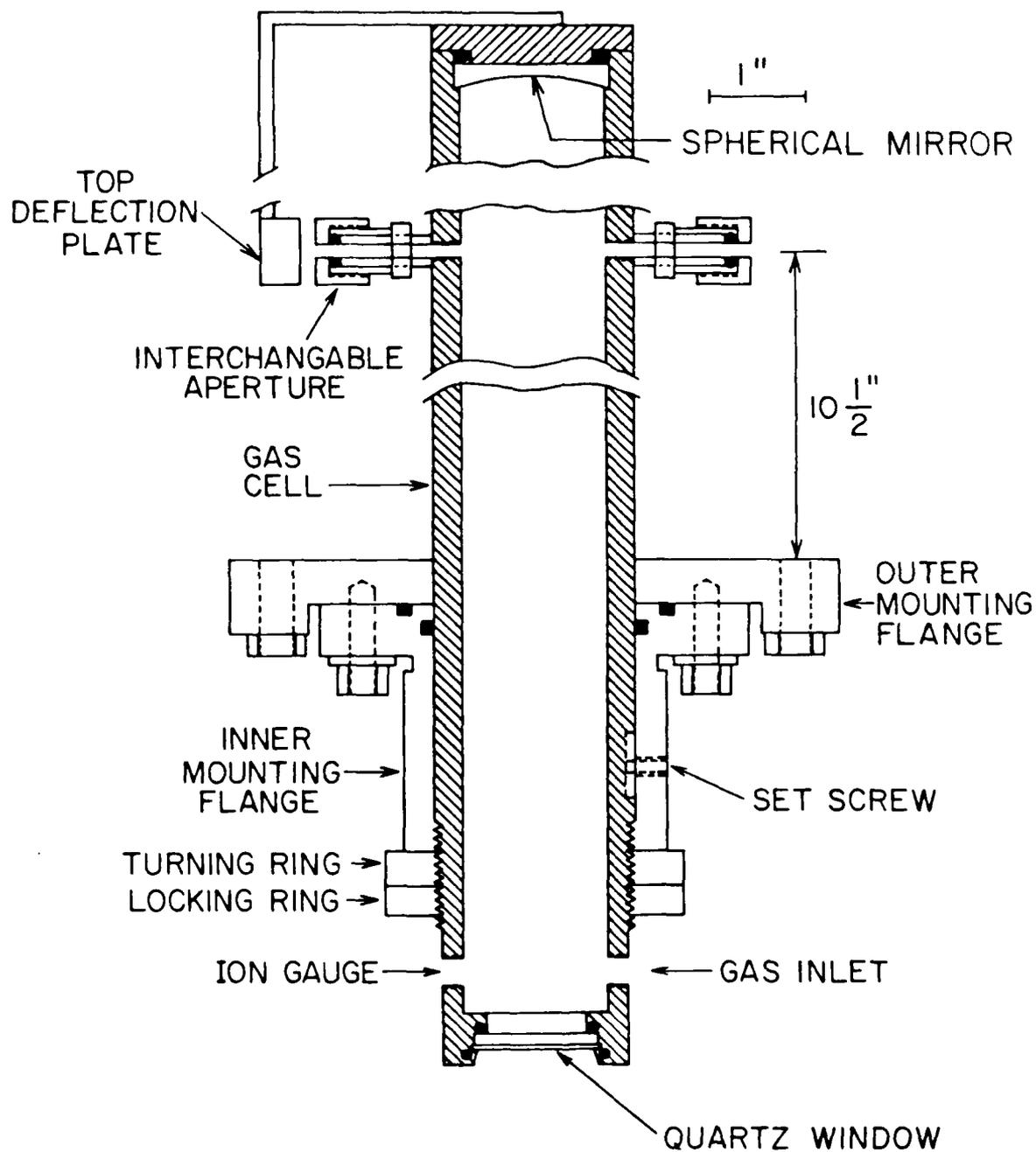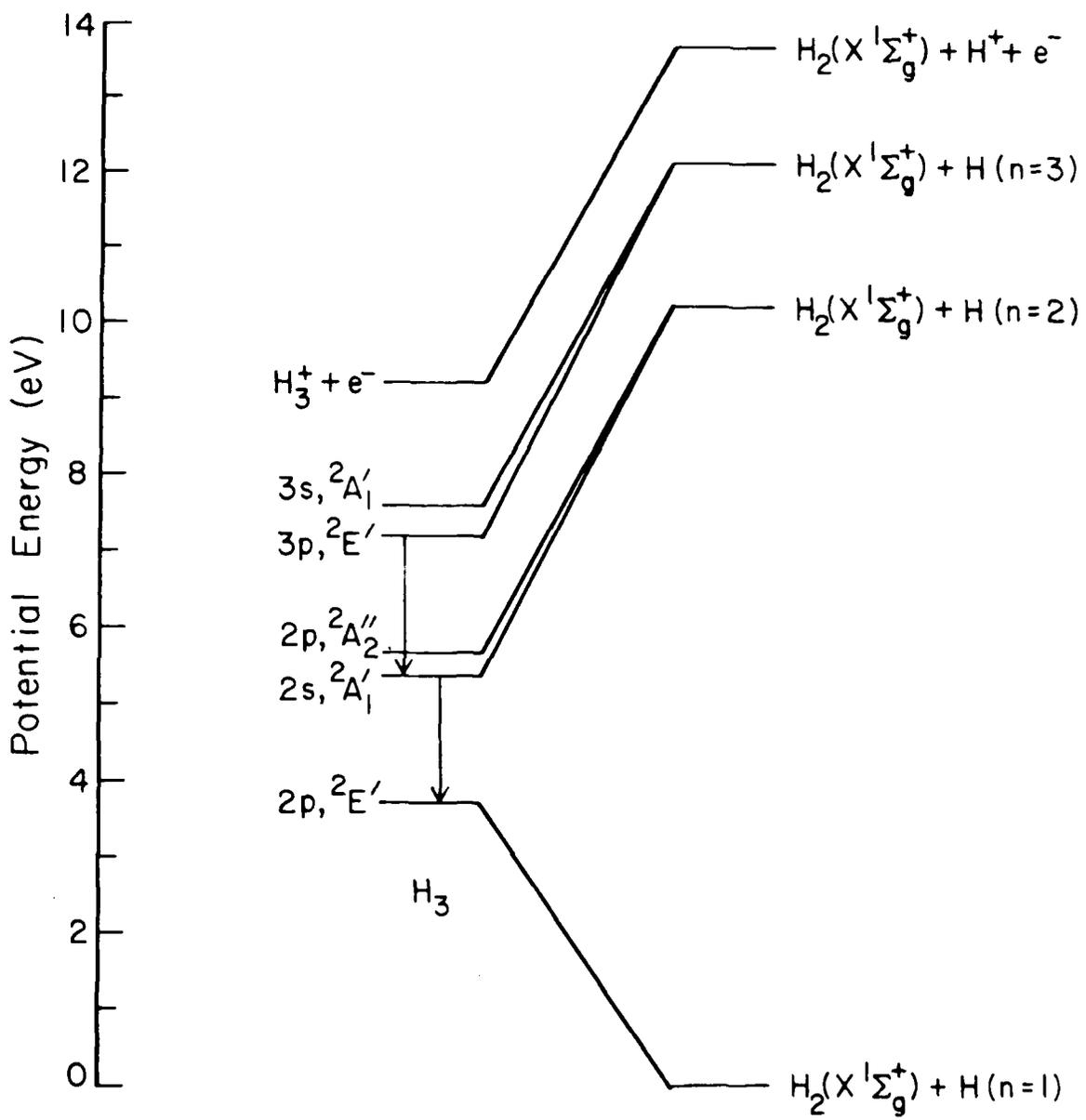
Figure 4

Figure 5

Figure 6
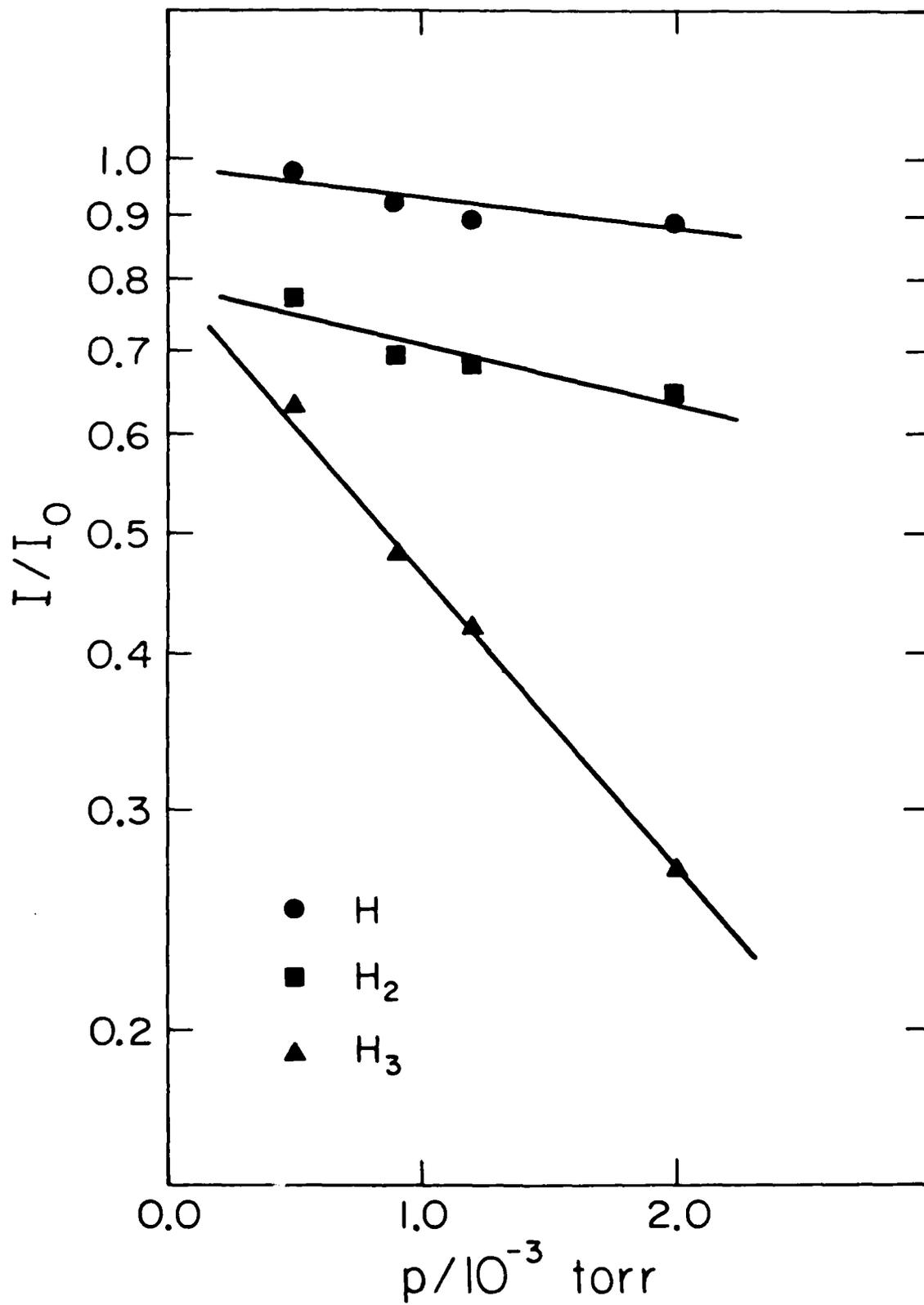
Figure 7
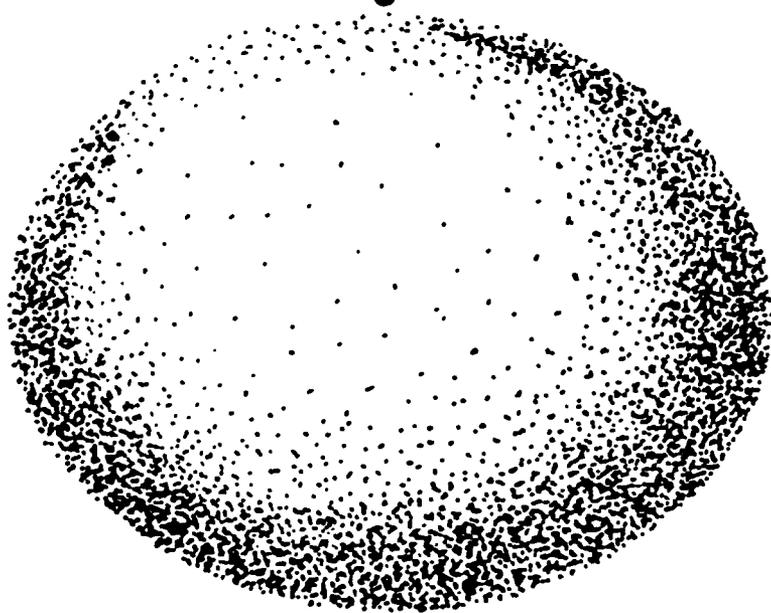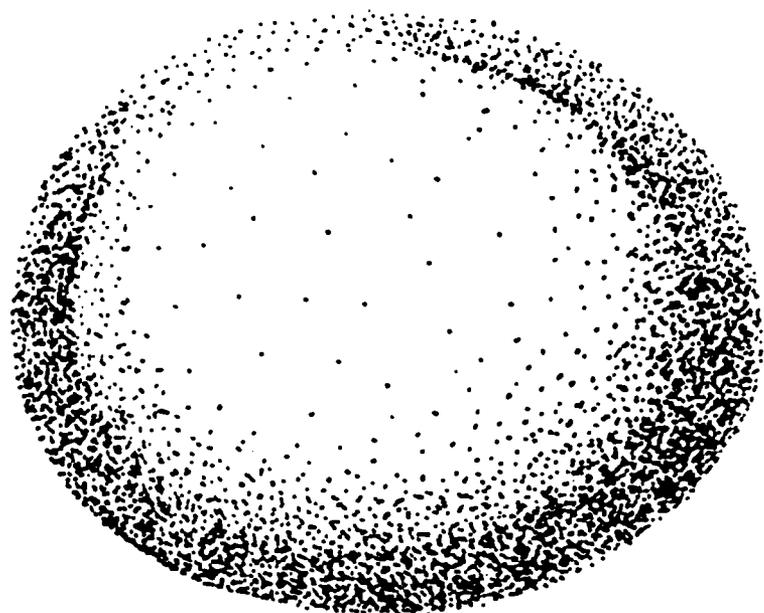
2Å
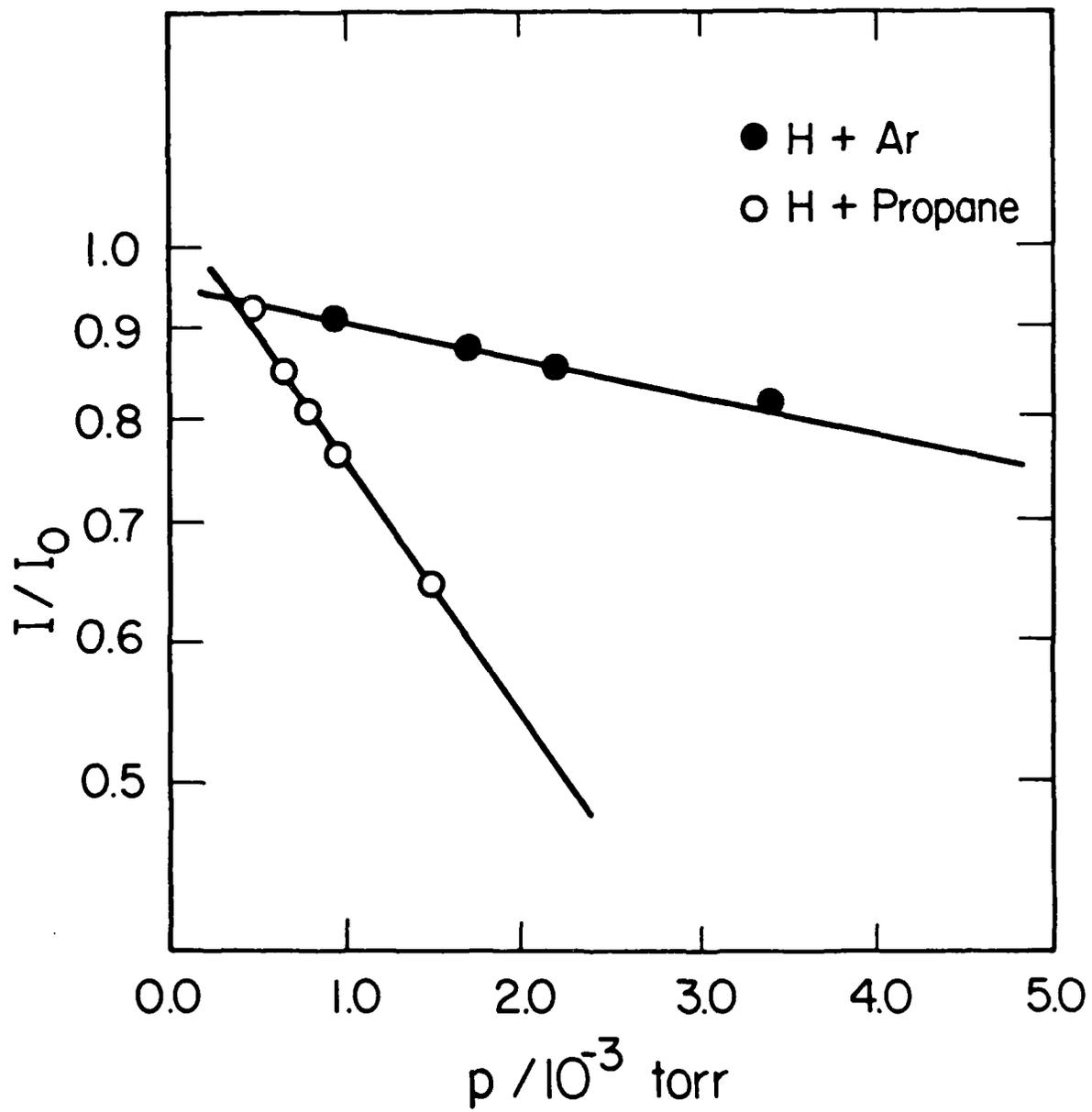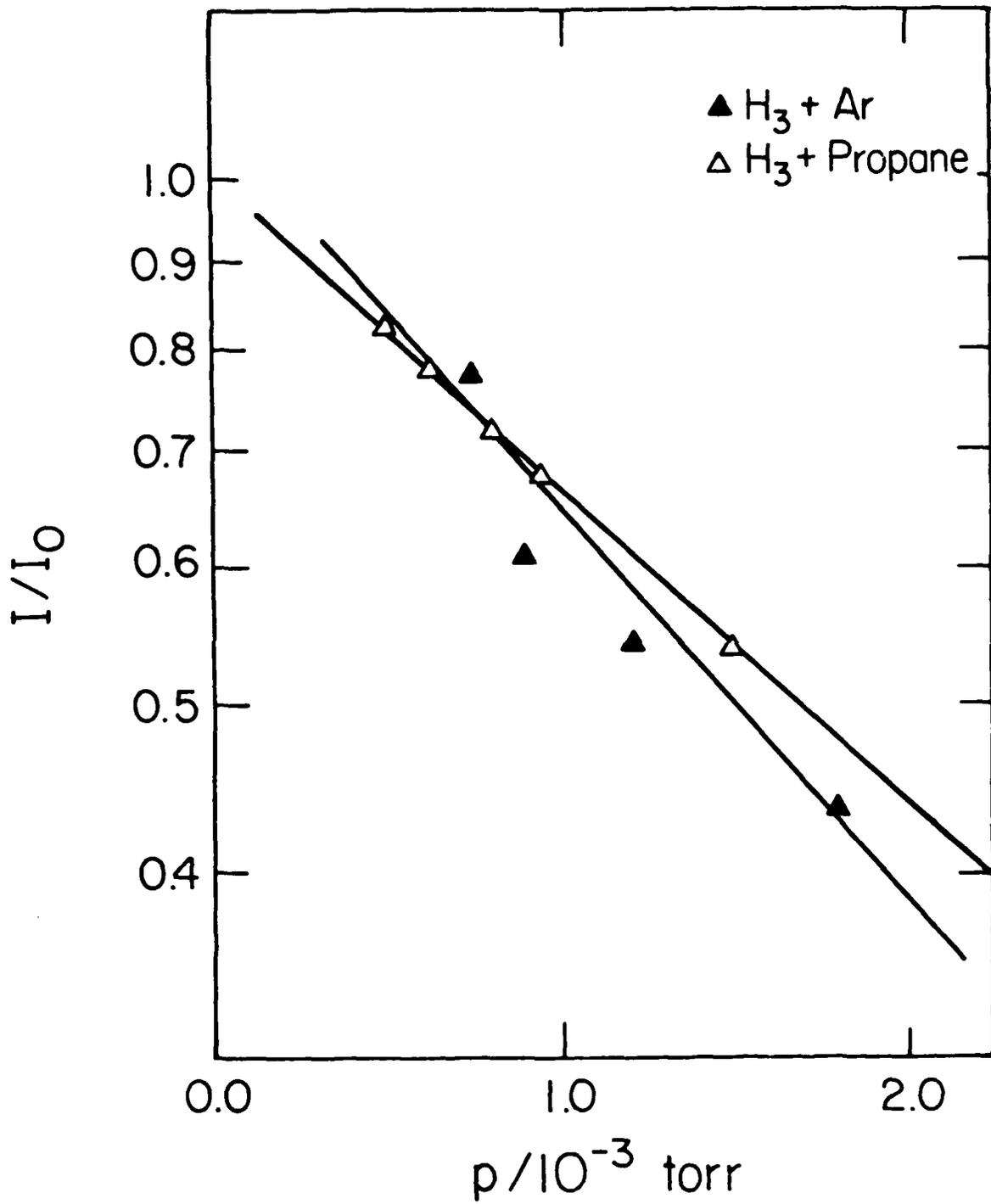
Figure 8

Figure 9

Figure 10
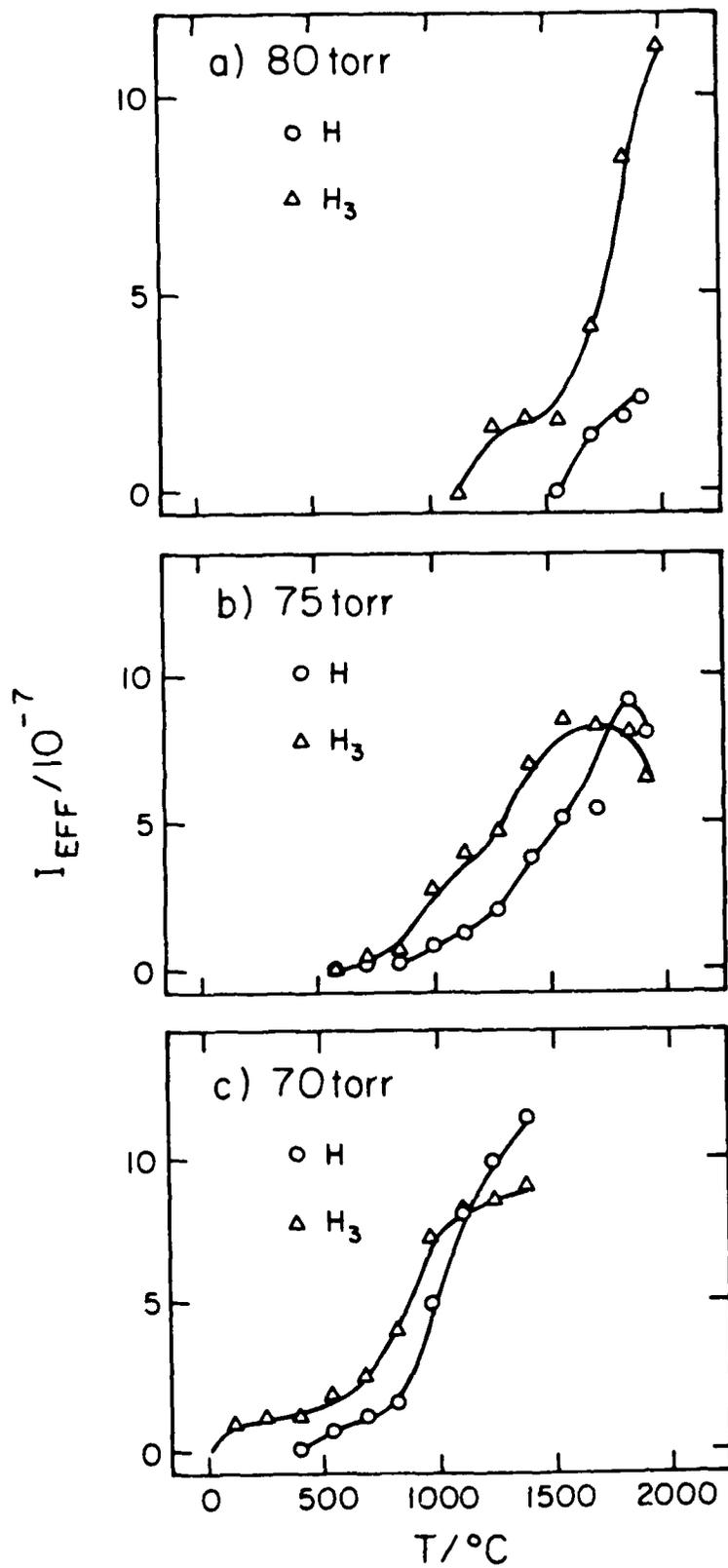
Figure 11
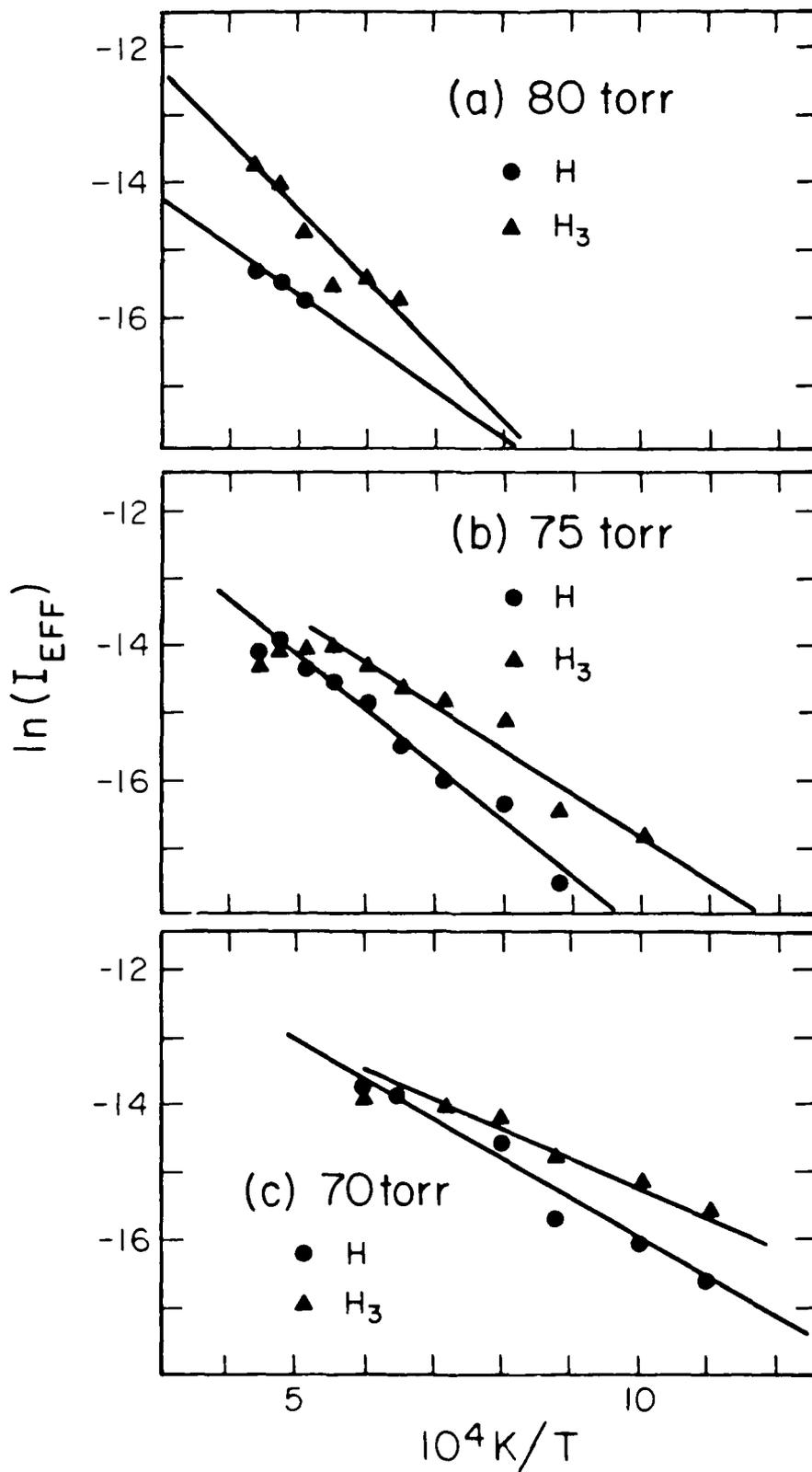
Figure 12
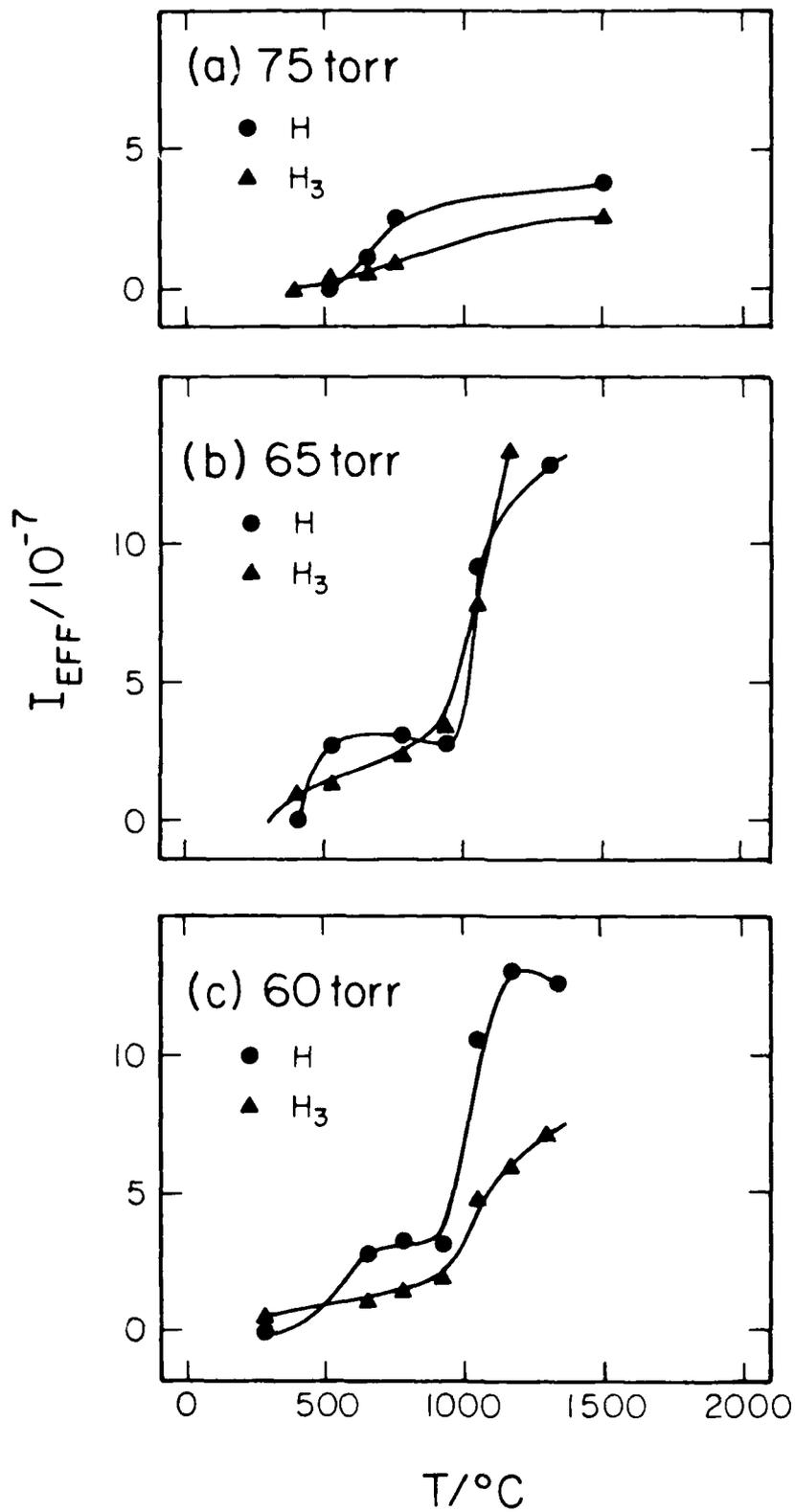
Figure 13
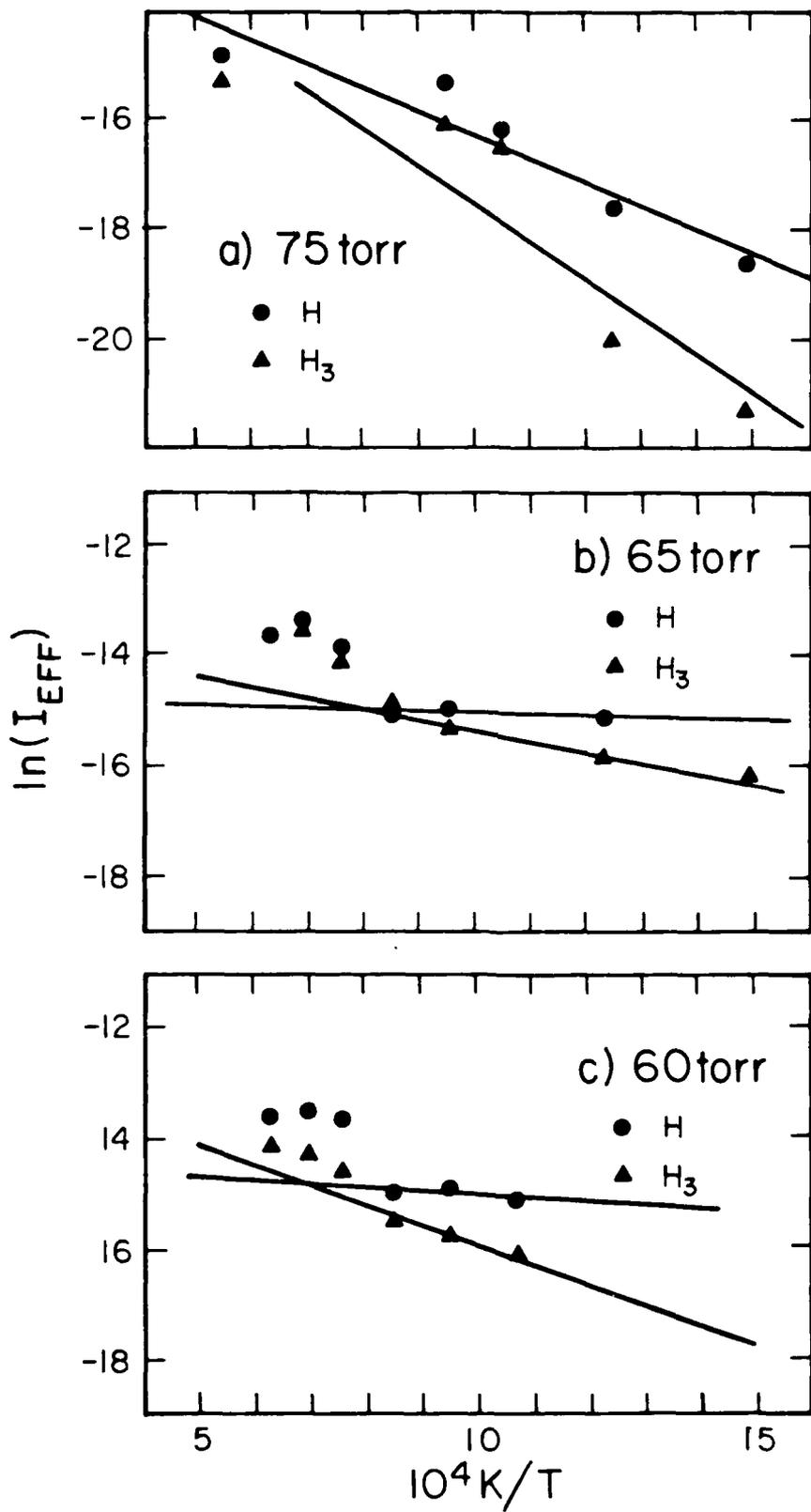
Figure 14
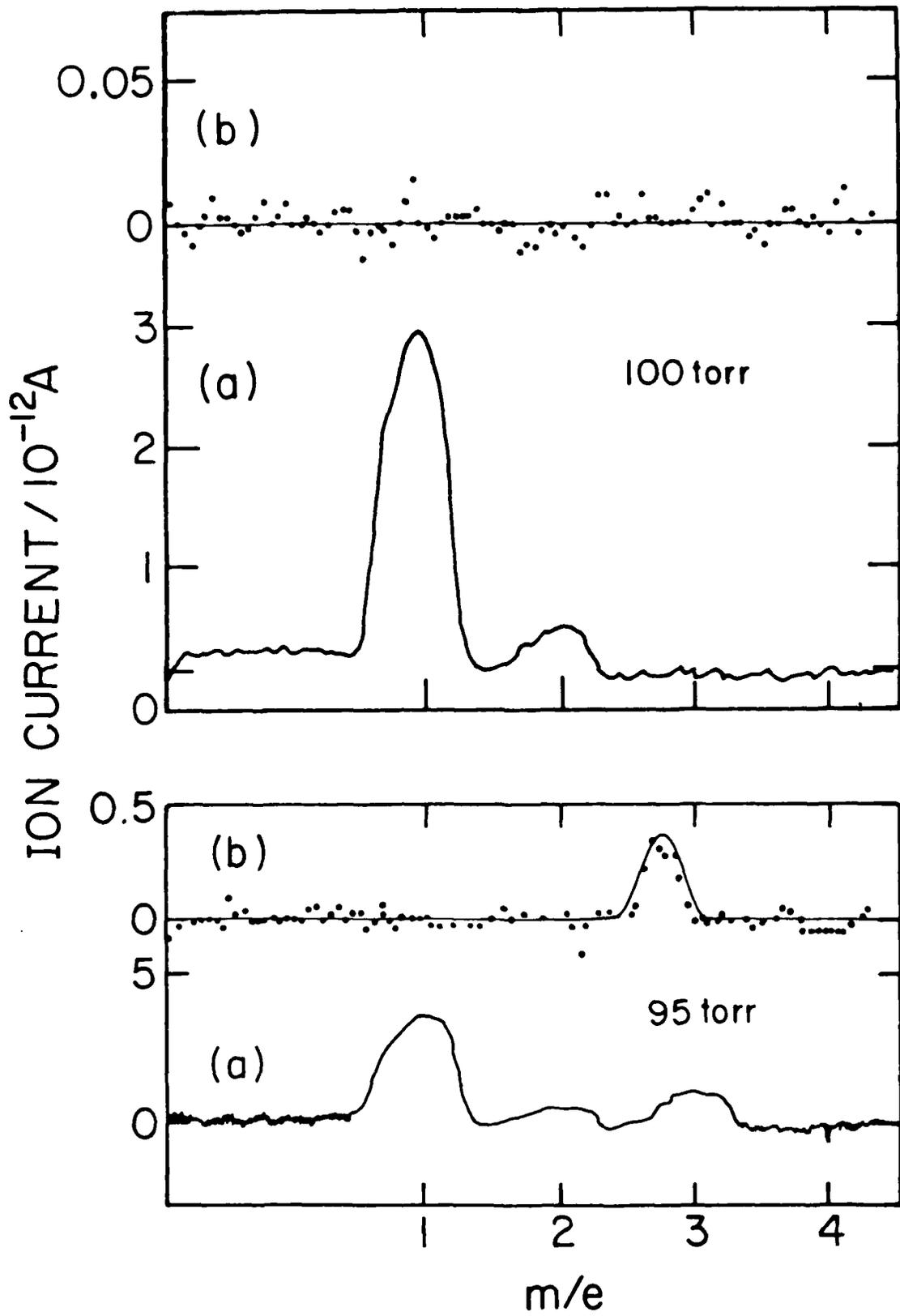
Figure 15
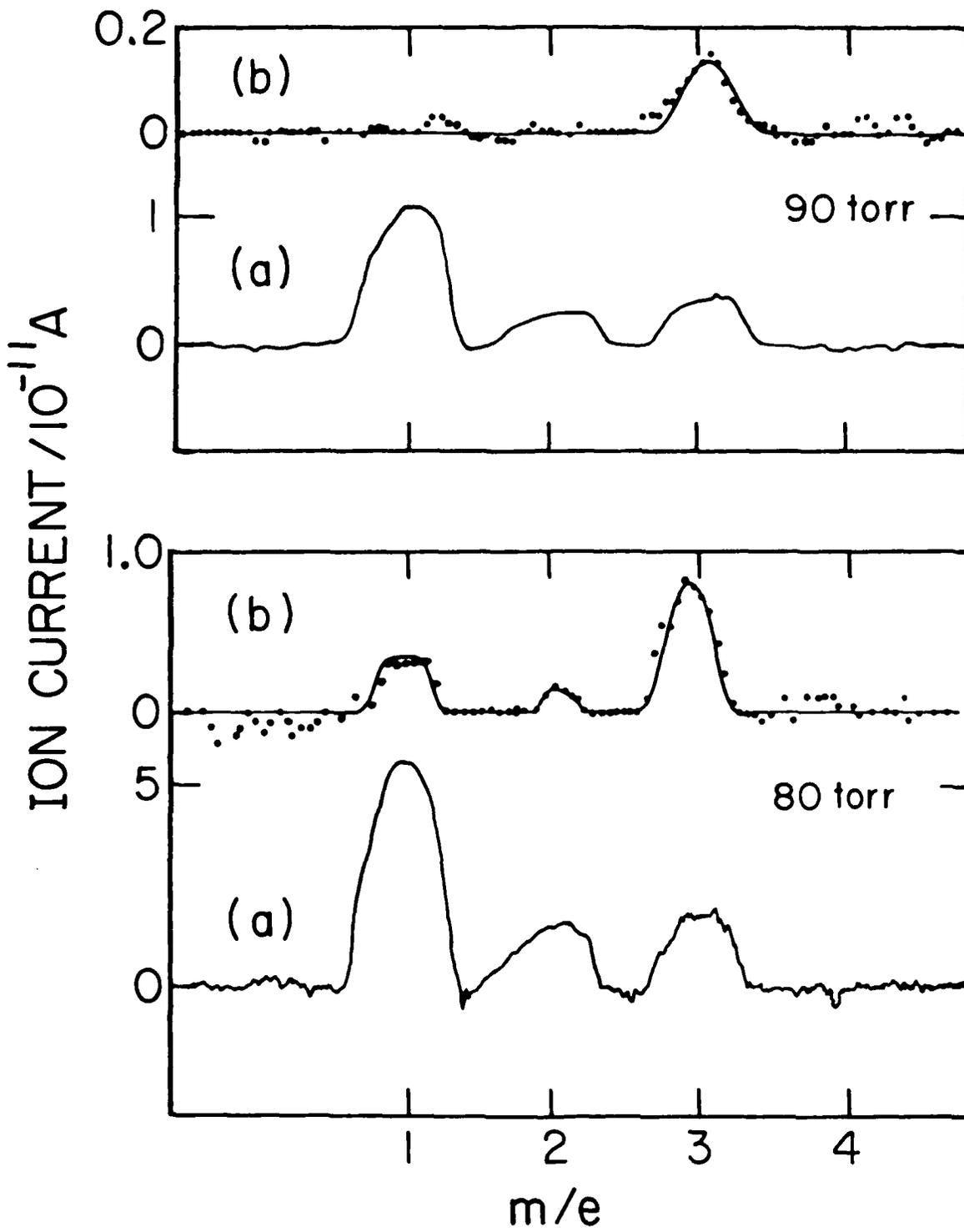
Figure 16

A Test of the Babamov-Marcus Vibrationally Adiabatic Theory of Hydrogen Atom Transfer Reactions[†]

Paul G. Hipes[§] and Aron Kuppermann

Arthur Amos Noyes Laboratory of Chemical Physics
California Institute of Technology,* Pasadena, CA 91125

Abstract

Accurate quantum mechanical reaction probability calculations for a collinear tri-atomic model of the abstraction of a hydrogen atom from a methane molecule by a methyl radical were performed. The calculations used the method of hyperspherical coordinates and a LEPS potential energy surface having a realistic (13.86 kcal/mole) barrier to reaction. With the same surface, the same reaction probabilities were calculated using the Babamov-Marcus vibrationally adiabatic model. It was found that for reagents in their ground and first two vibrationally excited states, this model displayed a dynamically correct qualitative behavior. In addition, the reaction probability from the ground vibrational state was accurate to within 6% for translational energies from 0.35 eV to 0.51 eV.

1. Introduction

The abstraction of a hydrogen atom from a molecule by a methyl radical is a commonly studied reaction. Arrhenius parameters derived from gas phase kinetics studies have been tabulated.[1] There has also been much interest in the hydrogen atom abstraction from small organic molecules by methyl radicals in frozen matrices.[2-6] This interest is stimulated by the observation of finite, temperature-independent rate constants at very low temperatures. This phenomenon is interpreted as a manifestation of quantum mechanical tunneling through a potential energy barrier. The low temperature experiments are often analyzed with the aid of corrections to transition state theory to account for tunneling.[7,8] The corrections are based on the solution of one-dimensional barrier penetration problems. A different approach is to model the tunneling in the hydrogen atom transfer by a collinear, three particle reaction. Although the collinear constraint is rather severe, some important aspects of the dynamics of light particle transfer can be gleaned from such a study, not only at the low translational energies at which tunneling is important, but also at significantly higher energies.

Collinear heavy-light-heavy (H-L-H) mass systems have generated substantial theoretical activity recently. Until the introduction of hyperspherical coordinates to collinear reactive scattering,[9,10] these systems were difficult to treat quantum mechanically.[11] Now a variety of symmetric[12-15] (A + BA) and asymmetric[16-19] (A + BC) systems have been solved accurately. Some general characteristics of reaction probabilities for the heavy-light-heavy systems have emerged: pronounced oscillatory dependence on collision energy and near conservation of translational energy.[12-15,20] The latter characteristic is equivalent to vibrational adiabaticity in symmetric systems, and has been exploited to develop efficient and accurate approximations for collinear reactive scattering in both symmetric[15,20-22] and asymmetric[18,19,23-25] systems. Resonance positions and widths have been approximated in heavy-light-heavy and in more general

2

systems using the ideas of adiabatic separation of degrees of freedom.[13,15,17,22,26-32] Efforts to extend the collinear heavy-light-heavy results to 3D[33-35] have suggested that the oscillatory collinear reactive probabilities may be manifest as oscillatory cross sections in the real world. It should be recognized that the current intense interest in adiabatic separation of variables has its origins in the early work of Marcus.[36]

In this paper, we present the results of accurate quantum mechanical calculations for a collinear model of the hydrogen atom exchange between a methane molecule and a methyl radical. The methyl moiety is represented by a structureless point having the mass of the methyl radical. Hyperspherical coordinates are used to formulate the scattering problem exactly.[9,10] Accurate solutions to the Schrödinger equation are generated numerically using a diabatic representation. Reaction probabilities from the lowest three vibrational levels are presented. In addition, transition probabilities calculated using the Babamov-Marcus vibrationally adiabatic model[21] for symmetric, collinear, heavy-light-heavy systems are compared with the accurate results. This model and its extension to asymmetric systems have been shown to be good at rather low translational energies for reaction from the lowest vibrational level[15,20,22] and from the first vibrationally excited level of the reagent.[19] We will examine the applicability of the adiabatic model for transitions from the first two excited vibrational levels of the reagent in addition to those from the lowest level.

2. Potential Energy Surface and Convergence

The potential energy surface is of the LEPS form[37,38] and potential contours are shown in figure 1. This surface was previously used by Ovchinnikova[39] and by Babamov and Marcus.[21] The barrier height is 13.86 kcal/mole, in accord with the gas phase activation energy. The LEPS parameters are listed in Table I along with some surface characteristics. It should be noted that the asymptotic Morse parameters do

3

not reproduce any spectroscopic transitions of methane.

The hyperspherical cocrdinate method used to accurately solve the Schrödinger equation for a collinear, three-particle system has been described elsewhere[9] and will not be repeated here. The adiabatic model will be discussed after the accurate results are presented. The convergence of the accurate numerical results with respect to basis size, projection distance, and other numerical parameters was investigated. A basis set of 4 even and 4 odd functions was found to be adequate for convergence of the P_{00}^R within 1% over the energy range studied (0.2 eV to 1.15 eV total energy, with respect to the bottom of the isolated H-CH$_3$ diatom potential energy curve). P_{11}^R required 5 even and 5 odd basis functions and P_{22}^R required 7 even and 7 odd basis functions for the same degree of convergence. The numerical method involves a projection of the solutions onto an asymptotic atom-diatom basis set prior to the calculation of the scattering matrix and transition probabilities. For the latter to become independent of the atom-diatom distance at which this projection is performed, to within the convergence mentioned, it sufficed to integrate the coupled radial equations from an initial value of the hyperradius of 5.4 bohr out to 20 bohr.

The adiabatic model used requires the solution of two uncoupled ordinary differential equations to obtain phase shifts, and convergence was obtained with respect to the corresponding discretization parameters.

3. Results of Accurate Calculations

Figure 2 shows the accurate reaction probabilities from the first three levels of the reagent. The first feature of the results which is noticed is the dominance of reactive transitions which preserve the vibrational quantum number (i.e. vibrationally adiabatic transitions). Reactive transitions between the states whose quantum numbers

4

differ by unity are an order of magnitude smaller than the adiabatic ones. A change of two vibrational quanta is two orders of magnitude less probable than conservation of the quantum number. (The small oscillations in the P_{02}^R curve of figure 2 probably represent numerical inaccuracies.) This near conservation of vibrational quantum number has been observed in a number of other collinear calculations consisting of the transfer of a light particle between two heavier ones (HLH) of equal mass.[12-15]

The effect is kinematic in origin, and is explained by an argument analogous to that used in the Born-Oppenheimer separation of nuclear and electronic motion.[21,40] At low translational energies, the light particle (the hydrogen atom in the present case) vibrates quickly on the time scale of the heavy particle motion. In an approximate sense, the two heavy particles approach and recede in a potential averaged over the vibrational motion of the light particle. As the translational energy of relative motion increases, the decoupling of the vibrational and translational motion is less accurate. It is inherent in this picture that the vibrational quantum number is unaffected by the collision of the atom and the diatomic molecule and hence is adiabatic. The concept that the transfer of a light particle between heavy ones can be approached via an adiabatic separation between the corresponding degrees of freedom has been used previously, as discussed in the introduction. It has also been argued that a natural adiabatic separation between the hyperradial and hyperangular motions exists for general mass combinations when hyperspherical coordinates are utilized.[26,41] This near adiabatic separation is responsible for the rapid convergence of coupled channel expansions. The general argument for the separation of time scales in reactive transitions focuses attention on the strong interaction region of the potential energy surface (figure 1). In this region, as the particle moves from reagent channel to product channel, the hyperangle (plane polar angle for collinear triatomic systems) changes by a large fraction of its allowed range while the hyperradius (plane polar radius for collinear triatomic systems) changes relatively little, which results in an adiabatic separation of angular and radial motion.[9b,26] However, as pointed out

5

by Babamov and Marcus,[21] the class of heavy-light-heavy mass combinations is the one for which the adiabatic separation is expected to be most valid. Under these conditions, only vibrationally adiabatic transfer processes would be expected. This agrees qualitatively with the results in figure 2.

Another prominent characteristic of the accurate results is the significant degree of tunneling from the lowest vibrational level of the reagent to that of the product. For energies above the classical barrier height, to determine the fraction of reactive probability flux which passes into the product channel via tunneling through classically forbidden regions of configuration space requires an analysis of the probability current density streamlines.[42a] However, below the classical barrier height, any reactive flux is necessarily due to tunneling. From figure 2a, we see that the probability for reaction from the n=0 level of the reagent to the n=0 level of the product is significant at energies below the classical barrier. For energies close to that barrier but still below it, the reactive pathway dominates over the nonreactive one. The physical reason for the prominence of tunneling is the heavy-light-heavy mass combination. Such mass combinations lead to small Delves skew angles[42b] A particle approaching the strong interaction region does not have to penetrate the barrier at the saddle point to move into the product channel. It can cut the corner over a significant portion of configuration space for which the classically forbidden region is narrow (i.e., has a width of the order of the system's local de Broglie wavelength or less [42c]). The heavy-light-heavy mass combination increases this region of configuration space. The result is increased tunneling for such combinations. In the low temperature abstraction of hydrogen atoms by radicals, the presence of apparent tunneling phenomena is not at all surprising from a theoretical standpoint. It has long been understood that tunneling probabilities in one dimension increase as the particle mass decreases. The collinear model, which involves two mathematical dimensions, has led us to a clearer perspective, namely that tunneling can occur by corner-cutting away from the saddle point.[42a]

6

In summary, the reaction dynamics of this collinear model of hydrogen atom abstraction from methane by a methyl radical is characterized by dominance of vibrational adiabaticity, and significant tunneling from the n=0 level.

4. Vibrationally Adiabatic Model

The treatment given here roughly parallels that of reference[21] and is provided for completeness. Let A_α, A_β, and A_γ represent the three atoms of mass m_α, m_β, and m_γ, respectively. We define two sets of coordinates R'_α, r'_α and R'_γ, r'_γ shown in figure 3, where $G_{\beta\gamma}$ and $G_{\alpha\beta}$ are the centers of mass of $A_\beta A_\gamma$ and $A_\alpha A_\beta$, respectively. Let the subscript λ take on the values α or γ. Both sets of coordinates can then be represented by R'_λ, r'_λ. We now define the Delves scaled coordinates[43,44] R_λ, r_λ as

$$R_\lambda = a_\lambda R'_\lambda \tag{1}$$

$$r_\lambda = a_\lambda^{-1} r'_\lambda \tag{2}$$

where

$$a_\lambda = \left(\frac{\mu_{\lambda,\nu\kappa}}{\mu_{\nu\kappa}} \right)^{1/4} \tag{3}$$

$$\mu_{\lambda,\nu\kappa} = \frac{m_\lambda(m_\nu + m_\kappa)}{m_\lambda + m_\nu + m_\kappa} \tag{4}$$

and

$$\mu_{\nu\kappa} = \frac{m_\nu m_\kappa}{m_\nu + m_\kappa} \tag{5}$$

The set of indices $\lambda, \nu\kappa$ stands for either $\alpha, \beta\gamma$ or $\gamma, \alpha\beta$.

The hyperspherical coordinates ρ and ϑ_λ are defined by [9,10,43,44]

$$\rho = \left(R_\lambda^2 + r_\lambda^2 \right)^{1/2} \tag{6}$$

7

$$\vartheta_\lambda = \arctan\left(\frac{r_\lambda}{R_\lambda}\right) \qquad 0 \le \vartheta_\lambda \le \pi/2 \tag{7}$$

The Schrödinger equation in these coordinates is

$$\left[\frac{-\hbar^2}{2\mu}\left(\frac{\partial^2}{\partial\rho^2} + \frac{1}{\rho}\frac{\partial}{\partial\rho} + \frac{1}{\rho^2}\frac{\partial^2}{\partial\vartheta_\lambda^2}\right) + V(\rho,\vartheta_\lambda) - E\right]\psi(\rho,\vartheta_\lambda) = 0 \tag{8}$$

where

$$\mu = \left(\frac{m_\alpha m_\beta m_\gamma}{m_\alpha + m_\beta + m_\gamma}\right)^{1/2} \tag{9}$$

A discrete basis set in the hyperangle ϑ_λ is defined by

$$\left[-\frac{\hbar^2}{2\mu\rho^2}\frac{d^2}{d\vartheta_\lambda^2} + V(\rho,\vartheta_\lambda) - \epsilon_n(\rho)\right]\chi_n(\vartheta_\lambda;\rho) = 0 \tag{10}$$

with

$$\chi_n(\vartheta_\lambda = 0;\rho) = \chi_n(\vartheta_\lambda = \vartheta_{\lambda\mathrm{max}};\rho) = 0 \tag{11}$$

and

$$\int_0^{\vartheta_{\lambda\mathrm{max}}} \chi_n(\vartheta_\lambda;\rho)\chi_{n'}(\vartheta_\lambda;\rho)d\vartheta_\lambda = \delta_n^{n'} \tag{12}$$

where ρ is considered a parameter and $\vartheta_{\lambda\mathrm{max}}$ is the Delves skew angle.

When the wave function $\psi(\rho,\vartheta_\lambda)$ is expanded in this basis set, according to

$$\psi(\rho,\vartheta_\lambda) = \rho^{-1/2}\sum_{n=0}^{\infty} g_n(\rho)\chi_n(\vartheta_\lambda;\rho) \tag{13}$$

an infinite set of coupled, ordinary differential equations, equivalent to the original Schrödinger equation, results:

$$\left[\frac{-\hbar^2}{2\mu}\frac{d^2}{d\rho^2} + \epsilon_n(\rho) - E - \frac{\hbar^2}{8\mu\rho^2}\right]g_n(\rho)$$

$$+\sum_{n'=0}^{\infty}\left(\frac{-\hbar^2}{2\mu}<\chi_n|\frac{\partial^2}{\partial\rho^2}|\chi_{n'}> - \frac{\hbar^2}{\mu}<\chi_n|\frac{\partial}{\partial\rho}|\chi_{n'}>\frac{d}{d\rho}\right)g_{n'}(\rho) = 0 \tag{14}$$

8

For a symmetric mass combination, the solutions can be chosen to have a definite parity, even or odd. Solutions of different parity are rigorously decoupled. If the entire sum over n' in eq.(14) is neglected, a single ordinary differential equation for each n and each parity results. This neglect is the central feature of the adiabatic approximation. The scattering matrix can then be expressed in terms of the resulting even and odd phase shifts.[21] The square of the elements of this matrix give the corresponding transition probabilities P_{nn}^R , according to

$$P_{nn}^R = \sin^2(\delta_n^s - \delta_n^a) \tag{15}$$

where δ_n^s is the phase shift for the symmetric solution for state n, and δ_n^a is that for the corresponding antisymmetric solution. The numerical procedure used for implementing the adiabatic approximation was as follows. The eigenvalue eq. (10) for $\epsilon_n(\rho)$ was solved for a grid of values of ρ. These eigenvalues form part of an effective potential for the $g_n(\rho)$. They are depicted in figure 4 for n=0,1,2 as asymptotically degenerate pairs of curves, the lower curve of each pair corresponding to even parity and the upper one to odd parity. The (uncoupled) ordinary differential equation for the adiabatic model $g_n(\rho)$ was then solved numerically, as an initial value problem, using an Adams-Moulton integrator, and from the asymptotic behavior of the $g_n(\rho)$ at large ρ, the phase shifts were obtained. It should be stressed that the scheme just outlined is two orders of magnitude faster than a solution of the set of coupled differential equations (14) which must be used in general. The diagonal term $\frac{\hbar^2}{2\mu} < \chi_n|\frac{\partial^2}{\partial\rho^2}|\chi_n >$ was not included in the effective potential used to calculate $g_n(\rho)$. Römelt[28] has shown that this diagonal term is important for the adiabatic modeling of resonances in non heavy-light-heavy systems. The diagonal term $< \chi_n|\frac{\partial}{\partial\rho}|\chi_n >$ is identically zero for real χ_n, as in the present case.

Figure 5 shows the reactive probabilities calculated with the adiabatic model along with the corresponding probabilities obtained from the accurate calculations. It can be seen that the adiabatic model results for n = 0 agree very well with the accurate

9

ones for low translational energies. For example, at translational energies in the range 0.35 eV to 0.51 eV, the difference between the two is only 6% or less. For higher energies, these approximate $n = 0$ results show the qualitative behavior of the accurate ones but are shifted in energy. The correct qualitative behavior is also displayed by the $n = 1$ and $n = 2$ adiabatic model results, again, with a slight energy shift. This suggests that improvements in this model may be possible via energy scaling, first order perturbation corrections, optical potentials, or other appropriate approaches. From these results, it appears that for heavy-light-heavy systems like the one studied in this paper, the hyperspherical adiabatic decoupling approximation provides a good qualitative picture of the dynamics even for vibrationally excited reagents. This is very significant since the difference in computational effort between the accurate and approximate methods is substantial and because of the insight this model provides. The qualitative correctness of the decoupling approximation for vibrationally excited reagent states for the present symmetric system is in accord with the results of Abusalbi, *et. al.*[19] for reaction from the first excited state of an asymmetric system. Low translational energy processes are chemically very important, and accurate dynamical approximations such as the one developed by Babamov and Marcus[21] are very useful.

5. Conclusions

We have presented the results of an accurate quantum mechanical calculation for a collinearly constrained model of the abstraction of a hydrogen atom from methane by a methyl radical. The dynamics have the general characteristics already noted for other heavy-light-heavy systems. The rather large barrier to reaction (13.86 kcal/mole), involving a saddle point whose energy is greater than that of the ground state reagent, allows tunneling to be observed clearly. For heavy-light-heavy systems with small barriers to reaction (less than 2 kcal/mole)[13,14,16] the detection of tunneling

is less straightforward. We have tested the hyperspherical vibrationally adiabatic model of Babamov and Marcus[21] and found that it describes the general dynamics of this system rather well for the ground and the first two vibrationally excited states of the reagents. In addition, the reaction probabilities for the ground state of the reagent are accurate to within 6% for translational energies in the range 0.35 eV to 0.51 eV.

11

References

(1) V. N. Kondratiev, "Rate Constants of Gas Phase Reactions"; Nauka: Moscow, 1970.

(2) E. D. Sprague and F. Williams, *J. Am. Chem. Soc.*,**93**, 787 (1971).

(3) R. J. LeRoy, E. D. Sprague, and F. Williams, *J. Phys. Chem.*,**76**, 546 (1972).

(4) R. L. Hudson, M. Shiotani, and F. Williams, *Chem. Phys. Letters*,**48**, 193 (1976).

(5) V. A. Benderskii, P. G. Philippov, Yu. I. Dakhnovskii, and A. A. Ovchinnikov, *Chem. Phys.*,**67**, 301 (1982).

(6) L. I. Trakhtenberg, V. L. Klochikhin, and S. Ya. Pshezhetsky, *Chem. Phys.*,**69**, 121 (1982).

(7) R. P. Bell, "The Tunnel Effect in Chemistry"; Chapman and Hall: New York, 1980.

(8) D. G. Truhlar, A. D. Isaacson, and B. C. Garrett, in "The Theory of Chemical Reaction Dynamics", edited by M. Baer (Chemical Rubber Company Press, Boca Raton, FL, 1985), Vol. IV.

(9) (a) A. Kuppermann, J. A. Kaye, and J. P. Dwyer, *Chem. Phys. Letters*,**74**, 257 (1980); (b) J. P. Dwyer, "Quantum Mechanical Studies of Reactive Scattering", Ph.D. Thesis, California Institute of Technology, 1977.

(10) G. Hauke, J. Manz, and J. Römelt, *J. Chem. Phys.*,**73**, 5040 (1980).

(11) M. Baer, *J. Chem. Phys.*,**62**, 305 (1975).

(12) J. Manz and J. Römelt, *Chem. Phys. Letters*,**76**, 337 (1980).

(13) J. A. Kaye and A. Kuppermann, *Chem. Phys. Letters*,**77**, 573 (1981).

(14) J. Manz and J. Römelt, *Chem. Phys. Letters*,**81**, 179 (1981).

(15) D. K. Bondi, J. N. L. Connor, J. Manz, and J. Römelt, *Mol. Phys.*, **50**, 467 (1983).

(16) J. A. Kaye and A. Kuppermann, *Chem. Phys. Letters*, 92, 574 (1982).

(17) P. L. Gertitschke, J. Manz, J. Römelt, and H. H. R. Schor, *J. Chem. Phys.*, 83, 208 (1985).

(18) P. V. Coveney, M. S. Child, and J. Römelt, *Chem. Phys. Letters*, 120, 349 (1985).

(19) N. Abusalbi, D. J. Kouri, V. Lopez, V. K. Babamov, and R. A. Marcus, *Chem. Phys. Letters*, 103, 458 (1984).

(20) C. Hiller, J. Manz, W. H. Miller, and J. Römelt, *J. Chem. Phys.*, 78, 3850 (1983).

(21) V. K. Babamov and R. A. Marcus, *J. Chem. Phys.*, 74, 1790 (1981).

(22) V. Aquilanti, S. Cavalli, and A. Lagana, *Chem. Phys. Letters*, 93, 179 (1982).

(23) V. K. Babamov, V. Lopez, and R. A. Marcus, *J. Chem. Phys.*, 78, 5621 (1983); *Chem. Phys. Letters*, 101, 507 (1983); *J. Chem. Phys.*, 80, 1812 (1984); *ibid.*, 81, 3962 (1984).

(24) H. Nakamura, *J. Phys. Chem.*, 88, 4812 (1984).

(25) H. Nakamura and A. Ohsaki, *J. Chem. Phys.*, 83, 1599 (1985).

(26) A. Kuppermann and J. P. Dwyer, in "Electronic and Atomic Collisions, Abstracts of Contributed Papers, 11th International Conference on the Physics of Electronic and Atomic Collisions", Society for Atomic Collision Research: Japan, 1979; pp. 888,889.

(27) J. M. Launay and M. LeDourneuf, *J. Phys. B*, 15, L455 (1982).

(28) J. Römelt, *Chem. Phys.*, 79, 197 (1983).

(29) J. Manz and H. H. R. Schor, *Chem. Phys. Letters*, 107, 542 (1984).

(30) K. C. Kulander, J. Manz, and H. H. R. Schor, *J. Chem. Phys.*, 82, 3088 (1985).

(31) J. Manz, E. Pollak, and J. Römelt, *Chem. Phys. Letters*, 86, 26 (1982).

13

(32) E. Pollak and J. Römelt, *J. Chem. Phys.*,**80**, 3613 (1984).

(33) E. Pollak, M. Baer, N. Abusalbi, and D. Kouri, *Chem. Phys.*,**99**, 15 (1985).

(34) N. Abusalbi, S. H. Kim, D. J. Kouri, and M. Baer, *Chem. Phys. Letters*,**112**, 502 (1984).

(35) M. Baer and I. Last, *Chem. Phys. Letters*,**119**, 393 (1985).

(36) R. A. Marcus, *J. Chem. Phys.*,**41**, 603 (1964); *ibid.*, **41**, 610 (1964); *ibid.*, **43**, 1598 (1965).

(37) S. Sato, *J. Chem. Phys.*,**23**, 592, 2465 (1955).

(38) P. J. Kuntz, in "Dynamics of Molecular Collisions - Part B", W. H. Miller, Ed.; Plenum: New York, 1976, pp. 65-69.

(39) M. Ya. Ovchinnikova, *Chem. Phys.*,**36**, 85 (1979).

(40) M. Born and J. R. Oppenheimer, *Ann. Phys.*, **84**, 457 (1927).

(41) U. Fano, *Phys. Rev. A*, **24**, 2402 (1981).

(42) A. Kuppermann in "Theoretical Chemistry: Advances and Perspectives"; Vol 6A; D. Henderson, Ed.; Academic Press: New York, 1981, (a)pp. 100-107; (b) p.85; (c) pp. 86-87.

(43) L. M. Delves, *Nucl. Phys.*,**9**, 391 (1959).

(44) L. M. Delves, *Nucl. Phys.*,**20**, 275 (1960).

(45) N. F. Mott and H. S. W. Massey, "Theory of Atomic Collisions"; Oxford University Press: Oxford, 1965, 3rd edition, p. 349.

Table I: LEPS Potential Energy Surface Parameters and Characteristics

	C-H interaction	C-C interaction
β/bohr^{-1}	0.9420	0.815
R_e/bohr	2.0662	2.910
D_e/eV	4.7270	3.660
$\triangle$	0.1850	0

Barrier height: 13.86 kcal/mol $\quad$ $M_H = 1.0078$ amu

Skew angle: 20.4° $\quad\quad\quad\quad\quad$ $M_{CH_s} = 15.0235$ amu

$E(n = 0) = 0.1803$ eV

$E(n = 1) = 0.5304$ eV

$E(n = 2) = 0.8665$ eV

FIGURE CAPTIONS

**Figure 1.** Potential energy contours for the model H_3C-H-CH_3 LEPS surface in Delves mass scaled coordinates (solid lines). The lowest contour is for 0.16 eV, the highest is for 0.8 eV, and the energy increment between consecutive contours is 0.04 eV. The dashed line is the minimum energy path.

Figure 2. Accurate transition probabilities as a function of energy. $P^R_{nn'}$ indicates the reaction probability from vibrational level n of the reagents to the vibrational level n' of the reaction products. The scale on the bottom abcissa on each panel denotes the translational energy of the reagent. The scale on the upper abcissa of the top panel denotes the total system energy measured from the bottom of the isolated reagent potential energy curve. This scale is common to all panels. The number in parenthesis beside some of the curves indicates the factor used to multiply the results before plotting. The arrows labeled "barrier" in the bottom abcissa of panels (a) and (b) indicate the energy of the classical barrier height.

Figure 3. Coordinates for a collinear triatomic system.

Figure 4. Eigenvalues $\epsilon_n(\rho)$ of the adiabatic basis as a function of the hyperradius. The eigenvalues are measured from the bottom of the isolated reagent potential energy curve. The tic marks on the right vertical axis represent the isolated reagent eigenvalues. These curves become pairwise degenerate as ρ increases. For each such pair, the lower (upper) curve corresponds to even (odd) parity.

Figure 5. Adiabatic model transition probabilities. The model results are represented by open circles (o) and the corresponding accurate results are represented by the solid lines and are the same as in figure 2. Scales are the same as in figure 2.

0.8eV

0.2eV

R_α/bohr

r_α/bohr

17
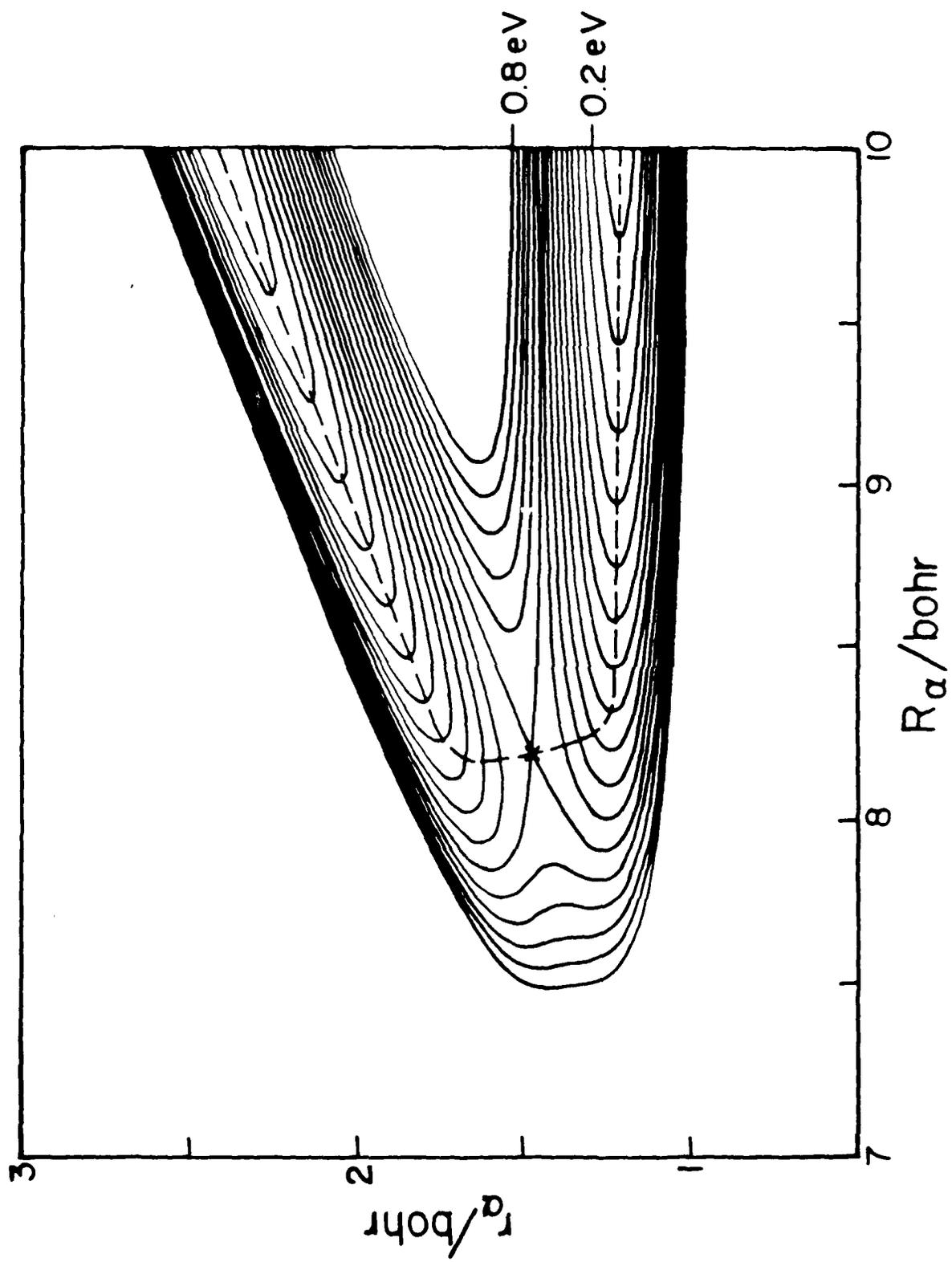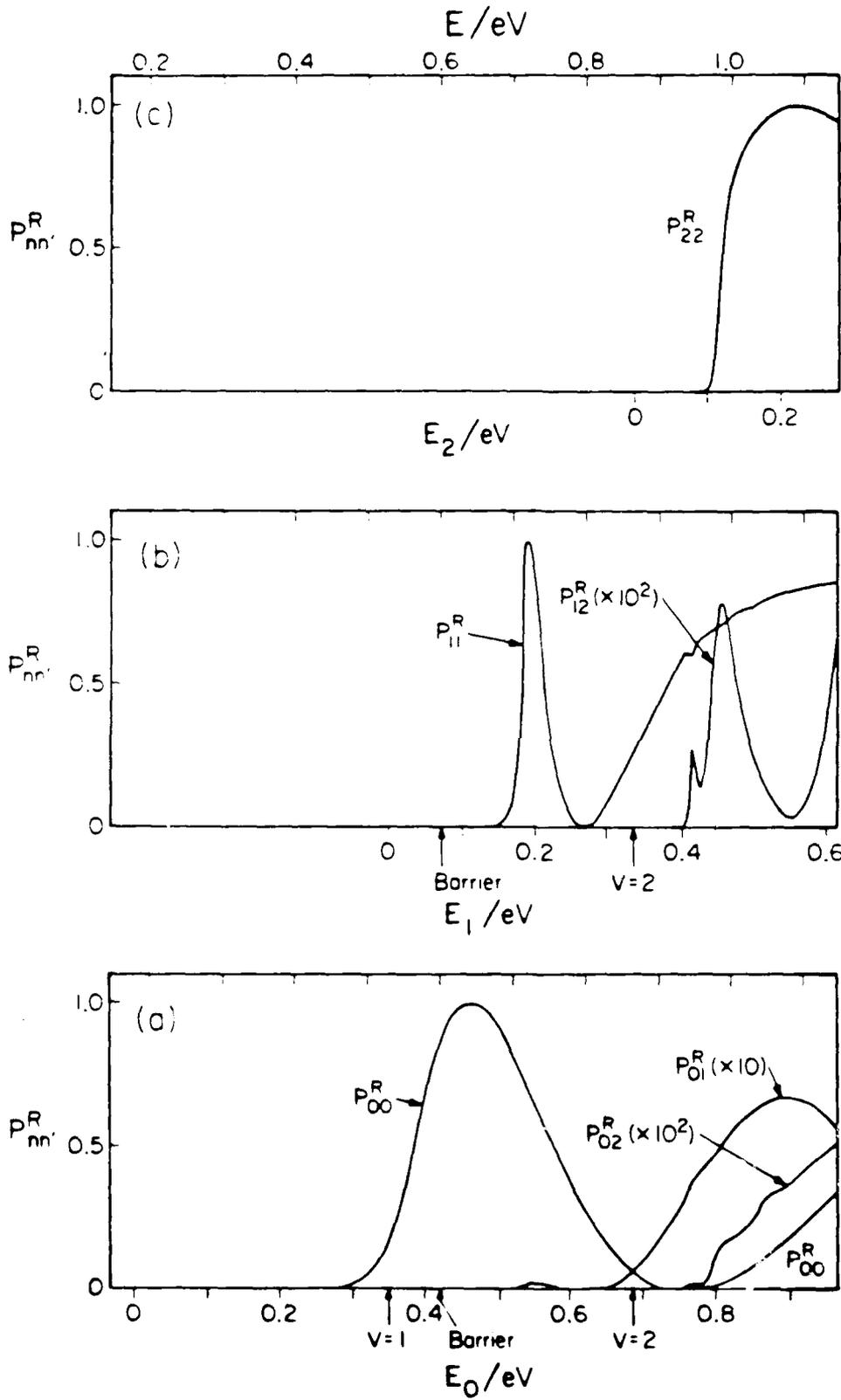
FIGURE 1.

FIGURE 2.

MICROCOPY RESOLUTION TEST CHART
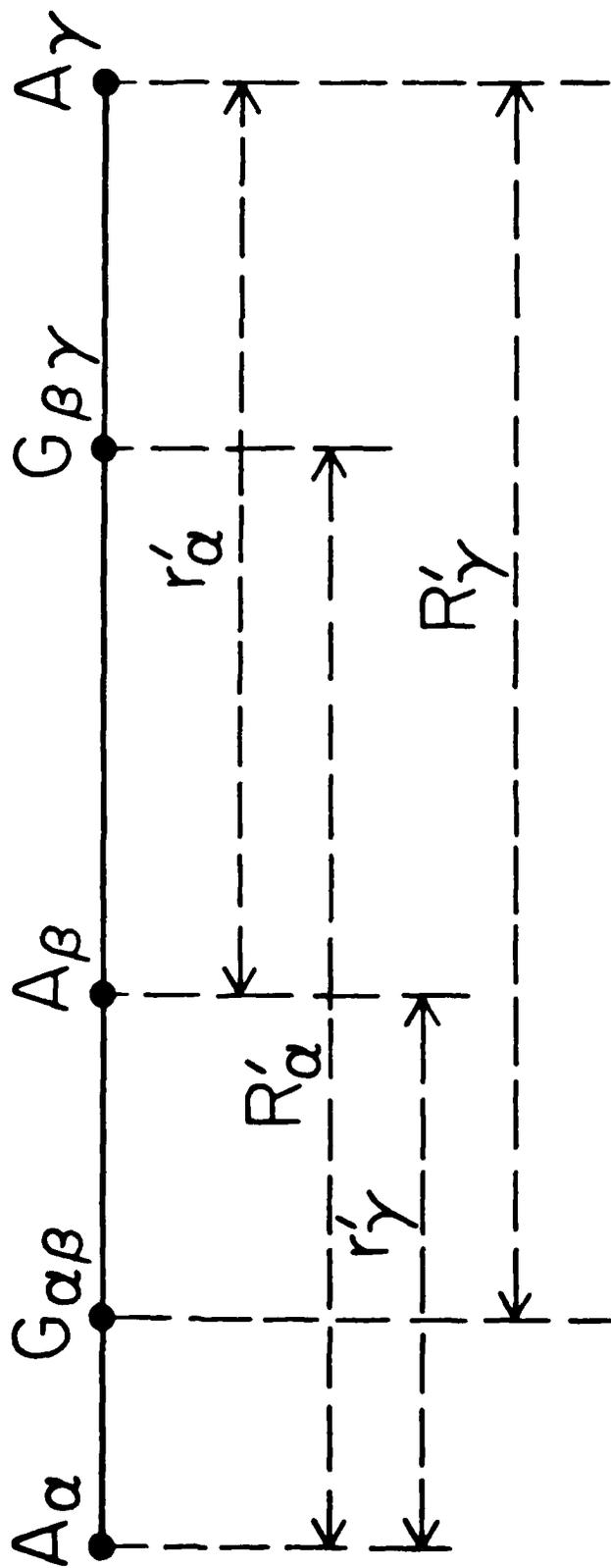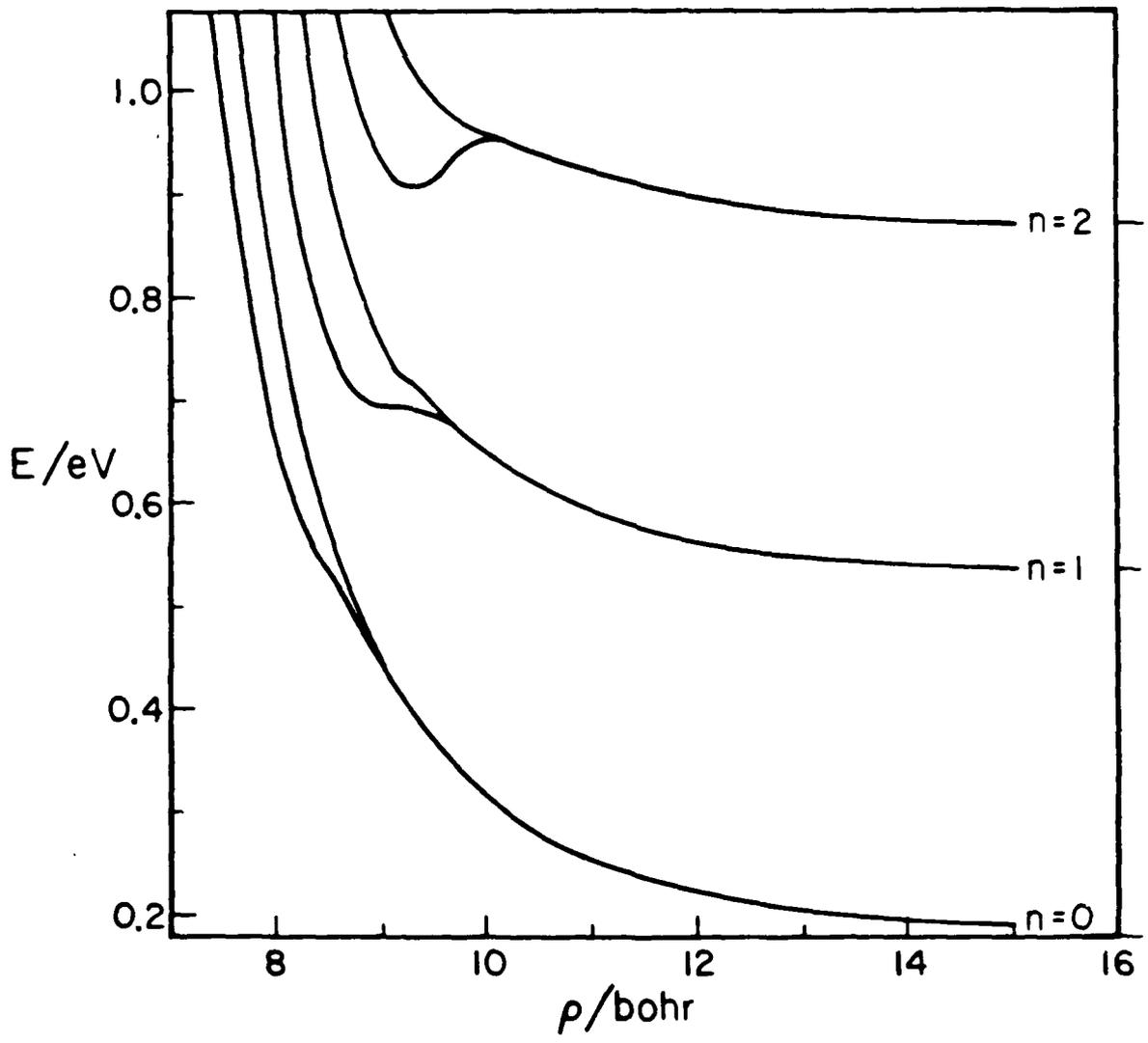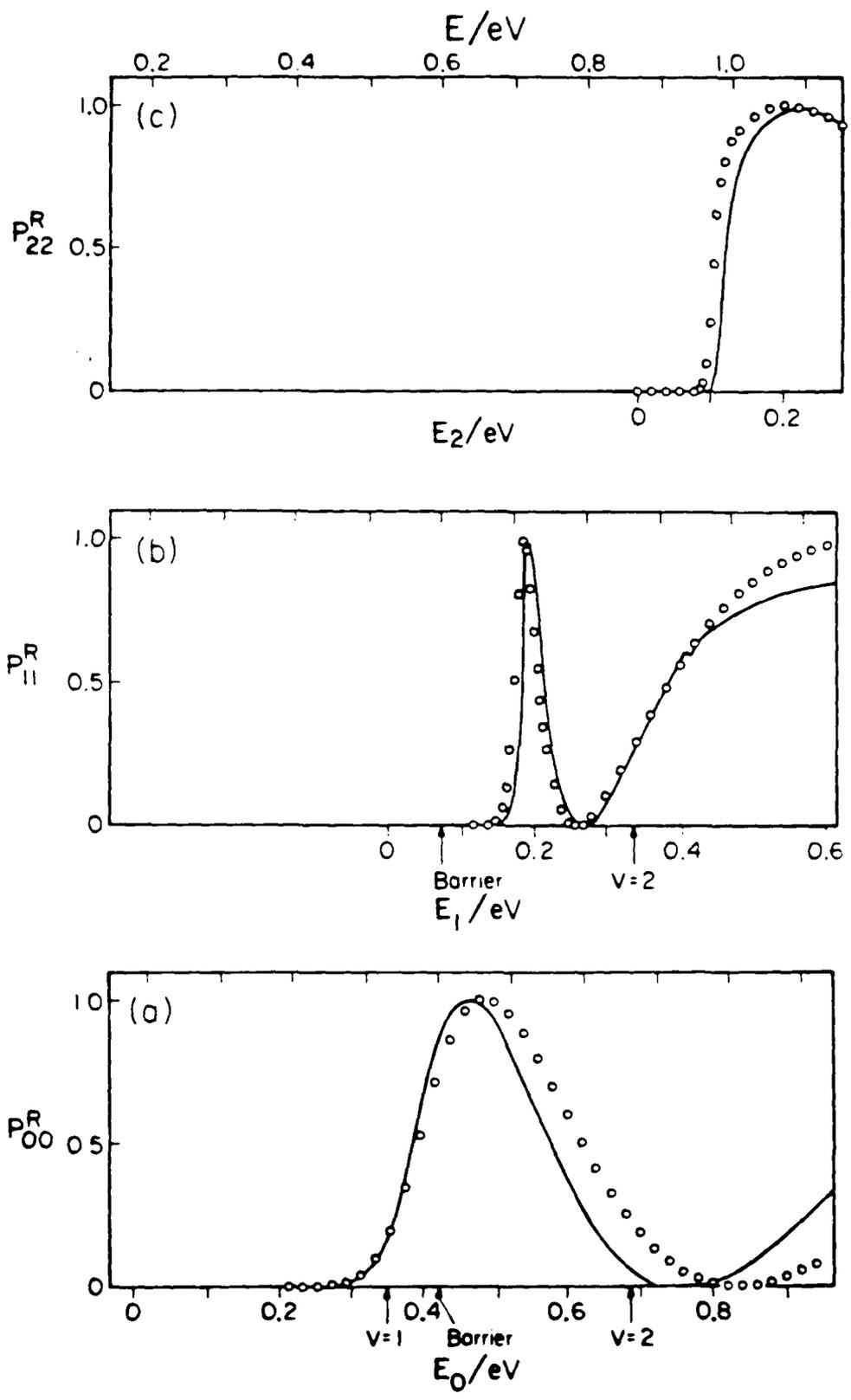
NATIONAL BUREAU OF STANDARDS 1963 A

FIGURE 3.

FIGURE 4.

FIGURE 5.

21

Three-dimensional quantum mechanical reactive scattering using symmetrized hyperspherical coordinates[a]

Aron Kuppermann and Paul G. Hipes[b]

Arthur Amos Noyes Laboratory of Chemical Physics, Division of Chemistry and Chemical Engineering,[c]
California Institute of Technology, Pasadena, California 91125

We report here the first three-dimensional (3D) reactive scattering calculations using symmetrized hyperspherical coordinates (SHC). They show that the 3D local hyperspherical surface function basis set leads to a very efficient computational scheme which should permit accurate reactive scattering calculations to be performed for a significantly larger number of systems than has heretofore been possible.

Approximately ten years ago the first accurate differential[1] and integral[1-3] cross section calculations for the 3D H + H$_2$ exchange reaction were reported. One of the methods[1] involved matching the solutions of the Schrödinger equation obtained for each of the three arrangement channel regions across half-planes in an internal configuration space separating those regions. The application of this method to less symmetric systems requires an excessive number of channels for satisfactory convergence. There have been no accurate 3D reactive scattering cross section calculations, involving competition among three arrangement channels,[4] reported since.

At about the same time, a system of SHC was developed.[5] Their usefulness in performing accurate and approximate 3D reactive scattering calculations was suggested,[5] and an appropriate computation methodology was outlined.[6] These coordinates are related to others introduced previously,[7] and are defined as follows. Let A, B, and C be three atoms, and $\mathbf{R}_a$ and $\mathbf{r}_a$ the mass scaled[8] vectors from the center of mass of BC to A and from B to C. We now define the hyperradius $\rho = (R_a^2 + r_a^2)^{1/2}$ and the hyperangle $\omega_a = 2 \tan^{-1}(r_a/R_a)$ in the 0 to π range. The factor of 2 in this definition is very important for symmetrizing the coordinates.[5] The body-fixed SHC are ρ, ω_a, θ_a, ϕ_a, γ_a, and ψ_a, where θ_a, ϕ_a are the space-fixed polar angles of $\mathbf{R}_a$ and γ_a, ψ_a the corresponding angles of $\mathbf{r}_a$ in a body-fixed frame whose polar axis is $\mathbf{R}_a$.

In these SHC, the 6D Hamiltonian H can be written as the sum of a hyperradial kinetic energy operator T(ρ) and a

hyperangular Hamiltonian $H(\mathbf{w}_a; \rho)$ which operates on the five angles $\mathbf{w}_a \equiv (\omega_a, \theta_a, \phi_a, \gamma_a, \psi_a)$. The eigenfunctions of H, called local hyperspherical surface functions (LHSF), form a complete discrete orthonormal basis set which spans the 5D hyperangular space defined by $\mathbf{w}_a$, for each value of ρ. They sample all regions of configuration space and, as $\rho \to \infty$, are related in a simple way to the isolated AB, BC, and CA diatom eigenfunctions. As a result, they constitute a very appropriate basis set for expanding the scattering wave function. Such an expansion leads to a set of coupled ordinary differential equations in the hyperradius, whose numerical solutions, together with a simple asymptotic analysis, furnishes the standard scattering matrix.

The usefulness of these ideas has been extensively tested for a variety of collinear systems, including H + H$_2$[9-11] and I + HI.[12,13] They have also been used as a tool for calculating dissociation probabilities,[14,15] and energy partitioning among the dissociation products[16] in collinear collision-induced dissociation. For collinear exchange reactions, an important feature of the surface function basis set is that it requires fewer asymptotically closed channels than do other approaches.[17-19] The reason for this high convergence efficiency with respect to the number of vibrational states is that, in the strong interaction region, the hyperangle acts as a rapidly changing variable whereas the hyperradius acts as a slow one.[20]

For 3D reactions, the corresponding LHSF can be expanded in the Wigner rotation functions of ϕ_a, θ_a, ψ_a[21] resulting in a set of coupled partial differential eigenfunction equations in the variables ω_a, γ_a. We have employed a finite element method[22] to solve these equations numerically for the H + H$_2$ system and total angular momentum $J = 0$. This approach is similar to a previous one[23] which employed a different variety of hyperspherical coordinates.[24] We then solved the associated scattering equations, using a logarithmic derivative method,[25] over the total energy range 0.5–1.0 eV, for the A_1, A_2, and E irreducible representations of the P_3
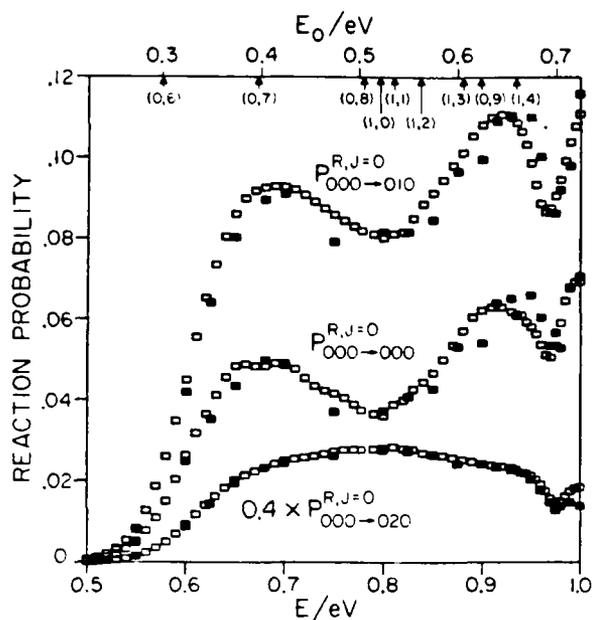
FIG. 1. Distinguishable atom $J = 0$ partial wave reaction probabilities as a function of energy for the $H + H_2(v,j,0) \rightarrow H_2(v',j',0)$ reaction on the Porter–Karplus potential energy surface (Ref. 29). The probabilities are denoted by the symbol $P^{R,J=0}_{v,j,0 \rightarrow v',j',0}$. The lower abcissa is the total energy and the upper abcissa the reagent translational energy. The vertical arrows on the upper abcissa denote the energy at which the corresponding $H_2(v,j)$ channel opens up. The open symbols represent the present results and the full ones those of a previous calculation (Ref. 1). The $P^{R,J=0}_{000 \rightarrow 020}$ results were multiplied by 0.4 prior to plotting.

symmetric group.[26] All LHSF were calculated for a grid of $40\,\omega_a$ and $50\,\gamma_a$ points. Up to 0.9 eV, $10 A_1$, $10 A_2$, and $20 E$ functions were used. Between 0.9 and 1.0 eV, where a Feshbach resonance occurs,[27] those numbers were increased to 14 and 28, respectively. In all these calculations, flux was conserved to 1%. With respect to basis set size, transition probabilities greater than 0.01 were converged to 5% and the corresponding phases to 2° over the entire energy range. The corresponding probabilities, within the $v = 0$ manifold, were symmetric to 2% and convergence with respect to the grid coarseness was 3% and 3° for those probabilities and phases. Including the $v = 1$ manifold, the probabilities greater than 0.01 were symmetric to 11% and convergence of those transitions with respect to grid coarseness was 10% and 15°.

From the irreducible representation scattering matrices, distinguishable atom reaction probabilities were calculated, some of which are displayed in Fig. 1, together with the results of previous calculations.[1] For energies below 0.9 eV the two methods agree to within 12% for the probabilities in this figure and 5° for the corresponding phases, which is very encouraging.

Once the LHSF and interaction matrix elements have been obtained, the solution of the scattering equations and the calculation of the scattering matrix is very efficient, taking on an FPS 164-VAX 11/780 system, about 23 s for 10 channels and about 3 min for 20 channels. This efficiency is

due in part to the absence of a matching procedure in the calculation. Instead, a simple asymptotic projection of the surface functions on the isolated diatom states is required. The surface functions themselves already span all three arrangement channels, and are energy independent.

Our finite element code for calculating the LHSF is accurate and efficient. The A_1 and A_2 functions (including the evaluation of all the interaction potential matrix elements needed for the scattering part of the calculation) required an average of only 17 s each, and the E functions utilized 34 s each. However, they were calculated at 140 values of ρ, which made their evaluation dominate the calculation, for the relatively small number of channels discussed here. A variational approach promises to be significantly faster. Recently, such a method has been developed for the $e + H$ system, which takes only about 0.3 s per surface function even for $J > 0$.[28] It is currently being adapted to triatomic systems and preliminary results indicate that it will speed up the calculation of the LHSF by one to two orders of magnitude.

In conclusion, the LHSF approach to 3D reactive scattering has been successfully tested and gives strong indications that it will become a powerful tool for studying the quantum dynamics of chemical reactions, which other accurate methods have so far not permitted.

[1] A. Kuppermann and G. C. Schatz, J. Chem. Phys. 62, 2502 (1975), 65, 4642, 4668 (1976).
[2] A. B. Elkowitz and R. E. Wyatt, J. Chem. Phys. 62, 2504 (1975), 63, 702 (1975).
[3] R. B. Walker, E. B. Stechel, and J. C. Light, J. Chem. Phys. 69, 2922 (1978).
[4] One accurate calculation, for the $H + BrH \rightarrow HBr + H$ exchange reaction, excluding competition with the $H_2 + Br$ abstraction channel, has been reported: D. J. Clary, J. Chem. Phys. 83, 1685 (1985)
[5] A. Kuppermann, Chem. Phys. Lett. 32, 374 (1975).
[6] R. T. Ling and A. Kuppermann, in Electronic and Atomic Collisions, edited by J. S. Risley and R. Geballe (University of Washington, Seattle, 1975), Vol. I, p. 353.
[7] R. C. Whitten and F. T. Smith, J. Math. Phys. 9, 1103 (1968), B. R. Johnson, J. Chem. Phys. 73, 5051 (1981).
[8] L. M. Delves, Nucl. Phys. 9, 391 (1959); 20, 275 (1960).
[9] A. Kuppermann, J. A. Kaye, and J. P. Dwyer, Chem. Phys. Lett. 74, 257 (1980), J. P. Dwyer, Ph.D. thesis, California Institute of Technology, 1977.
[10] G. Hauke, J. Manz, and J. Römelt, Chem. Phys. 73, 5040 (1980), J. Römelt, Chem. Phys. Lett. 74, 263 (1980).
[11] K. D. Bondi and J. N. L. Connor, Chem. Phys. Lett. 92, 570 (1982).
[12] J. A. Kaye and A. Kuppermann, Chem. Phys. Lett. 77, 573 (1981).
[13] J. Manz and J. Römelt, Chem. Phys. Lett. 81, 179 (1981).
[14] J. A. Kaye and A. Kuppermann, Chem. Phys. Lett. 78, 546 (1981).
[15] J. Manz and J. Römelt, Chem. Phys. Lett. 77, 172 (1981).
[16] J. A. Kaye and A. Kuppermann, Chem. Phys. Lett. 115, 158 (1985).
[17] C. C. Rankin and J. C. Light, J. Chem. Phys. 51, 1701 (1969), G. Miller and J. C. Light, ibid. 54, 1635, 1643 (1971); J. C. Light and R. B. Walker, ibid. 65, 4272 (1976).
[18] A. Kuppermann, in Proceedings of the Conference on Potential Energy Surfaces in Chemistry, edited by W. A. Lester (University of California, Santa Cruz, 1970), p. 121, Proceedings of the 7th International Conference on Physical and Electronic Atomic Collisions, 1972, p. 3, A. Kuppermann, in Theoretical Chemistry, Theory of Scattering Papers in Honor of Henry Eyring, edited by D. Henderson (Academic, New York, 1981), Vol. 6A, p. 79.

[19]B. R. Johnson, Chem. Phys. Lett. **13**, 172 (1972).

[20]A. Kuppermann and J. P. Dwyer, in *Electronic and Atomic Collisions, Abstracts of Contributed Papers, 11th International Conference on Electronic and Atomic Collisions* (Society for Atomic Collision Research, Tokyo, 1979), p. 888.

[21]A. S. Davydov, *Quantum Mechanics*, translated by D. ter haar (Addison-Wesley, Reading, MA, 1965), p. 151.

[22]G. Dhatt and G. Touzot, *The Finite Element Method Displayed*, translated by G. Cantin (Wiley, New York, 1984); K. J. Bathe, *Finite Element Analysis in Engineering Procedures* (Prentice-Hall, Englewood Cliffs, 1982), pp. 672–695.

[23]M. Mishra, J. Linderberg, and Y. Öhrn, Chem. Phys. Lett. **111**, 439 (1984); J. Linderberg, Int. J. Quantum Chem. (in press).

[24]C. A. Mead, Chem. Phys. **49**, 23 (1980); J. Chem. Phys. **72**, 3839 (1980).

[25]B. R. Johnson, J. Compl. Phys. **13**, 445 (1973), J. Chem. Phys. **67**, 4086 (1977); NRCC Workshop, Lawrence Berkeley Laboratory, Report No. LBL-9501, 1979.

[26]E. P. Wigner, *Group Theory* (Academic, New York, 1959), Chaps 7 and 13.

[27]G. C. Schatz and A. Kuppermann, Phys. Rev. Lett. **35**, 1266 (1975).

[28]D. M. Hood and A. Kuppermann, in *Theory of Chemical Reaction Dynamics*, edited by D. C. Clary (Reidel, Boston, 1986), D. M. Hood, Ph.D. thesis, California Institute of Technology, 1986.

[29]R. N. Porter and M. Karplus, J. Chem. Phys. **40**, 1105 (1964).

Total Scattering, Surface Ionization and Photoionization of

a Beam of H_3 Metastable Molecules[*]

James F. Garvey[†] and Aron Kuppermann

Arthur Amos Noyes Laboratory of Chemical Physics[§]

California Institute of Technology, Pasadena, CA, 91125

Abstract: In a previous paper we reported a technique for generating an intense hyperthermal beam of hydrogen atoms and metastable H_3 molecules. From the flight time of the H_3 species between the source and detector we estimated that its lifetime exceeds 40 μs and that it must therefore be in the 2p $^2A_2''$ excited Rydberg state. In this paper we report experiments utilizing this novel source of H_3 molecules. Beam - gas attenuation measurements indicate that the H_3-Ar cross section is roughly ten times larger than the H-Ar cross-section for translational energies in the 1 to 10 eV range. This observation is consistent with the assignment of the H_3 to that excited state, which has a much larger effective radius than a ground state hydrogen atom. The temperature dependence of the surface ionization of H_3 by heated tungsten and platinum filaments is used to obtain effective ionizational potentials of this species. These potentials suggest that upon interaction with a metal surface, the metastable state decays to the repulsive 2p $^2E'$ state which then surface ionizes to produce H_3^+. The production of H_3^+ and H^+ when the H_3 beam is irradiated with UV light from a high pressure mercury lamp was also observed and is attributed to the relatively low ionization potential ($\sim$ 3.7 eV) of the 2p $^2A_2''$ metastable state of H_3.

Chemistry, UCLA, Los Angeles, CA, 90024.

§ Contribution No. 7263

1. Introduction

For the past forty years the simplest neutral triatomic system, the triatomic hydrogen one, has been the subject of extensive investigations. The ground state potential energy surface of this species, relevant to the symmetric hydrogen exchange reaction has been calculated by many workers through a variety of techniques dating from the first Eyring and Polanyi calculations[1] to the present[2-4]. A thorough account of the history of these calculations is given by Truhlar and Wyatt[5]. That surface has no minima and H_3, in its electronic ground state, is unstable.

In apparent conflict with this theoretical result, several workers have reported the detection of a stable form of H_3. The first report of the existence of such a species came from Devienne and coworkers.[6-10] In their experiment a 1 to 12 KeV beam of H_3^+ is neutralized in a first charge exchange chamber containing He and the neutral beam formed, cleansed of ions by appropriate electrostatic deflection plates, is reionized in a second charge exchange chamber and detected in a mass spectrometer as ions with a mass to charge ration of 3. This was interpreted as evidence that some neutral H_3 molecules are formed in the first charge exchange cell and survived the traversal between that cell and the second charge-exchange chamber. Devienne observed that an appreciable fraction of these H_3 molecules lived for as long as a fraction of a microsecond.

A short time later Gray and Tomlinson[11] attempted to reproduce this result with either D_2H^+ or D_3^+ and observed no signal, suggesting that no neutral species had been generated. They concluded that Devienne's result was not due to neutral H_3 but rather to the presence of an HD isotopic impurity in his experiment. It was not until 1972 that Barnett and Ray [12] also reported the observation of H_3 claiming to have identified this species in an experiment identical to Devienne's, where the second charge-exchange process was now replaced by electric field ionization. That same year Nagasaki and co-workers[13], also in contrast to Gray and Tomlinson's

results, reported the generation of a beam of neutral D_3 using the same technique. In their paper they noted the apparent conflict between their estimated lifetime which was 10^6 times larger than the theoretically estimated life time of the ground state of D_3 of about 10^{-12} sec. They attempted to reconcile this disagreement by suggesting that the neutral species they had observed could indeed be in an excited electronic state of H_3, possessing a different lifetime from the ground state. In 1970, two years prior to the Nagasaki *et al.* results, the first theoretical study of the potential energy surfaces of excited electronic states of H_3 was carried out by Frenkel[14]. He performed restricted Hartree-Fock calculations in order to interpret collision experiments of H_2 with metastable 2s H atoms[15] and his results showed deep minima in the excited energy surfaces for H_3 (having D_{3h} symmetry) which could therefore support bound states.

The technique of neutralization and reionization of H_3^+ in order to study H_3 was not employed again until 1981 when Castro de Faria *et al.*[16] also reported the observation of that neutral species. From measurements of dissociation cross sections they suggested that the H_3^+ ions resulting from ionization of H_3 are not vibrationally excited. This indicates that the H_3 was in a excited Rydberg state since the capture or removal of an electron into or from a Rydberg state should leave the H_3^+ core unperturbed. This technique has been used again recently by Gaillard and co-workers[17]. By placing an electric field between the neutralization and reionization gas cells they were able to show that for fields of 1.5 to 50 kV/cm a fraction of the neutral triatomic molecules are destroyed. This indicates that the H_3 is in a weakly bound state with $n < 10$ (where n is the principal quantum number).

A different approach has entailed beam studies in which the dissociation products of the neutralized H_3^+ are detected directly. Vogler[18,19] used a time-of-flight difference method and observed the spontaneous dissociation products of H_3 which are formed by the non-resonant neutralization of H_3^+ with H_2. The H-H_2 fragment pairs are observed using two separate detectors operating in a coincidence mode such that the velocity vectors of the fragments may then be determined from the flight-

time difference of the two fragments. This technique was also used by Cisneros and co-workers[20] to observe the angular distribution of the dissociation products D_2 and D following electron transfer from Cs to D_3^+ . Curtis *et al.*[21,22] have also attempted this kind of experiment, producing H_3 by electron transfer from Mg to H_3^+ . However, in none of the above experiments[18-22] was there any evidence observed for a metastable state of H_3.

At roughly the same time new experimental evidence for H_3 came from a novel experiment by Herzberg. While running H_2 at 1 torr in a hollow cathode discharge different emission spectra were obtained from the cathode and anode regions. Subtraction of the two spectra resulted in a series of broad visble light bands that could be assigned to Rydberg to Rydberg transitions of H_3.[23-27]

The findings of Herzberg stimulated theoretical calculations[28-34] which have successfully described the rotation band spectra he observed. Recently, Mayne and co-workers[35] have calculated the absorption spectra of transition state configurations of H_3 and other theorists have already begun to extend electronic state calculations to larger systems, such as H_4[36,37], and H_5[38]. Because of this theoretical effort some interpretations of previous experiments have been changed. Watson[39], re-evaluating Vogler's past results[18,19], suggested that the energy distribution of the dissociation products observed is due to a predissociation from a Rydberg state of H_3. The King and Morokuma calculation[28] shows that the predissociation process of the lowest excited state is exoergic by approximately 5.57 eV. On the basis of this theoretical result Watson proposed that Vogler's product energy distribution was due to that predissociation, thereby making Vogler's work the first experimental determination of the energy of a known electronic state of H_3 relative to the dissociation products of H_2 and H.

In light of Herzberg's results and in view of a private communication of our own results, Porter recently repeated his own charge-exchange experiments in an attempt to observe a long-lived species of H_3. By increasing the angular resolution of his apparatus[40] as well as using K instead of Mg as the charge-exchange target,

he was able to observe a metastable state of H_3 [41,42].

Recently, a great deal of interest has been generated in the spectroscopy of H_3. Freeman and co-workers[43] attempted to reproduce Herzberg's result by colliding H_2 gas with high energy (0.5 MeV) electrons, but failed to detect any H_3 emission. However, Figger and co-workers[44,45] have recently begun to employ laser spectroscopy to study the hollow cathode discharge of H_3. By placing the discharge tube in the tuning arm of a color-center laser they observed the discharge emission at a selected line of D_3, as a function of laser frequency. This has proved extremely helpful in the observing and assigning of new spectral features of D_3. Figger *et al.*[46] have also begun to perform emmission spectroscopy on beams of D_3 created by charge-transfer D_3^+ with alkali metals. The D_3 molecules are produced in electronically excited states, such that after leaving the alkali metal cell they emit light in a collision free region, which is then measured spectroscopically. To date only transitions between the Rydberg states $n = 3$ and $n = 2$ have been observed but all the lifetimes measured by this technique are in good agreement with the *ab initio* calculation by King and Morokuma[28]. Additional spectroscopic experiments have recently been performed on beams of H_3 created by charge transfer of H_3^+ by Cs by Helm[47]. The H_3 metastable is further excited by a tunable laser beam, field ionized and detected by a mass spectrometer. Transitions to high Rydberg levels were dtected. In summary, with the exception of Herzberg's result[23-27], all of the H_3 experiments discussed so far have used H_3^+ ions (or their isotopes) having energies in the keV to MeV range which are then neutralized by charge exchange.

In a previous letter we have reported the first direct observation of a hyperthermal beam of metastable H_3 molecules, intense enough for scattering as well as spectroscopy experiments[48], which is generated directly as a neutral species from a high temperature arc-discharge source[49-52]. In this paper we report scattering, photoionization and surface ionization experiments utilizing this new source of H_3 metastables. These experimental results confirm the nature of H_3 as due to a Rydberg metastable species.

2. Experimental

2.1 H_3 Beam

Through characterization and development of an arc-discharge source for the production of hyperthermal hydrogen atoms, it was observed that this plasma source was capable of generating other novel molecular species. The beam apparatus is depicted schematically in Figure 1. The discharge source is similar to that described previously[48-52]. It is placed in a vacuum chamber [VC1], pumped by a 20″ Westinghouse oil diffusion pump, and is connected by a flexible bellows to a test stand consisting of a bell jar [VC2] pumped by a system comprising a 6″ mercury diffusion pump, a freon-cooled chevron baffle and a liquid nitrogen trap. Differential pumping between these two chambers is provided by a skimmer [S] with an orifice diameter of about 1 mm with a knife-sharp edge. Chamber VC2 contains a beam flag [F], a 10 Hz beam chopper [C1] which modulates and allows AC detection of the beam, a pair of electrostatic deflector plates [D] which eliminate ions from the beam, and an EAI 300 quadrupole mass spectrometer with an electron bombardment ion source [QMS].

The arc discharge in the H-atom source can be run continuously for many hours with a H_2 stagnation pressure of 50 to 100 torr such that the pressure in chamber VC1 is of the order of 10^{-2} torr and in chamber VC2 of the order of 10^{-5} torr. The source [AS] can be moved with respect to the skimmer with the help of a translation assembly [TA] permitting the apparatus to be operated in two modes. The first mode, in which the nozzle is far away (about 17 cm) from the skimmer allows spectroscopic observation of the intense red emission of the plasma plume in front of the nozzle (as depicted in Figure 1). The second mode involves moving the nozzle to within about 4 cm of the skimmer to maximize the intensity of the H-atom beam as detected by the mass spectrometer. This source produces a reliable, intense beam of hyperthermal hydrogen atoms.

As shown in figure 2, during the operation of the discharge we observed a $m/e = 3$ 10 Hz AC ion signal in the mass spectrometer when the beam was run with H_2 and chopped at that frequency, and a $m/e = 6$ ion signal when the beam was run with D_2. Figure 3 shows that by varying the stagnation pressure in our arc-heated source we are able to vary the ratio of the $m/e = 3$ to $m/e = 1$ signal from 0 to about 1. As seen in that figure the signals for H and H_3 increase and their ratio decreases as the stagnation pressure is reduced. As a result, we may use the stagnation pressure to control the relative amount of H_3 with respect to H.

We have determined that the $m/e = 3$ signal cannot be attributed to ions present in the beam before it enters the mass spectrometer. Indeed that beam passes through an electric field produced by a pair of deflector plates ([D], figure 1) which has sufficient strength (1 kV/cm) to deflect any charged particles out of the initial beam direction. Furthermore, as can be seen in figure 2, the signal virtually vanishes when the electron beam is turned off.

The additional possibility that the origin of the observed $m/e = 3$ signal is H_3^+ formed in the ionizer by some ion molecule reaction involving ions formed by electron bombardment is precluded by observing that under our experimental conditions the expected signal from such a process would be less than 10^{-3} of the observed $m/e = 3$ signal. This subject is treated in greater detail in appendix A.

A crude energy analysis of this metastable H_3 species utilizing ion-retarding elements in the optics of the mass spectrometer indicates a translational energy distribution function having, for a source stagnation pressure of 70 torr, a peak at about 8 eV and a width of about 7 eV. From these measurements we can estimate flight times and obtain a lower bound for the lifetime of the observed H_3 species of the order of 40 to 100 μs. A calibration of the detector indicates an absolute H_3 flux per unit solid angle of the order of 10^{21} molecules/(s sterad). Under identical experimental conditions the same peak position is obtained for the H atoms but the width is decreased to about 3 eV. This indicates that both the H and H_3 are heated to about the same extent in the plasma. Upon decreasing the arc source stagnation

pressure to 55 torr, the peak of the energy distribution function for both H and H_3 shifts upwards to about 13 eV. This observation indicates that decreasing the stagnation pressure increases the effective temperature of the plasma.

As additional confirmation of the presence of H_3 in our beam we observed emission spectra of the plasma plume which compares well with Herzberg's spectra[26]. This plasma plume appears directly in front of the nozzle of the beam source. Our spectra were obtained through a quartz port using a 0.5m Jarrell-Ash monochromator pointed at the plasma plume from a direction perpendicular to it as shown in figure 1. Figure 4 shows an energy level diagram for H_3 and its disociation products. The spacing of the H_3 energy levels correspond to the wquilateral triangle configuration and is the one calculated by King and Morokuma[28]. They were referred to the energy of those products using the calculated values of Kulander and Guest[53]. The two transitions which we observed previously[48] are also indicated.

The most likely candidate state for the H_3 metastable molecule produced in our beam[48] is 2p $^2A_2''$, the second excited state of this species. The first excited state, 2s $^2A_1'$, can predissociate to the 2p $^2E'$ repulsive ground state by coupling with a vibrational mode of symmetry e'. However, for the 2p $^2A_2''$ state there can be no vibronic predissociation[24] and only a rovibronic mechanism would permit predissociation to occur. We can also rule out any higher metastable Rydberg states for reasons outlined in appendix B of this paper.

2.2 Scattering Cell

Interesting information may be obtained by the study of the scattering of a beam of molecules by a gas target. From the measurement of the attenuation of the beam it is possible to derive a total collision cross section. Since the metastable H_3 would be expected to have a large radius, due to the Rydberg nature of the state it is in, we felt it would be informative to measure its total scattering cross section with a reference gas such as argon. For the experiment we utilized as a scattering chamber an aluminum cell whose suraces were black anodized. A sketch of this cell, together

with its mounting flanges, is given in Figure 5. The path length through the cell is 4.0 inches when the 1/4 inch diameter apertures indicated in that figure are in place, and 2 inches otherwise. A pair of deflection plates, between which a 1 kV/cm electric field is produced, are mounted before the entrance to the cell to deflect any ions out of the beam and permit only neutral species to enter the cell. Figure 6 shows the scattering cell in place in the bell jar (VC2). Approximately one and a half orders of magnitude pressure differential could be maintained between the cell and the bell jar such that pressure in the latter never rises above about 1×10^{-4} torr (while the arc discharge beam is on). The pressure in the scattering cell was measured using an uncalibrated Schulz-Phelps gauge and a Granville-Phillps high-pressure ionization gauge controller (series 224). The intensity of the beam was measured as usual by electron impact mass spectroscopy as described in section 2.1.

2.3 Surface Ionization

Since our metastable H_3 species has some similarities to an alkali atom in that they both have low ionization potentials (about 3.7 eV for 2p $^2A_2''$ H_3 [28]) and an outer shell having one electron only, it is expected to surface ionize when colliding with a heated filament having a high work function. Rubidium atoms have an IP (4.18 eV) close to that of metastable H_3 and exhibit an ionization efficiency of 90% on platinum at 1200 K and 100% on tungsten at 1400 K[54]. If metastable H_3 does indeed ionize upon interaction with a hot filament, this process could prove to be a highly selective detector for this species in the presence of high ionization potential atoms or molecules.

To perform this experiment it was necessary to modify the ionization region of the mass spectrometer. Two ceramic blocks were set on opposite sides of the mass spectrometer ionization chamber such that from these blocks either a platinum or tungsten filament could be suspended through the middle of the ionization region. This filament is electrically insulated from the rest of the electronics and does not affect the normal operation of the mass spectrometer ion source. This was verified

by testing the mass spectrometer with just background gas and observing no change in the original mass spectrum with either a hot or cold surface ionization filament. When surface ionization measurements are to be made, the electron impact ionizer is turned off and the filament wire may be heated by passing a DC current (0 to 2.0 A) through it with the help of an HP 6236A power supply. Any ions formed and detected under such conditions can be due only to surface ionization processes occurring on the filament.

By varying the current to the filament it is possible to control its temperature. The latter was measured using a micro-optical pyrometer (Pyrometer Instrument Co., Bergenfield, N. J. Model 95) having a reported accuracy[54] between $\pm$ 4° at 1000 K and $\pm$ 10° at 2800 K).

This arrangement permits us to measure the efficiency for producing any ion as a function of the temperature of the filament since the absolute intensity of the incident beam can be measured with the help of the electron bombardment ionizer (section 2.1) and is known as a function of stagnation pressure[48]. The .005″ diameter wire subtends about 5% of the cross-sectional area of the beam in the ionizer region, which permits us to estimate the flux incident on the wire. By taking the ratio of the ion flux of a particular mass emanating from the hot filament to the incident neutral flux of H_3 the ionization efficiency for the production of that particular ion is obtained (assuming that the H atoms and the H_2 molecules present in the beam cannot surface ionize under these experimental conditions).

2.4 Photoionization Cell

Due to the relatively low IP of its 2p $^2A_2''$ state, it should be possible in principle to photoionize H_3 with visible or ultraviolet light of an appropriate wavelength($\lambda <$ 3300 Å). To perform this experiment we used the same cell as for the total scattering experiments, as shown in figures 5 and 6. The inside of the cell may then be illuminated by focusing the light from an appropriate source through a quartz window into the cell. The light that is not absorbed by the beam is reflected by a spherical

mirror at the end of the cell, producing a double pass illumination. That light may excite or ionize some of the H_3 passing through the cell. Since the momentum carried away by the ejected electron is very small, the ions formed will not be significantly deflected and will traverse the cell to be ultimately detected by the mass spectrometer located at the end of the bell jar and in line with the neutral beam. The cell is made of aluminum and is black-anodized to help prevent light being reflected into VC2. In addition, the entrance and exit apertures help decrease the amount of the mercury lamp scattered light from entering the mass spectrometer and producing a background signal on the electron multiplier.

For these photoionization experiments we decided to use a broad, intense source of excitation that would extend well into the UV. A Bausch & Lomb (cat. no. 33-86-36-01) 200-watt, short-arc, super-pressure mercury lamp which is enclosed in a quartz envelope was selected. It has a high luminance and an exceptionally high spectral radiance in the ultraviolet. This light source is known to give a continuous, fairly uniform intensity spectrum covering the UV, visible and infrared region of the electromagnetic spectrum except for the very high-intensity discrete lines which are characteristic of the mercury arc spectrum. For the 440 nm mercury line (the most intense line in the output spectrum of the lamp) we calculate an intensity for it of 3.6×10^{14} photons cm^{-2} s^{-1}.[55]

Through the use of two quartz lenses (one inside the mercury lamp unit [ML] and one outside [L], figure 6) the output of the lamp is focused directly into the cell through which the neutral beam must pass before reaching the mass spectrometer. Figure 6 shows the lamp position on the exterior of the vacuum chamber. Testing the mass spectrometer with the lamp on produced no change in the background signal, indicating that any stray light which may be escaping from the cell does not interfere with the normal operation of the mass spectrometer.

3. Results and Discussion

3.1 Total Scattering

Figure 7 shows the logarithm of the transmittance I/I_o (ratio of the beam intensity measured by the electron bombardment mass spectrometer with target molecules in the cell to the beam intensity without scattering gas in the cell) for H, H_2, and H_3 as a function of the pressure of argon, measured by an uncalibrated Schulz-Phelps gauge. These points lie on a straight line as expected from theory.

With no gas in the scattering cell $(p = 0)$, by defination $I/I_o = 1$, but this reference point is not included in Figure 7. The lowest pressure at which we could make reproducible measurements was about 0.5×10^{-3} torr. The line for H in that figure does have a linear intercept of 1.0, as expected, but those for H_2 and H_3 do not, displaying a steeper slope between $p = 0$ and $p = 0.5 \times 10^{-3}$ torr than the rest of the corresponding line. This suggests the presence in the H_2 and H_3 beams components of larger cross section than those implied by the $p > 0.5 \times 10^{-3}$ torr measurements. For H_3, this may indicate higher Rydberg states than the $2p\ ^2A_2''$ one which, for reasons not presently understood, were not completely quenched by the deflection field, or did not decay radiatively by the time they reach the scattering cell (see Appendix A). We limit our discussion to the reproducible $p > 0.5 \times 10^{-3}$ torr results.

From these results one can obtain the effective total cross section, Q, and from it the corresponding interaction radii. The method we used to calculate Q is based on that of Rosin and Rabi[57] and is partially described by Levine and Bernstein[58a]. The probability that a beam molecule of laboratory velocity v_b will pass through a scattering chamber of length l without being deflected is given by

$$P(v_b) = \exp\left(-\frac{l}{\lambda}\right) \tag{1}$$

where λ is the mean free path. This means that the beam flux is an exponentially decreasing function of the length of the scattering path, a result similar to the Beer-Lambert law for the attenuation of a beam of light by absorption.

From the slope S of plots of ln (I/I_o) versus the target gas pressure in the scattering cell, Q may be approximately calculated using the Rosin-Rabi equation[57]. This equation is

$$Q = 2(\pi)^{\frac{1}{2}} J(z)\left(\frac{\ln\left(\frac{I}{I_o}\right)}{nl}\right) \tag{2}$$

where

$$J(z) = z^2 \int_0^\infty \left[\frac{x^5}{\Psi(x)}\right] \exp\left(-zx^2\right) dx \tag{3}$$

$$\Psi(x) = x \exp\left(-x^2\right) + (2x^2 + 1) \int_0^z e^{-\nu^2} dy \tag{4}$$

$$z = \frac{m_b T_t}{m_t T_b} \tag{5}$$

$$x = \frac{v_b}{\left(\frac{2kT_t}{m_t}\right)^{\frac{1}{2}}}. \tag{6}$$

In these expressions n is the scattering target gas number density, k the Boltzmann constant, l the scattering path length, and m, v and T stand for mass, velocity and temperature respectively, while the subscript b refers to the beam molecule and the subscript t refers to the target molecule. Rothe has shown that for I/I_o in the range of 0.1 to 1.0 the deviation between this approximate expression of equation 2 and the exact equation is 5% at most[59]. The quantity J(z) defined by equation 3 is obtained from Rosenberg's table[60]. The angle subtended by the entrance aperture to the mass spectrometer at the midpoint of the scattering center is about 1°. This leads to an underestimation of the integral cross sections, and in the absence of other errors would be a lower limit to the correct cross section.

We may now employ equation 2 to obtain the total cross section for scattering by argon (Figure 7). For our present measurements, substituting in the appropriate experimental values for our apparatus with a 4 inch path length, equation 2 yields

$$Q = [3.05 \times 10^{-18}(S)]\text{Å}^2 \tag{7}$$

where S is the slope in torr^{-1}. By using a least square fit of the data points of Figure 7 we can get values for S and therefore Q for collisions of H, H_2, and H_3 with Ar. These cross sections are listed in Table I for a source stagnation pressure of 57 torr. The uncertainties in Table I represent 95 % confidence level. Since however the pressures were measured with an uncallibrated Schulz-Phelps gauge, those uncertainties only represent reproducibility errors but not the accuracy of the measurements.

There have been many experimental[58,61] and theoretical[60] studies on the absolute total cross sections for scattering of atomic hydrogen by argon. However, these studies were done at energies up to only 1 eV and cannot be directly compared with our result since this is the first scattering experiment using H atoms in the 5 eV to 15 eV energy range. It has been shown[62] that at high energies the major contribution to the elastic cross section comes from scattering by the repulsive core, resulting in a linear dependence of the logarithm of the cross section on the logarithm of the velocity. If we use this functional form to extrapolate the results of Das and co-workers[63] to our energy ($\sim$ 13 eV), we obtain a cross section of 4.4 Å^2. This differs from our total cross section of 1.7 Å^2 by a factor of 2.5. This difference can be attributed to our angular resolution, our broad hydrogen atom energy distribution, the lack of callibration of our Schulz-Phelps ionization gauge and the fact that an extrapolation of over more than an order of magnitude in energy was involved.

Let us also discuss our results in terms of the relative cross section, Q^*, which is defined as

$$Q^*_{X-Ar} = \frac{Q_{X-Ar}}{Q_{H-Ar}} \tag{8}$$

where Q_{X-Ar} is the cross section of the beam species X with Ar, and Q_{H-Ar} is the cross section of the H with Ar. This ratio eliminates the errors due to the lack of callibration of the Schulz-Phelps gauge. Our experimental results for Q^* are also given in Table I. Rothe and Bernstein[64] report that in atom-molecule total cross section measurements, while the absolute cross sections may vary over a range of $\pm$ 10%, the ratio of the cross section of two gases were reproducible to within $\pm$ 3%. In the case of our data for H_2 we obtain a $Q^*_{H_2-Ar}$ of 1.9.

This value can be rationalized on the basis of a very simple energy-dependent hard sphere radius model for argon. Taking the radius of H to be 0.53 Å, the effective Ar radius (for high energy collisions) which will produce a value of Q_{H-Ar} of 1.7 Å^2 is 0.21 Å. Using an effective radius for H_2 as 0.90 Å ($\frac{1}{2}$ of the H_2 internuclear distance plus the H radius), this yields a H_2-Ar hard sphere collision cross section of 3.8 Å^2 and a $Q^*_{H_2-Ar}$ of 2.2. This is in reasonable agreement with the measured values of

3.3 Å^2 and 1.9 respectively. Independently, the $H_2 - Ar$ collision cross section has been measured as a function of relative energy up to 100 meV[65]. Extrapolation to ~ 13 eV furnishes a value of 12.4 Å^2 and a $Q^*_{H_2 - Ar}$ with respect to the Das *et al.* results[62] of 2.8, compared to our measured result of 1.9, which is not unreasonable, in view of the gross nature of the model and extrapolations used.

For H_3 we measure a Q^* of 10. This large value may at first appear excessive but this is not the case considering that the H_3 molecule is in an excited Rydberg state. With a bond distance some .02 Å smaller than H_3^+ (as determined by Herzberg *et al.*[26]), the metastable molecule may be pictured as a stable H_3^+ core having an equilateral triangle equilibrium geometry, with the Rydberg electron (which makes it neutral) in a 2p orbital perpendicular to the plane of the triangle. As a result, the triangle contracts slightly to accommodate the additional electron. Figure 8 shows a representation of this molecule with a hydrogenic $2p_z$ orbital (perpendicular to the plane of the nuclei) representing the 2p Rydberg orbital of H_3. The Bohr radius for a hydrogenic orbital in the $n = 2$ state is 2.12 Å. Taking this as the radius of H_3 in the 2p $^2A_2''$ state and the effective argon radius of 0.21 Å obtained from the H scattering experiment, this furnishes a $Q_{H_3 - Ar}$ of 17 Å^2 and a $Q^*_{H_3 - Ar} = 10$, in surprisingly good agreement with the measured values of 17 Å^2 and 10, respectively. From this simple analysis we see that it is quite reasonable for H_3 to have a collision cross section with Ar an order of magnitude greater than that with a hydrogen atom.

We also performed similar experiments with a higher stagnation pressure in the arc source. As previously observed in section 2.1, increasing the stagnation pressure lowers the translational energy of all species in the beam and thereby should increase its scattering cross section. Figures 9 and 10 show data for the scattering of H and of H_3 generated at a 65 torr stagnation pressure by argon and propane as target gases. The corresponding cross sections are shown in Tables II and III. The precision uncertainties listed represent a 95% confidence level. For the scattering of hydrogen atoms with argon we see that the cross section has increased by a factor of 1.7 as the stagnation pressure was increased from 57 to 65 torr.

Using the same analysis as before we calculate an effective Ar radius of .43 Å. Extrapolating again Das and co-workers[63] results to our peak energy of about 10 eV (pertaining to a 65 torr stagnation pressure) we get a cross section of 5.2 Å^2. This is greater than our measured value of 2.9 Å^2 by a factor of 1.8, but is closer to the 65 torr result than the 57 torr ones. As expected, as the stagnation pressure increases, with a concomitant lowering in translational energy, our cross sections move towards the Das *et al.* results.

For H$_3$ we see that the cross section for scattering by Ar has increased by a factor of 1.7 as well, in going from 57 torr to 65 torr stagnation pressure. The fact that both the H$_3$ and H cross sections increased by the same factor is not unreasonable. Both H$_3$ and H have roughly the same translational energy at the same stagnation pressure, presumably because they are heated to the same extent in the plasma discharge. Under these conditions, their cross sections should be affected in a similar manner, as observed. Using the effective Ar radius obtained at the 57 torr source stagnation pressure experiments and the H$_3$ radius of 2.12 Å we calculate a hard sphere scattering cross section for H$_3$ plus Ar to be 20 Å^2 and a $Q^*_{H_3-Ar}$ of 7. This is in reasonable agreement with our measured values of $Q_{H_3-Ar} = 30$ Å^2 and $Q^*_{H_3-Ar}$ = 10 respectively.

Lastly, we wanted to see what effect a larger scattering target would have on the cross sections. For this reason we chose to use propane as another scattering gas. The results obtained using propane at the same stagnation pressure (65 torr) of the previous experiment are also shown in Figures 9 and 10 and listed in Table III. We see that the H-propane cross section has increased by a factor of 7 compared to the H-Ar one at the same energy. An increase in the cross section is expected since the H atom is small compared to the target and will be very sensitive to a change in the latter's size. In contrast, there is no significant change in the cross section for H$_3$-propane ($[25.4 \pm 0.6]$Å^2) compared to H$_3$-Ar ((30 ± 7)Å^2). This as well is not unexpected since the large size of the metastable H$_3$ molecule will make it relatively insensitive to a change in the target size.

Using the same analysis as for the argon experiment at 57 torr we calculate an effective propane radius of 0.92 Å from the H plus propane scattering cross section at 65 torr (with 0.53 Å as the radius for H). Taking 2.12 Å as the radius of the H_3 molecule (as justified in the H_3 + Ar scattering analysis) and the effective propane radius we just calculated, we obtain a scattering cross section of 29 Å^2 for H_3 against propane at 65 torr stagnation pressure. Again, this compares well with the measured value of 25 Å^2. These values are listed in Table III.

The reason for the similar cross sections for H_3-Ar and H_3-propane becomes obvious by comparing the 'true' sizes of the two scattering molecules. For solid Ar the average radius (half the distance between closest atomic centers) is 1.6 Å[66]. For propane, by adding together the appropriate bond distances[67] (taking into account the geometry of propane), we get a spherical radius of $\sim$ 2.5 Å. The change in size in going from argon to propane is small compared to the radius of the H_3 but not of the H, suggesting that the scattering cross section of H_3 from those two molecules should be comparable in magnitude but the cross section of H should be significantly smaller, as observed.

3.2 Surface Ionization

Figure 11 shows plots of ionization efficency against filament temperature for different stagnation pressures using a tungsten filament. From this figure we see that at 80 torr stagnation pressure the onset of m/e = 3 ions occurs at approximately 1100°C and has a maximum value of approximately 10^{-6} at about 2000°C. It is interesting to analyze why such low ionization efficiencies were observed, since in the case of Rb atoms of similar ionization potential, efficiencies of 100% are observed for ionization by a tungsten filament[68]. However, as the H_3 in our beam is an electronically excited species, one should expect that the most likely process would be for the H_3 to de-excite electronically to the repulsive ground state when colliding with the metal surface, resulting in the production of neutral H_2 and H. This is consistent with our observation that surface ionization to H_3^+ is a very weak channel in the interaction of H_3 with a metal surface. Nevertheless, this production of H_3^+ ions

is the first reported observation of the surface ionization of a metastable molecule, the 2p $^2A_2''$ state of H_3. As a result, surface ionization could prove to be in the future a unique and highly selective detector of molecules which are in excited metastable electronic states.

As described previously, varying the stagnation pressure should allow us to probe the effect of higher translational energies on the surface ionization. Indeed, upon decreasing that pressure from 80 to 75 torr (Figure 11b), the onset of the m/e = 3 species drops from 1100°C to 500°C and the position of the corresponding inflection point decreases from 1800°C to 1200°C. Further lowering the stagnation pressure to 70 torr decreases the onset to 150°C and the position of the inflection point to 800°C. At all stagnation pressures the maximum ionization efficency observed is always approximately 10^{-6}. There are at least two factors which are capable of influencing the ionization efficiency versus filament temperature curves. First, as the translational energy increases, the temperature needed to produce significant surface ionization decreases. Second, as the filament temperature increases the amount of adsorbed material on it increases. This effect tends to shield the metal from the incident beam. Our onset and inflection point temperature results indicate a strong correlation with stagnation pressure and therefore with translational energy. However, the ionization efficiency at the inflection point temperature appears to be approximately independent of translational energy.

The ratio of the number of ions (n_+) to atoms (n_a) evaporating from a surface with which they are in equilibrium is given by the Saha-Langmuir equation[69-71]

$$\frac{n_+}{n_a} = \left(\frac{1-r_+}{1-r_a}\right)\frac{\omega_+}{\omega_a}\exp\left[\frac{e(\Phi-I)}{kT}\right] \qquad (9)$$

where r_a and r_+ are the reflection coefficients for atoms and ions, respectively; ω_+/ω_a is the ratio of the statistical weight of the ionic state and the atomic state involved; I is the ionization potential of the atoms; Φ is the thermionic work function of the surface; and e the electronic charge. A plot of the natural logarithm of the ionization efficiency vs. the inverse of the temperature of the filament should result in a straight line whose slope is proportional to the difference between the work function of the

filament and the ionization potential of the surface-ionized species. These types of plots have proved useful in determining work functions of surfaces by measuring the surface ionization of an atomic species having a known ionization potential[72].

Using this technique and the known tungsten work function (4.58 eV), one should be able to evaluate the ionization potential of H_3. The data of Figure 11 were replotted in this manner and are shown in Figure 12, with the resulting effective ionization potentials obtained from eq (9) given in Table IV. We first observe that the ionization potential increases slightly with increasing stagnation pressure. At low stagnation pressures the high translational energy of the H_3 may lower the effective ionization potential since some of that translational energy may become available for surface ionization. If this is the case, the more accurate ionization potential would be the one obtained at a higher stagnation pressure, which is 5.4 eV.

An inspection of the energy level diagram for H_3 in Figure 4 shows that this ionization potential is some 1.7 eV too large to be originating from the 2p $^2A_2''$ state, whose ionization potential is about 3.67eV[47]. However, it agrees reasonably well with the estimated ionization potential of 5.6 eV from the 2p $^2E'$ repulsive ground state obtained by adding to the 3.67 eV figure the splitting of 1.90 eV between the $^2A_2''$ and ground 2p $^2E'$ levels estimated theoretically, assuming that the latter can still be described as a Rydberg state[28]. We have already stated that the most likely process to occur when H_3 interacts with a metal surface is for it to de-excite electronically, probably to the ground repulsive state, which would result in the production of neutral H_2 and H. However, since the time scale for electron transfer ($\sim 10^{-14}$ s) is faster than for dissociation, ($\sim 10^{-12}$ s) it is possible that some of the molecules in this repulsive 2p $^2E'$ ground state could surface ionize to form H_3^+ before dissociation into neutral H_2 and H. Our measurements indicate that surface ionization to H_3^+ is indeed a weak channel, which is consistent with this interpretation. It would appear then that the majority of the 2p $^2A_2''$ H_3 deexcites to the 2p $^2E'$ repulsive state and a small fraction of those quickly surface ionize to form H_3^+. If this is indeed the case, this is the first measurement of the ionization potential of a repulsive state by surface

ionization

Due to the unexpected value of the ionization potential we repeated the measurements using a filament with a different work function in order to verify the consistency of the measurements. A platinum filament ($\Phi = 5.36$ eV) was used and the results are shown in Figure 13. An immediate difference which is observed between the tungsten and platinum filament results is their behavior with respect to the stagnation pressure of the beam. For platinum, no surface ionization was observed at 80 torr. At 75 torr (Figure 13a) a small amount of H_3^+ is observed. At 65 torr (Figure 13b) the H_3^+ ionization efficiency is about 10^{-6} at the inflection point temperature, which is also typical of the tungsten results. However, the ionization efficiency characteristic temperatures appear to be insensitive to stagnation pressure with an onset of about 300°C and an inflection at about 1100°C (figures 13 b and c). One explanation for this contrast in behavior between the platinum and tungsten filaments is that there is some species adsorbed on the latter which is not adsorbed on the platinum filament, resulting in a surface ionization efficiency process which is more sensitive to the translational energy of the H_3 in the tungsten case.

Figure 14 shows the Saha-Langmuir plots of the platinum surface ionization data. Table V displays the ionization potentials obtained from this data. Disregarding the result for 75 torr (because the signal was very weak and the errors large) the platinum results support the conclusion that the surface ionization to form H_3^+ occurs from from the repulsive ground state of H_3.

It should be mentioned that in this series of surface ionization experiments we were never able to detect H_2^+ formation. This is as expected since H_2 , having an IP of 15.6 eV, should not surface ionize on tungsten, whose work function is 4.58 eV. It was very surprising to observe that at high tungsten filament temperatures the production of H^+ was observed, as shown in Figure 11. At all stagnation presures the onset temperature of the $m/e = 1$ ions is always about 400°C greater than that of the $m/e = 3$ ions and the inflection point for $m/e = 1$ is always about 200°C greater than that for $m/e = 3$. For the platinum filament (Figure 13) the production

of H^+ is somewhat greater than the production of H_3^+ with the onset and inflection temperatures being about the same for both. One explanation for this behavior is that the beam contains metastable hydrogen atoms which (due to high translation energy) do not decay by the time they exit the 1 kV/cm electric field (which serves to sweep ions out of the beam), and are surface ionized at the filament. Since the IP for H $(n = 2)$ is about 3.4 eV an excited hydrogen atom would be expected to surface-ionize readily. However, this explanation must be discarded since the Saha-Langmuir plots (Tables IV and V) show the ionization potential for H^+ formation to be on the average 5.3 eV. However, this ionization potential compares well with the average ionization potential of 5.5 eV for H_3^+ which is calculated from the 65 torr and 60 torr results of Table V (leaving out the 75 torr results because of the low signals) and the 80 torr results of Table IV (which, as pointed out above, minimizes the effect of translational energy) This suggests that the H^+ production is due to the presence of H_3 in the beam. One possible explanation is that these H^+ ions are due to the dissociation of the H_3 molecule (not unlike dissociation of alkali halides on hot filaments[73,74]). An interaction which might explain the production of H^+ from H_3 is

$$H_3 \left(2p^2 A_2''\right) + M \rightarrow H_2 + H \left(n = 2\right) + M. \tag{10}$$
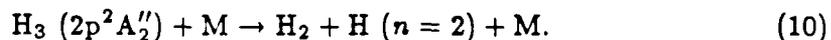
Although this process is endoergic by about 5.0 eV (Figure 4), that energy could be supplied by the translational energy of the H_3. Then in a second step the electronically excited H atom formed on the filament could ionize and desorb. However, if this is the correct mechanism, one would expect it to exhibit an ionization potential of 3.33 eV and not the observed 5.3 eV. The only other explanation for the generation of H^+ is that in the surface ionization of H_3 to H_3^+ some of the H_3^+ which is now adsorbed on the surface dissociates to form H^+ and H_2 before it has a chance to desorb as H_3^+. This would then give H^+ having the same effective ionization potential as H_3^+ since they both originate from the same precursor, H_3. However, the dissociation of H_3^+ to H^+ and H_2 is endoergic by some 4.3 eV. The strength of the bond between H and a Pt surface is about 3.5 eV[75], making the process $H_3^+ + 2Pt \rightarrow H^+ + 2\,Pt{-}H$

endoergic by 1.6 eV which could be suplied by the beam translational energy.

3.3 Photoionization

Figures 15 and 16 shows the preliminary resluts for this experiments. Curve (a) for the top panel of Figure 15 shows the electron impact spectrum for a stagnation pressure of 100 torr with the lamp off. As expected, the signal is virtually all due to H, but it is very weak due to the reduced temperature of the plasma characteristic of this stagnation pressure. Curve (b) of the same panel shows the photoionization mass spectrum (with the electron beam in the mass spectrometer ionizer turned off), correected for a small amount of background (i.e., lamp off) signal. As can be see, no photoionization is detected.

The bottom panel of Figure 15 shows the effect of having the stagnation pressure reduced to 95 torr. Curve (a) now shows the presence of some H_3, through the intensities of all species are still small due to the plasma temperature which is still relatively low. The photoionization mass spectrum displayed in curve (b) now shows a distinct peak at $m/e = 3$, whose intensity is about 0.38 times that of the electron impact mass spectrum (a). Lowering the stagnation pressure further to 90 torr (top panel of figure 16) results in stronger electron impact peak intensies as expected, due to the concomitant increase in the plasma temperature. The photoionization peak at $m/e = 3$ also increases, and the ratio of its intensity to that of the electron impact peak increases slightly to 0.42. Finally, decreasing the stagnation presure to 80 torr (bottom panel of figure 16) further increases the electron impact and photoionization peak intensities, the ratio of the $m/e = 3$ peaks now being about 0.5. The small increase in this ratio with decreasing stagnation pressure may be due to the faci that as the velocity of the H_3 species increases, the loss of the H_3^+ photoion, between the photoionization region and the mass spectrometer ionizer region (which are about 20 cm from one another), decreases. We interpret these results as indicating that we aree indeed photoionizing metastable H_3 and the the H_3^+ photocurrent is approximately proportional to the neutral metastable H_3 intensity.

This is the first direct observation of photoionization of metastable H_3.

As expected, no photoionization of H is seen at stagnation pressures of 100, 95 or 90 torr. However, at 80 torr stagnation pressure a small photoionization peak at $m/e = 1$ is seen, having an intensity which is 6% of that of the corresponding electron impact peak. At first one might think that it is due to the presence of metastable H atoms in the beam. This interpretation would be consistent with its appearance at the higher plasma temperature. However, this cannot be the case since any metastable hydrogen atoms should have been quenched by the electric field in front of the photoionization chamber. As has been shown previously[76,77] a field of 1000 V/cm lowers the lifetime of the 2s metastable state to about 5×10^{-9} s. For 8 eV hydrogen atoms traveling through the plates, which are about 1 cm long, they will remain in the field about 2.6×10^{-7} s. This corresponds to approximately fifty lifetimes of the 2s state; thus any metastable atoms should have relaxed by the time they have left the field. The presence of the small $m/e = 1$ photoionization mass peak cannot therefore be explained by invoking the photoionization of metastable hydrogen atoms and must remain unexplained for the time being.

4. Summary and Conclusions

We have investigated the scattering of a beam of neutral metastable 2p $^2A_2''$ H_3 molecules at translational energies in the 0.1 to 10 eV range by Ar and propane, as well as their surface ionization and photoionization. The total scattering cross section of H_3 by Ar was shown to be about ten times larger than the corresponding H-Ar cross section, in keeping with the large size of the metastable H_3 molecule. The use of the larger propane molecule in place of Ar as a scattering partner results in a large increase in the total cross section for hydrogen atoms but not for H_3 in agreement with that interpretation. These results suggest that due to its large size and high internal and translational energies, this H_3 metastable molecule may be expected to exhibit unusual properties, especially in the area of reaction dynamics.

We were able to observe surface ionization of H_3 to H_3^+ on both tungsten and platinum filaments. By measuring the production of H_3^+ as a function of filament temperature we determined an effective ionization potential of H_3 and concluded that upon interaction with the metal surface the metastable 2p $^2A_2''$ state first decays to the 2p $^2E'$ state, which can then surface ionize to produce H_3^+. This process is consistent with the small number of H_3^+ ions which are formed, since the greater fraction of the H_3 which decays on the filament surface to the 2p $^2E'$ state dissociates to form H and H_2.

We also observe the formation of H^+ by surface ionization but are unable to completely explain this observation. Further experiments are necessary to elucidate the mechanism of this process. By velocity selecting the H_3 beam one should be able to observe the effect of translational energy on surface ionization efficiency and gain insight into the mechanism which generates H^+.

Lastly, we observe the production of H_3^+ when the beam is irradiated with the light from a high pressure mercury lamp. This is the first direct observation of photoionization of metastable H_3.

Appendix A: Possible Alternative Origins of Detected H_3

Because of our interpretation of the $m/e = 3$ mass spectral peak as due to an H_3 metastable, it is necessary that any other mechanisms which could account for that peak be ruled out. As a result, a number of potential candidates have been considered.

A.1. Ion-Molecule Reactions

One possible explanation for the observation of a $m/e = 3$ signal could be a reaction which produces H_3^+ ions in the mass spectrometer ionizer by a mechanism other than electron impact ionization of neutral H_3. Since in this region a large number of ions as well as electronically excited species are produced, it is not unreasonable to consider that they might react with neutral molecules in the beam to form H_3^+ which would then be extracted and detected by the mass spectrometer. Ion-neutral reactions tend to have large cross sections (~ 100 Å^2)[58b] and therefore could contribute to the observed signal.

The most likely ion-molecule reaction which may occur in the ionizer and produce H_3^+ ions is

$$H_2^+ + H_2 \rightarrow H_3^+ + H. \qquad (A.1)$$
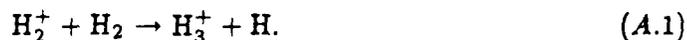
Rate constants for this reaction have been experimentally[78,79] measured as well as calculated[80] as a function of energy for thermal energies and lie in the range $(6 \text{ to } 20) \times 10^{-10}$ cm^3 s^{-1}. From these results, thermal cross section can be obtained which can be extrapolated to higher energies since they are known to be inversely proportional to the relative velocity of the reagents[80,81]. At a laboratory H_2 translational energy of 8 eV this cross section is estimated to be 6.6 Å^2. Using this value we conclude that only 0.004% of the observed H_3^+ mass peak intensity could be due to process (A.1). Even if a significant fraction of the H_2 molecules have an energy as low as 1 eV (which is very unlikely in view of the high temperature of the arc discharge), this figure would be about 0.01 %, which is still very small. As a result,

it can be concluded that this process contributes negligibly to the observed signal.

Since an electron current can trap positive ions in the ionizing region of the mass spectrometer such a trapping could amplify the likelyhood of process (A.1). However, the ratio of the $m/e = 3$ to $m/e = 1$ peak intensities did not vary with electron current over the range 30 to 130 μA. Thus ion-molecule reactions may be ruled out as the cause of our observed $m/e = 3$ signal. As an independent confirmation of this conclusion, we doubled the background pressure of the mass spectrometer detector by introducing D_2 into it. No increase in the size of the AC peaks at $m/e = 4$ or 5 was detected, with the electron bombardment ionizer on, when the arc discharge H/H_3 beam, modulated at 150 Hz by a chopper, was sent into the detector. This indicates that no DH_2^+ or D_2H^+ is formed by reaction of H_2^+ ions resulting from electron bombardment of beam molecules, with background D_2.

A.2. Three-body recombination processes

Recombination process of the type

$$H^+ + H_2 + M \rightarrow H_3^+ + M \qquad (A.2)$$

$$H + H_2^+ + M \rightarrow H_3^+ + M \qquad (A.3)$$

which are possible at sufficiently high pressures, can be ruled out. The pressure in the mass spectrometer ionizer region is of the order of 10^{-5} torr, resulting in a number density of 3.5×10^{12} molecules cm^{-3}. It is difficult to calculate the number of triple collisions that occur in a gas, but a fairly good estimate should be obtained by equating the ratio of triple collisions Z_{123} to binary ones Z_{12} to the ratio of the molecular diameter d to the mean free path[82]. Under our conditions $d \sim 10^{-8}$ cm and $\lambda \sim 760$ cm, Z_{123}/Z_{12} results in a ration of the order of 10^{-11}. This crude calculation shows that at the pressures at which our mass spectrometer detector is operated 3-body processes are highly unlikely.

A.3. Excited atom-molecule reactions

Since electronically excited H atoms can be formed in the mass spectrometer ionizer by electron bombardment of H atoms [83], the reaction of these species with

H_2 is another candidate for production of H_3^+:

$$H^\bullet + H_2 \rightarrow H_3^+ + e^-. \tag{A.4}$$

For this process to account for 10% of our observed H_3^+ signal it should have a cross section of about 1200 $\mathring{A}^2$, which is unrealistically high. Furthermore, the lack of the increase of the $m/e = 5$ peak when D_2 was introduced in the mass spectrometer (as described in the discussion of process (A.1)) confirms that (A.4) is does not contribute significantly to the observed H_3^+ signal.

Appendix B: Life-time of High-Lying Rydberg States

We examine here the possibility that the observed metastable H_3 is due to excited electronic states other than the 2p $^2A_2''$ state. In recent years there has been an increase in the number of studies of atoms[84-87] in which the valence electron is excited to a state of high n (the principle quantum number). In these Rydberg states the electron is very weakly bound. Simple Bohr theory indicates that for $n = 25$ the mean radius is approximately 500 Å and the ionization energy of the excited electron is only 20 meV. In thermal collisions such atoms can ionize or change their state. However, in a collisionless environment they are relatively long-lived. Quantum mechanical treatments[87,88] for excited H atoms show that for $n = 25$ the radiative lifetime can be anywhere from 3 to 500 μsec depending on the value of the orbital angular momentum quantum number l. These long lifetimes are a consequence of poor overlap between the wave functions of the excited state and the ground or lower excited states.

Due to these long lifetimes the possibility exists that the H_3 we have observed is not in the 2p $^2A_2''$ state as we proposed but some higher-lying Rydberg state. To rule this out it is necessary to analyze the ability of these higher states to survive field ionization when traversing the ion deflection plates.

When an atom is in a high Rydberg state it may be described to a good approximation as an ionic core with a single electron sufficiently far away from the core to be described by the single particle Hamiltonian[89]

$$H = -\frac{\hbar}{2\mu}\nabla^2 + V(r). \qquad (B.1)$$

In the presence of a constant electric field $\vec{E}$, which is taken to lie along the z axis, a zE term must be added to the right-hand side of this equation. This field not only will perturb the atomic energy levels (Stark effect) but will cause a local potential maximum to appear on the "down-field" side of the atom. Therefore, in the presence of such an electric field there are no true stationary states and the electron will have a finite probability of tunneling through this potential barrier to

the outside. As the field increases the barrier becomes lower and narrower, thereby increasing the probability that the electron will be emitted. The penetrability of this barrier was first calculated by Lanczos[90] and this result has since been extended by many workers[91-97]. If this simple hydrogenic model is assumed to hold for neutral atoms in general, then all Rydberg states with a principal quantum number greater than the critical value

$$n_C \approx 24 \left[E \ (kV/cm) \right]^{-\frac{1}{4}} \qquad (B.2)$$

are field ionized, in a field of intensity E. This has been experimentally verified[97-99], and the hydrogenic theory provides a good model of highly excited Rydberg states in other species such as rare gases and alkali atoms.

Assuming this theory to be valid for the Rydberg states of H_3, the 1 kV/cm field usd in the present experiments can be expected to field-ionize any H_3 with $n \geq 25$ and deflect the ions generated in this manner. We therefore expect that the species which we are detecting are not in highly excited Rydberg states.

With quenching of high Rydberg states accomplished by field ionization we still need to rule out the possibility of lower-lying Rydberg states. To do this it suffices to examine the radiative lifetimes for states with $n \leq 25$. As calculated from equations listed in Bethe and Salpeter[87], as well as experimental data from Stebbings[97] and Allen[100], such states should have radiative lifetimes less then 10 μsec. The Rydberg states of H_3 are expected to display a similar behavior and to have radiatively decayed before reaching the mass spectrometer detector in our apparatus, for states whose downward transitions are not optically forbidden. However, the results in Section 3.1 suggest that some H_3 may nevertheless be in higher Rydberg states than the 2p $^2A_2''$ one.

From this analysis and the discussion in Section 2.1 we can conclude that the metastable we observe is not predominantly a high lying Rydberg one and is most likely to a major extent the 2p $^2A_2''$ state.

Table 1. Total attenuation cross section by Argon target, at a source
stagnation pressure of 57 Torr.

		H	X H_2	H_3
Experiment	$Q/Å^2$	1.7 ± 0.7^a	3.3 ± 0.9^a	17.3 ± 0.8^a
	Q_{X-Ar}/Q_{H-Ar}	1.0	1.9	10
Theoretical Model	$Q/Å^2$	-	3.8	17
	Q_{X-Ar}/Q_{H-Ar}	-	2.2	10

a. Since the pressures were measured with an uncalibrated Schulz-Phelps
gauge, these uncertainties represent reproducilbility errors rather
than the absolute accuracy of the measurements.

Table II. Total attenuation cross section by Argon target, at a source stagnation pressure of 65 Torr.

		X	
		H	H_3
	$Q/Å^2$	2.9 ± 0.5[a]	30 ± 7[a]
Experiment			
	Q_{X-Ar}/Q_{H-Ar}	1.0	10
	$Q/Å^2$	-	20
Theoretical Model			
	Q_{X-Ar}/Q_{H-Ar}	-	7

a. Since the pressures were measured with an uncalibrated Schulz-Phelps gauge, these uncertainties represent reproducibility errors rather then the absolute accuracy of the measurements.

Table III. Total attenuation cross section by propane target, at a source stagnation pressure of 65 Torr.

		X	
		H	H_3
Experiment	$Q/Å^2$	20.9 ± 2.7[a]	25.4 ± 1.6[a]
	$Q_{\lambda-C_3H_8}/Q_{\lambda-Ar}$	7	0.85
Theoretical Model	$Q/Å^2$	-	29
	$Q_{\lambda-C_3H_8}/Q_{H-Ar}$	-	1.4

a. Since the pressures were measured with an uncalibrated Schulz-Phelps gauge, these uncertainties represent reproducibility error rather than the absolute accuracy of the measurements.

Table IV. Effective Surface Ionization Potential for a Tungsten Filament

	Ionization Potential/eV	
Pressure/Torr	H	H_3
70	5.1	4.9
75	5.3	5.1
80	5.2	5.4

Table V. Effective Surface Ionization Potential for a Platinum Filament

	Ionization Potential/eV	
Pressure/Torr	H	H_3
60	5.4	5.6
65	5.3	5.9
75	5.7	5.9

5. References

1. H. Eyring and M. Polanyi, *Z. Phys.Chem*, **B12**, 279 (1931).

2. J. O. Hirschfelder, H. Eyring, and H. Rosen, *J. Chem. Phys.*, **4**, 121 (1936).

3. I. Shavitt, R. M. Stevens, F. L. Minn, and M. Karplus, *J. Chem. Phys*, **48**, 2700 (1968).

4. P. Siegbahn and B. Liu, *J. Chem. Phys.*, **68**, 2466 (1978); D. G. Truhlar and C. J. Horowitz, *J. Chem. Phys.*, **68**, 2466 (1978).

5. D. G. Truhlar and R. E. Wyatt, *Ann. Rev. Phys. Chem.*, **27**, 1 (1976).

6. F. M. Devienne and J. C. Roustan, *C. R. Acad. Sci. Paris*, **263**, B-1389 (1966).

7. F. M. Devienne, *C. R. Acad. Sci. Paris*, **264**, B-1400 (1967); **267**, B-1279 (1968).

8. F. M. Devienne, *Entropie*, **24**, 35 (1968).

9. F. M. Devienne, *C. R. Acad. Sci. Paris*, **268**, B-1303 (1969).

10. F. M. Devienne, *Sixth International Conference on the Physics of Electronic and Atomic Collisions*, MIT Press, Cambridge, p. 789 (1969).

11. J. Gray and R. H. Tomlinson, *Chem. Phys. Lett.*, **4**, 251 (1969).

12. C. F. Barnett and J. A. Ray, *Phys. Rev. A.*, **5**, 2120 (1972).

13. T. Nagasaki, H Doi, K. Wada, K. Higashi, and F. Fukuzawa, *Phys. Lett.*, **38A**, 381 (1972).

14. E. Frenkel, *Z. Naturforsch.*, **25a**, 1265 (1970).

15. F. J. Comes and U. Wenning, *Z. Naturforsch.*, **24a**, 1227 (1969).

16. N. V. Castro de Faria, M. J. Gaillard, J. C. Poizat, and J. Remillieux, *Ann.*

Israël Phys. Soc., **4**, 134 (1981).

17. M. J. Gaillard, A. G. de Pinho, J. C. Poizat, J. Remillieux, and R. Saoudi, *Phys. Rev. A*, **28**, 1267 (1983).

18. M. Vogler and B. Meierjohann, *J. Chem. Phys*, **69**, 2450 (1978).

19. M. Vogler, *Phys. Rev. A*, **19**, 1 (1979).

20. C. Cisneros, I. Alvarez, R. Garcia G., C. F. Barnett, J. A. Ray, and A. Russek, *Phys. Rev. A*, **19**, 631 (1979).

21. P. M. Curtis, B. W. Williams, and R. F. Porter, *Chem. Phys. Lett.*, **65**, 296 (1979).

22. P. M. Curtis, Ph.D thesis, Cornell University, 1979. Available from University Microfilms, Inc., Ann Arbor, Michigan.

23. G. Herzberg, *J. Chem. Phys*, **70**, 4806 (1979).

24. I. Dabrowski and G. Herzberg, *Can. J. Phys.*, **58**, 1238 (1980).

25. G. Herzberg and J. K. G. Watson, *Can. J. Phys.*, **58**, 1250 (1980).

26. G. Herzberg, H. Lew, J. J. Sloan and J. K. G. Watson, *Can. J. Phys.*, **59**, 428 (1981).

27. G. Herzberg, J. T. Hougen and J. K. G. Watson, *Can. J. Phys.*, **60**, 1261 (1982).

28. H. R. King and K. Morokuma, *J. Chem. Phys*, **71**, 3213 (1979).

29. R. L. Martin, *J. Chem. Phys.*, **71**, 3541 (1979)

30. M. Jungen, *J. Chem. Phys.*, **71**, 3540 (1979).

31. G. Calzaferri, *Chem. Phys. Lett.*, **87**, 443 (1982).

32. J. Tennyson, *Chem. Phys. Lett*, **86**, 181 (1982).

33. S. Raynor and D. R. Herschbach, *J. Phys. Chem.*, **86**, 1214, 3592 (1982).

34. K. Hirao and S. Yamabe, *Chem Phys.*, **80**, 237 (1983).

35. H. R. Mayne, R. A. Poirier, and J. C. Polanyi, *J. Chem. Phys.*, *80*, 4025 (1984).

36. M. Jungen and V. Staemmler, *Chem. Phys. Lett.*, **103**, 191 (1983).

37. C. A. Nicolaides, G. Theodorakopoulos and I. D. Petsalakis, *J. Chem. Phys.*, **80**, 1705 (1984).

38. K. Kaufmann, M. Jungen, and V. Staemmler, *Chem. Phys.*, **79**, 111 (1983).

39. J. K. G. Watson, *Phys. Rev. A*, **22**, 2279 (1980).

40. G. I. Gellene, D. A. Cleary, R. F. Porter, *J. Chem. Phys.*, **77**, 3471 (1982).

41. G. I. Gellene and R. F. Porter, *J. Chem. Phys.*, **79**, 5975 (1983).

42. S.-J. Jeon, A. B. Raskit, G. I. Gellene, and R. F. Proter, *J. Chem. Phys.*, **82**, 4916 (1985).

43. C. G. Freeman, T. I. Quickenden, and D. F. Sangster, *J. of Photochemistry*, **24**, 403 (1984).

44. H. Figger, H. Moller, W. Schrepp,and H. Walther, *Chem. Phys. Lett.*, **90**, 90 (1982).

45. W. Schrepp, H. Figger, and H. Walther, *Lasers & Applications*, 77 (July 1984).

46. H. Figger, M. N. Dixit, R. Maier, W. Schrepp, and H. Walther, *Phys. Rev. Letters*, **52**, 906 (1984).

47. H. Helm, *Phys. Rev. Lett.*, **56**, 42 (1986).

48. J. F. Garvey and A. Kuppermann, *Chem. Phys. Lett.*, **107**, 491 (1984).

49. H. L. Knuth, *Appl. Mech. Rev.*, **17**, 751 (1964).

END

12-86

DTIC